

**University of Calgary**

**PRISM: University of Calgary's Digital Repository**

---

Graduate Studies

Legacy Theses

---

2011

# Beamforming of Broadband Bandpass Signals using Multidimensional FIR Filters

Gunaratne, Thushara Kanchana

---

Gunaratne, T. K. (2011). Beamforming of Broadband Bandpass Signals using Multidimensional FIR Filters (Unpublished doctoral thesis). University of Calgary, Calgary, AB.

doi:10.11575/PRISM/23074

<http://hdl.handle.net/1880/48863>

doctoral thesis

---

University of Calgary graduate students retain copyright ownership and moral rights for their thesis. You may use this material in any way that is permitted by the Copyright Act or through licensing that has been assigned to the document. For uses that are not allowable under copyright legislation or licensing, you are required to seek permission.

*Downloaded from PRISM: <https://prism.ucalgary.ca>*

UNIVERSITY OF CALGARY

Beamforming of Broadband Bandpass Signals using Multidimensional FIR Filters

by

Thushara Kanchana Gunaratne

A THESIS

SUBMITTED TO THE FACULTY OF GRADUATE STUDIES  
IN PARTIAL FULFILLMENT OF THE REQUIREMENTS FOR THE  
DEGREE OF DOCTOR OF PHILOSOPHY

DEPARTMENT OF ELECTRICAL AND COMPUTER ENGINEERING

CALGARY, ALBERTA

September, 2011

© Thushara Kanchana Gunaratne 2011



UNIVERSITY OF  
CALGARY

The author of this thesis has granted the University of Calgary a non-exclusive license to reproduce and distribute copies of this thesis to users of the University of Calgary Archives.

Copyright remains with the author.

Theses and dissertations available in the University of Calgary Institutional Repository are solely for the purpose of private study and research. They may not be copied or reproduced, except as permitted by copyright laws, without written authority of the copyright owner. Any commercial use or re-publication is strictly prohibited.

The original Partial Copyright License attesting to these terms and signed by the author of this thesis may be found in the original print version of the thesis, held by the University of Calgary Archives.

Please contact the University of Calgary Archives for further information:

E-mail: [uarc@ucalgary.ca](mailto:uarc@ucalgary.ca)

Telephone: (403) 220-7271

Website: <http://archives.ucalgary.ca>

# Abstract

Two novel beamforming methods based on multidimensional finite impulse response (FIR) filters are proposed for broadband-bandpassed signals received by uniformly distributed 1D/2D antenna arrays. For cognitive radio (CR) systems, an adaptive complex-coefficient 2D FIR asymmetric-trapezoidal filter-based beamforming method is proposed. The proposed beamforming 2D filter is designed such that its 2D trapezoidal passband closely encloses the region of support (ROS) of the spectral components of the desired subscriber signal and such that its 2D stopband encloses the ROSs of the spectra of the co-channel interfering subscriber signals and a dominant component of receiver noise. The proposed novel closed-form design method achieves near-optimal passband and stopband characteristics while instantaneously adapting to variations of the operation frequency band and bandwidth and of the time varying directions of arrival of the desired signal.

A novel method based on a complex-coefficient 3D FIR frustum filter has been proposed as a pre-coherent dedispersion broadband beamformer for pulsar timing/profile studies in order to significantly suppress off-dish signals such as radio frequency interference (RFI), ground thermal noise and receiver noise in focal plane array (FPA) signals. Accurate simulations of electromagnetic fields using the Focal Field Synthesizer (FFS) program imply that the ROSs of the spectra of space-time sampled FPA signals corresponding to dish-reflected celestial signals of interest (SOI) of the FPA is a 3D frustum-shaped volume  $F$ . Also, it is shown that the ROSs of the 3D power spectral density of RFI and ground thermal noise occupies the volume just outside the surface of the frustum  $F$ . The frustum-shaped passband of the proposed 3D filter is designed to encompass most of the volume of frustum  $F$ , ensuring that most of the energy of the SOIs is transmitted to the output, where as the 3D stopband attenuates the most of the spectral components of off-dish FPA signals. Simulation results show that the proposed 3D FIR frustum



filter-based beamformer achieves the lowest mean-square-error (MSE) compared to the conventional 2D spatial-only beamformer and 3D conjugate-field-matching beamformer.

## Acknowledgements

I owe my deepest gratitude to my supervisor, Dr. Leonard T. Bruton for all the ideas, advice, suggestions, guidance and encouragement given to me throughout the course of my doctoral research. Also, I admire his thirst for new knowledge, search for real-world applications for MDSP, his patience, kindness and generosity. Further, I'm lucky to have him as my supervisor as we share the interests of current world politics, history of the human civilization and the game of cricket, in which he imparts knowledge on me.

I thank my teachers and mentors at the University of Calgary including Dr. Jim Haslett, Dr. John Nielsen, Dr. Grant McGibney, Dr. Bob Davies and Dr. Abu Sesay, Dr. Graham Jullien, Dr. Vassil Dimitrov, Dr. Mike Potter, Dr. Brent Maundy, Dr. Laleh Behjat, Dr. Geoffrey Messier and Dr. Leonid Belostotski for all their support. I extend my appreciation to Professor Indra Dayawansa, Professor Dileeka Dias, Professor Nandana Rajatheva, Dr. Ajith Pasqual and Mr. Srimal Punchihewa at the University of Moratuwa, Sri Lanka for their guidance during my undergraduate studies. I also thank Dr. Bruce Veidt, Mr. Gary Hovey and Dr. Rick Smegal for their support.

I am especially grateful to my former senior colleague, Dr. Arjuna Madanayake for his thought-provoking conjectures. I thank my friends and colleagues, Ganesh Doluweera, Achala Nanayakkara, Sidhantha Weerakoon, Chamika Huththotuwa, Mehdi Ataei, Chamira Edussooriya, Udara Waraketiya and others for their wonderful friendship.

I thank my parents, parents-in-law and my (late) grandmother for their support and love. Last, but not least, my heartfelt thanks to my dearest wife Dulini for her patience, unconditional love, understanding, kindnesses and encouragement given to me.

This thesis was made possible by a scholarship from Micronet Canada, a grant from the Natural Sciences and Engineering Research Council (NSERC) of Canada and a Graduate Teaching/Research Assistantship at the University of Calgary.

*Dedicated to my dearest wife, parents, parents-in-law and (late) grandparents.*

# Table of Contents

Abstract . . . . .	ii
Acknowledgements . . . . .	iv
Dedication . . . . .	v
Table of Contents . . . . .	vi
List of Tables . . . . .	x
List of Figures . . . . .	xi
List of Symbols and Abbreviations . . . . .	xv
1 Beamforming of Broadband-Bandpassed Signals using Multidimensional FIR Filters . . . . .	1
1.1 Introduction . . . . .	1
1.2 Contributions of this Thesis . . . . .	5
1.3 Outline of this Thesis . . . . .	11
2 Propagating Broadband-Bandpassed Signals and the Corresponding Spectra	15
2.1 Introduction . . . . .	15
2.2 Propagation of EM Waves through the 3D Space . . . . .	17
2.2.1 Polarization of Propagating EM Waves: A Review . . . . .	18
2.3 Analysis of Spatio-Temporal Planes Waves and the Corresponding Spectra	21
2.3.1 4D BB-BP ST PWs and the Corresponding Spectra . . . . .	23
2.3.2 4D BB-BP ST PWs Observed on a Plane and the Corresponding Spectra . . . . .	26
2.3.3 4D BB-BP ST PWs Observed on a Line in 3D Space and the Corresponding Spectra . . . . .	32
2.4 EM BB-BP Signals Received by Arrays of Antennas . . . . .	36
2.4.1 Antenna Response Pattern . . . . .	38
2.4.2 The Relationship Between Antenna Response Pattern and Active Element Pattern . . . . .	38
2.4.3 An Example for an Active Element Pattern . . . . .	40
2.4.4 Signals Induced at an Elemental Antenna in Response to Propa- gating EM signals and the Corresponding Spectra . . . . .	41
2.5 3D Spectra of the Signals Observed at the Terminals of 2D Planar Array	47
2.6 2D Spectra of the Signals Observed at the Terminals of 1D Linear Array	52
2.7 Distortions of the Spectra of Finite Aperture Arrays . . . . .	59
2.7.1 Distortions in the Spectra of Antenna Responses of Finite Extent 2D-UDPAs . . . . .	60
2.7.2 Distortions in the Spectra of Antenna Responses of Finite Extent 1D-UDAAs . . . . .	63
2.8 Temporal Sampling of Signals Observed at the Terminals of Antenna Array	66
2.8.1 The Direct Nyquist Sampling Scheme . . . . .	67
2.8.2 The Complex-Quadrature Sampling Scheme . . . . .	69
2.8.3 The Real-IF Sampling Scheme . . . . .	70
2.9 Summary . . . . .	71

3	The Focal Region Signals of a Paraboloidal Reflector and the Corresponding Spectra . . . . .	73
3.1	Introduction . . . . .	73
3.2	The ROS of the Spectrum of the EM Field Observed on the Focal Region	75
3.2.1	Predicting the ROS of the Spectrum of the Focal Region Electric-Field . . . . .	76
3.2.2	Verification of the ROS of the Focal Plane EM Field by Numerical Simulation . . . . .	81
3.3	The Focal Field Synthesizer (FFS) . . . . .	88
3.3.1	The System Specifications and Notations used in the FFS . . . .	92
3.3.2	Focal Region EM Field Synthesis; A Review . . . . .	93
3.3.3	Numerical Integration of the Radiation Integral using a GPU . . .	97
3.3.4	Examples of the FFS Field Calculations and Comparisons between the FFS and the GRASP9 . . . . .	103
3.4	Summary . . . . .	114
4	Broadband-Bandpass Beamforming for Cognitive Radio (CR) Systems using Complex-Coefficient 2D FIR Trapezoidal Filters . . . . .	117
4.1	Introduction . . . . .	117
4.2	Cognitive Radio Systems; An Introduction . . . . .	122
4.3	Signal Processing at the SDR Front-End of the CR System . . . . .	126
4.3.1	A Review on Signals Observed at the Outputs of Elementals Antennas	126
4.3.2	Some Definitions of Parameters . . . . .	128
4.3.3	On the Complex-Quadrature Temporal-Sampling of LNA Outputs	129
4.3.4	Spectra of the Complex-Quadrature Sampled BB-BP ST PWs . .	131
4.4	Previously Proposed Broadband-Bandpass Beamforming Methods: A Review . . . . .	138
4.4.1	Digital Interpolation Beamforming for Broadband-Bandpassed Signals . . . . .	139
4.4.2	Frequency Domain Beamforming Methods for Broadband-Bandpassed Signals . . . . .	143
4.4.3	The Sekiguchi Method; A Beamforming 2D Complex-Coefficient FIR Filter Design Method using a Combined Spectral-Transformation and Window Method . . . . .	144
4.5	The Beamforming Complex-Coefficient 2D FIR Trapezoidal Filter . . . .	147
4.5.1	The Ideal Transfer Function for the Beamforming of Complex-Quadrature Sampled 1D-UDAA Signals . . . . .	148
4.5.2	Approximation of the Complex-Coefficient 2D FIR Filter with a Trapezoidal-Shaped Passband . . . . .	151
4.5.3	A Design Example of a Complex-Coefficient 2D FIR Trapezoidal Filter . . . . .	154
4.5.4	The Output Sequence of the Beamformer; An Analysis . . . . .	158
4.5.5	Implementation of the Beamforming Complex-Coefficient 2D FIR Trapezoidal Filters . . . . .	162
4.6	A Brief Comparison of Broadband-Bandpass Beamforming Methods . . .	164

4.7	An Example of the Application of the Proposed Adaptive Beamformer in the Receiving Arm of a CR System . . . . .	168
4.8	Summary . . . . .	173
5	Broadband Beamforming of Focal Plane Array Signals using Real-Time Spatio-Temporal 3D FIR Frustum Digital Filters . . . . .	176
5.1	Introduction . . . . .	176
5.2	The SKA Science Projects and Engineering Specifications; A Review . .	181
5.2.1	The SKA Science Projects . . . . .	181
5.2.2	The SKA Engineering Specifications . . . . .	185
5.3	FPA Signals and the Corresponding Spectra . . . . .	191
5.3.1	Elemental-Antenna Response to Dish-Reflected Celestial SOIs and the Corresponding Spectra . . . . .	195
5.3.2	Elemental-Antenna Response to the Off-Dish RFI Signals and the Corresponding Spectra . . . . .	200
5.3.3	Elemental-Antenna Response to the Ground Thermal Noise and the Corresponding Spectral-Density . . . . .	202
5.3.4	Signals at the Outputs of LNAs . . . . .	203
5.3.5	The Pre-Beamforming Signal Processing and Temporal Sampling of the LNA Outputs of FPAs . . . . .	206
5.4	Broadband Beamforming of Space-Time Sampled FPA Sequences using a Single 3D FIR Frustum Filter . . . . .	208
5.4.1	A Criteria for Determining the Ideal Transfer Function for the Beamforming 3D Filter . . . . .	208
5.4.2	A Combined Frequency-Sampling and 3D Window-Based Design Method for Beamforming 3D FIR Frustum Filters . . . . .	212
5.4.3	A Numerical Design Example of the Beamforming 3D FIR Frustum Filter . . . . .	216
5.4.4	The 1D Output Sequence of the Beamforming 3D FIR Frustum Filter . . . . .	218
5.4.5	Implementation of the Beamforming Complex-Coefficient 3D FIR Frustum Filters . . . . .	221
5.5	A Comparative Study of the Broadband Signal Recovery in the Presence of Off-Dish RFI, Ground Thermal Noise and Receiver Noise . . . . .	223
5.6	Summary . . . . .	227
6	Finite-Word-Length Effects of Beamforming MD FIR Filters and an Example of FPGA Implementation of a Beamforming 2D FIR Filter . . . .	230
6.1	Introduction . . . . .	230
6.2	Finite-Word-Length Effects of MD FIR Filters implemented with an Array of 1D FIR Filters; A Review . . . . .	233
6.2.1	Input-Data Quantization . . . . .	234
6.2.2	Multiplier-Product Quantization . . . . .	235
6.2.3	Filter Coefficient Quantization . . . . .	237
6.2.4	1D Filter Structures and Their Significance in the Product Quantization Noise and the Effects of Coefficient Quantization at the Output . . . . .	237

6.2.5	Adder-Overflow Errors . . . . .	239
6.3	The Distortions of the Transfer Functions of Beamforming MD FIR Filters due to Coefficient Quantization . . . . .	240
6.3.1	Examples of Transfer Function Distortions in Beamforming Polyphase 2D FIR Double-Trapezoidal Filters . . . . .	240
6.3.2	Examples of Transfer Function Distortions in Beamforming Complex- Coefficient 2D FIR Asymmetric-Trapezoidal Filters . . . . .	247
6.3.3	Examples of Transfer Function Distortions in Beamforming Complex- Coefficient 3D FIR Frustum Filters . . . . .	250
6.4	The Degradation of the SNDR of Beamforming MD FIR Filters due to Finite-Word-Length Digital Arithmetics . . . . .	253
6.4.1	A Theoretical Model for the SNDR at the Output of the Beamformer	254
6.4.2	Estimation of the SNDR at the Output of a Particular Beamformer	257
6.4.3	Comparison Between Estimated SNDRs and Calculated SNDRs with the Monte Carlo Simulations . . . . .	260
6.5	An Example of FPGA Implementation of Beamforming Polyphase 2D FIR Double-Trapezoidal Filter . . . . .	265
6.5.1	The FPGA Implementation of the Polyphase 1D FIR Building Block	265
6.5.2	Throughput and Computational Complexity of the Polyphase 1D FIR Building Block . . . . .	266
6.5.3	Estimated FPGA Resources for Filter Designs for Different $W_m$ .	266
6.5.4	Design Partitioning and a Multiple-FPGA Physical Implementation	266
6.5.5	Some Results of the On-chip Stepped Hardware Co-Simulations of the Modeled FPGA Implementation . . . . .	268
6.6	Summary . . . . .	269
7	Conclusions and Future Work . . . . .	271
7.1	Conclusions . . . . .	271
7.2	Future Work . . . . .	273
	Bibliography . . . . .	276
A	The Evaluation of MD Continuous-Domain Fourier Transform (CDFT) of a MD BB-BP ST PW . . . . .	302
A.1	The Evaluation of 4D CDFT of a 4D BB-BP ST PW . . . . .	302
A.2	The Evaluation of 3D CDFT of a 3D BB-BP ST PW . . . . .	305
A.3	The Evaluation of 2D CDFT of a 2D BB-BP ST PW . . . . .	307

## List of Tables

3.1	MRD values for focal electric-fields corresponding to different size grids on the reflector surface . . . . .	110
3.2	Calculated MRD and NMSD values between FFS and GRASP9 generated focal field patterns . . . . .	113
3.3	Calculated MRD between GRASP9 and MATLAB-DPFAO and between MATLAB-DPFAO and FFS . . . . .	114
5.1	The System Specifications for the SKA - Phase-I . . . . .	187
5.2	The Design Parameters of the Beamforming 3D FIR Frustum Filter. . . .	217
5.3	The MSE between the Recovered Pulses and the Ideal Dispersed Pulse for the Different Beamforming Methods. . . . .	227
6.1	Estimated $\gamma$ , $a$ , $\kappa$ and $M$ of $\bar{H}_{\text{TR-D}[W_c]}(z_x, z_t)$ for $W_c = 8, 10, 12, 14, 16$ and 18 and $\bar{H}_{\text{TR-D}[FP]}(z_x, z_t)$ . . . . .	258
6.2	Estimated FPGA Resources For the Beamforming Polyphase 2D FIR Double-Trapezoidal Filters with Different Word-Lengths Combinations. .	267



## List of Figures

1.1	A scenario in which a Cognitive Radio (CR) system is receiving signals from different subscribers. . . . .	3
1.2	A scenario in which an antenna in a radio telescope receives EM waves from different celestial sources. . . . .	4
2.1	A RF signal propagation between a point-source and a 1D uniformly distributed receiver-antenna-array. . . . .	18
2.2	An ideal 4D ST PW $pw_{4C}(x, y, z, t)$ in 3D space. . . . .	22
2.3	A ST PW $pw_{4C}(x, y, z, t)$ observed on the infinite extent plane $z = 0$ in 3D space. . . . .	27
2.4	The ROS of the spectrum $PW_{3CP}(f_x, f_y, f_{ct})$ of a 3D BB-BP ST PW is on the line of intersection between the two planes $d_x f_{ct} - f_x = 0$ and $d_y f_{ct} - f_y = 0$ . . . . .	30
2.5	The 3D double right-circular frustum volume is the range of ROSs of the spectra of all possible 4D BB-BP ST PWs observed on the plane $z = 0$ in 3D space. . . . .	31
2.6	A 4D ST PW is observed on the infinitely-long a continuous line on the $x$ axis. . . . .	33
2.7	The ROS of the spectrum $PW_{2CP}(f_x, f_{ct})$ and the double-fan area corresponding to the range of ROSs of the spectra of all possible 2D ST PWs observed on the line along $x$ -axis in 3D space. . . . .	35
2.8	A propagating EM ST PW is received by a 2D-UDPA consisted of broadband elemental antennas. . . . .	37
2.9	An example of an active element pattern; PHAD. . . . .	42
2.10	The plan-view of the range of ROSs of $A_{3MP}(e^{j\omega_x}, e^{j\omega_y}, f_{ct})$ . . . . .	52
2.11	1D-UDAA in receiving EM 4D BB-BP ST PW <b>empw</b> $_{4CP}(x, y, z, t)$ . . . . .	53
2.12	A typical active element pattern for wideband elemental antennas in pseudo-infinite 1D-UDAA . . . . .	54
2.13	ROSs of 2D-MDFT of $A_{2MP}(e^{j\omega_x}, f_{ct})$ and the regions subjected to spatial aliasing . . . . .	59
2.14	The normalized magnitude of the spectrum of the 2D rectangular window for $N_x = 16$ and $N_y = 8$ . . . . .	62
2.15	The normalized magnitude of the spectrum of the 2D Hanning window for $N_x = 16$ and $N_y = 8$ . . . . .	63
2.16	The normalized magnitude spectra of 1D rectangular window and 1D Hamming window for $N_x = 32$ . . . . .	66
2.17	The ROSs of the spectra of SOIs after being subjected to direct-Nyquist sampling . . . . .	68
2.18	Complex-quadrature temporal-demodulation applied to down-shift the spectral contents of the positive frequency bands of 3D/2D signal sequences to the baseband . . . . .	70

2.19	Real-IF temporal-demodulation applied to down-shift the positive frequency band and up-shift the negative frequency band of 3D/2D signal sequences to the IF-bands . . . . .	71
3.1	EM waves propagating from the surface of the paraboloidal reflector towards the focal plane . . . . .	77
3.2	Projections of the 4D ROS of the spectra of focal electric fields . . . . .	80
3.3	The equivalent iso-surface of the positive frequencies of the normalized spectrum of the $\hat{\mathbf{u}}_y$ -component of the focal electric-field . . . . .	83
3.4	Contour-plots of the spectra of the focal electric-field components at 1 GHz; simulated Vs predicted . . . . .	84
3.5	Contour-plots of the spectra of focal electric-field corresponding to different focal lengths; simulated Vs predicted . . . . .	85
3.6	Contour-plots of the spectra of focal electric-field corresponding to EM ST PWs arriving from different directions; simulated Vs predicted . . . . .	87
3.7	The considered arrangement of the reflector for the FFS and the used notations for specifying system parameters . . . . .	89
3.8	The architecture of a typical GPU . . . . .	91
3.9	Geometry of the reflector, incident PW and the reflected wave expressed using vector notation . . . . .	94
3.10	The pseudo-code for the FFS . . . . .	101
3.11	Field patterns from the FFS; $\hat{\mathbf{u}}_y$ - (left), $\hat{\mathbf{u}}_y$ - (center) and $\hat{\mathbf{u}}_z$ - (right) electric-field components . . . . .	105
3.12	Comparison between the focal field components evaluated using the FFS and GRASP9 . . . . .	107
4.1	A typical architecture of the receiving arm of a CR system . . . . .	118
4.2	An ideal architecture for the SDR front-end of a CR system . . . . .	125
4.3	A typical scenario where subscriber modules transmitting toward the 1D-UDAA of a CR system . . . . .	128
4.4	The ROS of the spectrum of a complex-quadrature sampled EM 4D BB-BP ST PW received by a 1D-UDAA . . . . .	136
4.5	A typical architecture of a interpolation delay-and-sum beamformer . . . . .	141
4.6	The ROSs of the spectrum $D(e^{j\omega_x}, e^{j\omega_t})$ inside of <b>PNS</b> and the ideal beam-shaped transfer function $IH_{\text{BEAM}}(e^{j\omega_x}, e^{j\omega_t})$ . . . . .	149
4.7	The ROS of the ideal spectrum $D(e^{j\omega_x}, e^{j\omega_t})$ inside of <b>PNS</b> and the ideal trapezoid-shaped transfer function $IH_{\text{TRAP}}(e^{j\omega_x}, e^{j\omega_t})$ . . . . .	151
4.8	The properties of the complex-coefficient 2D FIR trapezoidal filter of order $(40 \times 32)$ . . . . .	155
4.9	The average stopband gains of the series of beamforming 2D FIR trapezoidal filters for the temporal frequency band FB01 . . . . .	157
4.10	The compensated passband ripple of the series of beamforming 2D FIR trapezoidal filters for the temporal frequency band FB01 . . . . .	158
4.11	The average stopband gains of the series of beamforming 2D FIR trapezoidal filters for the temporal frequency band FB02 . . . . .	159

4.12	The compensated passband ripple of the series of beamforming 2D FIR trapezoidal filters for the temporal frequency band FB02 . . . . .	160
4.13	A proposed architecture for the beamforming complex-coefficient 2D FIR trapezoidal filter . . . . .	162
4.14	Outputs of different beamforming methods processing an identical test sequence . . . . .	166
4.15	A typical scenario for a CR system that is receiving RF signals transmitted by subscriber modules . . . . .	169
4.16	The averaged SIR (in dB) of the recovered signal transmitted from the commuter train and the apartment building as time progresses. . . . .	172
5.1	A paraboloidal reflector and a focal plane array (FPA) along with a broad-band single channel receiver . . . . .	177
5.2	The beamforming complex-valued 3D FIR frustum filter . . . . .	179
5.3	The relative sensitivities of main radio telescopes in the world . . . . .	182
5.4	The proposed antenna systems and their arrangement in the SKA . . . . .	189
5.5	The proposed system architecture for the aperture synthesis imaging with multi-beamforming FPA signals for the SKA . . . . .	190
5.6	A typical scenario of focal EM field reception by the FPA . . . . .	192
5.7	A typical instantaneous amplitude distribution of the focal electric field component in response to dish reflected ST PW . . . . .	196
5.8	A group of contour-lines that corresponds to the bases of the main lobes generated on the FPA in response to incident EM waves emanating from group of point-sources around the axis of the paraboloid . . . . .	198
5.9	The ROSs of the spectra of the SOIs, RFIs and ground-thermal noise contained in the space-time sampled FPA signals . . . . .	209
5.10	The iso-surface corresponding to -3 dB level of the magnitude response of the designed 3D FIR frustum filter. . . . .	218
5.11	The magnitude and phase properties of the designed 3D FIR frustum filter along the cross-sectional planes . . . . .	219
5.12	The proposed architecture for the beamforming complex-coefficient 3D FIR frustum filter . . . . .	222
5.13	The original pulse, the dispersed pulse after propagating through ISM and its spectrogram . . . . .	224
5.14	The comparison between among different beamforming methods in recovering broadband pulsar signals . . . . .	225
6.1	The input-data quantization-noise model and the multiplier-product quantization-noise model. . . . .	236
6.2	The common structures for 1D FIR filters. . . . .	238
6.3	The ROS of the ideal passband of the 2D double-trapezoidal filter and the ROSs of the spectra of the space-time sampled ST PWs. . . . .	241
6.4	The proposed hardware architecture of a polyphase 1D FIR building block. . . . .	244

6.5	The cross-sectional magnitude responses evaluated on $\omega_t = 0.5\pi$ across the passbands of floating-point and fixed-point represented beamforming polyphase 2D FIR double-trapezoidal-filters . . . . .	246
6.6	The normalized effective passband gains evaluated along the axes of the 2D double-trapezoidal passbands of floating-point and fixed-point represented beamforming polyphase 2D FIR double-trapezoidal-filters . . . . .	247
6.7	The expanded cross-sectional magnitude responses evaluated on $\omega_t = 0.5\pi$ across the passbands of floating-point and fixed-point represented beamforming polyphase 2D FIR double-trapezoidal-filters . . . . .	248
6.8	The cross-sectional magnitude responses evaluated on $\omega_t = 0$ across the passbands of floating-point and fixed-point represented beamforming 2D FIR asymmetric-trapezoidal filters . . . . .	250
6.9	The normalized effective passband gains evaluated along the axes of the 2D double-trapezoidal passbands of floating-point and fixed-point represented beamforming 2D FIR asymmetric-trapezoidal filters . . . . .	251
6.10	The cross-sectional magnitude responses evaluated on the line of intersection between the plane $\omega_t = -0.5\pi$ and $\omega_y =$ across the passbands of floating-point and fixed-point represented beamforming 3D FIR frustum filters . . . . .	253
6.11	The noise-model for the polyphase 1D FIR building block. . . . .	256
6.12	The parameter “ $a$ ” evaluated for different beamformers corresponding to fixed-point and floating point represented filters. . . . .	260
6.13	The parameter “ $\gamma$ ” evaluated for different beamformers corresponding to fixed-point and floating point represented filters. . . . .	261
6.14	The parameter “ $\kappa$ ” evaluated for different beamformers corresponding to fixed-point and floating point represented filters. . . . .	262
6.15	The parameter “ $M$ ” evaluated for different beamformers corresponding to fixed-point and floating point represented filters. . . . .	263
6.16	The comparison between the estimated SNDRs and the calculated SNDRs for $W_m = 10, 11, 12, 13, 14, 15$ and 16-bits and floating point represented filters for different input SIR levels. . . . .	264
6.17	The demodulated signal without beamforming, output of the beamformer with ideal floating point implementation and the output of the beamformer with proposed fixed point implementation. . . . .	269

## List of Symbols and Abbreviations

1D	One-Dimensional
2D	Two-Dimensional
<b>2PNR</b>	Two-Dimensional Principle Nyquist Region
3D	Three-Dimensional
<b>3PNR</b>	Three-Dimensional Principle Nyquist Region
4D	Four-Dimensional
ADC	Analog-to-Digital Converter
BB-BP	Temporally-Broadband-Bandpassed signal
<i>BW</i>	Temporal Bandwidth
CDFT	Continuous-Domain Fourier Transform
CFM	Conjugate-Field-Matching
CR	Cognitive Radio
DDFT	Discrete-Domain Fourier Transform
DFAO	Double-Precision Floating-Point Arithmetic Operation
DOA	Direction Of Arrival
DOP	Direction Of Propagation
DSM	Double Sideband Modulated
$\hat{\mathbf{E}}^{\text{pol}}$	The polarization unit vector of a propagating EM ST PW
EM	Electromagnetic
FFS	Focal Field Synthesizer Program (Formerly known as UC-FPFC)
FIR	Finite Impulse Response
FoV	Field of View
FPA	Focal Plane Array
FPGA	Field Programmable Gate Array

GP-GPU	General Purpose - Graphics Processing Unit Processing
GPU	Graphics Processing Unit
GSPS	Giga-Samples Per-Second
ICDFT	Inverse Continuous-Domain Fourier Transform
IDDFT	Inverse Discrete-Domain Fourier Transform
IMDFT	Inverse Mixed-Domain Fourier Transform
IIR	Infinite Impulse Response
ISM	Interstellar Medium
$K$	The bandwidth spread factor of a temporally-bandpassed signal
$K_I$	The instantaneous bandwidth spread factor of a temporally-bandpassed signal associated with a CR system
$L_I$	The instantaneous system utilization factor of a CR system
MD	Multidimensional
MDFT	Mixed-Domain Fourier Transform
MDSP	Multidimensional Signal Processing
MSE	Mean Square Error
MSPS	Mega-Samples Per-Second
NB-BP	Temporally-Narrowband-Bandpassed signal
PHAD	Phased Array Demonstrator
PNC	Principle Nyquist Cube
PNS	Principle Nyquist Square
PSD	Power Spectral Density
PW	Plane Wave
ROS	Region Of Support
RF	Radio Frequency
RFI	Radio Frequency Interference

SDR	Software Defined Radio
SFAO	Single-Precision Floating-Point Arithmetic Operation
SIMD	Single Instruction Multiple Data
SIQNR	Signal to Input-Quantization-Noise Ratio
SIR	Signal to Interference Ratio
SKA	Square Kilometre Array
SNDR	Signal to Noise and Distortion Ratio
SNR	Signal to Noise Ratio
SOI	Signal of Interest
ST	Spatio-Temporal
UC-FPFC	University of Calgary - Focal Plane Field Calculator (New name FFS)
UDAA	Uniformly Distributed Antenna Array
UDPA	Uniformly Distributed Planar Array
UDSA	Uniformly Distributed Sensor Array
$c$	Constant wave propagation speed in the medium
$\mathbf{d}$	$[d_x \ d_y \ d_z]^T$ , The unit vector specifying the DOA of a 4D ST PW in 3D space $(x, y, z) \in \mathbb{R}^3$
$f_C$	The center frequency of a temporally-bandpassed signal
$f_{\max}$	The maximum frequency of a temporally-bandpassed signal
$f_{\min}$	The minimum frequency of a temporally-bandpassed signal
$n_t$	Temporal sample index
$n_x$	Spatial sample index along the direction of $x$ -axis
$n_y$	Spatial sample index along the direction of $y$ -axis
$\Delta_x$ or $\Delta_{xy}$	Inter element distance between adjacent elemental antennas in an uniformly distributed array

$\alpha_{\max}$	The half-cone angle of a cone in 3D frequency-space
$\phi$	The azimuth angle specifying the DOA in 3D space or the orientation of a straight-line in 3D frequency-space
$\theta$	The inclination angle specifying the DOA in 3D space or the orientation of a straight-line in 3D frequency-space



# Chapter 1

## Beamforming of Broadband-Bandpassed Signals using Multidimensional FIR Filters

### 1.1 Introduction

Humans are immersed in a sea of signals, some of those are generated naturally and some of those are results of human activity. Also, some of these signals, such as propagating electromagnetic (EM) waves in the band 400-790 THz (i.e. the optical band) and propagating acoustic waves in the band 20-20,000 Hz (i.e. the audible band), can be directly perceived by human sensors. However, most of the signals such as EM radiation in radio, microwave, infrared, ultraviolet, X-ray and Gamma-ray bands in the environment are not perceived by human sensors. In order to extract the information carried by the directly unperceivable signals and to enhance the desired signals in the optical-band and audible-band, engineers have designed and implemented special *sensor & processing systems*. Many of these sensor & processing systems employ “*sensor arrays*” for receiving the propagating signals of interest. The received signals are processed in order to enhance the desired signals while suppressing interfering signals and contaminating noise. Examples of such sensor-array & processing systems, also known as array processing systems, include mobile and wireless communication systems [1][2], radio telescopes [3][4], fixed- and synthetic- aperture radar systems [5][6], active and passive sonar systems [7][8], ultrasound and tomographic biomedical imaging systems [9][10] and audio processing systems [11][12].

Among modern wireless communication systems, *Cognitive Radio* (CR) systems are of increasing interest for the optimal management of the available radio spectrum, trans-

mitting power, and wireless modulation techniques for the facilitation of a broad range of communication and entertainment applications [13][14][15][16]. Software defined radio (SDR) architectures have been proposed for CR systems that exploit dynamic allocation of the radio spectrum and modulation techniques [13][15][17], where real-time dynamic spectral utilization is achieved by maintaining several sub-bands for different subscriber/application clusters and is managed by sensing the spectral occupancy at regular time intervals [13][15]. Consider the scenario shown in Figure 1.1, where the 1D uniformly distributed antenna array (UDAA) of a CR system [14] is used to receive groups of co-channel RF signals transmitted by the mobile communication devices on a high-speed commuter train and by both mobile wireless and fixed wireless devices in an apartment building. In general, the group of signals transmitted by the mobile devices on the commuter train may be of low power compared to the group of signals transmitted from the wireless devices in the building. Hence, *receiving beams*, as shown in Figure 1.1, must be formed in order to faithfully recover the two groups of co-channel signals transmitted by the devices in the train and the devices in the building, respectively. Further, the beam pointed at the train must be regularly adapted in time in order to track the train as it moves along the tracks.

Also consider a different scenario shown in Figure 1.2, where the EM waves emanated from the celestial sources  $S_1$  and  $S_2$  are first reflected by the paraboloidal reflector and subsequently received by the 2D focal plane array (FPA) [18]. FPA's are under investigation as a means of increasing the field of view (FoV) for the observations in the lower mid-band (i.e. 0.5 - 1.7 GHz) of the Square Kilometre Array (SKA) [19]. The SKA will be the world's largest aperture synthesis radio telescope upon its completion in 2020 at an estimated cost of \$2 billion [19]. It has been proposed that approximately 1,000 - 2,000 paraboloidal reflector antennas in the SKA will be equipped with FPA's where, each FPA may contain 100-200 or more wideband elemental antennas, such as Vivaldi elements

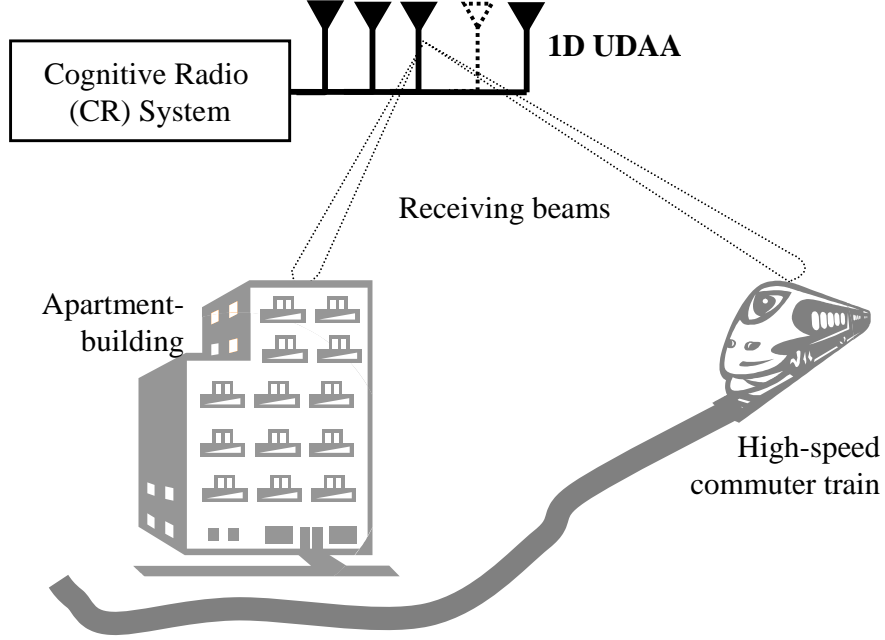


Figure 1.1: A scenario in which a CR system is receiving RF signals from many wireless mobile devices on a high-speed commuter train and many fixed and mobile communication devices in an apartment building.

[20]. In addition to the induced signals in response to the desired celestial signals of interests from  $S_1$  and  $S_2$ , the FPA outputs may also contain man-made radio frequency interference (RFI) [21], contaminating noise induced due to the thermal radiation in the vicinity of the receiver antenna and the noise induced in low noise amplifiers (LNAs). Given that the celestial EM waves are extremely weak, *highly sensitive receiving beams*, as shown in Figure 1.2, must be formed in order to extract the information carried by the celestial EM radiation from  $S_1$  and  $S_2$  in the presence of receiver noise, ground thermal radiation noise and RFI.

In both of above mentioned scenarios, the objective of forming receiving beams is to selectively enhance the desired signals and to suppress the co-channel interfering signals and the receiver noise, and is based on the *directions of arrival* (DOAs)<sup>1</sup> of the propagating signals received by an array of sensors [22]. Beamforming has been extensively used

<sup>1</sup>The direction of arrival is the direction unit vector of the source of a signal with respect to the receiver array. The exact definition of the DOA is given in chapter 2 of this thesis.

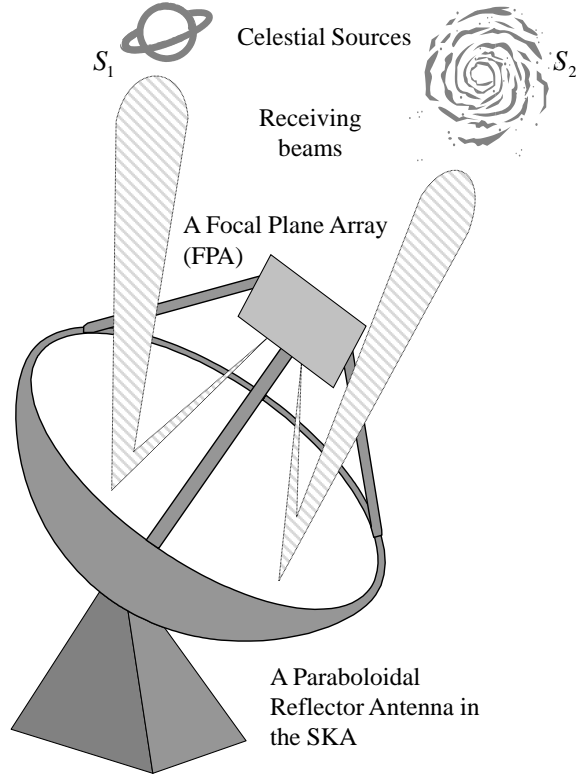


Figure 1.2: A scenario in which an antenna in a radio telescope receives EM waves from different celestial sources.

in various array processing applications including wireless and mobile communications [23][24], radio astronomy [25], radar [5], active and passive sonar [26] and directional audio systems [27][28]. However, in most legacy applications in wireless communications, radio astronomy and radar the signals of interests are temporally-narrowband-bandpassed<sup>2</sup> signals and thus, employ temporally-narrowband-bandpass beamforming methods. In such applications, the optimal performance of the employed narrowband-bandpass beamforming methods is designed to achieve for a single frequency<sup>3</sup>. However, in some of the modern array processing applications, specially for radio astronomy [18][29][30], radar [31][32] and wireless communications [23][33][34] the signals of interest are temporally-broadband-bandpassed signals. Therefore, such array processing applications require ad-

<sup>2</sup>The criterion for characterizing the temporally-narrowband-bandpassed (NB-BP) signal and the temporally-broadband-bandpassed (BB-BP) signal is given in chapter 2.

<sup>3</sup>In general at the carrier frequency of the narrowband-bandpassed signal.

vanced broadband-bandpass beamforming methods that yield optimal (or near-optimal) performance for the entire bandwidth of the signals of interest.

In general, beamforming systems can be implemented either in continuous-time with analog circuits or in discrete-time with digital circuits in hardware or software [35][36][37]. However, for some modern array processing applications, digital signal processing (DSP) methods are often preferred over the continuous-time analog alternatives because, DSP systems allow faster implementation, easy reconfiguration, higher accuracy, reliability and robustness, wider availability and lower cost of implementation and maintenance [38][39][40].

## 1.2 Contributions of this Thesis

This thesis presents the investigation of *optimal<sup>4</sup> or near optimal design methods and efficient-implementation techniques for discrete-time multidimensional (MD) finite impulse response (FIR) filters used in broadband-bandpass beamforming methods for real-time applications*. Here, two broadband-bandpass beamforming applications are considered in detail. The first is adaptive beamforming of broadband-bandpassed signals received by a 1D-UDAA of a CR system having a SDR front-end. Here, an adaptive complex-coefficient 2D FIR trapezoidal filter-based beamformer is proposed. The second application is beamforming of broadband-bandpassed FPA signals in paraboloidal receiver antennas for mitigating RFI and thermal radiation noise for broadband detection processes. Here, a complex-coefficient 3D FIR frustum filter-based beamformer is proposed. For both applications, *the concepts and theories of multidimensional signal processing (MDSP) [41][42][43][44][45][46] have been exploited in analyzing the properties, in both space-time and spectral domains, of propagating “spatio-temporal” (ST)<sup>5</sup> signals*

---

<sup>4</sup>In the sense of a given metric (i.e. mean-square-error, min-max, etc.)

<sup>5</sup>Here, the term “spatio” implies one or more spatial dimension where the term “temporal” implies time or a dimension proportional to time.

*that are received by an array of sensors placed in the propagation medium and in designing the ideal transfer functions for the MD FIR filters that lead to optimal receiving beamforming systems.* The proposed beamforming methods are expected to yield lower distortions of the desired signals, higher attenuation of the interfering signals and system noise with easy adaptability and lower computational complexity that improve the performance and reduce the cost of these real-time applications.

### **Broadband-Bandpass Beamforming for Cognitive Radio (CR) Systems using Complex-Coefficient 2D FIR Trapezoidal Filters**

A novel adaptive discrete-domain method based on a complex-coefficient 2D FIR trapezoidal filter is proposed for the beamforming of temporally-broadband-bandpassed signals in the context of a CR system. For CR systems, in almost all the cases, the receiver is in the far-field region of the transmitter. Hence, the simplified ST plane-wave (PW) propagation model [43] may be assumed for the received signals by 1D-UDAAs in CR systems. The proposed beamforming method is in two stages. In the first stage, pre-beamforming processing is applied at the front-end of the CR system where the outputs of 1D-UDAA elements are RF pre-filtered, amplified by LNAs, complex-temporal-demodulated and synchronously-sampled using software tunable analog and digital systems, thereby yielding a complex-valued 2D ST sample sequence. Then, in the second stage of the method, the above 2D ST sampled sequence is processed using a complex-coefficient 2D FIR filter having an asymmetric trapezoidal-shaped passband. This filter is designed so that its 2D passband closely encloses the region of support (ROS) of the spectral components of the desired ST PW and so that its 2D stopband encloses the ROSs of the spectra of the interfering ST PWs and a dominant component of the receiver noise. The proposed novel closed-form design method for the realization of this beamforming 2D filter achieves near-optimal passband and stopband characteristics while simultaneously and instantaneously adapting to variations of the operation-frequency band, of the bandwidth and

of the time varying DOAs of the signal. Further, the 2D filter is implemented using a parallel-connected array of complex-coefficient 1D FIR filter structures, whereby each of the 1D FIR filter structure can be implemented using low-cost DSP hardware having high throughputs. The simulation results show that the required filter coefficients may be evaluated within few hundredths of a second using the proposed method implemented on a general purpose computer. Here it is shown that, compared with previously reported methods, the proposed method achieves the best overall trade-off with respect to distortion of the desired passband signal, stopband attenuation of interfering signals and instantaneous adaptations of the operating frequency band, of the bandwidth and of the time varying DOAs. Parts of this work have been published in [47][48][49].

### **Broadband-Bandpass Beamforming of FPA Signals using 3D FIR Frustum Filters**

A novel discrete-domain method is proposed as a *pre-coherent-dedispersion* broadband beamformer for pulsar timing [30] and pulsar profile studies [50] in order to significantly suppress RFI signals, the dominant thermal noise from the ground and the receiver noise in FPA signals using a single real-time ST 3D FIR frustum filter. The proposed method depends on the following facts about the 3D regions of support (ROSs) of the spectra of space-time sampled FPA signals, which are explained in detail in chapters 3 and 5. First, that the ROS of the spectrum of far-field dish-reflected direct down-converted and *complex-quadrature-sampled* [51] FPA signals of interest is a 3D frustum<sup>6</sup>-shaped volume, within the principal Nyquist cube in 3D frequency space, where the dimensions of the corresponding 3D cone are primarily determined by the diameter ( $D$ ) and the focal length ( $F$ ) of the paraboloidal reflector. Also, it is shown that the ROS of the 3D power spectral density (PSD) of the dominant component of the spatio-temporally-sampled thermal noise from the ground occupies the volume that is just outside the

---

<sup>6</sup>i.e. a section of a cone dissected by two parallel planes that are perpendicular to the axis of the cone.

surface of the frustum that corresponds to the ROS of the celestial signals of interest. With similar analysis, it is also shown that the ROS of the 3D spectra of off-dish RFI signals also occupies the same region. However for simplicity, it is assumed that the ROS of the 3D PSD of the spatio-temporally-sampled broadband receiver noise occupies most of the volume of the Nyquist cube in 3D frequency space and is almost spectrally-flat over the lower-mid band temporal frequency range. In practice, the exact shape of the 3D receiver noise power-spectral density function within the Nyquist cube is determined by the 1D temporal-power-spectral-density function of the receiver noise and the non-ideal inter-elemental-antenna mutual-coupling of the noise across the FPA [52][53][54]. Based on the above properties of the ROSs of 3D spectra, the frustum-shaped passband of the proposed 3D filter is designed to encompass most of the 3D ROS of the focal-plane spectra of far-field dish-reflected celestial signals, implying that the resulting 3D stopband attenuates the major component of off-dish FPA signals. Simulation results show that the proposed 3D FIR frustum filter-based beamformer achieves the lowest MSE compared to the conventional 2D spatial only beamformer and 3D conjugate-field-matching (CFM) beamformer. Parts of this work have been published in [55][56].

### **The Focal Region Signals of a Paraboloidal Reflector and the Corresponding Spectra**

The electric fields observed around the focal region in response to the reflected far-field EM waves from an ideal circular-aperture prime-focus paraboloidal reflector and the corresponding spectra are analyzed using the “*Huygens’ Principle Approximation*” [57](pp. 34). Following Huygens’ Principle Approximation, it is shown that under certain assumptions, the focal region EM field can be modeled as a superposition of EM BB-BP ST PWs that are emanating from point sources on the surface of the reflector, which are induced in response to the incident far-field EM waves. Hence, the ROS the spectrum of focal electric-field is given by the composite ROSs of the spectra of EM BB-BP ST



PWs. In case of a circular-aperture prime-focus paraboloidal reflector, it is shown that ideally the ROS of the spectrum of the electric-field observed on the focal-plane is a 3D frustum. Also, it is shown that the shape of the frustum is determined by the diameter ( $D$ ) and the focal-length ( $F$ ) of the particular circular-aperture prime-focus paraboloidal reflector. This has been verified by using the **Focal Field Synthesizer (FFS)**, a computer program that is developed in order to evaluate focal region electric fields of a paraboloid by exploiting the extensive parallel processing capabilities of the graphics processing unit (GPU) of a computer for fast evaluation of computationally intensive numerical integrations. The accuracy of the electric fields calculated with the FFS is verified by the field patterns generated with GRASP9 [58], which is a EM field evaluation software that is widely used in analyzing reflector antennas. In this thesis, the details of the ROSs of the spectrum of the focal region electric fields are exploited in designing the beamforming 3D FIR frustum filters in chapter 5. The focal fields generated using the FFS is exploited in generating the ideal phase response of the 3D beamforming transfer function in chapter 5. Also in chapter 5, the test sequences for focal region electric fields, which are used in determining the performance of the broadband beamformers, are also synthesized by using the field patterns generated by the FFS. Parts of this work have been included in a manuscript for the subsequent publication in the Springer Journal on Electrical Engineering. The manuscript is currently under review.

### **Finite-Word-Length Effects of Beamforming MD FIR Filter Implementations**

The required throughputs for the proposed real-time beamforming applications for CR systems and FPAs are in the range of several hundred mega-samples per second (MSPS) to several Giga-samples per-second (GSPS). Such high throughputs necessitate the beamforming MD FIR filters proposed in this thesis including those proposed in [47][55][56][59], to be implemented using finite-word-length DSP hardware in high speed very large scale integrated (VLSI) circuits [60]. However, finite-word-length DSP implementation

may cause errors and degrade the maximum possible signal-to-noise-and-distortion ratio (SNDR) achievable at the output of the proposed beamforming MD FIR filters of particular order [61]. Hence, the careful assignments of register-lengths (i.e. word-lengths) for input data, filter coefficients of the MD FIR filters and the outputs of digital-multipliers and -adders are required to minimize the degradation of the SNDR and avoid overflow errors [62] in the output while minimizing the hardware complexity of the beamforming MD FIR filters of the particular order. Note that the structure of the MD FIR filters determines the transfer function distortion and the quantization noise contribution at the final output of the beamformer. Here, the proposed beamforming MD FIR filters are implemented with parallel connected array of direct-form or transformed direct-form real-valued 1D FIR filter structures.

With the example of the polyphase 2D FIR double-trapezoidal filter-based beamformer<sup>7</sup>, the degradations of the SNDR at the output of the proposed MD FIR filter-based beamformers implemented with parallel connected arrays of direct-form 1D FIR filters for a given configuration of DSP resources are investigated both theoretically and empirically. First, theoretical estimates of the SNDR at the output of the beamformers are made following the accepted models of quantization noise [61][65][66] for a given DSP configuration in terms of the assigned word-lengths for input-data, filter coefficients products from multipliers and partial-sums from adders. Then, the SNDR at the output of the beamformers is calculated empirically through *Monte Carlo simulations* under the same DSP configurations using the MATLAB<sup>®</sup> Fixed-Point Toolbox. It is observed that the theoretical estimates and simulation resulted agree well. Also, the steps for the implementation of the beamforming polyphase 2D FIR trapezoidal filter in a Xilinx Virtex-4 Sx35 ff668-10 FPGA chip [67] is also summarized in chapter 6. Parts of this work have been published in [68].

---

<sup>7</sup>This beamforming method has been proposed by the candidate in his MSc. thesis [63] and also published in [59][64].

### 1.3 Outline of this Thesis

The remainder of this thesis is arranged as follows. The key concepts and terminology used in this thesis are introduced in chapter 2. In section 2.2, the important properties of propagating EM waves are briefly reviewed. The spectra of 4D BB-BP ST PWs and the corresponding 3D/2D spatio-temporal signals observed on a plane and on a line in the 3D space in response to a propagating EM wave are derived in section 2.3, which refers to Appendix A. The concepts of the antenna response function and the antenna impulse response are introduced in section 2.4. A detailed spectral analysis is given in sections 2.5 and 2.6 for 3D/2D signal sequences observed in 2D-UDPAs and 1D-UDAAs in response to propagating EM BB-BP ST PWs. Also, the criteria for avoiding aliasing in 2D-UDPAs and 1D-UDAAs are stated there. The distortions of the spectra of signal sequences from finite-extent 2D-UDPAs and 1D-UDAAs are analyzed in section 2.7. Finally, three possible temporal sampling schemes are suggested for sampling 3D and 2D signal sequences from 2D-UDPAs and 1D-UDAAs.

The electric fields observed around the focal region in response to the reflected far-field EM waves from an ideal circular-aperture prime-focus paraboloidal reflector and the corresponding spectra are analyzed in chapter 3. The properties of the electric fields on the focal plane and the corresponding spectra are derived in section 3.2. The ROSs of the spectra of the focal electric-fields are deduced in subsection 3.2.1 using the Huygens' Principle Approximation and the concepts that have been introduced in chapter 2. In subsection 3.2.2, the predicted ROSs of the spectra of the focal electric fields are compared with the ROSs of the spectra of simulated focal electric fields, which are evaluated using the FFS. The design of the GPU-accelerated FFS program is explained in section 3.3. The system specifications and the input parameters for the FFS are stated in subsection 3.3.1. Using the fundamental Maxwell's equations and the physical optics (PO) approximation, the radiation integral for the focal region EM field is derived in subsection 3.3.2. In order

to fully exploit the extensive parallel processing capabilities of the GPU, the radiation integral is reorganized as a numerical summation using the Newton-Cotes algorithm in subsection 3.3.3. Examples of the electric-field patterns evaluated using the FFS are given in subsection 3.3.4. Here, the normalized focal electric-field patterns evaluated with the FFS are compared with the electric-field patterns evaluated with GRASP9 for the same set of specifications.

In chapter 4, a novel adaptive discrete-domain method based on a complex-coefficient 2D FIR trapezoidal filter is proposed for the beamforming of temporally-broadband-bandpassed signals in the context of a CR system. A brief introduction of CR systems is given in section 4.2. In section 4.3, a detailed mathematical analysis is carried out analyzing the signal processing conducted in the SDR front-end of a CR systems. Previously proposed beamforming methods that can be used in enhancing the temporally-broadband-bandpassed signals associated with CR systems are briefly reviewed in section 4.4. The design of the beamforming complex-coefficient 2D FIR filter having an asymmetric trapezoidal shaped passband is explained in detail in section 4.5. A design example of a beamforming 2D FIR trapezoidal filter that satisfies a selected group specifications is given in subsection 4.5.3. In subsection 4.5.4, the 1D output sequence of the beamforming 2D FIR filter is analyzed in detail. The implementation of the beamforming complex-coefficient 2D FIR filter is briefly discussed in subsection 4.5.5. The proposed 2D FIR trapezoidal filter-based beamforming method is compared with similar beamforming methods in section 4.6. In section 4.7, an example of an adaptive beamforming scenario for a receiving arm of a CR system has been simulated.

In chapter 5, a novel discrete-domain method is proposed for the suppression of RFI signals, the dominant thermal noise from the ground and the receiver noise in FPA signals using a single real-time ST 3D FIR frustum filter. In section 5.2, the key science projects and the engineering specifications of the SKA are briefly introduced. A detailed analysis

of the celestial SOIs, the off-dish RFI and noise due to ground thermal radiation observed at the outputs of the FPA elemental antennas and the corresponding spectra are given in subsections 5.3.1, 5.3.2 and 5.3.3, respectively. The various noise sources contributing to the outputs of the array of LNAs and the effects of noise coupling in the FPA receiver are briefly reviewed in subsection 5.3.4. In subsection 5.3.5, the pre-beamforming signal processing architecture of a typical FPA receiver is briefly reviewed. The design of beamforming complex-coefficient 3D FIR frustum filter for processing broadband pulsar signals is explained in detailed in section 5.4. In subsection 5.4.1, the 3D transfer function for the ideal beamformer is derived and in subsection 5.4.2, a combined frequency-sampling and 3D window-based method for the design of beamforming 3D FIR frustum filters is proposed. A design example of a beamforming 3D FIR frustum filter is given in subsection 5.4.3. In section 5.5, the proposed method is compared with the conventional 2D spatial-only beamformer and the 3D conjugate-field-matching (CFM) beamformer based on the means-square-error (MSE) estimate between the ideal dispersed pulse and the outputs of each beamformer.

In chapter 6, the finite-word-length effects of the SNDR of proposed MD FIR filter-based broadband beamforming methods are analyzed. A brief theoretical analysis on the sources of quantization noise and errors due to finite-word-length representation of input-data and the outputs of digital-multipliers and -adders and transfer function distortions due to finite-word-length representation of filter coefficients of MD FIR filters is given in section 6.2. The distortions of the transfer functions due to finite-word-length representation of filter-coefficients of the beamforming polyphase 2D FIR double-trapezoidal filter, the beamforming complex-coefficient 2D FIR asymmetric-trapezoidal filter and the beamforming complex-coefficient 3D FIR frustum filter are studied with examples in subsections 6.3.1, 6.3.2 and 6.3.3, respectively. In subsection 6.4.1, a theoretical model is developed for the estimation of the SNDR at the output of a beamforming MD FIR filters

with the example of the polyphase 2D FIR double-trapezoidal filter-based beamformer implemented with a parallel connected array of direct form 1D FIR filters. Following the proposed theoretical model, the estimates of the SNDRs are evaluated in subsection 6.4.2 for the beamforming polyphase 2D FIR double-trapezoidal filter implemented with different DSP configurations. For the same set of DSP configurations, the average SNDRs of the beamforming polyphase 2D FIR double-trapezoidal filters that are evaluated with Monte Carlo simulations are given in subsection 6.4.3. In section 6.5, an example of the FPGA implementation of the polyphase 2D FIR double-trapezoidal filter-based beamformer with a given DSP configuration is outlined. An estimate of the FPGA resources required for the full implementation of this beamformer for a set of different DSP configurations is given in Table 6.2.

Finally, the concluding remarks of the proposed beamforming MD FIR filters, the focal-field synthesis program, the combined theoretical and empirical estimation method for the SNDR at the outputs of beamforming MD FIR filters and an overview of the future work on the beamforming MD FIR filters are given in chapter 7.

## Chapter 2

# Propagating Broadband-Bandpassed Signals and the Corresponding Spectra

### 2.1 Introduction

A detailed review of the broadband-bandpassed signals and their spectra that correspond to propagating far-field EM signals received by planar and linear arrays is given in this chapter. It has been widely accepted that the propagating signals emanating from a far-field point source can be considered as a 4D *spatio-temporal*<sup>1</sup> (ST) *plane-wave* (PW) over a finite spatial region. This wave propagation model has been assumed in determining the criteria for optimum broadband beamformer design for wireless communications as explained in chapter 4 of the thesis. Also, the same model has been extended in chapter 3 in determining the distribution of spectral components of the focal-field of a paraboloidal reflector in response to far-field celestial signals. Here, emphasis is given to the spectral domain properties of the temporally-broadband-bandpassed (BB-BP) ST signals at various stages of the signal processing architecture prior to the beamforming operation.

This chapter is arranged as follows. The polarization properties of the EM waves propagating through the 3D space in the far-field are briefly studied in section 2.2. In Section 2.3, the important properties of 4D ST PWs, which corresponds to far-field propagating EM waves and the corresponding spectra are analyzed giving prominence to temporally-broadband-bandpassed (BB-BP) ST PWs. Further in this section, ST signals observed on a plane and on a line in the 3D space in response to 4D ST BB-BP PWs

---

<sup>1</sup>A Spatio-Temporal (ST) signal is a multidimensional (MD) signal that is a function of at least one spatial dimension in the three-dimensional (3D) space and one temporal dimension.

and the corresponding spectra are also studied. The reception of EM BB-BP signals using an array of wideband antennas is discussed in detailed in section 2.4. The ideal spectra of signal sequences observed at the output of elemental antennas in 2D uniformly distributed planar arrays (2D-UDPAs) and 1D uniformly distributed antenna arrays (1D-DUAAs) are evaluated in sections 2.5 and 2.6, respectively. In section 2.7, the spectral-spreading and the spectral-leakage distortions of the spectra of finite-extent 3D/2D signal sequences observed at the outputs of elemental antennas of 2D-UDPAs and 1D-DUAAs are discussed. Here, a compensation method that can achieve an acceptable trade-off between spectral-spreading and spectral-leakage is also suggested. Finally, in section 2.8, three possible temporal sampling schemes that can be used in periodic temporal sampling of the 3D/2D signal sequences from 2D-UDPAs and 1D-DUAAs are briefly introduced.

### **The Notation Scheme**

In this chapter, similar notational labels have been used in denoting the continuous-domain ST signals and the corresponding sampled mixed-domain and discrete-domain versions at the various stages of the signal processing architecture. However, in order to avoid any ambiguities, a subscript-based notation scheme is adopted. According to this scheme, an alpha-numeric subscript, which is up to three-characters long, is appended to the label in order to specify the dimension, domain and the spectral-occupancy of the specified ST signal, respectively. The numerical subscripts “4”, “3” and “2”, which appear first in the subscript, denote 4D, 3D and 2D ST signals<sup>2</sup> respectively, where the subscript letters “C”, “M” and “D”, which immediately follow the numerical-subscript, denote continuous-domain, mixed-domain and discrete-domain ST signals, respectively. Further, the subscript letters “B”, “P” and “F” may be added as the third character of the subscript in order to denote temporally-baseband, temporally-bandpassed and temporally-intermediate-frequency (IF) band ST signals, respectively. For example, a 2D

---

<sup>2</sup>Note, for brevity, the subscript “1” is not used to denote 1D temporal signals.



continuous-domain temporally-baseband ST PW is denoted by  $pw_{2CB}(x, t)$ . Also, second order subscripts are used to denote individual ST signals in a group of ST signals. For example,  $pw_{2CB_R}(n_x, n_t)$  is used to denote the desired 2D space-time sampled temporally baseband ST PW in the group  $pw_{2CB_q}(n_x, n_t)$ ;  $q = 1, 2, \dots, R, \dots, Q$ . The corresponding frequency domain spectra of the ST signals or sequences are specified by interchanging lowercase letters in their labels with uppercase letters. For example, the 4D continuous-domain Fourier transform (4D-CDFT) pair of a 4D continuous-domain plane-wave signal is denoted by

$$pw_{4C}(x, y, z, t) \xleftrightarrow{4D\text{-}CDFT} PW_{4C}(f_x, f_y, f_z, f_t).$$

However, this notation scheme may lead to longer labels and therefore, it is relaxed in later chapters if there is little ambiguity regarding the dimension and the domain of referred signals and sequences.

## 2.2 Propagation of EM Waves through the 3D Space

Consider the example shown in Figure 2.1, where a radio-frequency (RF) signal, emanating from the antenna of a modern mobile communication device, propagates towards the one-dimensional (1D) uniformly distributed antenna-array (UDAA) at the front-end of a CR system. Figure 2.1 also shows that the propagating wavefronts of the RF signal take a spherical shape in the *near field* of the transmitting antenna. However, as these spherical wavefronts propagate away from the transmitting antenna toward the *far field*, the wavefronts spread in such a manner that those can be approximated by planar wavefronts over a finite area. In case of EM signals emanating from celestial sources, which are at distances ranging from several millions of kilometers to several hundreds of light-years from the surface of the earth, this planar-wavefront approximation applies even better. Hence, *in the far field, propagating EM waves in 3D space  $(x, y, z) \in \mathbb{R}^3$  can be closely approximated by vector-valued 4D continuous-domain ST PWs over a finite area* [69].

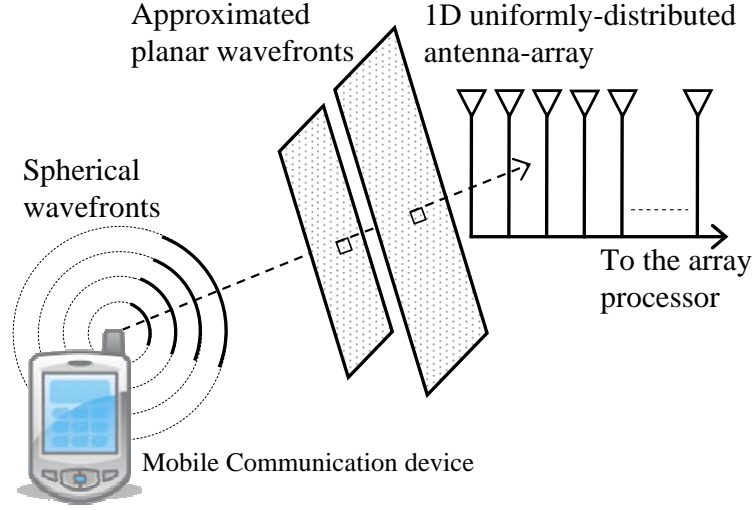


Figure 2.1: A RF signal originating from a modern mobile communication device propagates through the 3D space and is received by a 1D uniformly distributed antenna-array (1D-UDAA) of a CR System.

A detailed analysis on the transmission antennas and EM wave propagation according to the fundamental Maxwell's equations is out of the scope of this thesis. Nevertheless, a brief review of the “polarization” of propagating EM waves is given in the following because it is important in analyzing the antenna arrays for receiving EM waves.

### 2.2.1 Polarization of Propagating EM Waves: A Review

Propagating EM ST PWs are transversal waves<sup>3</sup> that consist of alternately oscillating electric and magnetic fields [70]. Hence, the electric-field component  $\mathbf{epw}_{4C}(x, y, z, t)$ , and the magnetic-field component  $\mathbf{mpw}_{4C}(x, y, z, t)$ , of an ideal continuous-domain vector-valued 4D ST PW  $\mathbf{empw}_{4C}(x, y, z, t)$  are related such that

$$\mathbf{epw}_{4C}(x, y, z, t) = Z (\mathbf{mpw}_{4C}(x, y, z, t) \times \hat{\mathbf{p}}), \quad (2.1)$$

$$\mathbf{mpw}_{4C}(x, y, z, t) = Z^{-1} (\hat{\mathbf{p}} \times \mathbf{epw}_{4C}(x, y, z, t)), \quad (2.2)$$

---

<sup>3</sup>i.e. The direction of wave propagation is perpendicular to both electric and magnetic fields.

where  $Z$  is the impedance of the propagation medium and  $\hat{\mathbf{p}}$  is the unit vector along the direction of propagation (DOP) of the vector-valued 4D ST PW [70](pp. 20). Note that both the electric-field component  $\mathbf{epw}_{4C}(x, y, z, t)$  and the magnetic-field component  $\mathbf{mpw}_{4C}(x, y, z, t)$  individually contain all the temporal information carried by the 4D ST PW  $\mathbf{empw}_{4C}(x, y, z, t)$ . According to [70](pp. 21-23), any EM ST PW  $\mathbf{empw}_{4C}(x, y, z, t)$ , can be decomposed into two EM ST PWs  $\mathbf{empw}_{4C_1}(x, y, z, t)$  and  $\mathbf{empw}_{4C_2}(x, y, z, t)$  such that the corresponding electric-field components are given by

$$\mathbf{epw}_{4C}(x, y, z, t) = \hat{\mathbf{E}}_1^{\text{pol}} pw_{4C_1}(x, y, z, t) + \hat{\mathbf{E}}_2^{\text{pol}} pw_{4C_2}(x, y, z, t), \quad (2.3)$$

where the unit vectors  $\hat{\mathbf{E}}_1^{\text{pol}}$ ,  $\hat{\mathbf{E}}_2^{\text{pol}}$  and  $\hat{\mathbf{p}}$  are orthogonal to each other. That is the vector dot product between any two of the three is zero;  $\hat{\mathbf{E}}_1^{\text{pol}} \bullet \hat{\mathbf{E}}_2^{\text{pol}} = \hat{\mathbf{E}}_1^{\text{pol}} \bullet \hat{\mathbf{p}} = \hat{\mathbf{E}}_2^{\text{pol}} \bullet \hat{\mathbf{p}} = 0$ . Note that  $pw_{4C_1}(x, y, z, t)$  and  $pw_{4C_2}(x, y, z, t)$  are ideal continuous-domain scalar-valued 4D ST PWs. The electric-field of  $\mathbf{empw}_{4C_1}(x, y, z, t)$  is confined to a plane along the vectors  $\hat{\mathbf{p}}$  and  $\hat{\mathbf{E}}_1^{\text{pol}}$  and the electric-field of  $\mathbf{empw}_{4C_2}(x, y, z, t)$  is confined to a plane along the vectors  $\hat{\mathbf{p}}$  and  $\hat{\mathbf{E}}_2^{\text{pol}}$  such that these two planes are orthogonal to each other.

If the scalar-valued 4D ST PWs  $pw_{4C_1}(x, y, z, t)$  and  $pw_{4C_2}(x, y, z, t)$  in (2.3) are uncorrelated then the vector-valued 4D ST PW  $\mathbf{empw}_{4C}(x, y, z, t)$  is a *completely unpolarized* EM ST PW. Such completely unpolarized EM ST PWs are commonly observed among the celestial EM radiation received on the surface of the earth [70](ch. 12). Nevertheless, if  $pw_{4C_1}(x, y, z, t)$  and  $pw_{4C_2}(x, y, z, t)$  are partially correlated then  $\mathbf{empw}_{4C}(x, y, z, t)$  is a *partially polarized* EM ST PW, as observed in EM radiation from the Sun in radio- and microwave- bands [70](ch. 12). However, if  $pw_{4C_1}(x, y, z, t) = \beta pw_{4C_2}(x, y, z, t)$ , where  $\beta$  is a complex-valued constant, then  $\mathbf{empw}_{4C}(x, y, z, t)$  is a *completely polarized or fully polarized* EM ST PW. Completely polarized EM ST PWs are commonly observed among signals transmitted from wireless communication devices and in weather radar [70](ch. 12).

The *type of polarization* of a completely polarized EM ST PW is specified by the

magnitude and phase of the complex constant  $\beta$  that in turn specifies the orientation of the electric field vector on a plane, which is perpendicular to the DOP unit-vector  $\mathbf{p}$  [70]. For the general case of  $\beta \neq 0$ , the electric-field vector of the fully polarized EM ST PW  $\mathbf{empw}_{4C}(x, y, z, t)$  traces a *perfect-ellipse* on the perpendicular plane thus, such EM ST PWs are called *elliptical-polarized* EM ST PWs. However, for the special case where  $|\beta| = 1$  and  $\angle\beta = \pm\pi/2$ , the electric-field vector of the fully polarized EM ST PW  $\mathbf{empw}_{4C}(x, y, z, t)$  traces a perfect circle on the perpendicular plane. Note that  $\angle\beta = +\pi/2$  corresponds to *right-circular polarization* and  $\angle\beta = -\pi/2$  corresponds to *left-circular polarization*, respectively. Hence, such EM ST PWs are called *circular-polarized* EM ST PWs. For another special case where  $\angle\beta = 0^\circ$  or  $\angle\beta = 180^\circ$ , the electric-field vector of the fully polarized EM ST PW  $\mathbf{empw}_{4C}(x, y, z, t)$  traces a *straight-line* on the perpendicular-plane thus, the electric-field is confined to a plane along the DOP. Such EM ST PWs are called *linear-polarized* EM ST PWs. According to the above mentioned property of linear-polarized EM ST PWs, each of the two decomposed EM ST PWs  $\mathbf{empw}_{4C_1}(x, y, z, t)$  and  $\mathbf{empw}_{4C_2}(x, y, z, t)$ , whose electric-field component is specified in (2.3), is a linear-polarized EM ST PW. *Therefore, any EM ST PW can be decomposed into two linear-polarized EM ST PWs, where the corresponding electric-field vectors are confined to two orthogonal planes along the DOP* [70](ch. 12).

According to (2.3), almost all the information carried by the vector-valued 4D ST PW  $\mathbf{empw}_{4C_1}(x, y, z, t)$  are contained jointly in the scalar-valued 4D ST PWs  $pw_{4C}(x, y, z, t)$  and  $pw_{4C_2}(x, y, z, t)$ . Therefore, the ST-domain and spectral-domain properties of the vector-valued 4D ST PWs can be deduced from the ST-domain and spectral-domain properties of the scalar-valued 4D ST PWs. For simplicity, in Section 2.3, the derivation of the MD CDFTs is limited to scalar-valued MD ST PWs. The spectra of vector-valued MD ST PWs are then deduced according to the linear relationship given in (2.3) with the substitution of respective MD-CDFTs of scalar-valued MD ST PWs.

### 2.3 Analysis of Spatio-Temporal Planes Waves and the Corresponding Spectra

An ideal scalar-valued 4D continuous-domain ST PW  $pw_{4C}(x, y, z, t)$ , shown in Figure 2.2, may be expressed in the form

$$pw_{4C}(x, y, z, t) = w_C(t + c^{-1}(d_x x + d_y y + d_z z)), \quad (2.4)$$

where  $\hat{\mathbf{d}} = [d_x \ d_y \ d_z]$  is the unit vector specifying the direction of arrival (DOA)<sup>4</sup> in the 3D space  $(x, y, z) \in \mathbb{R}^3$ ,  $c$  is the constant speed of wave propagation and  $w_C(\tau)$ ;  $\forall \tau = t + c^{-1}(d_x x + d_y y + d_z z) \in \mathbb{R}$  is the *1D temporal wavefront function* in the DOA [42](pp. 289-293). The dimensions  $\text{Dim}[x] = \text{Dim}[y] = \text{Dim}[z] = \text{m}$ ,  $\text{Dim}[t] = \text{s}$  and  $\text{Dim}[c] = \text{ms}^{-1}$ . Note that the DOA unit vector  $\hat{\mathbf{d}}$  can be expressed in terms of the *inclination-angle*  $\theta$ , and the *azimuth-angle*  $\phi$  of the point source of the signal, such that

$$\hat{\mathbf{d}} = [d_x \ d_y \ d_z] = [\sin(\theta) \cos(\phi) \ \sin(\theta) \sin(\phi) \ \cos(\theta)], \quad (2.5)$$

where  $\theta \in [0^\circ, 180^\circ]$  and where  $\phi \in [0^\circ, 360^\circ]$ . Further,

$$d_x^2 + d_y^2 + d_z^2 = 1, \quad (2.6)$$

according to the definition of the DOA unit vector  $\hat{\mathbf{d}}$ .

A 4D ST PW can be categorized according to the spectral content of the associated 1D temporal wavefront function  $w_C(t)$ . For example, a 4D temporally baseband ST PW  $pw_{4CB}(x, y, z, t)$  is associated with a real-valued 1D temporally baseband wavefront function  $w_{CB}(t)$  of temporal bandwidth  $BW$ . Here,  $W_{CB}(f_t) = 0$ ; for all  $f_t \notin (-BW, BW)$ , where the 1D-CDFT pair  $w_{CB}(t) \xleftrightarrow{1\text{D-CDFT}} W_{CB}(f_t)$  [71] (pp. 41). A temporally-bandpassed wavefront function  $w_{CP}(t)$ , having a bandwidth of  $BW$  and center-frequency  $f_C$  may be expressed as

$$w_{CP}(t) = \text{Re}[w_{CB}(t)e^{j2\pi f_C t}], \quad (2.7)$$

---

<sup>4</sup>The DOA unit vector is related to the DOP unit vector such that  $\hat{\mathbf{d}} = -\hat{\mathbf{p}}$ .

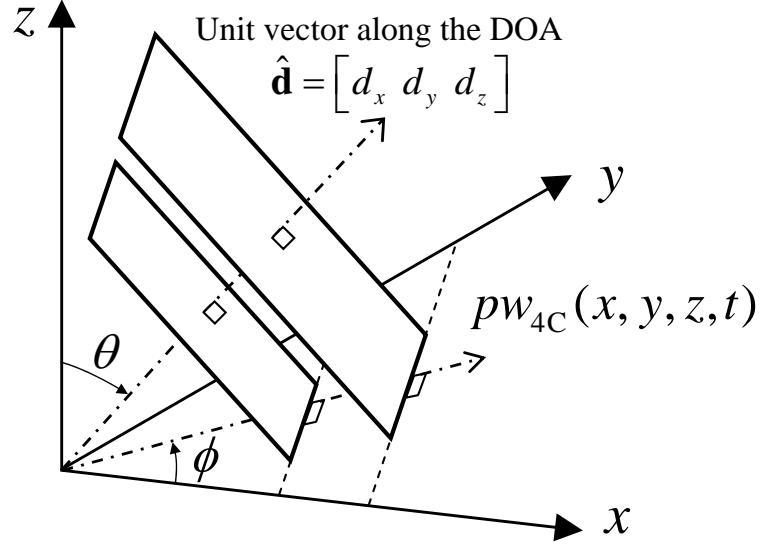


Figure 2.2: An ideal 4D ST PW  $pw_{4C}(x, y, z, t)$  in 3D space  $(x, y, z) \in \mathbb{R}^3$  having the DOA  $\hat{\mathbf{d}} = [d_x \ d_y \ d_z]$ .

in terms of  $w_{CB}(t)$ , a temporally baseband wavefront function of bandwidth  $0.5BW$  where  $f_C \geq 0.5BW > 0$  [71] (pp. 196-199). According to [71] (pp. 198), the 1D-CDFT of  $w_{CB}(t)$  can be expressed by

$$W_{CP}(f_t) = \frac{1}{2} \left( W_{CB}(f_t - f_C) + W_{CB}^*(-f_t - f_C) \right), \quad (2.8)$$

where “\*” denotes complex conjugation operation. According to (2.8),  $W_{CP}(f_t) = 0$ ; for all  $f_t \notin \{(-f_C - 0.5BW, -f_C + 0.5BW) \cup (f_C - 0.5BW, f_C + 0.5BW)\}$ .

The relative spread of the temporal bandwidth of a temporally-bandpassed wavefront function  $w_{CP}(t)$  is characterized by the bandwidth spread factor  $K$ , defined by

$$K \triangleq \frac{BW}{2f_{\max}}, \quad (2.9)$$

where  $f_{\max} = f_C + 0.5BW$  [59]. In this thesis, temporally-bandpassed wavefront functions having bandwidth spread factors higher than 0.125 are defined as *temporally-broadband-bandpassed* (BB-BP) wavefront functions and the associated 4D ST PWs are known as 4D BB-BP ST PWs. However, the remainder of temporally-bandpassed wavefront functions

(i.e.  $K < 0.125$ ) are defined as *temporally-narrowband-bandpassed* (NB-BP) wavefront functions and the associated 4D ST PWs are known as 4D NB-BP ST PWs. Here, the emphasis is given to the analyses of propagating BB-BP ST PWs because in this thesis, the main objectives are the design and implementation of MD filters for beamforming of propagating BB-BP signals.

### 2.3.1 4D BB-BP ST PWs and the Corresponding Spectra

In order to analyze the frequency domain properties of the 4D continuous-domain BB-BP ST PW, its 4D-CDFT is evaluated. The 4D-CDFT of the 4D continuous-domain BB-BP ST PW  $pw_{4CP}(x, y, z, t)$  is defined by

$$PW_{4CP}(f_x, f_y, f_z, f_t) \triangleq \iiint\limits_{x,y,z,t=-\infty}^{+\infty} pw_{4CP}(x, y, z, t) e^{-j2\pi f_x x} e^{-j2\pi f_y y} e^{-j2\pi f_z z} e^{-j2\pi f_t t} dx dy dz dt, \quad (2.10)$$

where  $(f_x, f_y, f_z, f_t) \in \mathbb{R}^4$  [41] and the dimensions  $\text{Dim}[f_x] = \text{Dim}[f_y] = \text{Dim}[f_z] = \text{m}^{-1}$  and  $\text{Dim}[f_t] = \text{s}^{-1}$ . Substituting for  $pw_{4CP}(x, y, z, t)$  in (2.10) with the equivalent temporally BB-BP wavefront function in (2.4) yields,

$$PW_{4CP}(f_x, f_y, f_z, f_t) = \iiint\limits_{x,y,z,t=-\infty}^{+\infty} w_{CP} \ t + c^{-1}(d_x x + d_y y + d_z z) \ e^{-j2\pi(f_x x + f_y y + f_z z + f_t t)} dx dy dz dt. \quad (2.11)$$

With a novel approach, the 4D CDFT (2.11) has been evaluated in detail in Appendix A.1.

As shown there

$$PW_{4CP}(f_x, f_y, f_z, f_t) = W_{CP} \ f_t \cdot \delta(c^{-1}d_x f_t - f_x) \cdot \delta(c^{-1}d_y f_t - f_y) \cdot \delta(c^{-1}d_z f_t - f_z), \quad (2.12)$$

where  $W_{CP}(f_t)$  is the 1D-CDFT of  $w_{CP}(t)$  and where  $\delta(f_t)$  is the *1D continuous-domain unit impulse function*.

For the ease of comparison among ST PWs propagating at different speeds, a scaled temporal-frequency space is defined such that  $f_{ct} \triangleq c^{-1}f_t$ , where the dimensions  $\text{Dim}[f_x]$

$= \text{Dim}[f_y] = \text{Dim}[f_z] = \text{Dim}[f_{ct}] = m^{-1}$ . Now the 4D spectrum of a propagating 4D BB-BP ST PW is rewritten as

$$PW_{4\text{CP}}(f_x, f_y, f_z, f_{ct}) = W_{\text{CP}}(cf_{ct}) \cdot \delta(d_x f_{ct} - f_x) \cdot \delta(d_y f_{ct} - f_y) \cdot \delta(d_z f_{ct} - f_z). \quad (2.13)$$

Following (2.8), (2.13) can also be expressed in terms of the equivalent 1D baseband spectrum  $W_{\text{CB}}(cf_{ct})$ , such as

$$\begin{aligned} PW_{4\text{CP}}(f_x, f_y, f_z, f_{ct}) = \\ \frac{1}{2} \{ W_{\text{CB}}(cf_{ct} - f_C) + W_{\text{CB}}^*(-cf_{ct} - f_C) \} \cdot \delta(d_x f_{ct} - f_x) \cdot \delta(d_y f_{ct} - f_y) \cdot \delta(d_z f_{ct} - f_z). \end{aligned} \quad (2.14)$$

The distribution of the spectral components of signals of interest is an important property in beamforming. The region in the respective domain where a multidimensional-function is specified to be non-zero is defined as the *region of support* (ROS) of that function<sup>5</sup> [41](ch. 1-2). Hence according to (2.13) and (2.14), the ROS of the spectrum  $PW_{4\text{CP}}(f_x, f_y, f_z, f_{ct})$  is given by the 4D *hyper-lines of intersection* among the three 4D hyper-planes  $d_x f_{ct} - f_x = 0$  and  $d_y f_{ct} - f_y = 0$  and  $d_z f_{ct} - f_z = 0$ ; in  $(f_x, f_y, f_z, f_{ct}) \in \mathbb{R}^4$  such that  $f_{ct} \in \{(-c^{-1}f_C - 0.5c^{-1}BW, -c^{-1}f_C + 0.5c^{-1}BW) \cup (-c^{-1}f_C - 0.5c^{-1}BW, c^{-1}f_C + 0.5c^{-1}BW)\}$  where  $W_{\text{CP}}(cf_{ct}) = 0$ .

The 4D parametric equations of the 4D hyper-line of intersection corresponding to the three 4D hyper-planes  $d_x f_{ct} - f_x = 0$  and  $d_y f_{ct} - f_y = 0$  and  $d_z f_{ct} - f_z = 0$  that passes through the origin O of the 4D frequency-space  $(f_x, f_y, f_z, f_{ct}) \in \mathbb{R}^4$  is given by

$$4\text{DHLin}_{\text{ROS}} = d_x f_{ct}, d_y f_{ct}, d_z f_{ct}, f_{ct}, \quad (2.15)$$

in terms of the Cartesian components  $[d_x \ d_y \ d_z]$  of the DOA vector  $\hat{\mathbf{d}}$  and

$$4\text{DHLin}_{\text{ROS}} = \sin(\theta) \cos(\phi) f_{ct}, \sin(\theta) \sin(\phi) f_{ct}, \cos(\theta) f_{ct}, f_{ct}, \quad (2.16)$$

---

<sup>5</sup>Either in spatio-temporal or spectral domains.



in terms of the inclination and azimuth angles  $\theta$  and  $\phi$ . As  $\theta$  varies in the range  $[0^\circ, 180^\circ]$  and  $\phi$  varies in the range  $[0^\circ, 360^\circ]$ , the 4D volume swept by the 4D hyper-line given in (2.16) represents a 4D *double right-spherical hyper-cone* [72]. Similar to a 3D double right-circular cone, a 4D double right-spherical hyper-cone consisted of two unbounded nappes, where the upper-nappe corresponds with the positive frequencies of  $f_{ct}$ , and the lower-nappe corresponds with the negative frequencies of  $f_{ct}$  [72]. Further, the projection of a 4D double right-spherical hyper-cone onto the 4D hyper-plane  $f_{ct} = 0$ , is a 3D *sphere* where the projections onto the 4D hyper-planes  $f_x = 0$ ,  $f_y = 0$  and  $f_z = 0$  are 3D *double right-circular cones* [72]. Therefore, the range of all ROSs of the spectra of all propagating 4D BB-BP ST PWs are given by a 4D double *right-spherical hyper-frustum*<sup>6</sup>, where upper-frustum corresponds to  $f_{ct} \in \{(-c^{-1}f_C - 0.5c^{-1}BW, -c^{-1}f_C + 0.5c^{-1}BW)\}$  and lower-frustum corresponds to  $f_{ct} \in \{(c^{-1}f_C - 0.5c^{-1}BW, c^{-1}f_C + 0.5c^{-1}BW)\}$ , respectively. It can be deduced that the projection of a 4D double right-spherical hyper-frustum onto the 4D hyper-plane  $f_{ct} = 0$ , is a 3D double *sphere-shell* of inner-radius  $(c^{-1}f_C - 0.5c^{-1}BW)$  and outer-radius  $(c^{-1}f_C + 0.5c^{-1}BW)$ , where the projections onto the 4D hyper-planes  $f_x = 0$ ,  $f_y = 0$  and  $f_z = 0$  are 3D *double right-circular frustas* (see Figure 2.5).

### The 4D-CDFT of EM 4D BB-BP ST PW

Following (2.3), the 4D CDFT  $\mathbf{EPW}_{4CP}(f_x, f_y, f_z, f_{ct})$  of the vector-valued electric-field component  $\mathbf{epw}_{4CP}(x, y, z, t)$  associated with EM 4D BB-BP ST PW  $\mathbf{empw}_{4CP}(x, y, z, t)$  can be defined as

$$\mathbf{EPW}_{4CP}(f_x, f_y, f_z, f_{ct}) \triangleq \hat{\mathbf{E}}_1^{\text{pol}} PW_{4CP_1}(f_x, f_y, f_z, f_{ct}) + \hat{\mathbf{E}}_2^{\text{pol}} PW_{4CP_2}(f_x, f_y, f_z, f_{ct}), \quad (2.17)$$

where the 4D-CDFT pairs of the scalar-valued 4D BB-BP ST PWs are denoted by

$$pw_{4CP_1}(x, y, z, t) \xleftrightarrow{4D\text{-}CDFT} PW_{4CP_1}(f_x, f_y, f_z, f_{ct})$$

---

<sup>6</sup>A frustum is the volume that corresponds to a section of cone between two parallel slicing planes [73].

and

$$pw_{4CP_2}(x, y, z, t) \xleftrightarrow{4D-CDF^T} PW_{4CP_2}(f_x, f_y, f_z, f_{ct}).$$

Because the unit vectors  $\hat{\mathbf{E}}_1^{\text{pol}}$  and  $\hat{\mathbf{E}}_2^{\text{pol}}$  are orthogonal to each other, the spectral components of  $PW_{4CP_1}(f_x, f_y, f_z, f_{ct})$  and  $PW_{4CP_2}(f_x, f_y, f_z, f_{ct})$  can be resolved separately even though their ROSs are coincided in 4D frequency-space  $(f_x, f_y, f_z, f_{ct}) \in \mathbb{R}^4$ .

In the next two subsections, ST signals observed on a plane and on a line in the 3D space in response to propagating 4D BB-BP ST PWs are analyzed giving prominence to their spectral domain properties. This analysis is a precursor for analyzing EM waves received by 2D-UDPAs and 1D-UDAAs in the following sections and chapters.

### 2.3.2 4D BB-BP ST PWs Observed on a Plane in the 3D Space and the Corresponding Spectra

Without the loss of generality, assume a propagating 4D BB-BP ST PW is observed on the infinite plane  $z = 0$  in the 3D space, as shown in Figure 2.3. Hence, the ST signal on the plane may be expressed by

$$\text{Plane}_{3CP}(x, y, t) = pw_{4CP}(x, y, 0, t) = w_{CP}(t + c^{-1}(d_x x + d_y y)), \quad (2.18)$$

that has the form of 3D continuous-domain ST PW according to the definition of the 4D continuous-domain ST PW given in (2.4). Hence,  $\text{Plane}_{3CP}(x, y, t)$  is redefined as a 3D continuous-domain BB-BP ST PW

$$pw_{3CP}(x, y, t) = \text{Plane}_{3CP}(x, y, t) = w_{CP}(t + c^{-1}(d_x x + d_y y)). \quad (2.19)$$

Note that  $pw_{3CP}(x, y, t)$  has no information of the exact value of the  $d_z$  component of the DOA  $\hat{\mathbf{d}}$  of the original  $pw_{4CP}(x, y, z, t)$ . *Therefore, the 3D BB-BP ST PWs  $pw_{3CP_O}(x, y, t)$  and  $pw_{3CP_I}(x, y, t)$  that correspond to the two propagating 4D BB-BP PWs; the first  $pw_{4CP_O}(x, y, z, t)$ , having the DOA  $\hat{\mathbf{d}}_O = [d_x \ d_y \ d_z]$ , and the second  $pw_{4CP_I}(x, y, z, t)$ , having the DOA  $\hat{\mathbf{d}}_I = [d_x \ d_y \ -d_z]$ , are indistinguishable on the basis of their DOAs*

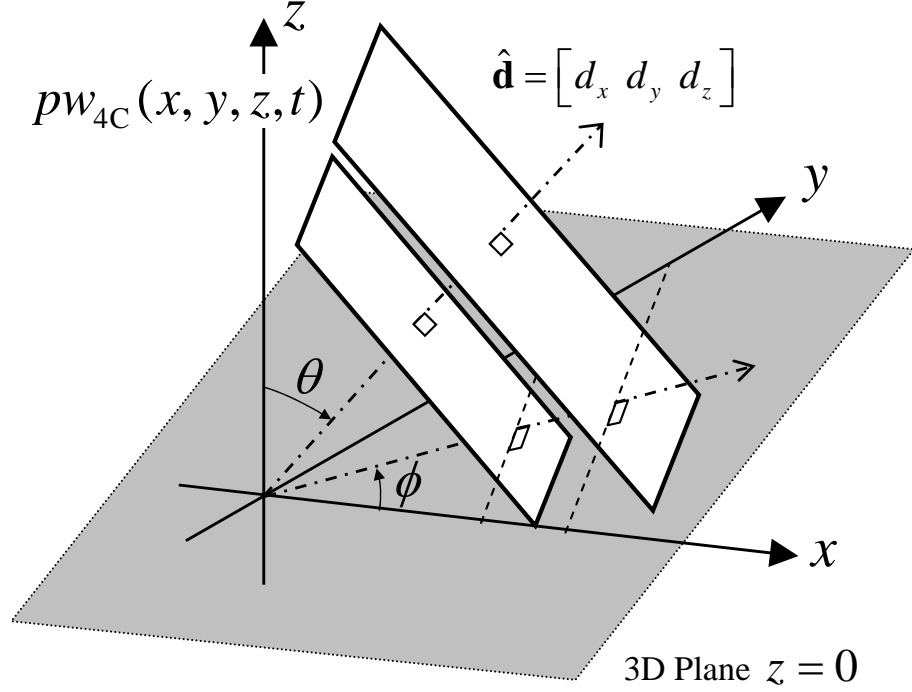


Figure 2.3: A ST PW  $pw_{4C}(x, y, z, t)$  having the DOA  $\hat{\mathbf{d}} = [d_x \ d_y \ d_z]$  is observed on the infinite extent plane  $z = 0$  in 3D space.

if those are observed on the plane  $z = 0$  in 3D space. Note that the unit vector  $\hat{\mathbf{d}}_I$  is the *mirror-image* of  $\hat{\mathbf{d}}_O$  on the plane  $z = 0$  in 3D space. In terms of the inclination angles and azimuth angles, two ST PWs observed on the plane  $z = 0$  in 3D space are indistinguishable if and only if the inclination angles for their DOAs are related such that  $\theta_O = \theta$  and  $\theta_I = 180^\circ - \theta$ , for any azimuth angle  $\phi$ . This implies that by observing propagating 4D BB-BP ST PWs on the plane  $z = 0$  in 3D space, is it impossible to determine whether the signals are arriving from the upper-hemisphere; such that  $\theta \in [0^\circ, 90^\circ]$  or the signals are arriving from the lower-hemisphere; such that  $\theta \in [90^\circ, 180^\circ]$ . However, for most applications this indistinguishability is of little concern because in such applications the interest is limited to the signals arriving from a single

hemisphere for  $\theta \in [0^\circ, 90^\circ]$ . For example, dense aperture arrays (DAAs) are designed in order to receive EM radiation from celestial sources distributed over the upper-hemisphere above the surface of the earth while suppressing the EM signals emanating from the surface of the earth [74].

Here, the 3D-CDFT of the 3D continuous-domain BB-BP ST PW  $pw_{3CP}(x, y, t)$  is defined<sup>7</sup> by

$$PW_{3CP}(f_x, f_y, f_{ct}) \triangleq \iiint_{x, y, t=-\infty}^{+\infty} pw_{3CP}(x, y, t) e^{-j2\pi f_x x} e^{-j2\pi f_y y} e^{-j2\pi c f_{ct} t} dx dy dt, \quad (2.20)$$

where  $(f_x, f_y, f_{ct}) \in \mathbb{R}^3$  [41] and the dimensions  $\text{Dim}[f_x] = \text{Dim}[f_y] = \text{Dim}[f_{ct}] = \text{m}^{-1}$ . Substituting for  $pw_{3CP}(x, y, t)$  in (2.20) with (2.19) yields

$$PW_{3CP}(f_x, f_y, f_{ct}) = \iiint_{x, y, t=-\infty}^{+\infty} w_{CP}(t + c^{-1}(d_x x + d_y y)) e^{-j2\pi f_x x} e^{-j2\pi f_y y} e^{-j2\pi c f_{ct} t} dx dy dt. \quad (2.21)$$

As evaluated in Appendix A.2

$$PW_{3CP}(f_x, f_y, f_{ct}) = W_{CP} \cdot cf_{ct} \cdot \delta(d_x f_{ct} - f_x) \cdot \delta(d_y f_{ct} - f_y), \quad (2.22)$$

in terms of 1D BB-BP spectral function  $W_{CP}(cf_{ct})$  and

$$PW_{3CP}(f_x, f_y, f_{ct}) = \frac{1}{2} \{W_{CB}(cf_{ct} - f_C) + W_{CB}^*(-cf_{ct} - f_C)\} \delta(d_x f_{ct} - f_x) \delta(d_y f_{ct} - f_y), \quad (2.23)$$

in terms of 1D baseband spectral function  $W_{CB}(cf_{ct})$ . Note that the projection of the 4D spectrum  $PW_{4CP}(f_x, f_y, f_z, f_{ct})$  of the original 4D BB-BP ST PW  $pw_{4CP}(x, y, z, t)$ , which is given in (2.13), onto the 4D hyper-plane  $f_z = 0$  in  $(f_x, f_y, f_z, f_{ct}) \in \mathbb{R}^4$ , such that

$$\begin{aligned} \text{Proj}_{3CP}(f_x, f_y, f_{ct}) &= \int_{f_z=-\infty}^{+\infty} W_{CP} \cdot cf_{ct} \cdot \delta(d_x f_{ct} - f_x) \cdot \delta(d_y f_{ct} - f_y) \cdot \delta(d_z f_{ct} - f_z) df_z \\ &= W_{CP} \cdot cf_{ct} \cdot \delta(d_x f_{ct} - f_x) \cdot \delta(d_y f_{ct} - f_y), \end{aligned} \quad (2.24)$$

---

<sup>7</sup>Note that  $f_t$  is now substituted with  $cf_{ct}$ .

yields the same result given in (2.22) for the corresponding 3D-CDFT  $PW_{3CP}(f_x, f_y, f_{ct})$ .

According to 2.22 and 2.23, the ROS of  $PW_{3CP}(f_x, f_y, f_{ct})$  is given by the two line segments  $PQ$  and  $P'Q'$  that are on the line of intersection between the two planes  $d_x f_{ct} - f_x = 0$  and  $d_y f_{ct} - f_y = 0$  in 3D frequency-space  $(f_x, f_y, f_{ct}) \in \mathbb{R}^3$ , as shown in Figure 2.4. Note that the line segment  $PQ$  corresponds to the *positive temporal frequencies*  $f_{ct} \in \{(c^{-1}f_C - 0.5c^{-1}BW, c^{-1}f_C + 0.5c^{-1}BW)\}$  and  $P'Q'$  corresponds to the *negative temporal frequencies*  $f_{ct} \in \{(-c^{-1}f_C - 0.5c^{-1}BW, -c^{-1}f_C + 0.5c^{-1}BW)\}$ , respectively. The 3D parametric equations of the line of intersection between the two planes  $d_x f_{ct} - f_x = 0$  and  $d_y f_{ct} - f_y = 0$  that passes through the origin O of the 3D frequency-space  $(f_x, f_y, f_{ct}) \in \mathbb{R}^3$  are given by

$$3DLine_{ROS} = d_x f_{ct}, d_y f_{ct}, f_{ct} , \quad (2.25)$$

in terms of the Cartesian components  $[d_x \ d_y \ d_z]$  of the DOA vector  $\hat{\mathbf{d}}$  and

$$3DLine_{ROS} = \sin(\theta) \cos(\phi) f_{ct}, \sin(\theta) \sin(\phi) f_{ct}, f_{ct} , \quad (2.26)$$

in terms of the inclination and azimuth angles  $\theta$  and  $\phi$ . As shown in Figure 2.4, the angle between the  $f_{ct}$ -axis and the line of intersection is  $\alpha = \tan^{-1}(\sin(\theta))$  where as the angle between  $f_x$ -axis and the projection of the line of intersection on to the  $f_{ct} = 0$  plane is  $\phi$ .

As  $\theta$  varies in the range  $[0^\circ, 90^\circ]$  and  $\phi$  varies in the range  $[0^\circ, 360^\circ]$ , the 3D volume swept by the line given in (2.26) represents a 3D *double right-circular cone* having half-cone angle  $\alpha_{\max} = 45^\circ$  in  $(f_x, f_y, f_{ct}) \in \mathbb{R}^3$ , as illustrated in Figure 2.5. The same volume is swept as  $\theta$  varies in the range  $[90^\circ, 180^\circ]$  and  $\phi$  varies in the range  $[0^\circ, 360^\circ]$ . Therefore, the range of ROSs of the spectra of all 3D BB-BP ST PWs observed on the plane  $z = 0$  in response to propagating 4D BB-BP ST PWs all possible DOAs, is given by the two 3D right-circular frustum regions shown in Figure 2.5 that correspond to temporal frequencies  $f_{ct} \in \{(-c^{-1}f_C - 0.5c^{-1}BW, -c^{-1}f_C + 0.5c^{-1}BW) \cup (c^{-1}f_C - 0.5c^{-1}BW, c^{-1}f_C + 0.5c^{-1}BW)\}$  in  $(f_x, f_y, f_{ct}) \in \mathbb{R}^3$ . This 3D double frustum-shaped range of ROSs of 3D BB-BP ST PWs corresponds to the projection of the 4D double

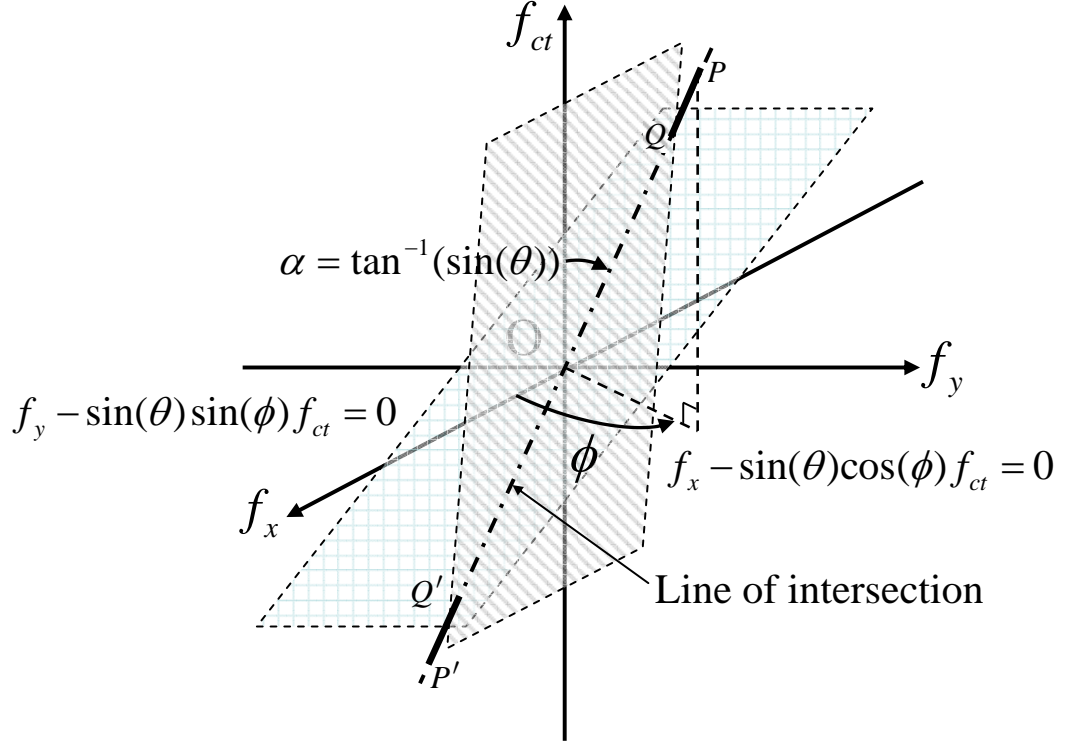


Figure 2.4: The ROS,  $PQ$  and  $P'Q'$ , of the spectrum  $PW_{3CP}(f_x, f_y, f_{ct})$  is on the line of intersection between the two planes  $d_x f_{ct} - f_x = 0$  and  $d_y f_{ct} - f_y = 0$ .

hyper-frustum-shaped range of ROSs of propagating 4D BB-BP ST PWs on to the 4D frequency hyper-plane  $f_z = 0$ , as mentioned in Section 2.3.1.

Also, the indistinguishability of propagating 4D BB-BP ST PWs observed on a plane in 3D space can be explained using the ROSs of the spectra of  $PW_{3CP}(f_x, f_y, f_{ct})$ . According to (2.25) and (2.26), the ROSs of  $PW_{3CP_0}(f_x, f_y, f_{ct})$  and  $PW_{3CP_1}(f_x, f_y, f_{ct})$ , which are corresponding to DOAs

$$\hat{\mathbf{d}}_0 = [d_x \ d_y \ d_z] = [\sin(\theta) \cos(\phi), \ \sin(\theta) \sin(\phi), \ \cos(\theta)],$$

and

$$\hat{\mathbf{d}}_1 = [d_x \ d_y \ -d_z] = [\sin(\theta) \cos(\phi), \ \sin(\theta) \sin(\phi), \ -\cos(\theta)],^8$$

coincide with each other. Hence, it is impossible to distinguish between the 4D BB-BP

---

<sup>8</sup>Where  $\sin(180^\circ - \theta) = \sin(\theta)$  and  $\cos(180^\circ - \theta) = -\cos(\theta)$ .

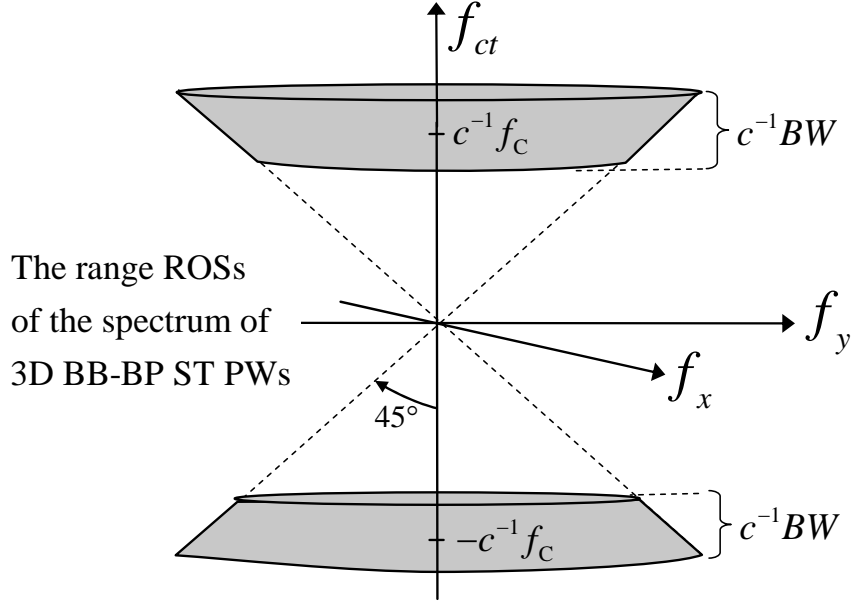


Figure 2.5: The 3D double right-circular frustum volume is the range of ROSs of the spectra  $PW_{3CP}(f_x, f_y, f_{ct})$  of all possible 4D BB-BP ST PWs observed on the plane  $z = 0$  in 3D space.

ST PWs  $pw_{4CP_O}(x, y, z, t)$  and  $pw_{4CP_I}(x, y, z, t)$  in terms of their DOAs by observing the ROSs of the spectra of observed 3D BB-BP ST PWs  $pw_{3CP_O}(x, y, t)$  and  $pw_{3CP_I}(x, y, t)$  on the plane  $z = 0$  in 3D space.

As deduced in (2.17), the spectrum  $\mathbf{EPW}_{3CP}(f_x, f_y, f_{ct})$  of the electric-field component  $\mathbf{epw}_{3CP}(x, y, t)$  observed on the plane  $z = 0$  in 3D space in response to 4D EM BB-BP ST PW  $\mathbf{empw}_{4CP}(x, y, z, t)$  can be expressed as

$$\mathbf{EPW}_{3CP}(f_x, f_y, f_{ct}) = \hat{\mathbf{E}}_1^{\text{pol}} PW_{3CP_1}(f_x, f_y, f_{ct}) + \hat{\mathbf{E}}_2^{\text{pol}} PW_{3CP_2}(f_x, f_y, f_{ct}), \quad (2.27)$$

where the 3D-CDFT pairs of the scalar-valued 3D BB-BP ST PWs are denoted by  $pw_{3CP_1}(x, y, t) \xleftrightarrow{\text{3D-CDFT}} PW_{3CP_1}(f_x, f_y, f_{ct})$  and  $pw_{3CP_2}(x, y, t) \xleftrightarrow{\text{3D-CDFT}} PW_{3CP_2}(f_x, f_y, f_{ct})$ . Note that the spectral components of  $PW_{3CP_1}(f_x, f_y, f_{ct})$  and  $PW_{3CP_2}(f_x, f_y, f_{ct})$  can be resolved separately even though their ROSs are coincided in 3D frequency-space  $(f_x, f_y, f_{ct}) \in \mathbb{R}^3$ , because the unit vectors  $\hat{\mathbf{E}}_1^{\text{pol}}$  and  $\hat{\mathbf{E}}_2^{\text{pol}}$  are orthogonal to each other.

### 2.3.3 4D BB-BP ST PWs Observed on a Line in 3D Space and the Corresponding Spectra

Without the loss of generality assume a propagating 4D BB-BP ST PW is observed on the infinite line in 3D space along the  $x$ -axis (i.e. the line of intersection between the two planes  $y = 0$  and  $z = 0$  in 3D space), as shown in Figure 2.6. Hence, the signal on the line may be expressed by

$$\text{Line}_{2\text{CP}}(x, t) = pw_{4\text{CP}}(x, 0, 0, t) = w_{\text{CP}}(t + c^{-1}d_x x), \quad (2.28)$$

that has the form of 2D continuous-domain ST PW according to the definition of the 4D continuous-domain ST PW given in (2.4). Hence,  $\text{Line}_{2\text{CP}}(x, t)$  is redefined as a 2D continuous-domain BB-BP ST PW

$$pw_{2\text{CP}}(x, t) = \text{Line}_{2\text{CP}}(x, t) = w_{\text{CP}}(t + c^{-1}d_x x). \quad (2.29)$$

Note that  $pw_{2\text{CP}}(x, t)$  has no information of exact values of the  $d_y$  and  $d_z$  components of the DOA  $\hat{\mathbf{d}}$  of the original  $pw_{4\text{CP}}(x, y, z, t)$ . *Therefore, the 2D BB-BP ST PWs  $pw_{2\text{CP}}(x, t)$  that correspond to propagating 4D BB-BP PWs  $pw_{4\text{CP}}(x, y, z, t)$ , which correspond to the DOAs  $\hat{\mathbf{d}}_C = [d_{x_C} \ d_y \ d_z]$ ; where  $d_{x_C}$  is a constant such that  $|d_{x_C}| \leq 1$ , and where  $d_y$  and  $d_z$  varies such that  $d_y^2 + d_z^2 = 1 - d_{x_C}^2$ , are indistinguishable on the basis of their DOAs if those are observed on the line along the  $x$ -axis.* In other words, any 4D BB-BP ST PW observed on the line along the  $x$ -axis is identical in terms of its DOAs if and only if the inclination angle  $\varphi$  (see Figure 2.6 (right)) between the  $x$ -axis and the DOA vector remains a constant for all propagating 4D BB-BP PWs. However, for some applications this indistinguishability is of little concern because in such applications the interest is limited to propagating 4D BB-BP ST PWs arriving along the plane  $z = 0$  in 3D space (i.e.  $\theta = 90^\circ$ ) and limited azimuth angular range (i.e.  $\phi \in [0^\circ, 180^\circ]$ ). For example, 1D uniformly distributed antenna arrays (1D-UDAAs) are designed to receive EM radiation emitted by wireless subscribers spread across a certain sector (e.g.  $\phi \in [30^\circ, 150^\circ]$ ) of the



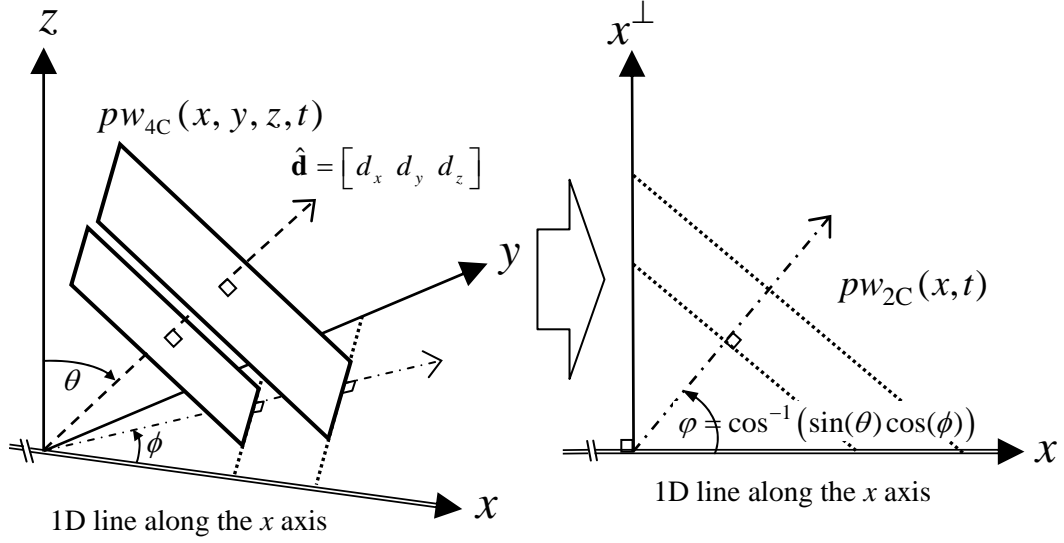


Figure 2.6: A 4D ST PW  $pw_{4C}(x, y, z, t)$  is observed on the infinitely-long continuous line along the  $x$  axis (left), reduces to a 2D ST PW  $pw_{2C}(x, t)$  (right).

coverage area on the surface of the earth (e.g.  $\theta \approx 90^\circ$ ) while minimizing the response from signals arriving in other directions [24]. In practice, several such 1D-UDAAs are used to cover all the sectors of the coverage area [24].

The 2D-CDFT of the 2D continuous-domain BB-BP ST PW  $pw_{2CP}(x, t)$  is defined<sup>9</sup> by

$$PW_{2CP}(f_x, f_{ct}) \triangleq \iint_{x, t=-\infty}^{+\infty} pw_{2CP}(x, t) e^{-j2\pi f_x x} e^{-j2\pi c f_{ct} t} dx dt, \quad (2.30)$$

where  $(f_x, f_{ct}) \in \mathbb{R}^2$  [41]. Substituting for  $pw_{2CP}(x, y, t)$  in (2.30) with (2.29) yields

$$PW_{2CP}(f_x, f_{ct}) = \iint_{x, t=-\infty}^{+\infty} w_{CP}(t + c^{-1}d_x x) e^{-j2\pi f_x x} e^{-j2\pi c f_{ct} t} dx dt, \quad (2.31)$$

As evaluated in Appendix A.3

$$PW_{2CP}(f_x, f_{ct}) = W_{CP} \ c f_{ct} \cdot \delta(d_x f_{ct} - f_x), \quad (2.32)$$

<sup>9</sup>Note that  $f_t$  is substituted with  $c f_{ct}$  and the dimensions  $\text{Dim}[f_x] = \text{Dim}[f_{ct}] = \text{m}^{-1}$ .

in terms of 1D BB-BP spectral function  $W_{\text{CP}}(cf_{ct})$  and

$$PW_{2\text{CP}}(f_x, f_y, f_{ct}) = \frac{1}{2} \{W_{\text{CB}}(cf_{ct} - f_C) + W_{\text{CB}}^*(-cf_{ct} - f_C)\} \cdot \delta(d_x f_{ct} - f_x), \quad (2.33)$$

in terms of 1D baseband spectral function  $W_{\text{CB}}(cf_{ct})$ . Note that two successive projections of the 4D spectrum  $PW_{4\text{CP}}(f_x, f_y, f_z, f_{ct})$  of the original 4D BB-BP ST PW  $pw_{4\text{CP}}(x, y, z, t)$ , which is given in (2.13), first onto the plane  $f_z = 0$  and then onto the plane  $f_z = 0$  in  $(f_x, f_y, f_z, f_{ct}) \in \mathbb{R}^4$ , such that

$$\begin{aligned} \text{Proj}_{2\text{CP}}(f_x, f_{ct}) &= \int_{f_y=-\infty}^{+\infty} \int_{f_z=-\infty}^{+\infty} W_{\text{CP}}(cf_{ct}) \cdot \delta(d_x f_{ct} - f_x) \cdot \delta(d_y f_{ct} - f_y) \cdot \delta(d_z f_{ct} - f_z) df_z df_y \\ &= W_{\text{CP}}(cf_{ct}) \cdot \delta(d_x f_{ct} - f_x), \end{aligned} \quad (2.34)$$

yields the same result given in (2.32) for the corresponding 2D-CDFT  $PW_{2\text{CP}}(f_x, f_{ct})$ .

According to (2.32) and (2.33), the ROS of  $PW_{2\text{CP}}(f_x, f_{ct})$  is given by the line segments  $RS$  and  $R'S'$  on the straight-line  $d_x f_{ct} - f_x = 0$  in the 2D frequency-space  $(f_x, f_{ct}) \in \mathbb{R}^2$ , as show in Figure 2.7. Note that the line segment  $RS$  corresponds to the *positive temporal frequencies*  $f_{ct} \in \{(c^{-1}f_C - 0.5c^{-1}BW, c^{-1}f_C + 0.5c^{-1}BW)\}$  and  $R'S'$  corresponds to the *negative temporal frequencies*  $f_{ct} \in \{(-c^{-1}f_C - 0.5c^{-1}BW, -c^{-1}f_C + 0.5c^{-1}BW)\}$ , respectively. The 2D parametric equations of the line in 3D space corresponding to the ROS of  $PW_{2\text{C}}(f_x, f_{ct})$ , which passes through the origin O of the 2D frequency space  $(f_x, f_{ct}) \in \mathbb{R}^2$  are given by

$$2\text{DLine}_{\text{ROS}} = [d_x f_{ct}, f_{ct}] , \quad (2.35)$$

in terms of the Cartesian components  $[d_x \ d_y \ d_z]$  of the DOA vector  $\hat{\mathbf{d}}$  and

$$2\text{DLine}_{\text{ROS}} = [\sin(\theta) \cos(\phi) f_{ct}, f_{ct}] , \quad (2.36)$$

in terms of the inclination and azimuth angles  $\theta$  and  $\phi$ .

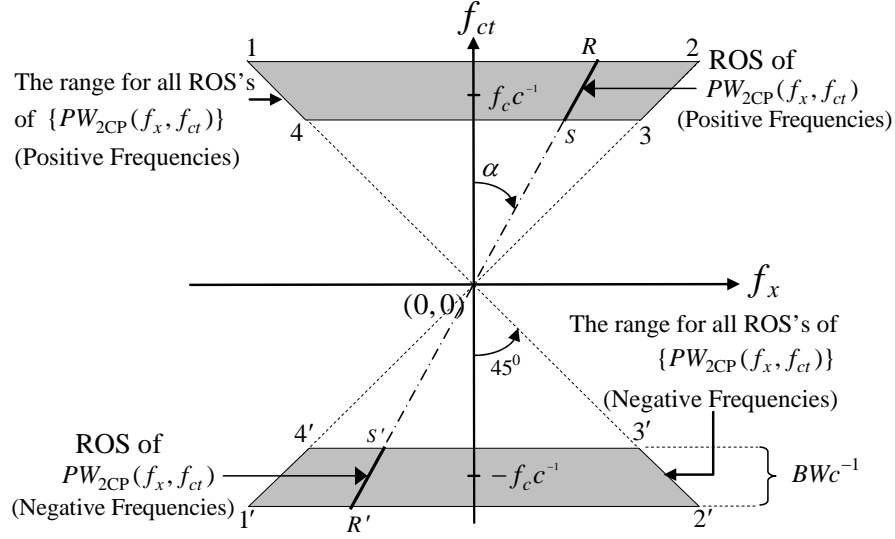


Figure 2.7: The ROS  $RS$  (positive frequencies) and  $R'S'$  (negative frequencies) of the spectrum  $PW_{2CP}(f_x, f_{ct})$  and the double isosceles-trapezoidal-shaped area corresponding to the range of ROSs of the spectra of all possible 2D ST PWs observed on the line along  $x$ -axis in 3D space.

As  $\theta$  varies in the range  $[0^\circ, 180^\circ]$  and  $\phi$  varies in the range  $[0^\circ, 360^\circ]$ , the 2D double fan-shaped area  $121'2'$  having half-apex angle  $\alpha_{\max} = 45^\circ$  in the 2D frequency-space  $(f_x, f_{ct}) \in \mathbb{R}^2$ , as illustrated in Figure 2.7, is swept by the line given in (2.36) multiple times. Hence, the range of ROSs of the spectra of all 2D BB-BP ST PWs observed on the line along the  $x$ -axis in response to propagating 4D BB-BP ST PWs of all possible DOAs, is given by the 2D *double isosceles-trapezoidal-shaped* shaded area  $1234 \cup 1'2'3'4'$  shown in Figure 2.7. Note that the area  $1234 \cup 1'2'3'4'$  corresponds to the projection of 3D double frustum-shaped volume shown in Figure 2.5 onto the 3D frequency plane  $f_y = 0$ .

Also, the indistinguishability of some propagating 4D BB-BP ST PWs observed on a line can be explained using the ROSs of the spectra  $PW_{2CP}(f_x, f_{ct})$ . According to (2.35), the ROS of any  $PW_{2CP}(f_x, f_{ct})$ , which is associated with a DOA  $\hat{\mathbf{d}}_C = [d_{x_C} \ d_y \ d_z]$ ; where  $d_{x_C}$  is a constant such that  $|d_{x_C}| \leq 1$  and  $d_y$  and  $d_z$  varies such that  $d_y^2 + d_z^2 = 1 - d_{x_C}^2$ , is

on the 2D parametric-line  $d_{x_C} f_{ct}, f_{ct}$ . Hence, it is impossible to distinguish 4D BB-BP ST PWs  $pw_{4CP}(x, y, z, t)$  in terms of the associated DOAs by observing the ROSs of the spectra of 2D BB-BP ST PWs  $pw_{2CP}(x, y, t)$  observed along the  $x$ -axis if the Cartesian components of the DOAs are related such that  $d_y^2 + d_z^2 = 1 - d_{x_C}^2$ , where the constant  $|d_{x_C}| \leq 1$ .

As deduced in (2.17) and (2.27), the spectrum  $\mathbf{EPW}_{2CP}(f_x, f_{ct})$  of the electric-field component  $\mathbf{epw}_{2CP}(x, t)$  observed on the line along the  $x$ -axis in 3D space in response to 4D EM BB-BP ST PW  $\mathbf{empw}_{4CP}(x, y, z, t)$  can be expressed as

$$\mathbf{EPW}_{2CP}(f_x, f_{ct}) = \hat{\mathbf{E}}_1^{\text{pol}} PW_{2CP_1}(f_x, f_{ct}) + \hat{\mathbf{E}}_2^{\text{pol}} PW_{2CP_2}(f_x, f_{ct}). \quad (2.37)$$

where the 2D-CDFT pairs of the scalar-valued 2D BB-BP ST PWs are denoted by  $pw_{2CP_1}(x, t) \xleftrightarrow{2D\text{-CDFT}} PW_{2CP_1}(f_x, f_{ct})$  and  $pw_{2C_2}(x, t) \xleftrightarrow{2D\text{-CDFT}} PW_{2CP_2}(f_x, f_{ct})$ . Here also, the spectral components of  $PW_{2CP_1}(f_x, f_t)$  and  $PW_{2CP_2}(f_x, f_t)$  can be resolved separately even though their ROSs are coincided in 2D frequency-space  $(f_x, f_{ct}) \in \mathbb{R}^2$ , because the unit vectors  $\hat{\mathbf{E}}_1^{\text{pol}}$  and  $\hat{\mathbf{E}}_2^{\text{pol}}$  are orthogonal to each other.

## 2.4 EM BB-BP Signals Received by Arrays of Antennas

In array processing applications considered here, the propagating EM waves are received by arrays of antennas; in particular, 2D uniformly distributed planar antenna arrays (2D-UDPAs) (e.g. FPAs) and 1D uniformly distributed antenna arrays (1D-UDAAs). The signals induced in the broadband elemental antennas in such arrays are subsequently processed in order to extract the desired information carried by the propagating EM waves. In the following, a detailed analysis is given on the reception of EM ST PWs by a broadband elemental antenna in an uniformly distributed array.

A typical scenario of a 2D-UDPA used in receiving EM ST PWs is shown in Figure 2.8. Here, it is assumed that the propagating EM 4D BB-BP ST PW  $\mathbf{empw}_{4DP}(x, y, z, t)$  emanating from a point source in the sky at the inclination angle  $\theta_0$  and azimuth angle

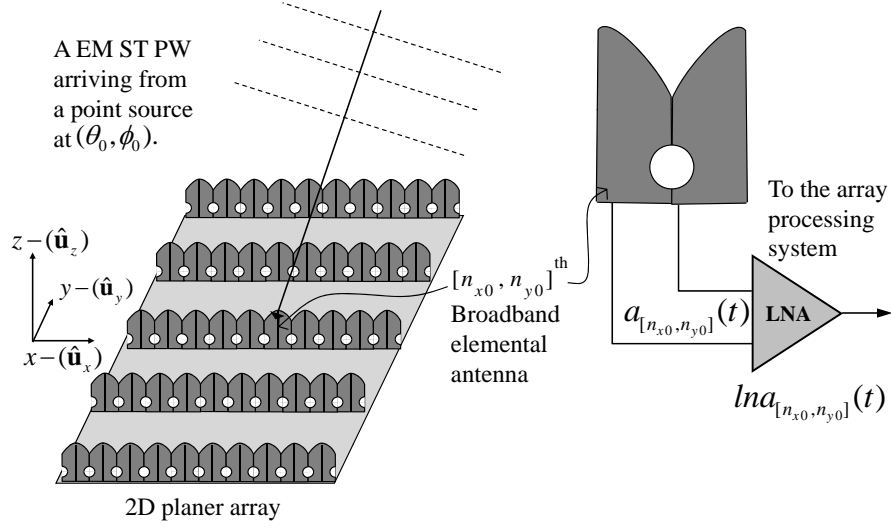


Figure 2.8: A propagating EM ST PW is received by a 2D-UDPA consisted of broadband elemental antennas. The signal  $a_{[n_{x0}, n_{y0}]}(t)$  is observed at the output of  $[n_{x0}, n_{y0}]^{\text{th}}$  element in response to the propagating EM 4D ST PW  $\mathbf{empw}_{4\text{CP}}(x, y, z, t)$  emanating from a point source at  $(\theta_0, \phi_0)$  on the sky.

$\phi_0$  is received on the 2D planar array on the plane  $z = 0$  in 3D space. Also, the output terminals of each elemental antenna of the array is connected to a low noise amplifier (LNA) having *matched input impedance* [75][76][77]. The signal observed at the output terminals of the  $[n_{x0}, n_{y0}]^{\text{th}}$  elemental antenna in response to the arriving EM 4D BB-BP ST PW  $\mathbf{empw}_{4\text{CP}}(x, y, z, t)$  is denoted by  $a_{[n_{x0}, n_{y0}]}(t)$ . According to [78](ch. 4),  $a_{[n_{x0}, n_{y0}]}(t)$  depends on the *vector valued antenna response pattern*  $\mathbf{AR}_{[n_x, n_y]}(\theta, \phi, f_{ct})$  at  $(\theta_0, \phi_0)$  for  $[n_{x0}, n_{y0}]^{\text{th}}$  elemental antenna and the spectral content of the wavefront function  $W_{\text{CP}}(cf_{ct})$  associated with the electric-field component  $\mathbf{epw}_{4\text{CP}}(x, y, z, t)$  of the 4D EM BB-BP ST PW  $\mathbf{empw}_{4\text{CP}}(x, y, z, t)$ .

### 2.4.1 Antenna Response Pattern

The vector-valued antenna response pattern  $\mathbf{AR}_{[n_x, n_y]}(\theta, \phi, f_{ct})$  of the  $[n_x, n_y]^{\text{th}}$  elemental antenna may be specified as the combined response

$$\mathbf{AR}_{[n_x, n_y]}(\theta, \phi, f_{ct}) = ARX_{[n_x, n_y]}(\theta, \phi, f_{ct}) \hat{\mathbf{u}}_x + ARY_{[n_x, n_y]}(\theta, \phi, f_{ct}) \hat{\mathbf{u}}_y + ARZ_{[n_x, n_y]}(\theta, \phi, f_{ct}) \hat{\mathbf{u}}_z, \quad (2.38)$$

of the  $\hat{\mathbf{u}}_x$ -,  $\hat{\mathbf{u}}_y$ - and  $\hat{\mathbf{u}}_z$ - components that are specified in terms of the scalar-valued response patterns  $ARX_{[n_x, n_y]}(\theta, \phi, f_{ct})$ ,  $ARY_{[n_x, n_y]}(\theta, \phi, f_{ct})$  and  $ARZ_{[n_x, n_y]}(\theta, \phi, f_{ct})$ , respectively. Note that  $ARX_{[n_x, n_y]}(\theta, \phi, f_{ct})$  determines the signal observed at the output terminals of the  $[n_x, n_y]^{\text{th}}$  elemental antenna in response to a unit amplitude linear-polarized EM 4D ST PW having the electric-field in the direction of unit vector  $\hat{\mathbf{u}}_x$  that has been emanating from a monochromatic point source of temporal frequency  $cf_{ct}$  where its position in the sky is given by the inclination angle  $\theta$  and azimuth angle  $\phi$ . Similarly,  $ARY_{[n_x, n_y]}(\theta, \phi, f_{ct})$  and  $ARZ_{[n_x, n_y]}(\theta, \phi, f_{ct})$  determine the antenna responses to linear-polarized EM 4D ST PWs having the electric-field along the direction of the unit vectors  $\hat{\mathbf{u}}_y$  and  $\hat{\mathbf{u}}_z$ , respectively.

### 2.4.2 The Relationship Between Antenna Response Pattern and Active Element Pattern

According to the *reciprocity-theorem* [79][80], for the  $[n_{x0}, n_{y0}]^{\text{th}}$  elemental antenna in a uniformly distributed array, the antenna response pattern  $\mathbf{AR}_{[n_{x0}, n_{y0}]}(\theta, \phi, f_{ct})$ , in receiving EM signals, and the *active element pattern* [81]  $\mathbf{AT}_{[n_{x0}, n_{y0}]}(\theta, \phi, f_{ct})$ , in transmitting EM signals, are related such that

$$\mathbf{AR}_{[n_{x0}, n_{y0}]}(\theta, \phi, f_{ct}) = C_{\text{TxRx}} \mathbf{AT}_{[n_{x0}, n_{y0}]}(\theta, \phi, f_{ct}), \quad (2.39)$$

where  $C_{\text{TxRx}}$  is the constant of proportionality [78](ch. 4). As defined in [53](pp. 106-112), the vector-valued active element pattern  $\mathbf{AT}_{[n_{x0}, n_{y0}]}(\theta, \phi, f_{ct})$  specifies the orientation, magnitude and phase of the electric-field at the direction given by the inclination angle

$\theta$  and azimuth angle  $\phi$  in the far-field, when the  $[n_{x0}, n_{y0}]^{\text{th}}$  element is excited with a unit amplitude signal of temporal frequency  $cf_{ct}$  while all other elemental antennas are terminated with matching impedances. The mutual coupling among the elemental antennas in the array effects the active element pattern therefore, it is different from the isolated antenna element pattern [81]. For example, active element patterns may have nulls called *scan blind spots* [53](pp. 103), even though the isolated element pattern shows no such nulls.

In hypothetical infinite-extent uniformly distributed arrays, the active element pattern is identical for each elemental antennas because each elemental antenna is subjected to the same mutual coupling scenario [81]. Hence, the active element pattern for an infinite-extent array may be given by

$$\mathbf{AT}_{[n_{x0}, n_{y0}]}(\theta, \phi, f_{ct}) = \mathbf{AT}_O(\theta, \phi, f_{ct}), \quad (2.40)$$

where  $\mathbf{AT}_O(\theta, \phi, f_{ct})$  is the elemental antenna pattern of the element at the origin O [81]. However, in finite-extent uniformly distributed arrays, the active element pattern  $\mathbf{AT}_{[n_x, n_y]}(\theta, \phi, f_{ct})$  depends on the position  $(n_x, n_y)$  of the elemental antenna in the array. For example, in a 2D-UDPA the active element pattern of an element near the center of the array may differ significantly from that of an element at the edge of the array due to the difference between the two mutual coupling scenarios [81]. However, given an array contain more than 100 elemental antennas, adding “*dummy-elements*” around the edge of an array is expected to create a mutual coupling scenario that is almost identical at each element resulting a *pseudo-infinite array*. This has been attempted in the “Phased Array Demonstrator” (PHAD) [20], which has been designed and implemented by the Dominion Radio Astrophysical Observatory (DRAO), BC, Canada. For such arrays, the active element pattern  $\mathbf{AT}_{[n_x, n_y]}(\theta, \phi, f_{ct})$  of any  $(n_x, n_y)^{\text{th}}$  element can be approximated with  $\mathbf{AT}_C(\theta, \phi, f_{ct})$  that corresponds to an element near the center of a finite array. This approximation simplifies the analysis of array response and subsequently eases the beam

synthesis.

In practice, the antenna response pattern  $\mathbf{AR}_C(\theta, \phi, f_{ct})$  of a pseudo infinite-extent array is determined using the reciprocity relationship given in (2.39) that in turn requires the evaluation of active element pattern  $\mathbf{AT}_C(\theta, \phi, f_{ct})$  for the respective array. Theoretical, numerical and empirical methods have been used in determining the active element patterns of antenna arrays of different element arrangements and those employ different types of elemental antennas. In [53], an extensive theoretical study is given on the infinite-extent and finite-extent antenna arrays using “Floquet Series” expansion of the EM modes associate with such arrays. Evaluation of wideband active element patterns using numerical methods based on Finite-Difference Time-Domain (FDTD), Method of Moments (MoM) and their variants are given in [82][83][84][85][86][87][88]. Finally, experimental analysis of active element patterns are given in [89][90][91][92].

#### 2.4.3 An Example for an Active Element Pattern

The Phased Array Demonstrator (PHAD) is a working engineering prototype that has been used as the front-end of a focal plane array (FPA) receiver [20][92]. In PHAD, 180 linear polarized wideband Vivaldi elements are arranged in a square grid, where two elements are fixed perpendicular to each other at each grid point in order to receive the two orthogonal polarized components of EM signals of interest [20]. PHAD has been designed to cover the frequency range 1-2 GHz and the inter element distance has been set to the half wavelength at 2 GHz [20]. As mentioned earlier, PHAD contains dummy elements around the edge of the array so that the active element pattern  $\mathbf{AT}_{[n_x, n_y]}(\theta, \phi, f_{ct})$  for any elemental Vivaldi antenna can be approximated by active element pattern  $\mathbf{AT}_C(\theta, \phi, f_{ct})$  of an element near the center of the array.

For a Vivaldi elemental antenna in PHAD that is arranged in the direction of  $\hat{\mathbf{u}}_x$  (see



Figure 2.8), the active element pattern is given by

$$\mathbf{AT}_C(\theta, \phi, f_{ct}) = ATX_C(\theta, \phi, f_{ct}) \hat{\mathbf{u}}_x, \quad (2.41)$$

where the  $\hat{\mathbf{u}}_y$ - and  $\hat{\mathbf{u}}_z$ - components are  $ATY_C(\theta, \phi, f_{ct}) = 0$  and  $ATZ_C(\theta, \phi, f_{ct}) = 0$ . At the temporal frequency  $cf_{ct_0} = 1.45$  GHz, the normalized magnitude of the  $\hat{\mathbf{u}}_x$ -component of the active element pattern  $ATX_C(\theta, \phi, f_{ct_0})$  for the azimuth angles  $\phi = 0^\circ, 45^\circ$  and  $90^\circ$  are shown in Figure 2.9 (right) and for the azimuth angles  $\phi = 135^\circ, 180^\circ$  and  $270^\circ$  are shown in Figure 2.9 (left). According to Figure 2.9,  $ATX_C(\theta, \phi, f_{ct})$  is almost independent of  $\phi$  therefore, it is nearly circular symmetric around the  $z$ -axis. Also according to Figure 2.9, there are no deep nulls in the upper-hemispherical angular-range  $\theta \in [0^\circ, 90^\circ]$  for  $\phi = 0^\circ, 45^\circ, 90^\circ, 180^\circ, 225^\circ$  and  $270^\circ$ ; thus,  $\mathbf{AT}_C(\theta, \phi, cf_{ct_0})$  of PHAD does not show any scan blindness at  $cf_{ct_0} = 1.45$  GHz in this angular-range. However, a gradual reduction of magnitude is observed as  $\theta$  increases from  $0^\circ$  to  $90^\circ$ . It is expected that  $\mathbf{AT}_C(\theta, \phi, f_{ct})$  remains almost identical to that of  $\mathbf{AT}_C(\theta, \phi, cf_{ct_0})$  for all temporal frequencies  $cf_{ct} \in [1, 2]$  GHz.

#### 2.4.4 Signals Induced at an Elemental Antenna in Response to Propagating EM signals and the Corresponding Spectra

Let's reexamine the scenario of EM wave reception using a 2D-UDPA as shown in Figure 2.8, exploiting the facts stated in subsections 2.4.1, 2.4.2 and 2.4.3. Specifically, the EM 4D BB-BP ST PW  $\mathbf{empw}_{4CP}(x, y, z, t)$  is emanating from a point source in the sky at the inclination angle  $\theta_0$  and azimuth angle  $\phi_0$  and it is received by a pseudo-infinite 2D-UDPA on the plane  $z = 0$  in 3D space. It is assumed that this 2D-UDPA contains linear-polarized elemental antennas oriented along the direction of  $\hat{\mathbf{u}}_x$  (e.g. PHAD; subsection 2.4.3) that are arranged on a rectangular grid at intervals of  $\Delta_x$  and  $\Delta_y$  along the  $x$ -axis and  $y$ -axis, respectively. The output of each elemental antenna is connected to a matching LNA.

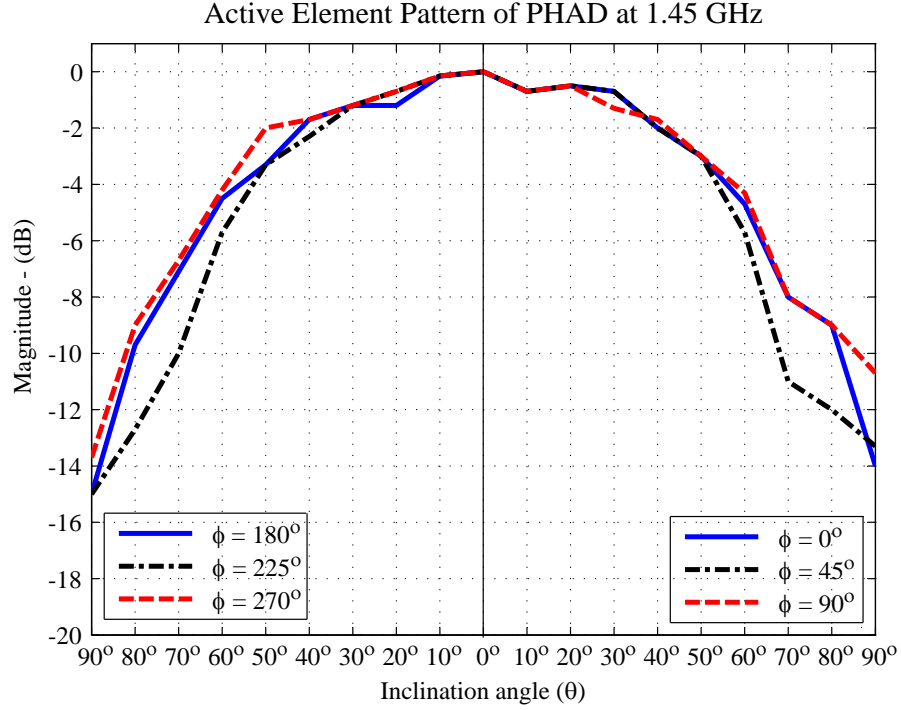


Figure 2.9: The normalized magnitude of the  $\hat{\mathbf{u}}_x$ -component of the active element pattern  $ATX_C(\theta, \phi, f_{ct_0})$  at  $cf_{ct_0} = 1.45$  GHz for the azimuth angles  $\phi = 0^\circ, 45^\circ$  and  $90^\circ$  (right) and for the azimuth angles  $\phi = 180^\circ, 225^\circ$  and  $270^\circ$  (left). (Recreated using the data extracted from the Figure 3 in [92].)

According to (2.39) and (2.41), the antenna response pattern of any elemental antenna in this pseudo-infinite 2D-UDPA may be expressed by

$$\mathbf{AR}_C(\theta, \phi, f_{ct}) = ARX_C(\theta, \phi, f_{ct}) \hat{\mathbf{u}}_x. \quad (2.42)$$

Also according to subsection 2.2.1, the electric-field component  $\mathbf{epw}_{4CP}(x, y, z, t)$  of the propagating EM 4D BB-BP ST PW  $\mathbf{empw}_{4CP}(x, y, z, t)$  may be decomposed with respect to the linear polarized antenna response pattern  $ARX(\theta, \phi, f_{ct}) \hat{\mathbf{u}}_x$ , such that

$$\mathbf{epw}_{4CP}(x, y, z, t) = pw_{4CP_O}(x, y, z, t) \hat{\mathbf{u}}_x + pw_{4CP_X}(x, y, z, t) \hat{\mathbf{u}}_x^\perp, \quad (2.43)$$

where  $\hat{\mathbf{u}}_x$  is the unit “*co-polar*” vector along the  $x$ -axis and  $\hat{\mathbf{u}}_x^\perp$  is the unit “*cross-polar*” vector, which is orthogonal to  $\hat{\mathbf{u}}_x$ . Hence, the scalar-valued 4D BB-BP ST PW

$pw_{4\text{CP}_O}(x, y, z, t)$  is called as the co-polar component where as  $pw_{4\text{CP}_X}(x, y, z, t)$  is called as the cross-polar component of  $\mathbf{epw}_{4\text{CP}}(x, y, z, t)$ . Thus following (2.17) and (2.13),  $\mathbf{EPW}_{4\text{CP}}(f_x, f_y, f_z, f_{ct})$ , the 4D-CDFT of  $\mathbf{epw}_{4\text{CP}}(x, y, z, t)$ , can be expressed as

$$\begin{aligned} \mathbf{EPW}_{3\text{CP}}(f_x, f_y, f_z, f_{ct}) = & W_{\text{CP}_O} cf_{ct} \delta(d_{x0}f_{ct} - f_x)\delta(d_{y0}f_{ct} - f_y)\delta(d_{z0}f_{ct} - f_z) \hat{\mathbf{u}}_x \\ & + W_{\text{CP}_X} cf_{ct} \delta(d_{x0}f_{ct} - f_x)\delta(d_{y0}f_{ct} - f_y)\delta(d_{z0}f_{ct} - f_z) \hat{\mathbf{u}}_x^\perp, \end{aligned} \quad (2.44)$$

where  $d_{x0} = \sin(\theta_0) \cos(\phi_0)$ ,  $d_{y0} = \sin(\theta_0) \sin(\phi_0)$  and  $d_{z0} = \cos(\theta_0)$ . In (2.44),  $W_{\text{CP}_O}(cf_{ct})$  and  $W_{\text{CP}_X}(cf_{ct})$  denote the 1D-CDFTs of 1D BB-BP wavefront functions  $w_{\text{CP}_O}(t)$  and  $w_{\text{CP}_X}(t)$ , which are associated with the co-polar component  $pw_{4\text{CP}_O}(x, y, z, t)$  and cross-polar component  $pw_{4\text{CP}_X}(x, y, z, t)$ , respectively.

### The Antenna Frequency Response

As shown in Figure 2.8, the signal observed at the output terminals of the  $[n_{x0}, n_{y0}]^{\text{th}}$  elemental antenna in response to the received EM 4D BB-BP ST PW  $\mathbf{epw}_{4\text{CP}}(x, y, z, t)$  is denoted by  $a_{[n_{x0}, n_{y0}]}(t)$ . Following [78](ch. 4) and [93], it can be shown that  $A_{[n_{x0}, n_{y0}]}(cf_{ct})$ , the 1D-CDFT of the observed signal  $a_{[n_{x0}, n_{y0}]}(t)$ , is given by

$$A_{[n_{x0}, n_{y0}]}(cf_{ct}) = ARX_C(\theta_0, \phi_0, f_{ct}) W_{\text{CP}_O}(cf_{ct}) PS_{[n_{x0}, n_{y0}]}(\theta_0, \phi_0, f_{ct}), \quad (2.45)$$

where

$$\begin{aligned} PS_{[n_{x0}, n_{y0}]}(\theta_0, \phi_0, f_{ct}) & \triangleq e^{j2\pi \sin(\theta_0) \cos(\phi_0) f_{ct} \Delta_x n_{x0}} e^{j2\pi \sin(\theta_0) \sin(\phi_0) f_{ct} \Delta_y n_{y0}}, \\ & \triangleq e^{j2\pi d_{x0} f_{ct} \Delta_x n_{x0}} e^{j2\pi d_{y0} f_{ct} \Delta_y n_{y0}}, \end{aligned} \quad (2.46)$$

which specifies the phase-shift of the signal due to the displacement of the elemental antenna from the origin of the 2D-UDPA. Here, it is assumed the cross-polar response of the elemental antenna is negligible. *Exploiting the unique relationship between the DOA of the propagating EM 4D BB-BP ST PW  $\mathbf{epw}_{4\text{CP}}(x, y, z, t)$ , specified by  $(\theta_0, \phi_0)$ , and the ROS of spectrum of its electric-field component  $\mathbf{EPW}_{4\text{CP}}(f_x, f_y, f_z, f_{ct})$ , specified by*

the parametric equations of the 4D hyper-line

$$d_{x0}f_{ct}, d_{y0}f_{ct}, d_{z0}f_{ct}, f_{ct} \equiv \sin(\theta_0)\cos(\phi_0)f_{ct}, \sin(\theta_0)\sin(\phi_0)f_{ct}, \cos(\theta_0)f_{ct}, f_{ct},^{10}$$

in  $(f_x, f_y, f_z, f_{ct}) \in \mathbb{R}^4$ , the vector valued **antenna frequency response function**  $\mathbf{AF}(f_x, f_y, f_z, f_{ct})$ , can be defined such that

$$\mathbf{AF}(d_{x0}f_{ct}, d_{y0}f_{ct}, d_{z0}f_{ct}, f_{ct}) \triangleq \mathbf{AR}_C(\theta_0, \phi_0, f_{ct}), \quad (2.47)$$

where the  $\hat{\mathbf{u}}_x$ -,  $\hat{\mathbf{u}}_y$ - and  $\hat{\mathbf{u}}_z$ - components of  $\mathbf{AF}(f_x, f_y, f_z, f_{ct})$  are given by

$$\begin{aligned} AFX(d_{x0}f_{ct}, d_{y0}f_{ct}, d_{z0}f_{ct}, f_{ct}) &= ARX_C(\theta_0, \phi_0, f_{ct}), \\ AFY(d_{x0}f_{ct}, d_{y0}f_{ct}, d_{z0}f_{ct}, f_{ct}) &= ARY_C(\theta_0, \phi_0, f_{ct}), \\ AFZ(d_{x0}f_{ct}, d_{y0}f_{ct}, d_{z0}f_{ct}, f_{ct}) &= ARZ_C(\theta_0, \phi_0, f_{ct}). \end{aligned} \quad (2.48)$$

According to the definition given in (2.47),  $\mathbf{AF}(f_x, f_y, f_z, f_{ct})$  is defined only in the inside of the volume of 4D double right-spherical hyper-cone in  $(f_x, f_y, f_z, f_{ct}) \in \mathbb{R}^4$  that is introduced in subsection 2.3.1. For the rest of 4D frequency space  $(f_x, f_y, f_z, f_{ct}) \in \mathbb{R}^4$ ,  $\mathbf{AF}(f_x, f_y, f_z, f_{ct})$  remains undefined.

Following (2.48) and *exploiting the sampling property of the unit impulse function*  $\delta(\cdot)$  [44] (pp. 14-15), (2.46) can be expressed as a *triple-integral*

$$\begin{aligned} A_{[n_{x0}, n_{y0}]}(cf_{ct}) &= \iiint_{f_x, f_y, f_z = -\infty}^{+\infty} AFX(f_x, f_y, f_z, f_{ct}) e^{j2\pi f_x \Delta_x n_{x0}} e^{j2\pi f_y \Delta_y n_{y0}} \\ &\quad W_{\text{CP}_O}(cf_{ct}) \delta(d_{x0}f_{ct} - f_x) \delta(d_{y0}f_{ct} - f_y) \delta(d_{z0}f_{ct} - f_z) df_x df_y df_z. \end{aligned} \quad (2.49)$$

in the 3D frequency space  $(f_x, f_y, f_z) \in \mathbb{R}^3$ . However, according to (2.44), (2.49) can be rewritten as

$$\begin{aligned} A_{[n_{x0}, n_{y0}]}(cf_{ct}) &= \\ &\iiint_{f_x, f_y, f_z = -\infty}^{+\infty} AFX(f_x, f_y, f_z, f_{ct}) PW_{4\text{CP}_O}(f_x, f_y, f_z, f_{ct}) e^{j2\pi f_x \Delta_x n_{x0}} e^{j2\pi f_y \Delta_y n_{y0}} df_x df_y df_z, \end{aligned} \quad (2.50)$$

---

<sup>10</sup>These equations for 4DHLin<sub>ROS</sub> have been stated previously in (2.15) and (2.16), respectively.

where  $PW_{4CP_O}(f_x, f_y, f_z, f_t)$  is the 4D-CDFT of  $pw_{4CP_O}(x, y, z, t)$ .

Generalizing (2.50), the spectral response  $A_{[n_{x0}, n_{y0}]}(cf_{ct})$  of the  $(n_{x0}, n_{y0})^{\text{th}}$  elemental antenna of a 2D-UDPA on the plane  $z = 0$  in 3D space, which is having an arbitrary antenna response function  $\mathbf{AF}(f_x, f_y, f_z, f_{ct})$ , to an arbitrary EM 4D BB-BP ST PW  $\mathbf{empw}_{4CP}(x, y, z, t)$ , can be expressed using the *vector dot product*, such that

$$A_{[n_{x0}, n_{y0}]}(cf_{ct}) = \int_{f_x, f_y, f_z=-\infty}^{+\infty} \left\{ \mathbf{AF}(f_x, f_y, f_z, f_{ct}) \bullet \mathbf{EPW}_{4CP}(f_x, f_y, f_z, f_{ct}) \right\} e^{j2\pi f_x \Delta_x n_{x0}} e^{j2\pi f_y \Delta_y n_{y0}} df_x df_y df_z, \quad (2.51)$$

where  $\mathbf{EPW}_{4CP}(f_x, f_y, f_z, f_{ct})$  is the 4D-CDFT of  $\mathbf{epw}_{4CP}(x, y, z, t)$ , which is the electric-field component of  $\mathbf{empw}_{4CP}(x, y, z, t)$ . Any arbitrary electric-field can be expressed as a linear combination of propagating EM 4D ST PWs such that  $\mathbf{ef}_{4C}(x, y, z, t) = \sum_i \mathbf{epw}_{4C_i}(x, y, z, t)$  [94](pp. 24). Hence, the spectrum  $A_{[n_{x0}, n_{y0}]}(cf_{ct})$  of the observed signal in response to  $\mathbf{ef}_{4C}(x, y, z, t)$ , is given by

$$A_{[n_{x0}, n_{y0}]}(cf_{ct}) = \int_{f_x, f_y, f_z=-\infty}^{+\infty} \left\{ \mathbf{AF}(f_x, f_y, f_z, f_{ct}) \bullet \mathbf{EF}_{4C}(f_x, f_y, f_z, f_{ct}) \right\} e^{j2\pi f_x \Delta_x n_{x0}} e^{j2\pi f_y \Delta_y n_{y0}} df_x df_y df_z, \quad (2.52)$$

where  $\mathbf{ef}_{4C}(x, y, z, t) \xleftrightarrow{4D\text{-CDFT}} \mathbf{EF}_{4C}(f_x, f_y, f_z, f_t)$ .

### The Antenna Impulse Response

The signal  $a_{[n_{x0}, n_{y0}]}(t)$ , observed at the terminals of  $[n_{x0}, n_{y0}]^{\text{th}}$  elemental antenna in response to an arbitrary EM field  $\mathbf{ef}_{4CP}(x, y, z, t)$ , can be determined by evaluating the inverse 1D-CDFT integral

$$a_{[n_{x0}, n_{y0}]}(t) = \int_{cf_{ct}=-\infty}^{+\infty} A_{[n_{x0}, n_{y0}]}(cf_{ct}) e^{j2\pi\{cf_{ct}\}t} d\{cf_{ct}\}. \quad (2.53)$$

Substituting for  $A_{[n_{x0}, n_{y0}]}(cf_{ct})$  in (2.53) with (2.52) yields a *quadruple-integral*

$$a_{[n_{x0}, n_{y0}]}(t) = \int_{f_x, f_y, f_z, cf_{ct}=-\infty}^{+\infty} \mathbf{AF}(f_x, f_y, f_z, f_{ct}) \bullet \mathbf{EF}_{4\text{CP}}(f_x, f_y, f_z, f_{ct}) e^{j2\pi f_x \Delta_x n_{x0}} e^{j2\pi f_y \Delta_y n_{y0}} e^{j2\pi cf_{ct} t} df_x df_y df_z dcf_{ct}, \quad (2.54)$$

in the 4D frequency space  $(f_x, f_y, f_z, f_{ct}) \in \mathbb{R}^4$ . According to [41](ch. 6), (2.54) is the inverse 4D-CDFT of the vector dot product  $\mathbf{AF}(f_x, f_y, f_z, f_{ct}) \bullet \mathbf{EF}_{4\text{CP}}(f_x, f_y, f_z, f_{ct})$  evaluated for  $t \in \mathbb{R}$  at  $x = \Delta_x n_{x0}$ ,  $y = \Delta_y n_{y0}$  and  $z = 0$ . Using the properties of *mD* CDFT [44](pp. 25), (2.54) can be evaluated such that

$$a_{[n_{x0}, n_{y0}]}(t) = \iiint_{x, y, z=-\infty}^{+\infty} \{\mathbf{ai}(x, y, z, t) \odot \odot \odot \odot \mathbf{ef}_{4\text{CP}}(x, y, z, t)\} \delta(x - \Delta_x n_{x0}) \delta(y - \Delta_y n_{y0}) \delta(z) dx dy dz, \quad (2.55)$$

where  $\mathbf{ai}(x, y, z, t)$  is defined as the *antenna impulse response* and where “ $\odot \odot \odot \odot$ ” denotes the combined *vector dot-product and 4D convolution* operation. Note that the vector-valued ***antenna impulse response***  $\mathbf{ai}(x, y, z, t)$  and the vector-valued antenna frequency response function  $\mathbf{AF}(f_x, f_y, f_z, f_{ct})$  are related through the 4D-CDFT, where the  $\hat{\mathbf{u}}_x$ -,  $\hat{\mathbf{u}}_y$ - and  $\hat{\mathbf{u}}_z$ - components of  $\mathbf{ai}(x, y, z, t)$  are given by

$$\begin{aligned} a_{ix}(x, y, z, t) &\stackrel{4\text{D-CDFT}}{\longleftrightarrow} AF_X(f_x, f_y, f_z, f_{ct}), \\ a_{iy}(x, y, z, t) &\stackrel{4\text{D-CDFT}}{\longleftrightarrow} AF_Y(f_x, f_y, f_z, f_{ct}), \\ a_{iz}(x, y, z, t) &\stackrel{4\text{D-CDFT}}{\longleftrightarrow} AF_Z(f_x, f_y, f_z, f_{ct}). \end{aligned} \quad (2.56)$$

According to [44](ch. 3.1-3.2), the mathematical operations in the right hand side of (2.55) can be interpreted as the *spatial-sampling* of electric-field component  $\mathbf{ef}_{4\text{CP}}(x, y, z, t)$  with the *non-ideal sampling function* of antenna impulse response  $\mathbf{ai}(x, y, z, t)$  at  $x = \Delta_x n_{x0}$ ,  $y = \Delta_y n_{y0}$  and  $z = 0$ , where the  $[n_{x0}, n_{y0}]^{\text{th}}$  elemental antenna is located in 3D space.

## 2.5 3D Spectra of the Signals Observed at the Terminals of 2D Planar Array

Consider an ideal infinite-extent 3D *mixed-domain*<sup>11</sup> signal sequence  $a_{3\text{MP}}(n_x, n_y, t)$  that corresponds to the group of temporal signals  $a_{[n_x, n_y]}(t)$  observed at the output of the  $(n_x, n_y)^{\text{th}}$  elemental antenna in a pseudo-infinite 2D-UDPA on the plane  $z = 0$  in 3D space in response to a propagating EM 4D BB-BP ST PW  $\mathbf{empw}_{4\text{CP}}(x, y, z, t)$  having the DOA  $[d_{x0} \ d_{y0} \ d_{z0}]$ . In this particular array, the elemental antennas are arranged in a square grid at intervals of  $\Delta_{xy}$  and the output of each elemental antenna is connected to a matching LNA. As in the case of PHAD (see subsection 2.4.3), each grid point of this array is fixed with two linear-polarized wideband elemental antennas (e.g. Vivaldi elements) perpendicular to each other along the directions  $\hat{\mathbf{u}}_x$  and  $\hat{\mathbf{u}}_y$  in order to receive the two orthogonally polarized components of  $\mathbf{empw}_{4\text{CP}}(x, y, z, t)$ . For simplicity, the following analysis of spectral properties is limited to a part of  $a_{3\text{MP}}(n_x, n_y, t)$ , which correspond to the elemental antennas oriented along the direction of  $\hat{\mathbf{u}}_x$ . Identical spectral properties are expected for the rest of  $a_{3\text{MP}}(n_x, n_y, t)$ , which correspond to the elemental antennas oriented along the direction of  $\hat{\mathbf{u}}_y$ .

For the elemental antennas oriented along the direction of  $\hat{\mathbf{u}}_x$  of this particular 2D-UDPA, according to (2.42), (2.48) and (2.56), the antenna impulse response can be expressed as

$$\mathbf{ai}(x, y, z, t) = a_{ix}(x, y, z, t) \hat{\mathbf{u}}_x. \quad (2.57)$$

Hence following (2.55), the 3D mixed-domain antenna signal sequence  $a_{3\text{MP}}(n_x, n_y, t)$  can be expressed as

$$a_{3\text{MP}}(n_x, n_y, t) = apwx_{3\text{CP}}(x, y, t) \sum_{n_x=-\infty}^{+\infty} \sum_{n_y=-\infty}^{+\infty} \delta(x - \Delta_{xy}n_x) \delta(y - \Delta_{xy}n_y), \quad (2.58)$$

---

<sup>11</sup>In this case, discrete in the spatial domain on the  $xy$ -plane and continuous in the temporal domain.

where the *equivalent 3D continuous-domain antenna output function* is defined as

$$apwx_{3\text{CP}}(x, y, t) \triangleq \int_{z=-\infty}^{+\infty} \{aix(x, y, z, t) * * * pw_{4\text{CP}_O}(x, y, z, t)\} \delta(z) dz, \quad (2.59)$$

where  $pw_{4\text{CP}_O}(x, y, z, t)$  is the co-polar component of  $\mathbf{empw}_{4\text{CP}}(x, y, z, t)$  along  $\hat{\mathbf{u}}_x$  (see (2.43)) and where “\*\*\*\*” denotes the 4D convolution operation.

In order to analyze the spectral properties of the 3D mixed-domain antenna signals  $a_{3\text{MP}}(n_x, n_y, t)$ , its 3D mixed-domain Fourier transform (3D-MDFT) is evaluated. The 3D-MDFT of  $a_{3\text{MP}}(n_x, n_y, t)$  defined by

$$A_{3\text{MP}}(e^{j\omega_x}, e^{j\omega_y}, f_{ct}) \triangleq \int_{t=-\infty}^{+\infty} \sum_{n_x=-\infty}^{+\infty} \sum_{n_y=-\infty}^{+\infty} a_{3\text{MP}}(n_x, n_y, t) e^{-j\omega_x n_x} e^{-j\omega_y n_y} e^{-j2\pi c f_{ct} t} dt, \quad (2.60)$$

where  $(\omega_x, \omega_y, f_{ct}) \in \mathbb{R}^3$  [41](ch.6). Nevertheless, according to [44](pp. 56-57), the 3D-MDFT  $A_{3\text{MP}}(e^{j\omega_x}, e^{j\omega_y}, f_{ct})$  may be expressed in the form

$$A_{3\text{MP}}(e^{j\omega_x}, e^{j\omega_y}, f_{ct}) = \frac{1}{\Delta_{xy}^2} \sum_{m_x=-\infty}^{+\infty} \sum_{m_y=-\infty}^{+\infty} APWX_{3\text{CP}_O} \left( \frac{\omega_x - 2\pi m_x}{2\pi \Delta_{xy}}, \frac{\omega_y - 2\pi m_y}{2\pi \Delta_{xy}}, f_{ct} \right), \quad (2.61)$$

where  $APWX_{3\text{CP}_O}(f_x, f_y, f_{ct})$  is the 3D-CDFFT of the equivalent 3D continuous-domain antenna output function  $apwx_{3\text{CP}}(x, y, t)$ , which is given in (2.59). It is implied in (2.61) that  $A_{3\text{MP}}(e^{j\omega_x}, e^{j\omega_y}, f_{ct})$  is given as the infinite series of periodic copies of  $APWX_{3\text{CP}_O} \left( \frac{\omega_x}{2\pi \Delta_{xy}}, \frac{\omega_y}{2\pi \Delta_{xy}}, f_{ct} \right)$  with 2D periodicity  $(2\pi, 2\pi)$  along  $\omega_x$ - and  $\omega_y$ - axes in  $(\omega_x, \omega_y, f_{ct}) \in \mathbb{R}^3$ . Here, the spectral properties of  $A_{3\text{MP}}(e^{j\omega_x}, e^{j\omega_y}, f_{ct})$  is determined by exploiting the relationship in (2.61) that in turn requires the evaluation of the spectral properties of  $APWX_{3\text{CP}_O}(f_x, f_y, f_{ct})$  in  $(f_x, f_y, f_{ct}) \in \mathbb{R}^3$ .

### The ROS of $APWX_{3\text{CP}_O}(f_x, f_y, f_{ct})$

Following (2.59), it can be shown that

$$APWX_{3\text{CP}_O}(f_x, f_y, f_{ct}) = \int_{f_z=-\infty}^{+\infty} AFX(f_x, f_y, f_z, f_{ct}) PW_{4\text{CP}_O}(f_x, f_y, f_z, f_{ct}) df_z, \quad (2.62)$$



where  $AFX(f_x, f_y, f_z, f_{ct})$  is the  $\hat{\mathbf{u}}_x$ -component of the antenna frequency response function and is given by the 4D-CDFT of  $aix(x, y, z, t)$  and where  $PW_{4\text{CP}_O}(f_x, f_y, f_z, f_{ct})$  is the 4D-CDFT of the  $pw_{4\text{CP}_O}(x, y, z, t)$ . Substituting  $PW_{4\text{CP}_O}(f_x, f_y, f_z, f_{ct})$  in (2.62) with (2.13) yields,

$$\begin{aligned} APWX_{3\text{CP}_O}(f_x, f_y, f_{ct}) &= \int_{f_z=-\infty}^{+\infty} AFX(f_x, f_y, f_z, f_{ct}) W_{\text{CP}_O}(cf_{ct}) \delta(d_{x0}f_{ct} - f_x) \delta(d_{y0}f_{ct} - f_y) \delta(d_{z0}f_{ct} - f_z) df_z, \\ &= AFX(f_x, f_y, d_{z0}f_{ct}, f_{ct}) W_{\text{CP}_O}(cf_{ct}) \delta(d_{x0}f_{ct} - f_x) \delta(d_{y0}f_{ct} - f_y). \end{aligned} \quad (2.63)$$

Note that in (2.63),  $AFX(f_x, f_y, d_{z0}f_{ct}, f_{ct})$  represents the slice of the 4D continuous-domain antenna response function ( $\hat{\mathbf{u}}_x$ -component)  $AFX(f_x, f_y, f_z, f_{ct})$  taken on the plane  $f_z = d_{z0}f_{ct}$  in 4D frequency-space. Such a relationship can be expressed as a 3D continuous-domain parametric-function  $AFX_{[d_z]}(f_x, f_y, f_{ct})$  of the parameter  $d_z$  in  $(f_x, f_y, f_{ct}) \in \mathbb{R}^3$  that is defined as

$$AFX_{[d_z]}(f_x, f_y, f_{ct}) \triangleq \int_{f_z=-\infty}^{+\infty} AFX(f_x, f_y, f_z, f_{ct}) \delta(d_z f_{ct} - f_z) df_z. \quad (2.64)$$

Hence, (2.63) can be rewritten as

$$APWX_{3\text{CP}_O}(f_x, f_y, f_{ct}) = AFX_{[d_{z0}]}(f_x, f_y, f_{ct}) PW_{3\text{CP}_O}(f_x, f_y, f_{ct}), \quad (2.65)$$

because according to (2.22),

$$W_{\text{CP}_O}(cf_{ct}) \delta(d_{x0}f_{ct} - f_x) \delta(d_{y0}f_{ct} - f_y) = PW_{3\text{CP}_O}(f_x, f_y, f_{ct}).$$

The ROS of  $APWX_{3\text{CP}_O}(f_x, f_y, f_{ct})$  is given by the *intersection* of the ROSs of  $PW_{3\text{CP}_O}(f_x, f_y, f_{ct})$  and  $AFX_{[d_z]}(f_x, f_y, f_{ct})$  in  $(f_x, f_y, f_{ct}) \in \mathbb{R}^3$ . According to subsection 2.3.2,  $PW_{3\text{CP}_O}(f_x, f_y, f_{ct})$  represents the spectrum of the 3D continuous-domain signal observed on the 3D-plane  $z = 0$  in response to the EM 4D BB-BP ST PW having the DOA  $\hat{\mathbf{d}}_0 = [d_{x0} \ d_{y0} \ d_{z0}]$ . As shown in Figure 2.4, the ROS of  $PW_{3\text{CP}_O}(f_x, f_y, f_{ct})$  is given by two line segments  $PQ$  and  $P'Q'$  on the line of intersection of the two 3D frequency

planes  $d_{x0}f_{ct} - f_x = 0$  and  $d_{y0}f_{ct} - f_y = 0$  in  $(f_x, f_y, f_{ct}) \in \mathbb{R}^3$ . Note that  $PQ$  corresponds to the positive temporal frequencies  $cf_{ct} \in \{f_C - 0.5BW, f_C + 0.5BW\}$  and  $P'Q'$  corresponds to the negative temporal frequencies  $cf_{ct} \in \{-f_C - 0.5BW, -f_C + 0.5BW\}$ . However, for all EM 4D BB-BP ST PWs having DOAs  $\hat{\mathbf{d}} = [d_x \ d_y \ d_z]$  such that  $d_x^2 + d_y^2 + d_z^2 = 1$ , the line segments corresponding to ROSs of the spectra lay inside the 3D double frustum region shown in the Figure 2.5.

Let's assume that the  $\hat{\mathbf{u}}_x$ -component of the active element pattern is *circular-symmetric* around the  $z$ -axis and its normalized-magnitude  $|ATX(\theta, \phi, f_{ct})| = 0$  in the angular-ranges  $\Theta_P = \bigcup_i \{(\theta_{Li}, \theta_{Ui})\}$  for all  $|f_{ct}| \in [c^{-1}f_C - 0.5c^{-1}BW, c^{-1}f_C + 0.5c^{-1}BW]$ . Note that according to (2.5), the DOA unit vectors  $\hat{\mathbf{d}}_P$  included in the vector-range

$$\mathbf{D}_P \in \{[d_{xP} \ d_{yP} \ d_{zP}] \mid [d_{xP} = \sin(\theta_P) \cos(\phi_P), \ d_{yP} = \sin(\theta_P) \sin(\phi_P) \ d_{zP} = \cos(\theta_P)]\}, \quad (2.66)$$

correspond to all  $\theta_P \in \Theta_P$  and  $\phi_P \in [0^\circ, 360^\circ]$ . Hence, according to the definitions (2.51) and (2.64), it can be shown that the 3D double frustum region, shown in Figure 2.5 in  $(f_x, f_y, f_{ct}) \in \mathbb{R}^3$ , is included in the ROS of  $AFX_{[d_{zP}]}(f_x, f_y, f_{ct})$  for all  $\hat{\mathbf{d}}_P \in \mathbf{D}_P$  but, is excluded in the ROS of  $AFX_{[\bar{d}_{zP}]}(f_x, f_y, f_{ct})$  for all  $\bar{\hat{\mathbf{d}}}_P \notin \mathbf{D}_P$ . Therefore, for any  $\hat{\mathbf{d}}_P \in \mathbf{D}_P$ , the ROS of  $APWX_{3\text{CPO}}(f_x, f_y, f_{ct})$  is determined by the ROS of  $PW_{3\text{CPO}}(f_x, f_y, f_{ct})$ , which is given by the two line segments  $PQ$  and  $P'Q'$  in  $(f_x, f_y, f_{ct}) \in \mathbb{R}^3$ . However, for any  $\bar{\hat{\mathbf{d}}}_P \notin \mathbf{D}_P$ ,  $APWX_{3\text{CPO}}(f_x, f_y, f_{ct}) = 0$  because there is no intersection between the ROSs of  $PW_{3\text{CPO}}(f_x, f_y, f_{ct})$  and  $AFX_{[\bar{d}_{zP}]}(f_x, f_y, f_{ct})$  in  $(f_x, f_y, f_{ct}) \in \mathbb{R}^3$ .

### The ROS of $A_{3\text{MP}}(e^{j\omega_x}, e^{j\omega_y}, f_{ct})$

Let  $A_{3\text{MP}}(e^{j\omega_x}, e^{j\omega_y}, f_{ct})$  be the 3D-MDFT of the infinite extent signal sequence  $a_{3\text{MP}}(n_x, n_y, t)$  observed at the output of pseudo infinite 2D uniform array in response to propagating EM 4D BB-BP ST PW of DOA  $\hat{\mathbf{d}}_{P0}$ , where  $\hat{\mathbf{d}}_{P0} \in \mathbf{D}_P$  (see (2.66)). Following

(2.61) and (2.65),  $A_{3\text{MP}}(e^{j\omega_x}, e^{j\omega_y}, f_{ct})$  is given by

$$A_{3\text{MP}}(e^{j\omega_x}, e^{j\omega_y}, f_{ct}) = \frac{1}{\Delta_{xy}^2} \sum_{m_x=-\infty}^{+\infty} \sum_{m_y=-\infty}^{+\infty} AFX_{[d_{zP0}]} \frac{\omega_x - 2\pi m_x}{2\pi \Delta_{xy}}, \frac{\omega_y - 2\pi m_y}{2\pi \Delta_{xy}}, f_{ct} \\ \times W_{\text{CPO}}(cf_{ct}) \delta_{d_{xP0}f_{ct} - \frac{\omega_x - 2\pi m_x}{2\pi \Delta_{xy}}} \delta_{d_{yP0}f_{ct} - \frac{\omega_y - 2\pi m_y}{2\pi \Delta_{xy}}}, \quad (2.67)$$

thus ROS of  $A_{3\text{MP}}(e^{j\omega_x}, e^{j\omega_y}, f_{ct})$  is given by an infinite series of line segments corresponding to  $PQ$  and  $P'Q'$  along  $\omega_x$ - and  $\omega_y$ - axes with 2D periodicity  $(2\pi, 2\pi)$  in  $(\omega_x, \omega_y, f_{ct}) \in \mathbb{R}^3$ . Therefore, the range of the ROSs of the spectra  $\{A_{3\text{MP}}(e^{j\omega_x}, e^{j\omega_y}, f_{ct})\}$  corresponding to all EM 4D BB-BP ST PWs having DOAs  $\hat{\mathbf{d}}_P \in \mathbf{D}_P$  is given by a series of double 3D right-circular frustum-shaped regions (see Figure 2.5) that are periodic along  $\omega_x$ - and  $\omega_y$ - axes with 2D periodicity  $(2\pi, 2\pi)$  in  $(\omega_x, \omega_y, f_{ct}) \in \mathbb{R}^3$ .

Figure 2.10 illustrates the plan-view of the range of ROSs of  $A_{3\text{MP}}(e^{j\omega_x}, e^{j\omega_y}, f_{ct})$  looking down at the  $(\omega_x, \omega_y)$ -plane. The periodic concentric inner- and outer- circles represents the narrow-base of the frustum and the wide-base of the frustum, respectively. The radius of the inner-circle is given by the angular-frequency  $\omega_{\min} = 2\pi \Delta_{xy} f_{\min} \sin(\theta_M)/c$ , where the inter-antenna distance  $\Delta_{xy}$ , the minimum temporal-frequency  $f_{\min} = f_C - 0.5BW$ ,  $c$  is the wave propagation speed and the inclination angle  $\theta_M \in \Theta_P$  such that  $\sin(\theta_M) \geq \sin(\theta)$  for all  $\theta \in \Theta_P$ . Similarly, the radius of the outer-circle is given by the angular-frequency  $\omega_{\max} = 2\pi \Delta_{xy} f_{\max} \sin(\theta_M)/c$ , where  $f_{\max} = f_C + 0.5BW$ . As defined in section 2.3,  $f_C$  denotes the center frequency and  $BW$  denotes the temporal bandwidth of the BB-BP wavefront functions associated with all propagating EM BB-BP ST PWs.

If  $\omega_{\max} \geq \pi$ , then the spectral components from the neighboring frusta overlap causing *spatial aliasing* in the spatial-angular frequency space  $(\omega_x, \omega_y) \in \mathbb{R}^2$ . Due to cross spectral contamination, aliasing prohibits accurate recovery of the desired signal [42]. For this particular array, spatial aliasing can be avoided for temporal frequencies  $f_{ct} \leq c^{-1}f_{\max}$ , if the inter element interval is selected such that  $\Delta_{xy} \leq 0.5c/(f_{\max} \sin(\theta_M))$  that in turn confine  $\omega_{\max} \leq \pi$ . Provided  $\Delta_{xy} \leq 0.5c/(f_{\max} \sin(\theta_M))$ , the spectral components  $A_{3\text{MP}}(e^{j\omega_x}, e^{j\omega_y}, f_{ct})$  of the 3D antenna array signal sequence  $a_{3\text{MP}}(n_x, n_y, t)$  in the 3D

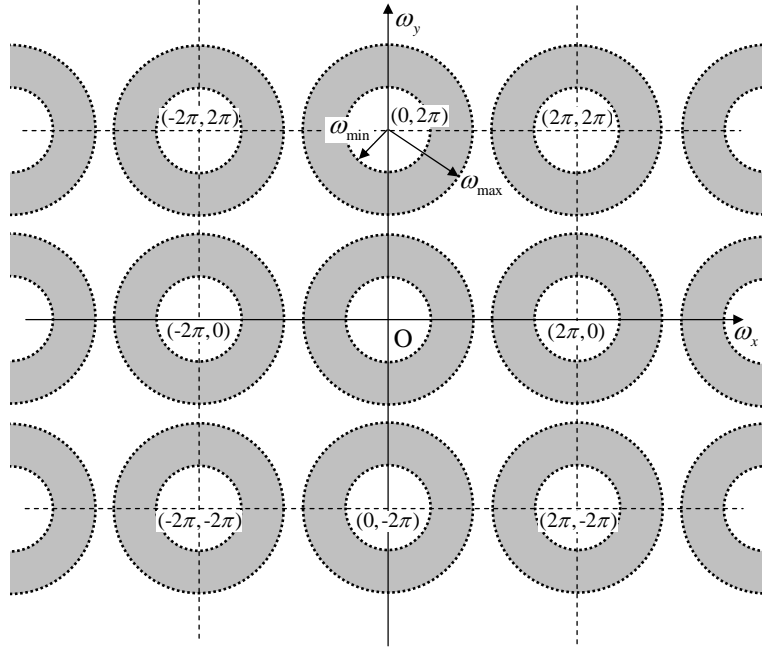


Figure 2.10: The plan-view of the range of ROs of  $A_{3MP}(e^{j\omega_x}, e^{j\omega_y}, f_{ct})$ . The inner-circle represent the narrow-base of the frustum having the radius  $\omega_{\min}$  where as the outer-circle represent the wide-base of the frustum having the radius  $\omega_{\max}$ .

*principle Nyquist region*  $\mathbf{3PNR} = \{|\omega_x; \omega_y| \leq \pi \cup |f_{ct}| \leq c^{-1}f_{\max}\}$  are given by

$$A_{3MP}(e^{j\omega_x}, e^{j\omega_y}, f_{ct})_{[\mathbf{3PNR}]} = \frac{1}{\Delta_{xy}^2} AF X_{[d_{zP0}]} \frac{\omega_x}{2\pi\Delta_{xy}}, \frac{\omega_y}{2\pi\Delta_{xy}}, f_{ct} \\ \times W_{CP0}(cf_{ct}) \delta_{d_{xP0}f_{ct} - \frac{\omega_x}{2\pi\Delta_{xy}}} \delta_{d_{yP0}f_{ct} - \frac{\omega_y}{2\pi\Delta_{xy}}} . \quad (2.68)$$

## 2.6 2D Spectra of the Signals Observed at the Terminals of 1D Linear Array

Let's consider a different scenario shown in Figure 2.11, where the propagating EM 4D BB-BP ST PW  $\mathbf{empw}_{4CP}(x, y, z, t)$  having the DOA  $[d_{x0} d_{y0} d_{z0}]$  is received by a pseudo-infinite 1D-UDAA containing linear-polarized wideband elemental antennas such as log periodic antennas or patch antennas [95]. The output of each elemental antenna of the 1D-UDAA is connected to a matching LAN. Without the loss of generality, assume that

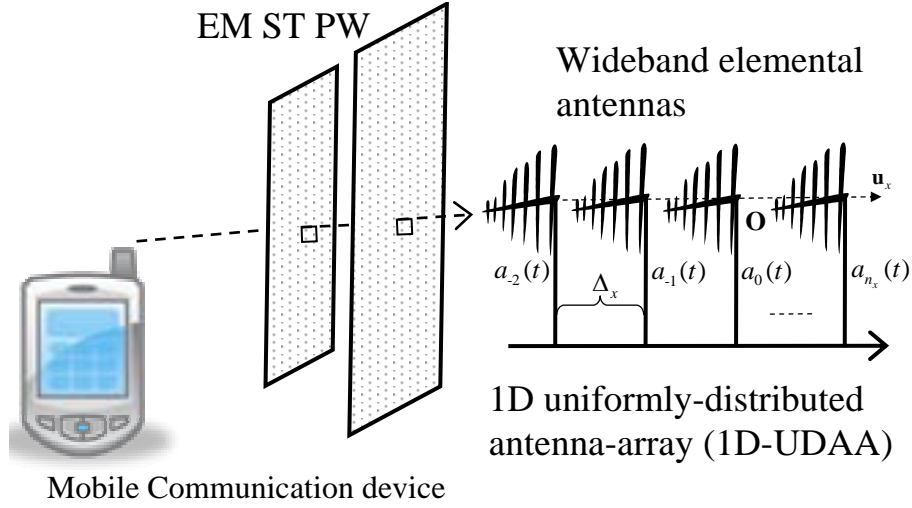


Figure 2.11: 1D uniformly distributed antenna array (1D-UDAA) in receiving EM 4D BB-BP ST PW  $\mathbf{empw}_{4CP}(x, y, z, t)$ .

the phase-centers [96](pp. 14-6) of the elemental antennas are arranged along the  $x$ -axis at uniform intervals of  $\Delta_x$  such that the electric-field of the corresponding active element pattern is oriented along the direction of  $\hat{\mathbf{u}}_z$ .

Assuming the  $\hat{\mathbf{u}}_x$ - and  $\hat{\mathbf{u}}_y$ - components are  $AE X_C(\theta, \phi, f_{ct}) = 0$  and  $AE Y_C(\theta, \phi, f_{ct}) = 0$ , the active element pattern of any elemental antenna in this pseudo-infinite 1D-UDAA may be expresses following (2.39) and (2.41), such that

$$\mathbf{AE}_C(\theta, \phi, f_{ct}) = AE Z_C(\theta, \phi, f_{ct}) \hat{\mathbf{u}}_z. \quad (2.69)$$

The typical normalized magnitude of  $z$ -component  $|AE Z_C(\theta, \phi, f_{ct})|$  at  $\theta = 90^\circ$  for  $\phi \in [0^\circ, 360^\circ]$  at the temporal frequency  $|cf_{ct0}| \in [f_C - 0.5BW, f_C + 0.5BW]$  is shown in Figure 2.12 (a). Also, the normalized  $|AE Z_C(\theta, \phi, f_{ct})|$  at  $\phi = 90^\circ$  for  $\theta \in [0^\circ, 90^\circ]$  and at  $\phi = -90^\circ$  for  $\theta \in [0^\circ, 90^\circ]$  at the temporal frequency  $|cf_{ct0}| \in [f_C - 0.5BW, f_C + 0.5BW]$  are shown in Figure 2.12 (b-right) and (b-left), respectively.

Following subsections 2.4.1, 2.4.2, 2.4.3 and 2.4.4, the corresponding vector valued antenna frequency response function  $\mathbf{AP}(f_x, f_y, f_z, f_{ct})$  can be defined with regards to

## Active Element Pattern for 1D-UDAA

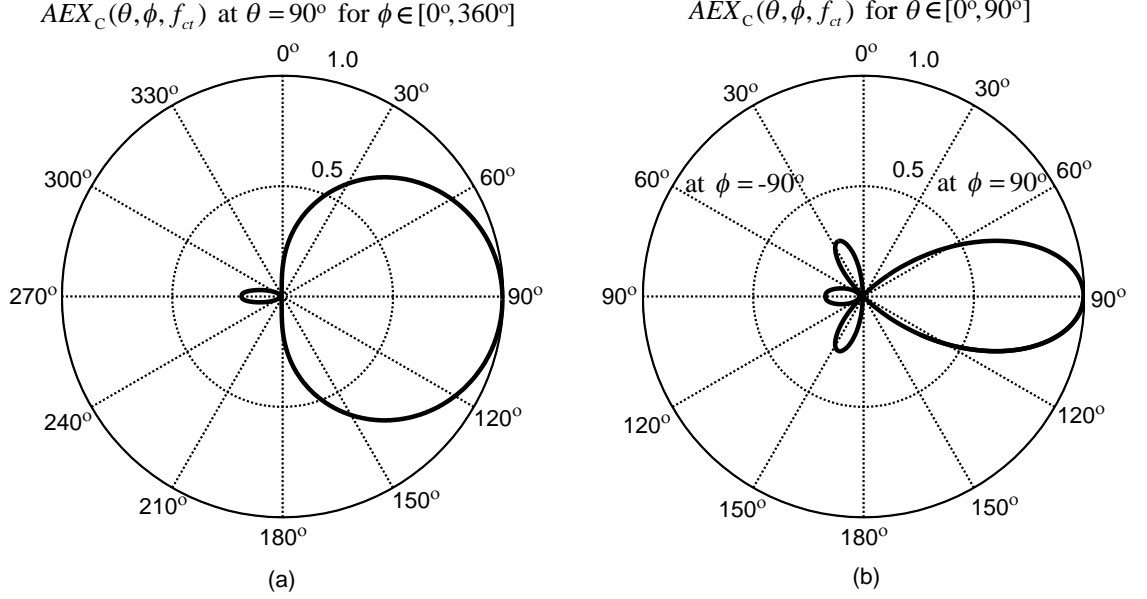


Figure 2.12: The  $\hat{\mathbf{u}}_z$ -component  $AEZ_C(\theta, \phi, f_{ct})$  of a typical active element pattern of a wideband elemental antenna in pseudo-infinite 1D-UDAA. The normalized  $|AEZ_C(\theta, \phi, f_{ct})|$  at  $\theta = 90^\circ$  for  $\phi \in [0^\circ, 360^\circ]$  at the frequency  $|cf_{cto}| \in [f_C - 0.5BW, f_C + 0.5BW]$  is shown in Figure 2.12 (a). The normalized  $|AEZ_C(\theta, \phi, f_{ct})|$  at  $\phi = 90^\circ$  for  $\theta \in [0^\circ, 90^\circ]$  and at  $\phi = -90^\circ$  for  $\theta \in [0^\circ, 90^\circ]$  at the frequency  $|cf_{cto}|$  are shown in Figure 2.12 (b-right) and (b-left), respectively.

$\mathbf{AE}_C(\theta, \phi, f_{ct})$  such that

$$\mathbf{AP}(d_x f_{ct}, d_y f_{ct}, d_z f_{ct}, f_{ct}) \triangleq C_{\text{TxRx}} \mathbf{AE}_C(\theta, \phi, f_{ct}), \quad (2.70)$$

where  $d_x = \sin(\theta) \cos(\phi)$ ,  $d_y = \sin(\theta) \sin(\phi)$  and  $d_z = \cos(\theta)$  and where  $C_{\text{TxRx}}$  is the constant of proportionality. Thus, according to (2.69),

$$\mathbf{AP}(f_x, f_y, f_z, f_{ct}) = APZ(f_x, f_y, f_z, f_{ct}) \hat{\mathbf{u}}_z, \quad (2.71)$$

and the corresponding the vector valued antenna impulse response is given by

$$\mathbf{aj}(x, y, z, t) = ajz(x, y, z, t) \hat{\mathbf{u}}_z, \quad (2.72)$$

where  $ajz(x, y, z, t) \xleftrightarrow{4\text{D-CDFT}} APZ(f_x, f_y, f_z, f_t)$ .

As shown in Figure 2.11, the signal observed at the output of the  $n_{x0}^{\text{th}}$  elemental antenna of this in response to a propagating EM 4D BB-BP ST PW  $\mathbf{empw}_{4\text{CP}}(x, y, z, t)$  is denoted by  $a_{n_{x0}}(t)$ . If the electric field component  $\mathbf{epw}_{4\text{CP}}(x, y, z, t)$  of  $\mathbf{empw}_{4\text{CP}}(x, y, z, t)$  is given by

$$\mathbf{epw}_{4\text{CP}}(x, y, z, t) = pw_{4\text{CP}_O}(x, y, z, t) \hat{\mathbf{u}}_z + pw_{4\text{CP}_X}(x, y, z, t) \hat{\mathbf{u}}_z^\perp, \quad (2.73)$$

where for this case  $\hat{\mathbf{u}}_z$  is the unit co-polar vector along the  $z$ -axis and  $\hat{\mathbf{u}}_z^\perp$  is the unit cross-polar vector, which is orthogonal to  $\hat{\mathbf{u}}_z$ . Hence,  $pw_{4\text{CP}_O}(x, y, z, t)$  and  $pw_{4\text{CP}_X}(x, y, z, t)$  are the co-polar component and the cross-polar component, respectively. According to (2.55), the signal observed at the output of  $n_{x0}^{\text{th}}$  elemental antenna may be given by

$$a_{n_{x0}}(t) = \iiint_{x,y,z=-\infty}^{+\infty} \{ajz(x, y, z, t) * * * pw_{4\text{CP}_O}(x, y, z, t)\} \delta(x - \Delta_x n_{x0}) \delta(y) \delta(z) dx dy dz. \quad (2.74)$$

Consider an ideal infinite-extent 2D mixed-domain<sup>12</sup> signal sequence  $a_{3\text{MP}}(n_x, t)$  that corresponds to the group of temporal signals  $a_{n_x}(t)$  observed at the output of the  $n_x^{\text{th}}$  elemental antenna in a 1D-UDAA along the  $x$ -axis in response to a propagating EM 4D BB-BP ST PW  $\mathbf{empw}_{4\text{CP}}(x, y, z, t)$ . Following (2.74), the 2D mixed-domain antenna signal sequence  $a_{2\text{MP}}(n_x, t)$  can be expressed as

$$a_{2\text{MP}}(n_x, t) = apwz_{2\text{CP}}(x, t) \sum_{n_x=-\infty}^{+\infty} \delta(x - \Delta_{xy} n_x), \quad (2.75)$$

where the *equivalent 2D continuous-domain antenna output function* is defined as

$$apwz_{2\text{CP}}(x, t) \triangleq \iint_{z,y=-\infty}^{+\infty} \{ajz(x, y, z, t) * * * pw_{4\text{CP}_O}(x, y, z, t)\} \delta(y) \delta(z) dy dz. \quad (2.76)$$

In order to analyze the spectral properties of the 2D mixed-domain antenna signals  $a_{2\text{MP}}(n_x, t)$ , its 2D mixed-domain Fourier transform (2D-MDFT) is evaluated. The 2D-MDFT of  $a_{2\text{MP}}(n_x, t)$  defined by

$$A_{2\text{MP}}(e^{j\omega_x}, f_{ct}) \triangleq \int_{t=-\infty}^{+\infty} \sum_{n_x=-\infty}^{+\infty} a_{2\text{MP}}(n_x, t) e^{-j\omega_x n_x} e^{-j2\pi f_{ct} t} dt, \quad (2.77)$$

---

<sup>12</sup>In this case, discrete in the spatial domain along  $x$ -axis and continuous in the temporal domain.

where  $(\omega_x, f_{ct}) \in \mathbb{R}^2$  [41](ch. 6). Nevertheless, according to [44] (pp. 52-53), the spectrum  $A_{2MP}(e^{j\omega_x}, f_{ct})$  may be expressed as in the form

$$A_{2MP}(e^{j\omega_x}, f_{ct}) = \frac{1}{\Delta_x} \sum_{m_x=-\infty}^{+\infty} APWZ_{2CP_O} \left( \frac{\omega_x - 2\pi m_x}{2\pi \Delta_x}, f_{ct} \right), \quad (2.78)$$

where  $APWZ_{2CP_O}(f_x, f_{ct})$  is the 2D-CDFT of the equivalent 2D continuous-domain antenna output function  $apwz_{2CP}(x, t)$ , which is given in (2.76). It is implied in (2.78), that  $A_{2MP}(e^{j\omega_x}, f_{ct})$  is given as the infinite series of periodic copies of  $APWZ_{2CP_O}(\frac{\omega_x}{2\pi \Delta_x}, f_{ct})$  along  $\omega_x$ -axis with periodicity  $2\pi$  in  $(\omega_x, f_{ct}) \in \mathbb{R}^2$ . Here also, the spectral properties of  $A_{2MP}(e^{j\omega_x}, f_{ct})$  is determined by exploiting the relationship in (2.78) that in turn requires the evaluation of the spectral properties of  $APWZ_{2CP_O}(f_x, f_{ct})$  in  $(\omega_x, f_{ct}) \in \mathbb{R}^2$ .

### The ROS of $APWZ_{2CP_O}(f_x, f_{ct})$

Following (2.76), it can be shown that

$$APWZ_{2CP_O}(f_x, f_{ct}) = \iint_{f_z, f_y=-\infty}^{+\infty} APZ(f_x, f_y, f_z, f_{ct}) PW_{4CP_O}(f_x, f_y, f_z, f_{ct}) df_y df_z, \quad (2.79)$$

where  $APZ(f_x, f_y, f_z, f_{ct})$  is the  $\hat{\mathbf{u}}_z$ -component of antenna frequency response function (see 2.71 at page 54) and  $PW_{4CP_O}(f_x, f_y, f_z, f_{ct})$  is the 4D-CDFT of  $pw_{4CP_O}(x, y, z, t)$ . Substituting  $PW_{4CP_O}(f_x, f_y, f_z, f_{ct})$  in (2.79) with (2.13) yields,

$$\begin{aligned} APWZ_{2CP_O}(f_x, f_{ct}) &= \iint_{f_z, f_y=-\infty}^{+\infty} APZ(f_x, f_y, f_z, f_{ct}) W_{CP_O}(cf_{ct}) \delta(d_x f_{ct} - f_x) \delta(d_y f_{ct} - f_y) \delta(d_z f_{ct} - f_z) df_y df_z, \\ &= APZ(f_x, d_y f_{ct}, d_z f_{ct}, f_{ct}) W_{CP_O}(cf_{ct}) \delta(d_x f_{ct} - f_x). \end{aligned} \quad (2.80)$$

Note that in (2.80),  $APZ(f_x, d_y f_{ct}, d_z f_{ct}, f_{ct})$  represents the slice of the 4D continuous-domain antenna response function ( $\hat{\mathbf{u}}_z$ -component)  $APZ(f_x, f_y, f_z, f_{ct})$  taken along to the line of intersection between two 4D-planes  $f_z = d_z f_{ct}$  and  $f_y = d_y f_{ct}$ . Such a relationship can be expressed as a 2D continuous-domain parametric-function  $APZ_{[d_y, d_z]}(f_x, f_{ct})$  of the parameters  $(d_y, d_z)$  in  $(f_x, f_{ct}) \in \mathbb{R}^2$  that is defined as

$$APZ_{[d_y, d_z]}(f_x, f_{ct}) \triangleq \iint_{f_z, f_y=-\infty}^{+\infty} APZ(f_x, f_y, f_z, f_{ct}) \delta(d_y f_{ct} - f_y) \delta(d_z f_{ct} - f_z) df_y df_z. \quad (2.81)$$



Hence, (2.80) can be rewritten as

$$APWZ_{2\text{CP}_O}(f_x, f_{ct}) = APZ_{[d_y, d_z]}(f_x, f_{ct}) PW_{2\text{CP}_O}(f_x, f_{ct}), \quad (2.82)$$

because according to (2.32)

$$PW_{2\text{CP}_O}(f_x, f_{ct}) = W_{\text{CP}_O}(cf_{ct})\delta(d_x f_{ct} - f_x).$$

The ROS of  $APWZ_{2\text{CP}_O}(f_x, f_{ct})$  is given by the intersection of the ROSs of  $APZ_{[d_y, d_z]}(f_x, f_{ct})$  and  $PW_{2\text{CP}_O}(f_x, f_{ct})$  in  $(f_x, f_{ct}) \in \mathbb{R}^2$ . According to subsection 2.3.3,  $PW_{2\text{CP}_O}(f_x, f_{ct})$  represents the spectrum of the 2D continuous-domain signal observed on the 3D-line along the  $x$ -axis in response to the 4D BB-BP ST PW having the DOA  $[d_{x0} \ d_{y0} \ d_{z0}]$ . As shown in Figure 2.7, the ROS of  $PW_{2\text{CP}_O}(f_x, f_{ct})$  is given by two line segments  $RS$  and  $R'S'$  on the line  $d_{x0}f_{ct} - f_x = 0$  in  $(f_x, f_{ct}) \in \mathbb{R}^2$ . Note that  $RS$  corresponds to the positive temporal frequencies  $cf_{ct} \in \{f_C - 0.5BW, f_C + 0.5BW\}$  and  $R'S'$  corresponds to the negative temporal frequencies  $cf_{ct} \in \{-f_C - 0.5BW, -f_C + 0.5BW\}$ .

Let's assume that for this particular array the normalized-magnitude of the  $\hat{\mathbf{u}}_z$ -component of the active element pattern  $|ATZ(\theta, \phi, f_{ct})| = 0$  in the angular-ranges  $\Psi_B = \bigcup_i \{(\theta_{Li}, \theta_{Ui}) \text{ and } (\phi_{Li}, \phi_{Ui})\}$  for all  $|f_{ct}| \in [c^{-1}f_C - 0.5c^{-1}BW, c^{-1}f_C + 0.5c^{-1}BW]$ . Note that according to (2.5), the DOA unit vectors  $\hat{\mathbf{d}}_B$  included in the vector-range

$$\mathbf{D}_B \in [d_{xB} \ d_{yB} \ d_{zB}] \mid [d_{xB} = \sin(\theta_B) \cos(\phi_B), \ d_{yB} = \sin(\theta_B) \sin(\phi_B), \ d_{zB} = \cos(\theta_B)] \ , \quad (2.83)$$

correspond to all  $(\theta_B, \phi_B) \in \Psi_B$ . Hence, according to the definitions (2.51) and (2.81), it can be shown that the 2D double trapezoidal region, shown in Figure 2.7 in  $(f_x, f_{ct}) \in \mathbb{R}^2$ , is included in the ROS of  $APZ_{[d_{yB}, d_{zB}]}(f_x, f_{ct})$  for all  $\hat{\mathbf{d}}_B \in \mathbf{D}_B$  but, is excluded in the ROS of  $APZ_{[\tilde{d}_{yB}, \tilde{d}_{zB}]}(f_x, f_{ct})$  for all  $\tilde{\hat{\mathbf{d}}}_B \notin \mathbf{D}_B$ . Therefore, for all  $\hat{\mathbf{d}}_B \in \mathbf{D}_B$ , the ROS of  $APWZ_{2\text{CP}_O}(f_x, f_{ct})$  is determined by the ROS of  $PW_{2\text{CP}_O}(f_x, f_{ct})$ , which is given by

the two line segments  $RS$  and  $R'S'$  in  $(f_x, f_{ct}) \in \mathbb{R}^2$  (see Figure 2.7). However, for all  $\bar{\mathbf{d}}_B \notin \mathbf{D}_B$ ,  $APWZ_{2\text{CPO}}(f_x, f_{ct}) = 0$  because there is no intersection between the ROSs of  $PW_{2\text{CPO}}(f_x, f_{ct})$  and  $APZ_{[\bar{d}_{yB}, \bar{d}_{zB}]}(f_x, f_{ct})$  in  $(f_x, f_{ct}) \in \mathbb{R}^2$ .

### The ROS of $A_{2\text{MP}}(e^{j\omega_x}, f_{ct})$

Let  $A_{2\text{MP}}(e^{j\omega_x}, f_{ct})$  be the 2D-MDFT of the infinite extent signal sequence  $a_{2\text{MP}}(n_x, t)$  observed at the output of pseudo infinite 1D-UDAA in response to propagating EM 4D BB-BP ST PW of DOA  $\hat{\mathbf{d}}_{B0}$ , where  $\hat{\mathbf{d}}_{B0} \in \mathbf{D}_B$  (see (2.83)). Following (2.78) and (2.82),  $A_{2\text{MP}}(e^{j\omega_x}, f_{ct})$  is given by

$$A_{2\text{MP}}(e^{j\omega_x}, f_{ct}) = \frac{1}{\Delta_x} \sum_{m_x=-\infty}^{+\infty} APZ_{[d_{yB0}, d_{zB0}]} \left[ \frac{\omega_x - 2\pi m_x}{2\pi \Delta_x}, f_{ct} \right] W_{\text{CPO}}(cf_{ct}) \delta_{d_{x0}f_{ct} - \frac{\omega_x - 2\pi m_x}{2\pi \Delta_x}}, \quad (2.84)$$

thus ROS of  $A_{2\text{MP}}(e^{j\omega_x}, f_{ct})$  is given by an infinite series of line segments shown in Figure 2.13 along  $\omega_x$ -axis with periodicity  $(2\pi)$  in  $(\omega_x, f_{ct}) \in \mathbb{R}^2$ . Therefore, the range of the ROSs of the spectra  $\{A_{3\text{MP}}(e^{j\omega_x}, f_{ct})\}$  corresponding to all EM 4D BB-BP ST PWs having DOAs  $\hat{\mathbf{d}}_B \in \mathbf{D}_B$  is given by a series of 2D double-trapezoid areas shown in Figure 2.13 that are periodic along  $\omega_x$ -axis with periodicity  $(2\pi)$  in  $(\omega_x, f_{ct}) \in \mathbb{R}^2$ .

According to Figure 2.13, the length of the narrow-base of the trapezoid is given by the angular-frequency  $\omega_{\min} = 2\pi \Delta_x f_{\min} \sin(\theta_M) \sin(\phi_M)/c$ , where  $\Delta_x$  is the inter-antenna distance,  $f_{\min} = f_C - 0.5BW$  is the minimum temporal-frequency,  $c$  is the wave propagation speed and  $(\theta_M, \phi_M) \in \Psi_P$  is the combined inclination angle and azimuth angle pair such that  $\sin(\theta_M) \sin(\phi_M) \geq \sin(\theta) \sin(\phi)$  for all  $(\theta, \phi) \in \Psi_P$ . Similarly, the length of the wide-base is given by the angular-frequency  $\omega_{\max} = 2\pi \Delta_{xy} f_{\max} \sin(\theta_M) \sin(\phi_M)/c$ , where  $f_{\max} = f_C + 0.5BW$ .

If  $\omega_{\max} \geq \pi$ , then the spectral components from the neighboring trapezoids overlaps causing spatial-aliasing in spatial-frequency space  $(\omega_x) \in \mathbb{R}$ . For this particular array, spatial aliasing can be avoided for temporal frequencies  $cf_{ct} \leq f_{\max}$ , if the inter element interval is selected such that  $\Delta_x \leq 0.5 c / (f_{\max} \sin(\theta_M) \sin(\phi_M))$  that in turn con-

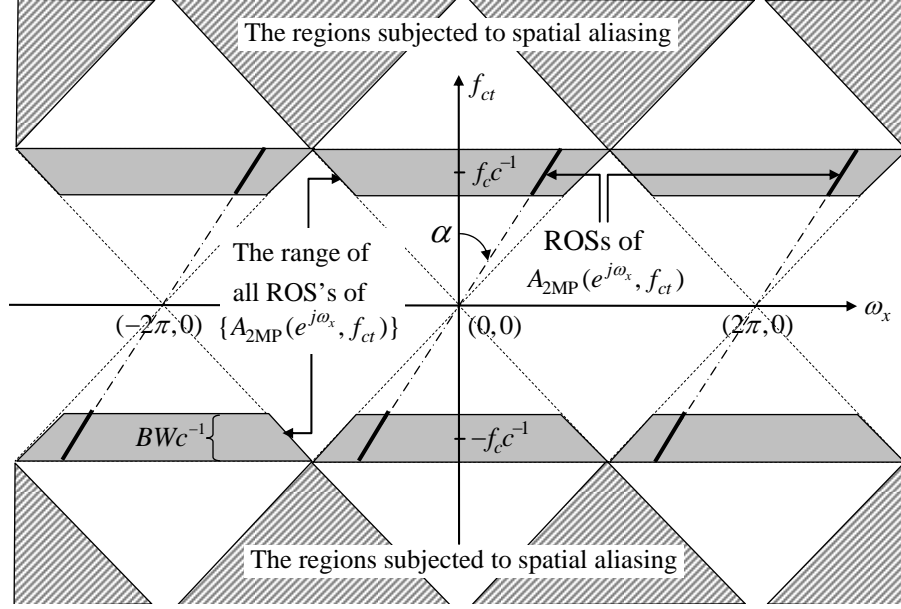


Figure 2.13: ROSs of 2D-MDFT of  $A_{2MP}(e^{j\omega_x}, f_{ct})$  and the regions subjected to spatial-aliasing.

fine  $\omega_{\max} \leq \pi$ . However, for temporal frequencies  $cf_{ct} \geq f_{\max}$ , spectral overlapping is unavoidable in some spectral regions as shown by the hatched-area in Figure 2.13. Further, these spatially-aliased spectral components can be removed from  $A_{2MP}(e^{j\omega_x}, f_{ct})$ , either by temporal lowpass filtering (having a cutoff-frequency  $f_{CF} = f_{\max}$ ) or temporal-bandpass filtering to retain the frequency band  $|cf_{ct}| \in \{f_c - 0.5BW, f_c + 0.5BW\}$ . Provided  $\Delta_x \leq 0.5c/(f_{\max} \sin(\theta_M) \sin(\phi_M))$ , the spectral components  $A_{2MP}(e^{j\omega_x}, f_{ct})$  of the 2D antenna array signal sequence  $a_{2MP}(n_x, t)$  in the 2D principle Nyquist region  $\mathbf{2PNR} = \{|\omega_x| \leq \pi \cup |f_{ct}| \leq c^{-1}f_{\max}\}$  are given by

$$A_{2MP}(e^{j\omega_x}, f_{ct})_{[\mathbf{2PNR}]} = APZ_{[d_{yB0}, d_{zB0}]} \frac{\omega_x}{2\pi\Delta_x}, f_{ct} W_{CPO}(cf_{ct}) \delta_{d_{xB0}f_{ct} - \frac{\omega_x}{2\pi\Delta_x}} \cdot (2.85)$$

## 2.7 Distortions of the Spectra of Finite Aperture Arrays

In subsection 2.5 and 2.6, infinite-extent 2D-UDPAs and 1D-UDAAs have been assumed in determining the *ideal spectral properties* of signals observed at the outputs of elemental

antennas in responses to propagating EM 4D BB-BP ST PWs. However in practice, both 2D-UDPAs and 1D-UDAs only extend over a *finite aperture* on particular planes or lines, respectively. In spectral analysis of signal sequences from finite aperture arrays, the straightforward application of MD Fourier transform leads to *spectral spreading* and *spectral leakage* [44] (pp. 186). Such distortions of the spectra of finite extent signal sequences are studied briefly in the following.

### 2.7.1 Distortions in the Spectra of Antenna Responses of Finite Extent 2D-UDPAs

Consider a 2D-UDPA containing  $(2N_x + 1) \times (2N_y + 1)$  wideband elemental antennas that are arranged in a rectangular-grid of  $(2N_x + 1)$ -columns along the  $\hat{\mathbf{u}}_x$ -direction and of  $(2N_y + 1)$ -rows along the  $\hat{\mathbf{u}}_y$ -direction. The finite-extent 3D mixed-domain signal sequence observed at the outputs of  $(2N_x + 1) \times (2N_y + 1)$  elemental antennas in response to a propagating EM 4D BB-BP ST PW  $\mathbf{empw}_{4CP}(x, y, z, t)$  may be expressed as

$$ar_{3MP}(n_x, n_y, t) = a_{3MP}(n_x, n_y, t) rect_{2D}(n_x, n_y), \quad (2.86)$$

where the infinite-extent 3D mixed-domain signal sequence  $a_{3MP}(n_x, n_y, t)$  is given in (2.58). Note that the “2D rectangular-window function” [97] (pp. 204) is defined by

$$rect_{2D}(n_x, n_y) \triangleq \begin{cases} 1; & \text{for } |n_x| \leq N_x \text{ and } |n_y| \leq N_y, \\ 0; & \text{elsewhere.} \end{cases} \quad (2.87)$$

Following [44] (pp. 58), the 3D-MDFT of finite-extent signal sequence  $ar_{3MP}(n_x, n_y, t)$  is given by

$$AR_{3MP}(e^{j\omega_x}, e^{j\omega_y}, f_{ct}) = A_{3MP}(e^{j\omega_x}, e^{j\omega_y}, f_{ct}) * * * \{RECT_{2D}(e^{j\omega_x}, e^{j\omega_y}) \delta(f_{ct})\}, \quad (2.88)$$

where  $RECT_{2D}(e^{j\omega_x}, e^{j\omega_y})$  is the 2D discrete-domain Fourier transform (2D-DDFT) of  $rect_{2D}(n_x, n_y)$ . According to [42] (pp. 66),  $RECT_{2D}(e^{j\omega_x}, e^{j\omega_y})$  may be expressed as

$$RECT_{2D}(e^{j\omega_x}, e^{j\omega_y}) = \frac{\sin(\omega_x(2N_x + 1)/2)}{\sin(\omega_x/2)} \times \frac{\sin(\omega_y(2N_y + 1)/2)}{\sin(\omega_y/2)}. \quad (2.89)$$

Let's consider the example of 2D rectangular window function  $rect_{2D}(n_x, n_y)$  of size  $N_x = 16$  and  $N_y = 8$ . The corresponding 2D normalized magnitude spectrum  $||RECT_{2D}(e^{j\omega_x}, e^{j\omega_y})||$  inside  $|(\omega_x, \omega_y)| \leq \pi$  is shown in Figure 2.14 (a). As shown there,  $RECT_{2D}(e^{j\omega_x}, e^{j\omega_y})$  has a main-lobe extending from  $\omega_x = -\frac{2\pi}{(2N_x+1)}$  to  $\omega_x = \frac{2\pi}{(2N_x+1)}$  along the  $\omega_x$ -axis and from  $\omega_y = -\frac{2\pi}{(2N_y+1)}$  to  $\omega_y = \frac{2\pi}{(2N_y+1)}$  along the  $\omega_y$ -axis that contains about 90% of the spectral energy of  $||RECT_{2D}(e^{j\omega_x}, e^{j\omega_y})||^2$ . Also shown there, the side-lobes of  $||RECT_{2D}(e^{j\omega_x}, e^{j\omega_y})||$  are slowly decaying and span the remaining space in  $|(\omega_x, \omega_y)| \leq \pi$ . The cross-sectional magnitude spectrum  $||RECT_{2D}(e^{j\omega_x}, e^{j\omega_y})||$  along the lines  $\omega_y = 0$  and  $\omega_x = 0$  are shown in Figure 2.14 (b) and (c), respectively. Note that the width of the main-lobe along  $\omega_y$ -axis is wider than the width of the main-lobe along  $\omega_x$ -axis. This due to the fact that the aperture is wider along the  $x$ -axis compared to the  $y$ -axis.

In section 2.5, it has been shown that, if it exists, the ROS of  $A_{3MP}(e^{j\omega_x}, e^{j\omega_y}, f_{ct})$  is given by an infinite series of periodic lines in  $(\omega_x, \omega_y, f_{ct}) \in \mathbb{R}^3$ . However, as a result of 3D convolution with the “ripply-function”  $\{RECT_{2D}(e^{j\omega_x}, e^{j\omega_y})\delta(f_{ct})\}$ , the spectral components of  $AR_{3MP}(e^{j\omega_x}, e^{j\omega_y}, f_{ct})$  are not confined to set of periodic line segments as in the case of  $A_{3MP}(e^{j\omega_x}, e^{j\omega_y}, f_{ct})$ . In fact, the ROS of  $AR_{3MP}(e^{j\omega_x}, e^{j\omega_y}, f_{ct})$  is distributed inside the entire 3D frequency space  $(\omega_x, \omega_y, f_{ct}) \in \mathbb{R}^3$ . However, the spectral components accounting to about 90% of the total-energy of  $AR_{3MP}(e^{j\omega_x}, e^{j\omega_y}, f_{ct})$  is concentrated in the vicinity of the line segments corresponding to the ROS  $A_{3MP}(e^{j\omega_x}, e^{j\omega_y}, f_{ct})$  within the interval  $\frac{4\pi}{(2N_x+1)}$  along the  $\omega_x$ -axis and the interval  $\frac{4\pi}{(2N_y+1)}$  along the  $\omega_y$ -axis for all temporal frequencies  $f_{ct}$ . This effect is called as spectral-spreading. The rest of the energy of  $AR_{3MP}(e^{j\omega_x}, e^{j\omega_y}, f_{ct})$  is distributed in a decaying set of side-lobes in  $(\omega_x, \omega_y, f_{ct}) \in \mathbb{R}^3$ . This effect is called spectral-leakage. Thus, the straightforward application of 3D-MDFT on  $ar_{3MP}(n_x, n_y, t)$  leads to spectral-leakage and spectral-spreading in  $(\omega_x, \omega_y, f_{ct}) \in \mathbb{R}^3$ .

*In spectral analysis of the finite-extent  $a_{3MP}(n_x, n_y, t)$ , an acceptable trade-off can be*

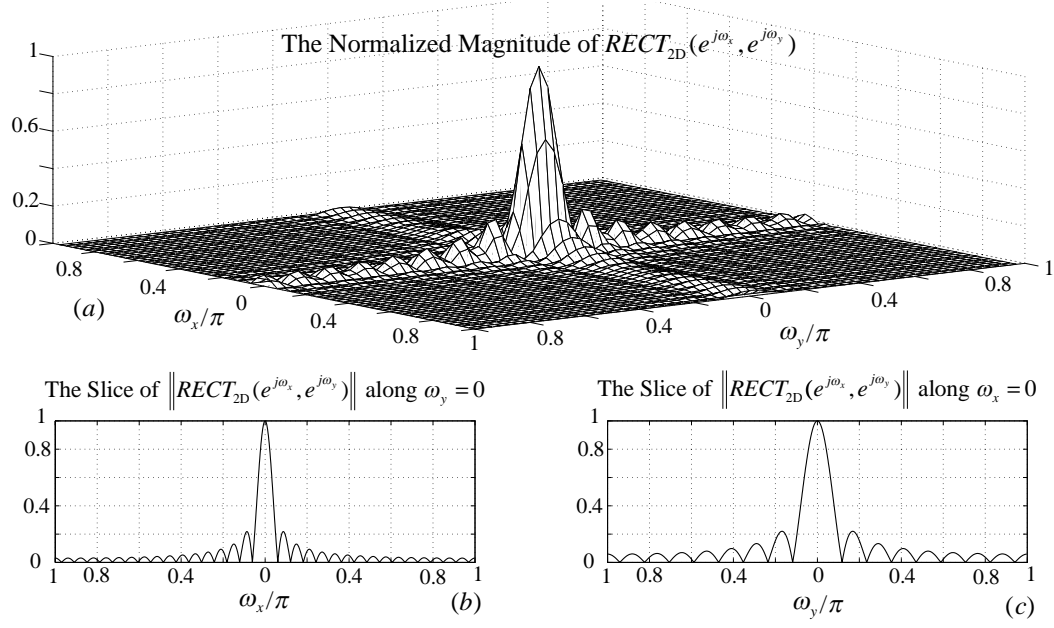


Figure 2.14: The normalized magnitude of the spectrum  $\|RECT_{2D}(e^{j\omega_x}, e^{j\omega_y})\|$  of the 2D rectangular window  $rect_{2D}(n_x, n_y)$  for  $N_x = 16$  and  $N_y = 8$ .

achieved between the spectral-leakage and the spectral-spreading by using a sufficient size 2D array along with an appropriate 2D window function [98] to weight [43] (pp. 88) the aperture of 2D-UDPA. Let's consider the example of "2D Hanning window function" [97] (pp. 204) that is defined with two cascading 1D Hanning functions  $han_{xD}(n_x) = han_D(n_x)$  of length  $(2N_x + 1)$  and  $hamy_D(n_y) = han_D(n_y)$  of length  $(2N_y + 1)$ , such that

$$han_{2D}(n_x, n_y) \triangleq han_{xD}(n_x) \times hany_D(n_y). \quad (2.90)$$

Note that  $han_{2D}(n_x, n_y) = 0$  for all  $|n_x| \geq N_x + 1$  and  $|n_y| \geq N_y + 1$ . Let's consider the example of  $han_{2D}(n_x, n_y)$  for  $N_x = 16$  and for  $N_y = 8$ . Given the 2D-DDFT pair  $han_{2D}(n_x, n_y) \xleftrightarrow{2D-DDFT} HAN_{2D}(e^{j\omega_x}, e^{j\omega_y})$ , Figure 2.15 (a) shows the 2D normalized magnitude spectrum  $\|HAN_{2D}(e^{j\omega_x}, e^{j\omega_y})\|$  in  $|(\omega_x, \omega_y)| \leq \pi$ . Compared to  $\|RECT_{2D}(e^{j\omega_x}, e^{j\omega_y})\|$  shown in Figure 2.14 (a), the ripples in  $\|HAN_{2D}(e^{j\omega_x}, e^{j\omega_y})\|$  decay rapidly as  $|(\omega_x, \omega_y)| \rightarrow \pi$ . However, according to Figure 2.15 (b) and (c), the width of the main-lobe is almost double in  $\|HAN_{2D}(e^{j\omega_x}, e^{j\omega_y})\|$  compared to that of

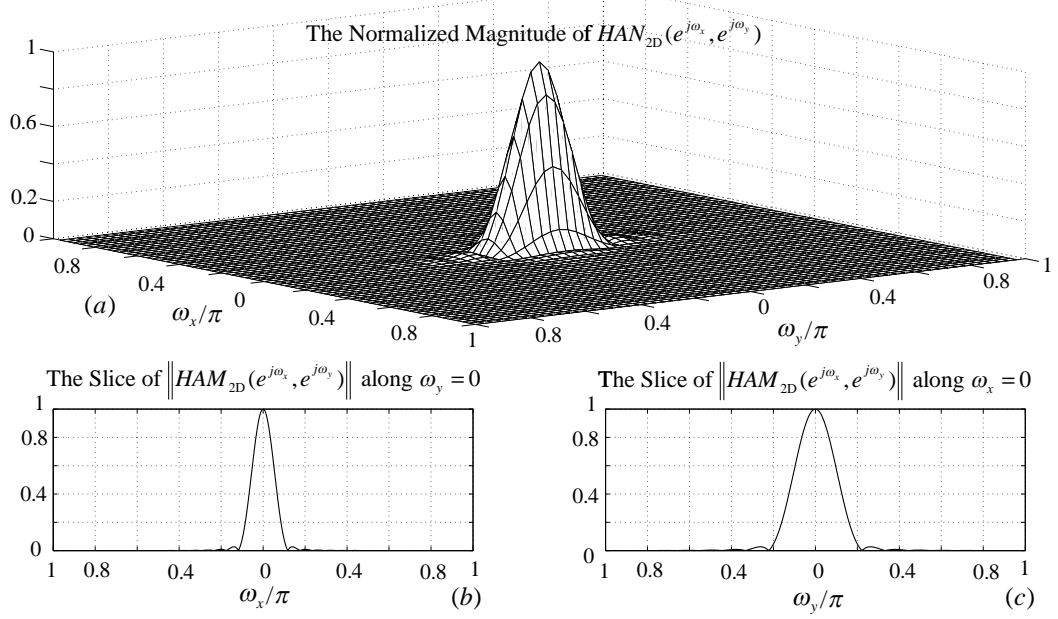


Figure 2.15: The normalized magnitude of the spectrum  $\|HAN_{2D}(e^{j\omega_x}, e^{j\omega_y})\|$  of the 2D Hanning window  $han_{2D}(n_x, n_y)$  for  $N_x = 16$  and  $N_y = 8$ .

$\|RECT_{2D}(e^{j\omega_x}, e^{j\omega_y})\|$ . Therefore, the 3D convolution between  $A_{3MP}(e^{j\omega_x}, e^{j\omega_y}, f_{ct})$  and  $\{HAN_{2D}(e^{j\omega_x}, e^{j\omega_y})\delta(f_{ct})\}$  spreads the spectral components accounting to 99% of the total-energy concentrated at the vicinity of the set of periodic line segments corresponding to the ROS of  $A_{3MP}(e^{j\omega_x}, e^{j\omega_y}, f_{ct})$ . However, here, the spectral components are distributed over a wider area. Hence, by using the 2D Hanning window function, a lower spectral leakage can be archived at the expense of higher spectral spreading. Using the 2D window function derived from two cascading 1D Kaiser window functions [66] (pp. 626), an arbitrary trade-off may be achieved between spectral-spreading and spectral-leakage in  $(\omega_x, \omega_y, f_{ct}) \in \mathbb{R}^3$ .

### 2.7.2 Distortions in the Spectra of Antenna Responses of Finite Extent 1D-UDAAs

Consider a 1D-UDAA containing  $(2N_x + 1)$  wideband elemental antennas that are arranged along the  $\hat{\mathbf{u}}_x$ -direction. The finite-extent 2D mixed-domain signal sequence observed at the outputs of  $(2N_x + 1)$  elemental antennas in response to a propagating EM

4D BB-BP ST PW **empw**<sub>4CP</sub>( $x, y, z, t$ ) may be expressed as

$$ar_{2MP}(n_x, t) = a_{2MP}(n_x, t) rect_D(n_x), \quad (2.91)$$

where the infinite-extent 2D mixed-domain signal sequence  $a_{2MP}(n_x, t)$  is given in (2.75).

Note that the “1D rectangular-window function” [66] (pp. 626) is defined by

$$rect_D(n_x) \triangleq \begin{cases} 1; & \text{for } |n_x| \leq N_x, \\ 0; & \text{elsewhere.} \end{cases} \quad (2.92)$$

Following [44] (pp. 55), the 2D-MDFT of finite-extent signal sequence  $ar_{2MP}(n_x, t)$  is given by

$$AR_{2MP}(e^{j\omega_x}, f_{ct}) = A_{2MP}(e^{j\omega_x}, f_{ct}) * * \{RECT_D(e^{j\omega_x}) \delta(f_{ct})\}, \quad (2.93)$$

where the 1D-DDFT pair  $rect_D(n_x) \xleftrightarrow{2D-DDFT} RECT_D(e^{j\omega_x})$ . According to [42] (pp. 66),  $RECT_D(e^{j\omega_x})$  may be expressed as

$$RECT_D(e^{j\omega_x}) = \frac{\sin(\omega_x(2N_x + 1)/2)}{\sin(\omega_x/2)}. \quad (2.94)$$

The 1D normalized magnitude spectrum  $\|RECT_D(e^{j\omega_x})\|$  of the 1D rectangular window  $rect_D(n_x)$  for  $N_x = 32$ , in  $|\omega_x| \leq \pi$  is shown in Figure 2.16 (left). As shown there,  $RECT_D(e^{j\omega_x})$  has a main-lobe extending from  $\omega_x = -\frac{2\pi}{(2N_x+1)}$  to  $\omega_x = \frac{2\pi}{(2N_x+1)}$  that contains about 90% of the spectral energy of  $\|RECT_D(e^{j\omega_x})\|^2$  and  $(2N_x - 1)$  slowly decaying side-lobes spanning the remainder of  $|\omega_x| \leq \pi$ . In section 2.6, it has been shown that, if it exists, the ROS of  $A_{2MP}(e^{j\omega_x}, f_{ct})$  is given by an infinite series of periodic lines in  $(\omega_x, f_{ct}) \in \mathbb{R}^2$  (see Figure 2.13). However, as a result of 2D convolution with the ripple-function  $(RECT_D(e^{j\omega_x})\delta(f_{ct}))$ , the spectral components of  $AR_{2MP}(e^{j\omega_x}, f_{ct})$  are also not confined to set of periodic line segments as in the case of  $A_{2MP}(e^{j\omega_x}, f_{ct})$ . In fact, the ROS of  $AR_{2MP}(e^{j\omega_x}, f_{ct})$  is distributed inside the entire 2D frequency space  $(\omega_x, f_{ct}) \in \mathbb{R}^2$ . However, it can be shown that spectral components accounting to about 90% of the total-energy is consenrated in the vicinity of the line segments corresponding to



the ROS  $A_{2\text{MP}}(e^{j\omega_x}, f_{ct})$  within the interval  $\frac{4\pi}{(2N_x+1)}$  along the  $\omega_x$ -axis for all temporal frequencies  $f_{ct}$ . The rest of the energy is distributed among  $(2N_x - 1)$  side-lobes in  $(\omega_x, f_{ct}) \in \mathbb{R}^2$ . Thus, the straightforward application of 2D-MDFT on  $ar_{2\text{MP}}(n_x, t)$  leads to spectral-spreading and spectral-leakage in  $(\omega_x, f_{ct}) \in \mathbb{R}^2$ .

In spectral analysis of finite-extent  $a_{2\text{MP}}(n_x, t)$ , an acceptable trade-off can be achieved between the spectral-leakage and the spectral-spreading by using a sufficient size 1D array along with an appropriate 1D window function *to weight* [43] (pp. 88) the aperture of 1D-UDAA. For an example, the “*1D Hamming window function*” [66] (pp. 626) is used to weight the 1D-UDAA signals such that

$$ah_{2\text{MP}}(n_x, t) = a_{2\text{MP}}(n_x, t) \times ham_D(n_x). \quad (2.95)$$

Note that  $ham_D(n_x) = 0$  for all  $|n_x| \geq N_x + 1$ . Following (2.93), the 2D-MDFT of  $ah_{2\text{MP}}(n_x, t)$  can be expressed as

$$AH_{2\text{MP}}(e^{j\omega_x}, f_{ct}) = A_{2\text{MP}}(e^{j\omega_x}, f_{ct}) * * HAM_D(e^{j\omega_x})\delta(f_{ct}), \quad (2.96)$$

where the 1D-DDFT pair  $ham_D(n_x) \xleftrightarrow{\text{1D-DDFT}} HAM_D(e^{j\omega_x})$ . The 1D normalized magnitude spectrum  $||HAM_D(e^{j\omega_x})||$  for  $N_x = 32$ , in  $|\omega_x| \leq \pi$  is shown in Figure 2.16 (right). The main-lobe of  $HAM_D(e^{j\omega_x})$  extends from  $\omega_x = -\frac{4\pi}{(2N_x+1)}$  to  $\omega_x = \frac{4\pi}{(2N_x+1)}$  and contains about 99.95% of the spectral energy of  $||HAM_D(e^{j\omega_x})||^2$ . Hence, the 2D convolution between  $HAM_D(e^{j\omega_x})$  and  $A_{2\text{MP}}(e^{j\omega_x}, f_{ct})$  results little spectral-leakage but significant spectral-spreading compared to  $RECT_D(e^{j\omega_x})$  for the same length  $N_x$ . A 1D Kaiser window function [66] (pp. 626) can be used to achieve an arbitrary trade-off between spectral-spreading and spectral-leakage in  $(\omega_x, f_{ct}) \in \mathbb{R}^2$ .

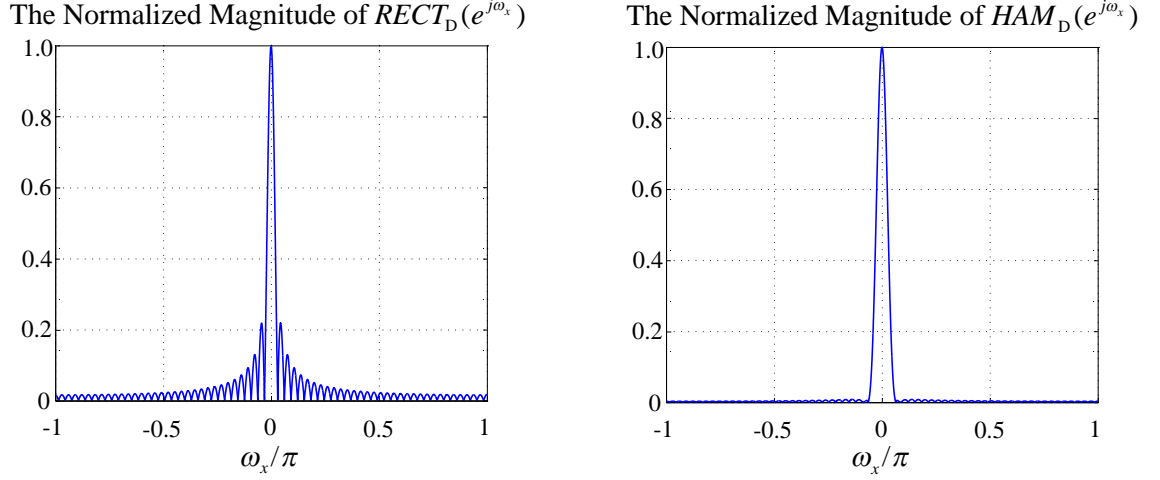


Figure 2.16: The normalized magnitude spectra of 1D rectangular window  $||RECT_D(e^{j\omega_x})||$  (left) and 1D Hamming window  $||HAM_D(e^{j\omega_x})||$  (right) in  $|\omega_x| \leq \pi$  for  $N_x = 32$ .

## 2.8 Temporal Sampling of Signals Observed at the Terminals of Antenna Array

In sections 2.4, 2.5 and 2.6 the reception of propagating EM BB-BP ST PWs by using array of antennas have been discussed in detail. The signals induced at the outputs of the elemental antennas of those arrays are subjected to pre-processing and temporal-sampling before being processed by the subsequent signal processing/detection/extraction stages. The main objective in temporal sampling schemes is to avoid distortion of the signal spectra. In the following, three possible synchronous-sampling schemes,

- The Direct Nyquist Sampling Scheme
- The Complex-Quadrature Sampling Scheme
- The Real-IF Sampling Scheme

that can be employed for temporal-sampling the temporally-bandpassed array signal sequences are outlined briefly. As mentioned in sections 2.4, 2.5 and 2.6, the spectra of the signals of interest (SOIs) observed at the outputs of the elemental antennas in response to

propagating EM BB-BP ST PWs occupy the temporal bandwidth spanning the positive frequencies  $cf_{ct} \in (f_C - 0.5BW, f_C + 0.5BW)$  and the negative frequencies  $cf_{ct} \in (-f_C - 0.5BW, -f_C + 0.5BW)$ . Also according to (2.8), either the positive or the negative frequency bands contain the desired information carried by the propagating EM BB-BP ST PWs. Hence, selecting either one of those sidebands of the array signal sequences is sufficient to extract that information. In the complex-quadrature sampling scheme, single sideband extraction is exploited to minimize the required sampling rate. However, lower pre-processing circuit complexities can be achieved with the direct Nyquist sampling scheme and the real-IF sampling scheme at the expense of higher sampling rate, where both the positive and negative frequency bands are extracted.

### 2.8.1 The Direct Nyquist Sampling Scheme

The Nyquist's<sup>13</sup> sampling theorem [71](pp. 347) specifies the conditions in order to avoid aliasing in the temporal frequency domain ( $\omega_t$ ) in sampling a real-valued band-limited continuous-time signal  $w_C(t)$  at regular time intervals. Given  $w_C(t) \xleftrightarrow{1D\text{-}CDFT} W_C(cf_{ct})$ , assume that the spectral components of  $W_C(cf_{ct})$  are confined to the band  $cf_{ct} \in (-f_{\max}, f_{\max})$ . Hence, according to the Nyquist's sampling theorem the required temporal sampling-rate in sampling  $w_C(t)$  should be  $f_S \geq 2f_{\max}$ .

In the direct Nyquist sampling scheme, first, each continuous-time signal from the output of the LNA, which is connected to an elemental antenna in a 2D-UDPAs or in a 1D-UDAAs, is processed by a lowpass filter. This is done to suppress spectral components outside of the band  $f_{ct} \in (-f_{\max}, f_{\max})$  that may lead to temporal aliasing. Then, each lowpass filtered signal is synchronously sampled at the rate  $f_S = 2f_{\max}$ , resulting 3D and 2D *discrete-domain* sample sequences  $a_{3DP}(n_x, n_y, n_t)$  and  $a_{2DP}(n_x, n_t)$ , respectively.

For 3D sample sequences  $a_{3DP}(n_x, n_y, n_t)$ , the direct Nyquist sampling scheme ide-

---

<sup>13</sup>Also known as Whittaker's cardinal theorem [99](pp. 32) or the Shannon's sampling theorem [100](ch. 1).

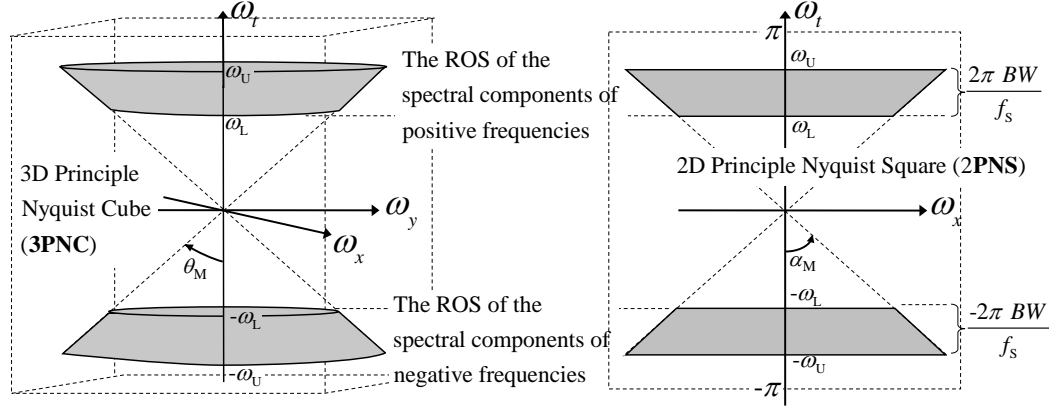


Figure 2.17: The ROSs of the spectra of SOIs contained in the 3D sample sequence  $a_{3DP}(n_x, n_y, n_t)$  (left) and 2D sample sequence  $a_{2DP}(n_x, n_t)$  (right) after being subjected to direct-Nyquist sampling of 3D/2D signal sequences  $a_{3MP}(n_x, n_y, t)$  and  $a_{2MP}(n_x, t)$ .

ally transforms the spectral components in the 3D double frustum region in **3PNR** =  $\{|\omega_x; \omega_y| \leq \pi \cup |f_{ct}| \leq c^{-1}f_{\max}\}$  (see page 52), into the *3D principle Nyquist cube* (**3PNC** =  $\{|\omega_x; \omega_y; \omega_t| \leq \pi\}$ ) shown in Figure 2.17 (left). Similarly, for 2D sample sequences  $a_{2DP}(n_x, n_t)$ , the direct Nyquist sampling scheme ideally transforms the spectral components in the 2D double trapezoidal region in **2PNR** =  $\{|\omega_x| \leq \pi \cup |f_{ct}| \leq c^{-1}f_{\max}\}$  (see page 59), into the *2D principle Nyquist square* (**2PNS** =  $\{|\omega_x; \omega_t| \leq \pi\}$ ) shown in Figure 2.17 (right).

As shown in Figure 2.17, the spectral components of the SOIs only occupy the temporal angular-frequency band  $|\omega_t| \in (\omega_L, \omega_U)$ , where  $\omega_L = \frac{2\pi(f_C - 0.5BW)}{f_s}$  and  $\omega_U = \frac{2\pi(f_C + 0.5BW)}{f_s}$ . The undesired spectral components in the rest of temporal angular-frequency band  $|\omega_t| \notin (\omega_L, \omega_U)$ , which corresponds to the continuous temporal frequency band  $|cf_{ct}| \in (0, f_C - 0.5BW)$ , are filtered out in subsequent signal processing stages. After removing these undesired spectral components the operating sample rate of these subsequent signal processing stages can be lowered significantly.

Instead of suppressing the undesired spectral components and subsequent down-sampling of the sequence after temporal sampling, the desired temporal frequency bands

$|cf_{ct}| \in (f_C - 0.5BW, f_C + 0.5BW)$  can be *first down-shifted, then lowpass filtered to remove all undesired spectral components and finally temporally sampled at much lower sampling rates than  $2f_{\max}$ , while avoiding temporal aliasing.* Although the frequency shifting operations require more sophisticated pre-processing analog-circuitry in such temporal-sampling process, the overall reduction in the computational complexity due to lower sampling rates may be substantial for some applications [101]. The following outlines the complex-quadrature sampling scheme and the real-IF sampling scheme that employ the frequency down-shifting prior to temporal sampling process in order to reduce the sampling rate.

### 2.8.2 The Complex-Quadrature Sampling Scheme

The complex-quadrature sampling scheme employs *complex-quadrature temporal-demodulation* [101] to down-shift<sup>14</sup> the spectral components inside the positive frequency band  $cf_{ct} \in (f_C - 0.5BW, f_C + 0.5BW)$ , of the 3D/2D signal sequences  $a_{3MP}(n_x, n_y, t)$  and  $a_{2MP}(n_x, t)$  to baseband without spectral overlapping as shown in Figure 2.18. The frequency down-shifting operation yields complex-valued 3D/2D signal sequences. Note that the desired spectral components are now in the temporal frequency band  $|cf_{ct}| \in (0, 0.5BW)$ . Next, these complex-valued 3D/2D signal sequences are lowpass-filtered in order to remove the undesired spectral components in  $|cf_{ct}| \notin (0, 0.5BW)$ . Finally, these lowpass-filtered complex-valued signal sequences may be sampled at the rate  $f_s = BW$  (i.e. at the temporal sampling interval  $T_s = \frac{1}{f_s} = \frac{1}{BW}$ ). According to Nyquist's sampling theorem, *the complex-quadrature sampling scheme achieves the minimum possible temporal-sampling rate* for a temporally-bandpassed signal having a bandwidth of  $BW$ . A detailed description of the complex-quadrature sampling scheme will be given in chapter 4.

---

<sup>14</sup>Or up-shift the spectral components inside the negative frequency band  $cf_{ct} \in (-f_C - 0.5BW, -f_C + 0.5BW)$ .

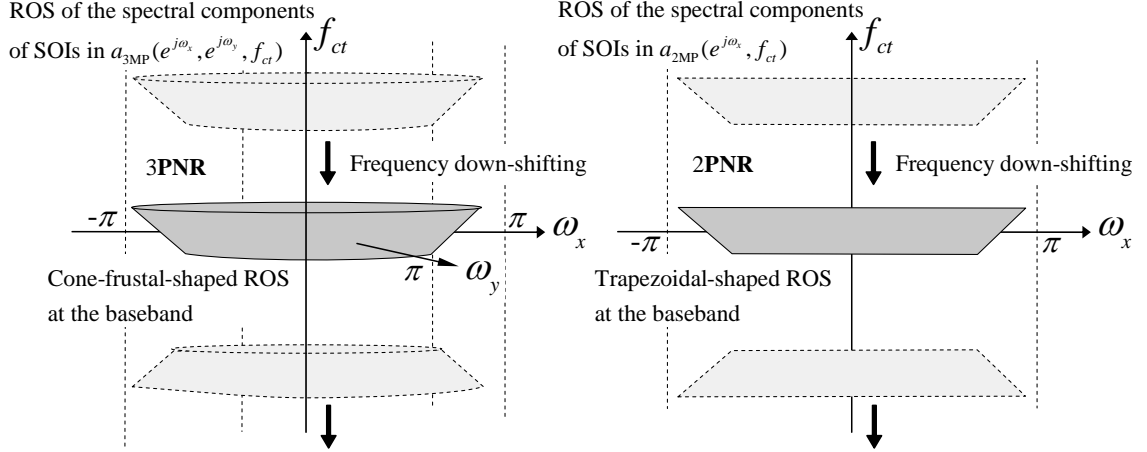


Figure 2.18: Complex-quadrature temporal-demodulation applied to down-shift the spectral contents of the positive frequency bands of 3D/2D signal sequences  $a_{3MP}(n_x, n_y, t)$  and  $a_{2MP}(n_x, t)$  to the baseband.

### 2.8.3 The Real-IF Sampling Scheme

The real-IF sampling scheme employs *real-IF temporal-demodulation* to down-shift the spectral contents in the positive frequency band  $cf_{ct} \in (f_C - 0.5BW, f_C + 0.5BW)$ , into the IF band  $cf_{ct} \in (0, BW)$  and up-shift the negative frequency band  $cf_{ct} \in (-f_C - 0.5BW, -f_C + 0.5BW)$ , into the IF band  $cf_{ct} \in (-BW, 0)$ , of the 3D/2D signal sequences  $a_{3MP}(n_x, n_y, t)$  and  $a_{2MP}(n_x, t)$  without any spectral overlapping as shown in Figure 2.19. The IF-temporal demodulation yield real-valued 3D/2D signal sequences. Note that the desired spectral components are now in the temporal frequency band  $|cf_{ct}| \in (0, BW)$ . Next, these real-valued 3D/2D signal sequences are lowpass-filtered in order to remove the undesired spectral components in  $|cf_{ct}| \notin (0, BW)$ . Finally, these lowpass-filtered complex-valued signal sequences may be sampled at the rate  $f_s = 2BW$  (i.e. at the temporal sampling interval  $T'_s = \frac{1}{f'_s} = \frac{1}{2BW}$ ). Because in the real-IF sampling scheme the 3D/2D signal sequences  $a_{3MP}(n_x, n_y, t)$  and  $a_{2MP}(n_x, t)$  are processed as real-valued signals, it has about 50% less pre-processing analog-circuit complexity compared to the complex-quadrature sampling scheme. The concept of down-shifting the positive

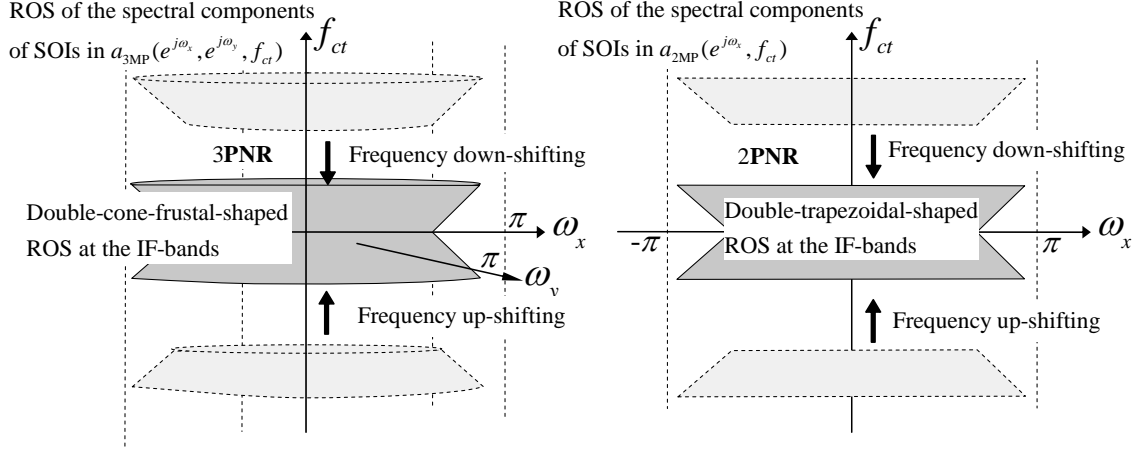


Figure 2.19: Real-IF temporal-demodulation applied to down-shift the positive frequency band and up-shift the negative frequency band of 3D/2D signal sequences  $a_{3MP}(n_x, n_y, t)$  and  $a_{2MP}(n_x, t)$  to the IF-bands.

frequency band and up-shifting the negative frequency band to IF bands is adopted in the real-IF tri-stage temporal sampler array, which has been proposed in [59].

## 2.9 Summary

In this chapter, the key concepts and terminology used in this thesis have been introduced. First, the important properties of propagating EM waves have been briefly reviewed in section 2.2. It has been shown that propagating EM waves can be closely approximated by 4D ST PWs. The spectra of 4D BB-BP ST PWs and the corresponding 3D/2D signals observed on a plane and on a line in 3D space in response to a propagating EM wave have been derived in section 2.3. Next in section 2.4, the concepts of the antenna response function and the antenna impulse response have been introduced by extending the concept of the active element pattern of the respective arrays. In the proceeding chapters, the signals observed at the outputs of elemental antennas in 2D/1D uniformly distributed antenna arrays in response to propagating EM 4D BB-BP ST PWs have been specified in terms of the antenna response function and the antenna impulse response.

A detailed spectral analysis has been given in sections 2.5 and 2.6, for 3D/2D signal sequences observed in 2D-UDPAs and 1D-UDAAAs, respectively. Also, the criteria for avoiding aliasing in 2D-UDPAs and 1D-UDAAAs have been stated there. In section 2.7, the distortions of the spectra of signal sequences from finite-extent 2D-UDPAs and 1D-UDAAAs have been analyzed. It has been shown that using proper 2D/1D window function an acceptable trade-off can be achieved between the spectral-spreading and spectral-leakage. Finally, three possible temporal sampling schemes have been suggested for sampling 3D and 2D signal sequences from 2D-UDPAs and 1D-UDAAAs.



## Chapter 3

# The Focal Region Signals of a Paraboloidal Reflector and the Corresponding Spectra

### 3.1 Introduction

Paraboloidal reflector antennas have widespread applications that include radio astronomy, microwave-imaging, remote-sensing, space-science, deep-space communications, satellite broadcasting and satellite communications [102][103][104][105][106][107][108][109]. It is expected that about 3,000 paraboloidal “dish” reflector antennas of 15 m diameter will be used in the Square Kilometer Array (SKA) in receiving celestial EM radiation in the frequency range of 0.5 - 10 GHz [110]. The SKA will be the largest aperture synthesis radio telescope system in the world and is planned to be fully commissioned by the year 2020 [19][110][111]. The principal engineering design goals for the SKA include achieving extremely high system sensitivity that is facilitated by the large collecting area and low noise receiver systems [19][110]. The system sensitivity of the SKA is expected to exceed that of current systems at least by a factor of 50 [111]. For achieving high sky survey scanning-speeds in the lower-mid frequency band (e.g. 0.5-1.7 GHz), it has been proposed that novel *focal plane array* (FPA) receivers to be used with some of the paraboloidal reflector antennas in the SKA [19][110][111]. In order to achieve such high sensitivity in the lower-mid frequency band using FPAs, it is essential to have an accurate modeling of focal EM fields of a paraboloidal reflector.

The electric-fields observed around the focal region in response to the reflected far-field EM waves from an ideal circular-aperture prime-focus paraboloidal reflector and the corresponding spectra are analyzed in this chapter. The diffraction of reflected EM waves

in the focal region concentrates the power of propagating EM waves into a finite spatial region on the focal plane. Using the “*Huygens’ Principle Approximation*” [57](pp. 34), it is shown that ideally the ROS of the spectrum of the resulted electric-field on the focal plane in response to an incident EM BB-BP ST PW is given by a 3D double right-circular frustum. It is also shown that the dimensions of this frustum can be specified in terms of the *focal length* ( $F$ ) and the *diameter* ( $D$ ) of the paraboloid. This is verified by using the **Focal Field Synthesizer (FFS)**, a GPU<sup>1</sup>-accelerated computer program that is developed in order to evaluate focal region electric-fields of a paraboloid. Here, the focal electric-field is determined by integrating the electric-field components originated by the infinitesimal currents induced on the perfectly conducting surface of the paraboloid in response to an incident monochromatic EM ST PW. The extensive parallel processing capabilities of the GPU are exploited for fast evaluation of computationally intensive numerical integrations. It is shown that for the same set of specifications the focal region electric-fields evaluated with the FFS are almost identical to the focal region electric-fields evaluated by the GRASP9<sup>2</sup>. In this thesis, the details of the ROSs of the spectra of the focal region electric-fields are exploited in designing the beamforming 3D FIR frustum filters in chapter 5. Also in chapter 5, the test sequences for focal region electric-fields, which are synthesized using the FFS, are used in determining the performance of the broadband beamformers.

This chapter is organized as follows. In section 3.2, the properties of the electric-fields on the focal region and the corresponding spectra are derived. Given that an arbitrary EM field can be expressed as a superposition of EM ST PWs [94](pp. 18), the ROS of the spectrum of the focal EM field is deduced in subsection 3.2.1 using the Huygens’ Principle Approximation and the concepts introduced in chapter 2 regarding propagating EM ST PWs received on a plane in 3D space, specifically in sections 2.3.1, 2.3.2, 2.4, 2.5 and

---

<sup>1</sup>The Graphics Processing Unit of a personal computer or a workstation.

<sup>2</sup>GRASP9 - is a EM field evaluation software that has been widely used in reflector antenna analysis [58].

2.7.1. In subsection 3.2.2, the predicted ROSs of the spectra of the focal electric-fields are compared against the ROSs of the spectra of simulated focal electric-fields, which are evaluated using the FFS. The design of the GPU-accelerated FFS program is explained in section 3.3. The system specifications and the input parameters for the FFS are stated in subsection 3.3.1. The radiation integral for the focal region EM field is derived in subsection 3.3.2 using the *fundamental Maxwell's equations and the physical optics (PO) approximation* [112](ch. 5). In subsection 3.3.3, the radiation integral is reorganized as a numerical summation using the *Newton-Cotes algorithm* [113] (pp. 247-264) in order to fully exploit the extensive parallel processing capabilities of the GPU. Examples of the electric-field patterns evaluated using the FFS are given in subsection 3.3.4. Also in this subsection, the normalized focal electric-field patterns evaluated with the FFS are compared against the electric-field patterns evaluated with GRASP9 for the same set of specifications.

## 3.2 The ROS of the Spectrum of the EM Field Observed on the Focal Region

Previously, various attempts have been made to determine the distribution of EM fields in the focal region of a paraboloidal reflector in response to an incident EM ST PW. As given in [114](part II), some of these attempts were aimed at deriving a closed-form expression for the EM fields in the focal region. However, such expressions contain so-called special functions (e.g. Bessel functions and their variants [115](pp. 219-223)) and, therefore, in general are too complicated to visualize and interpret for a general understanding of the properties of the focal electric-field and their corresponding spectra. In the following, a simple method has been proposed that deduce the ROS of the spectrum of focal region EM-field of a paraboloidal reflector in response to an incident EM ST PW.

### 3.2.1 Predicting the ROS of the Spectrum of the Focal Region Electric-Field

For simplicity, a *circular-aperture prime-focus paraboloidal-dish reflector* [57] is assumed here. In response to incident EM ST PWs, surface currents are induced on the ideally conducting inner-surface of the paraboloidal-dish [57](pp. 34-39). According to the “*Huygens’ Principle Approximation*” [57](pp. 34), these surface-currents act as point sources that emit infinitesimal EM spherical wavefronts toward the focal region of the paraboloidal-dish as shown in Figure 3.1 [112](ch. 5). *It is assumed that over a finite region around the focal point (O), these spherical wavefronts can be closely approximated by infinitesimal EM 4D ST PWs.* Thus, over this region, the EM field is formed by the superposition of such infinitesimal EM 4D ST PWs that radiate from all points on the reflector surface. Hence following section 2.3.1, the ideal infinite extent focal EM field may be written in the form of the summation of infinitesimal EM 4D ST PWs

$$\mathbf{efr}(x, y, z, t) = \sum_{\theta} \sum_{\phi} \hat{\mathbf{E}}_{\theta, \phi}^{\text{Pol}} pw_{\theta, \phi}(x, y, z, t), \quad (3.1)$$

where  $\hat{\mathbf{E}}_{\theta, \phi}^{\text{Pol}}$  is the polarization unit vector associated with each infinitesimal scalar-valued 4D ST PW that is given by

$$pw_{\theta, \phi}(x, y, z, t) = w_{\theta, \phi} c^{-1}(\sin(\theta) \cos(\phi)x + \sin(\theta) \sin(\phi)y + \cos(\theta)z) + t. \quad (3.2)$$

Here, the DOA of this infinitesimal EM 4D ST PW is specified by the inclination angle  $\theta$  and the azimuth angle  $\phi$ , which correspond to the *point of origin of the infinitesimal EM wave* on the surface of the reflector dish. Note that the wavefront function  $w_{\theta, \phi}(\tau)$  corresponds to the 1D temporal wavefront function  $w(\tau)$  that is associated with the incident EM ST PW arriving from a far-field source. However in (3.1), the polarization unit vector  $\hat{\mathbf{E}}_{\theta, \phi}^{\text{Pol}}$  depends on both the polarization of the incident EM ST PW and the *unit normal-vector* (i.e.  $\hat{\mathbf{n}}(\mathbf{r}')$  in Figure 3.9) at the point of origin  $(\theta, \phi)$  on the inner surface of the paraboloid. For the EM 4D ST PWs corresponding to this particular paraboloidal reflector, the associated azimuth angles are in the range  $\phi \in (0^\circ, 360^\circ)$ ,

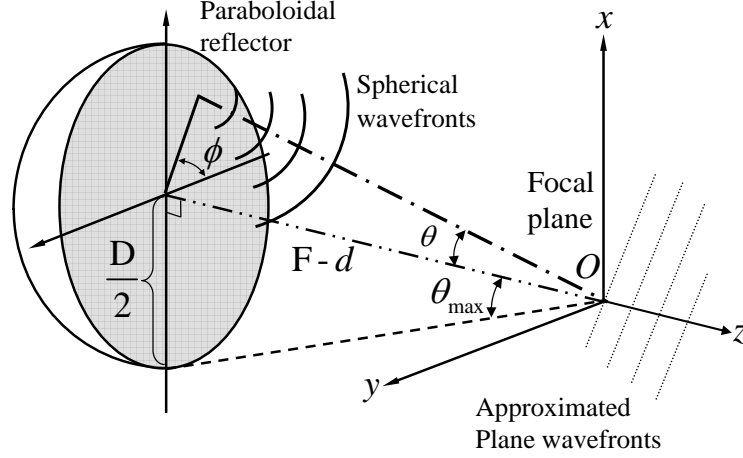


Figure 3.1: Surface currents are induced in response to the incident EM PWs. The induced surface currents act as point sources that emits infinitesimal EM waves towards to focal plane.

whereas the inclination angles are in the range  $\theta \in (0^\circ, \theta_{\max})$ . Given that the geometry of this particular paraboloidal dish is specified by the focal length  $F$ , and the aperture diameter  $D$ , it can be shown that

$$\theta_{\max} = \tan^{-1} \left( \frac{8(F/D)}{16(F/D)^2 - 1} \right). \quad (3.3)$$

In the focal region, the vector-valued electric-field  $\mathbf{efr}(x, y, z, t)$  can also be expressed with its components along directions of  $\hat{\mathbf{u}}_x$ ,  $\hat{\mathbf{u}}_y$  and  $\hat{\mathbf{u}}_z$ , such that

$$\mathbf{efr}(x, y, z, t) = xfr(x, y, z, t) \hat{\mathbf{u}}_x + yfr(x, y, z, t) \hat{\mathbf{u}}_y + zfr(x, y, z, t) \hat{\mathbf{u}}_z. \quad (3.4)$$

Substituting for  $\mathbf{efr}(x, y, z, t)$  in (3.1) with (3.4) yields

$$xfr(x, y, z, t) \hat{\mathbf{u}}_x + yfr(x, y, z, t) \hat{\mathbf{u}}_y + zfr(x, y, z, t) \hat{\mathbf{u}}_z = \sum_{\theta} \sum_{\phi} \hat{\mathbf{E}}_{\theta, \phi}^{\text{Pol}} pw_{\theta, \phi}(x, y, z, t), \quad (3.5)$$

that implies

$$xfr(x, y, z, t) = \sum_{\theta} \sum_{\phi} (\hat{\mathbf{E}}_{\theta, \phi}^{\text{Pol}} \bullet \hat{\mathbf{u}}_x) pw_{\theta, \phi}(x, y, z, t), \quad (3.6a)$$

$$yfr(x, y, z, t) = \sum_{\theta} \sum_{\phi} (\hat{\mathbf{E}}_{\theta, \phi}^{\text{Pol}} \bullet \hat{\mathbf{u}}_y) pw_{\theta, \phi}(x, y, z, t), \quad (3.6b)$$

$$zfr(x, y, z, t) = \sum_{\theta} \sum_{\phi} (\hat{\mathbf{E}}_{\theta, \phi}^{\text{Pol}} \bullet \hat{\mathbf{u}}_z) pw_{\theta, \phi}(x, y, z, t). \quad (3.6c)$$

Following the *linearity-property of mD Fourier transform* [41] (ch. 6), the 4D-CDFTs of  $xfr(x, y, z, t)$ ,  $yfr(x, y, z, t)$  and  $zfr(x, y, z, t)$  may be given by

$$XFR(f_x, f_y, f_z, f_{ct}) = \sum_{\theta} \sum_{\phi} (\hat{\mathbf{E}}_{\theta, \phi}^{\text{Pol}} \bullet \hat{\mathbf{u}}_x) PW_{\theta, \phi}(f_x, f_y, f_z, f_{ct}), \quad (3.7a)$$

$$YFR(f_x, f_y, f_z, f_{ct}) = \sum_{\theta} \sum_{\phi} (\hat{\mathbf{E}}_{\theta, \phi}^{\text{Pol}} \bullet \hat{\mathbf{u}}_y) PW_{\theta, \phi}(f_x, f_y, f_z, f_{ct}), \quad (3.7b)$$

$$ZFR(f_x, f_y, f_z, f_{ct}) = \sum_{\theta} \sum_{\phi} (\hat{\mathbf{E}}_{\theta, \phi}^{\text{Pol}} \bullet \hat{\mathbf{u}}_z) PW_{\theta, \phi}(f_x, f_y, f_z, f_{ct}), \quad (3.7c)$$

where the 4D-CDFT pair for the infinitesimal 4D ST PW and its spectrum are denoted by  $pw_{\theta, \phi}(x, y, z, t) \xrightarrow{\text{4D-CDFT}} PW_{\theta, \phi}(f_x, f_y, f_z, f_{ct})$ . According to (3.7a), the ROS of  $XFR(f_x, f_y, f_z, f_{ct})$  is given by the composite ROSs of  $PW_{\theta_x, \phi_x}(f_x, f_y, f_z, f_{ct})$  for all angle-pairs  $(\theta_x, \phi_x)$  such that  $\hat{\mathbf{E}}_{\theta_x, \phi_x}^{\text{Pol}} \bullet \hat{\mathbf{u}}_x = 0$  where  $\theta_x \in (0^\circ, \theta_{\max})$  and  $\phi_x \in (0^\circ, 360^\circ)$ . Similarly, the ROS of  $YFR(f_x, f_y, f_z, f_{ct})$  is given by the composite ROSs of  $PW_{\theta_y, \phi_y}(f_x, f_y, f_z, f_{ct})$  for all  $(\theta_y, \phi_y)$  such that  $\hat{\mathbf{E}}_{\theta_y, \phi_y}^{\text{Pol}} \bullet \hat{\mathbf{u}}_y = 0$  and the ROS of  $ZFR(f_x, f_y, f_z, f_{ct})$  is given by the composite ROSs of  $PW_{\theta_z, \phi_z}(f_x, f_y, f_z, f_{ct})$  for all  $(\theta_z, \phi_z)$  such that  $\hat{\mathbf{E}}_{\theta_z, \phi_z}^{\text{Pol}} \bullet \hat{\mathbf{u}}_z = 0$ , where  $\theta_{y;z} \in (0^\circ, \theta_{\max})$  and  $\phi_{y;z} \in (0^\circ, 360^\circ)$ .

Assume a scenario where a linearly  $\hat{\mathbf{u}}_y$ -polarized far-field EM BB-BP ST PW is incident on the prime-focus paraboloidal reflector. For the resultant infinitesimal EM ST PWs  $\hat{\mathbf{E}}_{\theta, \phi}^{\text{Pol}} pw_{\theta, \phi}(x, y, z, t)$ , it can be shown that  $\hat{\mathbf{E}}_{\theta, \phi}^{\text{Pol}} \bullet \hat{\mathbf{u}}_y = 0$  for all  $\theta \in (0^\circ, \theta_{\max})$  and all  $\phi \in (0^\circ, 360^\circ)$ . Therefore, the ROS of  $YFR(f_x, f_y, f_z, f_{ct})$  is given by the composite ROSs of the spectra  $PW_{\theta, \phi}(f_x, f_y, f_z, f_{ct})$ . In section 2.3.1, it has been shown that the ROS of  $PW_{\theta, \phi}(f_x, f_y, f_z, f_{ct})$  in the 4D frequency space  $(f_x, f_y, f_z, f_{ct}) \in \mathbb{R}^4$  is on the line of inter-

section between the three 4D hyper-planes  $f_x = \sin(\theta)\cos(\phi) f_{ct}$ ,  $f_y = \sin(\theta)\sin(\phi) f_{ct}$  and  $f_z = \cos(\theta) f_{ct}$  for temporal frequencies  $\forall |cf_{ct}| \notin (f_C - 0.5BW, f_C + 0.5BW)$ . As  $\phi$  and  $\theta$  varies in the respective ranges  $\phi \in (0^\circ, 360^\circ)$  and  $\theta \in (0^\circ, \theta_{\max})$ , the line of intersection sweeps the 4D hyper-volume  $HV_{4CP}(f_x, f_y, f_z, f_{ct})$ . The properties of  $HV_{4CP}(f_x, f_y, f_z, f_{ct})$  can be interpreted by its projection into different 4D hyper-planes, which results 3D objects. The projection of  $HV_{4CP}(f_x, f_y, f_z, f_{ct})$  onto the 4D hyper-plane  $f_z = 0$  is a 3D double right-circular frustum that corresponds to a 3D double right-circular cone that has its main axis along  $f_{ct}$  and a half-cone-angle

$$\alpha_{\max} = \tan^{-1}(\sin(\theta_{\max})), \quad (3.8)$$

as shown in Figure 3.2 (a). Given that prime-focus paraboloidal-dish reflectors of  $F/D$ -ratios in the range (0.4, 0.6) have been proposed for the SKA [18], the half-cone angle associated with such dishes varies in the range  $\alpha_{\max} \in (35^\circ, 42^\circ)$ . Further, the projection of  $HV_{4CP}(f_x, f_y, f_z, f_{ct})$  onto the 4D hyper-plane  $f_{ct} = 0$  is given by the intersection between a 3D double right-circular cone along the axis  $f_z$  and having a half-cone-angle  $\theta_{\max}$  and a 3D sphere-shell of inner- and outer- radius  $c^{-1}(f_C - 0.5BW)$  and  $c^{-1}(f_C + 0.5BW)$  as shown in Figure 3.2 (b). Also, the 3D projections of  $HV_{4CP}(f_x, f_y, f_z, f_{ct})$  onto 4D hyper-planes  $f_x = 0$  and  $f_y = 0$  yield an identical 3D volume that corresponds to a section of 3D double right-circular cone by an oblique plane is shown in Figure 3.2 (c).

For a circular-polarized far-field EM BB-BP ST PW incident on the prime-focus paraboloidal reflector, it can be shown that both  $\hat{\mathbf{E}}_{\theta, \phi}^{\text{Pol}} \bullet \hat{\mathbf{u}}_x = 0$  and  $\hat{\mathbf{E}}_{\theta, \phi}^{\text{Pol}} \bullet \hat{\mathbf{u}}_y = 0$  for all  $\theta \in (0^\circ, \theta_{\max})$  and all  $\phi \in (0^\circ, 360^\circ)$ . Therefore as predicted above, the ROSs of  $XFR(f_x, f_y, f_z, f_{ct})$  and  $YFR(f_x, f_y, f_z, f_{ct})$ , which are the spectra of the  $\hat{\mathbf{u}}_x$ -component  $xfr(x, y, z, t)$ , and the  $\hat{\mathbf{u}}_y$ -component  $yfr(x, y, z, t)$ , of the focal-region electric-field  $\mathbf{efr}(x, y, z, t)$ , take the shape of  $HV_{4CP}(f_x, f_y, f_z, f_{ct})$ .

Because  $\hat{\mathbf{E}}_{\theta, \phi}^{\text{Pol}} \bullet \hat{\mathbf{u}}_z \approx 0$  for  $\theta \approx 0$  and  $\phi \in (0^\circ, 360^\circ)$ , for any incident far-field EM BB-BP ST PW, the ROS of  $ZFP(f_x, f_y, f_z, f_{ct})$ , which is the spectrum of the  $\hat{\mathbf{u}}_z$ -component

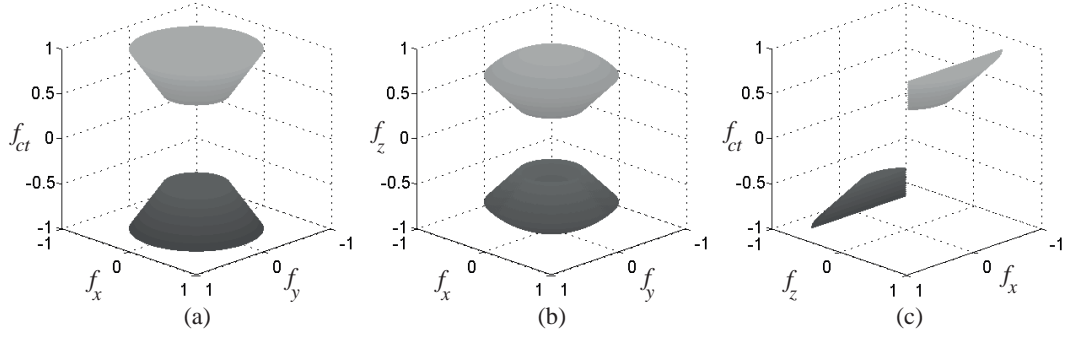


Figure 3.2: Projections of the 4D ROS of the spectra of focal electric fields on to the 4D hyper-planes (a)  $f_z = 0$  (b)  $f_{ct} = 0$  and (c)  $f_y = 0$ .

of  $\mathbf{efr}(x, y, z, t)$ , does not corresponds to 4D hyper-volume  $HV_{4C}(f_x, f_y, f_z, f_{ct})$  as in the case of  $\hat{\mathbf{u}}_x$ -component  $xfr(x, y, z, t)$  and  $\hat{\mathbf{u}}_y$ -component  $yfr(x, y, z, t)$ . Nevertheless, it can be shown that  $\hat{\mathbf{E}}_{\theta, \phi}^{\text{Pol}} \bullet \hat{\mathbf{u}}_z = 0$  for some  $\theta \approx \alpha_{\max}$  and for some  $\phi \in (0^\circ, 360^\circ)$ . Hence and because  $\hat{\mathbf{E}}_{\theta, \phi}^{\text{Pol}} \bullet \hat{\mathbf{u}}_z = 0$  for all  $\theta \geq \alpha_{\max}$  and for all  $\phi \in (0^\circ, 360^\circ)$ , all the spectral components of  $ZFP(f_x, f_y, f_z, f_{ct})$  remain inside the 4D volume of  $HV_{4CP}(f_x, f_y, f_z, f_{ct})$ .

### The Electric-Field on the Focal Plane and the Corresponding Spectrum

On the focal plane  $z = 0$ , the electric filed  $\mathbf{efp}(x, y, t)$  may be expressed with respect to the focal region electric field  $\mathbf{efr}(x, y, z, t)$  such that

$$\begin{aligned} \mathbf{efp}(x, y, t) &= \mathbf{efr}(x, y, z = 0, t), \\ &= xfr(x, y, z = 0, t) \hat{\mathbf{u}}_x + yfr(x, y, z = 0, t) \hat{\mathbf{u}}_y + zfr(x, y, z = 0, t) \hat{\mathbf{u}}_z. \end{aligned} \quad (3.9)$$

Following section 2.3.2, given that the  $\hat{\mathbf{u}}_x$ -component of the focal plane electric field  $xfp(x, y, t) = xfr(x, y, z = 0, t)$ , the corresponding spectrum  $XFP(f_x, f_y, f_{ct})$  can be evaluated by the projection of  $XFR(f_x, f_y, f_z, f_{ct})$  on to the 4D hyper plane  $f_z = 0$ . Similarly, the 3D spectra  $YFP(f_x, f_y, f_{ct})$  and  $ZFP(f_x, f_y, f_{ct})$  can be evaluated by projecting  $YFR(f_x, f_y, f_z, f_{ct})$  and  $ZFR(f_x, f_y, f_z, f_{ct})$  on to the 4D hyper-plane  $f_z = 0$ , respectively. Hence, the ROS of the spectrum  $YFP(f_x, f_y, f_{ct})$  of the  $\hat{\mathbf{u}}_y$ -component  $yfp(x, y, t)$  of the vector-valued focal electric-field  $\mathbf{efp}(x, y, t)$  resulted by an incident linearly  $\hat{\mathbf{u}}_y$ -polarized



*far-field EM BB-BP ST PW incident on a prime-focus paraboloidal reflector is predicted to be a 3D right-circular double frustum (see Figure 2.5 in page 31) that corresponds to a 3D cone of half-cone angle  $\alpha_{\max}$  in  $(f_x, f_y, f_{ct}) \in \mathbb{R}^3$ . The same region is occupied by the spectral components of  $XFP(f_x, f_y, f_{ct})$  and  $YFP(f_x, f_y, f_{ct})$ , the spectra of  $\hat{\mathbf{u}}_y$ - and  $\hat{\mathbf{u}}_x$ - components  $xfp(x, y, t)$  and  $yfp(x, y, t)$  of focal plane electric field in response to a circular-polarized far-field EM BB-BP ST PW incident on the circular-aperture prime-focus paraboloidal reflector.*

### 3.2.2 Verification of the ROS of the Focal Plane EM Field by Numerical Simulation

The above predicted ROS of the 3D spectrum of the focal plane electric-field  $\mathbf{efp}(x, y, t)$  is verified using the sampled sequences of focal plane electric-field that are synthesized using the FFS, the GPU accelerated focal EM field evaluation software<sup>3</sup>. In the following, spectra of focal field components corresponding to different paraboloidal geometries (i.e. the focal length  $F$ , and the diameter  $D$  combinations), temporal frequencies, types of polarization and the DOAs of the incident far-field EM ST PW, are evaluated and the corresponding ROSs are compared with the predicted ROS in section 3.2.1.

#### **ROSs of the Spectra of Synthesized Focal Electric-Field for a Band of Frequencies**

Let's assume a prime-focus paraboloidal-reflector with  $D = 15$  m and  $F = 6.75$  m (i.e.  $F/D = 0.45$ ). Here, the synthesized test-sequence of the focal electric-fields correspond to an incident linearly- $\hat{\mathbf{u}}_y$  polarized EM ST PW that arrives along the prime-axis of the paraboloid (i.e.  $\theta = 0^\circ$  and  $\phi = 0^\circ$ ) and containing all temporal frequencies in the band spanning 1.2 GHz from 0.5 to 1.7 GHz. The focal electric-field is synthesized on the square area of size  $(1.7648 \times 1.7648)$  m<sup>2</sup>, which is centered at the focal point (O) of the focal plane (i.e.  $z = 0$ ) (see Figure 3.1). It is observed that the area of the focal plane is

---

<sup>3</sup>The design of FFS is described in the second part of this chapter

much larger than the “focal spot” where the power of the incident PWs are focused in. Given the 3D-CDFT pair  $yfp(x, y, t) \xleftrightarrow{3D-CDFT} YFP(f_x, f_y, f_{ct})$  for the  $\hat{\mathbf{u}}_y$ -component of the synthesized focal electric-field  $\mathbf{efp}(x, y, t)$  and its spectrum, the *equivalent iso-surface of the positive frequencies of the normalized spectrum*  $||YFP(f_x, f_y, f_{ct})|| = 0.5$ , is shown in Figure 3.3. Note that spatial-frequency axes  $f_x$  and  $f_y$  are normalized. As shown in Figure 3.3 the “frustum-shaped” iso-surface agrees well with the predicted ideal ROS of the positive frequencies of the normalized spectrum of the focal electric-field.

The contour plots corresponding to  $||YFP(f_x, f_y, f_{ct})|| = 0.5$ ,  $||XFP(f_x, f_y, f_{ct})|| = 0.5$  and  $||ZFP(f_x, f_y, f_{ct})|| = 0.5$  of the normalized spectra of  $\hat{\mathbf{u}}_y$ -,  $\hat{\mathbf{u}}_x$ - and  $\hat{\mathbf{u}}_z$ - components of the focal electric-field  $\mathbf{efp}_{\text{Liny}}(x, y, t)$ , pertain to a linearly  $\hat{\mathbf{u}}_y$ -polarized monochromatic EM ST PW of temporal frequency ( $cf_{ct}$ ) 1 GHz that is arriving along the prime-axis of the paraboloid of  $D = 15$  m and  $F/D = 0.45$ , are shown by the solid-lines in Figure 3.4 (a), (b) and (c) (top-row). Similarly, the contour plots corresponding to  $||YFP(f_x, f_y, f_{ct})|| = 0.5$ ,  $||XFP(f_x, f_y, f_{ct})|| = 0.5$  and  $||ZFP(f_x, f_y, f_{ct})|| = 0.5$  of the normalized spectra of  $\hat{\mathbf{u}}_y$ -,  $\hat{\mathbf{u}}_x$ - and  $\hat{\mathbf{u}}_z$ - components of the focal electric-field  $\mathbf{efp}_{\text{Circ}}(x, y, t)$ , pertain to a right-circular polarized monochromatic EM ST PW of temporal frequency ( $cf_{ct}$ ) 1 GHz that is arriving along the prime-axis of the paraboloid of  $D = 15$  m and  $F/D = 0.45$  m, are shown by the solid-lines in Figure 3.4 (d), (e) and (f) (bottom-row). Note that the dashed-lines in the Figure 3.4 (a), (b), (c), (d), (e) and (f) represent the boundaries of the ROSs predicted in subsection 3.2.1 according to the Huygens’ Principle Approximation.

For the spectra of  $\mathbf{efp}_{\text{Liny}}(x, y, t)$ , which corresponds to the incident linearly  $\hat{\mathbf{u}}_y$ -polarized monochromatic EM ST PW, the contour-plot  $||YFP(f_x, f_y, f_{ct})|| = 0.5$  is almost coincide with the predicted boundary as shown in Figure 3.4 (a). Also according to Figure 3.4 (b) and (c), the contour-plots  $||XFP(f_x, f_y, f_{ct})|| = 0.5$  and  $||ZFP(f_x, f_y, f_{ct})|| = 0.5$  indicate that the spectral components of  $YFP(f_x, f_y, f_{ct})$  and  $ZFP(f_x, f_y, f_{ct})$  are remain inside of the predicted boundary. It has been observed that at any temporal fre-

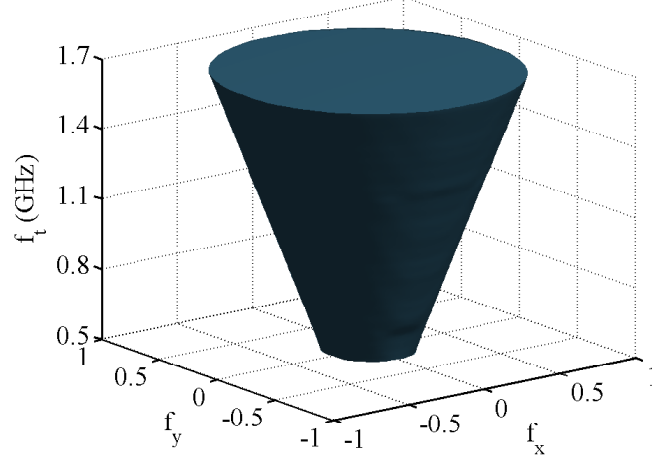


Figure 3.3:  $\|YFP(f_x, f_y, f_{ct})\| = 0.5$ ; The equivalent iso-surface of the positive frequencies of the normalized spectrum of the  $\hat{\mathbf{u}}_y$ -component of the focal electric-field for temporal frequencies in the band 0.5 - 1.7 GHz.

quency  $f_{ct} \in (0.5, 1.7)$  GHz, the contour plot  $\|YFP(f_x, f_y, f_{ct})\| = 0.5$ , which corresponds to an incident linearly  $\hat{\mathbf{u}}_y$ -polarized EM BB-BP ST PW on a prime-focus paraboloidal reflector having  $D = 15$  m and  $F/D = 0.45$ , is in good agreement with the boundary of the ROS that has been predicted in subsection 3.2.1.

On the other hand, for the spectra of  $\mathbf{efp}_{\text{Circ}}(x, y, t)$ , which corresponds to the incident right-circular polarized monochromatic EM ST PW, the contour-plots  $\|YFP(f_x, f_y, f_{ct})\| = 0.5$  and  $\|XFP(f_x, f_y, f_{ct})\| = 0.5$  are almost coincided with the predicted boundary as shown in Figure 3.4 (a) and (b). Also according to Figure 3.4 (c), the contour-plot  $\|ZFP(f_x, f_y, f_{ct})\| = 0.5$  indicates that the spectral components of  $ZFP(f_x, f_y, f_{ct})$  remain inside of the predicted boundary. It has been observed that at any temporal frequency  $f_{ct} \in (0.5, 1.7)$  GHz, the contour plots  $\|YFP(f_x, f_y, f_{ct})\| = 0.5$  and  $\|XFP(f_x, f_y, f_{ct})\| = 0.5$ , which correspond to an incident right-circular polarized EM BB-BP ST PW on a prime-focus paraboloidal reflector having  $D = 15$  m and  $F/D = 0.45$ , are in good agreement with the identical-boundary of the ROSs that has been predicted in subsection 3.2.1.

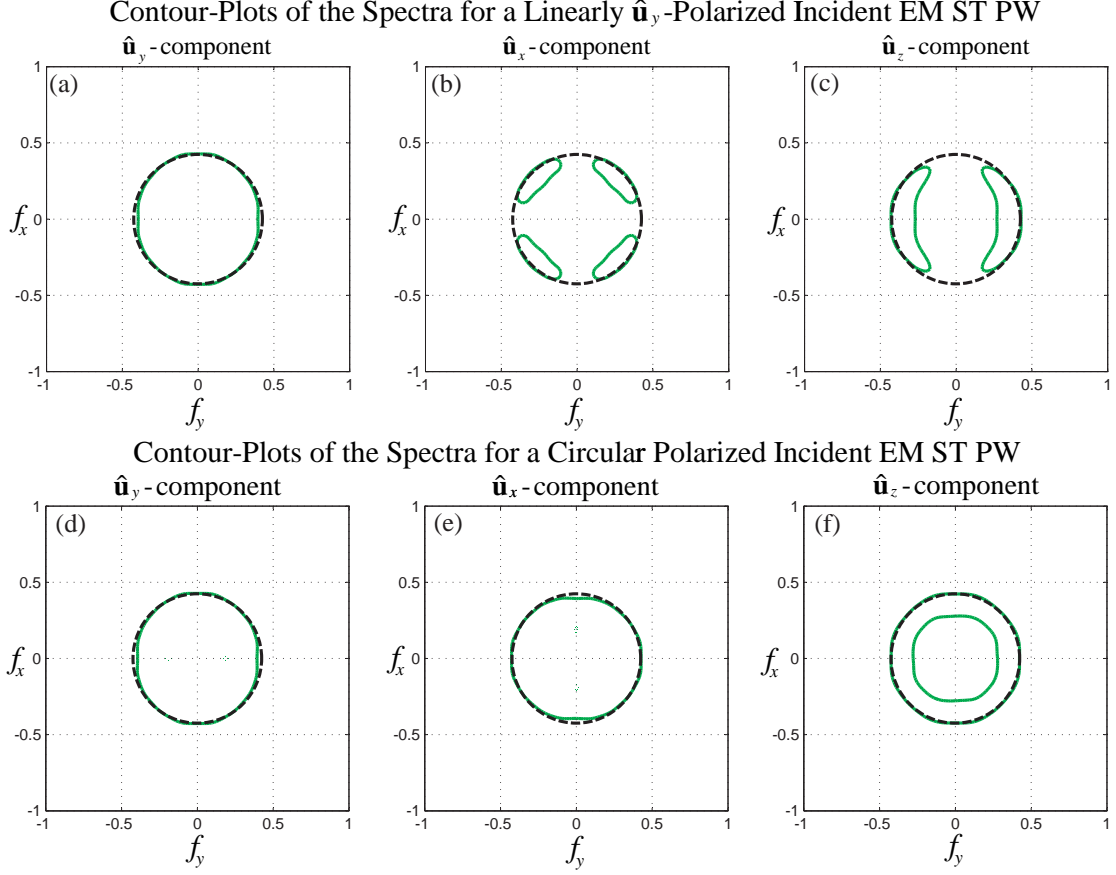


Figure 3.4: Contour-plots  $\|YFP(f_x, f_y, f_{ct})\| = 0.5$  (left),  $\|XFP(f_x, f_y, f_{ct})\| = 0.5$  (center) and  $\|ZFP(f_x, f_y, f_{ct})\| = 0.5$  (right) of the spectra of focal electric-field synthesized at 1 GHz (solid) and the boundary of the ROS predicted by Huygens' Principle Approximation (dashed). The top-row corresponds to an incident linearly  $\hat{\mathbf{u}}_y$ -polarized EM ST PW and the bottom-row corresponds to an incident right-circular polarized EM ST PW.

### The ROSs of the Spectra of Synthesized Focal Electric-Field for Different Focal Lengths

Figure 3.5 (a) - (l) illustrate the predicted boundary lines of the ROSs (dashed) and the contour plots  $\|YFP(f_x, f_y, f_{ct})\| = 0.5$  (solid) of the normalized spectra of  $\hat{\mathbf{u}}_y$ -component of the focal electric-field  $\mathbf{efp}(x, y, t)$ , pertain to a linearly  $\hat{\mathbf{u}}_y$ -polarized monochromatic EM ST PW of temporal frequency  $(cf_{ct})$  1 GHz that is arriving along the prime-axis of a series of prime-focus paraboloidal reflectors having a constant diameter  $D = 15$  m and different focal lengths  $F = 0.25D^4$ ,  $F = 0.30D$ ,  $F = 0.35D$ ,  $F = 0.40D$ ,  $F = 0.45D$ ,  $F = 0.50D$ ,

<sup>4</sup>For  $F/D = 0.25$ , the circular-aperture of a prime-focus paraboloid falls on the focal plane.

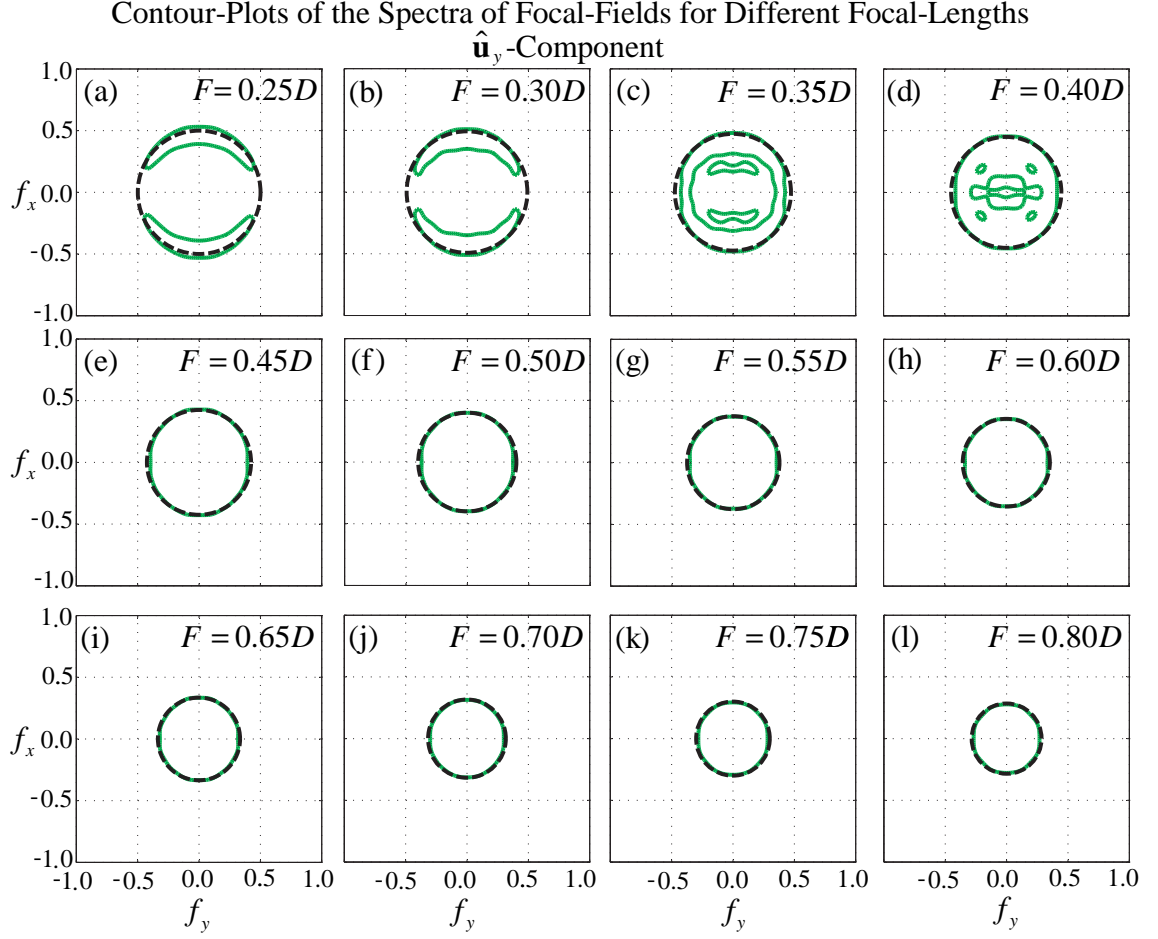


Figure 3.5: Contour-plots  $||YFP(f_x, f_y, f_{ct})|| = 0.5$  (solid) of the spectra of focal electric-field evaluated for paraboloidal reflectors having different focal lengths and the boundaries (dashed) of the ROSs predicted by Huygens' Principle Approximation.

$F = 0.55D$ ,  $F = 0.60D$ ,  $F = 0.65D$ ,  $F = 0.70D$ ,  $F = 0.75D$  and  $F = 0.80D$ . Note that as the focal lengths  $F$  and there by  $F/D$ -ratios increase, both the predicted and evaluated ROSs of the spectra of focal electric-field contract. As shown in Figure 3.5 (a) and (b), the contour plots  $||YFP(f_x, f_y, f_{ct})|| = 0.5$  corresponding to focal lengths  $F = 0.25D$  and  $F = 0.30D$  are not agreeing with the predicted boundaries for the ROSs. Also, for  $F = 0.35D$  and  $F = 0.40D$ , the corresponding contour plots  $||YFP(f_x, f_y, f_{ct})|| = 0.5$  show variations in the magnitude of  $YFP(f_x, f_y, f_{ct})$ . This may be due to the fact that at distances as short as  $F = 0.25D$ ,  $F = 0.30D$ ,  $F = 0.35D$  and  $F = 0.40D$ , the reflected

EM waves of temporal frequency 1 GHz can not be assumed to be EM ST PWs on the focal plane. Nevertheless, the contour plots  $||YFP(f_x, f_y, f_{ct})|| = 0.5$  shown in Figure 3.5 (e) - (l) are almost coincide with the predicted ROSs. Moreover, all contour plots shown in Figure 3.5 (a) - (l) imply that the spectral components of the focal electric-field remain inside of the boundaries of the predicted ROS with Huygens' Principle Approximation.

### **The ROSs of the Spectra of Synthesized Focal Electric-Field for Different DOAs**

The predicted boundary lines (dashed) and the contour plots  $||YFP(f_x, f_y, f_{ct})|| = 0.5$  (solid) of the normalized spectra of  $\hat{\mathbf{u}}_y$ -component of the focal electric-field  $\mathbf{efp}(x, y, t)$ , pertain to a prime-focus paraboloidal reflector having the diameter  $D = 15$  m and the focal length  $F = 6.75$  m (i.e.  $F/D = 0.45$ ), in response to a series of right-circular polarized monochromatic EM ST PWs of temporal frequency ( $cf_{ct}$ ) 1 GHz that are having different DOAs are shown in Figure 3.6. The polar-grid in Figure 3.6 specifies the DOAs of monochromatic EM ST PWs in terms of the inclination angle  $\theta$  and azimuth angle  $\phi$ . *Note that all the predicted boundary lines (dashed) and all the contour plots  $||YFP(f_x, f_y, f_{ct})|| = 0.5$  (solid) are centered at the origin  $(0, 0)$  (not shown in Figure 3.6) of the normalized 2D frequency space  $(f_x, f_y) \in \mathbb{R}^2$  as in the cases shown in Figures 3.4 and 3.5.* As shown in Figure 3.6, for DOAs specified by all combinations of  $\theta \in (0^\circ, 0.5^\circ, 1^\circ, 1.5^\circ, 2^\circ)$  and  $\phi \in (0^\circ, 45^\circ, 90^\circ, 135^\circ, 180^\circ, 225^\circ, 270^\circ, 315^\circ)$ , the contour plots  $||YFP(f_x, f_y, f_{ct})|| = 0.5$  are almost coincide with the predicted boundary for the ROS of the spectra of  $\hat{\mathbf{u}}_y$ -component of  $\mathbf{efp}(x, y, t)$  for a prime focus paraboloid of  $F/D = 0.45$  at  $cf_{ct} = 1$  GHz. The same has been observed that for any DOA specified by  $\theta \in (0^\circ, 3.5^\circ)$  and  $\phi \in (0^\circ, 360^\circ)$  at any temporal frequency  $cf_{ct} \in (0.5, 1.7)$  GHz. This verifies that, if the DOA of the incident EM BB-BP ST PW remains within the small angular range from the axis of the paraboloid, then the ROS of the spectrum of resultant focal electric-field is given by a 3D double right-circular frustum as predicted

### Contour Plots of the Focal-Field Spectra for Different DOAs

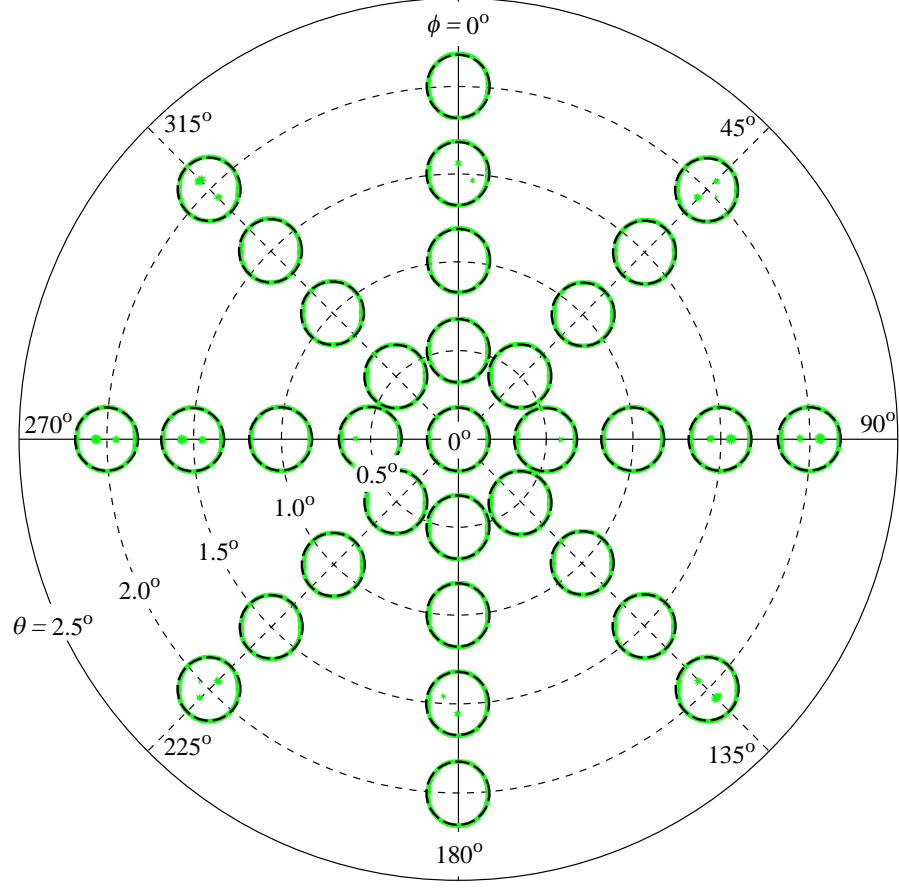


Figure 3.6: Contour-plots  $\|YFP(f_x, f_y, f_{ct})\| = 0.5$  (solid) of the spectra of the focal electric-fields resulted by right-circular polarized incident EM ST PWs having different DOAs and the boundary (dashed) of the ROS predicted by Huygens' Principle Approximation.

in subsection 3.2.1.

*From the observations made above using synthesized test sequences of the focal electric-field patterns, which correspond to prime focus paraboloidal reflectors of different focal lengths<sup>5</sup> and for both linear- and circular- polarized incident EM BB-BP ST PWs in the temporal frequency band (0.5, 1.7) GHz that are having different DOAs within the small angular range from the axis of the paraboloid, it can be confirmed that the ROSs of the spectra focal electric-field is given by a 3D double right-circular frustum as predicted*

<sup>5</sup>Provided the EM ST PW assumption holds for the infinitesimal EM waves originated by the surface currents on the reflector.

*by the Huygens' Principle Approximation.* Even though this model is not sophisticated enough to predict the magnitude and phase of the spectrum of the focal electric-fields, the concept of the ROS of the spectra of focal electric-field provides valuable insight for the effective design of FPA signal processors. In chapter 5 of this thesis, the shape of the ROS of the spectrum of the focal electric-field is exploited in the design of the beamforming 3D FIR frustum filters.

### 3.3 The Focal Field Synthesizer (FFS)

The Focal Field Synthesizer (FFS) is a computer program that evaluates the electric-field within the focal region of a paraboloidal reflector using numerical integration techniques that exploit the extensive parallel processing capabilities of the GPU. The FFS achieves high computational efficiency in evaluating focal electric-fields for different combinations of paraboloidal dish geometries in response to incident EM ST PWs having different temporal frequencies, polarizations and DOAs. Therefore, it is a viable and a low-cost CAD tool for FPA receiver design for the SKA and other applications. *In particular, the FFS is a frequency domain electric-field synthesis program that calculates the electric-field in the focal region in response to an incident monochromatic fully-polarized EM ST PW on a perfectly conducting paraboloidal reflector with no aperture blockage* (see Figure 3.7). The focal field patterns in response to non-monochromatic EM ST PWs can often be determined by appropriate superposition of monochromatic responses using the Fourier series representation of the wave front of the non-monochromatic EM ST PW.

Since late seventies various computer programs have been developed to numerically simulate EM fields in the focal region using mini-computers and personal-computers (PCs) [116][117][118][119]. As summarized in [114][120], in the development of these computer programs, many analysis/synthesis techniques have been employed to approximate the EM wave propagation and the induced surface current density at the reflector,



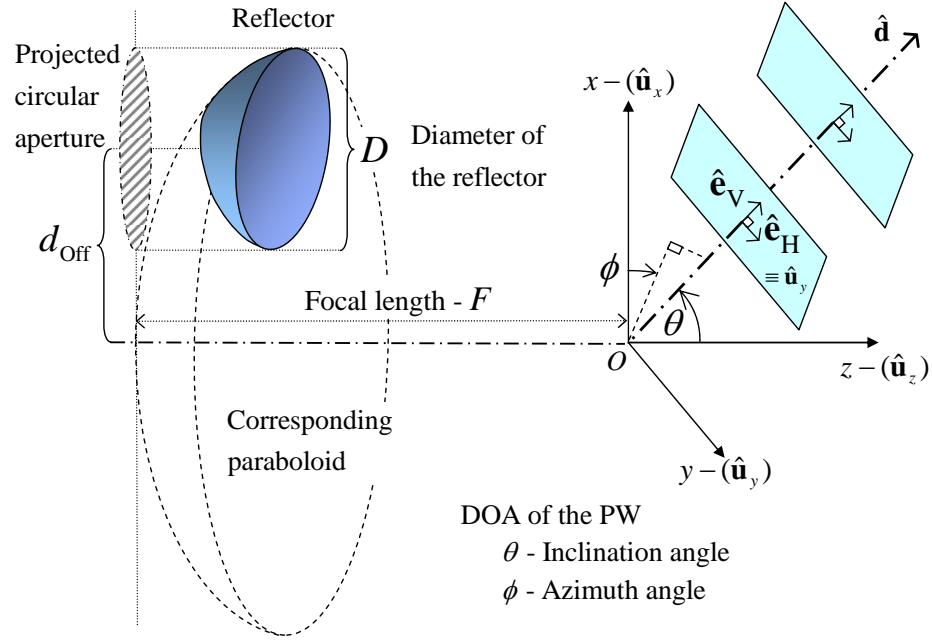


Figure 3.7: The considered arrangement of the reflector for the FFS and the used notations for specifying system parameters.

such as (a) geometrical optics (GO), (b) physical optics (PO), (c) the geometrical theory of diffraction (GTD), (d) the physical theory of diffraction (PTD), (e) the method of moments (MOM), (f) the Gaussian beam method and (g) the finite-time-time-domain (FTTD) method (e.g. with Yee algorithm). The above mentioned analysis/synthesis techniques have advantages and disadvantages for determining EM fields for different reflector configurations, both in terms of accuracy and computational complexity in evaluation. In general, the MOM method and FTTD method achieve the most accurate results although their respective computational complexities are comparatively very high because of the electrically larger paraboloidal reflector [120]. The GO and Gaussian-beam methods are accurate only for specific orientations of the reflector. For most practical cases of reflectors, PO and PTD methods, in combination with the GTD method, can achieve sufficiently accurate results with acceptable computation times [120]. Hence, in the FFS, the PO approximation is used in determining the surface current density

induced by the incident EM ST PW.

Specialized parallel processing hardware devices, such as field programmable gate arrays (FPGAs) and graphics processor units (GPUs), have been used to increase the speed of numerical calculations for FDTD, MOM techniques [121][122][123][124][125]. GPUs are now widely used in modern personal computers (PCs) for manipulating high-definition (HD) 3D graphical-objects in real time for applications in computer games and in animation [126][127]. As shown in Figure 3.8, a typical GPU architecture contains many processor cores and a common random access memory (RAM) module. Each processor core consists of a control unit, a cache memory and multiple arithmetic and logic units (ALUs) [128]. This many-core multi-threaded architecture facilitates the high-speed parallel execution of single-instruction-multiple-data (SIMD) operations, which is the case for graphics processing.

As a result of the rapid growth in the computer gaming industry over the last five years, there have been significant advances in GPU processing capabilities [126]. Also in the current market, PCs in the mid- to high-priced ranges are typically equipped with GPUs of moderate processing capabilities. NVIDIA, the largest GPU manufacturer in the world, foresaw the potential of GPU processing for “General Purpose - GPU” (GP-GPU) applications for non-graphical data and therefore developed the computational engine called Compute Unified Device Architecture (CUDA) and an integrated software development kit (SDK), based on the C programming language [126]. Further, third party software, known as “wrappers”, have been developed for other programming languages, such as Python, Fortran, Java and MATLAB, to interface CUDA with the respective development environments [126][129][130]. These wrappers provide researchers with the capability of rapid deployment of previously developed source codes with very few modifications in the respective development environment (e.g. MATLAB, Fortran). Nevertheless, the increased processing speeds that are achieved using wrapper

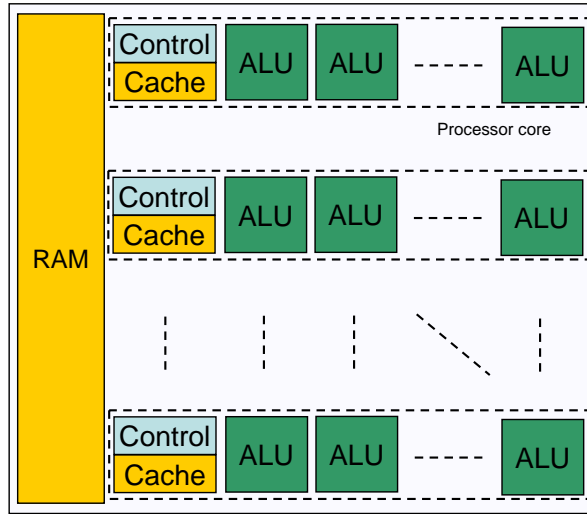


Figure 3.8: The architecture of a typical GPU.

programs may be lower than that achieved using direct CUDA implementation. In the FFS, GPUmat [130], a wrapper for MATLAB, is exploited to transfer the SIMD operations and data of the focal electric-field calculations to the GPU for high-speed parallel execution.

In order to validate the functionality of the FFS, the EM fields that are synthesized using the FFS has been compared with the focal fields<sup>6</sup> generated by GRASP9 [58] from TICRA. GRASP9 is a widely used commercial CAD tool for analyzing EM fields scattered by reflector antennas [58]. Here, the focal EM fields calculated using the FFS have been compared against the electric-field patterns calculated by the GRASP9 for same sets of input specifications. The results show that the focal EM fields calculated by both the FFS and the GRASP9 are in good agreement. Further, it has been observed that the FFS achieves reductions of field evaluation processing times that range from 150% to 280% compared to GRASP9.

---

<sup>6</sup>GRASP9 simulations were conducted by Dr. Bruce Veidt and Dr. Rick Smegal of Dominion Radio Astrophysical Observatory (DRAO), Penticton, BC, Canada. This candidate is utterly grateful for both Dr. Veidt and Dr. Smegal for generating these test sequences.

### 3.3.1 The System Specifications and Notations used in the FFS

In the FFS, the input specifications are the diameter ( $D$ ), the focal length ( $F$ ), and the lateral offset ( $d_{\text{Off}}$ ), which specify the geometry of the paraboloidal dish, and the temporal frequency ( $f_t \equiv cf_{ct}$ ), the type of polarization ( $\hat{\mathbf{E}}^{\text{Pol}}$ ), and the DOA ( $\hat{\mathbf{d}}$ ), of the incident monochromatic fully-polarized EM ST PW. The co-ordinate system of choice, the arrangement of the paraboloidal reflector and the orientation and the polarization of the incident monochromatic EM ST PW of the FFS are shown in Figure 3.7 (see page 89). As shown there, the focal point of the paraboloidal reflector is selected as the origin (O) of the Cartesian coordinate system of choice. For the FFS, only the paraboloidal reflectors of circular-apertures are considered. For the reflector arrangement shown in Figure 3.7, the lateral offset  $d_{\text{Off}}$ , is the distance between the center of the projected circular-aperture on the  $z = 0$  plane (i.e.  $x - y$  plane) and the  $z$ -axis, which coincides with the prime-axis [57] of the corresponding paraboloid of focal length  $F$ . Hence, the surface of the reflector is defined as

$$g(x, y, z) \triangleq z + F - \frac{1}{4F} x^2 + y^2 = 0, \quad (3.10)$$

such that  $\sqrt{(x - d_{\text{Off}})^2 + y^2} \leq 0.5D^2$ . Note that  $\sqrt{(x - d_{\text{Off}})^2 + y^2} \leq 0.5D^2$  corresponds to the projected circular-aperture PCA( $x, y$ ) shown in Figure 3.7, which remains inside the square region  $x \in [d_{\text{Off}} - 0.5D, d_{\text{Off}} + 0.5D]$  and  $y \in [-0.5D, 0.5D]$ .

The magnitude  $A$  and the phase  $\varphi$  of the incident monochromatic EM ST PW is specified with respect the origin (O), with the complex-valued scaling-factor  $M = Ae^{j\varphi}$ . The orientation of the incident monochromatic EM ST PW is specified by its DOA with the inclination angle  $\theta$  and the azimuth angle  $\phi$ , where both angles are measured as shown in Figure 3.7. The corresponding DOA unit vector  $\hat{\mathbf{d}}$  is given by

$$\hat{\mathbf{d}} \equiv \cos(\phi) \sin(\theta) \hat{\mathbf{u}}_x + \sin(\phi) \sin(\theta) \hat{\mathbf{u}}_y + \cos(\theta) \hat{\mathbf{u}}_z. \quad (3.11)$$

As mentioned in section 2.2.1, the electric-field component of a fully-polarized monochro-

matic EM ST PW may be given by

$$\mathbf{epw}(x, y, z, t) = pw(x, y, z, t)\hat{\mathbf{e}}_H + \beta pw(x, y, z, t)\hat{\mathbf{e}}_V, \quad (3.12)$$

where the orthogonal unit vectors  $\hat{\mathbf{e}}_H$  and  $\hat{\mathbf{e}}_V$  are oriented as shown in Figure 3.7. The parameter  $\beta$  specify the *type of polarization* of  $\mathbf{epw}(x, y, z, t)$ . For example, if  $\angle\beta = 0^\circ$  or  $\angle\beta = 180^\circ$ , then  $\mathbf{epw}(x, y, z, t)$  is a linear-polarized EM ST PW, where the direction of the electric-field is given by the vector combination  $\hat{\mathbf{e}}_H + \beta\hat{\mathbf{e}}_V$ . On the other hand, if  $|\beta| = 1$  and  $\angle\beta = \pm\pi/2$ , then  $\mathbf{epw}(x, y, z, t)$  is a circular-polarized EM ST PW, where “+” sign corresponds to right-circular polarization and “−” sign corresponds to left-circular polarization, respectively. For all other values of  $\beta$ ,  $\mathbf{epw}(x, y, z, t)$  is a elliptical-polarized EM ST PW. However for the FFS, the type of polarization of the incident monochromatic EM ST PW is specified by the unit vector  $\hat{\mathbf{E}}^{\text{Pol}}$  in terms of the parameter  $\beta$ , the inclination angle  $\theta$ , and the azimuth angle  $\phi$ , of the EM ST PW, such that

$$\hat{\mathbf{E}}^{\text{Pol}} = \frac{\beta \cos(\phi) - \sin(\phi) \hat{\mathbf{u}}_x + \cos(\phi) + \beta \sin(\phi) \hat{\mathbf{u}}_y + -\beta \tan(\theta) \hat{\mathbf{u}}_z}{(\beta^2 \sec^2(\theta) + 1)} \quad (3.13)$$

which satisfies the orthogonality condition  $\hat{\mathbf{d}} \bullet \hat{\mathbf{E}}^{\text{Pol}} = 0$ , where  $\hat{\mathbf{d}}$  is the DOA unit vector of the incident EM ST PW that is given in (3.11).

### 3.3.2 Focal Region EM Field Synthesis; A Review

Consider the paraboloidal reflector surface shown in Figure 3.9, where its orientation in 3D space is specified according to an arbitrarily selected co-ordinate system. Given  $\epsilon$  denotes the permittivity and  $\mu$  denotes the permeability of the medium that the EM ST PW propagates, the electric-field  $\mathbf{E}(\mathbf{r})$ , at a point specified by the position vector  $\mathbf{r} = x \hat{\mathbf{u}}_x + y \hat{\mathbf{u}}_y + z \hat{\mathbf{u}}_z$ , can be expressed as

$$\mathbf{E}(\mathbf{r}) = -j\omega\mu\mathbf{A}(\mathbf{r}) + \frac{1}{j\omega\epsilon}\nabla[\nabla \bullet \mathbf{A}(\mathbf{r})], \quad (3.14)$$

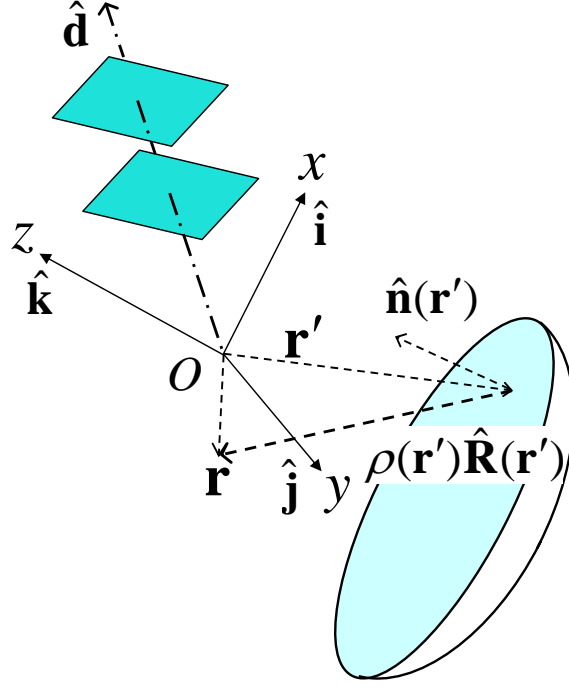


Figure 3.9: Geometry of the reflector, incident PW and the reflected wave expressed using vector notation.

[57] (pp. 30), where  $\nabla$  denotes the gradient operation [115](pp. 446-447) and  $\nabla \bullet$  denotes the divergence operation [115](pp. 453-454). According to the Maxwell's equations, the magnetic vector potential  $\mathbf{A}(\mathbf{r})$  [57] (pp. 30), in (3.14) is defined as a surface integral

$$\mathbf{A}(\mathbf{r}) \triangleq \iint_S \mathbf{J}(\mathbf{r}') G(\rho') dS', \quad (3.15)$$

of the *surface current density*  $\mathbf{J}(\mathbf{r}')$ , which is induced in response to the incident monochromatic EM ST PW of temporal angular frequency  $\omega (= 2\pi f_t)$ , and the *Green's function*  $G(\rho')$  [69](pp. 407-411) over the surface  $S'$  of the paraboloidal reflector. Note that the Green's function is defined as

$$G(\rho') \triangleq \frac{e^{-j k \rho}}{4 \pi \rho'} = \frac{e^{-j k |\mathbf{r} - \mathbf{r}'|}}{4 \pi |\mathbf{r} - \mathbf{r}'|}, \quad (3.16)$$

with reference to the point on the reflector surface, which is specified by the position vector  $\mathbf{r}' = x' \hat{\mathbf{u}}_x + y' \hat{\mathbf{u}}_y + z' \hat{\mathbf{u}}_z$ , and the point  $\mathbf{r}$ , where the electric-field is evaluated. The

separation vector between  $\mathbf{r}$  and  $\mathbf{r}'$  is defined as

$$\mathbf{r} - \mathbf{r}' \triangleq \rho' \hat{\mathbf{R}}', \quad (3.17)$$

with the magnitude  $\rho'$  and the direction of the unit vector  $\hat{\mathbf{R}}'$ . Also,  $k = \omega/c$  is the corresponding *wavenumber* and  $c = 1/\sqrt{\varepsilon\mu}$  is the *speed of wave propagation* in the medium where the incident EM ST PWs propagates [112]. Substituting (3.15) and (3.16) into (3.14) yields the *radiation integral*,

$$\mathbf{E}(\mathbf{r}) = -\frac{j}{\omega\varepsilon} \iint_S \left[ k^2 \mathbf{J}(\mathbf{r}') + (\nabla \bullet \mathbf{J}(\mathbf{r}')) \nabla \right] G(\rho') dS'. \quad (3.18)$$

According to [120](pp. 15-4-15-5), the evaluation of the gradient ( $\nabla$ ) and divergence ( $\nabla \bullet$ ) operations in (3.18) results in

$$\mathbf{E}(\mathbf{r}) = \frac{-j}{\omega\varepsilon} \iint_S \left[ \left( k^2 - \frac{jk}{\rho'} - \frac{1}{\rho'^2} \right) \mathbf{J}(\mathbf{r}') + \left( -k^2 + \frac{3jk}{\rho'} + \frac{3}{\rho'^2} \right) (\mathbf{J}(\mathbf{r}') \bullet \hat{\mathbf{R}}') \hat{\mathbf{R}}' \right] G(\rho') dS'. \quad (3.19)$$

Assuming the contribution from the factors  $jk/\rho'$  and  $1/\rho'^2$  are negligible,  $\mathbf{E}(\mathbf{r})$  in (3.19) can be approximated by

$$\mathbf{E}(\mathbf{r}) \approx \frac{-jk^2}{\omega\varepsilon} \iint_S \left[ \mathbf{J}(\mathbf{r}') - (\mathbf{J}(\mathbf{r}') \bullet \hat{\mathbf{R}}') \hat{\mathbf{R}}' \right] G(\rho') dS'. \quad (3.20)$$

Assuming the inner surface of the paraboloidal reflector is *near-perfect electric conductor with no aperture blockage*, here, the *physical-optics* (PO) [120](pp. 15-4-15-6) approximation is used in determining the surface current density  $\mathbf{J}(\mathbf{r}')$  induced on the reflector surface. The PO approximation yields

$$\mathbf{J}(\mathbf{r}') = 2\hat{\mathbf{n}}(\mathbf{r}') \times \mathbf{H}^{\text{Inc}}(\mathbf{r}'), \quad (3.21)$$

where  $\mathbf{H}^{\text{Inc}}$  is the incident magnetic field vector *just outside* the reflector surface at point  $\mathbf{r}'$  and  $\hat{\mathbf{n}}(\mathbf{r}')$  is the unit normal vector at point  $\mathbf{r}'$  on the reflector surface as shown in Figure 3.9. Here, by considering only the PO approximation, the possible reflected fields

at the edges of the reflector have been ignored [112]. Further, this approximation ignores the edge conditions, which requires the normal components of the surface current density to be zero and the tangential components of the same to be singular [112]. Nevertheless, it has been shown that the PO approximation can achieve highly accurate results in predicting EM fields, even for small reflectors having at least 5 wavelengths in diameter [120](pp. 15-4). According to PW propagation model given in section 2.2, the magnetic field at the point ( $\mathbf{r}'$ ) just outside the reflector surface is given by

$$\mathbf{H}^{\text{Inc}}(\mathbf{r}') = \frac{1}{Z} \mathbf{E}^{\text{Inc}}(\mathbf{r}') \times \hat{\mathbf{d}}, \quad (3.22)$$

where  $Z = \sqrt{\mu/\varepsilon}$  is the characteristic impedance of the propagation medium,  $\mathbf{E}^{\text{Inc}}(\mathbf{r}')$  is the incident electric-field and  $\hat{\mathbf{d}}$  is the unit DOA vector shown in Figure 3.9. For a monochromatic EM ST PW, both  $\mathbf{H}^{\text{Inc}}(\mathbf{r}')$  and  $\mathbf{E}^{\text{Inc}}(\mathbf{r}')$  can be expressed relative to the EM fields  $\mathbf{H}_O^{\text{Inc}}$  and  $\mathbf{E}_O^{\text{Inc}}$ , at the origin O (or any other reference point), using a unit-magnitude scaling-factor to compensate the phase-change due to the propagation such that

$$\mathbf{H}^{\text{Inc}}(\mathbf{r}') = \mathbf{H}_O^{\text{Inc}} e^{jk[\mathbf{r}' \cdot \hat{\mathbf{d}}]} \quad \text{and} \quad \mathbf{E}^{\text{Inc}}(\mathbf{r}') = \mathbf{E}_O^{\text{Inc}} e^{jk[\mathbf{r}' \cdot \hat{\mathbf{d}}]}, \quad (3.23)$$

where  $\mathbf{H}_O^{\text{Inc}} = 1/Z(\mathbf{E}_O^{\text{Inc}} \times \hat{\mathbf{d}})$  and where  $\mathbf{E}_O^{\text{Inc}} = M\hat{\mathbf{E}}^{\text{Pol}}$ . Note that the complex-valued scaling-factor  $M$ , specifies the magnitude and phase of the monochromatic EM ST PW at the reference point O.

Substituting (3.23), (3.22) and (3.21) into (3.20) yields

$$\mathbf{E}(\mathbf{r}) = \frac{-j\omega}{2\pi c} \iint_S \hat{\mathbf{n}}(\mathbf{r}') \times (\mathbf{E}_O^{\text{Inc}} \times \hat{\mathbf{d}}) - \hat{\mathbf{n}}(\mathbf{r}') \times (\mathbf{E}_O^{\text{Inc}} \times \hat{\mathbf{d}}) \cdot \hat{\mathbf{R}}' \hat{\mathbf{R}}' \frac{e^{-jk(\rho - [\mathbf{r} \cdot \hat{\mathbf{d}}])}}{\rho'} dS'. \quad (3.24)$$

According to [115](pp. 496-497), the surface integral given in (3.24) can be rewritten as a 2D integral

$$\mathbf{E}(\mathbf{r}) = \frac{-j\omega}{2\pi c} \iint_{(x,y) \in \text{PCA}(x,y)} \hat{\mathbf{n}}(\mathbf{r}') \times (\mathbf{E}_O^{\text{Inc}} \times \hat{\mathbf{d}}) - \hat{\mathbf{n}}(\mathbf{r}') \times (\mathbf{E}_O^{\text{Inc}} \times \hat{\mathbf{d}}) \cdot \hat{\mathbf{R}}' \hat{\mathbf{R}}' \frac{e^{-jk(\rho - [\mathbf{r} \cdot \hat{\mathbf{d}}])}}{\rho'} J'_\Sigma dx' dy'. \quad (3.25)$$



of  $x'$  and  $y'$  variables spanning the projected circular-aperture PCA( $x, y$ ) of the reflector (see Figure 3.7). Also according to [115](pp. 502-503), the *Jacobian* of the integral transform is given by

$$J'_\Sigma = \overline{(x'^2 + y'^2 + 4F^2)}/2F, \quad (3.26)$$

which is only valid on PCA( $x, y$ ). The unit-normal vector to a 3D surface  $g(x', y', z') = 0$  is defined by

$$\hat{\mathbf{n}}(\mathbf{r}') \triangleq \frac{\nabla(g(x', y', z'))}{|\nabla(g(x', y', z'))|}, \quad (3.27)$$

[115](pp. 493-494). Hence, the unit normal vector at the point  $\mathbf{r}' \equiv (x', y', z')$  on the paraboloidal reflector surface, which is defined in (3.10), is given by

$$\hat{\mathbf{n}}(\mathbf{r}') \equiv \frac{\mathbf{n}(\mathbf{r}')}{|\mathbf{n}(\mathbf{r}')|} = \frac{-x\hat{\mathbf{u}}_x - y\hat{\mathbf{u}}_y + 2F\hat{\mathbf{u}}_z}{(x'^2 + y'^2 + 4F^2)}. \quad (3.28)$$

In (3.25), substituting for  $J'_\Sigma$  with (3.26) and  $\hat{\mathbf{n}}(\mathbf{r}')$  with (3.28), yields the radiation integral

$$\mathbf{E}(\mathbf{r}) = \frac{-j\omega}{4\pi F c} \iint_{(x, y) \in \text{PCA}(x, y)} \mathbf{n}(\mathbf{r}') \times (\mathbf{E}_O^{\text{Inc}} \times \hat{\mathbf{d}}) - \mathbf{n}(\mathbf{r}') \times (\mathbf{E}_O^{\text{Inc}} \times \hat{\mathbf{d}}) \bullet \hat{\mathbf{R}}' \hat{\mathbf{R}}' \frac{e^{-jk(\rho - [\mathbf{r} \bullet \hat{\mathbf{d}}])}}{\rho'} dx' dy'. \quad (3.29)$$

### 3.3.3 Numerical Integration of the Radiation Integral using a GPU

#### Selecting of a Suitable Numerical Integration Method for GPU Processing

In subsection 3.3.2, it has been shown that the electric-field at point  $\mathbf{r}$  (see Figure 3.9) in the focal region of a paraboloidal reflector in response to an incident monochromatic EM ST PW can be obtained by evaluating the radiation integral (3.29). *Previously, for determining the far field radiation of a reflector antenna, slightly different versions of (3.29) has been evaluated in [116][117][131][132][133] using different approaches. For example, a closed-form solution has been derived for a special case of the feed pattern in [131], whereas various numerical-integration techniques have been used in [116][117][132][133]. In general, the far-field close-form method and far-field numerical integration techniques*

(e.g. [112] (pp. 42-44)) may be modified to evaluate the focal electric-field in 3.29. Further, according to [134], Monte Carlo and Quasi-Monte Carlo methods can also be used in evaluating multiple integrals. Such methods use iterative algorithms, which are numerically efficient for general evaluation in a central processing unit (CPU).

The architectures of CPUs and GPUs are fundamentally different [128]. The CPUs are designed for execution of general purpose instructions while the GPUs are designed for execution of a limited set of instructions on a large set of data. Compared to a CPU, a GPU achieves the best acceleration when it is used for executing non-iterative arithmetic-type SIMD operations [126]. Hence, the numerical integration methods that has been optimized for execution in a CPU may not be directly deployable in a GPU, or if deployed may not yield optimum results. For example, the libraries available for CUDA are limited and therefore, may not include the optimized instruction sets to evaluate the special functions, which are required in the integration methods summarized in [112][116][117], in the GPU. Also, the methods employing iterative evaluation to implement Monte Carlo and Quasi-Monte Carlo integration algorithms become inefficient when implemented in GPUs, because excessive data transfers in and out of the GPU may slow down the execution. However, the direct numerical integration algorithms [134] can be formulated into an algorithm of non-iterative arithmetic-type SIMD operations. Hence, for the FFS, the 2D extension of the *simplest rectangular Newton-Cotes algorithm* [113](pp. 247-264) has been selected for evaluating the radiation integral (3.29), using a GPU. Also for the FFS, it has been observed that the direct integration method yields better accuracy compared to the 2D FFT based integration method proposed in [112](pp. 42-44).

Following the 2D rectangular Newton-Cotes algorithm, (3.29) can be approximated

by

$$\begin{aligned} \mathbf{E}(\mathbf{r}) \approx & \frac{-j\omega\Delta_m\Delta_n}{4\pi Fc} \sum_m \sum_n \mathbf{n}(\mathbf{r}'_{m'n'}) \times (\mathbf{E}_O^{\text{Inc}} \times \hat{\mathbf{d}}) \\ & - \mathbf{n}(\mathbf{r}'_{m'n'}) \times (\mathbf{E}_O^{\text{Inc}} \times \hat{\mathbf{d}}) \bullet \hat{\mathbf{R}}'_{m'n'} \hat{\mathbf{R}}'_{m'n'} \frac{e^{-jk(\rho_{m'n'} - [\mathbf{r}_{m'n'} \bullet \hat{\mathbf{d}}])}}{\rho'_{m'n'}}, \quad (3.30) \end{aligned}$$

where  $\Delta_m$  and  $\Delta_n$  are the horizontal and vertical sampling intervals on the surface of the reflector. According to [113](pp. 253-254), as  $\Delta_m \rightarrow 0$  and  $\Delta_n \rightarrow 0$ , the accuracy of the approximation in (3.30) improves, while increasing the computational complexity of the numerical integration. Hence, the selection of  $\Delta_m$  and  $\Delta_n$  in FFS is a trade-off between the accuracy and the computational complexity, and therefore the computation time.

### Arranging the Numerical Radiation Integral to Achieve the Maximum Possible Acceleration with a Typical GPU

According to the system architecture of a GPU shown in Figure 3.8 (see page 91), a typical GPU contains many-processor-cores, where each core is assigned with a cache memory and many dedicated ALUs. Also, there is a common RAM shared by all processor cores. Therefore, Compared to general-purpose CPUs, GPUs are better designed for evaluating *computationally-intensive arithmetic algorithms in SIMD format* [128]. However, extensive data transfers between the CPU and the GPU may diminish the accelerations achieved with GPU processing [126]. Hence, in the FFS, (3.30) is re-formulated in such a way that the bulk of the computationally intensive processing is presented in SIMD form. Also in the FFS, steps has been taken to minimize data transfers between CPU to GPU.

In typical FPA applications, the focal field  $\mathbf{E}(\mathbf{r})$  is evaluated at a set of  $L$  points  $\mathbf{r}_l = x_l \hat{\mathbf{u}}_x + y_l \hat{\mathbf{u}}_y + z_l \hat{\mathbf{u}}_z$ ;  $l = 1, \dots, L$ , either on a plane, on a surface or inside a volume, which requires repeated evaluations of the numerical radiation integral (3.30), for each point  $\mathbf{r}_l$ . In repeated evaluations of (3.30), *pre-calculation of the common components*

for any  $\mathbf{r}_l$ , namely  $\mathbf{n}(\mathbf{r}'_{m,n}) \times (\mathbf{E}_O^{\text{Inc}} \times \hat{\mathbf{d}})$ ,  $e^{jk[\mathbf{r}_{m,n} \cdot \hat{\mathbf{d}}]}$  and  $\frac{-j\omega\Delta_m\Delta_n}{4\pi Fc}$ , and using these arrays for all  $\mathbf{r}_l$ 's yields considerable reduction of the computational complexity of the total evaluation. However, the repeated calculations of (3.30) at each  $\mathbf{r}_l$ , require independent re-calculations of

$$\rho'_{m,n} @_{\mathbf{r}_l} = \sqrt{(x_l - x'_{m,n})^2 + (y_l - y'_{m,n})^2 + (z_l - z'_{m,n})^2}, \quad (3.31)$$

$$\hat{\mathbf{R}}'_{m,n} @_{\mathbf{r}_l} = \frac{(x_l - x'_{m,n})\hat{\mathbf{u}}_x + (y_l - y'_{m,n})\hat{\mathbf{u}}_y + (z_l - z'_{m,n})\hat{\mathbf{u}}_z}{\rho'_{m,n}}, \quad (3.32)$$

and  $e^{-jk\rho_{m,n}}/\rho'_{m,n} @_{\mathbf{r}_l}$ . Given  $\mathbf{r}'$  is on the paraboloidal reflector surface, which is specified in (3.10),  $z'_{m,n} = (x'^2_{m,n} + y'^2_{m,n})/4F - F$ .

A typical pseudo-code for the FFS is shown in Figure 3.10, where both CPU and GPU are employed in processing for the evaluation of the numerical radiation integral (3.30). According to Figure 3.10, after specifying the reflector arrangement and PW parameters, the common components  $\mathbf{n}(\mathbf{r}'_{m,n}) \times (\mathbf{E}_O^{\text{Inc}} \times \hat{\mathbf{d}})$ ,  $e^{jk[\mathbf{r}_{m,n} \cdot \hat{\mathbf{d}}]}$  and  $\frac{-j\omega\Delta_m\Delta_n}{4\pi Fc}$ , of (3.30) are evaluated through CPU processing. The lack of parallelism of these three variables makes such evaluations unsuitable for GPU processing. On the other hand, the required repeated evaluations of  $\rho'_{m,n}$ ,  $\hat{\mathbf{R}}'_{m,n}$ ,  $e^{-jk\rho_{m,n}}$  and finally  $\mathbf{E}(\mathbf{r})$  for any  $L_P$  points can be arranged into SIMD format to be simultaneously evaluated in a GPU. However, in practice,  $L_P$  is limited by the available computational resources of the GPU, implying a maximum of  $L_{P\text{max}}$  simultaneous evaluations of  $\mathbf{E}(\mathbf{r})$ . In this case the FFS requires to perform  $\lceil L/L_{P\text{max}} \rceil^7$  number of evaluations of the section of the pseudo-code denoted by \* in order to evaluate (3.30) for all  $L$  points. For the FFS, it has been observed that the limitations of the common RAM and the processor cache memory of the particular GPU limit the number of simultaneous evaluations of (3.30). Thus, the operational code of the FFS is refined in order to minimize the peak-memory requirement for evaluating the variables in (3.31) and 3.32 such that the optimal number of  $L_{P\text{max}}$  is achieved for the particular GPU.

---

<sup>7</sup> $\lceil N_p/N_q \rceil$  denotes the *ceiling operation* that *rounds-up* the quotient of  $N_p/N_q$  to the nearest integer.

Start

Initialize : ( $c \equiv 3 \times 10^8 ms^{-1}$ ).

Input : For the PW :  $M, \omega, \hat{\mathbf{d}}, \hat{\mathbf{E}}^{\text{Pol}}$ ,  
 : For the reflector :  $F, D, d_{\text{off}}$ .

Define :  $L$  point grid:  $\mathbf{r}_l = x_l \hat{\mathbf{u}}_x + y_l \hat{\mathbf{u}}_y + z_l \hat{\mathbf{u}}_z$ .

Select :  $\Delta_{m'}, \Delta_{n'}$ .

Calculate in CPU,

:  $\hat{\mathbf{E}}_{\text{O}}^{\text{Inc}} = M \hat{\mathbf{E}}^{\text{Pol}}$ ,  
 :  $\mathbf{r}'_{m',n'} = x'_{m',n'} \hat{\mathbf{u}}_x + y'_{m',n'} \hat{\mathbf{u}}_y + z'_{m',n'} \hat{\mathbf{u}}_z$ ; use (3.24),  
 :  $\mathbf{n}(\mathbf{r}'_{m',n'})$ ; use (3.24),  
 :  $\mathbf{n}(\mathbf{r}'_{m',n'}) \times (\hat{\mathbf{E}}_{\text{O}}^{\text{Inc}} \times \hat{\mathbf{d}}), e^{jk(\mathbf{r}'_{m',n'} \cdot \hat{\mathbf{d}})}$ ,  
 :  $j\omega \Delta_{m'} \Delta_{n'} / 4\pi cF$ .

Convert  $\mathbf{n}(\mathbf{r}'_{m',n'}) \times (\hat{\mathbf{E}}_{\text{O}}^{\text{Inc}} \times \hat{\mathbf{d}})$  &  $e^{jk(\mathbf{r}'_{m',n'} \cdot \hat{\mathbf{d}})}$  to SF format.

Send SF variables to GPU.

Calculate in GPU,

for  $l = 1 : \lceil L / L_{\text{Pmax}} \rceil$

Distribute to $L_{\text{Pmax}}$ GPU cores : $\mathbf{n}(\mathbf{r}'_{m',n'}) \times (\hat{\mathbf{E}}_{\text{O}}^{\text{Inc}} \times \hat{\mathbf{d}}), e^{jk(\mathbf{r}'_{m',n'} \cdot \hat{\mathbf{d}})}$ . Assign : $\mathbf{r}_t$ ; $t = 1 : L_{\text{Pmax}}$ , Calculate : $\rho'_{m',n'}, \hat{\mathbf{R}}'_{m',n'}$ & $e^{-jk\rho'_{m',n'}}$ @ $\mathbf{r}_t$ ; use (3.27) & (3.28), Evaluate summations in $\mathbf{E}(\mathbf{r}_t)$ ; $t = 1 : L_{\text{Pmax}}$ ; use (3.26)	}	*
---	---	---

end.

Send variable to CPU.

Assemble  $\mathbf{E}(\mathbf{r}_l)$ ;  $l = 1 \dots L$ .

Calculate  $-j\omega \Delta_{m'} \Delta_{n'} \mathbf{E}(\mathbf{r}_l) / 4\pi cF$ .

Stop.

Figure 3.10: The pseudo-code for the FFS. This code illustrates the use of the CPU and the GPU for processing different variables of (3.30) in order to achieve the maximum possible acceleration for the FFS.

### Single Precision vs Double Precision Arithmetic in GPU Processing

It is expected that using double-precision floating-point arithmetic operations (DFAOs) would lead to a better accuracy in evaluating the numerical radiation integral (3.30) compared to that evaluated using single-precision floating-point arithmetic operations (SFAOs). According to [128](Appendix A), low-end and mid-range GPUs only support SFAOs where high-end GPUs support both SFAOs and DFAOs. Nevertheless in GPUs, DFAOs has longer execution times compared to SFAOs [128]. Hence, in order to minimize the computational time in GPU processing, SFAOs are employed in the FFS. However, in the FFS, the intermediate data sequences (e.g.  $\mathbf{n}(\mathbf{r}'_{m'n'}) \times (\mathbf{E}_O^{\text{Inc}} \times \hat{\mathbf{d}})$ ,  $e^{jk[\mathbf{r}_{m'n'} \cdot \hat{\mathbf{d}}]}$  and  $\frac{-j\omega\Delta_m\Delta_n}{4\pi Fc}$ ) evaluated in the CPU are in double-precision floating-point (DF) format. Hence, before being transferred into the GPU for subsequent processing, these intermediate data variables are transformed into single-precision floating-point (SF) format (see Figure 3.10). It has been observed that there is no significant reduction in the accuracy of the focal field calculated with the FFS using SFAOs in GPU processing compared to the focal field calculated using DFAOs in CPU processing with the corresponding MATLAB code.

### Using a Wrapper Program vs Using the Direct CUDA Implementation for GPU Processing

In the implementation of the FFS, MATLAB commands has been used for CPU processing and extended MATLAB commands of the GPUmat [130], which is a wrapper for MATLAB that interfaces MATLAB with CUDA [126], for GPU processing. Even though it is expected that the direct implementation of the SIMD operation in CUDA would lead to the best possible acceleration of the numerical integration, the use of a wrapper program to interface CUDA for GPU processing has a few other advantages. First, the wrapper programs allow the rapid deployment of the original source code, which has been developed for the respective development environments (e.g. MATLAB, Java,

FORTRAN, etc.), with only a few modifications [130]. The choice of development environment may depend on the language familiarity of the developer. Second, knowledge of the architecture of the GPU is not required for the implementation in order to achieve considerable increases in the processing speed of the execution [130]. Also, the added features, such as the GPUMat compiler, allow the development of special sub-routines and saving those in GPU memory, which speed up the execution in repeated evaluations of the same program [130].

### 3.3.4 Examples of the FFS Field Calculations and Comparisons between the FFS and the GRASP9

Some examples of focal electric-field patterns achieved using the FFS are presented in the following. Also, here, the focal electric-field patterns evaluated with the FFS are compared against the electric-field patterns evaluated using GRASP9 for the same set of specifications. GRASP9, which has been developed by TICRA, is a widely used CAD tool for analyzing EM fields scattered by reflector antennas [58]. In [90][135][136], researchers have used either GRASP9 or its predecessors in order to model focal field patterns. In GRASP9, for single reflector analysis, the PO approximation is assumed in determining the induced surface current density and the PTD approximation is assumed in determining the edge conditions [137]. It would be highly desirable had both the FFS and GRASP9 yielded identical field patterns for the same set of specifications. However, partly because the ignored edge conditions in the FFS, and also because of differences between the employed integration methods in GRASP9 and the FFS, minor differences have been observed between the calculated focal field patterns by the two field synthesis programs.

In this example, a prime-focus (i.e.  $d_{\text{Off}} = 0$ ) paraboloidal reflector with  $D = 10$  m and  $F = 6$  m (i.e.  $F/D = 0.6$ ) having a near-perfect conducting surface is considered. A linearly- $\hat{\mathbf{u}}_y$  polarized (i.e.  $\hat{\mathbf{E}}^{\text{Pol}} = \hat{\mathbf{u}}_y$ ) monochromatic EM ST PW of temporal frequency

( $cf_{ct}$ ) 1 GHz and the scaling-factor at the origin (O)  $M = 1$ , which is arriving from the direction specified by the inclination angle  $\theta = 1.5^\circ$  and the azimuth angle  $\phi = 0^\circ$ , is incident on the paraboloidal reflector. The magnitude and the phase of the  $\hat{\mathbf{u}}_y$ -,  $\hat{\mathbf{u}}_x$ - and  $\hat{\mathbf{u}}_z$ - components of the electric-field  $\mathbf{E}_{\text{FFS}}$  on the focal plane (i.e.  $z = 0$  see Figure 3.7), that has been evaluated using the FFS, are shown in Figure 3.11. Note the shown region, which corresponds to an area of  $0.75 \times 0.75 \text{ m}^2$  centered at the origin O, is uniformly sampled into a grid of  $(51 \times 51)$  points. In this example, for the numerical integration, a sampling grid of size was selected such that  $\Delta_m = \Delta_n = D / \lceil D/\lambda \rceil$ . In order to evaluate  $\hat{\mathbf{u}}_y$ -,  $\hat{\mathbf{u}}_x$ - and  $\hat{\mathbf{u}}_z$ - components of  $\mathbf{E}_{\text{FFS}}$  at a total of 2601 points, the FFS takes about 0.825 s on a Dell XPS-600 computer equipped with an Intel Pentium-IV (clock speed 3.4 GHz) CPU, 2 GB RAM and NVIDIA GeForce GTX 260 (Processor clock speed 1242 MHz and Internal RAM 896 MB) GPU.

### Comparing the Focal Electric-Fields Evaluated by the FFS and GRASP9: A Qualitative Study

The focal electric-field patterns  $\mathbf{E}_{\text{FFS}}$ , evaluated with the FFS, and  $\mathbf{E}_{\text{GRASP9}}$ , evaluated with GRASP9, for the same set of specifications are compared in the following. For ease of comparison between  $\mathbf{E}_{\text{FFS}}$ , and  $\mathbf{E}_{\text{GRASP9}}$ , both  $\hat{\mathbf{u}}_y$ -components are normalized by multiplying with the corresponding scaling-factors, which are defined as

$$\text{SCF}_{\text{FFS}} \triangleq \frac{1}{\max[|\mathbf{E}_{\text{FFS}} \bullet \hat{\mathbf{u}}_y|]} \quad \text{and} \quad \text{SCF}_{\text{GRASP9}} \triangleq \frac{1}{\max[|\mathbf{E}_{\text{GRASP9}} \bullet \hat{\mathbf{u}}_y|]},$$

and the respective  $\hat{\mathbf{u}}_x$ - and  $\hat{\mathbf{u}}_z$ - components of  $\mathbf{E}_{\text{FFS}}$  and  $\mathbf{E}_{\text{GRASP9}}$  are scaled by the corresponding  $\text{SCF}_{\text{FFS}}$  and  $\text{SCF}_{\text{GRASP9}}$ . Note that the phase angle of the  $\hat{\mathbf{u}}_x$ -,  $\hat{\mathbf{u}}_x$ - and  $\hat{\mathbf{u}}_z$ - components of  $\mathbf{E}_{\text{FFS}}$  and  $\mathbf{E}_{\text{GRASP9}}$  is given in degrees. For both  $\mathbf{E}_{\text{FFS}}$  and  $\mathbf{E}_{\text{GRASP9}}$ , compared to the  $\hat{\mathbf{u}}_y$ -component, the maximum relative magnitude of the  $\hat{\mathbf{u}}_x$ -component is

$$20 \log_{10} \frac{\max[|\mathbf{E}_{\text{FFS};\text{GRASP9}} \bullet \hat{\mathbf{u}}_x|]}{\max[|\mathbf{E}_{\text{FFS};\text{GRASP9}} \bullet \hat{\mathbf{u}}_y|]} = -28 \text{ dB},$$



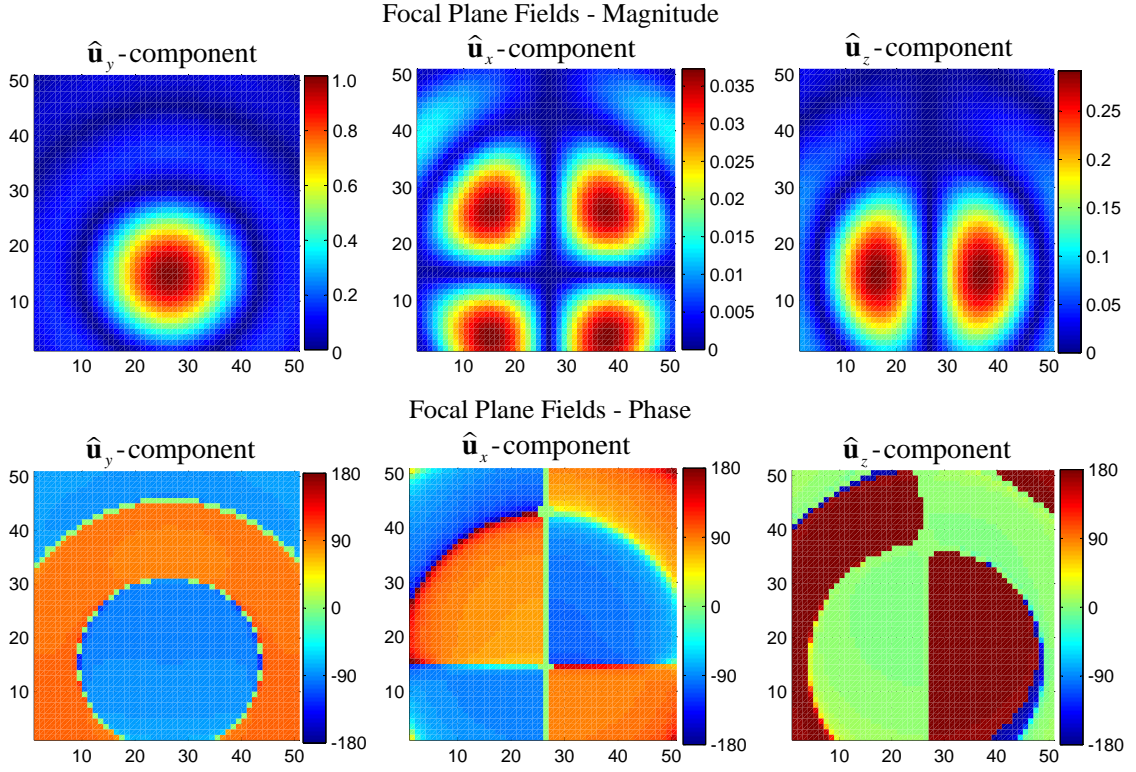


Figure 3.11: The electric-field pattern  $\mathbf{E}_{\text{FFS}}$  evaluated with the FFS. The magnitude (upper-row) and the phase (bottom-row) of the  $\hat{\mathbf{u}}_y$ - (left),  $\hat{\mathbf{u}}_x$ - (center) and  $\hat{\mathbf{u}}_z$ - (right) components of  $\mathbf{E}_{\text{FFS}}$  is sampled into a grid of  $(51 \times 51)$  points on an area of  $0.75 \times 0.75 \text{m}^2$ , in response to an incident linearly- $\hat{\mathbf{u}}_y$  polarized EM ST PW of frequency 1 GHz. The DOA of the PW is specified by  $\theta = 1.5^\circ$  and  $\phi = 0^\circ$ .

and the maximum relative magnitude of the  $\hat{\mathbf{u}}_z$ -component is

$$20 \log_{10} \frac{\max[|\mathbf{E}_{\text{FFS};\text{GRASP9}} \bullet \hat{\mathbf{u}}_z|]}{\max[|\mathbf{E}_{\text{FFS};\text{GRASP9}} \bullet \hat{\mathbf{u}}_y|]} = -10.5 \text{ dB}.$$

Also, as shown in Figure 3.11 (bottom-left) and Figure 3.11 (bottom-right), the phase within the “main-lobes” of the  $\hat{\mathbf{u}}_y$ -component and the  $\hat{\mathbf{u}}_z$ -component are approximately constant. However, according to Figure 3.11 (bottom-center), the phase for the  $\hat{\mathbf{u}}_x$ -components is approximately quadratic. Note that there are some inconsistencies of phase at some regions of the focal field, prominently at the edges of the main lobes where the magnitudes are relatively low (e.g. Figure 3.11 (bottom-right)). It is suspected that this effect is caused by quantization effects due to numerical integration.

A typical example of the electric-field difference

$$\Delta \mathbf{E} \triangleq \mathbf{E}_{\text{FFS}} - \mathbf{E}_{\text{GRASP9}}, \quad (3.33)$$

between the focal plane electric-field patterns  $\mathbf{E}_{\text{FFS}}$  and  $\mathbf{E}_{\text{GRASP9}}$  are shown in Figure 3.12, where the corresponding  $\mathbf{E}_{\text{FFS}}$  and  $\mathbf{E}_{\text{GRASP9}}$  are evaluated using the same set of parameters that had been used to evaluate the focal electric-field shown in Figure 3.11. Here, the magnitude and phase of the  $\hat{\mathbf{u}}_y$ -,  $\hat{\mathbf{u}}_x$ - and  $\hat{\mathbf{u}}_z$ - components of  $\Delta \mathbf{E}$  are shown in the top- and bottom- rows of Figure 3.12. Note that for the ease of comparison, the magnitude differences are normalized for the  $\hat{\mathbf{u}}_y$ -,  $\hat{\mathbf{u}}_x$ - and  $\hat{\mathbf{u}}_z$ - components such that  $|\Delta \mathbf{E} \bullet \hat{\mathbf{u}}_{x;y;z}| / \max[|\Delta \mathbf{E} \bullet \hat{\mathbf{u}}_{x;y;z}|]$ . By comparing the magnitude of electric-field  $|\mathbf{E}_{\text{FFS}}|$  and the corresponding normalized magnitude differences  $||\Delta \mathbf{E}||$ , which are shown in the top-rows of Figure 3.11 and Figure 3.12, respectively, it can be seen that in the regions where the magnitude of the electric-field is higher, the normalized magnitude difference is lower. Hence, the magnitudes of the electric-field components evaluated by the FFS and GRASP9 are in good agreement. As shown in Figure 3.12 (bottom-center) for the  $\hat{\mathbf{u}}_x$ -component, there are no significant differences between the phase of  $\mathbf{E}_{\text{FFS}}$  and  $\mathbf{E}_{\text{GRASP9}}$ . Also shown in Figure 3.12 (bottom-left) and (bottom-right), the phase of the  $\hat{\mathbf{u}}_y$ - and  $\hat{\mathbf{u}}_z$ -components of  $\mathbf{E}_{\text{FFS}}$  and  $\mathbf{E}_{\text{GRASP9}}$  differ only at very few points at the edges of the main lobes (see Figure 3.11). For most applications such differences can be ignored because the magnitudes at these edge points are relatively very small.

### Comparing the Focal Electric-Fields Evaluated by the FFS and GRASP9: A Quantitative Study

Here, two figures of merit, the *maximum-relative-difference* (MRD) and the *normalized-mean-square-difference* (NMSD), are used to *quantify the differences in magnitudes* of the  $\hat{\mathbf{u}}_y$ -,  $\hat{\mathbf{u}}_x$ - and  $\hat{\mathbf{u}}_z$ - components of the focal plane electric-field patterns  $\mathbf{E}_{\text{FFS}}$  and  $\mathbf{E}_{\text{GRASP9}}$ , which are evaluated by the FFS and GRASP9, respectively. For the  $\hat{\mathbf{u}}_y$ -,  $\hat{\mathbf{u}}_x$ - and  $\hat{\mathbf{u}}_z$ -

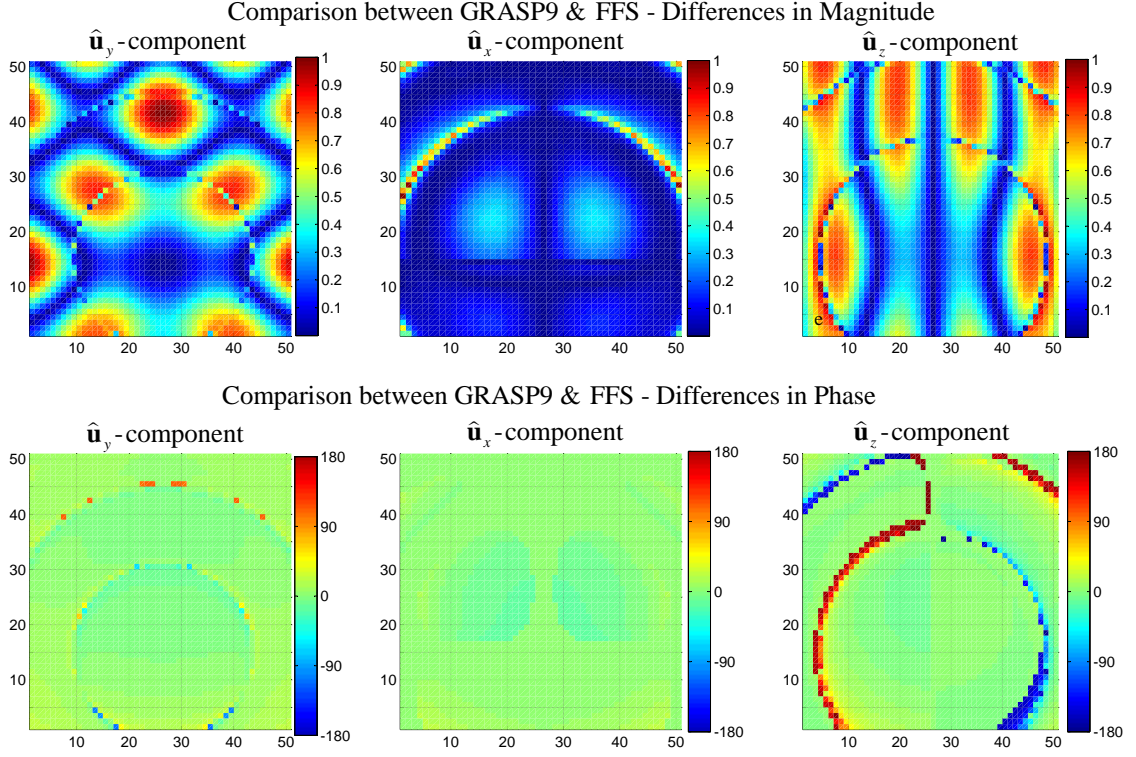


Figure 3.12: The magnitude and phase of the  $\hat{\mathbf{u}}_y$ -,  $\hat{\mathbf{u}}_x$ - and  $\hat{\mathbf{u}}_z$ - components of the electric-field difference  $\Delta \mathbf{E}$  between  $\mathbf{E}_{\text{FFS}}$  and  $\mathbf{E}_{\text{GRASP9}}$ , which are evaluated using the FFS and GRASP9 for the same set of specifications.

components, the MRD and the NMSD are defined as

$$\text{MRD}_{x;y;z} \triangleq \frac{\max [|\Delta \mathbf{E} \bullet \hat{\mathbf{u}}_{x;y;z}|]}{\max [|\mathbf{E}_{\text{FFS}} \bullet \hat{\mathbf{u}}_{x;y;z}|]} \times 100\%, \quad (3.34)$$

where  $\Delta \mathbf{E}$  is defined in (3.33) and

$$\text{NMSD}_{x;y;z} \triangleq \text{Mean} \left[ \frac{|\Delta \mathbf{E} \bullet \hat{\mathbf{u}}_{x;y;z}|^2}{\max [|\Delta \mathbf{E} \bullet \hat{\mathbf{u}}_{x;y;z}|]} \right]. \quad (3.35)$$

The MRD specifies the maximum difference between the magnitudes of the focal electric-field component relative to the maximum of the magnitude of the corresponding electric-field component. On the other hand the NMSD specifies the distribution of the differences between focal electric-field components. For example, a lower NSMD implies the error distribution is limited to a narrow region of the focal plane, similar to Figure 3.12 (top-center).

In the following, firstly, MRD and NMSD values are calculated for a series of focal plane electric-field patterns  $\mathbf{E}_{\text{FFS}}$  and  $\mathbf{E}_{\text{GRASP9}}$ , where the FFS employed different size grids over the surface of the reflector to perform the numerical integration. This leads to determination of the optimum grid size of the paraboloidal reflector that achieves the fastest computation time of the FFS while maintaining the accuracy. Secondly, MRD and NMSD values are evaluated for a series of  $\mathbf{E}_{\text{FFS}}$  patterns, which have been evaluated by using the speed optimized FFS, are compared against  $\mathbf{E}_{\text{GRASP9}}$  patterns that corresponds to a series of EM ST PWs having different DOAs. Also, it has been mentioned in subsection 3.3.3 (see page 102), that the accuracy of  $\mathbf{E}_{\text{FFS}}$  depends on the precision of the intermediate numerical processing carried in the GPU. Finally, in order to determine the degradation of the accuracy due to the use of SFAOs for GPU processing, MRD and NMSD values are calculated for a series of  $\mathbf{E}_{\text{FFS}}$ ,  $\mathbf{E}_{\text{GRASP9}}$  and  $\mathbf{E}_{\text{MATLAB}}$  that corresponds to a series of EM ST PWs having different DOAs. Here,  $\mathbf{E}_{\text{MATLAB}}$  patterns are evaluated using the FFS's equivalent version in MATLAB<sup>8</sup>, where DFAOs are used in the numerical evaluation of focal region electric-fields.

Using different size grids on the reflector surface for the evaluation of the radiation integral in the FFS

According to section 3.3.3, the accuracy of the numerical integration, which is given in (3.30), improves as the grid intervals on the reflector surface  $\Delta_m \rightarrow 0$  and  $\Delta_n \rightarrow 0$  but, as a result, the computational complexity increases. Therefore,  $\Delta'_m$  and  $\Delta_n$  have to be selected such that the required accuracy is achieved while minimizing the computational time. In the FFS, the surface of the reflector is segmented into a square-grid of size ( $N \times N \equiv N^2$ ). In order to determine the optimal grid size for the FFS, a series of focal electric-field patterns  $\mathbf{E}_{\text{FFS}}^{N^2}$  have been evaluated for different size grids  $N^2 = 8^2, 16^2, 32^2, 64^2, 128^2, 256^2, 512^2$  and  $1024^2$ . Here, a prime-focus paraboloidal reflector of

---

<sup>8</sup>The original source code for FFS developed in MATLAB that runs exclusively in the CPU.

$D = 10$  m and  $F = 6$  m (i.e.  $F/D = 0.6$ ) and a linearly- $\hat{\mathbf{u}}_y$  polarized monochromatic EM ST PW of temporal frequency ( $cf_{ct}$ ) 1 GHz that is arriving from the direction  $\theta = 0.5^\circ$  and  $\phi = 0^\circ$  are assumed in evaluating the series of  $\mathbf{E}_{\text{FFS}}^{N^2}$ . The average execution times for the FFS in evaluating the series of  $\mathbf{E}_{\text{FFS}}^{N^2}$  is given in the column 1 of Table 3.1. MRD values that correspond to the  $\hat{\mathbf{u}}_y$ -  $\hat{\mathbf{u}}_x$ - and  $\hat{\mathbf{u}}_z$ - components of the series of  $\mathbf{E}_{\text{FFS}}^{N^2}$  and  $\mathbf{E}_{\text{GRASP9}}$ , the focal electric-field components calculated by GRASP9, are given in columns 2, 4 and 6 in Table 3.1. Also, MRD values that correspond to the  $\hat{\mathbf{u}}_y$ -  $\hat{\mathbf{u}}_x$ - and  $\hat{\mathbf{u}}_z$ - components of the series of  $\mathbf{E}_{\text{FFS}}^{N^2}$  and  $\mathbf{E}_{\text{FFS}}^{1024^2}$ , the focal electric-field components calculated by the FFS with the grid size  $1024^2$ , are given in columns 3, 5, and 7 in Table 3.1.

For  $\Delta\mathbf{E}_{\text{FFS}} = \mathbf{E}_{\text{FFS}}^{N^2} - \mathbf{E}_{\text{FFS}}^{1024^2}$ , which correspond to the magnitude differences of the electric-field resulted by the FFS operating on a grid of  $N^2$  points and a grid of  $1024^2$  points on the reflector surface, the values of  $\text{MRD}_{x;y;z}$  are measures of the convergence of the  $\hat{\mathbf{u}}_y$ -  $\hat{\mathbf{u}}_x$ - and  $\hat{\mathbf{u}}_z$ - components of the numerical radiation integral given in (3.30). According to Table 3.1, the  $\hat{\mathbf{u}}_x$ -component is the fastest to converge, followed by the  $\hat{\mathbf{u}}_y$ -component component and the slowest to converge is the  $\hat{\mathbf{u}}_z$ -component. Nevertheless for  $\Delta\mathbf{E}_{\text{GRASP9}} = \mathbf{E}_{\text{FFS}}^{N^2} - \mathbf{E}_{\text{GRASP9}}$ , which correspond to the magnitude differences of the electric-field resulted by the FFS operating on a grid of  $N^2 \equiv (N \times N)$  points and the electric-field resulted by GRASP9, the values of  $\text{MRD}_{y;z}$  that correspond to the  $\hat{\mathbf{u}}_y$ - and  $\hat{\mathbf{u}}_z$ - components reduce and converge to 0.435% and 1.15%, as the grid size increases. Further it has been observed that the  $\text{NMSD}_{y;z}$  also reduces with the increasing number of grid points, which implies that the distribution of  $|\Delta\mathbf{E}_{\text{GRASP9}}|^2$  reduces with the increase in the grid size. Hence,  $\hat{\mathbf{u}}_y$ - and  $\hat{\mathbf{u}}_z$ - components of  $\mathbf{E}_{\text{FFS}}^{N^2}$  and  $\mathbf{E}_{\text{GRASP9}}$  converge as the grid size increases. Note that as number in grid points increases from  $(16^2)$ , the values of  $\text{MRD}_x$  increase slightly as given in column 4 of the Table 3.1. However, it has been observed that the  $\text{NMSD}_x$  monotonically reduces with the increase in the grid size. This indicates that for the  $\hat{\mathbf{u}}_y$ -component of  $\Delta\mathbf{E}_{\text{GRASP9}}$  is only limited to a very narrow

Table 3.1: MRD values for  $\hat{\mathbf{u}}_y$ -  $\hat{\mathbf{u}}_x$ - and  $\hat{\mathbf{u}}_z$ - components of  $\Delta\mathbf{E}_{\text{GRASP9}}$  and  $\Delta\mathbf{E}_{\text{FFS}}$  corresponding to different size grids ( $N \times N \equiv N^2$ ) on the reflector surface.

Sampling grid size & the average run time for the FFS	MRD of the $\hat{\mathbf{u}}_y$ -component (%)		MRD of the $\hat{\mathbf{u}}_x$ -component (%)		MRD of the $\hat{\mathbf{u}}_z$ -component (%)	
	$\Delta\mathbf{E}_{\text{GRASP9}}$	$\Delta\mathbf{E}_{\text{FFS}}$	$\Delta\mathbf{E}_{\text{GRASP9}}$	$\Delta\mathbf{E}_{\text{FFS}}$	$\Delta\mathbf{E}_{\text{GRASP9}}$	$\Delta\mathbf{E}_{\text{FFS}}$
$8^2$ - 0.6875 s	8.8971	8.8367	18.652	17.779	19.242	19.184
$16^2$ - 0.6875 s	3.2240	3.1765	6.3557	1.9341	4.6349	4.6873
$32^2$ - 0.7500 s	1.1910	1.1349	6.9674	1.4815	2.2212	2.1382
$64^2$ - 1.1094 s	0.45604	0.3623	7.3608	0.4901	1.3473	0.7125
$128^2$ - 3.4844 s	0.43986	0.1285	7.3707	0.1866	1.1579	0.2178
$256^2$ - 17.219 s	0.43701	0.0524	7.4282	0.0404	1.1549	0.0783
$512^2$ - 125.58 s	0.43637	0.0152	7.4533	0.0316	1.1528	0.0305
$1024^2$ - 1262.53 s	0.43568	-	7.4545	-	1.1498	-

region similar to Figure 3.12 (top-center).

The average run times of the FFS for different numbers of grid points on the reflector surface grid are given in the first column of Table 3.1. These run times have been achieved with a Dell-XPS computer equipped with an Intel Pentium-IV (clock speed 3.4 GHz) CPU, 2 GB RAM and NVIDIA GeForce GTX 260 (processor clock speed 1242 MHz and internal RAM 896 MB) GPU. Note, the average run time for GRASP9 for an identical field calculation is 2.5 s on a generic PC equipped with an Intel Pentium-IV (clock speed 3.0 GHz) CPU and 1 GB RAM at DRAO Penticton, BC, Canada. According to Table 3.1, the run times grow exponentially as the numbers of grid points increase.

Moreover, it has been observed that for lower number of grid points, for example for  $8^2$  and  $16^2$ , the processing time remained same. This is due to the fact that the GPU, which has been used for this particular example, has sufficient computational resources to simultaneously evaluate (3.30) at all  $(51 \times 51)$  points in the focal plane, where each focal plane point corresponds to  $8^2$  or  $16^2$  grid on the reflector surface. Therefore, the time consuming data transfers between the CPU and the GPU need to be performed twice only. However, as the grid size increases, the available computational resources in the GPU are not sufficient to simultaneously evaluate (3.30) at all points. Therefore, such evaluations require several data transfers between the CPU and the GPU for the full evaluation. The data transfers between the CPU and the GPU are time consuming and therefore slow down the execution of the FFS. However, as given in Table 3.1, increasing the sampling grid size beyond  $32^2$  yields marginal increases in the accuracy of the focal EM fields calculated with the FFS even though the evaluation times are increased exponentially. Further, it has been observed that if the grids size is  $34^2$  then  $\text{MRD}_y \leq 1\%$  for  $\Delta \mathbf{E}_{\text{GRASP9}}$ . The average computation time for the FFS, which employs a grid of  $34^2$ , is around 0.825 s. Hence, compared to GRASP9 that takes about 2.5 s for the evaluation of  $\mathbf{E}_{\text{GRASP9}}$ , the FFS is 284% faster in evaluating  $\mathbf{E}_{\text{FFS}}$  for the same set of specifications.

#### **$\mathbf{E}_{\text{FFS}}$ Vs $\mathbf{E}_{\text{GRASP9}}$ ; At different inclination angles ( $\theta$ )**

Consider the series of focal electric-fields,  $\mathbf{E}_{\text{FFS}}$  and  $\mathbf{E}_{\text{GRASP9}}$ , that correspond to focal plane (i.e.  $z = 0$ ) electric-fields of a prime focus paraboloidal reflector of diameter  $D = 10$  m and focal length  $F = 6$  m (i.e.  $F/D = 0.6$ ) that are resulted by a series of linear- $\hat{\mathbf{u}}_y$  polarized monochromatic EM ST PWs of temporal frequency ( $cf_{ct}$ ) 1 GHz, which are arriving from different directions that are specified by inclination angles  $\theta = 0^\circ, 0.5^\circ, 1^\circ, 1.5^\circ, 2^\circ, 2.5^\circ$  and  $3^\circ$  and the azimuth angle  $\phi = 0$ . Here, the FFS is speed optimized by selecting the grid size of the reflector surface to be  $34^2$  such that the

sampling intervals are  $\Delta_m = \Delta_n \approx 30 \text{ cm}$  ( $= \lambda$  at  $cf_{ct}$  1 GHz). Calculated MRD and NMSD values for  $\hat{\mathbf{u}}_y$ -  $\hat{\mathbf{u}}_x$ - and  $\hat{\mathbf{u}}_z$ - components of  $\mathbf{E}_{\text{FFS}}$  and  $\mathbf{E}_{\text{GRASP9}}$  that correspond to different  $\theta$ , are given in Table 3.2. According to Table 3.2, for all considered  $\theta$ ,  $\text{MSD}_y$  fluctuates in the neighborhood of 0.9% and  $\text{MSD}_x$  fluctuates in the neighborhood of 6.5%. Nevertheless with increasing  $\theta$ , in general,  $\text{NMSD}_y$  and  $\text{NMSD}_x$  increase, which imply that the magnitude differences between  $\Delta \mathbf{E} \bullet \hat{\mathbf{u}}_y$  and  $\Delta \mathbf{E} \bullet \hat{\mathbf{u}}_x$  spread as  $\theta$  increases. Also according to Table 3.2, as  $\theta$  increases, both  $\text{MSD}_z$  and  $\text{NMSD}_z$  increase in general, which imply that the magnitude differences  $\Delta \mathbf{E} \bullet \hat{\mathbf{u}}_z$  increase as  $\theta$  increases.

#### The precision of the intermediate calculations of the radiation integral; DFAOs Vs SFAOs

It has been mentioned in subsection 3.3.3 (see page 102) that DFAOs are only supported in high-end GPUs and if supported, DFAOs have longer execution times compared to SFAOs in the same GPU. Hence, SFAOs are used for the GPU processing in the FFS, assuming that it may lead to faster evaluation times. However, this could lead to a reduction of accuracy of the focal electric-field patterns  $\mathbf{E}_{\text{FFS}}$  evaluated with the FFS. In order to determine the significance of the error due to the use of SFAOs instead of DFAOs, MRD and NMSD values are evaluated for the difference  $\Delta \mathbf{E}_{\text{GRASP9}} = \mathbf{E}_{\text{GRASP9}} - \mathbf{E}_{\text{MATLAB}}$  between the focal plane electric-fields that are determined by GRASP9 and the FFS's equivalent version in MATLAB that employs DFAOs and for the difference  $\Delta \mathbf{E}_{\text{MATLAB}} = \mathbf{E}_{\text{MATLAB}} - \mathbf{E}_{\text{FFS}}$  between the focal electric-fields that are determined by the FFS and FFS's equivalent version in MATLAB. Here, the focal electric-fields  $\mathbf{E}_{\text{GRASP9}}$ ,  $\mathbf{E}_{\text{MATLAB}}$  and  $\mathbf{E}_{\text{FFS}}$  correspond to a series of linear- $\hat{\mathbf{u}}_y$  polarized monochromatic EM ST PWs of temporal frequency ( $cf_{ct}$ ) 1 GHz, which are arriving from different directions that are specified by inclination angles  $\theta = 0^\circ, 0.5^\circ, 1^\circ, 1.5^\circ, 2^\circ, 2.5^\circ$  and  $3^\circ$  and the azimuth angle  $\phi = 0$  that are reflected by a prime-focus paraboloidal reflector of  $D = 10 \text{ m}$  and  $F = 6 \text{ m}$ . Note that in the FFS, a grid of size  $34^2$  is used for evaluating  $\mathbf{E}_{\text{MATLAB}}$  and  $\mathbf{E}_{\text{FFS}}$ . The



Table 3.2: Calculated MRD and NMSD values for  $\hat{\mathbf{u}}_y$ -  $\hat{\mathbf{u}}_x$ - and  $\hat{\mathbf{u}}_z$ - components of  $\Delta\mathbf{E} = \mathbf{E}_{\text{GRASP9}} - \mathbf{E}_{\text{FFS}}$  at different inclination angles ( $\theta$ ) and at  $\phi = 0^\circ$ .

Inclination angle $\theta$	$\hat{\mathbf{u}}_y$ -component		$\hat{\mathbf{u}}_x$ -component		$\hat{\mathbf{u}}_z$ -component	
	MRD(%)	NMSD	MRD(%)	NMSD	MRD(%)	NMSD
0.0°	0.883	0.37400	6.1145	0.08606	1.5992	0.42609
0.5°	0.927	0.36953	6.8798	0.07544	1.6134	0.42589
1.0°	0.922	0.38013	6.1870	0.08066	1.6265	0.43053
1.5°	0.919	0.37020	6.3246	0.08706	1.6388	0.43402
2.0°	0.915	0.37536	6.4830	0.11303	1.6507	0.44150
2.5°	0.918	0.39254	6.4440	0.11700	1.6631	0.45319
3.0°	0.923	0.39890	6.3031	0.11789	1.6773	0.45105

corresponding MRD values for  $\Delta\mathbf{E}_{\text{GRASP9}}$  and  $\Delta\mathbf{E}_{\text{MATLAB}}$  are given in Table 3.3. Note that MRD values for  $\Delta\mathbf{E} = \mathbf{E}_{\text{GRASP9}} - \mathbf{E}_{\text{FFS}}$  (Table 3.2) and MRD values for  $\Delta\mathbf{E}_{\text{GRASP9}}$  that corresponds to focal electric-fields of GRASP9 and the FFS's equivalent version in MATLAB that employs DFAOs (Table 3.3; labeled with DP) are almost identical. This implies that there is no significant error due to the reduction of the precision by using SFAOs instead of DFAOs in GPU processing. This is further corroborated by the low MRD values, given in Table 3.3, for  $\Delta\mathbf{E}_{\text{MATLAB}}$ , which corresponds to the FFS and the FFS's equivalent version in MATLAB that employs DFAOs.

Table 3.3: Calculated MRD values for  $\hat{\mathbf{u}}_y$ -  $\hat{\mathbf{u}}_x$ - and  $\hat{\mathbf{u}}_z$ - components of  $\Delta\mathbf{E}_{\text{GRASP9}}$  and  $\Delta\mathbf{E}_{\text{MATLAB}}$  for different inclination angles ( $\theta$ ) for  $\phi = 0^\circ$ .

Incli angle $\theta$	MRD of the $\hat{\mathbf{u}}_y$ -component (%)		MRD of the $\hat{\mathbf{u}}_x$ -component (%)		MRD of the $\hat{\mathbf{u}}_z$ -component (%)	
	$\Delta\mathbf{E}_{\text{GRASP9}}$	$\Delta\mathbf{E}_{\text{MATLAB}}$	$\Delta\mathbf{E}_{\text{GRASP9}}$	$\Delta\mathbf{E}_{\text{MATLAB}}$	$\Delta\mathbf{E}_{\text{GRASP9}}$	$\Delta\mathbf{E}_{\text{MATLAB}}$
$0.0^\circ$	0.883	0.37400	6.1145	0.08606	1.5992	0.42609
$0.5^\circ$	0.927	0.36953	6.8798	0.07544	1.6134	0.42589
$1.0^\circ$	0.922	0.38013	6.1870	0.08066	1.6265	0.43053
$1.5^\circ$	0.919	0.37020	6.3246	0.08706	1.6388	0.43402
$2.0^\circ$	0.915	0.37536	6.4830	0.11303	1.6507	0.44150
$2.5^\circ$	0.918	0.39254	6.4440	0.11700	1.6631	0.45319
$3.0^\circ$	0.923	0.39890	6.3031	0.11789	1.6773	0.45105

### 3.4 Summary

The electric-fields observed around the focal region in response to the reflected far-field EM waves from an ideal paraboloidal reflector and the corresponding spectra have been analyzed in this chapter. In section 3.2, the ROS of the spectra of focal region electric-field, which resulted by an incident EM BB-BP ST PW, has been predicted according to the Hyguens' Principle Approximation. As derived in subsection 3.2.1, the predicted ROSs of the focal plane electric-field of a prime-focus paraboloidal reflector is given by a 3D double right-circular frustum that corresponds to a 3D cone of half-cone angle  $\alpha_{\text{max}}$ , which is specified in (3.8) in terms of the diameter  $D$  and the focal length  $F$  of the paraboloid. The properties of the predicted ROSs have been verified in subsection 3.2.2

by using focal region electric-field test-sequences synthesized with the FFS. Provided that the EM ST PW assumption holds for the infinitesimal EM waves originated by the surface currents on the reflector, the spectra of synthesized test sequences confirmed that the ROS of focal plane electric-field correspond to both linear- and circular- polarized incident EM BB-BP ST PWs in the temporal frequency band (0.5, 1.7) GHz that are having different DOAs within the small angular range from the axis of the paraboloid is indeed given by a 3D double right-circular frustum predicted in subsection 3.2.1. In chapter 5 of this thesis, the shape of the ROS of the spectrum of the focal electric-field predicted in section 3.2 is exploited in the design of the beamforming 3D FIR frustum filters.

The design of the Focal Field Synthesizer (FFS), a GPU-accelerated computer program has been explained in section 3.3. The FFS evaluates electric-fields in the focal region of a paraboloidal reflector in response to an incident monochromatic EM ST PW. One of the main objective in the design the FFS is to facilitate the design of the FPA receivers for the lower-mid frequency band (e.g. 0.5 - 1.7 GHz) of the SKA and evaluating the subsequent signal processing techniques (i.e. beamformers) for the FPAs as done in chapter 5. According to subsection 3.3.1, the input specifications of the FFS are the geometry of the paraboloidal reflector and the orientation, polarization and temporal frequency of the incident monochromatic EM ST PW. As shown in Figure 3.7, the geometry of the paraboloid has been specified by the diameter  $D$ , focal length  $F$  and the offset of the circular-aperture  $d_{\text{Off}}$ . The orientation of the incident monochromatic PW has been specified by the DOA with the inclination angle  $\theta$  and the azimuth angle  $\phi$ , which are measured with respect to the axis of the paraboloid and the polarization of the incident Em ST PW is specified by the polarization unit vector  $\hat{\mathbf{E}}_{\text{Pol}}$ . In subsection 3.3.2, the PO approximation has been used to determine the induced surface current density on the near-perfect conducting reflector surface with no aperture blocking. Also in this subsec-

tion, the focal electric-field has been expressed as a double integral using Maxwell's EM field equations, and evaluated numerically. Here for the numerical evaluation, the 2D Newton-Cotes method has been reformulated into SIMD format in order to achieve the best acceleration using a GPU. Further, the wrapper called GPUmat, has been exploited for interfacing the NVIDIA CUDA and Mathworks MATLAB development environments. This enables the straightforward deployment of MATLAB source code<sup>9</sup> for the CPU and GPU combine processing of the FFS. The focal EM field components calculated by the FFS has been validated using TICRA GRASP9, which a commercial CAD tool. It has been shown that the electric-field patterns from both programs are in good agreement but, the CPU and GPU combined implementation of the FFS achieves 250% to 280% faster evaluations of focal electric-fields compared to the GRASP9.

---

<sup>9</sup>With few slightly modified commands.

## Chapter 4

# Broadband-Bandpass Beamforming for Cognitive Radio (CR) Systems using Complex-Coefficient 2D FIR Trapezoidal Filters

### 4.1 Introduction

Cognitive radio (CR) systems are of increasing interest for the optimal management of the *radio-spectrum* in the next generation wireless communication systems, which will facilitate a broad range of communication/entertainment applications and services [13][14][15][16]. “*Software Defined Radio*” (SDR) architectures have been proposed for CR systems that exploit the dynamic allocation of the operational frequency band, the signal bandwidth, the transmission power, and the signal modulation techniques [13][15][17]. Non-conflicting spectral utilization in CR systems is achieved by sensing the spectral occupancy of the allocated frequency bands in real-time [13][14][15]. Using “*Smart Antennas*” for the adaptive beamforming, CR systems effectively allocate the radio-spectrum and efficiently control the power of transmitting signals so as to reduce interference [13][23][45]. Typically, CR systems span several designated frequency bands and inherently employ temporally-broadband-bandpassed (BB-BP) signals [13][14][15][23].

A typical architecture of the receiving-arm of a CR system [13] (ch. 4) that contains software-tunable hardware at the front-end is shown in Figure 4.1. In order to cater to a geographically spread subscriber population by effective utilization of signal spectrum and transmission power, this particular CR system employs adaptive broadband-bandpass beamforming. Here, the signals transmitted by the subscriber modules are received by the 1D uniformly-distributed antenna array (1D-UDAA). It is assumed that

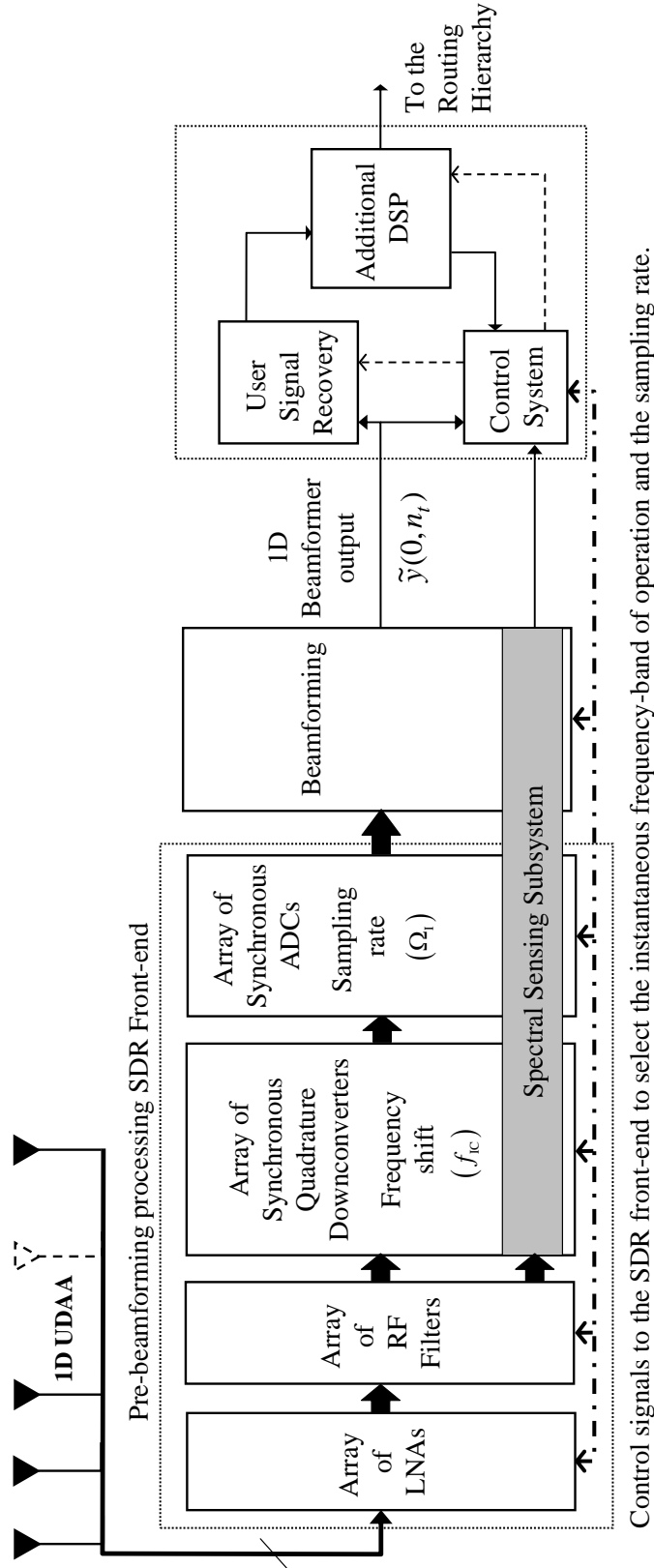


Figure 4.1: A typical architecture for the receiving arm of a CR system that employs adaptive broadband-bandpass beamforming for the effective utilization of signal spectrum and power catering a geographically spread subscriber population. The SDR front-end instantly determines the frequency-band of operation and signal bandwidth. The signals received by the 1D uniformly-distributed antenna array (1D-UDAA) are RF pre-filtered, low-noise-amplified, complex-quadrature-downconverted and synchronously sampled during the pre-beamforming processing. Subsequently the 2D sampled sequence is processed by a beamformer and the 1D beamformer output sequence is further processed to retrieve the subscriber signal.

for this CR system, almost all the time the 1D-UDAA is in the far-field region of the transmitters. Hence, the propagating EM waves transmitted by the subscriber modules of the CR system can be approximated as EM 4D BB-BP ST PWs in the finite region around the 1D-UDAA. Therefore, the signals observed at the outputs of elemental antennas in a 1D-UDAA in response to EM 4D BB-BP ST PWs can be modeled as given in sections 2.4 and 2.6 of chapter 2. The received signals at the outputs of the 1D-UDAA are *pre-filtered, complex-temporal-downconverted and synchronously sampled using an adaptive complex-quadrature temporal-sampler-array* implemented with hybrid analog-digital circuitry based on the SDR architecture, thereby yielding a complex-valued 2D spatio-temporal (ST) sample-sequence. The spectral sensing subsystem measures the signals at various stages of the front-end of the CR system in order to determine the spectral occupancy of the allocated frequency bands.

The 2D ST sample-sequence is processed by a beamformer as shown in Figure 4.1. In the receiving arm, the objectives of beamforming are to selectively enhance the desired signals according to their directions of arrival (DOAs) and to attenuate interfering signals, such as other co-channel signals and receiver noise [42][43]. Those real-time adaptive broadband-bandpass beamforming methods used by the CR systems must accommodate the movement of subscriber modules within the coverage area [23][45] as well as the instantaneous changes of the operating frequency band and the bandwidth [13][15]. As shown in Figure 4.1, the 1D beamformer output sequence is further processed to demodulate and recover the subscriber module signals.

In this chapter, a discrete-domain beamforming method is proposed for the adaptive beamforming of the desired temporally-broadband-bandpassed signals received by an 1D-UDAA of a CR system having a SDR-based receiver front-end. Here, the proposed beamformer is a *complex-coefficient 2D FIR trapezoidal filter* that operates on the complex-valued 2D ST sample-sequence, which corresponds to complex-quadrature sam-

pled 1D-UDAA outputs. The beamforming complex-coefficient 2D FIR filter is having *an asymmetric-trapezoidal shaped passband*, which is arranged to closely enclose the region of support (ROS) of the spectral components of the desired EM BB-BP ST PW. The corresponding 2D stopband encloses the ROSs of the spectra of interfering EM BB-BP ST PWs. It is expected that the novel closed-form design method proposed here can achieve near-optimal passband and stopband characteristics while instantaneously adapting for changing carrier frequencies and operating bandwidth. It is shown that, compared with previously reported methods [101][138][139], the method proposed in this chapter achieves best overall trade-off considering the passband distortion of the desired signal, stopband attenuation of the interfering signals and instantaneous adaptation with the changing of operating frequency band and sampling rate. Further, the proposed design method allows easy tracking and thereby enhancing the desired EM BB-BP ST PWs having gradually time varying DOAs. Also, the beamforming filter is implemented with a parallel-connected array of complex-coefficient 1D FIR filters, whereby each of the 1D FIR filters can be implemented using low-cost DSP hardware at high throughputs.

First, let's distinguish the proposed method from other methods that employ 2D FIR trapezoidal filters. In [59][64], a broadband-bandpass beamforming method has been proposed that is based on a real-coefficient 2D FIR filter having a rotationally symmetric double-trapezoidal passband along with an IF sampling scheme where the special case of double sideband modulated (DSB) temporally-broadband-bandpassed signals is assumed (and then exploited) in order to reduce the operational sampling rate of the beamformer by 50%. In contrast, here the objective is to design a broadband beamformer for CR systems that have SDR front-ends and which invariably employ single sideband modulated (SSB) signals as well as a baseband complex-quadrature sampling scheme. In [48], a nonadaptive beamforming method has been proposed for such complex-quadrature sampled signals, where the complex-coefficient 2D FIR filter has an asymmetric trapezoidal-



shaped passband. Unlike in [48], in this chapter<sup>1</sup>, firstly, a novel algebraic closed-form design method has been proposed and secondly and most importantly, the proposed method facilitates the instantaneous adaptation of the operational frequency band and of the bandwidth. Finally, it has been shown through experimental means that the proposed method is capable of real-time tracking and enhancement of desired signals having time-varying DOAs.

This chapter is arranged as follows. A brief introduction of CR systems is given in section 4.2 discussing their importance in the next generation wireless communications and the SDR architectures used in realizing real-time adaptation of spectral resources. A detailed mathematical analysis on the signal processing conducted in the SDR front-end of a CR systems is given in section 4.3. In this analysis, the spectral properties of the complex-quadrature-sampled antenna signals are evaluated. Previously proposed beamforming methods that can be used in enhancing the temporally-broadband-bandpassed signals associated with CR systems are briefly reviewed in section 4.4. Here, attention is given to the interpolation delay-and-sum beamforming method, DFT based frequency domain beamforming method and the “Sekiguchi method” that employs a beamforming 2D complex-coefficient FIR filter that has been designed using a combined approach of the spectral-transformation and the window methods. In section 4.5, the design of the beamforming complex-coefficient 2D FIR filter having an asymmetric trapezoidal shaped passband is explained in detail. The shape and orientation of the ideal asymmetric trapezoidal-shaped passband of the beamforming complex-coefficient 2D FIR filter is proposed in subsection 4.5.1. Also, the limitation of the previously proposed broadband-beamforming methods are briefly discussed here. The derivation of the ideal infinite extent 2D unit impulse response is given in subsection 4.5.2 where the beamforming complex-coefficient 2D FIR filter is approximated by truncating the infinite extent 2D unit impulse response with a 2D window function. A design example of a beamforming

---

<sup>1</sup>Note that parts of this work have been published in [47].

2D FIR trapezoidal filter that satisfies a selected group specifications is given in subsection 4.5.3. The 1D output sequence of the beamforming 2D FIR filter is analyzed in detail in subsection 4.5.4 and the implementation of the beamforming complex-coefficient 2D FIR filter is briefly discussed in subsection 4.5.5. The proposed 2D FIR trapezoidal filter-based beamforming method is compared against similar beamforming methods in section 4.6 using typical synthesized complex-quadrature sampled antenna signal sequences. In section 4.7, an example of an adaptive beamforming scenario for a receiving arm of a CR system has been simulated. The main objective of this simulation experiment is to study the ability of the proposed adaptive broadband beamforming method to maintain the signal to interference ratio (SIR) above a given threshold as the subscriber modules move around the coverage area.

## 4.2 Cognitive Radio Systems; An Introduction

The radio spectrum is the most valuable asset of modern wireless communication systems. Wireless communication service providers all around the world are competing for shares of the radio spectrum that have been auctioned for billions of dollars by telecommunication regulatory bodies [140]. Nevertheless, subscribers of modern wireless communication systems, in billions, are demanding a plethora of communication/entertainment applications and services that require large chunks of the radio spectrum. Examples of such applications and services include video conference calls, mobile high-Definition (HD) television (TV) and multi-player hyper-reality video games [141]. The demand for these applications and services has been steadily growing for the past few years and the CR systems may be able to meet this by effective management of the radio spectrum [13].

CR System may assist the stability and robustness of the supporting radio network [15]. For example, if the signal quality drops due to over congestion of subscribers in a particular channel then, the CR system can reassign some of the subscribers to a

different channel such that the overall signal quality may increase. If this move does not increase the signal quality, the same group or a different group of subscribers may be transferred to a close by base-station, which is having resources to handle the new group. This allows the communications between subscribers to continue uninterrupted while maintaining the quality of services. Further, a subscriber module in a CR system can select the most appropriate wireless communication standard for different service requests of the subscribers. For example, a subscriber module can select a Bluetooth communication standard to access a local printer, rather than using the WiFi communication standard. On the other hand, the same subscriber module may use the WiFi communication standard for Internet access and WCDMA communication standard for the voice or video calls. In order to accommodate the global seamless connectivity and economical transition among different applications and services, different wireless communication standards such as WCDMA, GSM, EDGE, CDMA2000, HSPA, WiMAX, WiFi, Bluetooth, ZigBee, ect. are supported in CR systems [15].

For the wireless network regulators, the most important feature of the CR systems is the policy engine [13]. The role of the policy engine is to implement the spectral utilization rules for a particular CR system, which have been specified by the telecommunication regulatory body. Spectral utilization rules may vary for different wireless communication standards and for different regions of the world. Additional rules such as network usage policies (e.g. for fair use), network operator policies (e.g. for preventing illegal activities), and manufacturer policies (e.g. for locating lost or stolen devices) can be incorporated into the policy engine [13].

The software defined radio (SDR) front-ends enables the adaptive use of the radio spectrum in CR systems [13]. The concept of SDR has been developed since the early 1990s, when the computational resources available in digital signal processors (DSPs) and General Purpose Processors (GPPs) became sufficient for the real time implementa-

tion of modulation and signal processing functions and network management functions of wireless communication systems. Since the late 90's, almost all wireless communication systems have been implemented using DSPs and GPPs [13]. This SDR architecture allows the basic hardware structure to be reused for new wireless system designs, thereby reducing the time and cost of engineering design, enabling volume purchasing, and optimizing production of a common platform, while retaining the flexibility for sophisticated protocols and generation of waveforms [13].

An ideal SDR architecture, which is shown in Figure 4.2, consists of three main units; which are (a) the reconfigurable digital circuitry, (b) the software tunable analog RF circuitry with embedded impedance synthesizer and (c) the software tunable antenna system [13]. The reconfigurable digital circuitry perform signal processing functions such as modulation/demodulation, waveform generation/detection and control of the analog RF circuitry and the antenna system. The software tunable analog circuitry perform signal up/down-conversion, analog-to-digital/digital-to-analog conversion, RF filtration, power amplification, low-noise amplification, separation and combination of RF signals. Note that the embedded impedance synthesizer effectively matches the transmitter/receiver impedances with the antenna array for different frequency bands. However, due to the limitation of state of the art technology the ideal SDR architecture is too costly and bulky to implement in practice.

A contemporary architecture<sup>2</sup> of the receiving arm of a typical SDR, which is supported by the state of the art technology, is shown in Figure 4.1. As shown there, the signals received by the 1D-UDAA are the input to an array of matching low noise amplifiers (LNAs). The amplified signals are then subjected to bandpass filtering in order to suppress undesired out-of-band signals. The filtered RF signals are processed by an array of "Variable Gain Amplifiers" (VGAs). Here, the signals are either amplified or

---

<sup>2</sup>The architecture that include both the transmitting and the receiving arms is given in Fig. 4.3 of [13].

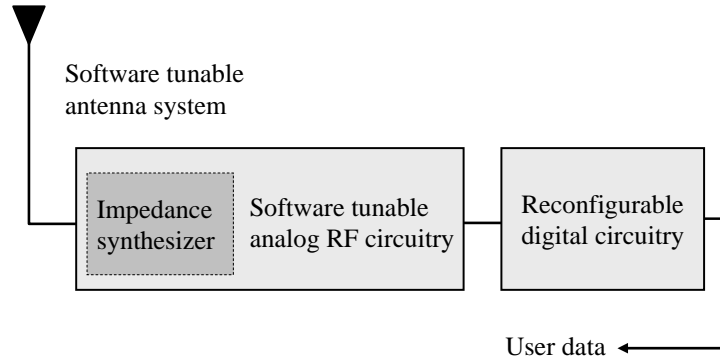


Figure 4.2: An ideal architecture for the SDR front-end of a CR system.

attenuated in order to maintain the amplitude of the signals approximately constant. The VGA is controlled by the control system of the CR system. The amplified RF signals containing bandpassed signals centered at frequency  $f_{Ic}$  are down-converted to a intermediate-frequency (IF) stage [71] using an array of synchronous software-tunable quadrature-downconverters [51]. The down-conversion process can be performed in either single or multiple demodulator stages [13]. A typical software-tunable quadrature-downconverter consists of software tunable internal “Automatic Gain Controller” (AGC) with peak detector and externally selectable IF filters to support different frequency bands and bandwidths. Consequently, software tunable analog-to-digital converters (ADC) synchronously sample the inphase (I) and the quadrature (Q) components of the continuous-time down-converted IF signals at the sample rate ( $\Omega_I$ ) that yield the corresponding digitalized complex-valued (i.e I - Q) sample sequences. In some cases, these complex-valued sample sequences are subjected to decimation [142] in order to reduce the data rate to  $\Omega_I$ , such that it matches with the bandwidth of the signals of interest. In order to determine the spectral occupancy of the allocated frequency bands, the spectral sensing subsystem measures the signals in the software-tunable quadrature-downconverters and software-tunable ADCs. A detailed mathematical analysis of the signal processing stages in SDR front-end of the CR system is given in section 4.3.

Wireless communication systems are interference limited systems [23]. Hence, *smart antennas* and beamforming networks have been exploited in modern wireless communications systems in order to increase the capacity and to maintain the quality of service [24]. In CR systems, mainly two types of beamforming methods, which are the switched beam methods and the adaptive beam methods, have been employed. In switched beam methods, the beamformer is switched between a predefined set of beams in order to achieve the best signal to interference ratio (SIR). In adaptive beam methods, the beamformer is adapted in real time to track and enhance the desired signals transmitted by a particular subscriber group as that group moves around the geographical area, while maintaining the SIR above the acceptable threshold. However, both switch and adaptive beam methods should be able to accommodate the instantaneous changes of the operating frequency band and the bandwidth in CR systems. The beamformer outputs are processed further in order to demodulate and recover the subscriber signals. Given the reciprocity between the signals in the receiving and transmitting arms of the front-end of the SDR [13] (ch. 4), the reciprocated application of the broadband beamforming methods that had been proposed for the receiving arm may also be used for beamforming for the transmission arms of a CR system. However for brevity, here, the focus is limited to adaptive beamforming in the receiving arm of a CR system.

### 4.3 Signal Processing at the SDR Front-End of the CR System

#### 4.3.1 A Review on Signals Observed at the Outputs of Elementals Antennas

Let's reconsider the scenario shown in Figure 2.11 (see page 53), where the EM waves transmitted by the subscriber module of a CR system are propagating toward the pseudo-infinite 1D-UDAA, which consisted of  $(2N_x + 1)$  linear-polarized wideband elemental antennas such as log periodic antennas or patch antennas [95] arranged at the inter element distance of  $\Delta_x$ . It is assumed here that the subscriber module is in the far-field

of the 1D-UDAA and therefore, the propagating EM wave can be closely approximated by a EM 4D BB-BP ST PW over the region of the 1D-UDAA. In practice, the subscriber modules of a CR systems are located at heights that are within a hundred meters from the surface of the earth and therefore, the inclination angles corresponding to the DOAs of propagating EM ST PWs are  $\theta_q \approx 90^\circ$ . According to example shown in Figure 2.12 (see page 54), the gain of the antenna active element pattern is approximately unity for  $\phi \in [30^\circ, 150^\circ]$  for  $\theta_q \approx 90^\circ$ . According to section 2.3 and section 2.6 of chapter 2, the signal  $a_{n_x}(t)$  observed at the output of  $n_x^{\text{th}}$  elemental antenna, where  $n_x \in [-N_x, N_x]$ , in response to the EM 4D BB-BP ST PW  $\mathbf{epw}_{4\text{CP}}(x, y, z, t)$  having the DOA  $\hat{\mathbf{d}} = [d_x, d_y, d_z]$  is given by

$$a_{n_x}(t) = \iiint_{x,y,z=-\infty}^{+\infty} \{\mathbf{ai}(x, y, z, t) \odot \odot \odot \odot \mathbf{epw}_{4\text{CP}}(x, y, z, t)\} \delta(x - \Delta_x n_x) \delta(y) \delta(z) dx dy dz, \quad (4.1)$$

where  $\mathbf{ai}(x, y, z, t)$  is the vector-valued the antenna impulse response corresponding to the elemental antennas of the pseudo-infinite 1D-UDAA and  $\mathbf{epw}_{4\text{CP}}(x, y, z, t)$  of is the electric field component of  $\mathbf{epw}_{4\text{CP}}(x, y, z, t)$ . Note that  $\odot \odot \odot \odot$  denotes the combined vector dot-product and 4D convolution operation.

Now consider a scenario as shown in Figure 4.3 where  $Q$  different subscriber modules of the CR system are transmitting toward the 1D-UDAA. These EM waves may occupy different temporal frequency bands that have been allocated to the CR system. The electric-field  $\mathbf{ef}_{4\text{CP}}(x, y, z, t)$  around the 1D-UDAA may be modeled as a superposition of linear-polarized EM 4D BB-BP ST PWs

$$\mathbf{ef}_{4\text{CP}}(x, y, z, t) = \sum_{q=1}^Q \mathbf{epw}_{4\text{CP}}(x, y, z, t) = \sum_{q=1}^Q pw_{4\text{CP}_q}(x, y, z, t) \hat{\mathbf{u}}_z, \quad (4.2)$$

which have DOAs  $\hat{\mathbf{d}}_q = [d_{xq}, d_{yq}, d_{zq}]$ ;  $q = 1, \dots, Q$ . Hence, the signals observed at the outputs of the elemental antennas can be rewritten as

$$a_{n_x}(t) = \sum_{q=1}^Q a_{qn_x}(t), \quad (4.3)$$

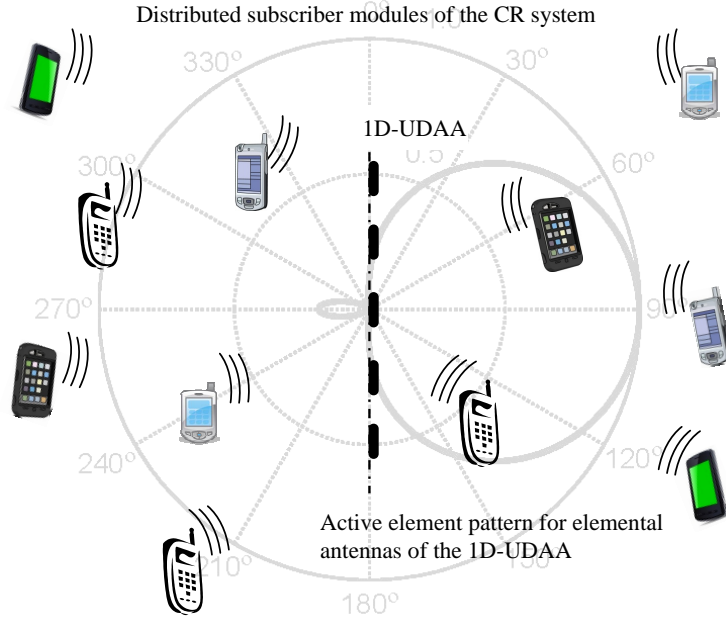


Figure 4.3: A typical scenario where subscriber modules transmitting toward the 1D-UDAA of a CR system. A typical active element pattern at  $\theta = 90^\circ$  that corresponds to each of the elemental antennas in the 1D-UDAA is shown in the background.

where according to (4.1) the antenna response for each linear-polarized EM 4D BB-BP ST PW  $pw_{4CP_q}(x, y, z, t) \hat{\mathbf{u}}_z$ ;  $q = 1, \dots, Q$ , is given by

$$a_{qn_x}(t) = \iiint_{x,y,z=-\infty}^{+\infty} a_{iz}(x, y, z, t) * * * pw_{4CP_q}(x, y, z, t) \delta(x - \Delta_x n_x) \delta(y) \delta(z) dx dy dz, \quad (4.4)$$

where the  $\hat{\mathbf{u}}_x$ - and  $\hat{\mathbf{u}}_y$ - components of  $\mathbf{a}_i(x, y, z, t)$  are  $a_{ix}(x, y, z, t) = 0$  and  $a_{iy}(x, y, z, t) = 0$ . Note that each  $pw_{4CP_q}(x, y, z, t)$ ;  $q = 1, \dots, Q$ , is associated with a 1D temporal-bandpassed wavefront function  $w_q(t)$  such that

$$pw_{4CP_q}(x, y, z, t) = w_q(t + c^{-1}(d_{xq}x + d_{yq}y + d_{zq}z)). \quad (4.5)$$

#### 4.3.2 Some Definitions of Parameters

According to section 2.3 (see page 21), the 1D temporal-bandpassed wavefront function  $w_{CP_q}(t)$  with instantaneous-bandwidth  $\Omega_I$ , and the instantaneous center frequency  $f_{Ic}$ ,



may be expressed as

$$w_{\text{CP}_q}(t) = \text{Re}[\tilde{b}_q(t)e^{j2\pi f_{\text{ic}}t}], \quad (4.6)$$

where  $\tilde{b}_q(t)$  is the *baseband equivalent of the analytic function of the temporal-bandpassed wavefront function*  $w_{\text{CP}_q}(t)$  and  $f_{\text{ic}} \geq \Omega_{\text{I}} > 0$  [66] (pp. 738 - 742). Note that the modulated subscriber information is carried by  $\tilde{b}_q(t)$ , which is having a instantaneous temporal bandwidth of  $0.5 \Omega_{\text{I}}$  [71] (pp. 194 - 195). As in section 2.3, here, the relative bandwidth of a temporally-bandpassed signal is characterized by the *instantaneous bandwidth spread factor*  $K_{\text{I}}$ , defined as

$$K_{\text{I}} \triangleq \frac{\Omega_{\text{I}}}{2f_{\text{Imax}}}, \quad (4.7)$$

where  $f_{\text{Imax}} (= f_{\text{ic}} + 0.5\Omega_{\text{I}})$  is the instantaneous maximum temporal frequency of  $w_{\text{CP}_q}(t)$ . The full allocated temporal bandwidth of the CR system is denoted by  $\Omega_{\text{Full}}$ . Here also, if a temporally-bandpassed signal  $w_{\text{CP}_q}(t)$  has  $K_{\text{I}} \geq 0.125$ , then it is considered to be a *temporally-broadband-bandpassed* signal. The utilization of the spectrum by the CR system is characterized by the *instantaneous system utilization factor*  $L_{\text{I}}$ , defined as

$$L_{\text{I}} \triangleq \frac{f_{\text{Imax}}}{f_{\text{SYSmax}}}, \quad (4.8)$$

where  $f_{\text{SYSmax}}$  is the upper limit of the temporal frequency of operation of the particular CR system considered here. Thus according to section 2.6, in order to avoid spatial aliasing, the inter-element distance of the 1D-UDAA has been selected as  $\Delta_x = 0.5 c/f_{\text{SYSmax}}$ .

#### 4.3.3 On the Complex-Quadrature Temporal-Sampling of LNA Outputs

In general, the signals observed at the output of the elemental antennas in response to the propagating desired EM BB-BP ST PWs are contaminated with the signals induces in response to the propagating undesired *out-of-band interfering* EM ST PWs. As shown in Figure 4.1, the signals observed at the output of the elemental antennas are processed by an array of LNAs. The signal at the output of the LNA connected to the  $n_x^{\text{th}}$  elemental

antenna of the 1D-UDAA can be expressed as

$$lna_{n_x}(t) = \sum_{q=1}^Q a_{qn_x}(t) + \gamma_{n_x}(t) + \eta_{n_x}(t), \quad (4.9)$$

where  $\gamma_{n_x}(t)$  corresponds set of superimposed, out-of-band interfering signals and  $\eta_{n_x}(t)$  is the receiver noise<sup>3</sup>. In the SDR front end of the CR system, the LNA outputs are processed by an array of software-tunable RF filters that suppresses the out-of-band interfering signals  $\gamma_{n_x}(t)$ . The remaining RF signals are the input to an array of VGAs that scales the signals such that the average magnitude of these signals remains a constant. Next, these signals are processed by an array of synchronous software-tunable quadrature-downconverters, where the BB-BP signals  $\sum_{q=1}^Q a_{qn_x}(t)$  having the center frequency  $f_{Ic}$  are modulated by the inphase (I) sinusoid  $\cos(2\pi f_{Ic}t)$  and the quadrature (Q) sinusoid  $\sin(2\pi f_{Ic}t)$  [51]. The modulated I and Q signals are filtered to remove the undesired images at frequencies  $|cf_{ct}| \geq 0.5\Omega_{Ic}$ , where  $0.5\Omega_I$  is the instantaneous bandwidth of the desired baseband signal. *Ideally, this process transfers the spectral components in the temporal frequency band  $cf_{ct} \in [f_{Ic} - 0.5\Omega_I, f_{Ic} + 0.5\Omega_I]$  into the baseband  $cf_{ct} \in [-0.5\Omega_I, 0.5\Omega_I]$  and filters out the remaining spectral components.*

Ideally the outputs of the software-tunable quadrature-downconverters  $\tilde{dc}_{n_x}(t)$ , may be expressed with *the analytic functions* [51]  $a_{qn_x}^+(t)$ ;  $q = 1, \dots, Q$  and  $\eta_{n_x}^+(t)$ , of  $a_{qn_x}(t)$ ;  $q = 1, \dots, Q$  and  $\eta_{n_x}(t)$ , respectively, such that

$$\tilde{dc}_{n_x}(t) = \left( \sum_{q=1}^Q a_{qn_x}^+(t) + \eta_{n_x}^+(t) \right) e^{-j2\pi f_{Ic}t}. \quad (4.10)$$

According to [66] (pp. 738 - 742), the analytic functions  $a_{qn_x}^+(t)$  and  $\eta_{n_x}^+(t)$ , are defined as

$$a_{qn_x}^+(t) \triangleq a_{qn_x}(t) + j\check{a}_{qn_x}(t); \quad q = 1, \dots, Q, \quad \text{and} \quad (4.11)$$

$$\eta_{n_x}^+(t) \triangleq \eta_{n_x}(t) + j\check{\eta}_{n_x}(t), \quad (4.12)$$

---

<sup>3</sup>For ease of analysis receiver noise is referred to the input of the LNA connected to the  $n_x^{\text{th}}$  antenna element.

where  $\check{a}_{qn_x}(t)$ ;  $q = 1, \dots, Q$  and  $\check{\eta}_{n_x}(t)$ , are the Hilbert transforms [51] of  $a_{qn_x}(t)$ ;  $q = 1, \dots, Q$  and  $\eta_{n_x}(t)$ , respectively. According to [66] (pp. 738 - 742), the Hilbert transforms of  $a_{qn_x}(t)$ ;  $q = 1, \dots, Q$  and  $\eta_{n_x}(t)$  are defined as

$$\check{a}_{qn_x}(t) \triangleq \frac{1}{\pi} \int_{\tau=-\infty}^{\infty} \frac{a_{qn_x}(\tau)}{t - \tau} d\tau; \quad q = 1, \dots, Q, \quad \text{and} \quad (4.13)$$

$$\check{\eta}_{n_x}(t) \triangleq \frac{1}{\pi} \int_{\tau=-\infty}^{\infty} \frac{\eta_{n_x}(\tau)}{t - \tau} d\tau. \quad (4.14)$$

The downconverted signals  $\tilde{d}c_{n_x}(t)$ ;  $n_x = 1, \dots, 2N_x + 1$  are synchronously sampled by an array of software-tunable ADCs at the instantaneous sampling rate  $f_{\text{SI}} = \Omega_{\text{I}} (= \Delta_{\text{It}}^{-1})$  that yields a 2D complex-valued sample sequence

$$\begin{aligned} \tilde{x}(n_x, n_t) &\equiv xi_{n_x}(n_t) + jxq_{n_x}(n_t), \\ &= \sum_{q=1}^Q a_{qn_x}^+(\Delta_{\text{It}} n_t) + \eta_{n_x}^+(\Delta_{\text{It}} n_t) e^{-j2\pi f_{\text{Ic}} \Delta_{\text{It}} n_t}, \end{aligned} \quad (4.15)$$

for  $n_x \in [-N_x, N_x]$  and  $n_t \in \mathbb{Z}$ , where the residual baseband equivalent noise component represented by  $\check{\eta}_{n_x}(\Delta_{\text{It}} n_t)$ . Note that  $xi_{n_x}(n_t)$  and  $xq_{n_x}(n_t)$  denote the I (real) and Q (imaginary) components of the complex-valued sample sequence  $\tilde{x}(n_x, n_t)$ .

#### 4.3.4 Spectra of the Complex-Quadrature Sampled BB-BP ST PWs

According to (4.15), the ideal infinite extent complex-valued 2D sample sequence  $\tilde{d}(n_x, n_t)$  that corresponds to a complex-quadrature sampled antenna signals, which are induced by a EM 4D BB-BP ST PW  $pw_{4\text{CP}_p}(x, y, z, t) \hat{\mathbf{u}}_z$ , is given by

$$\tilde{d}(n_x, n_t) = a_{pn_x}^+(\Delta_{\text{It}} n_t) e^{-j2\pi f_{\text{Ic}} \Delta_{\text{It}} n_t}, \quad (4.16)$$

for  $(n_x, n_t) \in \mathbb{Z}^2$ . In order to analyze the frequency domain properties of the complex-quadrature sampled antenna signals that are induced by a linear-polarized EM 4D BB-BP ST PW  $pw_{4\text{CP}_p}(x, y, z, t) \hat{\mathbf{u}}_z$ , the 2D discrete-domain Fourier transform (2D-DDFT) [42] (pp. 32) of the 2D sample sequence  $\tilde{d}(n_x, n_t)$  is evaluated.

The 2D-DDFT  $D(e^{j\omega_x}, e^{j\omega_t})$ , of the complex-valued 2D sample-sequence  $\tilde{d}(n_x, n_t)$ , is defined as

$$D(e^{j\omega_x}, e^{j\omega_t}) \triangleq \sum_{n_x=-\infty}^{+\infty} \sum_{n_t=-\infty}^{+\infty} \tilde{d}(n_x, n_t) e^{-jn_x\omega_x} e^{-jn_t\omega_t}, \quad (4.17)$$

for  $(\omega_x, \omega_t) \in \mathbb{R}^2$  [42] (pp. 32). Nevertheless, according to [44] (pp. 54-55),  $D(e^{j\omega_x}, e^{j\omega_t})$  may be expressed in the form

$$D(e^{j\omega_x}, e^{j\omega_t}) = \frac{1}{\Delta_x \Delta_{It}} \sum_{m_x=-\infty}^{+\infty} \sum_{m_t=-\infty}^{+\infty} DC \left( \frac{\omega_x - 2\pi m_x}{2\pi \Delta_x}, \frac{\omega_t - 2\pi m_t}{2\pi \Delta_{It}} \right), \quad (4.18)$$

where  $DC(f_x, f_t)$  is the 2D-CDFFT of the *equivalent 2D continuous domain complex-quadrature downconverted signal*  $\tilde{dc}(x, t)$ . It is implied in (4.18) that  $D(e^{j\omega_x}, e^{j\omega_t})$  may be expressed as an infinite series of periodic copies of  $DC \left( \frac{\omega_x}{2\pi \Delta_x}, \frac{\omega_t}{2\pi \Delta_{It}} \right)$  with 2D-periodicity  $(2\pi, 2\pi)$  along  $\omega_x$ - and  $\omega_t$ - axes in  $(\omega_x, \omega_t) \in \mathbb{R}^2$ . Here,  $D(e^{j\omega_x}, e^{j\omega_t})$  is determined by exploiting the relationship in (4.18) that in turn requires the evaluation of  $DC(f_x, f_{ct})$  in  $(f_x, f_{ct}) \in \mathbb{R}^2$ .

According to (4.15),  $\tilde{d}(n_x, n_t)$ ,  $\tilde{dc}(x, t)$  and the analytic antenna output function  $a_{pn_x}^+(t)$  are related as

$$\tilde{d}(n_x, n_t) = a_{pn_x}^+(\Delta_{It} n_t) e^{-j2\pi f_{lc} \Delta_{It} n_t} = \tilde{dc}(\Delta_x n_x, \Delta_{It} n_t). \quad (4.19)$$

According to (4.11),  $a_{pn_x}^+(t)$  may be given in terms of the equivalent 2D continuous-domain antenna output function  $apwz_{2CP}(x, t)$  that is defined in (2.76) (see page 55), such that

$$a_{pn_x}^+(t) = apwz_{2CP}(\Delta_x n_x, t) + \frac{j}{\pi} \int_{\tau=-\infty}^{\infty} \frac{apwz_{2CP}(\Delta_x n_x, \tau)}{t - \tau} d\tau. \quad (4.20)$$

Hence, the *equivalent 2D continuous-domain temporal analytic antenna output function*  $apwz_{2CP}^+(x, t)$  can be defined as

$$apwz_{2CP}^+(x, t) \triangleq apwz_{2CP}(x, t) + \frac{j}{\pi} \int_{\tau=-\infty}^{\infty} \frac{apwz_{2CP}(x, \tau)}{t - \tau} d\tau. \quad (4.21)$$

According to (4.19), (4.20) and (4.21),  $\tilde{dc}(x, t)$  and  $apwz_{2CP}^+(x, t)$  are related as

$$\tilde{dc}(x, t) = apwz_{2CP}^+(x, t) e^{-j2\pi f_{lc} t}. \quad (4.22)$$

Thus, following the frequency shifting properties of the Fourier transform [41] (ch. 6), it can be shown that

$$DC(f_x, f_{ct}) = APWZ_{2CP}^+(f_x, f_{ct} + c^{-1}f_{1c}), \quad (4.23)$$

where  $APWZ_{2CP}^+(f_x, f_{ct})$  is the 2D-CDFT of  $apwz_{2CP}^+(x, t)$ . According to (4.23), in order to evaluate  $DC(f_x, f_{ct})$ , first,  $APWZ_{2CP}^+(f_x, f_{ct})$  has to be evaluated for  $(f_x, f_{ct}) \in \mathbb{R}^2$ .

According to the properties of the Hilbert transform [66] (pp. 738 - 742), it can be shown that

$$APWZ_{2CP}^+(f_x, f_{ct}) = APWZ_{2CP}(f_x, f_{ct}) - jSGN(f_{ct})APWZ_{2CP}(f_x, f_{ct}), \quad (4.24)$$

where  $SGN(f_{ct})$  is defined such that

$$SGN(f_{ct}) \triangleq \begin{cases} 1; & f_{ct} > 0 \\ 0; & f_{ct} = 0 \\ -1; & f_{ct} < 0. \end{cases} \quad (4.25)$$

Note that  $APWZ_{2CP}(f_x, f_{ct})$ , the 2D-CDFT of the equivalent 2D continuous-domain antenna output function  $apwz_{2CP}(x, t)$  has been derived in section 2.6 and given in (2.82) as

$$APWZ_{2CP_p}(f_x, f_{ct}) = APZ_{[d_{py}, d_{pz}]}(f_x, f_{ct}) PW_{2CP_p}(f_x, f_{ct}),$$

where the 2D continuous-domain parametric-function  $APZ_{[d_{py}, d_{pz}]}(f_x, f_{ct})$  of the parameters  $(d_{py}, d_{pz})$  has been defined in (2.81) as

$$APZ_{[d_{py}, d_{pz}]}(f_x, f_{ct}) \triangleq \iint_{f_z, f_y = -\infty}^{+\infty} APZ(f_x, f_y, f_z, f_{ct}) \delta(d_{py}f_{ct} - f_y) \delta(d_{pz}f_{ct} - f_z) df_y df_z.$$

In (2.81),  $APZ(f_x, f_y, f_z, f_{ct})$  represent the  $\hat{\mathbf{u}}_z$ -component of antenna frequency response function that relates to the vector-valued active element pattern  $\mathbf{A}\mathbf{E}_C(\theta, \phi, f_{ct})$  as defined in (2.70). Note that the spectrum of the 2D BB-BP ST PW  $PW_{2CP_p}(f_x, f_{ct})$ , which is

observed on the 3D line along the  $x$ -axis in response to a 4D BB-BP ST PW having the DOA  $\hat{\mathbf{d}}_p = [d_{px} \ d_{py} \ d_{pz}]$ , has been derived in subsection 2.3.3 such that

$$PW_{2CP_p}(f_x, f_{ct}) = W_{CP_p}(cf_{ct})\delta(d_{px}f_{ct} - f_x).$$

Substituting the above in (4.24) yields

$$\begin{aligned} APWZ_{2CP}^+(f_x, f_{ct}) = \\ APZ_{[d_{py}, d_{pz}]}(f_x, f_{ct}) W_{CP_p}(cf_{ct}) - jSGN(f_{ct})W_{CP_p}(cf_{ct}) \delta(d_{px}f_{ct} - f_x). \end{aligned} \quad (4.26)$$

According to the definition of the 1D temporal-bandpassed wavefront function  $w_{CP_q}(t)$  given in (4.6) and the definition of the analytic function given in (4.11), the analytic function  $w_{CP_p}^+(t)$  of  $w_{CP_q}(t)$  may be expressed in terms of the baseband equivalent of the analytic function  $\tilde{b}_q(t)$ , such that

$$w_{CP_p}^+(t) = w_{CP_p}(t) + j\check{w}_{CP_p}(t) = \tilde{b}_p(t)e^{j2\pi f_{Ic}t}. \quad (4.27)$$

Therefore, following the properties of Fourier transform and Hilbert transform, it can be shown that

$$W_{CP_p}^+(cf_{ct}) = W_{CP_p}(cf_{ct}) - jSGN(f_{ct})W_{CP_p}(cf_{ct}) = B_p(cf_{ct} - f_{Ic}), \quad (4.28)$$

where the 1D-CDFT pairs are  $w_{CP_p}^+(t) \xleftrightarrow{1D-CDFT} W_{CP_p}^+(cf_{ct})$ ,  $w_{CP_p}(t) \xleftrightarrow{1D-CDFT} W_{CP_p}(cf_{ct})$  and  $\tilde{b}_p(t) \xleftrightarrow{1D-CDFT} B_p(cf_{ct})$ . Hence, (4.26) can be rewritten as

$$APWZ_{2CP}^+(f_x, f_{ct}) = APZ_{[d_{py}, d_{pz}]}(f_x, f_{ct})B_p(cf_{ct} - f_{Ic})\delta(d_{px}f_{ct} - f_x). \quad (4.29)$$

Now,  $DC(f_x, f_{ct})$  can be evaluated by substituting (4.29) into (4.23), that results

$$DC(f_x, f_{ct}) = APZ_{[d_{py}, d_{pz}]}(f_x, f_{ct} + c^{-1}f_{Ic})B_p(cf_{ct})\delta(d_{px}(f_{ct} + c^{-1}f_{Ic}) - f_x). \quad (4.30)$$

In the following, the properties of  $DC \xrightarrow{\frac{\omega_x}{2\pi\Delta_x}, \frac{\omega_t}{2\pi\Delta_{It}}} \text{analyzed}$  because, according to (4.18), the 2D spectrum  $D(e^{j\omega_x}, e^{j\omega_t})$  may be represented as an infinite series of periodic copies of  $DC \xrightarrow{\frac{\omega_x}{2\pi\Delta_x}, \frac{\omega_t}{2\pi\Delta_{It}}} \text{with 2D-periodicity } (2\pi, 2\pi) \text{ along } \omega_x\text{- and } \omega_t\text{-axes in } (\omega_x, \omega_t) \in \mathbb{R}^2$ .

**The ROS of  $DC$**   $\frac{\omega_x}{2\pi\Delta_x}, \frac{\omega_t}{2\pi\Delta_{It}}$

Substituting (4.30) with  $f_x = \frac{\omega_x}{2\pi\Delta_x}$  and  $cf_{ct} = \frac{\omega_t}{2\pi\Delta_{It}}$ , results

$$DC \quad \frac{\omega_x}{2\pi\Delta_x}, \frac{\omega_t}{2\pi\Delta_{It}} = \frac{1}{\Delta_x \Delta_{It}} APZ_{[d_{py}, d_{pz}]} \quad \frac{\omega_x}{2\pi\Delta_x}, \frac{c^{-1}\omega_t}{2\pi\Delta_{It}} + c^{-1}f_{Ic} \\ \times B_p \quad \frac{\omega_t}{2\pi\Delta_{It}} \quad \delta \quad \frac{\omega_x}{2\pi\Delta_x} - c^{-1}d_x \quad \frac{\omega_t}{2\pi\Delta_{It}} + f_{Ic} \quad . \quad (4.31)$$

Given that the instantaneous bandwidth spread factor is  $K_I = \Omega_I/2f_{I\max}$  (see (4.7)), the instantaneous system utilization factor is  $L_I = f_{I\max}/f_{SYS\max}$  (see (4.8)), the inter-element distance is  $\Delta_x = 0.5cf_{SYS\max}^{-1}$  and the instantaneous temporal-sampling-interval is  $\Delta_{It} = \Omega_{It}^{-1}$ , (4.31) can be rewritten as

$$DC \quad \frac{\omega_x}{2\pi\Delta_x}, \frac{\omega_t}{2\pi\Delta_{It}} = \frac{1}{\Delta_x \Delta_{It}} APZ_{[d_{py}, d_{pz}]} \quad \frac{\omega_x}{2\pi\Delta_x}, \frac{c^{-1}\omega_t}{2\pi\Delta_{It}} + c^{-1}f_{Ic} \\ \times B_p \quad \frac{\omega_t}{2\pi\Delta_{It}} \quad \delta \quad \frac{\omega_x - L_I d_{px} (K_I \omega_t + (1 - K_I)\pi)}{2\pi\Delta_x} \quad , \quad (4.32)$$

According to (4.32), the ROS of  $DC$   $\frac{\omega_x}{2\pi\Delta_x}, \frac{\omega_t}{2\pi\Delta_{It}}$  is given by the intersection of ROSs of  $APZ_{[d_{py}, d_{pz}]}$   $\frac{\omega_x}{2\pi\Delta_x}, \frac{c^{-1}\omega_t}{2\pi\Delta_{It}} + c^{-1}f_{Ic}$ ,  $B_p \quad \frac{\omega_t}{2\pi\Delta_{It}}$  and  $\delta \quad \frac{\omega_x - L_I d_{px} (K_I \omega_t + (1 - K_I)\pi)}{2\pi\Delta_x}$  in  $(\omega_x, \omega_t) \in \mathbb{R}^2$ . Because  $\tilde{b}_p(t)$  is a temporally-baseband signal with temporal bandwidth  $0.5\Omega_I$ ,  $B_p(cf_{ct}) = 0; \forall |cf_{ct}| > 0.5\Omega_I$  and therefore  $B_p \quad \frac{\omega_t}{2\pi\Delta_{It}} = 0; \forall |\omega_t| > \pi$ . Thus, the intersection of ROSs between  $B_p \quad \frac{\omega_t}{2\pi\Delta_{It}}$  and  $\delta \quad \frac{\omega_x - L_I d_{px} (K_I \omega_t + (1 - K_I)\pi)}{2\pi\Delta_x}$  is given by the straight-line segment  $PQ$  shown in Figure 4.4, which is on

$$\omega_x = L_I d_{px} \quad K_I \omega_t + \pi(1 - K_I) \quad , \quad (4.33)$$

for  $|\omega_t| > \pi$ . In case of EM waves transmitted from the subscriber modules of the CR system, the azimuth angles associated with the corresponding EM 4D BB-BP ST PW varies in the range  $\phi_p \in [0^\circ, 360^\circ]$ , while the inclination angle is  $\theta_p \in [85^\circ, 95^\circ]$ . For the varying  $\phi_p$ , the corresponding straight-line segment sweeps the *2D trapezoidal-shaped area marked with 1234*<sup>4</sup> multiple times.

---

<sup>4</sup>The shaded region in Figure 4.4

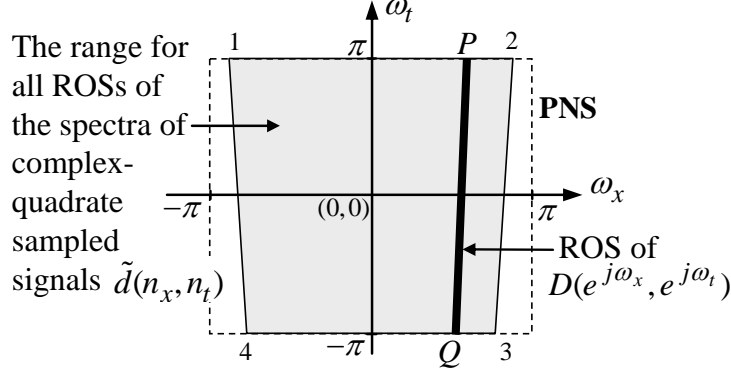


Figure 4.4: The ROS of the spectrum  $D(e^{j\omega_x}, e^{j\omega_t})$  in  $\mathbf{PNS}\{|\omega_x; \omega_t| \leq \pi\}$ . The range of all ROSs of  $D(e^{j\omega_x}, e^{j\omega_t})$  corresponding to DOAs corresponding to  $\phi_p \in [0^\circ, 180^\circ]$ .

Let's assume that for this particular 1D-UDAA the normalized-magnitude of the  $\hat{\mathbf{u}}_z$ -component of the active element pattern  $|ATZ(\theta, \phi, f_{ct})| = 0$  in the angular-ranges  $\Psi_P = \bigcup\{\theta_p \in (85^\circ, 95^\circ) \text{ and } \phi_p \in (0^\circ, 180^\circ)\}$  for all temporal frequencies used by the CR system  $|cf_{ct}| \in [f_{\text{SYSmax}} - \Omega_{\text{Full}}, f_{\text{SYSmax}}]$ . Note that according to (2.5), the DOA unit vectors  $\hat{\mathbf{d}}_P$  included in the vector-range

$$\mathbf{D}_P \in [d_{xP} \ d_{yP} \ d_{zP}] \mid [d_{xP} = \sin(\theta_P) \cos(\phi_P), \ d_{yP} = \sin(\theta_P) \sin(\phi_P), \ d_{zP} = \cos(\theta_P)] \ , \quad (4.34)$$

correspond to all  $(\theta_P, \phi_P) \in \Psi_P$ . According to (4.34),  $d_{px} \approx \cos(\phi_P)$ , because  $\sin(\theta_P) \approx 1$  for  $\theta_P \in (85^\circ, 95^\circ)$ . According to the definitions (2.51) and (2.81), it can be shown that the 2D trapezoidal shaped area 1234, shown in Figure 4.4 in  $(\omega_x, \omega_t) \in \mathbb{R}^2$ , is included in the ROS of  $APZ_{[d_{yP}, d_{zP}]} \frac{\omega_x}{2\pi\Delta_x}, \frac{c^{-1}\omega_t}{2\pi\Delta_{It}} + c^{-1}f_{Ic}$  for all  $\hat{\mathbf{d}}_P \in \mathbf{D}_P$  but, is excluded in the ROS of  $APZ_{[\bar{d}_{yP}, \bar{d}_{zP}]} \frac{\omega_x}{2\pi\Delta_x}, \frac{c^{-1}\omega_t}{2\pi\Delta_{It}} + c^{-1}f_{Ic}$  for all  $\bar{\hat{\mathbf{d}}}_P \notin \mathbf{D}_P$ . Therefore, for all  $\hat{\mathbf{d}}_P \in \mathbf{D}_P$ , the ROS of  $DC \frac{\omega_x}{2\pi\Delta_x}, \frac{\omega_t}{2\pi\Delta_{It}}$  is determined by the ROS of  $B_p \frac{\omega_t}{2\pi\Delta_{It}} \delta \frac{\omega_x - L_I \cos(\phi_P)(K_I \omega_t + (1-K_I)\pi)}{2\pi\Delta_x}$ , which is given by the line segment  $PQ$  in  $(\omega_x, \omega_t) \in \mathbb{R}^2$  (see Figure 4.4). However, for all  $\bar{\hat{\mathbf{d}}}_P \notin \mathbf{D}_P$ ,  $DC \frac{\omega_x}{2\pi\Delta_x}, \frac{\omega_t}{2\pi\Delta_{It}} = 0$ , because there is no intersection between the ROSs of  $B_p \frac{\omega_t}{2\pi\Delta_{It}} \delta \frac{\omega_x - L_I \cos(\phi_P)(K_I \omega_t + (1-K_I)\pi)}{2\pi\Delta_x}$  and  $APZ_{[\bar{d}_{yP}, \bar{d}_{zP}]} \frac{\omega_x}{2\pi\Delta_x}, \frac{c^{-1}\omega_t}{2\pi\Delta_{It}} + c^{-1}f_{Ic}$  in  $(\omega_x, \omega_t) \in \mathbb{R}^2$ .

Given that the parameters  $|d_{px}| \leq 1; \forall [d_{px} \ d_{py} \ d_{pz}] \in \mathbf{D}_P$ ,  $|L_I| \leq 1$  and  $|K_I| \leq 0.5$ , it



can be shown that the spatial frequency components corresponding to the line-segment  $PQ$  are confined to the frequency range  $\omega_x \in (-\pi, \pi)$  for  $\forall \omega_x \in (-\pi, \pi)$ . Therefore, the ROS of  $DC \frac{\omega_x}{2\pi\Delta_x}, \frac{\omega_t}{2\pi\Delta_{It}}$  remains inside *the principle Nyquist square (PNS)*  $\{|\omega_x; \omega_t| \leq \pi\}$ . This confirms that the selected inter-element distance  $\Delta_x$  and the instantaneous temporal sampling-interval  $\Delta_{It}$  prevent spatial- and temporal- aliasing in the complex-quadrature sampling performed by the SDR front end. This implies that inside the **PNS**,  $D(e^{j\omega_x}, e^{j\omega_t})$  may be given by

$$D(e^{j\omega_x}, e^{j\omega_t})_{\{|\omega_x, \omega_t| \leq \pi\}} = \frac{1}{\Delta_x \Delta_{It}} APZ_{[d_{py}, d_{pz}]} \left[ \frac{\omega_x}{2\pi\Delta_x}, \frac{c^{-1}\omega_t}{2\pi\Delta_{It}} + c^{-1}f_{lc} \right. \\ \left. \times B_p \frac{\omega_t}{2\pi\Delta_{It}} \delta \left[ \frac{\omega_x - L_I d_{px} (K_I \omega_t + (1 - K_I)\pi)}{2\pi\Delta_x} \right] \right], \quad (4.35)$$

The spectral density  $\overline{\overline{Z}}(e^{j\omega_x}, e^{j\omega_t})$ , where the 2D-DDFT pair for the auto-correlation function for the 2D noise sequence is  $\text{AutoCorr } \eta_{n_x}(\Delta_{It}n_t) \xleftrightarrow{2D-DDFT} \overline{\overline{Z}}(e^{j\omega_x}, e^{j\omega_t})$ , of the equivalent complex-quadrature sampled receiver noise  $\eta_{n_x}(\Delta_{It}n_t)$  is expected to occupy the entire **PNS**  $\{|\omega_x; \omega_t| \leq \pi\}$  shown in Figure 4.4.

#### On Spectral Leakage and Spectral Spreading

The ideal complex-quadrature sampled antenna signals corresponds to EM 4D BB-BP ST PWs  $\tilde{d}(n_x, n_t)$  has an infinite number of spatial samples whereas the output  $\tilde{x}(n_x, n_t)$  (see (4.15)) of the complex-quadrature temporal sampler array is limited to  $2N_x + 1$  spatial samples. As discussed in section 2.7, the straightforward 2D spectral analysis of  $\tilde{x}(n_x, n_t)$ , leads spectral spreading and spectral leakage [42][44] in the direction of the spatial frequency  $\omega_x$ . However, an acceptable trade-off can be achieved between this spectral spreading and spectral leakage by using a sufficient number of sensors along with an appropriate 1D window function [42][66] to weight [43] (pp. 88) the aperture of the 1D-UDAA.

## 4.4 Previously Proposed Broadband-Bandpass Beamforming Methods: A Review

In this section, a few examples of the previously proposed discrete-domain broadband-beamforming methods that can be employed to enhance desired signals in CR systems are briefly reviewed. Most previously proposed discrete-domain broadband-beamforming methods can be categorized as either *frequency-domain broadband-beamforming* methods or *time-domain broadband-beamforming* methods. The frequency-domain broadband-beamforming methods [138][143][144] typically evaluate the discrete Fourier transform (DFT) of a segment of the sampled ST PW signals. Because of higher latency, the frequency-domain broadband-beamforming methods are not well suited for real-time adaptive applications. The *legacy* time-domain broadband-beamforming methods [145][42][43][101][146][147] have been derived from the basic *delay-and-sum* concept [148]. Even though these delay-and-sum methods can be used for real-time adaptive broadband beamforming, the errors between the required exact time delays and the corresponding implemented approximate time delays typically result in considerable distortion of the desired beam-formed signal [145][146][149]. As a remedy, the frequency-invariant broadband beamforming methods [150][151][152][153][154] have been realized by extrapolating the narrowband beamforming methods for several different temporal frequencies in the desired frequency band using iterative optimization techniques. Even though these methods minimize the distortion, the design process is typically too computationally intensive for the real-time adaptive tracking of ST PWs. In yet another approach to time-domain broadband-beamforming, *multidimensional (MD) filters* have been used as broadband beamformers [139][155][156][157].

The frequency domain beamforming method proposed in [138], the digital interpolation delay-and-sum beamforming method proposed in [101] and the “Sekiguchi Method”, which employs a 2D FIR filter, proposed in [139] are briefly reviewed in the following.

In section 4.6, the proposed 2D FIR asymmetric-trapezoidal filter-based beamforming method is compared against the beamforming methods [101][138][139] based on the attenuation of the interfering signals, the distortion of the desired signal and the evaluation time of the beamforming coefficients.

#### 4.4.1 Digital Interpolation Beamforming for Broadband-Bandpassed Signals

The digital interpolation beamforming method that has been proposed in [101] is a modification of the basic delay-and-sum [42] beamforming method. In the basic delay-and-sum beamforming, the sensor signals are delayed to match the propagation delays of the desired ST PW arriving at the 1D uniformly distributed sensor array along a specified DOA. Here, it is expected that the coherent combination of antenna signals corresponding to the desired ST PW would enhance the associated wavefront signal with respect to the other propagating ST PWs having different DOAs and the receiver noise. In general, the antenna signals are scaled by 1D window-function in order to control the width of the main-lobe and the magnitude of the side-lobes of the beam-pattern [101].

The main objective of the digital interpolation beamforming method is to reduce the prohibitively high sampling rates that are required for the beamforming of BB-BP ST PWs using the basic delay-and-sum beamforming method. The requirement of the high sampling rates arises from two factors. First, the direct Nyquist sampling (see subsection 2.8.1) of BB-BP signals requires about 4 - 12 times higher sampling rates compared to the complex-quadrature sampling of the same signals. Secondly, in order to *“steer” the beam towards the desired direction*, the sampled sequences are required to be delayed by fractions of the Nyquist sampling interval. Hence for efficient beam steering, the antenna signals must be oversampled at 20 - 100 times higher rates compared to the Nyquist sampling rate [43].

A typical architecture of an interpolation beamformer is shown in Figure 4.5. As shown there the antenna signals  $a_{n_x}(t)$ ;  $n_x = [N_x, \dots, -1, 0, 1, \dots, N_x]$ , are subjected to

complex-quadrature sampling. Next, 1D temporal sequence of  $\tilde{x}(n_x, n_t)$  for each  $n_x$  is subjected to  $M$ -fold temporal interpolation that oversample the information carrying baseband equivalent signal sequences by a factor of  $M$ . Followed by that, the interpolated 1D sequence  $\widetilde{xd}(n_x, n_t)$  for each  $n_x$  is scaled by the “phase-rotating-factor”, that is defined as

$$c_{\hat{\phi}_0}(n_x) \triangleq e^{-j\pi \cos(\hat{\phi}_0)L_I(1-K_I)n_x}, \quad (4.36)$$

where the anticipated azimuth angle  $\hat{\phi}_0$  of the DOA of the desired EM wave varies in the range  $\hat{\phi}_0 \in [0^\circ, 180^\circ]$ . As proposed in [101], for each  $n_x = [N_x, \dots, -1, 0, 1, \dots, N_x]$ , the phase-rotated 1D sequence  $c_{\hat{\phi}_0}(n_x)\widetilde{xd}(n_x, n_t)$  is delayed by  $N_{\hat{\phi}_0}(n_x)$ -samples, scaled by the coefficient  $w_D(n_x)$  and summed together such that

$$\tilde{y}_{DS}(n_t) = \sum_{n_x=-N_x}^{N_x} w_D(n_x) c_{\hat{\phi}_0}(n_x) \widetilde{xd}_{n_x, n_t - N_{\hat{\phi}_0}(n_x)}, \quad (4.37)$$

in order to achieve the output  $\tilde{y}_{DS}(n_t)$  of the digital interpolation beamformer. Note that the samples delays for each  $n_x$  is given by

$$N_{\hat{\phi}_0}(n_x) = \left\lfloor M L_I K_I \cos(\hat{\phi}_0) \right\rfloor n_x. \quad (4.38)$$

Note that the symbol  $\lfloor \tau \rfloor$  denotes the nearest integer of the real-number  $\tau$ . In (4.37),  $w_D(n_x)$  specifies the 1D discrete-domain window-function of length  $(2N_x+1)$  that controls the main-lobe width and side-lobe magnitude of the beam-pattern. However, due to the  $M$ -fold interpolation,  $\tilde{y}_{DS}(n_t)$  is over-sampled by a factor of  $M$ , where the temporal bandwidth of  $\tilde{y}_{DS}(n_t)$  is confined to  $\omega_t \in [-\pi/M, \pi/M]$ . Therefore, without distorting the information content,  $\tilde{y}_{DS}(n_t)$  can be *decimated by a factor of  $M$*  [142] (ch. 4), as shown in Figure 4.5.

The digital interpolation beamforming process specified in (4.37) can be expressed as a 2D FIR filtering process. The unit impulse response  $\tilde{h}_{DS}(n_x, n_t)$  of this delay-and-sum beamforming 2D FIR filter is defined by

$$\tilde{h}_{DS}(n_x, n_t) \triangleq w_D(n_x) c_{\hat{\phi}_0}(n_x) \delta_{2D} [n_x, n_t - N_{\hat{\phi}_0}(n_x)], \quad (4.39)$$

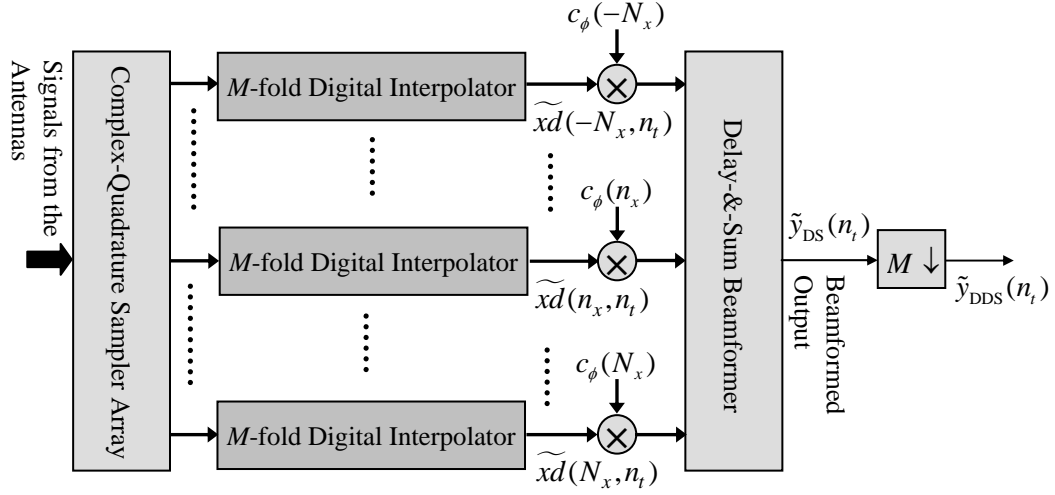


Figure 4.5: A typical architecture of a interpolation delay-and-sum beamformer that has been proposed in [101].

where  $\delta_{2D} \ n_x, n_t$  is the *2D Kronecker delta-function* [42] (ch. 1). The 2D input sequence of this 2D beamforming filter is given by the interpolated complex-valued 2D sequence  $\widetilde{x}d(n_x, n_t)$ . According to [44] (pp. 54 - 55), the transfer function of the interpolation delay-and-sum beamforming 2D FIR filter may be given by

$$H_{DS}(e^{j\omega_x}, e^{j\omega_t}) = \sum_{m_x=-\infty}^{\infty} \sum_{m_t=-\infty}^{\infty} HC_{DS} \frac{\omega_x - 2\pi m_x}{2\pi \Delta_x}, \frac{\omega_t - 2\pi m_t}{2\pi \Delta_{It} M^{-1}} \quad , \quad (4.40)$$

where  $HC_{DS}(f_x, f_{ct})$  the 2D-CDFT of the equivalent continuous-domain unit impulse response of the delay-and-sum beamformer  $\widetilde{h}c_{DS}(x, t)$ . Note that in this case the temporal sampling interval is  $\Delta_{It} M^{-1}$ . Following (4.39),  $\widetilde{h}c_{DS}(x, t)$  can be expressed as

$$\widetilde{h}c_{DS}(x, t) = \left\{ w_C(x) cc_{\hat{\phi}_0}(x) \delta \left( t + c^{-1} \frac{ML_I K_I \cos(\hat{\phi}_0)}{ML_I K_I} x \right) \right\} * \frac{\text{sinc}(\Omega_I t)}{\Omega_I}, \quad (4.41)$$

where  $w_C(x)$  is the 1D equivalent continuous-domain window-function and where the phase rotations are resulted by the 1D equivalent continuous-domain phase-shift function  $cc_{\hat{\phi}_0}(x) \triangleq e^{\frac{-j2\pi \cos(\hat{\phi}_0) L_I (1-K_I) x}{2\Delta_x}}$ . Given that  $\frac{\text{sinc}(\Omega_I t)}{\Omega_I} \xleftrightarrow{\text{1D-CDFT}} \text{rect}(\frac{f_x}{\Omega_I})$ , where  $\text{rect}(\frac{f_x}{\Omega_I}) = 1$  for  $|f_x| \leq 0.5\Omega_I$  and where  $\text{rect}(\frac{f_x}{\Omega_I}) = 0$  for  $|f_x| > 0.5\Omega_I$ , the convolution with  $\frac{\text{sinc}(\Omega_I t)}{\Omega_I}$  limits the filter response to  $|f_{ct}| \leq [-0.5\Omega_{It}, 0.5\Omega_{It}]$ . Following the properties of Fourier

transform and the derivation of the 2D-CDFT of a 2D BB-BP ST PW in Appendix A.3, it can be shown that

$$\begin{aligned}
HC_{\text{DS}}(f_x, f_{ct}) &= \left\{ W_C(f_x) * * \delta_{f_x - \frac{\cos(\hat{\phi}_0)L_I(1-K_I)}{2\Delta_x}} * * \delta_{f_x - \frac{ML_I K_I \cos(\hat{\phi}_0)}{ML_I K_I} f_{ct}} \right\} \text{rect} \frac{f_{ct}}{\Omega_{\text{It}}} , \\
&= W_C \left( f_x - \frac{ML_I K_I \cos(\hat{\phi}_0)}{ML_I K_I} f_{ct} - \frac{\cos(\hat{\phi}_0)L_I(1-K_I)}{2\Delta_x} \right) \text{rect} \frac{f_{ct}}{\Omega_{\text{It}}} . \tag{4.42}
\end{aligned}$$

where the 1D-CDFT pair  $w_C(x) \xleftrightarrow{\text{1D-CDFT}} W_C(f_x)$ . Hence, inside the **PNS**, *the transfer function of the equivalent digital interpolation delay-and-sum beamforming process after the decimation* can be expressed as

$$[H_{\text{DDS}}(e^{j\omega_x}, e^{j\omega_t})]_{\{|\omega_x, \omega_t| \leq \pi\}} = W_C \left( \frac{\omega_x - \frac{ML_I K_I \cos(\hat{\phi}_0)}{2\pi\Delta_x} M^{-1}\omega_t - \pi \cos(\hat{\phi}_0)L_I(1-K_I)}{2\pi\Delta_x} \right). \tag{4.43}$$

According to [42] (ch. 6), *the transfer function given in (4.43) corresponds to a 2D beam having uniform beamwidth* along the axis that is on the straight line

$$\omega_x = \frac{ML_I K_I \cos(\hat{\phi}_0)}{M} M^{-1}\omega_t + \pi \cos(\hat{\phi}_0)L_I(1-K_I) \tag{4.44}$$

inside the **PNS**. Note that the gradient of the axis can only take the fractional values  $\frac{\lfloor ML_I K_I \cos(\hat{\phi}_0) \rfloor}{M}$ . Therefore,  $H_{\text{DDS}}(e^{j\omega_x}, e^{j\omega_t})$  can only be directed at certain azimuth angles  $\hat{\phi}_D$  such that  $ML_I K_I \cos(\hat{\phi}_D) \in \mathbb{Z}$ . The width of the main-lobe of the beam and the side-lobe levels corresponding to  $H_{\text{DDS}}(e^{j\omega_x}, e^{j\omega_t})$  are determined by the magnitude response of the 1D window functions  $w_D(n_x)$ . Examples of normalized magnitude responses of the 1D rectangular window function and 1D Hamming window function are given in section 2.7.

#### 4.4.2 Frequency Domain Beamforming Methods for Broadband-Bandpassed Signals

In [138], several different versions of digital frequency-domain beamforming methods for direct Nyquist sampled ST PWs have been summarized and compared on the basis of the required computational complexity and memory. In these methods, the exact or an approximate of the DFT of a segment of the sampled ST PW signals has been evaluated along the an anticipated ROS, which corresponds to the anticipated DOA of the desired ST PW, in order to recover its spectral components. Hence, in digital frequency-domain broadband-bandpass beamforming of complex-quadrature sampled antenna sequences, in order to recover the spectral components of the desired BB-BP ST PW, the DFT of a segment of the sample sequence is evaluated along the anticipated ROS of the spectrum of the desired BB-BP ST PW, which has been given in (4.33) where  $d_{qx} \approx \cos(\hat{\phi}_0)$ . The exact DFT evaluation methods proposed in [138] (sec II-A), can be modified to evaluate the DFT along the anticipated ROS  $\omega_x = L_I K_I \cos(\hat{\phi}_0) \omega_t + \pi \cos(\hat{\phi}_0) L_I (1 - K_I)$  in the **PNS** such that

$$Y_{\text{FB}}(e^{j\omega_t}) = \sum_{n_t=0}^{N_t} \sum_{n_x=-N_x}^{N_x} w_D(n_x) \tilde{x}(n_x, n_t) e^{-j \cos(\hat{\phi}_0) L_I K_I \omega_t + \pi(1-K_I) n_x} e^{-j\omega_t n_t}, \quad (4.45)$$

where  $w_D(n_x)$  is the 1D discrete-domain window function, which controls the width of the mainlobe and the amplitude of the sidelobes.

The digital frequency-domain broadband-bandpass beamforming process specified in (4.45) can also be expressed as a 2D FIR filtering process. The transfer function of the digital frequency-domain broadband-bandpass beamforming 2D FIR filter inside the PNS may be given by

$$[H_{\text{FB}}(e^{j\omega_x}, e^{j\omega_t})]_{\{|\omega_x, \omega_t| \leq \pi\}} = W_C \frac{\omega_x - \cos(\hat{\phi}_0) L_I (K_I \omega_t + \pi(1 - K_I))}{2\pi \Delta_x}. \quad (4.46)$$

where the 1D-CDFT pair  $w_C(x) \xleftrightarrow{\text{1D-CDFT}} W_C(f_x)$  of the equivalent 1D continuous domain window function of  $w_D(n_x)$ . Note that the transfer function for digital interpolation delay-and-sum beamformer given in (4.43) and the transfer function of the digital frequency-

domain broadband-bandpass beamformer given in (4.46) are almost identical. For the digital frequency-domain broadband-bandpass beamformer, the axis of the 2D beam-shaped transfer function is given by

$$\omega_x = \cos(\hat{\phi}_0) L_I (K_I \omega_t + \pi(1 - K_I)). \quad (4.47)$$

However, the gradient of the axis of the transfer function of the frequency-domain broadband-bandpass beamformer can take any real value  $L_I K_I \cos(\hat{\phi}_0)$  unlike the gradient of the axis of the interpolation delay-and-sum beamformer, which can take only fractional values.

#### 4.4.3 The Sekiguchi Method; A Beamforming 2D Complex-Coefficient FIR Filter Design Method using a Combined Spectral-Transformation and Window Method

A *nearly frequency-independent* broadband-bandpass beamformer for signals received by a 1D-UDAA has been proposed by Sekiguchi et. al. in [139]. In the Sekiguchi method, a 2D FIR ST filter has been proposed to process the complex-quadrature sampled antenna signals and selectively enhance the desired signals. The transfer function of the 2D FIR filter has been achieved using the spectral-transformation method [158] (ch. 6.4) such that the *main-lobe and the side-lobe characteristics of the spatial beam-pattern are nearly independent of the temporal frequency*. Also, a window method has been employed to truncate the prohibitively high order of the direct frequency transformed 2D FIR filter.

A two-stage design process has been proposed in [139] for the design of the beamforming 2D FIR filter. At the first stage, the 2D frequency-space  $(F_x, F_t)^5$  is mapped to a 1D frequency parameter  $F$  using the 2D to 1D spectral-transform that is defined by

$$F \triangleq \frac{F_x}{(\Omega_I/f_{Ic})F_t + 1} - \Delta_x c^{-1} f_{Ic} \cos(\hat{\phi}_0). \quad (4.48)$$

Equation (4.48) can be rewritten using the usual group of parameters defined in subsec-

---

<sup>5</sup> $F_x$  and  $F_t$  are normalized spatial and temporal frequencies, respectively.



tion 4.3.2 and by substituting  $F_x = \omega_x/2\pi$  and  $F_t = \omega_t/2\pi$  such that

$$F = \frac{\omega_x - L_I \cos(\hat{\phi}_0) (K_I \omega_t + (1 - K_I)\pi)}{2 \frac{K_I \omega_t}{(1 - K_I)} + \pi}. \quad (4.49)$$

Note that if  $F = 0$ , then  $\omega_x = L_I \cos(\hat{\phi}_0) (K_I \omega_t + (1 - K_I)\pi)$ , which specifies the line segment  $PQ$  (see (4.33) in page 135), the ROS of the spectra of the complex-quadrature sampled desired signal. Also note that for non-zero  $|F| = F'$ , the contour of  $(\omega_x, \omega_t)$  that satisfies (4.49) inside the **PNS** is an asymmetric-trapezoid<sup>6</sup>. Given that the ideal 2D frequency transform function inside the **PNS** may be expressed as

$$[IT(e^{j\omega_x}, e^{j\omega_t})]_{\{|\omega_x, \omega_t| \leq \pi\}} = \frac{\omega_x - L_I \cos(\hat{\phi}_0) (K_I \omega_t + (1 - K_I)\pi)}{2 \frac{K_I \omega_t}{(1 - K_I)} + \pi}, \quad (4.50)$$

an approximate of associated 2D unit impulse response  $\tilde{it}(n_x, n_t)$  can be evaluated by taking the 2D-IDFT of sampled  $IT(2\pi m_x/M_x, 2\pi m_t/M_t)$  for  $m_x = 0, 1, \dots, M_x - 1$  and  $m_t = 0, 1, \dots, M_t - 1$ . Generally, almost all of the elements of  $\tilde{it}(n_x, n_t)$  are non-zero and if the 2D sequence of size  $(M_x \times M_t)$  employed directly in the following filter design process it would have led to an extremely high order 2D FIR filter. Therefore in [139],  $\tilde{it}(n_x, n_t)$  is truncated by a 2D window function  $win_{2D}(n_x, n_t)$  (see section 2.7.1) of size  $(2N_x + 1) \times (2N_t + 1)$  such that

$$\tilde{at}(n_x, n_t) = win_{2D}(n_x, n_t) \tilde{it}(n_x, n_t). \quad (4.51)$$

According to [139], the 2D rectangular window has been deemed unsuitable for the truncation process. Usually the window sizes for  $win_{2D}(n_x, n_t)$  in (4.51) are restricted to  $N_x = 1, 2, 3$  and  $N_t = 2, 3, 4$ . The transform function  $AT(e^{j\omega_x}, e^{j\omega_t})$  that corresponds to  $\tilde{at}(n_x, n_t)$  can be evaluated by taking its 2D-DDFT. Finally,  $\tilde{at}(n_x, n_t)$  is scaled by the scaling factors  $c_1 \triangleq 2/(T_{\max} - T_{\min})$  and  $c_2 \triangleq c_1 T_{\max} - 1$  such that

$$\tilde{ct}(n_x, n_t) = \begin{cases} c_1 \tilde{at}(0, 0) - c_2; & (n_x, n_t) = (0, 0) \\ c_1 \tilde{at}(n_x, n_t); & (n_x, n_t) \neq (0, 0). \end{cases} \quad (4.52)$$

---

<sup>6</sup>Note that the trapezoid-shaped passband specified in (4.49) is different than the trapezoid-shaped passband that corresponds to the ideal frequency invariant beam pattern proposed in section 4.5.

With this scaling, the range of scaled transform function  $CT(e^{j\omega_x}, e^{j\omega_t})$  has been limited to  $(-1, 1)$  as in the case of sinusoids.

In the second stage, the McClellan-transform [159] has been used to evaluate the corresponding transfer function  $H_{\text{SKG}}(e^{j\omega_x}, e^{j\omega_t})$ . However, first, a *zero-phase prototype 1D FIR filter* [66] (pp. 641) has to be designed. The passband of the prototype filter determines the selectivity of the beamformer and the passband ripple and stopband attenuation of the prototype filter determine the distortions of the desired signal and the interference from the co-channel interfering signals, respectively. Given the coefficients of the 1D prototype filter of order  $2N$  are  $p(n)$ ;  $n = -N, \dots, -1, 0, 1, \dots, N$ , the frequency response of the beamforming 2D FIR filter is given by

$$H_{\text{SKG}}(e^{j\omega_x}, e^{j\omega_t}) = p(0) + \sum_{n=-N}^N p(n) T_n \quad CT(e^{j\omega_x}, e^{j\omega_t}) \quad , \quad (4.53)$$

where  $T_n(\cdot)$  is the  $n^{\text{th}}$ -order *Chebyshev polynomial of the first kind* that can be expressed with the recursive relationship given in [44] (pp. 210). Next the 2D-IDFT of evaluated for the 2D sample sequence  $H_{\text{SKG}}(e^{j2\pi m_x/M_x}, e^{j2\pi m_t/M_t})$  for  $m_x = 0, 1, \dots, M'_x - 1$  and  $m_t = 0, 1, \dots, M'_t - 1$  that yields  $\tilde{h}_{\text{SKG}}(n_x, n_t)$ . Finally, a 2D window function  $\text{win}_{2\text{D}}(n_x, n_t)$  of size  $(2N_x + 1, N_t)$  has been used to truncate  $\tilde{h}_{\text{SKG}}(n_x, n_t)$  such that

$$\tilde{h}_{\text{SKG}}(n_x, n_t) = \text{win}_{2\text{D}}(n_x, n_t) \tilde{h}l(n_x, n_t). \quad (4.54)$$

The simulation results shown in [139] confirm that the proposed method can achieve lower distortion in the passband. However, for the adaptive beamforming as required in the CR systems, instantaneous determination of several key design parameters such as prototype 1D FIR trapezoidal filter and window sizes requires highly sophisticated design process that may take up to several seconds to evaluate all the beamformer coefficients.

## 4.5 The Beamforming Complex-Coefficient 2D FIR Trapezoidal Filter

The main objective of the beamformer to be used in the CR system is to process the complex-quadrature sampled antenna signals in order to recover the desired 1D temporally baseband user data signals transmitted by subscriber modules by selectively enhancing EM waves on the basis of DOAs in the presence of severe co-channel interference and receiver noise. Further, this beamforming method should be able to adapt instantaneously following the changes in the operational frequency-band in terms of the bandwidth and the center-frequency and facilitate the real-time tracking of desired signals associated with the gradually time varying DOAs due to the movement of the subscriber modules.

Reconsider the typical scenario of subscriber module distribution for a CR system shown in Figure 4.3 (see page 128), where the 1D-UDAA receives the EM waves transmitted by  $Q_T + 1$  different subscriber modules that are distributed around the geographical area. However, due to the directional nature of the active element pattern shown in Figure 4.3, only the EM waves corresponding to azimuth angles in the range  $\phi_q \in [30^\circ, 150^\circ]$  for  $q = 0, 1, \dots, Q_D$ , are effectively received by this particular 1D-UDAA. In order to distinguish the different groups of subscriber modules distributed in the geographical area, the CR system estimates the azimuth angle  $\hat{\phi}_q$  that corresponds to the DOA of the EM waves transmitted by each of the subscriber modules.

According to analysis of the spectral properties of the complex-quadrature sampled antenna signals given in subsection 4.3.4, inside the **PNS**, the ROS of the spectrum of a space-times sampled EM wave transmitted by a desired subscriber module is given by (4.33) and shown by the lines-segment  $PQ$  in Figure 4.4. Also, it has been derived that the range of the ROSs of the space-times sampled EM waves having DOAs specified by the inclination angles  $\theta_p \approx 90^\circ$  and the azimuth angle in the range  $\phi_q \in [0^\circ, 180^\circ]$  is given by the shaded trapezoidal-shaped area denoted by 1234 in Figure 4.4. The spectra

of the desired subscriber signals and co-channel interfering signals occupy the area 1234 where the spectral-density of receiver noise occupy the entire **PNS**. In order to selectively enhance the spectral components of the desired subscriber signal and to minimize the interference caused by other co-channel EM waves having different DOAs, the transfer function of the beamformer must *closely enclose*  $PQ$ , the ROS of the desired spectrum.

In the following, first, the beam-shaped transfer functions of previously proposed methods [101][138] are briefly discussed highlighting the limitations of these methods. Next, the ideal transfer function that yields the minimum distortion of the desired subscriber signals associated with time varying DOAs is proposed.

#### 4.5.1 The Ideal Transfer Function for the Beamforming of Complex-Quadrature Sampled 1D-UDAA Signals

##### **The Ideal 2D Uniform Bandwidth Beam-Shaped Transfer Function**

First, let's consider the ideal 2D beam-shaped transfer function  $IH_{\text{BEAM}}(e^{j\omega_x}, e^{j\omega_t})$  having a uniform bandwidth as shown by the region  $STUV$  inside the **PNS** in Figure 4.6. Note that ideally  $|IH_{\text{BEAM}}(e^{j\omega_x}, e^{j\omega_t})| = 1$  inside  $STUV$  and  $|IH_{\text{BEAM}}(e^{j\omega_x}, e^{j\omega_t})| = 0$  elsewhere in the **PNS** in  $(\omega_x, \omega_t) \in \mathbb{R}^2$ . Given that  $PQ$ , the ROS of  $D_0(e^{j\omega_x}, e^{j\omega_t})$ , is perfectly aligned with the axis of  $STUV$  as shown Figure 4.6 (left), the axis of the ideal 2D beam-shaped transfer function is given by (4.33). Therefore, the four parameters, namely the instantaneous bandwidth spread factor  $K_I$ , the instantaneous system utilization factor  $L_I$ , the shift-angle  $\alpha = \tan^{-1}(\cos(\phi_0))$  and the uniform bandwidth  $\Delta$ , determine the orientation of  $STUV$  in the **PNS**.

In practice, the exact azimuth angle  $\phi_0$  of the desired subscriber module signal is not precisely known at the CR system. Nevertheless, if the subscriber module moves, then  $\phi_0$  may change during the transmission period. Hence, due to the difference between the actual DOA and anticipated DOA of the desired signal, there may be a small deviation between the axis of the ideal transfer function  $IH_{\text{BEAM}}(e^{j\omega_x}, e^{j\omega_t})$  and  $PQ$ , the ROS

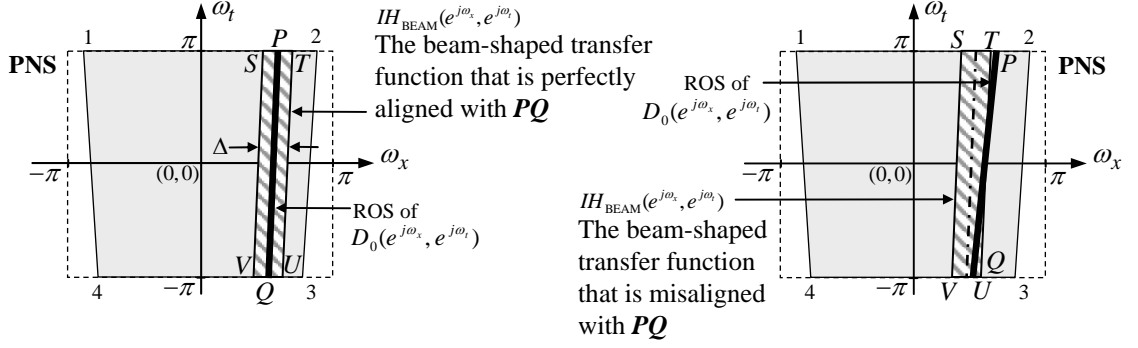


Figure 4.6: The ROS of the spectrum  $D_0(e^{j\omega_x}, e^{j\omega_t})$  inside of **PNS**, which is denoted by  $PQ$ , and the ideal beam-shaped transfer function  $IH_{\text{BEAM}}(e^{j\omega_x}, e^{j\omega_t})$ . Instances where the axis of  $IH_{\text{BEAM}}(e^{j\omega_x}, e^{j\omega_t})$  and  $PQ$  are perfectly aligned (left) and misaligned (right).

of the spectrum of desired signal as shown in Figure 4.6 (right). If the misalignment between the axis of  $IH_{\text{BEAM}}(e^{j\omega_x}, e^{j\omega_t})$  and  $PQ$  is sufficiently large, then parts of  $PQ$  may fall outside the  $STUV$  region as shown in Figure 4.6 (right). This may suppress the spectral components of the desired signals that lay outside of  $STUV$  and may cause severe distortion in the final output. As a remedy, the uniform bandwidth  $\Delta$  can be increased to reduce the chance of such misalignment distortions but, wider bandwidths allow more spectral components of co-channel interfering signals and receiver noise to contaminate the spectral components of the desired signals that ultimately degrades the signal to noise and interference ratio (SNIR) of the user data sequence.

The non-ideal 2D beam-shaped transfer functions corresponding to the digital interpolation delay-and-sum beamformer  $H_{\text{DS}}(e^{j\omega_x}, e^{j\omega_t})$  and the digital frequency domain beamformer  $H_{\text{FB}}(e^{j\omega_x}, e^{j\omega_t})$ , which have been introduced in subsections 4.4.1 and 4.4.2, are also susceptible to the distortions of the desired signal due to the misalignment of the axis of the 2D beam-shaped transfer functions and the actual ROS of the desired signal. Between the transfer functions  $H_{\text{DS}}(e^{j\omega_x}, e^{j\omega_t})$  and  $H_{\text{FB}}(e^{j\omega_x}, e^{j\omega_t})$ , the distortion of the desired signal can be even higher for  $H_{\text{DS}}(e^{j\omega_x}, e^{j\omega_t})$  because it can only be directed at certain azimuth angles  $\hat{\phi}_D$ . Further, variations of the magnitude responses  $|H_{\text{DS}}(e^{j\omega_x}, e^{j\omega_t})|$

and  $|H_{\text{FB}}(e^{j\omega_x}, e^{j\omega_t})|$ , within the main-lobe may also contribute to the distortion of the desired signal. Also, the non zero magnitude responses  $|H_{\text{DS}}(e^{j\omega_x}, e^{j\omega_t})|$  and  $|H_{\text{FB}}(e^{j\omega_x}, e^{j\omega_t})|$  outside the main-lobe may cause the energy of the co-channel interfering signals that are having ROSs outside the main-lobe to leak in to the output. However, with the choice of the 1D window function  $w_{\text{D}}(n_x)$ , the suppression of co-channel interfering signals can be controlled at the expense of the selectivity.

### The Ideal 2D Asymmetric Trapezoid-Shaped Transfer Function

Let's assume that in estimating the azimuth angles  $\phi_q$ ;  $q = 1, \dots, Q$  of the EM waves transmitted by  $Q$  subscriber modules, the experimental process [45] employed by the CR system considered here is associated with an uncertainty  $\Delta\phi$ . This implies that  $\phi_q$ , the actual azimuth angle of the  $q^{\text{th}}$  EM wave lies in the range  $[\hat{\phi}_q - \Delta\phi, \hat{\phi}_q + \Delta\phi]$ . Therefore, the ROS of the spectra  $D_0(e^{j\omega_x}, e^{j\omega_t})$ , of complex-quadrature sampled antenna signals that corresponds to the EM wave transmitted by  $0^{\text{th}}$  subscriber module, lies inside the *2D asymmetric trapezoidal region ABCD* shown in Figure 4.7, which is bounded by the straight lines

$$\begin{aligned} AD \rightarrow \omega_x &= L_{\text{I}}(K_{\text{I}}\omega_t + (1 - K_{\text{I}})\pi) \cos(\hat{\phi}_0 + \Delta\phi), \\ BC \rightarrow \omega_x &= L_{\text{I}}(K_{\text{I}}\omega_t + (1 - K_{\text{I}})\pi) \cos(\hat{\phi}_0 - \Delta\phi), \end{aligned} \quad (4.55)$$

inside the **PNS**  $|\omega_x; \omega_t| \leq \pi$ . Therefore, the *ideal transfer function*  $IH_{\text{TRAP}}(e^{j\omega_x}, e^{j\omega_t})$  of the *frequency-invariant beamformer* is proposed such that the ideal magnitude response  $|IH_{\text{TRAP}}(e^{j\omega_x}, e^{j\omega_t})| = 1$  inside *ABCD* and  $|IH_{\text{TRAP}}(e^{j\omega_x}, e^{j\omega_t})| = 0$  elsewhere in the **PNS**. According to (4.55), the four parameters, namely the instantaneous bandwidth spread factor  $K_{\text{I}}$ , the instantaneous system utilization factor  $L_{\text{I}}$ , the estimated azimuth angle  $\hat{\phi}_0$  and the uncertainty in azimuth angle estimation  $\Delta\phi$ , determine the orientation of *ABCD* in the **PNS**. Note that irrespective of small estimation errors between  $\hat{\phi}_0$  and  $\phi_0$ , *PQ*, the ROS of the desired spectra  $D_0(e^{j\omega_x}, e^{j\omega_t})$ , remains inside of the ideal trapezoidal shaped region *ABCD* as shown in Figure 4.7 (right). Ideally, the beamformer

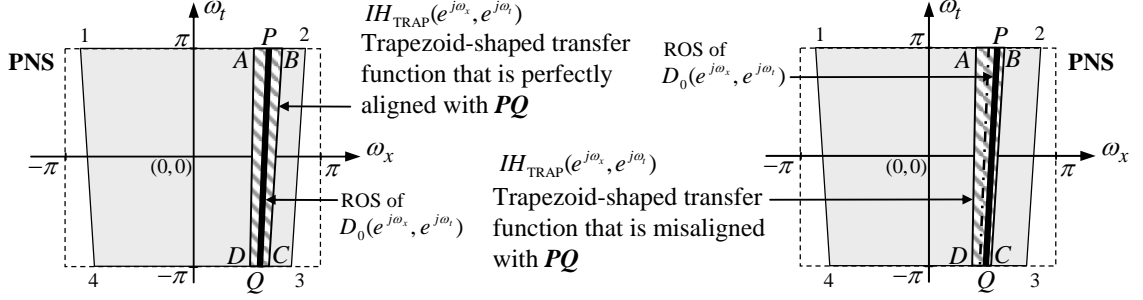


Figure 4.7: The ROS of the spectrum  $D_0(e^{j\omega_x}, e^{j\omega_t})$  inside of **PNS**, which is denoted by  $PQ$ , and the ideal trapezoid-shaped transfer function  $IH_{\text{TRAP}}(e^{j\omega_x}, e^{j\omega_t})$ . Instances where the axis of  $IH_{\text{TRAP}}(e^{j\omega_x}, e^{j\omega_t})$  and  $PQ$  are perfectly aligned (left) and misaligned (right).

having the transfer function  $IH_{\text{TRAP}}(e^{j\omega_x}, e^{j\omega_t})$  can suppress all the co-channel interfering signals provided that the ROSs of the spectra of the co-channel interfering EM waves lie outside  $ABCD$ .

As mentioned in subsection 4.4.3, the beamforming 2D FIR filter proposed by Sekiguchi et. al. in [139] also has an asymmetric trapezoid-shaped passband. However inside the **PNS**, the trapezoidal contour of  $(\omega_x, \omega_t)$  that satisfies (4.49) is different from the trapezoid specified in (4.55). Hence, for some values of  $\phi_q$  and  $\hat{\phi}_q$ , parts of  $PQ$ , the ROS of  $D_0(e^{j\omega_x}, e^{j\omega_t})$ , may fall outside of the 2D trapezoid-shaped passband of  $H_{\text{SKG}}(e^{j\omega_x}, e^{j\omega_t})$ , which has been proposed in [139]. This may lead to distortion of the desired signal at the output of the beamformer.

#### 4.5.2 Approximation of the Complex-Coefficient 2D FIR Filter with a Trapezoidal-Shaped Passband

Because of the inherent stability and linear phase property of MD FIR filters [42][158], here, a transfer function associated with a 2D FIR filter-structure has been selected to approximate the proposed asymmetrical-trapezoidal-shaped passband that has been specified in (4.55). In the following, a 2D window-based method [42][44][158] has been employed to derive algebraic closed-form expressions for the coefficients of the beamform-

ing 2D FIR trapezoidal filter as functions of the parameters  $K_I$ ,  $L_I$ ,  $\hat{\phi}_0$  and  $\Delta\phi$ .

As specified in subsection 4.5.1, the ideal magnitude response  $|IH(e^{j\omega_x}, e^{j\omega_t})|$ , which corresponds to the 2D transfer function  $IH(z_x, z_t)$ , equals unity inside the passband area given by  $ABCD$  in Figure 4.7 and zero elsewhere inside the **PNS**  $|\omega_x; \omega_t| \leq \pi$ . The ideal phase response is  $\angle [IH(e^{j\omega_x}, e^{j\omega_t})] = 0$  inside the **PNS**. According to these specifications and given the boundaries of the asymmetric-trapezoidal-shaped passband  $ABCD$  are specified in (4.55), the ideal infinite-extent complex-valued 2D unit impulse response  $\tilde{h}(n_x, n_t)$  of the ideal beamforming 2D FIR trapezoidal filter  $IH(z_x, z_t)$  may be evaluated following the definition of the inverse 2D discrete domain Fourier transform (2D-IDDF) [42] (pp. 29-31) such that

$$\tilde{h}(n_x, n_t) = \frac{1}{(2\pi)^2} \int_{\omega_t=-\pi}^{+\pi} \int_{\omega_x=L^-(\omega_t)}^{L^+(\omega_t)} 1 e^{j\omega_x n_x} e^{j\omega_t n_t} d\omega_x d\omega_t, \quad (4.56)$$

for  $(n_x, n_t) \in \mathbb{Z}^2$ , where the limits are defined as

$$\begin{aligned} L^+(\omega_t) &\triangleq L_I(K_I\omega_t + (1 - K_I)\pi) \cos(\hat{\phi}_0 - \Delta\phi) \quad \text{and} \\ L^-(\omega_t) &\triangleq L_I(K_I\omega_t + (1 - K_I)\pi) \cos(\hat{\phi}_0 + \Delta\phi). \end{aligned}$$

Evaluating (4.56) yields a *closed-form algebraic function*  $\tilde{h}(n_x, n_t)$  of parameters  $K_I$ ,  $L_I$ ,  $\hat{\phi}_0$  and  $\Delta\phi$ . However for brevity, the detailed derivation of  $\tilde{h}(n_x, n_t)$  is omitted here. For all  $(n_x, n_t) \in \mathbb{Z}^2$ ,  $\tilde{h}(n_x, n_t)$  is given by the following expressions where  $a \triangleq \cos(\hat{\phi}_0 + \Delta\phi)$  and  $b \triangleq \cos(\hat{\phi}_0 - \Delta\phi)$ .

For the most general case where  $n_x = 0$ ,  $(aL_I K_I n_x + n_t) = 0$  and  $(bL_I K_I n_x + n_t) = 0$

$$\tilde{h}(n_x, n_t) = \frac{\sin(\pi(bL_I K_I n_x + n_t)) e^{j\pi L_I(1-K_I)bn_x}}{j2\pi^2 n_x (bL_I K_I n_x + n_t)} - \frac{\sin(\pi(aL_I K_I n_x + n_t)) e^{j\pi L_I(1-K_I)an_x}}{j2\pi^2 n_x (aL_I K_I n_x + n_t)}. \quad (1.57(a))$$

### The special cases

For  $n_x = 0$ ,  $n_t = 0$ ,

$$\tilde{h}(0, 0) = \frac{L_I(1 - K_I)(b - a)}{2}. \quad (1.57(b))$$



For  $n_x = 0, n_t = 0$ ,

$$\tilde{h}(0, n_t) = \frac{(-1)^{n_t} L_I K_I (b - a)}{j 2 \pi n_t}. \quad (1.57(c))$$

For  $n_x = 0, (a L_I K_I n_x + n_t) = 0$  and  $(b L_I K_I n_x + n_t) = 0$

$$\tilde{h}(n_x, n_t) = \frac{\sin(\pi (b L_I K_I n_x + n_t)) e^{j \pi L_I (1 - K_I) b n_x}}{j 2 \pi^2 n_x (b L_I K_I n_x + n_t)} - \frac{e^{j \pi L_I (1 - K_I) a n_x}}{j 2 \pi^2 n_x}. \quad (1.57(d))$$

For  $n_x = 0, (a L_I K_I n_x + n_t) = 0$  and  $(b L_I K_I n_x + n_t) = 0$

$$\tilde{h}(n_x, n_t) = \frac{e^{j \pi L_I (1 - K_I) b n_x}}{j 2 \pi^2 n_x} - \frac{\sin(\pi (a L_I K_I n_x + n_t)) e^{j \pi L_I (1 - K_I) a n_x}}{j 2 \pi^2 n_x (a L_I K_I n_x + n_t)}. \quad (1.57(e))$$

For  $n_x = 0, (a L_I K_I n_x + n_t) = 0$  and  $(b L_I K_I n_x + n_t) = 0$

$$\tilde{h}(n_x, n_t) = \frac{e^{j \pi L_I (1 - K_I) b n_x} - e^{j \pi L_I (1 - K_I) a n_x}}{j 2 \pi^2 n_x}. \quad (1.57(f))$$

Because  $\tilde{h}(n_x, n_t)$  extends infinitely in both the spatial and temporal dimensions and is non-causal in the temporal dimension, ideally  $\tilde{h}(n_x, n_t)$  cannot be realized using a 2D ST FIR filter structure. Therefore, a 2D windowed [42] temporally-causal 2D unit impulse response has been defined such that

$$\tilde{g}(n_x, n_t + N_t) \triangleq \text{win}_{2D}(n_x, n_t) \tilde{h}(n_x, n_t), \quad (4.58)$$

where the 2D window function  $\text{win}_{2D}(n_x, n_t) = 0$  for  $|n_x| > N_x$  and  $|n_t| > N_t$ . In (4.58), the 2D impulse response  $\tilde{g}(n_x, n_t)$  of size  $(2N_x + 1) \times (2N_t + 1)$  corresponds to the beamforming 2D FIR trapezoidal filter  $G(z_x, z_t)$  of order  $(2N_x \times 2N_t)$ . For the subsequent beamforming 2D FIR trapezoidal filter designs, a 2D Hamming window  $\text{ham}_{2D}(n_x, n_t)$  of size  $((2N_x + 1) \times (2N_t + 1))$  has been assumed. As given in section 2.7,  $\text{ham}_{2D}(n_x, n_t)$  corresponds to two cascading 1D Hamming window functions  $\text{ham}_D(n_x)$  of length  $(2N_x + 1)$  and  $\text{ham}_D(n_t)$  of length  $(2N_t + 1)$  such that  $\text{ham}_{2D}(n_x, n_t) = \text{ham}_D(n_x) \text{ham}_D(n_t)$ .

In order to change the shape and orientation of the passband of  $G(z_x, z_t)$  with instantaneously selected frequency band and the sampling rate of the CR system, specified by

$L_I$  and  $K_I$ , as well as to track and enhance the desired signals with time varying DOA, specified by  $\hat{\phi}_0$  and  $\Delta\phi$ , the complex valued filter coefficients  $\tilde{g}(n_x, n_t)$  can be calculated instantaneously using the closed form expressions given in equations (1.57(a)) - (1.57(f)) multiplied by the 2D window function as given in (4.58) [44].

#### 4.5.3 A Design Example of a Complex-Coefficient 2D FIR Trapezoidal Filter

Let the beamforming complex-coefficient 2D FIR trapezoidal filter  $G(z_x, z_t)$  of order  $(40 \times 32)$  be required to meet the specifications  $\hat{\phi}_0 = 70^\circ$ ,  $\Delta\phi = 4^\circ$ ,  $K_I = 0.1$  and  $L_I = 0.9$ . The corresponding unit impulse response  $\tilde{g}(n_x, n_t)$  is evaluated from (4.58) using the closed-form expressions given in equations (1.57(a)) - (1.57(f)). A simple computer program implemented in MATLAB<sup>®</sup>, takes around 0.125 s to evaluate the 1353 coefficients of  $\tilde{g}(n_x, n_t)$  using a Dell XPS-600 computer equipped with an Intel Pentium-IV (clock speed 3.4 GHz) CPU and 2 GB of RAM.

The properties of the frequency response  $G(e^{j\omega_x}, e^{j\omega_t})$  of the beamforming complex-coefficient 2D FIR trapezoidal filter  $G(z_x, z_t)$  are shown in Figure 4.8. The resultant magnitude-frequency response  $|G(e^{j\omega_x}, e^{j\omega_t})|$  is shown by the 3D surface plot of in Figure 4.8(a), which specifies the selectivity of the beamformer. The -3 dB and -50 dB contours of  $|G(e^{j\omega_x}, e^{j\omega_t})|$  and the ideal trapezoidal passband boundary  $ABCD$ , specified in (4.55), are shown in Figure 4.8(b). As shown there, the -3 dB contour closely approximates the ideal passband boundary  $ABCD$ .

The typical cross-sectional magnitude response and cross-sectional phase (wrapped) response taken along the passband of  $G(e^{j\omega_x}, e^{j\omega_t})$  (for the slanted cross-sectional plane shown in Figure 4.8(b)) and projected onto the  $\omega_t$ -axis are shown in Figure 4.8(c) and Figure 4.8(e), respectively. Similarly, a typical cross-sectional magnitude response and a cross-sectional phase response, taken across the passband of (horizontal cross-sectional plane shown in Figure 4.8(b)) and projected onto the  $\omega_x$ -axis, are shown in Figure 4.8(d) and Figure 4.8(f), respectively. According to the cross-sectional magnitude response

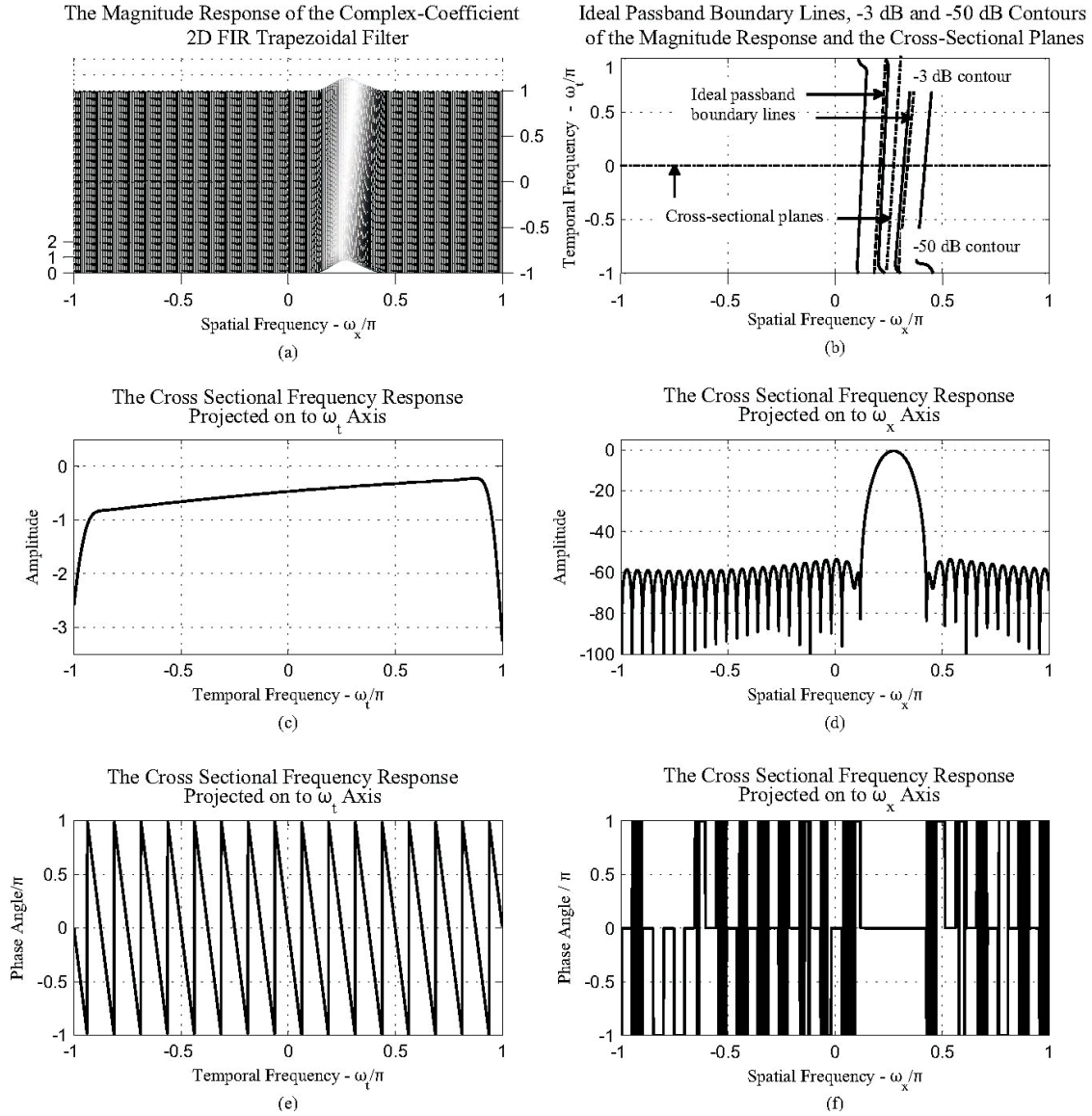


Figure 4.8: The properties of the 2D FIR trapezoidal filter of order  $(40 \times 32)$  designed to meet the specifications  $\hat{\phi}_0 = 70^\circ$ ,  $\Delta\theta = 4^\circ$ ,  $K_I = 0.1$  and  $L_I = 0.9$ . The normalized magnitude-frequency response  $|G(e^{j\omega_x}, e^{j\omega_t})|$  (a). The boundary lines the ideal trapezoidal passband, -3 dB and -50 dB contours of  $|G(e^{j\omega_x}, e^{j\omega_t})|$  and the cross-sectional planes taken along and across the passband (b). The cross-sectional magnitude (c) and phase (wrapped) (e) responses taken along the trapezoidal shaped passband. The cross-sectional magnitude (d) and phase (wrapped) (f) responses taken across the trapezoidal shaped passband.

shown in Figure 4.8(c) and the contour plots shown in Figure 4.8(b), the passband magnitude error is less than 0.5 dB within the central 90% of the operational temporal bandwidth and less than 1 dB within the central 95% of the operational temporal bandwidth, respectively. This implies that the proposed 2D FIR trapezoidal filter beamformer has a frequency-invariant beam-pattern over more than 90% of the temporal bandwidth. By observing many such cross-sectional magnitude responses (e. g. Figure 4.8(c) and Figure 4.8(d)) and cross-sectional phase (wrapped) responses (e. g. Figure 4.8(e) and Figure 4.8(f)), it has been confirmed that the frequency response inside the passband of is indeed of unity magnitude and given by

$$G(e^{j\omega_x}, e^{j\omega_t}) \simeq 1 e^{-j\omega_t N_t} \quad (4.59)$$

According to Figure 4.8(d), the average attenuation level in the stopband of  $G(z_x, z_t)$  is around 60 dB.

The average stopband gains and the compensated passband ripples of a series beamforming 2D FIR trapezoidal filters  $G(z_x, z_t)$  of order  $(40 \times 32)$ , which has been designed to be directed at a series of azimuth angles  $\hat{\phi}_0 \in [30^\circ, 150^\circ]$  for different angular widths  $\Delta\phi \in \{3^\circ, 3.25^\circ, 3.5^\circ, 4^\circ, 4.5^\circ, 5^\circ, 5.5^\circ, 6^\circ, 6.5^\circ\}$  for the temporal frequency band of operation FB01 that corresponds to  $K_I = 0.1$  and  $L_I = 1.0$ , are shown in Figure 4.9 and Figure 4.10, respectively. Here, in evaluating the compensated passband ripple, the passband is approximated with a first order polynomial of temporal frequency  $\omega_t$  for a 90% spectral occupancy. Also, the average stopband gains and the compensated passband ripples of a series beamforming 2D FIR trapezoidal filters  $G(z_x, z_t)$  of order  $(40 \times 32)$ , which has been designed to be directed at a series of azimuth angles  $\hat{\phi}_0 \in [30^\circ, 150^\circ]$  for different angular widths  $\Delta\phi \in \{4^\circ, 4.25^\circ, 4.5^\circ, 5^\circ, 5.5^\circ, 6^\circ, 6.5^\circ, 7^\circ, 7.5^\circ, 8^\circ\}$  for the temporal frequency band of operation FB01 that corresponds to  $K_I = 0.125$  and  $L_I = 0.8$ , are shown in Figure 4.11 and Figure 4.12, respectively.

Note that Figures 4.9 and 4.11, the stopband attenuation of the beamformers max-

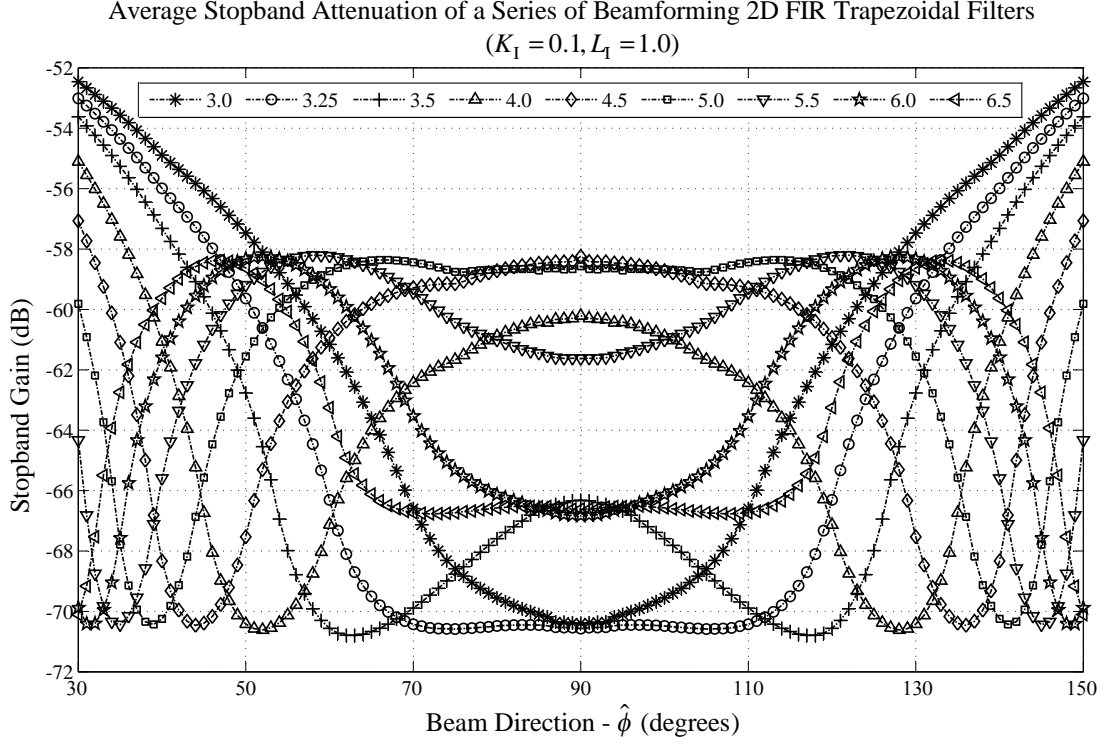


Figure 4.9: The average stopband gains of the series of beamforming 2D FIR trapezoidal filters of order  $(40 \times 32)$  for the operational temporal frequency band FB01 (i.e.  $K_I = 0.1$  and  $L_I = 1.0$ ). This series of beamforming 2D FIR trapezoidal filters are designed to be directed at  $\hat{\phi}_0 \in [30^\circ, 150^\circ]$  for  $\Delta\phi \in \{3^\circ, 3.25^\circ, 3.5^\circ, 4^\circ, 4.5^\circ, 5^\circ, 5.5^\circ, 6^\circ, 6.5^\circ\}$ .

imizes for a given angular range  $\Delta\phi$  at certain beam direction  $\hat{\phi}$ . For example, for the beam directions  $\hat{\phi}_0 \in [70^\circ, 110^\circ]$ , the maximum stopband attenuations are achieved for  $\Delta\phi = 3.25^\circ$ , in FB01 and for  $\Delta\phi = 4.25^\circ$ , in FB02. It was observed in Figures 4.9 and 4.11, for the beams directed at  $\hat{\phi} \in [30^\circ, 70^\circ]$  and  $\hat{\phi} \in [110^\circ, 150^\circ]$ , higher stopband attenuation may be achieved at the expense of selectivity by increasing the angular widths. Also note that, considerably lower passband ripples are observed for wider angular ranges (e.g.  $\Delta\phi = 60^\circ, 6.5^\circ$  for FB02 and  $\Delta\phi = 7.5^\circ, 8^\circ$  for FB02) for beam direction  $\hat{\phi} \in [80^\circ, 100^\circ]$  as shown in Figures 4.12 and 4.12. However according to Figures 4.9 and 4.11, for the particular beam directions  $\hat{\phi} \in [80^\circ, 100^\circ]$  and angular widths, the stopband attenuations are relatively high.

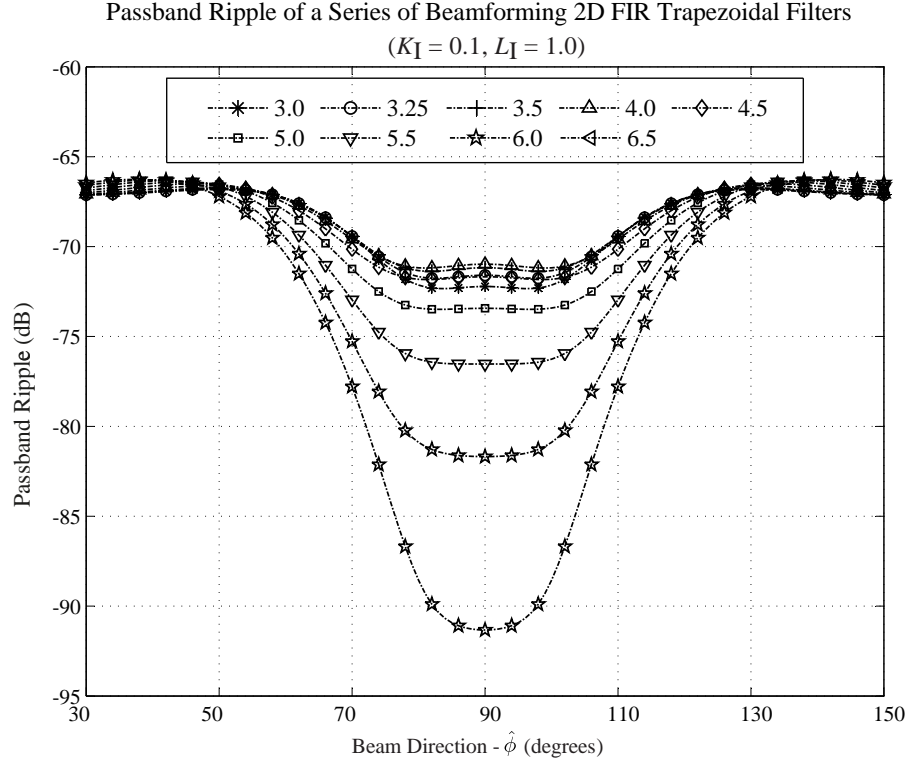


Figure 4.10: The compensated passband ripple of the series of beamforming 2D FIR trapezoidal filters of order  $(40 \times 32)$  for the operational temporal frequency band FB01 (i.e.  $K_I = 0.1$  and  $L_I = 1.0$ ). This series of beamforming 2D FIR trapezoidal filters are designed to be directed at  $\hat{\phi}_0 \in [30^\circ, 150^\circ]$  for  $\Delta\phi \in \{3^\circ, 3.25^\circ, 3.5^\circ, 4^\circ, 4.5^\circ, 5^\circ, 5.5^\circ, 6^\circ, 6.5^\circ\}$ .

#### 4.5.4 The Output Sequence of the Beamformer; An Analysis

As shown in Figure 4.1 and Figure 4.13 the output of the beamforming complex-coefficient 2D FIR trapezoidal filter is a 1D complex-valued sequence. An analysis of the temporal and spectral properties of the 1D sequence is given in the following. The 1D output sequence of the proposed beamformer is given by  $\tilde{y}(0, n_t)$ , where

$$\tilde{y}(n_x, n_t) = \tilde{x}(n_x, n_t) ** \tilde{g}(n_x, n_t), \quad (4.60)$$

and where  $\tilde{x}(n_x, n_t)$  is the 2D complex-quadrature sampled antenna signals, which is given in (4.15), and  $\tilde{g}(n_x, n_t)$  is the filter-coefficients of the 2D FIR trapezoidal filter of order  $(2N_x + 1) \times (2N_t + 1)$ , which is given in (4.58). (Note that  $**$  denotes 2D

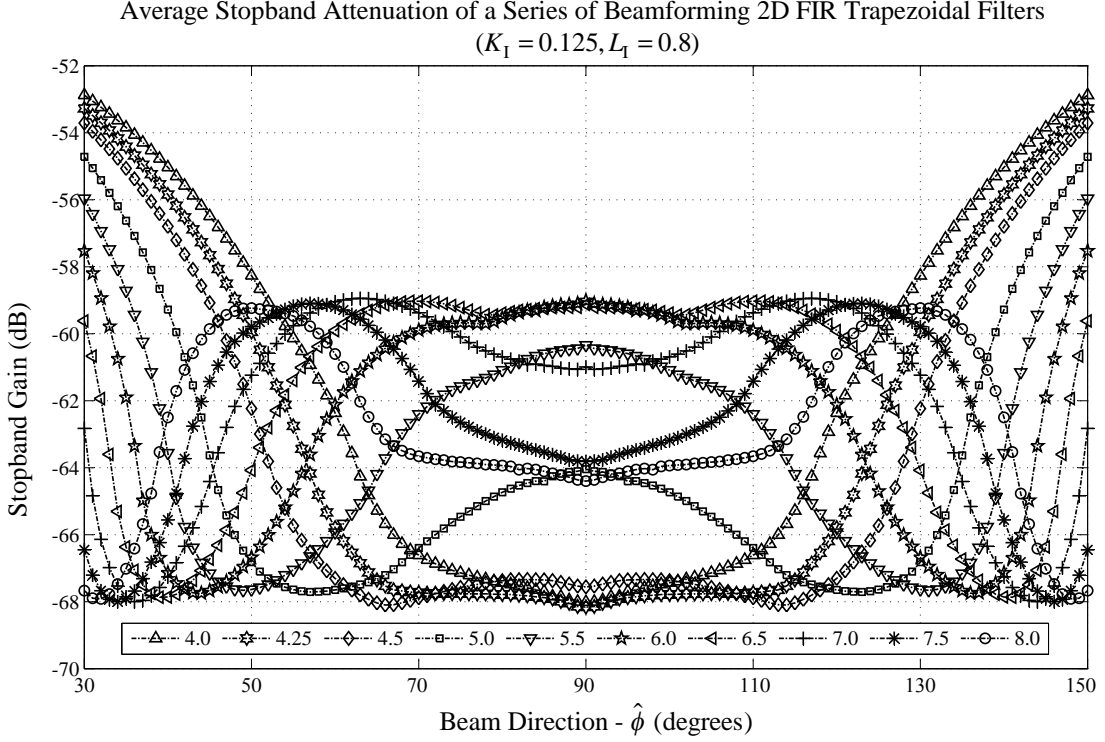


Figure 4.11: The average stopband gains of the series of beamforming 2D FIR trapezoidal filters of order  $(40 \times 32)$  for the operational temporal frequency band FB01 (i.e.  $K_I = 0.125$  and  $L_I = 0.8$ ). This series of beamforming 2D FIR trapezoidal filters are designed to be directed at  $\hat{\phi}_0 \in [30^\circ, 150^\circ]$  for  $\Delta\phi \in \{4^\circ, 4.25^\circ, 4.5^\circ, 5^\circ, 5.5^\circ, 6^\circ, 6.5^\circ, 7^\circ, 7.5^\circ, 8^\circ\}$ .

convolution.) Taking the 2D-DDFT of both sides yields,

$$Y(e^{j\omega_x}, e^{j\omega_t}) = X(e^{j\omega_x}, e^{j\omega_t}) G(e^{j\omega_x}, e^{j\omega_t}). \quad (4.61)$$

According to (4.15) and (4.16),

$$X(e^{j\omega_x}, e^{j\omega_t}) = \sum_{q=0}^Q D_q(e^{j\omega_x}, e^{j\omega_t}) + Z(e^{j\omega_x}, e^{j\omega_t}), \quad (4.62)$$

where the 2D-DDFT pair for the complex-quadrature sampled antenna signals corresponding to  $q^{\text{th}}$ -subscriber module and its spectrum is given by  $\tilde{d}_q(n_x, n_t) \xleftrightarrow{2\text{D-DDFT}} D_q(e^{j\omega_x}, e^{j\omega_t})$ . Note that  $Z(e^{j\omega_x}, e^{j\omega_t})$  represents the instantaneous spectrum of 2D sequence corresponding to sampled receiver noise. If only the ROS of the desired spectrum  $D_0(e^{j\omega_x}, e^{j\omega_t})$ , is inside the passband of  $G(z_x, z_t)$ , according to (4.35) the spectral com-

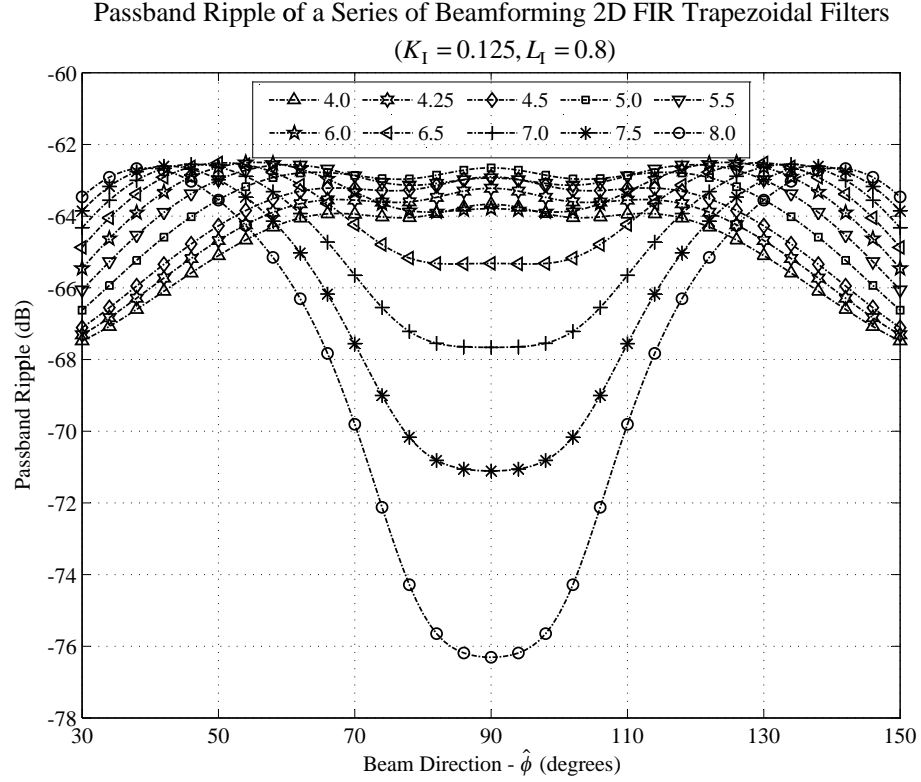


Figure 4.12: The compensated passband ripple of the series of beamforming 2D FIR trapezoidal filters of order  $(40 \times 32)$  for the operational temporal frequency band FB01 (i.e.  $K_I = 0.125$  and  $L_I = 0.8$ ). This series of beamforming 2D FIR trapezoidal filters are designed to be directed at  $\hat{\phi}_0 \in [30^\circ, 150^\circ]$  for  $\Delta\phi \in \{4^\circ, 4.25^\circ, 4.5^\circ, 5^\circ, 5.5^\circ, 6^\circ, 6.5^\circ, 7^\circ, 7.5^\circ, 8^\circ\}$ .

ponents of  $Y(e^{j\omega_x}, e^{j\omega_t})$  inside **PNS** are given by

$$\begin{aligned}
 Y(e^{j\omega_x}, e^{j\omega_t})_{\{|\omega_x, \omega_t| \leq \pi\}} &\cong \frac{G(e^{j\omega_x}, e^{j\omega_t})}{\Delta_x \Delta_{It}} \\
 &\times APZ_{[d_{0y}, d_{0z}]} \left[ \frac{\omega_x}{2\pi \Delta_x}, \frac{c^{-1}\omega_t}{2\pi \Delta_{It}} + c^{-1}f_{Ic} \right] B_0 \left[ \frac{\omega_t}{2\pi \Delta_{It}} \right] \delta \left[ \frac{\omega_x - L_I \cos(\phi_0) K_I \omega_t + (1 - K_I)\pi}{2\pi \Delta_x} \right] \\
 &+ G(e^{j\omega_x}, e^{j\omega_t}) Z(e^{j\omega_x}, e^{j\omega_t}).
 \end{aligned} \tag{4.63}$$

According to Figure 4.3, the normalized-magnitude of the  $\hat{\mathbf{u}}_z$ -component of the active element pattern  $|ATZ(\theta, \phi, f_{ct})| \approx 1$  in the angular-ranges  $\phi_p \in (30^\circ, 150^\circ)$  and  $\theta_p \in (85^\circ, 95^\circ)$  for all  $|cf_{ct}| \in [f_{\text{SYSmax}} - \Omega_{\text{Full}}, f_{\text{SYSmax}}]$ . Therefore, following (2.70) (see page 54), it can be shown that  $\left| APZ_{[d_{0y}, d_{0z}]} \left[ \frac{\omega_x}{2\pi \Delta_x}, \frac{c^{-1}\omega_t}{2\pi \Delta_{It}} + c^{-1}f_{Ic} \right] \right| \approx 1$  inside the region 1234 shown in Fig-



ure 4.4. Also according to (4.59),  $G(e^{j\omega_x}, e^{j\omega_t}) = 1 e^{-j\omega_t N_t}$  inside the passband  $ABCD$ , therefore, (4.63) can be rewritten as

$$Y(e^{j\omega_x}, e^{j\omega_t})_{\{|\omega_x, \omega_t| \leq \pi\}} \cong \frac{1 e^{-j\omega_t N_t}}{\Delta_x \Delta_{It}} B_0 \frac{\omega_t}{2\pi \Delta_{It}} \delta \left( \frac{\omega_x - L_I \cos(\phi_0) K_I \omega_t + (1 - K_I) \pi}{2\pi \Delta_x} \right) + G(e^{j\omega_x}, e^{j\omega_t}) Z(e^{j\omega_x}, e^{j\omega_t}). \quad (4.64)$$

The required 1D output sequence  $\tilde{y}(0, n_t)$  can be evaluated by taking the 2D inverse discrete-Fourier-transform (2D-IDFT) integral of (4.63) for  $n_x = 0$ , which simplifies to

$$\tilde{y}(0, n_t) \cong \tilde{\vartheta}(n_t) + \frac{1}{2\pi \Delta_{It}} \int_{\omega_t = -\pi}^{\pi} B_0 \frac{\omega_t}{2\pi \Delta_{It}} I(\omega_t) e^{j\omega_t(n_t - N_t)} d\omega_t, \quad (4.65)$$

where

$$\tilde{\vartheta}(n_t) = \frac{1}{(2\pi)^2} \int_{\omega_x = -\pi}^{\pi} \int_{\omega_t = -\pi}^{\pi} G(e^{j\omega_x}, e^{j\omega_t}) Z(e^{j\omega_x}, e^{j\omega_t}) e^{j\omega_t n_t} d\omega_x, \quad (4.66)$$

and

$$I(\omega_t) = \int_{\omega_x = -\pi}^{\pi} \delta \left( \frac{\omega_x - L_I \cos(\phi_0) K_I \omega_t + (1 - K_I) \pi}{2\pi \Delta_x} \right) d \frac{\omega_x}{2\pi \Delta_x}. \quad (4.67)$$

However, for the given values  $|L_I| \leq 1$ ,  $|K_I| \leq 0.5$ ,  $\phi_0 \in (30^\circ, 150^\circ)$  and  $|\omega_t| \leq \pi$ , it can be shown that  $|L_I \cos(\phi_0) K_I \omega_t + (1 - K_I) \pi| \leq \pi$ ; hence for (4.67),  $I(\omega_t) = 1$  for  $|\omega_t| \leq \pi$ . Therefore, the integral in (4.65) simplifies to  $\int_{\omega_t = -\pi}^{\pi} B_0 \frac{\omega_t}{2\pi \Delta_{It}} e^{j\omega_t(n_t - N_t)} d \frac{\omega_t}{2\pi \Delta_{It}}$ , which can be evaluated following [44] (pp. 99-101) such that

$$\tilde{b}_0 \Delta_{It}(n_t - N_t) = \int_{\omega_t = -\pi}^{\pi} B_0 \frac{\omega_t}{2\pi \Delta_{It}} e^{j\omega_t(n_t - N_t)} d \frac{\omega_t}{2\pi \Delta_{It}}, \quad (4.68)$$

where  $\tilde{b}_0(\Delta_{It}(n_t - N_t))$  is the sampled 1D baseband equivalent wavefront function  $\tilde{b}_0(t)$ , delayed by  $N_t$  samples. Now the 1D complex-valued sample sequence of the beamforming 2D FIR filter can be given by

$$\tilde{y}(0, n_t) \cong b_0 \Delta_{It}(n_t - N_t) + \tilde{\vartheta}(n_t); \quad \forall n_t \in \mathbb{Z}. \quad (4.69)$$

According to (4.69),  $\tilde{y}(0, n_t)$  is a combination of  $\tilde{b}_0(\Delta_{It}(n_t - N_t))$ , which contains the modulated-data of 0<sup>th</sup>-subscriber, and  $\tilde{\vartheta}(n_t)$ , which corresponds to a fraction of the contaminating receiver noise.

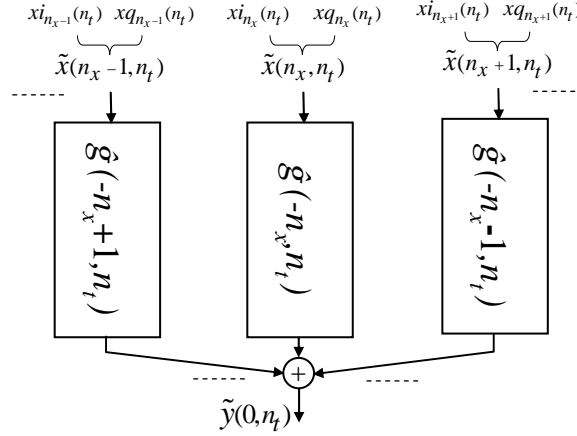


Figure 4.13: A section of the structure for the beamforming complex-coefficient 2D FIR trapezoidal filter  $G(z_x, z_t)$  implemented with parallel connection of complex-coefficient 1D FIR filters.

In subsection 4.3.4, it has been mentioned that the ROS of the spectral density function  $\overline{\overline{Z}}(e^{j\omega_x}, e^{j\omega_t})$ , of the equivalent complex-quadrature sampled receiver noise  $\eta_{n_x}(\Delta_{\text{It}} n_t)$  is expected to occupy the entire **PNS**, where the 2D-DDFT pair of the 2D auto-correlation function and its spectrum is  $\text{AutoCorr } \eta_{n_x}(\Delta_{\text{It}} n_t) \xrightarrow{2\text{D-DDFT}} \overline{\overline{Z}}(e^{j\omega_x}, e^{j\omega_t})$ . If the spectral density  $\overline{\overline{Z}}(e^{j\omega_x}, e^{j\omega_t}) = \text{constant}$  inside the **PNS**, then following [71][158] it can be shown that the output noise power  $E[\tilde{\vartheta}(n_t)]^2$  is proportional to the area of  $ABCD$ .

#### 4.5.5 Implementation of the Beamforming Complex-Coefficient 2D FIR Trapezoidal Filters

In CR systems, the computational complexity of the broadband beamformer, which accounts for significant portion of the base-station hardware and operational costs, is an important design parameter [16]. In the following, the computational complexities of the beamforming complex-coefficient 2D FIR trapezoidal filter of order  $(2N_x) \times (2N_t)$  is briefly discussed.

Following (4.60),  $\tilde{y}(0, n_t)$  can be evaluated using the 2D convolution-sum

$$\tilde{y}(0, n_t) = \sum_{m_x=-N_x}^{+N_x} \sum_{m_t=0}^{2N_t} \tilde{x}(m_x, n_t - m_t) \tilde{g}^*(-m_x, m_t), \quad (4.70)$$

where “\*” denotes complex-conjugation. Hence, the beamforming complex-coefficient 2D FIR trapezoidal filter  $G(n_x, n_t)$  of order  $(2N_x) \times (2N_t)$  can be implemented using an array of  $(2N_x + 1)$  direct-form [66] (pp. 503-504) parallel-connected complex-coefficient 1D FIR filters of order  $2N_t$ , as shown in Figure 4.13. Note, the unit impulse responses of the  $m_x^{th}$  complex-coefficient 1D FIR filter  $G_{m_x}(z_t)$  is given by  $\tilde{g}^*(-m_x, n_t)$ . Following [51], each complex-coefficient 1D FIR filter  $G_{m_x}(z_t)$  can be implemented with four real-valued 1D FIR filters. It follows from (4.70) that  $4(2N_x + 1)(2N_t + 1)$  real-number-multiplications and  $(4(2N_x + 1)(2N_t + 1) - 1)$  real-number-additions are required per output sample  $\tilde{y}(0, n_t)$ . With the proposed parallel-connected structure, the computational complexity of the filtering are divided among the 1D FIR filters. By exploiting well established 1D FIR filter implementation techniques [66] (pp. 502-519), higher throughput may be achieved by employing  $(2N_x + 1)$  parallel-connected low cost DSP hardware modules (e.g. FPGA or ASIC), where each module is dedicated to a 1D FIR filter. With this structure, additional 1D FIR filters can be easily incorporated to increase the spatial order of the beamformer. Using a folded structure similar to the direct-form structure given in Figure 7.2 in [66] (pp. 504), the number of multiplications can be reduced by half without increasing the number of additions. However, this requires the complex-coefficient 1D FIR filters  $G_{m_x}(z_t)$  and  $G_{-m_x}(z_t)$  to be implemented in a single DSP hardware module. Hence, the conjugate symmetry of  $\tilde{g}(n_x, n_t)$  has not been exploited here.

## 4.6 A Brief Comparison of Broadband-Bandpass Beamforming Methods

In the following, the performance and the design complexity of the proposed complex-coefficient 2D FIR trapezoidal filter-based beamformer are briefly compared against the different beamforming methods outlined in section 4.4, which can be employed in CR systems for broadband-bandpass beamforming. The considered methods are the digital DFT beamformer [138] (see subsection 4.4.2), the digital interpolation delay-and-sum beamformer [101] (see subsection 4.4.1), the *Sekiguchi-method*, a different 2D FIR filter-based beamformer that claims to be nearly frequency-independent [139] (see subsection 4.4.3).

The performance of these beamforming methods has been evaluated using 2D test sequences  $\tilde{x}(n_x, n_t)$  synthesized to simulate space-time sampled EM ST PWs that correspond to signals transmitted by different subscriber modules of the CR system. The complex-valued 2D test sequences  $\tilde{x}(n_x, n_t)$  are synthesized following the properties discussed in section 4.3 such that those 2D test sequences are associated with different 1D baseband equivalent wavefront functions  $\tilde{b}_q(t)$ ;  $q = 0, 1, \dots, Q$ , different instantaneous bandwidth spread factors  $K_I$ , different instantaneous system utilization factors  $L_I$ , and different DOAs  $\mathbf{d}_q$ . Because of the geographical spread of the subscribers and the limited angular coverage of the active element pattern of the 1D-UDAA, only the EM ST PWs arriving from DOAs  $\mathbf{d}_q$  that correspond to the inclination angular range  $\theta_q \in (85^\circ, 95^\circ)$  and the azimuth angular range  $\phi_q \in (30^\circ, 150^\circ)$  are effectively received by the 1D-UDAA. In the given example,  $\tilde{x}(n_x, n_t)$ , of 41 spatial samples by 256 temporal samples ( $41 \times 256$ ), encompasses five superimposed 2D space-time sampled ST PWs  $\tilde{p}w_q(n_x, n_t)$ ;  $q = 0, 1, 2, 3, 4$  having  $K_I = 0.1$ ,  $L_I = 0.9$  and are associated with azimuth angles  $\phi_0 = 70^\circ$ ,  $\phi_1 = 150^\circ$ ,  $\phi_2 = 95^\circ$ ,  $\phi_3 = 130^\circ$  and  $\phi_4 = 40^\circ$ , respectively. The instantaneous amplitude of the interference signals  $\tilde{p}w_q(n_x, n_t)$ ;  $q = 1, 2, 3, 4$  may be 100 times higher than that of the desired signal  $\tilde{p}w_0(n_x, n_t)$  where the overall signal to system noise ratio (SNR) of  $\tilde{x}(n_x, n_t)$  is 20 dB. In this example,  $\tilde{b}_q(t) = \text{sinc}(\Omega_I(t - \tau_q \Delta_{It}))$ ;  $q = 0, 1, 2, 3, 4$ , is selected as the

baseband equivalent wavefront function where the associated delays of the PWs  $\tau_0 = 10$ ,  $\tau_1 = 60$ ,  $\tau_2 = 110$ ,  $\tau_3 = 160$  and  $\tau_4 = 210$ . The equivalent continuous-time signal recovered by temporal-demodulation with no beamforming is shown in Figure 4.14 (a). The ROSs of the spectra of the input sequences are shown in Figure 4.14 (b). As explained in section 2.7.2 and section 4.3.4, the finite widths of the ROSs are due to spectral spreading. Note that, if all  $\tilde{b}_q(t)$ ;  $q = 0, 1, 2, 3, 4$  had identical delays  $\tau_q$ , then the desired  $\tilde{b}_0(t)$  would be irrecoverably suppressed by the four co-channel interfering signals  $\tilde{b}_q(t)$ ;  $q = 1, 2, 3, 4$ . For this case, the signal-to-interference-ratio (SIR) is -46 dB.

Given the initial estimation of the DOA angle of the desired ST PW is  $\hat{\phi}_0 = 70^\circ$ , the beamforming complex-coefficient 2D FIR trapezoidal filter  $G(z_x, z_t)$  of order  $(40 \times 32)$  is designed here to meet the specifications  $\hat{\phi}_0 = 68^\circ$ ,  $\Delta\phi = 5^\circ$ ,  $L_I = 0.9$  and  $K_I = 0.1$  and implemented using the FIR filter structure shown in Figure 4.13. The output of the 2D FIR trapezoidal filter beamformer  $\tilde{y}(0, n_t)$ , shown in Figure 4.14 (c), confirms the *near-perfect* recovery of the desired signal  $\tilde{b}_0(t)$ . The co-channel interfering signals are attenuated by more than 50 dB.

In DFT based broadband-beamforming, algorithms have been developed [138] to evaluate only the required points of the sampled DFT spectrum of the desired ST PWs in order to increase the algorithmic efficiency. The output of the direct-DFT based frequency domain broadband-beamformer, proposed in [138](Sec-II.A.1, pp. 1815), is shown in Figure 4.14 (d). In this method, a 1D Hamming window function is used to reduce the spectral leakage along  $\omega_x$  [43] (pp. 88). However, according to Figures 4.14 (d) and 4.14 (c), the signal distortion of the DFT based-beamformer is higher relative to that of 2D FIR trapezoidal filter-based beamformer. Even though more computationally efficient algorithms are proposed in [138][144], in general DFT based broadband beamforming methods have drawbacks such as the requirement of higher data storage and higher latency.

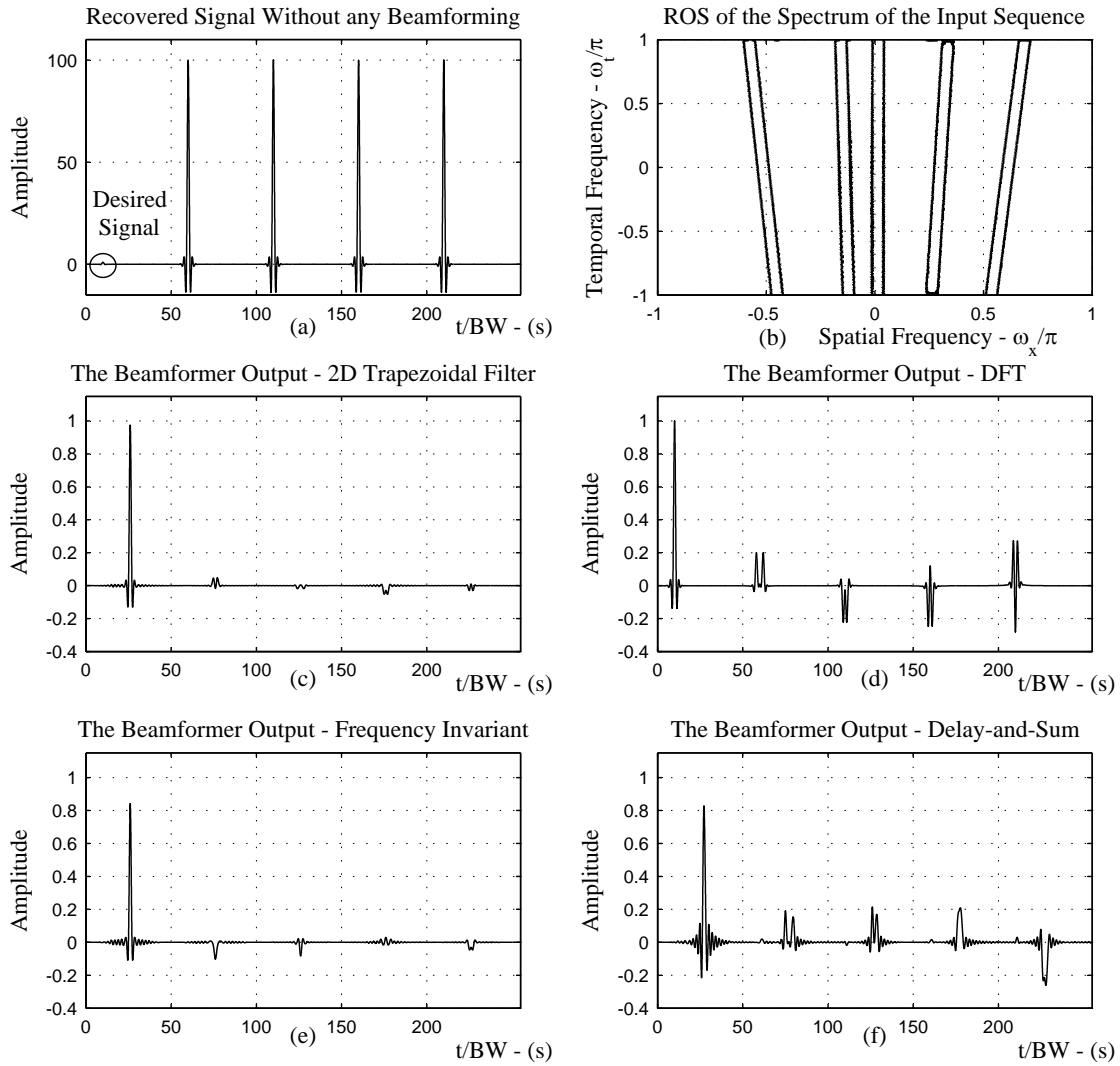


Figure 4.14: The directly demodulated signal without any beamforming (a), the distribution of spectral components inside the 2D Nyquist square (b), the output signal of the 2D Trapezoidal filter beamformer (c), the output of the DFT beamformer (d), the output of the sekiguchi-method, a nearly-frequency invariant beamformer (e) and the output signal of the delay and sum beamformer (f) in response to identical test sequences.

Both the interpolation delay-and-sum beamformer [101] and the Sekiguchi-method [139] may be implemented with the FIR filter structure shown in Figure 4.13. Hence, here, these two beamforming methods are implemented to have the same computational complexity of the 2D FIR trapezoidal filter beamformer. As shown in Figure 4.14 (f), performance of the interpolation delay-and-sum beamformer is the worst compared to other methods. This may be due to the misalignment of the beam-shaped transfer function corresponding to the interpolation delay-and-sum beamformer because, according to subsection 4.4.1, the interpolation delay-and-sum method is only capable of synthesizing a limited number of beams directed at specified azimuth angles  $\phi_D$ . As shown in Figure 4.14 (e), the performance of the Sekiguchi-method is similar to that of the 2D FIR trapezoidal filter beamformer. This result conforms that the beam-pattern achieved by the proposed 2D FIR trapezoidal filter beamformer is frequency invariant for more than 90% of the operational temporal bandwidth as claimed in section 4.5.3. Moreover, the design method of the 2D FIR trapezoidal filter is closed-form and therefore allows for the instantaneous evaluation of the filter coefficients, which is more time consuming with the iterative and complicated design methods proposed for the Sekiguchi-method [139]. Hence, considering a CR system where the instantaneous selection of operational bandwidth and sampling frequency as well as the real-time tracking of temporally-broadband-bandpassed ST PWs is required, the proposed 2D FIR trapezoidal filter-based beamformer achieves the best overall performance considering the factors of low distortion of the desired signal, higher attenuation of the interfering signals with a given computational complexity.

## 4.7 An Example of the Application of the Proposed Adaptive Beamformer in the Receiving Arm of a CR System

In order to provide an optimal quality of service for various communication/entertainment applications and services, the CR system must dynamically allocate the operational frequency bands, the bandwidths and the signal power for the subscribed communication devices [13][14][15][16]. Hence, the beamformer should be able to adapt according to the changing operational frequency-bands and the beam-directions in order to maintain the SIRs of the recovered desired signals above threshold levels [16]. A typical scenario for the multi-user subscriber management in CR systems has been introduced in chapter 1, where a 1D-UDAA of a CR system that is receiving groups of co-channel RF signals transmitted by the mobile communication devices on a high-speed commuter train and by both mobile wireless and fixed wireless devices in an apartment building as depicted in Figure 1.1. In order to faithfully recover the two groups of co-channel signals transmitted by the subscriber devices in the train and the devices in the building, receiving beams have to be formed. Further, the beam pointed at the commuter train has to be adapted in real-time in order to track the train as it moves along. In this scenario, the performance of the proposed beamforming 2D FIR trapezoidal filter as an adaptive broadband-bandpass beamformer in the receiving arm of a CR system is analyzed through simulation in the following. Given the reciprocity between the signals in the receiving and transmitting arms of the front-end of the SDR [13] (ch. 4), the reciprocated application of the proposed adaptive 2D FIR trapezoidal filter-based beamformer may also be used in beamforming within the transmitting arm of a CR system. However for brevity, the discussion is limited to the receiving arm beamforming process.

For this example, a section of the setup is illustrated in Figure 4.15, where the signals transmitted by the mobile devices on a high-speed commuter train and both mobile-



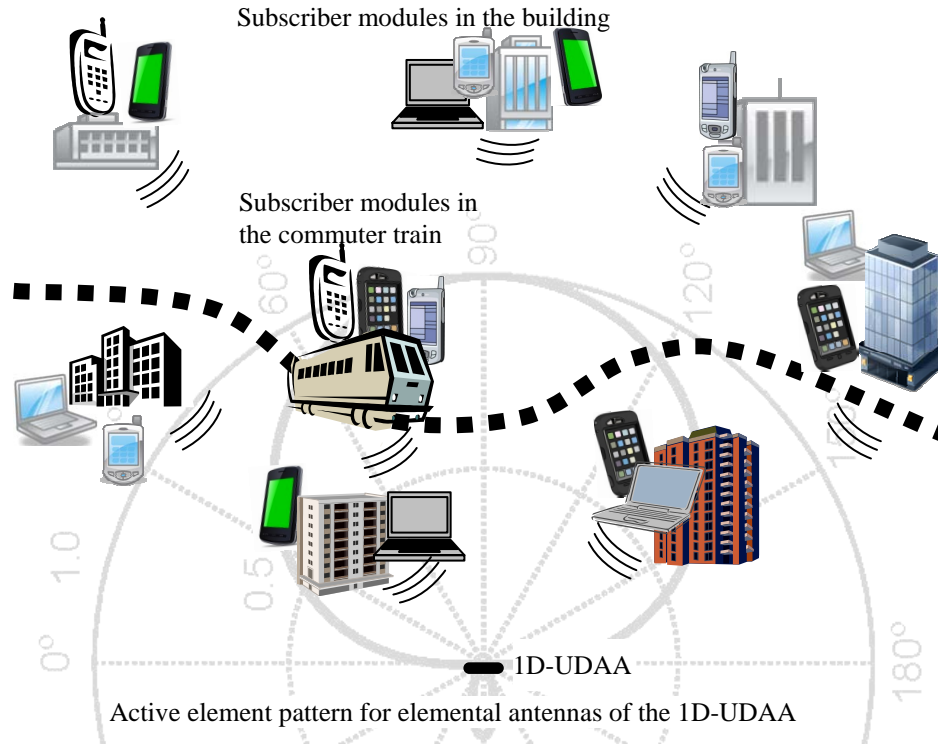


Figure 4.15: A typical scenario in which the CR system is receiving signals from many wireless mobile devices on a high-speed commuter train and many fixed and mobile communication devices in apartment buildings.

wireless and fixed-wireless devices in an apartment-building are received by the 1D-UDAA of a CR system. In this scenario, initially, the DOA ( $\theta_T$ ) of the group of signals

$w_T(t, \phi_T)$  that is transmitted from the mobile devices in the train is set at  $\phi_T = 70^\circ$  and the azimuth angle of the DOA ( $\phi_B$ ) of the group of signals  $w_B(t, \phi_B)$  transmitted from the wireless communication devices in the building is set at  $\phi_B = 91^\circ$ . Along with

$w_T(t, \phi_T)$  and  $w_B(t, \phi_B)$ , EM signals transmitted from three other buildings located in the directions along the azimuth angles  $50^\circ$ ,  $115^\circ$  and  $145^\circ$  have been allocated the operational-band FB1, corresponding to  $L_I = 1.0$  and  $K_I = 0.1$ , by the CR system. It is assumed here that amplitudes of  $w_B(t, \phi_B)$  and the signals transmitted from other buildings are 100 times stronger than the amplitudes of  $w_T(t, \phi_T)$ . *In order to minimize the interference from other co-channel signals, an adaptive beam should obviously be*

formed to track and receive  $w_T(t, \phi_T)$  and a fixed beam should be formed to receive  $w_B(t, \phi_B)$ . Therefore in this example, initially, two beamforming 2D FIR trapezoidal filters  $G_T(z_x, z_t)$  and  $G_B(z_x, z_t)$ , both of order  $(40 \times 32)$  have been designed. In order to receive  $w_T(t, \theta_T)$  with minimum distortion,  $G_T(z_x, z_t)$  must meet the specifications  $\hat{\phi}_T = 70^\circ$ ,  $\Delta\phi = 4^\circ$ ,  $L_I = 1.0$  and  $K_I = 0.1$  where as, in order to receive  $w_B(t, \phi_B)$  must meet the specifications  $\hat{\phi}_B = 91^\circ$ ,  $\Delta\phi = 4^\circ$ ,  $L_I = 1.0$  and  $K_I = 0.1$ . The output sequences of the beamforming 2D FIR filters  $G_T(z_x, z_t)$  and  $G_B(z_x, z_t)$  are denoted by  $y_T(n_t)$  and  $y_B(n_t)$ , respectively. The averaged SIRs,  $\text{SIR}[y_T(n_t)]$  and  $\text{SIR}[y_B(n_t)]$ , of  $y_T(n_t)$  and  $y_B(n_t)$ , that correspond to the transmitted signals  $w_T(t, \phi_T)$  and  $w_B(t, \phi_B)$ , have been evaluated using the Monte Carlo method and are shown in Figure 4.16 at Time = 0.

Given that the train is moving towards the building as time progresses,  $\phi_T$  gradually decreases and deviates from the initially estimated azimuth angle  $\hat{\phi}_T = 70^\circ$ . Therefore, the ROS of the spectrum of  $w_T(t, \theta_T)$  gradually moves towards the edge of the passband of  $G_T(z_x, z_t)$  causing the gain of the recovered desired signal group  $y_T(n_t)$  at the output of  $G_T(z_x, z_t)$  to gradually decrease. This leads to a corresponding gradual reduction of  $y_T(n_t)$  and  $y_B(n_t)$ , which is observed in Figure 4.16 between Time = 1 and Time = 3.5. However, for the fixed direction beamformer, the SIR of the recovered signals  $y_B(n_t)$  is generally expected to remain approximately constant, which is observed in Figure 4.16 between Time = 1 and Time = 3.5. Given that the quality of the recovered signal may severely degrade if the SIR of  $y_T(n_t)$  drops below a certain lower-threshold (e.g. 8 dB), the tracking beam should be redirected towards the new position of the train in order to maintain an adequate SIR such that the communication applications performed by the mobile devices in the train can continue without interruptions. In order to achieve this, the control unit of the CR systems should regularly evaluate the SIRs of all the recovered signals  $\text{SIR}[y_T(n_t)]$  and  $\text{SIR}[y_B(n_t)]$  etc and adapt the

beamformers accordingly. Usually, the decision to redirect the beam is taken when the observed SIR level reaches a higher threshold (e.g. 11 dB), in order to give enough time to design and commission a new beamforming 2D FIR filter  $G_T(z_x, z_t)$ . In this example, the threshold for redirecting the beam for  $y_T(n_t)$  is crossed at Time = 3.0. As illustrated in Figure 4.16 between Time = 3.0 and 3.2, it takes a finite time to evaluate the coefficients for  $G_T(z_x, z_t)$  and apply them to the filter structure. For this example, it is assumed that the maximum time available for designing (e.g. 0.125 s) and commissioning the redirected  $G_T(z_x, z_t)$  is much larger than the time it takes the SIR to degrade from 11 dB to 8 dB. In order to provide uninterrupted reception, both the “new” and the “old” beamformers operate simultaneously for a short period of time until the operation of the new beamformer is verified. In this example, the redirection process is repeated at Time = 5.5, Time = 8.5 and Time = 11.5 until Time = 14 in order to maintain the SIR  $[y_T(n_t)]$  above 8 dB.

As the train moves further towards the building, the angular selectivity of the beamformer may not be sufficient to effectively suppress the co-channel interfering signals. Therefore, the CR system should reallocate the frequency-bands of operation to different users such that the angular separations of the co-channel signals are sufficiently large. For the proposed beamforming 2D FIR trapezoidal filters  $G_T(z_x, z_t)$  and  $G_B(z_x, z_t)$ , of order  $(40 \times 32)$ , about  $10^\circ$  angular separation is required to achieve 50 dB attenuation of the co-channel interfering signals in the frequency-band of operation corresponding to  $L_I = 1.0$  and  $K_I = 0.1$ . In this example, such a situation arises at Time = 14. Here, it is assumed that at Time = 14, the CR system reallocates the signals  $w_B(t, \phi_B)$  (where  $\phi_B = 91^\circ$ ), frequency-band FB2, which corresponds to  $L_I = 0.8$  and  $K_I = 0.125$ , whereas the signals  $w_T(t, \phi_T)$  remain in the frequency band FB1. After the frequency reallocation,  $w_T(t, \theta_T)$  and the signals transmitted from three other buildings (where the corresponding DOAs are  $30^\circ, 60^\circ$  and  $145^\circ$ ) are accommodated in the frequency-band

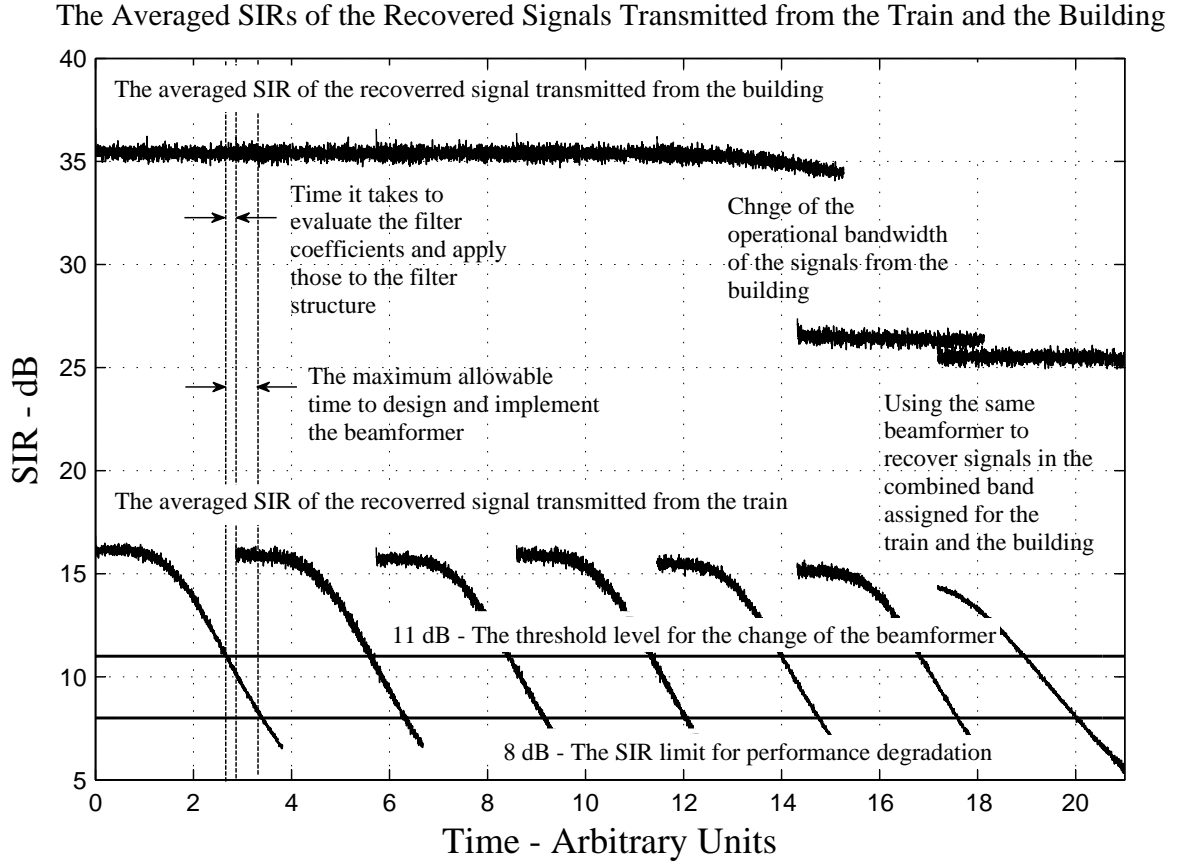


Figure 4.16: The averaged SIR (in dB) of the recovered signal transmitted from the commuter train and the apartment building as time progresses.

FB1, whereas  $w_B(t, \phi_B)$  and the signals transmitted from the three other buildings (where the corresponding azimuth angles are  $45^\circ$ ,  $105^\circ$  and  $125^\circ$ ) are accommodated in frequency-band FB2. In order to recover the desired signals  $y_B(t)$  after the frequency reallocation, the beamforming 2D FIR filter  $G_B(z_x, z_t)$  has to be redesigned to meet the specifications  $\hat{\phi}_0 = 91^\circ$ ,  $\Delta\phi = 4^\circ$ ,  $L_I = 0.8$  and  $K_I = 0.125$ . Also, the beamforming 2D FIR filter  $G_B(z_x, z_t)$  is required to be redesigned to direct the beam towards the new location of the train. As shown in Figure 4.16, between Time = 14.2 and Time = 18, the averaged SIR of  $y_B(t)$  is reduced to 27 dB, which is about 8 dB lower than the 35 dB that is the average SIR of  $y_B(t)$  between Time = 0 and Time = 14. This may be due to fact that the spectral components of the co-channel interfering signals are more

closely distributed in the respective **PNS** for the frequency band of operation FB2 than the frequency band of operation FB1.

As the train approaches the building (i.e. the azimuth angle  $\phi_T \rightarrow 1^\circ$  of  $w_T(t, \phi_T)$ ), instead of forming a tracking beam in FB1 and a fixed beam in FB2, a combined beam can be formed to cover the larger frequency-band FB12, corresponding to  $L_I = 1.0$  and  $K_I = 0.2$ . In the example, such a scenario arises at Time = 17. Hence, in order to recover both  $y_T(t)$  and  $y_B(t)$ , a beamforming 2D FIR filter  $G_{TB}(z_x, z_t)$  is designed to meet the specifications  $\hat{\phi}_0 = 88^\circ$ ,  $\Delta\phi = 4^\circ$ ,  $L_I = 1.0$  and  $K_I = 0.2$ . The variation of the respective SIRs of the recovered output sequences  $y_T(t)$  and  $y_B(t)$  at the output of  $G_{TB}(z_x, z_t)$  is shown in Figure 4.16 between Time = 17.2 and Time = 21. However, as the azimuth angle  $\phi_T$  goes beyond  $\phi = 91^\circ$ , in order to maintain the required SIR levels, it is necessary to design two beamforming 2D FIR filters  $G_T(z_x, z_t)$  and  $G_B(z_x, z_t)$  for FB1 and FB2 to track and enhance the signals  $y_T(t)$  and to enhance the signals  $y_B(t)$ , respectively.

The simulation results shown in section 4.6 and 4.7 indicate that, compared with previously reported broadband-beamforming methods [101][138][139], the proposed method achieves the best overall performance for a CR system with respect to lower distortion of the desired signal, higher attenuation of the co-channel interference signals for a given level of computational complexity while achieving instantaneous adaptability in terms of changing frequency band of operation, bandwidth and the time varying DOA of the desired signals.

## 4.8 Summary

In this chapter, a novel discrete-domain beamforming method has been proposed for the beamforming of temporally-broadband-bandpassed EM ST PWs using complex-coefficient 2D FIR trapezoidal filters for a cognitive radio (CR) system having a soft-

ware defined radio (SDR) based receiver front-end. The significance of CR systems in future wireless communications systems and the enabling technologies such as the SDR architectures have been briefly discussed in section 4.2. In section 4.3, signal processing carried by the SDR front-end of a CR system has been analyzed in detail. As given there, the EM ST PWs transmitted by subscriber modules are received by a 1D-UDAA, then the antenna signals are pre-filtered, complex-temporal-demodulated and synchronously sampled using a SDR implemented complex-quadrature-temporal sampler array. The SDR-based complex-quadrature-temporal sampler array achieves the minimum possible temporal sampling rate while instantaneously selecting the operational bandwidth. In subsection 4.3.4, it has been derived that inside the **PNS**, the ROS of the spectrum of complex-quadrature sampled antenna signals corresponding to EM waves transmitted by a subscriber module is given by the straight line segment specified in (4.33). Further, it has been derived that the range of the ROSs of the spectra is given by the trapezoidal shaped region 1234 shown in Figure 4.4.

A few of the previously proposed broadband-bandpass beamforming methods, which may be applicable for broadband-bandpass beamforming in CR systems, have been briefly reviewed in section 4.4. The design of the beamforming complex-coefficient 2D FIR filter having an asymmetric trapezoidal shaped passband has been explained in detail in section 4.5. The shape and orientation of the ideal asymmetric trapezoidal-shaped passband  $ABCD$  of the proposed beamforming complex-coefficient 2D FIR filter is proposed in subsection 4.5.1. In this subsection, the limitation of the previously proposed broadband-beamforming methods have also been discussed. A 2D FIR filter structure has been used in subsection 4.5.2 to approximate ideal transfer function that corresponds to the ideal 2D asymmetric trapezoidal shaped passband  $ABCD$  shown in Figure 4.7. A closed-form design method has been proposed in subsection 4.5.2, in order to determine the filter coefficients  $\tilde{g}(n_x, n_t)$  of the proposed 2D FIR trapezoidal filter  $G(z_x, z_t)$  for dif-

ferent azimuth angles  $\hat{\phi}_q$ , the beam-width  $\Delta\phi$ , the instantaneous bandwidth spread-factor  $K_I$  and the instantaneous system utilization factor  $L_I$ . Employing this closed-form design method, beamforming 2D FIR trapezoidal filters can be easily designed to adapt for the instantaneous changes of the operational frequency band and the sampling rate of the CR system as well as to track and enhance temporally-broadband-bandpassed ST PWs in real time with time varying DOAs. As mentioned in subsection 4.5.4, the complex-valued 2D sample sequence  $\tilde{x}(n_x, n_t)$  is processed by the beamforming complex-coefficient 2D FIR trapezoidal filter  $G(z_x, z_t)$ , which enhances the spectral components of the desired subscriber signal that lie inside the asymmetric 2D trapezoidal shaped passband and suppresses the spectral components of the co-channel interfering subscriber signals and broadband receiver noise that lie inside the stopband. For the implementation of the beamforming 2D FIR trapezoidal filters, the parallel connected 1D FIR structure has been proposed in subsection 4.5.5. The proposed structure can exploit the low-cost DSP hardware while achieving high throughputs. Also, with this structure, additional 1D FIR filters can be easily incorporated to increase the spatial order of the beamformer.

According to the simulation results given in sections 4.6 and 4.7, compared to the broadband-beamforming methods [101][138][139] and many other similar methods, the proposed method achieves the best overall performance for a CR system considering instantaneous adaptability, lower distortion of the desired signal and higher attenuation of the co-channel interference signals with given computational complexity.

## Chapter 5

# Broadband Beamforming of Focal Plane Array Signals using Real-Time Spatio-Temporal 3D FIR Frustum Digital Filters

### 5.1 Introduction

The Square Kilometre Array (SKA) will be World's largest aperture synthesis radio telescope when it is completed in 2020 at an estimated cost of \$ 2 billion [110][111][160]. At the maximum baseline, the SKA is expected to span over 3000 kms and it is expected to cover the frequency range 70 MHz to 10 GHz [110][111]. Key science projects of the SKA include probing the dark ages, determination of the epoch of re-ionization, studies of the evolution of galaxies, dark energy, the origin and evolution of cosmic magnetism, search for the cradle of life and strong field tests of gravity to verify the general theory of relativity [111][160]. Some of these key science projects are to be achieved by analyzing broadband “transient” electromagnetic (EM) celestial signals of interest (SOIs), which are typically of less than 5 s duration and as short as 1 ns in the case of pulsars [29][50][161].

Full sampling radio frequency focal plane arrays (FPAs) have been proposed as a means of increasing the field of view (FoV) of the paraboloidal reflector antenna array based aperture synthesis systems [162]. Essentially, a FPA is a 2D-UDPA that is assembled on the focal plane of a paraboloidal reflector as shown in Figure 5.1. For the SKA, FPAs are under consideration for deployment in as many as 1,000 - 2,000 paraboloidal reflectors of 15 m diameter [110][111][160]. A FPA of  $3.24\text{ m}^2$  area associated with a 15 m diameter paraboloidal reflector dish is capable of covering a  $25\text{ deg}^2$  FoV for the so-called SKA lower mid-band (i.e. the frequency range 0.5 to 1.7 GHz) without significant diffraction losses [136]. Over this frequency range, it is expected that the multiple-beam



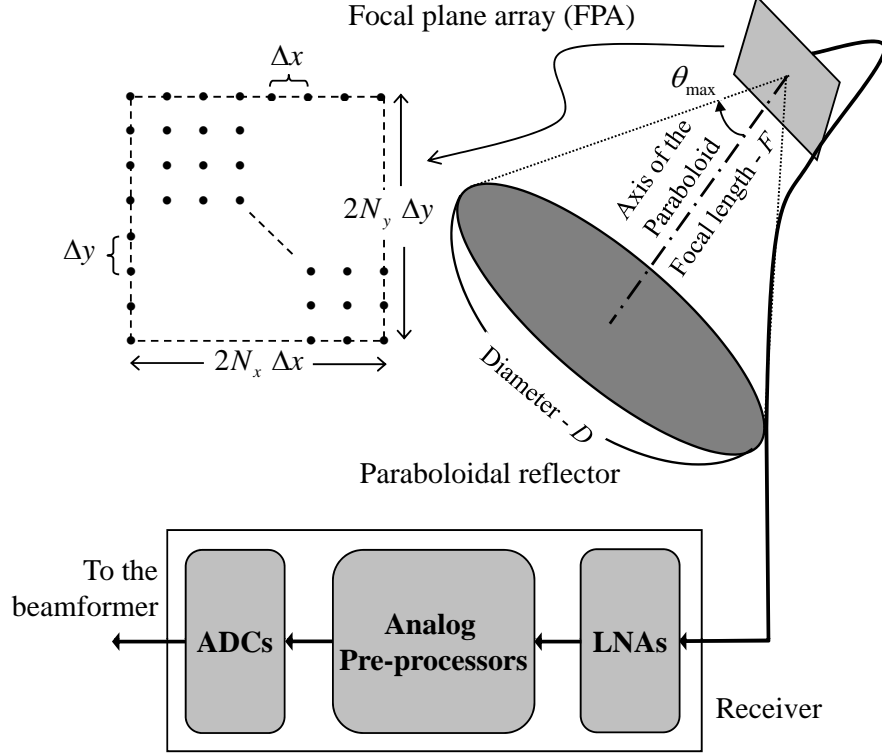


Figure 5.1: A prime-focus paraboloidal reflector having a circular-aperture and a focal plane array (FPA) consist of  $(2N_x + 1) \times (2N_y + 1)$  elements arranged uniformly on a plane. Each elemental antenna is connected to a single channel receiver.

capability of the FPAs, combined with the large collecting area of the complete system and the low-noise receiver systems will simultaneously facilitate both the high sensitivities and the high sky-survey speeds for applications in aperture synthesis imaging for the SKA [163][164].

A typical arrangement of a FPA on the focal plane of a prime-focus paraboloidal reflector and subsequent signal processing systems are illustrated in Figure 5.1. The EM waves originated from celestial sources are reflected from the paraboloidal dish onto the focal plane where they are received by a rectangular array containing coplanar uniformly-spaced wideband elemental-antennas, such as Vivaldi antennas [20][165] (see Figure 2.8) or patch antennas [166]. Currently, the number of elemental-antennas in an FPA is in the range of 100-200 [20][167][166]. The photonic response of each wideband elemental-

antenna is converted to electronic form and amplified by corresponding elemental low noise amplifiers (LNAs) [166]. The outputs of the LNAs are subjected to analog pre-processing that shifts the desired frequency band (i.e. 0.5 - 1.7 GHz) to the baseband. The down-shifted signals are synchronously sampled by array of ADCs that results in a complex-valued 3D sample sequence [166]. This complex-quadrature-sampled [51] 3D sequence is then processed using a *broadband beamformer* in order to remove contaminating RFI, ground thermal noise and parts of the receiver noise, which is contributed mainly by the LNAs. Subsequently, digital signal processing (DSP) algorithms are applied to recover the SOIs from the beamformer outputs. It has been proposed to deploy around 1,000 - 2,000 paraboloidal dishes fixed with FPAS in the SKA [110][111], which alone requires between 100,000 to nearly half a million elemental-antennas, LNAs, mixers and ADCs just for the front-end processing.

In this chapter, a real-time spatio-temporal 3D filter is proposed for the potential beamforming application of digital pre-processing of the 3D sample sequence corresponding to broadband FPA signals of a circular-aperture prime-focus paraboloidal reflector antenna in the SKA. More specifically, here, it is proposed that a single real-time spatio-temporal (ST) 3D FIR filter shown in Figure 5.2, having a frustum-shaped passband, can be employed as a *pre-coherent-dedispersion*<sup>1</sup> *broadband beamformer* for pulsar timing [30] and pulsar profile studies [50] in order to significantly suppress terrestrial RFI, the ground thermal noise and a dominant component of the LNA noise that contaminate the FPA signals. The proposed method depends on the following facts about the 3D regions of support (ROSs) of the spectra of space-time sampled FPA signals. Following chapter 3, it is shown in section 5.3.1, that the ROS of the spectrum of far-field dish-reflected direct down-converted and complex-quadrature-sampled FPA signals of interest (SOIs) is a frustum-shaped volume, within the Nyquist cube in 3D frequency space. Also, it is

---

<sup>1</sup>The coherent-dedispersion is a signal processing method that reconstructs the sharp pulses emitted by celestial objects reversing the dispersion due to the interstellar media (ISM) [168].

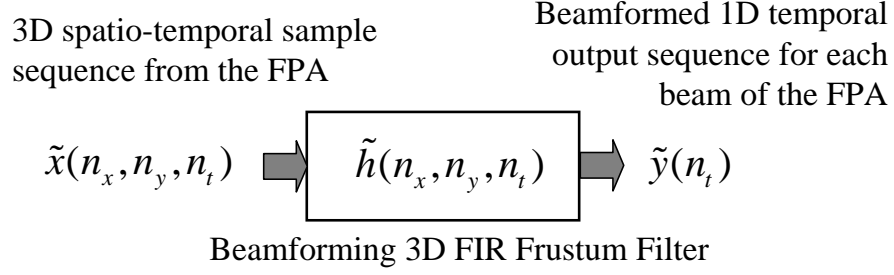


Figure 5.2: The beamforming 3D FIR frustum filter  $H(\mathbf{z})$ , having the 3D unit impulse response  $\tilde{h}(\mathbf{n})$ , for real-time pre-processing of FPA sample-sequences  $\tilde{x}(\mathbf{n})$ .

shown that the dimensions of the cone are primarily determined by the active element pattern of the FPA and the diameter ( $D$ ) and the focal length ( $F$ ) of the paraboloidal reflector having a circular-aperture. The shape of this ROS of the spectrum is virtually independent of the direction of the point celestial source on the sky. Also, it is shown in section 5.3.3 that the ROS of the 3D power spectral density (PSD) for the dominant component of the spatio-temporally-sampled ground thermal noise occupies the volume outside the surface of the frustum that corresponds to the ROS of the spectra of celestial SOIs. Similar analysis shows that the ROS of the 3D spectra of off-dish RFI signals also occupies the same region as the PSD of the ground noise. Finally, for simplicity, it is assumed<sup>2</sup> that the ROS of the 3D power spectral density (PSD) of the spatio-temporally-sampled broadband LNA noise occupies most of the volume of the Nyquist cube in 3D frequency space and is almost spectrally-flat over the lower-mid band temporal frequency range. Based on the above properties of the ROSs of 3D spectra, the frustum-shaped passband of the proposed 3D filter is designed to encompass most of the 3D ROS of the focal-plane spectra of far-field dish-reflected celestial signals, and thereby transmit most of the energy to the beamformer output. However, the 3D stopband is designed to encompass the spectral components of the undesired signals and noise such as terrestrial

<sup>2</sup>In practice, the exact shape of the 3D LNA noise power-spectral density function within the Nyquist cube is determined by the 1D temporal-power-spectral-density function of the LNA noise and the non-ideal inter-elemental-antenna mutual-coupling of the noise across the FPA [52][53][54].

RFI, ground thermal noise, and thereby attenuate the major component of off-dish FPA signals from the beamformer output. Parts of this work have been published in [55][56].

In order to verify the performance of the proposed beamforming 3D FIR frustum filter, here, noisy FPA signals (that are contaminated with off-dish RFI signals, ground thermal noise, and receiver noise) are synthesized for the FPAs of a number of dish-receivers, all of which are pointed at a distant emulated pulsar. For comparative purposes, these FPA signals are processed by a proposed 3D FIR frustum filter-based beamformer and also by the conventional 2D spatial-only beamformer and finally by the 3D conjugate-field-matching (CFM) beamformer. These three groups of outputs of each of the beamformers are time aligned, averaged and then normalized. The resulting three time sequences, corresponding to the three beamforming methods, contain recovered normalized pulses and some residual receiver noise. Each of these normalized pulses is compared with the normalized ideal dispersed-pulse in order to compute the mean-square-error (MSE). Simulation results show that the proposed 3D FIR frustum filter-based beamformer achieves the lowest MSE.

This chapter is arranged as follows. The key science projects and the engineering specifications of the SKA are briefly introduced in section 5.2. Section 5.3 is dedicated to the analysis of FPA signals and contaminating noise. A detailed analysis of the celestial SOIs, the off-dish RFI and noise due to ground thermal radiation observed at the outputs of FPA elemental antennas and the corresponding spectra, is given in subsections 5.3.1, 5.3.2 and 5.3.3, respectively. The various noise sources contributing to the outputs of the array of LNAs in the FPA receiver are reviewed in subsection 5.3.4. Here, the effects of noise coupling and the methods of modeling coupled FPA noise are briefly discussed. In subsection 5.3.5, the pre-beamforming signal processing architecture of a typical FPA receiver is briefly reviewed.

Based on the space-time and spectral domain properties of FPA signals and the

contaminating noise, the design of beamforming complex-coefficient 3D FIR frustum filter for processing broadband pulsar signals is explained in detailed in section 5.4. The 3D transfer function for the ideal beamformer is derived in subsection 5.4.1. It is proposed that a 3D FIR filter structure be used in approximating this ideal 3D transfer function. In subsection 5.4.2, a combined frequency-sampling and 3D window-based method for the design of beamforming 3D FIR frustum filters is proposed. A design example of a beamforming 3D FIR frustum filter is given in subsection 5.4.3. Here, the design is evaluated by comparing ideal and realized 3D frequency transfer functions of the beamforming 3D FIR trapezoidal filter. The results of a numerical study that is conducted to evaluate the performance of the proposed 3D FIR frustum filter-based beamformer in pre-processing broadband pulsar signals are given in section 5.5. Here, the proposed method is compared with the conventional 2D spatial-only beamformer and the 3D conjugate-field-matching (CFM) beamformer based on the means-square-error (MSE) estimate between the ideal dispersed pulse and the outputs of each beamformer.

## 5.2 The SKA Science Projects and Engineering Specifications; A Review

### 5.2.1 The SKA Science Projects

The effective collection area of the SKA, as implied by the adjective “square kilometre” is nearly a million square meters. Such a large effective collection area is unprecedented for radio telescopes and therefore is the key aspect that facilitates the potential new discoveries in many branches of modern science including fundamental physics, astrophysics, cosmology and astrobiology [169]. Supported by the modern low noise receiver technologies and efficient and flexible signal processing systems, the expected system sensitivity for the SKA is about 50 fold higher than the existing aperture synthesis radio telescopes (see Figure 5.3) [160]. Such unprecedented system sensitivity allows probing of previously unexplored regions of the universe using the SKA [169]. Based on the current

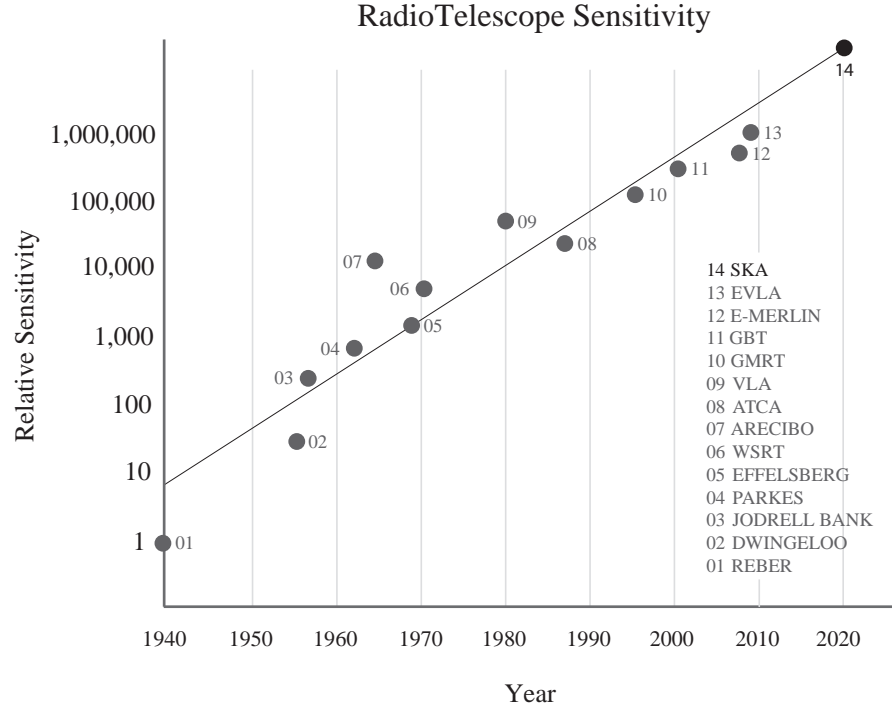


Figure 5.3: The relative sensitivities of main radio telescopes in the world and the expected sensitivity of the SKA. Source [170].

understanding of the universe, scientists have identified several key science projects to be conducted using the commissioned SKA [111]. These are,

- Probing the dark ages (i.e. up to 300,000 years after the big bang)
- Evolution of galaxies, cosmology and dark energy
- Studies of the origin and evolution of cosmic magnetism
- Searching the cradle of life
- Conducting extreme tests of general relativity.

However, with the observations made using the SKA, the possibility is always there to make unexpected discoveries that may lead to paradigm-shifts in modern science. In whichever case, the current frontiers of the modern science will be expanded.

In most of the above key science projects, the primary observation is the distribution of the spectral density of celestial EM radiation around 1.4 GHz (i.e. at wavelength around 21 cm), which is commonly known as HI-line, that corresponds to the strongest photonic emission of neutral hydrogen [169]. Hydrogen is believed to be the most common element in the universe. In probing the dark ages between the big bang and the epoch of reionization, HI densities corresponding to red-shifts higher than 10 are mapped by the SKA [169]. Similarly, HI densities corresponding to red-shifts up to 10 are observed in the studies of galaxy evolution [169]. The same data set may provide information of the dark energy distribution in the universe. With its unprecedented system sensitivity, the SKA will be able to detect the faint emissions of intergalactic hydrogen clouds with no star formation activity and distant dwarf galaxies, which have been hardly detected by the existing radio telescopes so far. The “Faraday rotation”, which is the rotation of the polarization plane when a polarized radio wave passes through a magnetic field, may be used to determine the magnetic field distribution in the universe [169]. With the SKA, the Faraday rotation of naturally polarized radio waves emitted by quasars will be measured in order to map the distribution of the magnetic fields around the intervening celestial structures, such as, the Milky Way, distant spiral galaxies, clusters of galaxies, and in intergalactic space [169]. Probing for the cradle of life is an important quest for humankind. Such efforts draw attention to the new discipline of astrobiology, a combination of radio astronomy and biology, which are distantly related branches of the modern science. The SKA’s approach to the searches of cradle of life is multipronged. Firstly, the SKA may facilitate searches for thermal radio emission from centimeter-sized “pebbles” in *protoplanetary systems*, which are thought to be the first step in assembling Earth-like planets [169]. With the specified sensitivity, the SKA is capable of detecting a protoplanet at distances ranging up to 3000 light years. Secondly, the synthesized aperture of the SKA facilitates optimal spatial resolutions associated with an adequate

signal strength for the detection of emission from the complex organic molecules formed in the hot core analogs within regions of low mass star formation [169]. Finally in searches for extraterrestrial intelligence (SETI), the sensitivity of the SKA allows the detection of unintentional “leakage” emissions (i.e. from TV transmitters, radars) from nearby solar systems up to several thousand light years [169].

Radio pulsars provide unique experimental observations that can lead to important insights about gravity and both the origin and evolution of the Universe [171]. Hence, a full sky survey that is intended for detecting new pulsars is one of the first astronomical observations that have been proposed for the SKA [161][50]. Such sky surveys will cover the galactic plane, intermediate longitudes, the galactic center, globular clusters and galaxies that are closest and furthest from the Earth [161][50]. With the unprecedented sensitivity of the SKA, it is expected that between 15,000 to 30,000 new pulsars will be detected during these sky surveys [171]. Some of these pulsars may be used as precise clocks to test the strong gravitational fields around black holes as predicted by Einsteins Theory of General Relativity [168]. In subsequent astronomical experiments, pulsar-timing observations and pulse-profile studies will be conducted for these newly discovered pulsars [50][168]. Systematic delays and advances in pulsar timing in a particular direction in the sky are measures of the space-time changes due to the propagation of gravitational waves [169]. Pulsar profiles studies may reveal the physics of radio pulse emissions and the nature of the ionized interstellar medium (ISM) [172]. The beamforming method proposed in this chapter is intended to be used in the front-end pre-processing in pulsar timing observations and pulsar profile studies.

The high energy radio-bursts originated from pulsars are subjected to (a) dispersion, (b) scintillation and (c) scattering while propagating through the ISM [168]. In brief, the dispersion causes frequency dependent phase rotation that spreads the intrinsically sharp pulse in time, where the scintillation causes frequency selective fluctuation of the



pulse and where the scattering causes the pulse to spread in time with a characteristic “exponential-tail” [168]. Because of these adverse propagation effects and because the pulsars are intrinsically weak radio sources [168], a radio telescope of extremely high system sensitivity such as the SKA is required for the detection of distorted EM radiation corresponding to the intrinsic sharp pulses. In order to recover the intrinsic sharp pulses for pulsar surveys, pulsar timing observations and pulse profile studies, removal of these adverse propagation effects is essential. Fortunately, effects of dispersion by the ionized ISM can be completely (or to a large extent) removed [168]. However, it is not possible to remove the effects of scattering [168].

There are two methods for dedispersion (i.e. the removal of the effects of dispersion) of the received pulses. The first method, the incoherent dedispersion method, employs an analog or a digital filter-bank in order to divide the broadband received signal into a number of channels [168]. The magnitudes of the signals in these channels are delayed in time such that the pulses in each channel are aligned so that, when added, they constructively superimpose to suppress the noise. The incoherent detection method is sufficient for new pulsar surveys [173][174] although the time resolutions may not be sufficiently accurate for pulsar timing observations and pulse profile studies [30]. The second method, the coherent dedispersion [175] method uses a deconvolution filter that operates on the entire broadband signals. The deconvolution filter corrects the phase rotation caused by ionized ISM and yields the intrinsic sharp pulse although the effects of ISM scattering remains [168].

### 5.2.2 The SKA Engineering Specifications

The SKA is proposed to be an aperture synthesis radio telescope where the collection area (i.e the aperture) is synthesized with a number of smaller antennas spread over a larger area [160]. At a given frequency, the angular resolution of an aperture synthesis system is determined by the largest baseline between the antennas. According to the Van

Cittert-Zernike theorem [3], for a quasi-monochromatic temporal frequency-band, the sky images are formed by evaluating the 2D Fourier transform of the *visibility functions* (i.e. measures of spatial coherence) over the synthesized aperture of the radio telescope. Given that the celestial EM radiation is extremely weak at the observation points on the surface of the Earth, the observed signals have to be integrated for a period of time to achieve the required signals to noise ratio (SNR) [3]. In practice, the visibility function is evaluated using a digital *cross-correlator* [176][177], that evaluates the cross-correlation for each baseline corresponding to all receiver antenna-pairs of the aperture synthesis system [176].

In case of radio telescopes including the SKA, radio frequency interference (RFI) is a major cause of degradation of the expected system sensitivity [21]. Because, RFI is due to human activities, sparsely-populated areas are often preferred for antennas sites of the radio telescopes. For constructing the “main-core” (see Figure 5.4) of the SKA, two candidate sites, (a) in the Karoo region of central South Africa and (b) in the state of Western Australia, have been identified after preliminary investigations [111]. In order to achieve the required sensitivities to successfully conduct the SKA science experiments outlined in subsection 5.2.1, the engineering design of the SKA must fulfill the basic specifications given in Table 5.1. In order to meet these stringent design specifications, low cost broadband antenna structures and low noise receiver technologies are required in receiving the celestial SOIs [160]. Further, low power ADCs and efficient high throughput data transfer networks are required to move raw or partially processed data to the main processing center at the rate of several hundred Gbps [111]. The data processing requirement in the main processing center can be as high as several Exa-FLOPs<sup>3</sup> [111]. The processed data throughput of the main processing center is expected to be in the range of hundreds of Giga-bytes per second [111]. Hence, high density data storage systems associated with fast data retrieval technologies are required to store the processed data

---

<sup>3</sup>An Exa-FLOP accounts for  $1 \times 10^{18}$  floating-point operations per second.

Table 5.1: The System Specifications for the SKA - Phase-I [170]

Parameter	Specifications
Frequency Range	70 MHz - 10 GHz
Sensitivity (see (5.1))	$5000 \text{ m}^2\text{k}^{-1}$ ; for 70 MHz - 300 MHz
Field of View (FoV)	$200 \text{ deg}^2$ ; for 70 MHz - 300 MHz $1 - 200 \text{ deg}^2$ ; for 300 MHz - 1 GHz $1 \text{ deg}^2$ ; for 1 GHz - 10 GHz
Survey Speed	$4 \times 10^4 - 2 \times 10^{10} \text{ m}^4/\text{k}^{-2}\text{deg}^2$
Figure of Merit (see (5.2))	(Depending on the receiver technology and frequency)
Angular Resolution	$< 0.1 \text{ arcseconds}$
Number of Spectral Channels	16,384; per band per baseline
Calibrated Polarization Purity	10,000:1 (i.e. 40 dB)
Dynamic Range for the Synthesized Image	$> 10^6$

and provide access to the hundreds of online users all around the world.

For the SKA, non traditional antenna technologies have been investigated for the synthesis of nearly one million square meters of collecting area for receiving celestial EM radiation [111]. In order to achieve the required sensitivity, the design of antennas should supplement the design of receiver systems. For the SKA, the key design factors for the antenna systems are the efficiency, frequency coverage, cost and multi-beamforming capabilities where the key feature of the receiver design are the low noise capabilities, cost and the compactness [111]. Based on the above factors, three key antenna technologies have been selected to cover the 70 MHz to 10 GHz frequency range of the SKA. They are,

1. The sparse aperture arrays; Constructed with non-uniformly distributed dual-polarized dipole-antennas to cover the frequency band 70 MHz - 300 MHz.
2. The dense aperture arrays; Constructed with 2D-UDPAs that contains linearly-arranged wideband Vivaldi elements to cover the frequency band 300 MHz - 500 MHz.
3. The paraboloidal reflector antenna array; Constructed with non-uniformly distributed paraboloidal reflectors. Two types of receiver element arrangements are proposed for reflector arrays.
  - FPA Receiver - Each reflector is fixed with a 2D-UDPA on the focal plane. Covers the frequency band 500 MHz - 1.7 GHz.
  - Single-Pixel Receiver - Each reflector is fixed with a single wideband antenna element at the focal point. Covers the frequency band 1.7 GHz - 10 GHz.

The proposed main-core of the SKA that accounts for 50% of the collection area corresponding to the three circular regions is shown in the center of Figure 5.4 [111]. Each of the three circular regions shown in the center of Figure 5.4, which corresponds to a diameter of 5 km, will contain a sparse aperture array, a dense aperture array and a array of paraboloidal reflector antennas. The rest of the antennas will be arranged along the arms of a spiral as shown in the bottom-right corner of Figure 5.4. However, according to the latest specifications [178][179], a different arrangement has been proposed. According to that only the sparse aperture arrays and the paraboloidal reflector arrays fixed with single-pixel receivers are included in the Phase-I implementation of the SKA where the dense aperture arrays and the paraboloidal reflector arrays fixed with FPA receivers left to the Phase-II implementation of the SKA.

For most of the key science projects outlined in subsection 5.2.1 that require mapping of HI density over the sky, the SKA will be used in the aperture synthesis mode. A typical architecture of a aperture synthesis imaging system that employs multi-beamformed

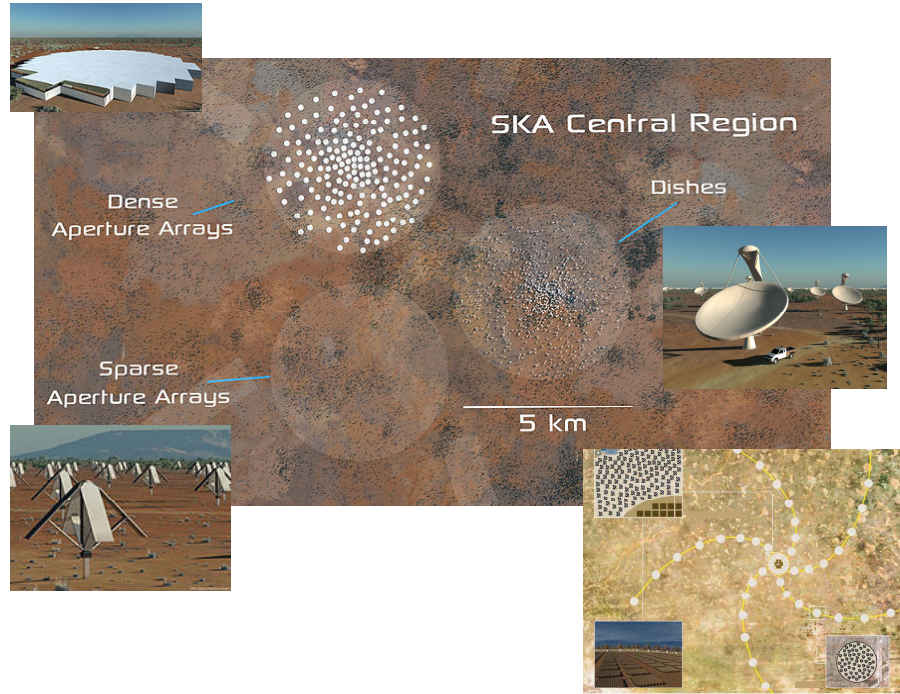


Figure 5.4: The proposed antenna systems for the SKA. (a) sparse aperture arrays, (b) dense aperture arrays and (c) paraboloidal reflector arrays. The arrangement of the antenna arrays in the main core and along the arms of a spiral. Source [170].

FPA signals [90][135][180] is shown in Figure 5.5. As shown there, first, the FPA signals are processed by a filter-bank that divides the broadband signal into a number of narrowband channels and then, the narrowband signals are processed by multiple arrays of digital beamformers, synthesizing many simultaneous sky-beams, each pointed at different directions in the sky. For a particular sky-beam associated with a single FPA, the ability of the beamformer to extract the power associated with the celestial SOIs determines the *effective beam-collecting-area*  $A_{\text{Beff}}$  [181]. Also for a particular sky-beam, the ability of the beamformer to suppress the contribution of the receiver system determines the *equivalent noise temperature for the beam*  $T_B$  [181]. Throughout the mid-frequency range, the dominant components of  $T_B$  are the equivalent ground noise and the equivalent receiver noise due to noise contributions from each individual LNA, antenna element and feed-line [182]. For the entire aperture synthesis system, the total effective collecting area

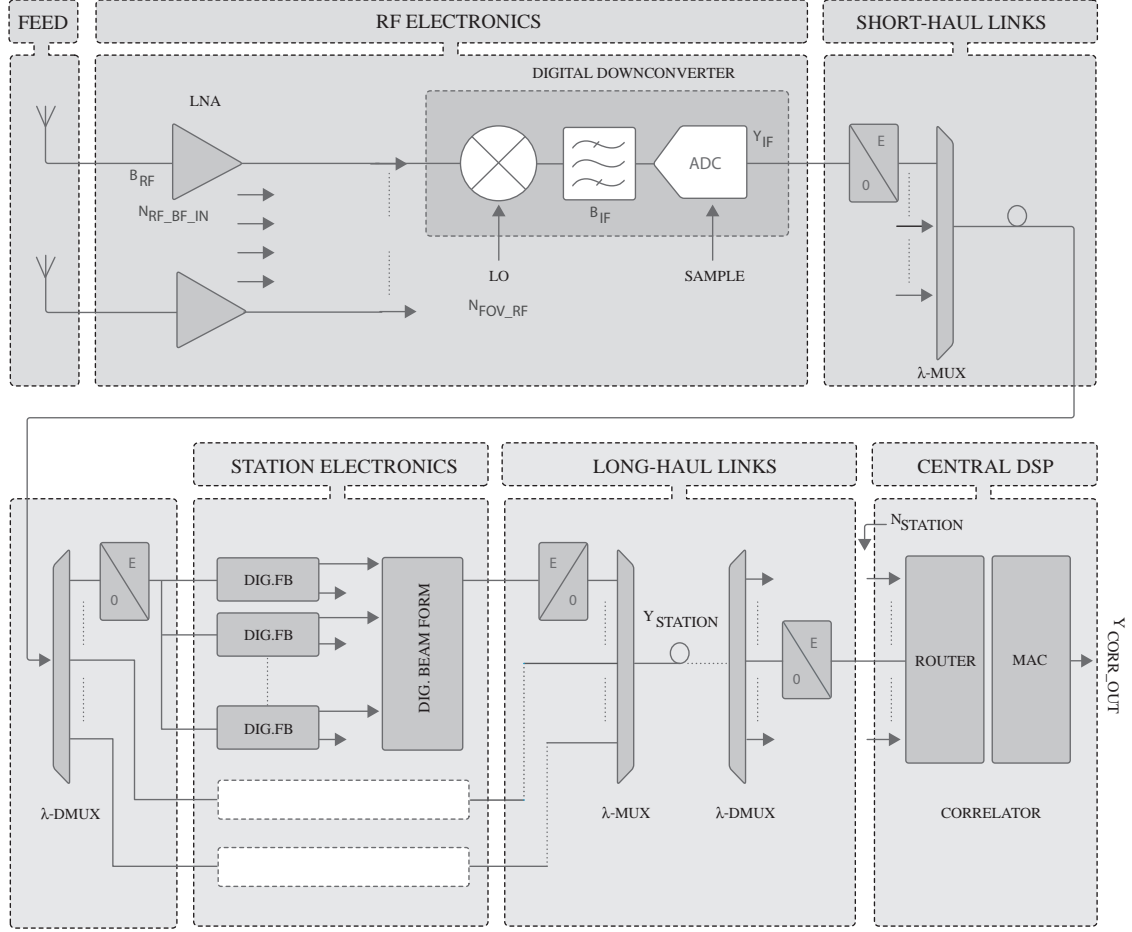


Figure 5.5: The proposed system architecture for the aperture synthesis imaging with multi-beamforming FPA signals for the SKA. Source [170].

of the system is denoted by  $A_{Teff}$  and the overall frequency-dependent *equivalent system noise temperature* is denoted by  $T_{Tsys}$ <sup>4</sup> [181]. According to [181], the performance metric of an aperture synthesis radio telescope at a particular temporal frequency is given by the total sensitivity  $S_{Tsys}$ , that is defined as

$$S_{Tsys} \triangleq \frac{A_{Teff}}{T_{Tsys}}. \quad (5.1)$$

In the design of aperture synthesis radio telescopes such as the SKA, much effort is dedicated to reducing  $T_{LNA}$  because its effects are critical for achieving the required  $S_{Tsys}$

<sup>4</sup>Note that here, 'T' in the subscripts refers to total system-wide parameters.

[182][183]. Given that the instantaneous field of view achieved with multi-beamforming is  $\mathbf{FoV}$ , the measure of the sky survey speed of this aperture synthesis system is defined as

$$\text{Survey Speed Figure-of-Merit} \triangleq S_{\text{Tsys}}^2 \times \mathbf{FoV}, \quad (5.2)$$

[164].

For pulsar searches, pulsar timing studies and pulsar profile studies, the aperture synthesis mode of the SKA is not applicable. In case of pulsar searches, the channelized-narrowband beamforming method may be used because the non-coherent dedispersion method employs channelized signals [161]. However, for pulsar timing studies and pulsar profile studies, the coherent dedispersion method is employed in order to recover the intrinsic sharp pulses. According to [168], the accuracy of the pulsar profiles and therefore the pulsar timings are proportional to the instantaneous bandwidth of the signal that is subjected to coherent dedispersion. Hence for such studies, an architecture that facilitate broadband front-end processing and broadband beamforming (e.g. the architecture shown in Figure 5.1) is much suited.

### 5.3 FPA Signals and the Corresponding Spectra

In the following, a detailed mathematical analysis is given on the characteristics of the signals and the corresponding spectra at various stages of the signal processing architecture of a FPA receiver, which is assembled on the focal plane of a *circular-aperture prime-focus paraboloidal reflector* as shown in Figure 5.1. Here it is assumed that the composite focal EM field consists of dish-reflected celestial SOIs, off-dish RFI signals and contaminating radiation from the thermal sources in the vicinity on the ground that are arriving from range of directions as shown in Figure 5.6. The electronic signal observed at the output of each elemental-antenna in the FPA in response to the composite focal EM field is amplified by a *matched LNA* [75]. However at the output of each LNA, the

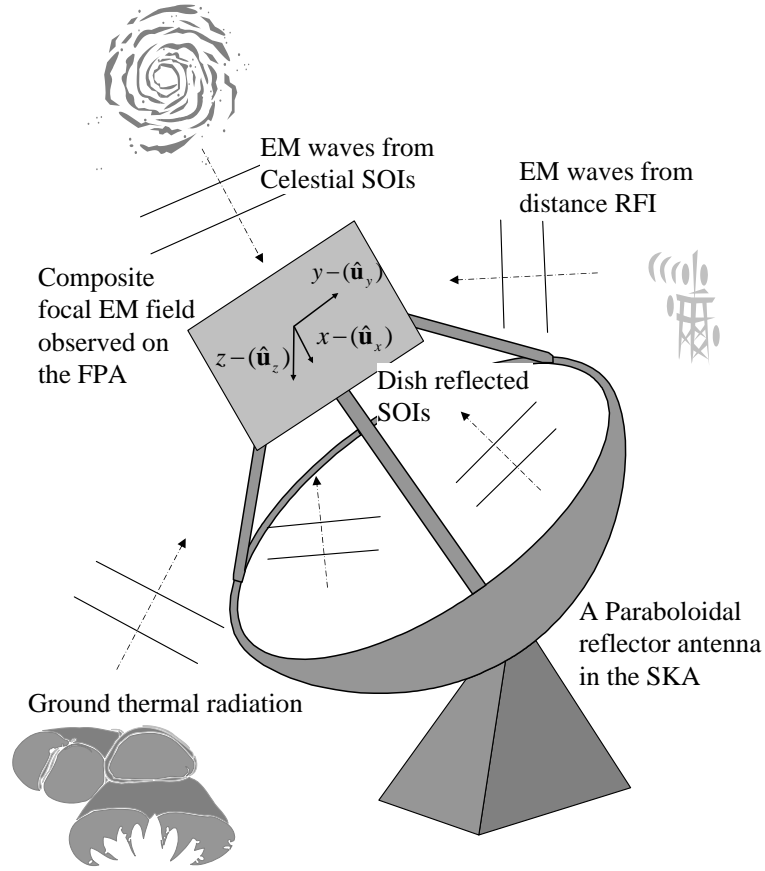


Figure 5.6: A typical scenario of focal EM field reception by the FPA. The composite focal EM field is consisted of dish-reflected celestial SOIs, RFI from far away terrestrial transmitters and ground noise radiation, which are arriving from different directions.

antenna response is contaminated with receiver noise. Receiver noise mainly consists of LNA-noise and thermal noise due to the Ohmic resistance in the elemental-antennas and feed-lines [184].

The PHAD [20] by DRAO, the APERTIF by ASTRON [165] and the “checkerboard array” by ASKAP [166] are three FPA prototypes that have been employed in proof-of-concept path-finder projects for the SKA. The checkerboard array employs rectangularly-distributed wideband patch-antennas [166] where as the PHAD and the APERTIF employ wideband Vivaldi-elements [20][165]. In the PHAD [20] and in the APERTIF [165], two Vivaldi elemental-antennas are fixed perpendicular to each other at each sample-



point on a square-grid in order to receive the two orthogonal linear polarizations. Also, the PHAD contains “matched dummy-elements” around the edge of the rectangular array outside of elements that are connected to matched receivers [20]. As explained in section 2.4, this results in a *pseudo-infinite 2D array*, where the active element patterns of all elements connected to matched receivers, are almost identical [53].

Consider a *pseudo-infinite* FPA consisted of  $(2N_x + 1) \times (2N_y + 1)$  linear  $\hat{\mathbf{u}}_x$ -polarized elemental-antennas<sup>5</sup>, arranged in a square grid at intervals  $\Delta_{xy}$ , as shown in Figure 5.1, where each of the elemental-antennas is connected to a matched LNA as in the case of 2D-UDPA, which has been analyzed in section 2.4 and section 2.5. As derived there, in order to “fully sample” [162] the composite focal EM field while avoiding spatial aliasing, the inter-elemental distances  $\Delta_{xy}$  of the FPA should be selected as  $\Delta_{xy} \leq 0.5\lambda_{\min}$ . Here,  $\lambda_{\min}$  is the minimum wavelength that is associated with the maximum temporal frequency  $f_{\max}$  such that  $\lambda_{\min} = c/f_{\max}$ , for a particular FPA design that is expected to cover the temporal frequency band  $|cf_{ct}| \in [f_C - 0.5BW, f_C + 0.5BW]$ , where  $f_{\max} = f_C + 0.5BW$ . For the following analysis, the inter-element distance for the FPA has been selected as  $\Delta_{xy} = 0.5\lambda_{\min} = 0.5cf_{\max}^{-1}$ . At particular temporal frequency, the directional response of each antenna element is determined by the active element pattern [53]. An example of the active element pattern of the PHAD is shown in Figure 2.9 (see page 42). In the following analysis the DOA of the propagating EM waves are measured with respect to the axis system shown in Figure 5.6. In this axis system, the focal plane is assigned as the  $z = 0$  plane (i.e.  $xy$ -plane), which allows direct comparison with the analysis that has been done in section 2.4 and section 2.5 regarding the use of 2D-UDPAs for receiving EM BB-BP ST PWs.

Following Figure 5.6, the composite focal EM field  $\mathbf{cfp}(x, y, z, t)$  may be expressed in

---

<sup>5</sup>For simplicity, only outputs of the elemental-antennas arranged along the  $\hat{\mathbf{u}}_x$ -direction are considered for the analysis. Nevertheless, a similar analysis could be conducted for the other group of elemental antennas, which are perpendicular to the first group.

the form

$$\mathbf{cfp}(x, y, z, t) = \mathbf{soi}(x, y, z, t) + \mathbf{rfi}(x, y, z, t) + \mathbf{g}\eta(x, y, z, t), \quad (5.3)$$

where  $\mathbf{soi}(x, y, z, t)$  corresponds to the dish-reflected celestial SOIs,  $\mathbf{rfi}(x, y, z, t)$  corresponds to the combination of off-dish RFIs and  $\mathbf{g}\eta(x, y, z, t)$  corresponds to the component of ground-noise radiation picked up by the FPA. According to section 2.4 and section 2.5 of chapter 2, the signal  $a_{[n_x, n_y]}(t)$  observed at the output of  $[n_x, n_y]^{\text{th}}$  elemental antenna of the FPA, where  $n_x \in [-N_x, N_x]$  and where  $n_y \in [-N_y, N_y]$ , in response to the composite focal EM field  $\mathbf{cfp}(x, y, z, t)$  is given by

$$a_{[n_x, n_y]}(t) = \int\limits_{x, y, z = -\infty}^{+\infty} \{\mathbf{ai}(x, y, z, t) \odot \odot \odot \odot \mathbf{ecfp}(x, y, z, t)\} \delta(x - \Delta_{xy} n_x) \delta(y - \Delta_{xy} n_y) \delta(z) dx dy dz, \quad (5.4)$$

where  $\mathbf{ai}(x, y, z, t)$  is the vector-valued antenna impulse response corresponding to the elemental antennas of the pseudo-infinite FPA and  $\mathbf{ecfp}(x, y, z, t)$  of is the electric field component of  $\mathbf{cfp}(x, y, z, t)$ . Note that  $\odot \odot \odot \odot$  denotes the combined vector dot-product and 4D convolution operation. The relationships among the vector-valued antenna impulse response  $\mathbf{ai}(x, y, z, t)$ , the vector-valued antenna frequency response  $\mathbf{AF}(f_x, f_y, f_z, f_{ct})$ , the antenna response pattern  $\mathbf{AR}_C(\theta, \phi, f_{ct})$  and the active element pattern  $\mathbf{AT}_C(\theta, \phi, f_{ct})$  have been discussed in detail in section 2.4. For simplicity, only the signals observed at the outputs of the group of linearly-polarized elemental antennas of the FPA, which are arranged along the  $\hat{\mathbf{u}}_x$ -direction (see Figure 2.8), are considered in the following analysis. Therefore, the corresponding vector-valued the antenna impulse response and the vector-valued antenna frequency response may be expressed as  $\mathbf{ai}(x, y, z, t) = a_{ix}(x, y, z, t) \hat{\mathbf{u}}_x$  and  $\mathbf{AF}(f_x, f_y, f_z, f_{ct}) = AFX(f_x, f_y, f_z, f_{ct}) \hat{\mathbf{u}}_x$ , respectively, where  $a_{ix}(x, y, z, t) \xleftrightarrow{4\text{D-CDFIT}} AFX(f_x, f_y, f_z, f_{ct})$ .

### 5.3.1 Elemental-antenna Response to Dish-Reflected Celestial SOIs and the Corresponding Spectra

The FFS program, which has been explained in chapter 3, can be used to model the focal region electric fields of a given paraboloidal reflector arrangement. For example, a typical instantaneous  $\hat{\mathbf{u}}_x$ -component  $soix(x, y, z, t)$ , of the focal electric field of  $\mathbf{soi}(x, y, z, t)$ , that is observed on the aperture of the FPA at time  $t = t_0$  is shown in Figure 5.7. Here, in this arrangement, a FPA of size  $(1.8 \times 1.8) = 3.24 \text{ m}^2$  is assembled on the focal-plane  $z = 0$ , which is centered at the focal-point of a circular-aperture prime-focus paraboloidal reflector having the focal length  $F = 6.75 \text{ m}$  and diameter  $D = 15 \text{ m}$  (i.e.  $F/D = 0.45$ ). The focal EM field is generated in response to a strong circular-polarized broadband EM wave, which occupies the temporal frequency band  $|cf_{ct}| \in [0.5, 1.7] \text{ GHz}$ , emanating from a celestial point-source in the sky at the angular position  $\theta_0 = 2.25^\circ$  and  $\phi_0 = 33.5^\circ$  with respect to the axis of the paraboloid (see Figure 5.6). Note that all most all the power of the BB-BP ST PW that is incident on the paraboloidal reflector is now diffracted onto a “focal-spot” [136] on the FPA. If the point-source moves to a new position within a small angular range, correspondingly the focal-spot also moves in the opposite direction on the focal plane. It has been observed that the displacement of the focal-spot primarily depends on the  $F/D$ -ratio of the paraboloidal reflector<sup>6</sup>. However, as the point-source moves further away from the axis of the paraboloid, portions of the signal power may now be diffracted away from the finite size FPA, such that parts of focal-spot may fall outside of the FPA. This implies that the sensitivity of the FPA received celestial signals emanating from point-sources is gradually reduced as those point-sources move away from the axis of the paraboloid. Note that for broadband celestial signals, the low frequencies are subjected to higher reduction in sensitivity compared to high frequencies. Hence

---

<sup>6</sup>The displacement of the focal-spot with respect to the movement of the celestial point-source is important in the design of 3D beamforming frustum filters for receiving pulsar signals arriving from off-axis directions.

A typical distribution of the  $\hat{\mathbf{u}}_x$  – component of the focal-plane electric field

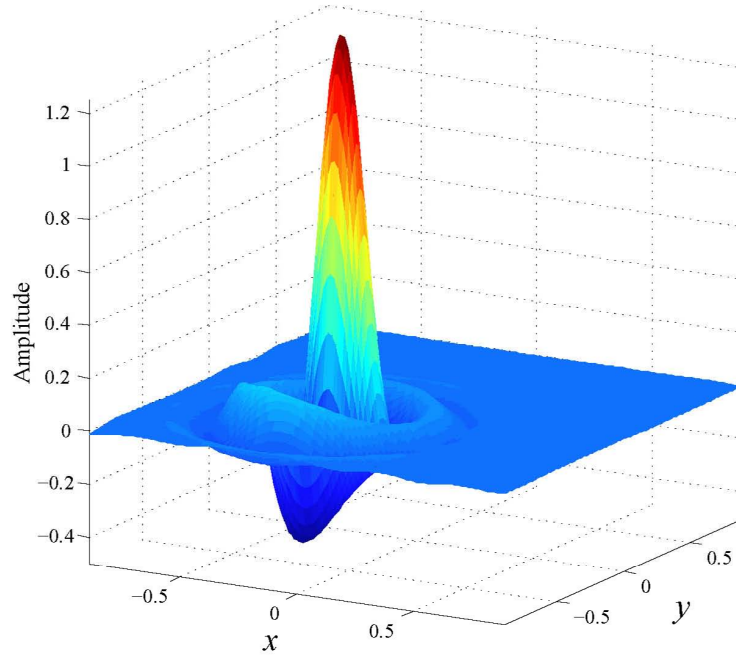


Figure 5.7: A typical instantaneous amplitude distribution of the  $\hat{\mathbf{u}}_x$ -component  $soix(x, y, z, t)$  of the electric field on the focal-plane  $z = 0$ , which is observed at time  $t = t_0$ , in response to dish reflected EM BB-BP ST PW emanating from a point source at the angular position  $\theta_0 = 2.25^\circ$  and  $\phi_0 = 33.5^\circ$ .

for a particular reflector-FPA arrangement, the field of view (FoV) specifies the angular range around the paraboloidal-axis, that facilitates a certain sensitivity level at a given frequency. The FFS may also be used in determining the FoV for a given reflector-FPA arrangement. Assume a circular-aperture prime-focus paraboloidal reflector having the focal length  $F = 6.75$  m and the diameter  $D = 15$  m (i.e.  $F/D = 0.45$ ), a FPA that contains elemental-antennas connected to receivers occupying an area of  $3.24\text{m}^2$ , and where the lowest frequency of interest of the receiver is  $0.5$  GHz. For this paraboloidal-reflector-FPA arrangement, the group of circular contour-lines  $|soix(x, y, z = 0, t = t_0)| = 0.1$  of the main lobe of the focal electric field generated by a group of narrowband point-sources of temporal frequency  $cf_{ct} = 0.5$  GHz that are located in the sky at the angular positions specified by  $(\theta, \phi) = \{(0^\circ, 0^\circ), (2.5^\circ, 0^\circ), (2.5^\circ, 90^\circ), (2.5^\circ, 180^\circ), (2.5^\circ, 270^\circ),$

$(5^\circ, 0^\circ), (5^\circ, 90^\circ), (5^\circ, 180^\circ), (5^\circ, 270^\circ)\}$  is shown in Figure 5.8. Hence, a FoV of  $25 \text{ deg}^2$  is comfortably achieved with this arrangement at the temporal frequency  $cf_{ct} = 0.5 \text{ GHz}$ .

Following (5.4), the 1D continuous-time signal  $s_{[n_x, n_y]}(t)$ , observed at the output of  $[n_x, n_y]^{\text{th}}$  elemental-antenna in the FPA in response to the dish-reflected celestial SOIs is given by

$$s_{[n_x, n_y]}(t) = \iiint_{x, y, z = -\infty}^{+\infty} \{a_{ix}(x, y, z, t) * * * soix(x, y, z, t)\} \delta(x - \Delta_{xy} n_x) \delta(y - \Delta_{xy} n_y) \delta(z) dx dy dz, \quad (5.5)$$

where  $soix(x, y, z, t)$  is the  $\hat{\mathbf{u}}_x$ -component of the focal region electric field of  $\mathbf{soi}(x, y, z, t)$  that is generated by the dish reflected EM celestial SOIs. As derived in section 3.2.1 in chapter 3, the electric field  $\mathbf{esoi}(x, y, z, t)$  observed in the focal region of a circular-aperture prime-focus paraboloidal reflector in response to the dish-reflected EM waves arriving from celestial sources can be modeled as a collection of infinitesimal 4D EM BB-BP ST PWs. Further, it has been shown that the ROS of the spectrum  $\mathbf{ESOI}(f_x, f_y, f_z, f_{ct})$  of the focal region electric field  $\mathbf{esoi}(x, y, z, t)$  is the composite ROS of the spectra of the infinitesimal dish-reflected 4D EM BB-BP ST PWs and is specified by the 4D hyper-volume  $HV_{4CP}(f_x, f_y, f_z, f_{ct})$  for  $|cf_{ct}| \in [f_C - 0.5BW, f_C + 0.5BW]$  in the 4D frequency space  $(f_x, f_y, f_z, f_{ct}) \in \mathbb{R}^4$ . The projections of  $HV_{4CP}(f_x, f_y, f_z, f_{ct})$ , on to 4D hyper-planes  $f_z = 0$ ,  $f_{ct} = 0$  and  $f_y = 0$  are shown in Figure 3.2 (a), (b) and (c), respectively (see page 80). It has been deduced that the ROS of the spectrum of electric-field on the focal-plane  $z = 0$  (i.e.  $\mathbf{esoi}(x, y, z = 0, t)$ ) is given by the 3D double right-circular frustum that is corresponding to a 3D double right-circular cone having the half-cone angle  $\alpha_{\max}$  as shown in Figure 2.5. According to (3.3) and (3.8),

$$\alpha_{\max} = \tan^{-1}(\sin(\theta_{\max})), \text{ where } \theta_{\max} = \tan^{-1} \frac{8(F/D)}{16(F/D)^2 - 1},$$

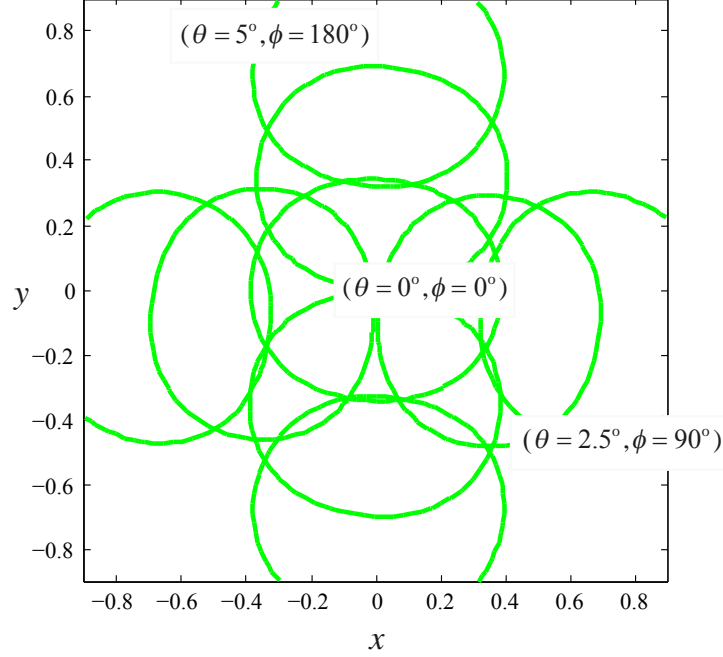


Figure 5.8: A group of contour-lines  $|soix(x, y, z = 0, t = t_0)| = 0.1$  of the main lobes generated on the FPA in response to incident narrowband EM waves of temporal frequency  $cf_{ct} = 0.5$  GHz that are emanating from group of point-sources located at the angular positions specified by  $(\theta, \phi) = \{(0^\circ, 0^\circ), (2.5^\circ, 0^\circ), (2.5^\circ, 90^\circ), (2.5^\circ, 180^\circ), (2.5^\circ, 270^\circ), (5^\circ, 0^\circ), (5^\circ, 90^\circ), (5^\circ, 180^\circ), (5^\circ, 270^\circ)\}$ . Area of the FPA ( $1.8 \times 1.8$ ) =  $3.24 \text{ m}^2$  and the circular-aperture prime-focus paraboloidal reflector having the focal length  $F = 6.75$  m and the diameter  $D = 15$  m (i.e.  $F/D = 0.45$ ).

where  $F$  is the focal-length and  $D$  is the diameter of the circular-aperture prime-focus paraboloidal reflector as shown in Figure 5.1. Note that for paraboloidal reflectors having  $F/D$ -ratios in the range  $[0.45, 0.6]$  the corresponding half-cone angle varies in the range  $[45.24^\circ, 58.11^\circ]$ . Also, it has been deduced that irrespective of the changes in the DOAs, the ROSs of the spectra of focal fields generated by EM ST PWs emanating point-sources inside the FoV of the particular reflector-FPA arrangement are given by the identical 3D frustum-shaped volume. The above results have been verified through accurate computer simulations using the FFS in subsection 3.2.2.

Let's consider the ideal infinite extent 3D mixed-domain signal-sequence  $s(n_x, n_y, t)$  that corresponds to the 1D-temporal signals  $s_{[n_x, n_y]}(t)$ ;  $(n_x, n_y) \in \mathbb{Z}^2$ , which are observed

at the outputs of elemental antennas in a hypothetical infinite-extent FPA. Following (2.61) in section 2.6, the 3D-MDFT of  $s(n_x, n_y, t)$  may be expressed in the form

$$S(e^{j\omega_x}, e^{j\omega_y}, f_{ct}) = \frac{1}{\Delta_{xy}^2} \sum_{m_x=-\infty}^{+\infty} \sum_{m_y=-\infty}^{+\infty} ASX \left( \frac{\omega_x - 2\pi m_x}{2\pi \Delta_{xy}}, \frac{\omega_y - 2\pi m_y}{2\pi \Delta_{xy}}, f_{ct} \right), \quad (5.6)$$

where  $ASX(f_x, f_y, f_{ct})$  is expressed as

$$ASX(f_x, f_y, f_{ct}) = \int_{f_z=-\infty}^{+\infty} AFX(f_x, f_y, f_z, f_{ct}) SOIX(f_x, f_y, f_z, f_{ct}) df_z, \quad (5.7)$$

where  $AFX(f_x, f_y, f_z, f_{ct})$  is the  $\hat{\mathbf{u}}_x$ -component of the antenna frequency response and  $SOIX(f_x, f_y, f_z, f_{ct})$  is the 4D-CDFT of  $soix(x, y, z, t)$ , which is the  $\hat{\mathbf{u}}_x$ -component of the focal region electric field of  $\mathbf{soi}(x, y, z, t)$ . According to subsection 2.3.2, the integral in (5.7) represent the projection of the integrand  $AFX(f_x, f_y, f_z, f_{ct})SOIX(f_x, f_y, f_z, f_{ct})$  onto the 4D hyper-plane  $f_z = 0$ . Hence, the ROS of  $ASX(f_x, f_y, f_{ct})$  in  $(f_x, f_y, f_{ct}) \in \mathbb{R}^3$  is given by the projection of the intersection of the ROSs of  $AFX(f_x, f_y, f_z, f_{ct})$  and  $SOIX(f_x, f_y, f_z, f_{ct})$  onto  $f_z = 0$  in  $(f_x, f_y, f_z, f_{ct}) \in \mathbb{R}^4$ . According to the active element pattern example of PHAD shown in Figure 2.9, for the  $\hat{\mathbf{u}}_x$ -component of a EM ST PW having a DOA corresponding to the range of inclination angles  $\theta \in [45.24^\circ, 58.11^\circ]$  the attenuation is just 2 - 4 dBs. This implies that the ROS of  $SOIX(f_x, f_y, f_z, f_{ct})$  remains inside of the ROS of the antenna response  $AFX(f_x, f_y, f_z, f_{ct})$ . Therefore, the intersection of ROSs of  $AFX(f_x, f_y, f_z, f_{ct})$  and  $SOIX(f_x, f_y, f_z, f_{ct})$  is given by the 4D hyper-volume  $HV_{4CP}(f_x, f_y, f_z, f_{ct})$ , where its projection onto the  $f_z = 0$  is the 3D double right-circular frustum that is corresponding to a 3D double right-circular cone having the half-cone angle  $\alpha_{\max}$  as shown in Figure 3.2 (a). Hence, the ROS of  $S(e^{j\omega_x}, e^{j\omega_y}, f_{ct})$ , 3D-MDFT of the ideal infinite extent signals-sequence observed at the output of the FPA in response to dish reflected celestial BB-BP SOIs, is given by an infinite array of 3D double right-circular frusta distributed at 2D interval  $(2\pi, 2\pi)$  in  $(\omega_x, \omega_y, f_{ct}) \in \mathbb{R}^3$  as shown in Figure 2.10 (see page 52). Provided the inter element distance  $\Delta_{xy} = c f_{\max}^{-1}$ , there is no spectral overlapping in the infinite periodic array of frusta for the temporal

frequency range  $|cf_{ct}| \in [f_C - 0.5BW, f_C + 0.5BW]$ . Hence, the 3D mixed domain spectra of  $S(e^{j\omega_x}, e^{j\omega_y}, f_{ct})$  in  $\mathbf{3PNR} = \{|\omega_x; \omega_y| \quad \pi \cup |f_{ct}| \quad c^{-1}f_{\max}\}$  is given by

$$S(e^{j\omega_x}, e^{j\omega_y}, f_{ct})_{[\mathbf{3PNR}]} = \frac{1}{\Delta_{xy}^2} ASX \frac{\omega_x}{2\pi\Delta_{xy}}, \frac{\omega_y}{2\pi\Delta_{xy}}, f_{ct} . \quad (5.8)$$

### 5.3.2 Elemental-Antenna Response to the Off-Dish RFI Signals and the Corresponding Spectra

For FPAs, RFI is mainly caused by terrestrial radio sources, such as spurious EM radiation from the electronic systems within the observation stations of the SKA itself, from broadcasting and wireless communication transmissions and from satellite broadcasting and communication transmissions. In the case of the RFI signals that are transmitted by satellites and received by a FPA, the ROS of the corresponding spectra is identical to the ROS of the spectra of celestial SOIs. Such interference is extremely difficult to suppress without attenuating the weak celestial SOIs that are in the angular vicinity of the RFI sources. However, the terrestrial RFI signals that are received directly by the FPA without being reflected from the paraboloidal-dish can be considered as ST PWs having typical inclination angles  $\theta \geq \theta_{\max}$  in the focal region. Therefore following sections 2.3.1 and 2.3.2, the EM field due to off-dish RFI signals  $\mathbf{rfi}(x, y, z, t)$  in the focal region can be expressed as a combination of EM 4D ST PWs such that

$$\begin{aligned} \mathbf{rfi}(x, y, z, t) &= \sum_l \mathbf{E}_{[\theta_l, \phi_l]}^{\text{Pol}} pw_{\theta_l, \phi_l}(x, y, z, t), \\ &= \sum_l \mathbf{E}_{[\theta_l, \phi_l]}^{\text{Pol}} r_l \quad c^{-1}(\sin(\theta_l) \cos(\phi_l)x + \sin(\theta_l) \sin(\phi_l)y + \cos(\theta)z) + t , \end{aligned} \quad (5.9)$$

where the typical DOA range  $\theta \geq \theta_{\max}$  and  $\phi \in [0^\circ, 360^\circ]$ .

The 1D continuous-time signal  $r_{[n_x, n_y]}(t)$  observed at the output of  $[n_x, n_y]^{\text{th}}$  elemental-



antenna in the FPA in response to the off-dish RFI is given by

$$r_{[n_x, n_y]}(t) = \int_{x, y, z=-\infty}^{+\infty} \{aix(x, y, z, t) * * * rfix(x, y, z, t)\} \delta(x - \Delta_{xy} n_x) \delta(y - \Delta_{xy} n_y) \delta(z) dx dy dz, \quad (5.10)$$

where  $rfix(x, y, z, t)$  is the  $\hat{\mathbf{u}}_x$ -component of the focal region electric field of  $\mathbf{rfi}(x, y, z, t)$  that is generated by the off-dish terrestrial RFIs. Following (2.68) in section 2.5, inside **3PNR** for the temporal frequency range  $|cf_{ct}| \in [f_C - 0.5BW, f_C + 0.5BW]$ , the 3D-MDFT  $R(e^{j\omega_x}, e^{j\omega_y}, f_{ct})$  of an ideal infinite extent 3D mixed-domain signal-sequence  $r(n_x, n_y, t)$ , may be expressed as

$$R(e^{j\omega_x}, e^{j\omega_y}, f_{ct})_{[\mathbf{3PNR}]} = \frac{1}{\Delta_{xy}^2} \sum_l AFX_{[d_{zl}]} \frac{\omega_x}{2\pi\Delta_{xy}}, \frac{\omega_y}{2\pi\Delta_{xy}}, f_{ct} \times CR_l(cf_{ct}) \delta(d_{xl}f_{ct} - \frac{\omega_x}{2\pi\Delta_{xy}}) \delta(d_{yl}f_{ct} - \frac{\omega_y}{2\pi\Delta_{xy}}). \quad (5.11)$$

where  $AFX_{[d_{zl}]}(f_x, f_y, f_{ct})$  is defined in (2.64) such that,

$$AFX_{[d_{zl}]}(f_x, f_y, f_{ct}) \triangleq \int_{f_z=-\infty}^{+\infty} AFX(f_x, f_y, f_z, f_{ct}) \delta(d_{zl}f_{ct} - f_z) df_z,$$

and where  $CR_l(cf_{ct}) \delta(d_{xl}f_{ct} - f_x) \delta(d_{yl}f_{ct} - f_y)$  represents the spectrum of the  $l^{\text{th}}$  RFI signal observed on the focal-plane  $z = 0$ . In section 2.5, it has been shown that inside the **3PNR**, the ROS of  $R(e^{j\omega_x}, e^{j\omega_y}, f_{ct})$  is given by the lines of intersection between  $f_x = \sin(\theta_l) \cos(\phi_l) f_{ct}$  and  $f_y = \sin(\theta_l) \sin(\phi_l) f_{ct}$ , for all  $l$ , where  $d_{xl} = \sin(\theta_l) \cos(\phi_l)$  and  $d_{yl} = \sin(\theta_l) \sin(\phi_l)$ . Given that  $\theta_l \geq \theta_{\max}$ , the inclination angles  $\alpha_l$  between the axis  $f_{ct}$  and the lines of interaction are in the range  $[\alpha_{\max}, 45^\circ]$ . If received by the PHAD, RFI EM ST PWs arriving along the ranges of DOAs that correspond to inclination angles  $\theta \geq \theta_{\max}$ , where typical  $\theta_{\max} \in (45^\circ, 58^\circ)$ , are subjected to attenuations of 2.5 - 15 dBs as shown in Figure 2.9. Also, note that for RFI EM ST PWs arriving along  $\theta \geq 90^\circ$ , the attenuation can be as high as 30 dB due to the back-plane of the FPA and therefore

can be ignored. Hence, it can be shown that inside the **3PNR**, the range of ROSs of the spectra of signals induced in the array of elemental-antennas in response to off-dish RFIs  $R(e^{j\omega_x}, e^{j\omega_y}, f_{ct})$ , is given by the 3D volume between the two surfaces of 3D double right-circular frusta that corresponds to half-cone angles  $\alpha_I = \alpha_{\max}$  and  $\alpha_U = 45^\circ$ , respectively. *Hence, ideally there is no intersection between the ROSs of  $R(e^{j\omega_x}, e^{j\omega_y}, f_{ct})$  and  $S(e^{j\omega_x}, e^{j\omega_y}, f_{ct})$ , which corresponds to the spectrum of FPA signals in response to celestial SOIs.*

### 5.3.3 Elemental-Antenna Response to the Ground Thermal Noise and the Corresponding Spectral-Density

The ground thermal noise is due to the radiation from distributed thermal sources such as rocks, earth, foliage, ect., at the vicinity of the paraboloidal reflector antenna [184][185]. Here, distributed ground noise sources are modeled as a collection of independent point radiators and the corresponding EM field in the focal region  $\mathbf{g}\eta(x, y, z, t)$ , is approximated by a superposition of EM ST PWs radiated from these point radiators. As shown in Figure 5.6, the FPA is only receiving the ground radiation EM ST PWs for inclination angles  $\theta > \theta_{\max}$  because for  $\theta \leq \theta_{\max}$  the thermal radiation PWs are blocked by the paraboloidal-dish. Also, ground radiation EM ST PWs for inclination angles  $\theta > 90^\circ$  are effectively blocked by the back-plane of the FPA. Here, the thermal noise contribution from the reflector is ignored because its *brightness-temperature is only a small fraction of its actual temperature due to the low emissivity* [185]. It has been proposed in [186] to cover the “hot-ground” in the vicinity of the paraboloidal reflector with a conducting mesh in order to shield the FPA from ground thermal noise radiation.

The 1D continuous-time signal  $g_{[n_x, n_y]}(t)$  observed at the output of  $[n_x, n_y]^{\text{th}}$  elemental-

antenna in the FPA in response to the ground noise is given by

$$g_{[n_x, n_y]}(t) = \int_{x, y, z = -\infty}^{+\infty} \{a_{ix}(x, y, z, t) * * * g_{\eta x}(x, y, z, t)\} \delta(x - \Delta_{xy} n_x) \delta(y - \Delta_{xy} n_y) \delta(z) dx dy dz, \quad (5.12)$$

where  $g_{\eta x}(x, y, z, t)$  is the  $\hat{\mathbf{u}}_x$ -component of the focal region electric field of  $\mathbf{g}_{\eta}(x, y, z, t)$  that is generated by the ground noise sources. Following the arguments given in sections 5.3.1 and 5.3.2, it can be shown that the range of ROS of the power spectral density (PSD) function  $\overline{\overline{G}}(e^{j\omega_x}, e^{j\omega_y}, f_{ct})$  inside the **3PNR** is given by the volume that is identical to the range of ROSs of the spectra of RFIs at the outputs of the FPA elements. However, the magnitude of PSD function  $\overline{\overline{G}}(e^{j\omega_x}, e^{j\omega_y}, f_{ct})$  is a function of the tilt-angle of the reflector.

#### 5.3.4 Signals at the Outputs of LNAs

The signal  $a_{[n_x, n_y]}(t)$  observed at the  $[n_x, n_y]^{\text{th}}$  elemental-antenna in the FPA in response to the composite focal region EM field  $\mathbf{c}_{\mathbf{fp}}(x, y, z, t)$  may be expressed following (5.3), (5.4), (5.5), (5.10) and (5.12), such that

$$a_{[n_x, n_y]}(t) = s_{[n_x, n_y]}(t) + r_{[n_x, n_y]}(t) + g_{[n_x, n_y]}(t). \quad (5.13)$$

As shown in Figure 5.1, the electric response  $a_{[n_x, n_y]}(t)$  of elemental-antennas in the FPAs are amplified by an array of identically matched LNAs. The continuous-time signal-sequence  $l_{[n_x, n_y]}(t)$ ;  $n_x \in [-N_x, N_x]$  and  $n_y \in [-N_y, N_y]$ , observed at the outputs of the array of LNAs may be written in the form

$$l_{[n_x, n_y]}(t) = a_{[n_x, n_y]}(t) + n_{[n_x, n_y]}(t), \quad (5.14)$$

where the total receiver-noise component  $n_{[n_x, n_y]}(t)$  is specified by

$$n_{[n_x, n_y]}(t) = [n_{\text{lina}}(t) + n_{\text{ant}}(t) + n_{\text{feed}}(t)]_{[n_x, n_y]} \quad (5.15)$$

where  $n_{\text{lina}}(t)$  denotes the noise component contributed by the LNA and  $n_{\text{ant}}(t)$  and  $n_{\text{feed}}(t)$  denote the thermal noise originate from the Ohmic resistances in each elemental-antenna and each feed line connecting the elemental-antennas and the LNAs, respectively [184][185]. Note that the 3D MDFT pair for the 3D auto-correlation function  $nc_{[n_x, n_y]}(t)$  of  $tn_{[n_x, n_y]}(t)$  and the PSD is given by  $nc_{[n_x, n_y]}(t) \xleftrightarrow{\text{3D-CDF}^T} \overline{\overline{NC}}(e^{j\omega_x}, e^{j\omega_y}, f_{ct})$ . If the individual components  $[n_{\text{lina}}(t)]_{[n_x, n_y]}$ ,  $[n_{\text{ant}}(t)]_{[n_x, n_y]}$  and  $[n_{\text{feed}}(t)]_{[n_x, n_y]}$  are uncorrelated for  $n_x \in [-N_x, N_x]$  and  $n_y \in [-N_y, N_y]$  then the PSD function  $\overline{\overline{NC}}(e^{j\omega_x}, e^{j\omega_y}, f_{ct})$  is uniform inside the entire **3PNR** [44]. However, It has been observed by means of numerical simulations [184] and measurement [92] that there is strong coupling of the noise between the antenna elements in an FPA that would lead to a non-uniform distribution of the total noise PSD inside the **3PNR**.

The impedance match between the elemental antennas and the input of the LNA determines the contributions of  $n_{\text{lina}}(t)$ ,  $n_{\text{ant}}(t)$  and  $n_{\text{feed}}(t)$  to the LNA output  $n_{[n_x, n_y]}(t)$  in (5.14) [187]. Hence, the output impedances of the elemental antennas must be properly matched with the input impedances of the LNAs in order to minimized the contamination of the weak celestial SOIs in FPAs and to achieve the optimum sensitivity at the outputs of the beamformers [188]. However, input matching for optimal sensitivity is complicated by noise coupling between elemental antennas [188]. In the literature, there are several noise matching techniques for phased arrays; namely, (a) the multi-port decoupling, (b) the self impedance noise matching, and (c) the active impedance matching [187]. With the active impedance matching, the elemental antennas in the FPA can be matched with the LNAs to achieve the minimum noise power for a particular beam direction [189]. Given that the active element impedance and the active element pattern of a particular phased array are uniquely interrelated [190], the input matching also determines the antenna frequency response function  $\mathbf{AF}(f_x, f_y, f_z, f_{ct})$  defined in subsection 2.4.4.

Various attempts have been made to model the noise coupling in 1D-UDAAs and

2D-UDPAs [54][191][192][193]. According to [191], the active reflection coefficient<sup>7</sup> of the array elements determines the coupling of noise between elements, which can either be measured or calculated using numerical simulations. A more detailed model that may be used to evaluate the *SNR element-patterns* of large-finite and infinite 2D-UDPAs has been proposed in [54] and it has been revised in [192] in order to include spatial correlation of thermal noise sources in the elemental antennas of a 2D-UDPA. The novel concept of SNR element-pattern may be used as a proper objective function in the optimal design of 2D-UDPA where a given sensitivity has to be achieved within a broad FoV [54]. In this model, the signal-to-noise pattern is evaluated by taking the ratio between the total signal power and the total system noise at the output after beamforming, for the beams pointed at different directions specified by the angular pairs  $(\theta, \phi)$ , where  $\theta \in (0^\circ, 90^\circ)$  and  $\phi \in (0^\circ, 360^\circ)$ . Here, the proposed model has been verified using the simulation results achieved using the method-of-moment (MoM). The large-finite array considered in [54] is consisted of 64 tapered-slot antennas<sup>8</sup> arranged in a  $8 \times 8$  uniform-square grid. The infinite arrays simulation has considered the same type of element with no truncation at the boundaries of the antenna-cell. For loss-less elemental antennas, the variation of noise contribution for the temporal band at 635 MHz from each amplifier for both large-finite and infinite arrays with the elevation angle  $\theta$  is shown by Figure 9 in [54]. As shown there, for the infinite array, the amplifier noise contribution steeply rises to the maximum as  $\theta \rightarrow 90^\circ$ . Further, with the inclusion of spatially correlated thermal noise from the lossy elemental antennas [192], the revised model clearly predicts higher system noise temperatures for  $\theta \approx 90^\circ$  as shown in Figure 3 in [192]. One of the main drawbacks of this model is that it indirectly specifies the noise spectral density only for a circular sub-region inside the boundary  $\overline{\omega_x^2 + \omega_y^2} = L_I f_{ct}^9$ , where the noise spectral density in

---

<sup>7</sup>Also referred as the scanning reflection coefficient.

<sup>8</sup>Tapered-slot antennas is the term used in referring to a more generalized group of linear-polarized wideband elemental antennas that includes Vivaldi elements [194]

<sup>9</sup>Note that the parameter  $L_I$  is depend on the inter-element distance  $\Delta_{xy}$  of the FPA.

the rest of the signal-space  $|(\omega_x, \omega_y)| \leq \pi$  is left unspecified.

A simple analytical model for the inter-element broadband noise coupling that is based on MD wave-propagation concept has been proposed in [193]. In this model, it is assumed that a part of the noise generated at the antennas, feed lines and the input terminal of the LNA are radiated by the associated elemental antenna and picked up by the adjacent elemental antennas. Here, the radiation of the EM noise wave has been modeled as a spatially decaying circular wave that is propagating along the length/surface of the 1D-UDAA/2D-UDPA. Experimental justification of this model has been attempted in [193] with the s-parameters transmission coefficient measurements made with the PHAD [92]. One of the most interesting observations made in [193] is the estimation of noise PSD of a 2D-UDPA with respect to the damping-factor associated with the decaying circular wave. According to simulation results, for strongly coupled noise waves (i.e. lower damping factors), the noise PSD is high in the region just outside the surface of a 3D right-circular frustum corresponding to half-cone angle of  $45^\circ$ . However, as the damping factor increases the inter element noise coupling becomes weaker and the noise spectral density tends to be uniform inside the **3PNR**.

### 5.3.5 The Pre-Beamforming Signal Processing and Temporal Sampling of the LNA Outputs of FPAs

The continuous-time signal from each LNA output is subjected to analog pre-processing prior to sampling and subsequent digital beamforming. First, the LNA output signals  $l_{[n_x, n_y]}(t)$ ;  $n_x \in [-N_x, N_x]$  and  $n_y \in [-N_y, N_y]$ , are amplified by an array of second-stage amplifiers. The outputs of the second stage amplifiers are bandpass filtered in order to isolate the desired frequency band of interest  $|cf_{ct}| \in [f_C - 0.5BW, f_C + 0.5BW]$ , by suppressing the out of band signals. Next, bandpass-filtered signals are frequency down converted to baseband. For this analysis, complex-quadrature frequency-downconversion [51] is assumed, where only the positive temporal frequencies of  $l_{[n_x, n_y]}(t)$  is retained. Ide-

ally the outputs  $\tilde{d}_{[n_x, n_y]}(t)$  of the complex-quadrature-downconversion process may be expressed with the corresponding *analytic functions* [51] of SOIs  $s_{[n_x, n_y]}^+(t)$ , RFIs  $r_{[n_x, n_y]}^+(t)$ , ground noise  $g_{[n_x, n_y]}^+(t)$  and receiver noise  $n_{[n_x, n_y]}^+(t)$  such that

$$\tilde{d}_{[n_x, n_y]}(t) = s_{[n_x, n_y]}^+(t) + r_{[n_x, n_y]}^+(t) + g_{[n_x, n_y]}^+(t) + n_{[n_x, n_y]}^+(t) e^{-j2\pi f_C t}, \quad (5.16)$$

where  $f_C$  is the center frequency (e.g. = 1.1 GHz) of the bandwidth of interest  $|cf_{ct}| \in [f_C - 0.5BW, f_C + 0.5BW]$  (e.g. [0.5, 1.7] GHz). According to [66] (pp. 738 - 742), the analytic function  $a_{[n_x, n_y]}^+(t)$  of any bandpassed signal  $a_{[n_x, n_y]}(t)$  is defined as

$$a_{[n_x, n_y]}^+(t) \triangleq a_{[n_x, n_y]}(t) + \frac{j}{\pi} \int_{\tau=-\infty}^{\infty} \frac{a_{[n_x, n_y]}(\tau)}{t - \tau} d\tau. \quad (5.17)$$

The corresponding transformation of the ROS of the spectrum of the SOIs due to direct down-conversion is shown in Figure 2.18 (left) (see page 70).

Each down-converted LNA output  $\tilde{d}_{[n_x, n_y]}(t)$  is subjected to synchronous sampling at the rate of  $F_S$  (e.g 1.2 GHz). Ideally the sampling process transfers the 3D-cube

$$\mathbf{V} = \{|\omega_x; \omega_y| \quad \pi \cup f_{ct} \in (-0.5F_S, 0.5F_S)\},$$

which is centered at the origin of the **3PNR**, into principle Nyquist cube, **PNC** =  $\{|\omega_x; \omega_y; \omega_t| \quad \pi\}$ , without distortion. Hence, the 3D frustum-shaped volume shown in Figure 3.3 (see page 83), which is inside of the volume **V**, is transferred into the **PNC** without distortion. The complex-valued 3D spatio-temporal sample-sequence from a FPA  $\tilde{x}(\mathbf{n})$ ,  $\mathbf{n} \equiv (n_x, n_y, n_t)$  such that  $n_x \in [-N_x, N_x]$  and  $n_y \in [-N_y, N_y]$  and  $n_t \in \mathbb{Z}$ , may be written as

$$\tilde{x}(\mathbf{n}) = \tilde{s}(\mathbf{n}) + \tilde{r}(\mathbf{n}) + \tilde{g}(\mathbf{n}) + \tilde{n}(\mathbf{n}), \quad (5.18)$$

where the complex-valued sequence  $\tilde{s}(\mathbf{n})$  corresponds to the space-time sampled SOIs,  $\tilde{r}(\mathbf{n})$  corresponds to the space-time sampled off-dish RFI,  $\tilde{g}(\mathbf{n})$  corresponds to the space-time sampled ground noise radiation and  $\tilde{n}(\mathbf{n})$  corresponds to the sampled receiver noise that include receiver noise and quantization noise.

## 5.4 Broadband Beamforming of Space-Time Sampled FPA Sequences using a Single 3D FIR Frustum Filter

A *beamforming complex-coefficient 3D FIR filter having a non-separable frustum shaped passband* is proposed here in order to selectively enhance the broadband celestial SOIs  $\tilde{s}(\mathbf{n})$  contained in the 3D complex-valued sequence  $\tilde{x}(\mathbf{n})$  that is contaminated by RFI  $\tilde{r}(\mathbf{n})$ , ground noise  $\tilde{g}(\mathbf{n})$  and receiver noise  $\tilde{n}(\mathbf{n})$ . In particular, this filter is proposed for the pre-processing of dish-reflected broadband pulsar signals, for the subsequent pulsar-timing and pulsar-profile studies. The design parameters of this beamforming complex-coefficient 3D FIR frustum filter of spatial orders  $(2N_x, 2N_y)$  and temporal order  $N_t$  include the half-cone angle  $\alpha_{\max}$  of the associated cone, the temporal bandwidth  $BW$ , and the center frequency  $f_C$  that in turn specify the shape of the frustum inside the **PNC**. However, first, a criteria that determines the ideal 3D transfer function  $H_I(\mathbf{e}^{j\omega})$ ;  $\mathbf{e}^{j\omega} \equiv (e^{j\omega_x}, e^{j\omega_y}, e^{j\omega_t})$ , of the beamformer is given in the following.

### 5.4.1 A Criteria for Determining the Ideal Transfer Function for the Beamforming 3D Filter

In subsection 5.3.1, it has been derived that the 3D ROS of the spectrum of the digitized dish-reflected broadband celestial SOIs is a 3D frustum, as shown by the shaded volume in Figure 5.9. Also in subsection 5.3.2 and subsection 5.3.3, it has been derived that the 3D ROSs of the spectra of the interfering RFI signals and ground noise signals are given by the 3D volume in between the outer 3D frustum, shown by the dashed-lines, and the inner 3D frustum, shown by the shaded region volume in Figure 5.9. Furthermore, according to the FPA noise analyses reviewed in subsection 5.3.4, it is expected that the spectral density of 3D broadband receiver noise is higher outside the shaded 3D frustum, which corresponds to the ROS of spectra of dish-reflected SOIs. Therefore, the proposed ideal transfer function  $H_I(\mathbf{e}^{j\omega})$  of the ideal beamformer  $H_I(\mathbf{z})$ ;  $\mathbf{z} = (z_x, z_y, z_t)$ , is designed



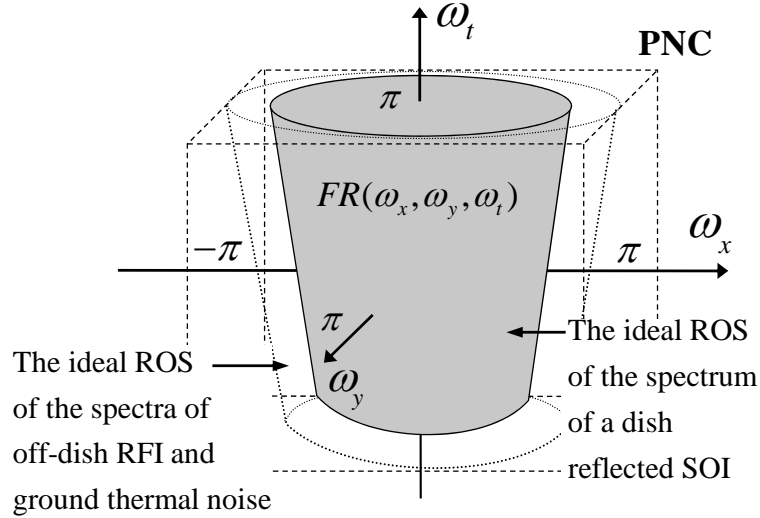


Figure 5.9: The ROSs of the spectra of the SOIs, RFIs and ground-thermal noise contained in the space-time sampled FPA signals.

such that the frustum-shaped passband closely encompasses, and therefore transmits, most of the spectral components of the dish-reflected celestial broadband SOIs to the output, where as the 3D stopband covers the 3D ROSs of the spectra of the RFI signals, of the ground noise signals and, to a large extent, of the receiver noise and therefore suppresses the off-dish undesired signals.

In order to facilitate observations for pulsar-profile studies and pulsar-timing studies that involve inherently broadband detection algorithms, *the principal objective of the broadband beamformer is to recover the broadband pulse while minimizing the distortion of it's shape*. Ideally, this requires that the magnitude response  $|H_I(\mathbf{e}^{j\omega})|$  of the ideal beamformer to be unity inside the shaded 3D frustum shown in Figure 5.9, while  $|H_I(\mathbf{e}^{j\omega})| = 0$  everywhere else in the **PNC** in order to suppress the spectral components of RFI, ground-thermal noise and part of the receiver noise. Finally, the ideal phase response  $\angle H_I(\mathbf{e}^{j\omega})$  of  $H_I(\mathbf{z})$  should be selected such that the corresponding spatial-beam is directed at the pulsar of interest<sup>10</sup>.

<sup>10</sup>Note that this particular pulsar should be within the FoV of the FPA.

The focal-spot that corresponds to a point-source at the angular position  $\theta = 0^\circ$ ;  $\phi = 0^\circ$ <sup>11</sup>, is at the “focal-point” of the paraboloid. In subsection 5.3.1, it has been shown that as this point-source moves inside the FoV, away to a new angular position  $\theta = \theta_N$ ;  $\phi = \phi_N$ , the focal-spot moves from the focal-point towards the opposite direction of the movement of the point-source. Also with FFS simulations, it has been observed that the phase of the electric-field on the focal-plane in response to an off-axis point source is not exactly the linearly-shifted version of the phase of the focal-field in response to the same point-source, it is on the angular position  $\theta = 0^\circ$ ;  $\phi = 0^\circ$ . Hence, in order to direct the spatial-beam of the beamformer towards a desired point within the FoV, the ideal magnitude response,  $|H_I(\mathbf{e}^{j\omega})|$  must be *modulated across the spatial-frequency space*  $(\omega_x; \omega_y)$  [44] (pp. 25), so that the phase-center<sup>12</sup> of the transfer function  $H_I(\mathbf{e}^{j\omega})$  coincides with the phase-center of the sampled focal field  $\tilde{a}_{[\theta_N, \phi_N]}(\mathbf{n})$  (see Figure 5.7) that resulted from a EM BB-BP ST PW emanating from a point-source at the angular position  $\theta = \theta_N$ ,  $\phi = \phi_N$ . Given the 1D temporal spectrum of the point-source is  $A_C(cf_{ct}) = 1$  in the temporal frequency band  $|cf_{ct}| \in [f_C - 0.5BW, f_C + 0.5BW]$  and  $A_C(cf_{ct}) = 0$  everywhere else in  $cf_{ct} \in \mathbb{R}$ , the ideal phase-response of  $H_I(\mathbf{z})$ , inside the shaded 3D frustum shaped volume shown in Figure 5.9, is defined as

$$\angle H_I(\mathbf{e}^{j\omega}) \triangleq -\angle A_{[\theta_N, \phi_N]}(\mathbf{e}^{j\omega}), \quad (5.19)$$

where  $\tilde{a}_{[\theta_N, \phi_N]}(\mathbf{n}) \xrightarrow{3D-DDFT} A_{[\theta_N, \phi_N]}(\mathbf{e}^{j\omega})$ . Note that  $\tilde{a}_{[\theta_N, \phi_N]}(\mathbf{n})$  act as a calibrating field and can be determined either with measurements or through numerical simulations (e.g. FFS, GRASP9, ect.).

Let's assume that a pulsar at angular position  $(\theta, \phi)$  is emanating a broadband temporal signal having an arbitrary temporal spectrum  $S_C(cf_{ct})$  such that  $S_C(cf_{ct}) = 0$ ;  $\forall |cf_{ct}| \notin [f_C - 0.5BW, f_C + 0.5BW]$ , where the corresponding space-time sampled sequence

<sup>11</sup>Measured with respect to the axis of the paraboloid.

<sup>12</sup>The phase-center is the point on the FPA that appears to be the origin of a spherical wave that spreads out to form the far-field beam pattern [96](pp. 14-6).

of the focal electric field is denoted by  $\tilde{s}_{[\theta,\phi]}(\mathbf{n})$ . Hence,  $S_{[\theta,\phi]}(\mathbf{e}^{j\omega})$ , the spectrum of  $\tilde{s}_{[\theta,\phi]}(\mathbf{n})$  may be expressed in terms of  $A_{[\theta,\phi]}(\mathbf{e}^{j\omega})$ , the spectrum of the calibrating field  $\tilde{a}_{[\theta,\phi]}(\mathbf{n})$  in the direction  $(\theta, \phi)$  such that

$$S_{[\theta,\phi]}(\mathbf{e}^{j\omega}) = S_D(e^{j\omega}) A_{[\theta,\phi]}(\mathbf{e}^{j\omega}), \quad (5.20)$$

where  $S_D(e^{j\omega})$  is the equivalent sampled temporal spectrum corresponding to the original continuous-domain spectrum  $S_C(cf_{ct})$ . Given the ideal space-time sampled FPA signal sequence  $\tilde{s}_{[\theta,\phi]}(\mathbf{n})$  is processed by the ideal beamformer  $H_I(\mathbf{z})$ , which is specified by the transfer function  $H_I(\mathbf{e}^{j\omega})$ , it can be shown<sup>13</sup> that the 1D temporal-spectrum of the 1D output sequence  $y_I(n_t)$  may be expressed as

$$Y_I(e^{j\omega_t}) = \frac{1}{(2\pi)^2} \iint_{[(\omega_x, \omega_y) \in [-\pi, \pi]]} S_{[\theta,\phi]}(\mathbf{e}^{j\omega}) H_I(\mathbf{e}^{j\omega}) d\omega_x d\omega_y. \quad (5.21)$$

Because  $|H_I(\mathbf{e}^{j\omega})| = 1$  inside the ROS of  $S(\mathbf{e}^{j\omega})$ , following (5.20) and (5.19), (5.21) can be rewritten as

$$\begin{aligned} Y_I(e^{j\omega_t}) &= \frac{S_D(e^{j\omega_t})}{(4\pi)^2} \iint_{[(\omega_x, \omega_y) \in [-\pi, \pi]]} |A_{[\theta,\phi]}(\mathbf{e}^{j\omega})| e^{j\angle A_{[\theta,\phi]}(\mathbf{e}^{j\omega})} 1 e^{-j\angle A(\mathbf{e}^{j\omega})} d\omega_x d\omega_y, \\ &= \frac{S_D(e^{j\omega_t})}{(4\pi)^2} \iint_{[(\omega_x, \omega_y) \leq \pi]} |A_{[\theta,\phi]}(\mathbf{e}^{j\omega})| d\omega_x d\omega_y. \end{aligned} \quad (5.22)$$

With different focal field patterns generated using the FFS (see chapter 3), it has been verified within the numerical limits that

$$\iint_{[(\omega_x, \omega_y) \in [-\pi, \pi]]} |A_{[\theta,\phi]}(\mathbf{e}^{j\omega})| d\omega_x d\omega_y \approx \text{Constant}, \quad (5.23)$$

therefore, according to (5.22), the ideal beamformer  $H_I(\mathbf{z})$  recovers the desired signal without any distortion.

---

<sup>13</sup>The expression in (5.21) is derived in subsection 5.4.4.

#### 5.4.2 A Combined Frequency-Sampling and 3D Window-Based Design Method for Beamforming 3D FIR Frustum Filters

For real-time processing of FPA sample-sequences, the beamforming 3D frustum filters must be implemented in high-speed digital hardware. Hence, the ideal transfer function of the beamforming 3D Frustum filter  $H_I(\mathbf{e}^{j\omega})$  must be approximated with a realizable transfer function [158]. Even with the advancement of modern MD-filter design techniques such as [195][196][197][198][199], approximating the 3D non-separable magnitude and phase responses of  $H_I(\mathbf{e}^{j\omega})$  with an efficient 3D filter-structure for practical implementation is a non-trivial task. In this section, a combined frequency sampling and window-based design method is used in approximating  $H_I(\mathbf{e}^{j\omega})$ , such that resultant transfer function can be implemented on a direct-form 3D FIR filter structure. Further, it is recognized that fine refinements of the filter-coefficients that corresponds to the 3D FIR filter structure may be necessary in order to achieve the optimum performance in practical situations.

The design of a 3D FIR frustum filter  $H(\mathbf{z})$ , for the beamforming of space-time sampled signal-sequences from a FPA that consists of  $(2N_x + 1) \times (2N_y + 1)$  elemental antennas is explained in the following. In the prototype FPAs, (e.g. the PHAD [20] and the APERTIF [165]), at each sampled point, two elemental antennas are arranged perpendicular to each other in order to receive both the  $\hat{\mathbf{u}}_x$ - and  $\hat{\mathbf{u}}_y$ - polarized components of celestial SOIs in the operational frequency band (e.g. 0.5 - 1.7 GHz). However, for simplicity, only one polarization is considered in the proposed design method for the 3D FIR frustum filter-based FPA beamformer. The design of the beamforming 3D FIR frustum filter is done in two stages. In the first stage, a prototype 3D FIR filter  $H_F(\mathbf{z})$ , having a *frustum-shaped passband of unity gain and zero-phase* is designed using the 3D window method. This prototype filter approximates the ideal transfer function  $H_I(\mathbf{e}^{j\omega})$  of the FPA beamformer directed towards a pulsar at the angular position  $\theta = 0^\circ$ ;  $\phi = 0^\circ$ ,

with respect to the axis of the paraboloid. In order to direct the spatial-beam towards a pulsar located at a general angular position  $(\theta, \phi)$  in the FoV, in the second stage of the design process, the transfer function of the prototype 3D filter  $H_F(\mathbf{z})$  is modulated by the phase  $e^{-j\angle A_{[\theta, \phi]}(\mathbf{e}^{j\omega})}$ , which has been defined in (5.19) in subsection 5.4.1. Note that  $A_{[\theta, \phi]}(\mathbf{e}^{j\omega})$  is the spectrum of the calibrating focal-field  $\tilde{a}_{[\theta_N, \phi_N]}(\mathbf{n})$ , which can be either measured or simulated.

### The Design of the Prototype 3D FIR Frustum Filter

A 3D window-based method is used in the design of the prototype 3D FIR frustum filter  $H_F(\mathbf{z})$  is explained in the following. According to the specifications of the ideal beam-former transfer function  $H_I(\mathbf{e}^{j\omega})$  given in subsection 5.4.1, the *ideal magnitude response of the 3D frustum filter*  $H_{FI}(\mathbf{z})$  is  $H_{FI}(\mathbf{e}^{j\omega}) = 1$  inside the frustum-shaped passband, which is shown by the shaded volume in Figure 5.9 that corresponds to a 3D right-circular cone having the half-angle  $\alpha_{\max}$ . Also,  $H_{FI}(\mathbf{e}^{j\omega}) = 0$  elsewhere in **PNC**. Here, the *ideal phase response of the prototype 3D FIR frustum filter*  $H_F(\mathbf{z})$ , is  $\angle H_{FI}(\mathbf{e}^{j\omega}) = 0$  in **PNC**. The *ideal 3D unit impulse response*  $\tilde{h}_{FI}(\mathbf{n})$ ;  $\mathbf{n} \in \mathbb{Z}^3$  of  $H_{FI}(\mathbf{z})$  can be evaluated by taking the 3D inverse discrete-domain Fourier transform (IDDFT) [44] of the transfer function  $H_{FI}(\mathbf{e}^{j\omega})$ . Thereby,  $\tilde{h}_{FI}(\mathbf{n})$  is evaluated by solving the triple-integral

$$\tilde{h}_{FI}(\mathbf{n}) = \frac{1}{8\pi^3} \int_{\omega_x=-\pi}^{+\pi} \int_{\omega_y=-\pi}^{+\pi} \int_{\omega_t=-\pi}^{+\pi} H_{FI}(\mathbf{e}^{j\omega}) e^{j\omega_x n_x} e^{j\omega_y n_y} e^{j\omega_t n_t} d\omega_x d\omega_y d\omega_t, \quad (5.24)$$

where

$$H_{FI}(\mathbf{e}^{j\omega}) = \begin{cases} 1; & \overline{\omega_x^2 + \omega_y^2} \leq K \tan(\alpha_{\max})(\omega_t + \omega_C), \\ 0; & \text{otherwise,} \end{cases}$$

where where  $K$  is the so-called bandwidth spread-factor defined as

$$K \triangleq \frac{F_S}{2f_{\max}}, \quad (5.25)$$

and where  $\omega_C = 2\pi f_C/F_S$ . The resultant ideal infinite extent 3D unit impulse response  $\tilde{h}_{FI}(\mathbf{n})$  is subsequently used in determining the coefficients of the proposed beamforming

3D FIR frustum filter  $H(\mathbf{z})$ .

Let's define the 1D spectral-response function corresponding to  $(n_x, n_y)^{\text{th}}$ -element such that

$$\tilde{d}_{\text{FI}}[n_x, n_y](e^{j\omega_t}) \triangleq \frac{1}{4\pi^2} \int_{\omega_x=-\pi}^{+\pi} \int_{\omega_y=-\pi}^{+\pi} H_{\text{FI}}(\mathbf{e}^{j\omega}) e^{j\omega_x n_x} e^{j\omega_y n_y} d\omega_x d\omega_y, \quad (5.26)$$

for  $\omega_t \in [-\pi, \pi]$ . Now (5.24) can be rewritten as

$$\tilde{h}_{\text{FI}}(\mathbf{n}) = \frac{1}{2\pi} \int_{\omega_t=-\pi}^{+\pi} \tilde{d}_{\text{FI}}[n_x, n_y](e^{j\omega_t}) e^{j\omega_t n_t} d\omega_t. \quad (5.27)$$

Substituting  $\omega_x = \omega_{xy} \cos(\beta)$  and  $\omega_y = \omega_{xy} \sin(\beta)$  such that  $\omega_{xy} \in [0, \omega_K(\omega_t)]$ , where  $\omega_K(\omega_t) = K \tan(\alpha_{\max})(\omega_t + \omega_C)$ , and where  $\beta \in [0, 2\pi]$ , into (5.26) yields

$$\tilde{d}_{\text{FI}}[n_x, n_y](e^{j\omega_t}) = \frac{1}{4\pi^2} \int_{\omega_{xy}=0}^{\omega_K(\omega_t)} \int_{\beta=0}^{2\pi} \omega_{xy} e^{j\omega_{xy}(n_x \cos(\beta) + n_y \sin(\beta))} d\omega_{xy} d\beta, \quad (5.28)$$

Following [158] (pp. 147 - 148) and [42] (pp. 30 - 31), (5.28) can be evaluated as

$$\begin{aligned} \tilde{d}_{\text{FI}}[n_x, n_y](e^{j\omega_t}) &= \frac{1}{2\pi} \int_{\omega_{xy}=0}^{\omega_K(\omega_t)} \omega_{xy} J_0 \left( \omega_{xy} \sqrt{n_x^2 + n_y^2} \right) d\omega_{xy}, \\ &= \frac{\omega_K(\omega_t)}{2\pi} \frac{J_1 \left( \omega_K(\omega_t) \sqrt{n_x^2 + n_y^2} \right)}{\sqrt{n_x^2 + n_y^2}}, \end{aligned} \quad (5.29)$$

where  $J_0(\cdot)$  and  $J_1(\cdot)$  are the 0<sup>th</sup>- and 1<sup>st</sup>- order Bessel functions of the first kind, respectively [115] (pp. 218 - 220). Now (5.27) can be rewritten as

$$\tilde{h}_{\text{FI}}(\mathbf{n}) = \frac{K \tan(\alpha_{\max})}{4\pi^2 \sqrt{n_x^2 + n_y^2}} \int_{\omega_t=-\pi}^{+\pi} (\omega_t + \omega_C) J_1 \left( \sqrt{n_x^2 + n_y^2} \tan(\alpha) K(\omega_t + \omega_C) \right) e^{j\omega_t n_t} d\omega_t, \quad (5.30)$$

where closed form trigonometric expressions of  $\tilde{h}_{\text{FI}}(\mathbf{n})$  are only available for few trivial combinations in  $\mathbf{n} \equiv (n_x, n_y, n_t) \in \mathbb{Z}^3$ , such as

$$\tilde{h}_{\text{FI}}(0, 0, 0) = \frac{\pi \tan^2(\alpha_{\max}) K^2}{12} \frac{3\omega_C^2}{\pi^2} + 1 \quad (5.31)$$

and

$$\tilde{h}_I(0, 0, n_t) = \frac{(-1)^{n_t} \tan^2(\alpha_{\max}) K^2}{2\pi} \left( \frac{1}{n_t^2} - \frac{j\omega_C}{n_t} \right), \quad (5.32)$$

for  $n_t = 0$ . A numerical integration method [200] can be used to evaluate 5.30 for the rest of the combinations of  $\mathbf{n} \in \mathbb{Z}^3$ .

In order to determine the *temporally-causal* 3D unit impulse response  $\tilde{h}_C(\mathbf{n})$  of the beamforming 3D FIR frustum filter  $H_C(\mathbf{z})$  of spatial-orders  $2N_x$  and  $2N_y$  and temporal-order  $N_t$ , in this design example, the ideal unit impulse response  $\tilde{h}_I(\mathbf{n})$  is windowed by the causal cubic-window function  $w_C(\mathbf{n})$  such that

$$\tilde{h}_C(n_x, n_y, n_t) = w_C(n_x, n_y, n_t) \tilde{h}_I(n_x, n_y, n_t + 0.5N_t) \quad (5.33)$$

where  $w_C(\mathbf{n}) = 1$ ; for  $|n_x| \leq N_x$ ,  $|n_y| \leq N_y$  and  $|n_t| \leq 0.5N_t$  and  $w_C(\mathbf{n}) = 0$  otherwise.

### Phase Modulation for Directing the Beam towards a Desired Direction

The required phase response for the transfer function  $H(\mathbf{e}^{j\omega})$  of the 3D FIR frustum filter based-beamformer to direct its receiving beam towards a point source at the angular position  $\theta_N$  and  $\phi_N$  is specified in (5.19) in subsection 5.4.1. In order to achieve the specified phase response inside the 3D frustum-shaped passband of  $H_C(\mathbf{z})$ , first, the 3D-DDFT of  $\tilde{h}_C(\mathbf{n})$  is evaluated on a 3D uniform grid  $\mathbf{w}_k \equiv (w_{xk}, w_{yk}, w_{zk})$  inside the **PNC**, such that  $w_{xk} \in \{-\pi, \dots, -2\pi/2M, 0, 2\pi/2M, \dots, \pi\}$ , where  $M > 2N_x$ . Second, the ideal phase response  $\angle A_{[\theta_N, \phi_N]}(\mathbf{e}^{j\omega})$  is evaluated with the calibrating focal field sequence  $\tilde{a}_{[\theta_N, \phi_N]}(\mathbf{n})$  at each of the grid points  $\mathbf{w}_k$ . As mentioned in subsection 5.4.1,  $\tilde{a}_{[\theta_N, \phi_N]}(\mathbf{n})$  may be either measured with a strong artificial point source such as a satellite-downlink or calculated using a focal field synthesis program (e.g. FFA, GRASP9, ect.). Next, the *sampled frequency response* of the 3D FIR frustum filter-based beamformer having the beam directed at the desired angular position  $\theta_N$  and  $\phi_N$  is evaluated such that

$$H(\mathbf{e}^{j\mathbf{w}_k}) = H_C(\mathbf{e}^{j\mathbf{w}_k}) \mathbf{e}^{\angle -jA_{[\theta_N, \phi_N]}(\mathbf{e}^{j\mathbf{w}_k})}; \quad \forall \mathbf{w}_k. \quad (5.34)$$

Finally, the 3D IDFFT of  $H(\mathbf{e}^{j\omega})$  is evaluated for all  $\mathbf{n} \equiv (n_x, n_y, n_t)$  such that  $|n_x| \leq N_x$ ,  $|n_y| \leq N_y$  and  $|n_t| \leq 0.5N_t$ , that yields the filter coefficients  $\tilde{h}(\mathbf{n})$  of the beamforming 3D FIR frustum filter of spatial-orders  $2N_x$  and  $2N_y$  and temporal-order  $N_t$ .

#### 5.4.3 A Numerical Design Example of the Beamforming 3D FIR Frustum Filter

A design example of a beamforming 3D FIR frustum filter  $H_D(\mathbf{z})$  of order  $N_x = 16$ ,  $N_y = 16$  and  $N_t = 10$ , which is to be used for the front-end broadband beamforming of pulsar-timing observations and pulsar-profile studies, is considered here. The spatial-order for the frustum filter has been selected by assuming an FPA that contains 289 individual (i.e.  $17 \times 17$ ) elemental-antennas arranged in a square array as shown in Figure 5.1. The design parameters considered in this design are specified in Table 5.2. First, the coefficients  $\tilde{h}_D(\mathbf{n})$  of the beamforming 3D FIR filter  $H_D(\mathbf{z})$  are evaluated using the expressions given in (5.30), (5.31), (5.32), (5.33) and (5.34). Here, MATLAB<sup>®</sup>'s “quad” function [201] is used in evaluating (5.30) for non trivial combinations of  $\mathbf{n} \in \mathbb{Z}^3$ . Also, the calibration focal field  $\tilde{a}_{[\theta_N, \phi_N]}(\mathbf{n})$  is determined using the FFS, which has been explained in chapter 3.

The iso-surface  $|H_D(\mathbf{e}^{j\omega})| = 1/\sqrt{2}$ , which corresponds to the -3 dB level of the magnitude-response of the passband inside the **PNC**, is shown in Figure 5.10. It is observed, as expected, that the iso-surface shown in Figure 5.10 closely approximates the predicted ideal frustum-shaped passband as required for the beamforming frustum filter for  $\omega_t \in [-0.95\pi, 0.95\pi]$ .

Further analysis of the frequency-response has been conducted and the resulted cross sectional magnitude and phase responses  $H_D(\mathbf{e}^{j\omega})$  are shown in Figure 5.11. The -3 dB and -20 dB contour plots for the squared magnitude response  $|H_D(\mathbf{e}^{j\omega})|^2$  on the cross sectional plane  $\omega_t = 0.75\pi$  are shown with solid lines in Figure 5.11 (top-left) where the dashed lines indicate the edge of the ideal passband of  $H_I(\mathbf{e}^{j\omega})$  on  $\omega_t = 0.75\pi$ . Note that the -3 dB contour line of  $|H_D(\mathbf{e}^{j\omega})|^2$  coincides closely with the edge of the ideal



Table 5.2: The Design Parameters of the Beamforming 3D FIR Frustum Filter.

Design Parameter	Value
Center Frequency of the Temporal Band - $F_C$	1.1 GHz
Bandwidth of the Temporal Band - $BW$	1.2 GHz
Maximum Operational Frequency - $f_{\max}$	1.7 GHz
Minimum Operational Frequency - $f_{\min}$	0.5 GHz
Half-Cone Angle - $\alpha_{\max}$	$30^\circ$
Bandwidth Spread Factor (5.25) - $K$	0.353
Normalized Center Frequency in the <b>PNC</b> - $\omega_C$	5.76

passband. The magnitude and phase responses along the line of penetration, which is illustrated by the dot-and-dashed straight-line in Figure 5.11 (top-left), are shown in Figure 5.11 (middle-left) and Figure 5.11 (bottom-left), respectively. According to Figure 5.11 (middle-left), the average stopband attenuation is around 20 dB. It is observed that the phase response  $\angle H_D(\mathbf{e}^{j\omega})$  follows (5.19), as expected. The -3 dB and -20 dB contour plots of  $|H_D(\mathbf{e}^{j\omega})|^2$  on the cross sectional plane  $\omega_y = 0$  are shown in Figure 5.11 (top-right) along with the edges of the ideal passband on the same cross sectional plane. Similarly, the edge of the ideal passband coincides closely with the -3 dB contour line for  $|H_D(\mathbf{e}^{j\omega})|^2$ . The magnitude and phase (wrapped) responses along the axis of the frustum-shaped passband, which is illustrated by the dot-and-dashed straight-lines in Figure 5.11 (top-right), are shown by the solid lines in Figure 5.11 (middle-right) and Figure 5.11 (bottom-right), respectively. According to Figure 5.11 (middle-right), along the axis of the frustum-shaped passband the gain is approximately 0 dB for frequen-

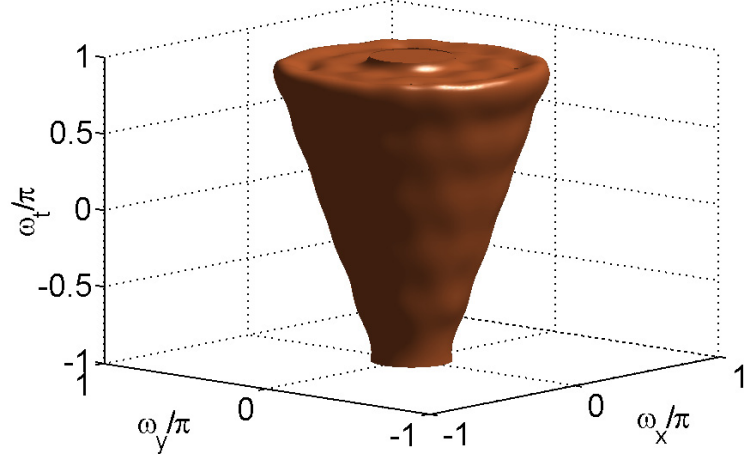


Figure 5.10: The iso-surface  $H_D(\mathbf{e}^j\omega) = 1/\sqrt{2}$  of the magnitude response of the 3D frustum filter  $H_D(\mathbf{z})$  inside the **PNC**.

cies  $\omega_t \in [-\pi, \pi]$ . Further according to Figure 5.11 (bottom-right), the phase (wrapped) response along the axis of the frustum-shaped passband of  $H_D(\mathbf{z})$  is ideally linear as expected. The above example of a typical frequency response of 3D FIR frustum filter confirms that the proposed design method in section 5.4.2 is capable of designing the beamforming 3D FIR filters that satisfy the specifications given in section 5.4.2 for near optimal FPA beamforming of broadband celestial signals.

#### 5.4.4 The 1D Output Sequence of the Beamforming 3D FIR Frustum Filter

As shown in Figure 5.2 and Figure 5.12, the input to the beamforming complex-coefficient 3D FIR frustum filter  $H(\mathbf{z})$  is  $\tilde{x}(\mathbf{n})$ , the complex-valued 3D spatio-temporal sample-sequence from the FPA pre-processors. The composition of  $\tilde{x}(\mathbf{n})$  has been discussed in subsection 5.3.5. The 1D output sequence of the proposed beamformer is given by  $\tilde{y}(n_t) = \tilde{y}_{3D}(n_x = 0, n_y = 0, n_t)$ , where

$$\tilde{y}_{3D}(n_x, n_y, n_t) = \tilde{x}(n_x, n_y, n_t) *** \tilde{h}(n_x, n_y, n_t), \quad (5.35)$$

and where  $\tilde{h}(n_x, n_y, n_t)$  is the 3D impulse response of the beamforming complex-coefficient 3D FIR frustum filter  $H(\mathbf{z})$  of order  $[2N_x, 2N_y, N_t]$ . (Note that  $***$  denotes 2D convolu-

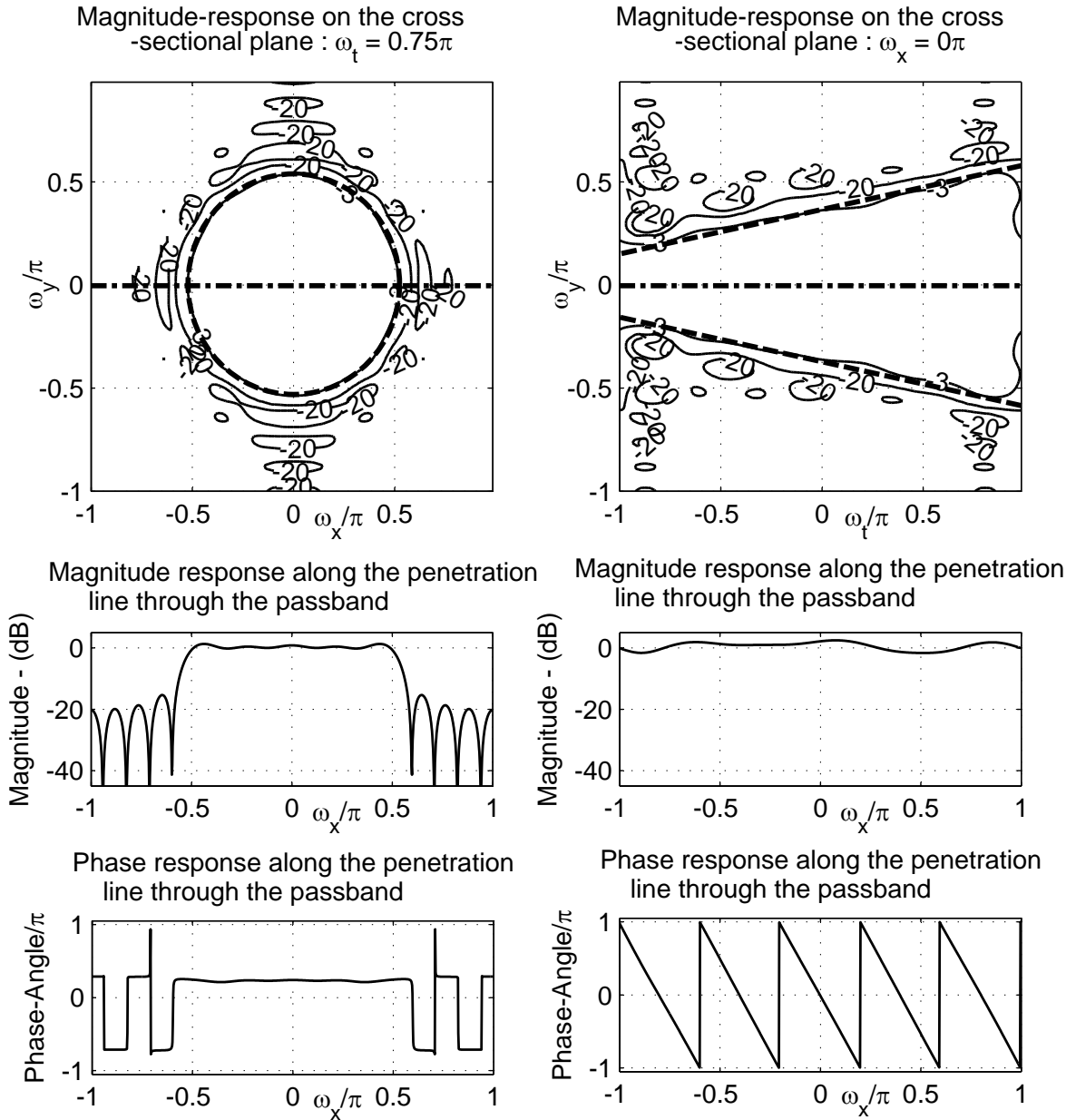


Figure 5.11: The -3 dB and -20 dB contour plots (solid) evaluated across and along the passband of the 3D frustum filter  $H_D(\mathbf{z})$  corresponding to  $H_D(\mathbf{z})$  of order  $[16, 16, 10]$  along with the edge of the ideal passband (dashed) are shown in the top-row. The magnitude and phase (wrapped) responses evaluated on the line of penetration through the passband are shown in middle and bottom rows, respectively.

tion.) Taking the 3D discrete-domain Fourier transform (DDFT) of both sides of (5.35) yields,

$$Y_{3D}(\mathbf{e}^{\mathbf{j}\omega}) = X(\mathbf{e}^{\mathbf{j}\omega}) H(\mathbf{e}^{\mathbf{j}\omega}), \quad (5.36)$$

where  $\mathbf{e}^{\mathbf{j}\omega} \equiv (e^{j\omega_x}, e^{j\omega_y}, e^{j\omega_t})$ . According to (5.18), the spectrum of the 3D input sampled sequence  $\tilde{x}(\mathbf{n})$ , is given by

$$X(\mathbf{e}^{\mathbf{j}\omega}) = S(\mathbf{e}^{\mathbf{j}\omega}) + R(\mathbf{e}^{\mathbf{j}\omega}) + G(\mathbf{e}^{\mathbf{j}\omega}) + N(\mathbf{e}^{\mathbf{j}\omega}), \quad (5.37)$$

where the 3D-DDFT pairs are denoted as

$$\tilde{x}(\mathbf{n}) \xleftrightarrow{3D-DDFT} X(\mathbf{e}^{\mathbf{j}\omega}), \quad \tilde{s}(\mathbf{n}) \xleftrightarrow{3D-DDFT} S(\mathbf{e}^{\mathbf{j}\omega}) \quad \text{and} \quad \tilde{r}(\mathbf{n}) \xleftrightarrow{3D-DDFT} R(\mathbf{e}^{\mathbf{j}\omega}).$$

Also in (5.37), the 3D DDFT pairs of the 3D noise autocorrelation functions and the corresponding power spectral density functions are given by

$$\widetilde{nc}(\mathbf{n}) \xleftrightarrow{3D-DDFT} \overline{\overline{N}}(\mathbf{e}^{\mathbf{j}\omega}) \quad \text{and} \quad \widetilde{gc}(\mathbf{n}) \xleftrightarrow{3D-DDFT} \overline{\overline{G}}(\mathbf{e}^{\mathbf{j}\omega}),$$

where  $\widetilde{nc}(\mathbf{n})$  and  $\widetilde{gc}(\mathbf{n})$  are the 3D autocorrelation functions of receiver noise  $\tilde{n}(\mathbf{n})$  and FPA ground thermal noise contribution  $\tilde{g}(\mathbf{n})$ , respectively. Following [42][44], the 1D temporal-spectrum  $Y(e^{j\omega_t})$  of the output  $\tilde{y}(n_t)$ , where  $y(n_t) \xleftrightarrow{1D-DDFT} Y(e^{j\omega_t})$ , is given by

$$Y(e^{j\omega_t}) = \frac{1}{(4\pi)^2} \iint_{[(\omega_x, \omega_y) \in [\pi, \pi]]} Y_{3D}(\mathbf{e}^{\mathbf{j}\omega}) d\omega_x d\omega_y = \frac{1}{(4\pi)^2} \iint_{[(\omega_x, \omega_y) \in [\pi, \pi]]} X(\mathbf{e}^{\mathbf{j}\omega}) H(\mathbf{e}^{\mathbf{j}\omega}) d\omega_x d\omega_y, \quad (5.38)$$

where  $\tilde{h}(\mathbf{n}) \xleftrightarrow{3D-DDFT} H(\mathbf{e}^{\mathbf{j}\omega})$ . Let the 1D temporal-spectrum of the recovered SOI corresponding to a narrow pulse is given by

$$OS(e^{j\omega_t}) = \frac{1}{(4\pi)^2} \iint_{[(\omega_x, \omega_y) \in [-\pi, \pi]]} S(\mathbf{e}^{\mathbf{j}\omega}) H(\mathbf{e}^{\mathbf{j}\omega}) d\omega_x d\omega_y, \quad (5.39)$$

and following (5.20), (5.22) and (5.34), (5.39) can be rewritten as

$$OS(e^{j\omega_t}) = \frac{S_D(e^{j\omega_t})}{(4\pi)^2} \iint_{[(\omega_x, \omega_y) \in [-\pi, \pi]]} |A_{[\theta, \phi]}(\mathbf{e}^{\mathbf{j}\omega})| |H(\mathbf{e}^{\mathbf{j}\omega})| d\omega_x d\omega_y. \quad (5.40)$$

As verified in subsection 5.4.3  $|H(\mathbf{e}^{j\omega})| \approx 1$  inside the 3D frustum-shaped passband, thus,

$$OS(e^{j\omega_t}) \approx \text{Const} \cdot S_D(e^{j\omega_t})e^{-j\omega_t N_t} \quad (5.41)$$

because

$$\iint_{[(\omega_x, \omega_y) \in [-\pi, \pi]]} |A_{[\theta, \phi]}(\mathbf{e}^{j\omega})| d\omega_x d\omega_y \approx \text{Constant},$$

according to (5.23) and because a phase shift  $e^{-j\omega_t N_t}$  is added due to the causal cubic-window function  $w_C(\mathbf{n})$  in (5.33).

The 1D spectral density function of residual attenuated receiver noise, ground thermal noise and interference is given by

$$NR(e^{j\omega_t}) = \frac{1}{(2\pi)^2} \iint_{[(\omega_x, \omega_y) \in [-\pi, \pi]]} N(\mathbf{e}^{j\omega}) + G(\mathbf{e}^{j\omega}) + R(\mathbf{e}^{j\omega}) H(\mathbf{e}^{j\omega}) d\omega_x d\omega_y. \quad (5.42)$$

Hence according to (5.41) and (5.42), the spectrum of the 3D FIR frustum filter-based beamformer is given by

$$Y(e^{j\omega_t}) = \text{Const} \cdot S_D(e^{j\omega_t})e^{-j\omega_t N_t} + NR(e^{j\omega_t}). \quad (5.43)$$

#### 5.4.5 Implementation of the Beamforming Complex-Coefficient 3D FIR Frustum Filters

The 1D output sequence  $\tilde{y}(n_t)$ , corresponding to the 3D FIR frustum filter based beamformer may be expressed as a discrete-domain convolution sum such that

$$\tilde{y}(n_t) = \sum_{m_x=-L_x}^{L_x} \sum_{m_y=-L_y}^{L_y} \sum_{m_t=0}^{N_t} \tilde{x}(m_x, m_y, n_t - m_t) \tilde{h}^*(-m_x, -m_y, m_t), \quad (5.44)$$

where “ $*$ ” denotes complex-conjugation. Note that  $L_i = N_i$ ; for  $i = x, y$ , and the FPA contains  $(2N_x + 1) \times (2N_y + 1)$  elements so that the order of  $H(\mathbf{z})$  is  $[2N_x, 2N_y, N_t]$ . Following [66],  $H(\mathbf{z})$  of order  $[2N_x, 2N_y, N_t]$  can be implemented using a 2D array of  $(2N_x + 1) \times (2N_y + 1)$  parallel-connected complex-coefficient 1D FIR filters of order  $N_t$ , as shown in Figure 5.12. Following [51], each complex-coefficient 1D FIR filter can be

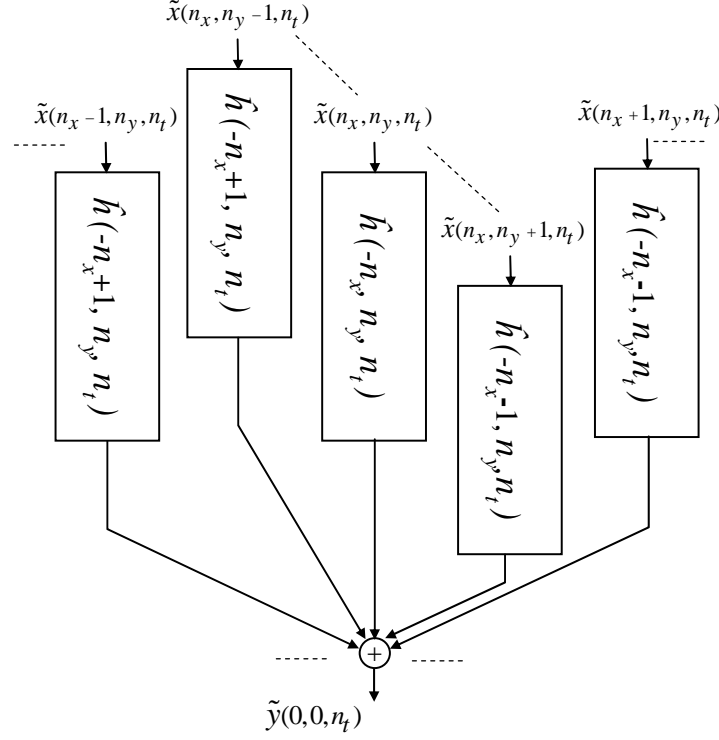


Figure 5.12: The section of the structure for the beamforming complex-coefficient 3D FIR frustum filter  $H(\mathbf{z})$  implemented with parallel connected array of complex-coefficient 1D FIR filters.

implemented with four real-valued 1D FIR filters. It follows from (5.44) that  $4(2N_x + 1)(2N_y + 1)(N_t + 1)$  real-number-multiplications and  $(4(2N_x + 1)(2N_y + 1)(N_t + 1) - 1)$  real-number-additions are required per output sample  $\tilde{y}(n_t)$ . With the proposed parallel-connected structure, the computational complexity of the filtering are divided among the 1D FIR filters. As in the case of complex-coefficient 2D FIR trapezoidal filters, by exploiting well established 1D FIR filter implementation techniques [66] (pp. 502-519), higher throughput may be achieved by employing  $(2N_x + 1)(2N_y + 1)$  parallel-connected low cost DSP hardware modules (e.g. FPGA or ASIC), where each module is dedicated to a 1D FIR filter.

## 5.5 A Comparative Study of the Broadband Signal Recovery in the Presence of Off-Dish RFI, Ground Thermal Noise and Receiver Noise

Here, the performance of the proposed real-time beamforming 3D FIR frustum filter is compared against the conventional 2D spatial-only beamformer and 3D conjugate-field-matching (CFM) beamformer that is based on a 3D FIR filter structure of the same order as the proposed 3D FIR frustum filter. The performance evaluation is based on the recovery of a dispersed pulse that is contaminated with strong off-dish RFI, thermal ground noise and receiver noise. Given that pulsars are typically weak radio sources, a group of (e.g. 100 - 1,000) 15 m FPA paraboloidal-dish receivers are needed in order to achieve the required SNR for pulsar-profile studies. For such studies, sub groups of the 1,000 - 2,000 FPA paraboloidal-dish receivers in the main-core of the SKA (see Figure 5.4) are expected to be used. Thus, for this example it is assumed that 1,000 FPA paraboloidal-dish receivers of diameter ( $D =$ ) 15 m, and focal-length ( $F =$ ) 6.75 m, are directed at a distant emulated pulsar having *an intrinsic twin-peak profile* as shown in Figure 5.13 (center-left). It is assumed that the intrinsic profile is *dispersed* while propagating through the ISM where the hypothetical “Dispersion Measure” (DM) is 0.025 [168]. The corresponding normalized original and dispersed pulses are shown in Figure 5.13 (top). The quadratic-phase of the dispersed pulse is shown in Figure 5.13 (center-right). The spectrogram of the dispersed pulse is shown in Figure 5.13 (bottom).

For the FPAs considered in this particular example the bandwidth of operations is 0.5 - 1.7 GHz. Each FPA contains ( $17 \times 17$ ) elemental antennas arranged in a square-grid with the inter-element distance  $\Delta_{xy} = 8.817$  cm as shown in Figure 5.1. The photonic responses of the FPAs are contaminated with receiver noise, ground noise and off-dish RFI spanning the bandwidth [0.74, 1.7] GHz. For this simulation, the noisy and RFI contaminated test sequences  $\tilde{x}_k(\mathbf{n})$ ;  $k = 1, \dots, 1000$  are synthesized according to the properties outlined in section 5.3 using the FFS, the focal field synthesis program introduced in chapter 3 and

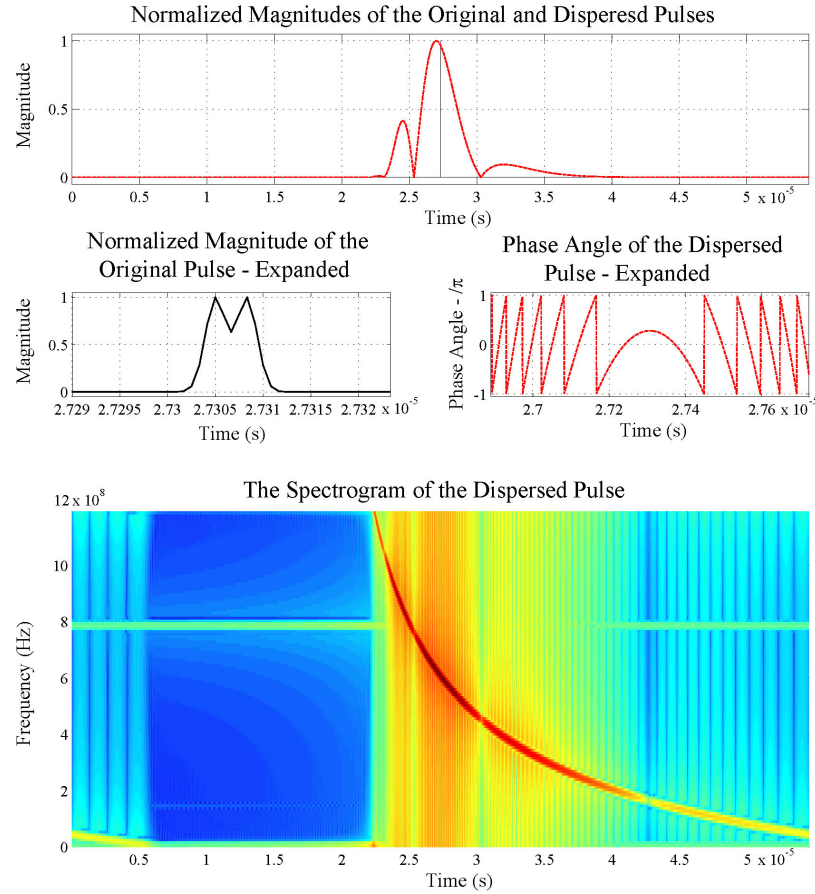


Figure 5.13: Dispersion of sharp-pulses while propagating through ISM. The normalized original pulse and the dispersed pulse (top). The expanded original pulse (center-left) and the expanded phase angle of the dispersed pulse (center-right) and the spectrogram of the dispersed pulse (bottom).

MD Fourier techniques [44][42]. Each of the 1,000 test sequences  $\tilde{x}_k(\mathbf{n})$ ;  $k = 1, \dots, 1000$  of size  $(17 \times 17 \times 2^{16})$  contains a dispersed-pulse contaminated with noise and RFI, which is sampled at the rate of 1.2 GHz. Note, each of the 289 time records of  $\tilde{x}_k(\mathbf{n})$  spans a duration of approximately 0.853 microseconds. For each  $\tilde{x}_k(\mathbf{n})$ , the signal to receiver noise ratio (SRNR) was chosen as -10 dB, the signal to ground noise ratio (SGNR) as -20 dB and the signal to interference ratio (SIR) as -30 dB.

For the purpose of comparison, each  $\tilde{x}_k(\mathbf{n})$  is processed by the proposed 3D FIR frustum filter-based beamformer, which corresponds to a cone having half-cone angle  $\alpha_{\max}$ , of order [16, 16, 10], the 2D spatial-only beamformer of order [16, 16] and the 3D



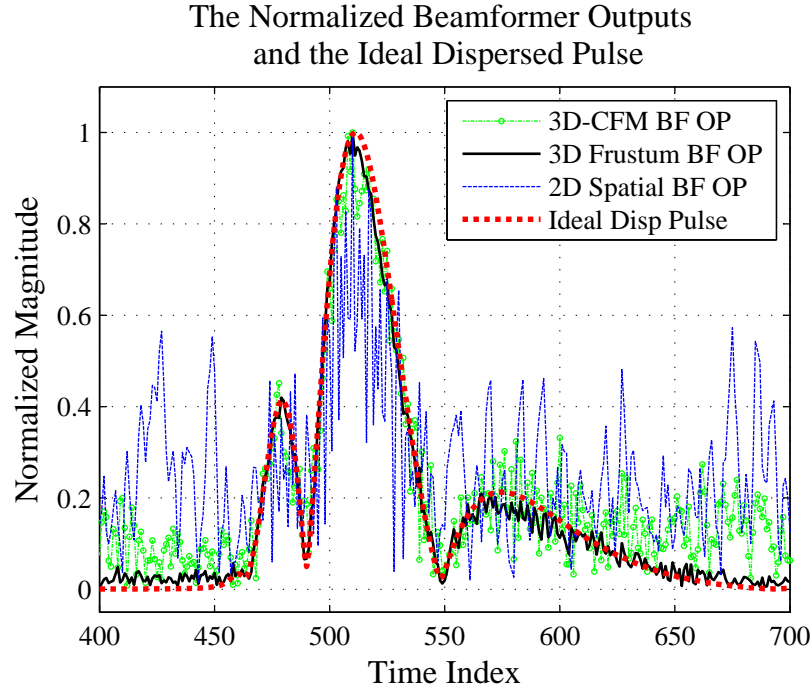


Figure 5.14: Examples of the normalized magnitudes of the recovered dispersed-pulses  $|\hat{y}_{\text{CFM}}(n_t)|$  (dot-dashed),  $|\hat{y}_{\text{Frustum}}(n_t)|$  for  $\alpha_{\text{max}} = 30^\circ$  (solid), and  $|\hat{y}_{\text{2DSP}}(n_t)|$  (dashed) along with the magnitude of the ideal-dispersed pulse (dotted).

CFM beamformer of order  $[16, 16, 10]$ . Hence, in order to evaluate one output sample  $\tilde{y}_{\text{Frustum}}(n_t)$  or  $\tilde{y}_{\text{CFM}}(n_t)$  of the proposed 3D FIR frustum filter-based beamformer of order  $[16, 16, 10]$ , or the 3D CFM beamformer of order  $[16, 16, 10]$ , it requires  $3179 = ((17 \times 17 \times 11))$  complex-arithmetic-multiply-add (CAMA) operations. However, in order to evaluate a single output sample of  $\tilde{y}_{\text{2DSP}}(n_t)$ , the 2D spatial-only beamformer of order  $[16, 16]$  requires only  $289 = (17 \times 17)$  CAMA operations.

The three groups of beamformed outputs are time aligned, averaged and normalized. The resulting three time sequences  $\hat{y}_{\text{CFM}}(n_t)$ ,  $\hat{y}_{\text{Frustum}}(n_t)$  and  $\hat{y}_{\text{2DSP}}(n_t)$  corresponding to the three beamforming methods, contain the normalized recovered dispersed-pulses. Figure 5.14 shows the examples of such normalized dispersed-pulse  $|\hat{y}_{\text{Frustum}}(n_t)|$  (solid), that has been recovered with the proposed 3D FIR frustum filter-based beamformer of order  $[16, 16, 10]$  where  $\alpha_{\text{max}} = 30^\circ$ ,  $|\hat{y}_{\text{CFM}}(n_t)|$  (dot-dashed), that has been recovered with the

3D CFM beamformer of order [16, 16, 10] and  $|\hat{y}_{2\text{DSP}}(n_t)|$  (dashed), that has been recovered with the 2D spatial-only beamformer. The ideal-dispersed pulse  $|\hat{d}(n_t)|$  (dotted), is also shown in Figure 5.14.

The mean square error (MSE) between each of the normalized-pulses and  $|\hat{d}(n_t)|$  is evaluated by

$$\text{MSE}_{[\text{CFM/Frust/2DSP}]} = \sqrt{\hat{d}_1(n_t) - \hat{y}_{[\text{CFM/Frust/2DSP}]}(n_t)}^2. \quad (5.45)$$

Note that the  $\text{MSE}_{[\text{CFM/Frust/2DSP}]}$  specify the distortion caused by the front-end beamforming methods. Table 5.3 contains the numerically evaluated MSE for the 3D CFM beamformer, the 2D Spatial-only beamformer and a group of 3D FIR Frustum filter-based beamformers corresponding to  $\alpha_{\max} = 25^\circ, 30^\circ$ , and  $35^\circ$ , respectively. According to Table 5.3 the 3D FIR frustum filter-based beamformer corresponding to  $\alpha_{\max} = 30^\circ$  achieves the minimum MSE. The high MSE value indicates that the beamforming 3D FIR frustum filter corresponding to  $\alpha_{\max} = 25^\circ$  has a smaller passband, which does not encompass the dominant spectral components of the SOI in the respective noise and RFI environments encountered in this test. On the other hand, the high MSE value indicates that the beamforming 3D FIR frustum filter corresponding to  $\alpha_{\max} = 35^\circ$  does not effectively suppress the dominant spectral components of the RFI and noise in the respective noise and RFI environment encountered in this test. Also, as expected, the 2D spatial-only beamformer performs the worst, where the MSE is more than 10 times that of the proposed 3D FIR frustum filter-based beamformer. For sensitive pulsar timing observations and pulsar profile studies the improvement of the MSE justifies the additional computational complexity of the proposed beamforming method over the 2D spatial-only beamforming. However with the same computational complexity, the MSE is 3.9 times higher for the 3D CFM beamformer compared to the proposed 3D FIR frustum filter-based beamformer. These results show that the proposed 3D FIR frustum filter based beamformer achieves lower distortion of the recovered broadband signals compared to

Table 5.3: The MSE between the Recovered Pulses and the Ideal Dispersed Pulse for the Different Beamforming Methods.

Beamforming Method	MSE
3D Conjugate Field Matching (CFM) Beamformer	0.09883
2D Spatial-Only Beamformer	0.26184
3D FIR Frustum Filter: $\alpha_{\max} = 25^\circ$	0.03120
3D FIR Frustum Filter: $\alpha_{\max} = 30^\circ$	0.02534
3D FIR Frustum Filter: $\alpha_{\max} = 35^\circ$	0.09571

the 3D CFM beamformer and 2D spatial-only beamformer.

## 5.6 Summary

In this chapter, a 3D FIR frustum filter-based beamformer has been proposed for the real-time pre-processing of FPA signals for broadband detection applications of the SKA such as pulsar timing observations and pulsar profile studies using coherent de-dispersion. The SKA will be World's largest aperture synthesis telescope upon its completion in 2020 and it is expected that the unprecedented systems sensitivity of the SKA may lead to many potential new discoveries in various branches of modern science including fundamental physics, astrophysics, cosmology and astrobiology. A description of key science projects that is expected to be conducted with the SKA observations has been given in subsection 5.2.1. Further, the specifications of the engineering design of the SKA has been outlined in subsection 5.2.2. Employing non traditional antenna technologies such as dense aperture arrays (DAAs) and focal plane arrays (FPAs) in order to increase the FoV of the aperture syntheses system is one of the key features of the SKA engineering

design.

In section 5.3, the signals received by the FPAs and the corresponding spectra have been analyzed in detail. In subsection 5.3.1, it has been shown that the power of an incident EM BB-BP ST PW emanating from a celestial point-source is concentrated to a finite size focal-spot after being reflected on the inner-surface of a circular-aperture prime-focus paraboloid. Also, it has been shown that the ROSs of the spectra of the space-time sampled FPA elemental antenna signals induced in response to dish-reflected EM waves are given by a 3D frustum inside the **PNC**. As shown there the shape of the 3D frustum is determined by the focal-length  $F$ , diameter  $D$ , of the reflector and the temporal bandwidth of the incident EM wave. As derived in subsections 5.3.2 and 5.3.3, the ROSs of the spectra of space-time sampled FPA signals that correspond to non-dish-reflected (i.e. off-dish) RFIs and ground thermal radiation are given by the 3D volume between two frusta shown in Figure 5.9. A brief review of the different noise sources in the FPA receiver system has been given in subsection 5.3.4. As given there, due to the noise coupling between elements of the FPA, the corresponding noise spectral density function is non-uniform inside the **PNC**. In subsection 5.3.5, the pre-beamforming signal processing model for the front-end of the FPA receiver has been briefly reviewed.

The design of the beamforming 3D FIR frustum filter has been explained in details in section 5.4. First, in subsection 5.4.1, the criteria for the determination of the ideal transfer function of broadband beamformer has been introduced. Here, the stopband and the passband characteristics of the 3D frustum filter have been determined such that the dominant spectral components of the receiver noise, off-dish RFI and the thermal ground noise are suppressed in the stopband while the dominant spectral components of the SOIs are enhanced in the passband. This leads to a non-separable transfer function having a non-trivial phase response. A combined frequency-sampling and 3D window-based design method has been proposed in subsection 5.4.2 in order to approximate the

required non-separable 3D transfer function of the beamforming 3D FIR frustum filter. In subsection 5.4.3, it has been verified that the proposed design method is capable of meeting the specification of the beamformer. The spectrum of the beamformer output has been briefly analyzed in subsection 5.4.4.

The numerical analysis presented in section 5.5, has confirmed that the proposed 3D FIR frustum filter-based beamformer achieves lower distortion compared to the conventional 2D spatial-only beamformer and the 3D CFM beamformer. The 2D spatial-only beamformer resulted in the highest distortion because its passband is designed considering the properties of only the center frequency of the SOIs. On the other hand for the 3D CFM beamformer, the spatio-temporal characteristics of SOIs for the entire operational bandwidth have been considered in its design however, it does not consider the spatio-temporal characteristics of off-dish RFI and ground noise.

## Chapter 6

# Finite-Word-Length Effects of Beamforming MD FIR Filters and an Example of FPGA Implementation of a Beamforming 2D FIR Filter

### 6.1 Introduction

The required throughputs for modern real-time array processing applications in wireless communications [32][34][202] and in radio astronomy [18][74][203] are in the range of several hundred mega-samples per-second (MSPS) to several Giga-samples per-second (GSPS). Such high throughputs necessitate the beamforming MD FIR filters proposed in chapter 4 and chapter 5, including those proposed in [47][55][56][59], to be implemented using finite-word-length [66][65] DSP hardware in high speed VLSI circuits [60][204][205][206][207]. Finite-word-length DSP implementation of beamforming MD FIR filters leads to the so called “quantization-noise” generation, transfer function distortion and in some instances cause errors due to adder-overflows and therefore, degrade the maximum achievable SNDR at the output of these beamforming MD FIR filters of particular order. Hence, the careful assignments of register-lengths (i.e. word-lengths) for input-data, filter-coefficients and the outputs of digital-multipliers and digital-adders are required in order to minimize the degradation of the SNDR and avoid errors in the output while minimizing the hardware complexity of the proposed beamforming MD FIR filters of the particular order.

According to chapters 4 and 5, beamforming MD FIR filters can be implemented with *parallel connected arrays of real-valued 1D FIR filter structures*. The efficient implementation of real-valued 1D FIR filters using VLSI finite-precision digital arithmetic

processors has been studied in detail in the literature [60][65][66][204][205][206][207]. For beamforming 2D FIR asymmetric-trapezoidal filters that have been proposed in chapter 4 for applications in wireless communications, the implementations must support real-time adaptation of filter coefficients. Nevertheless, for beamforming polyphase 2D FIR double-trapezoidal filters that have been proposed in [59], and for beamforming 3D FIR frustum filters that have been proposed in chapter 5 for applications in radio astronomy, the implementations must facilitate non-real time adaptation of filter coefficients. Hence, *reconfigurability* is the key aspect of the VLSI implementation of both real-time and non-real-time adaptive MD FIR filter-based beamforming methods proposed here and in [59] for applications in wireless communications and radio astronomy. In order to facilitate reconfigurability while minimizing transfer function distortion and quantization noise, here, the *parallel-connected direct-form 1D FIR filter structures* are selected for the implementation of the beamforming MD FIR filters using finite-word-length DSP hardware in VLSI circuits.

In this chapter, the distortions in the transfer functions due to finite-word-length representation of filter-coefficients of beamforming MD FIR filters are analyzed in terms of the changes in the stop-band attenuation and the passband-ripple of the corresponding transfer functions. Three examples of MD FIR filters, (a) a beamforming polyphase 2D FIR double-trapezoidal filter [59], (b) a beamforming complex-coefficient 2D FIR asymmetric-trapezoidal filter (see chapter 4) and (c) a beamforming complex-coefficient 3D FIR frustum filter (see chapter 5), are considered in this analysis. Also in this chapter, a theoretical model is developed for estimating the degradation of SNDR at the output of the beamforming MD FIR filters implemented with a parallel connected 1D FIR direct-form structures for different DSP configurations<sup>1</sup>. In order to verify the proposed theoretical model, the estimated SNDRs with the proposed model are compared against the averaged SNDRs calculated with empirical data obtained through *Monte*

---

<sup>1</sup>The assigned of word-lengths for input-data, filter-coefficients, multiplier-products and partial-sums.

*Carlo simulations* for the identical sets DSP configurations in implementing the beamforming polyphase 2D FIR double-trapezoidal filter [59] using the MATLAB *Fixed-Point Toolbox*. Finally, an example of a FPGA implementation of a beamforming MD FIR filter having a specific DSP configuration is briefly discussed here. With collaboration of Arjuna Madanayake, a then colleague of the MDSP Group, the beamforming polyphase 2D FIR double-trapezoidal filter is partially implemented in a Xilinx Virtex-4 Sx35 ff668-10 FPGA chip [67] using the “Xilinx System Generator” [208] and associated “Xilinx Block Set” for Simulink in MATLAB. Parts of the above work have been published in [68].

This chapter is arranged as follows. In section 6.2, a brief theoretical analysis is given on the sources of quantization noise and errors due to finite-word-length representation of input-data and the outputs of digital-multipliers and -adders and transfer function distortions due to finite-word-length representation of filter coefficients of MD FIR filters. The distortions of the transfer functions due to finite-word-length representation of filter-coefficients of the beamforming polyphase 2D FIR double-trapezoidal filter<sup>2</sup> [59], the beamforming complex-coefficient 2D FIR asymmetric-trapezoidal filter and the beamforming complex-coefficient 3D FIR frustum filter are studied with examples in subsections 6.3.1, 6.3.2 and 6.3.3, respectively.

In subsection 6.4.1, a theoretical model is developed for the estimation of the SNDR at the output of a beamforming MD FIR filters with the example of the polyphase 2D FIR double-trapezoidal filter-based beamformer [59] implemented with a parallel connected array of direct form 1D FIR filters. According to the proposed theoretical model, the estimates of the SNDRs are evaluated in subsection 6.4.2 for the beamforming polyphase 2D FIR double-trapezoidal filters implemented with different DSP configurations. For different DSP configurations, the average SNDRs of the beamforming polyphase 2D FIR double-trapezoidal filters evaluated with Monte Carlo simulations are given in subsec-

---

<sup>2</sup>A brief review of the polyphase 2D FIR double-trapezoidal filter-based beamformer and the proposed polyphase building block is given in subsection 6.3.1.



tion 6.4.3.

An example of the FPGA implementation of the polyphase 2D FIR double-trapezoidal filter-based beamformer with a given DSP configuration is outlined in section 6.5. An estimate of the FPGA resources required for the full implementation of this beamformer for a set of different DSP configurations is given in Table 6.2. A comparison between the outputs of the beamforming polyphase 2D FIR double-trapezoidal filter in response to a severely contaminated input 2D sample-sequence that are evaluated with floating point digital arithmetics in MATABL and with finite-word-length implementation, which is simulated with “bit-true cycle-accurate” *on-chip stepped hardware co-simulation* feature of the Xilinx Block Set for Simulink, is shown in Figure 6.17.

## 6.2 Finite-Word-Length Effects of MD FIR Filters implemented with an Array of 1D FIR Filters; A Review

In the implementation of MD FIR filters for real time applications in wireless communications and radio astronomy, filter-coefficients, input-data, products from multipliers and partial-sums from adders are stored in finite-length registers of finite-precision digital arithmetic processors [204]. Filter-coefficients and input-data are quantized and coded [62] prior to be stored in finite-length registers. At the outputs of digital-multipliers, the products are quantized because, in general the number of bits of the product between a coefficient and an input-data sample exceeds the assigned fixed register-length for that product in the filter structure. The coefficient-quantization causes *transfer function distortion* where as data and product quantization cause *quantization noise* [65](ch. 14). Both transfer function distortions and quantization noise degrade the SNDR of the output of the beamforming MD FIR filter. Further, possible overflows at the outputs of the digital-adders may cause significant errors in the output of the beamforming MD filter.

In this section, a brief theoretical analysis is given regarding the quantization noise,

the transfer function distortion and errors in MD FIR filters implemented with parallel connected arrays of real-valued 1D FIR filters due to finite-word-length representation of input-data, filter-coefficients and the outputs of digital-multipliers and -adders. Two's complement binary coding [62] and rounding-quantization [61] are assumed in the following analysis.

### 6.2.1 Input-Data Quantization

At the analog-to-digital converter (ADC), the continuous-time continuous-range input signal  $x_C(t)$  is sampled at regular time intervals  $t = nT$ ;  $n \in \mathbb{Z}$  and the values of these samples  $x_C(nT)$  are converted into a set of  $W$ -bit code-words  $\{[b_0, b_1, \dots, b_{W-1}]\}$ ;  $b_k \in [0, 1]$  for  $k = 0, 1, \dots, W-1$ . In two's complement binary coding, the value  $x_D(n)$ , of the  $W$ -bit code word  $[b_0, b_1, \dots, b_{W-1}]$  is given by

$$x_D(n) = \alpha \left( -b_0 + \sum_{k=1}^{W-1} b_k 2^{-k} \right), \quad (6.1)$$

where  $\alpha$  is a positive scaling factor [62]. The input-data quantization-error is defines as

$$e_i(n) \triangleq x_C(nT) - x_D(n), \quad (6.2)$$

[66](pp.750-753). In practice, the input signal  $x_C(t)$  can be scaled in the analog pre-processing stage such that the *probability of  $\{|x_C(nT)| \geq 1 - 2^{-W}\}$  is arbitrary small*. Under rounding-quantization process [61](pp.93-99), the maximum absolute input-data quantization error for a scaled sample sequence  $\{x_C(nT)\}$  is given by

$$\max[|e_i(n)|] = 2^{-W} \cdot \alpha. \quad (6.3)$$

With out the loss of generality from this point onwards it is assumed that  $\alpha = 1$ . In the following analysis, the input-data quantization-error  $e_i(n)$  is modeled as an *additive-noise* component that contaminates the sample  $x_C(nT)$  (see Figure 6.1 (top)).

If the dynamic range of the ADC is set to 2 (i.e. range of the ADC input is  $[-1, 1]$ ), the word-length  $W \geq 8$ -bits for the input-samples and at least few least-significant-bits<sup>3</sup>

---

<sup>3</sup>i.e. the right-most bits of the code-word

change for every input-sample then the following conditions hold for  $e_i(n)$  [66](pp. 752-753).

1.  $e_i(n)$  is uniformly distributed in the range  $[-2^{-W}, 2^{-W}]$ .
2.  $e_i(n)$  and  $e_i(m)$  are uncorrelated for  $n \neq m$ . In other words,  $e_i(n)$  is a stationary white noise sequence.
3. The error sequence  $e_i(n)$  is uncorrelated with the signal sequence  $x_C(nT)$ .

According to above conditions, the variance of the input quantization noise  $e_i(n)$  can be calculated to be  $\sigma_i^2 = 2^{-2W}/3$  [66] (pp. 753-756). Hence, it can be shown that at the output of the ADC, the signal-to-input-quantization-noise ratio (SIQNR) of a temporal sample sequence  $x_D(n)$  coded into  $W$ -bits two's-complement format, is given by

$$\text{SIQNR}_{\text{dB}} = 6.02W + 4.77 + 20 \log_{10}(\sigma_x), \quad (6.4)$$

where  $\sigma_x^2$  is the variance of  $\{x_C(nT)\}$ , which is bounded such that  $|x_C(nT)| \leq 1$  [66] (pp. 753-754). Therefore, in order to achieve the tolerable SIQNR for the beamforming application,  $W$  should be selected by considering the statistical properties (i.e.  $\sigma_x$ ) of the ensemble of scaled input signals  $x_C(t)$ . According to [209], the state of the art ADCs support different combinations of sampling rates and sample word-lengths and are available at various price ranges.

### 6.2.2 Multiplier-Product Quantization

In two's complement coding,  $(W_c + W - 1)$ -bits are typically required to represent the exact product  $(h_k \cdot x_D(n))$  of two two's-complement numbers  $h_k$  and  $x_D(n)$  of length  $W$ - and  $W_c$ -bits, respectively [62]. Given such product is to be stored in a register of  $W_m$ -bits, a product-quantization error may occurs if  $W_m < (W_c + W - 1)$  [66] (pp. 564-568). Under rounding-quantization process [66](pp. 564-568), the maximum absolute product-

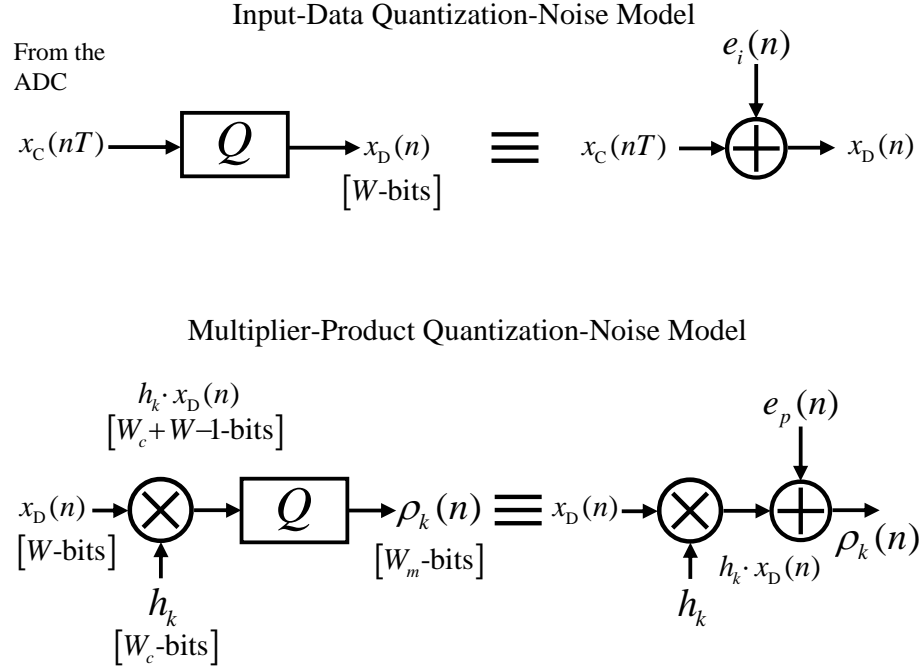


Figure 6.1: The input-data quantization-noise model (top) and the multiplier-product quantization-noise model (bottom).

quantization error is  $\max[|e_p(n)|] = 2^{-W_m}$ . In the following analysis, the multiplier-product quantization error  $e_p(n)$  is also modeled as an additive noise component contaminating the exact multiplier-product  $\rho_k(n)$  (see Figure 6.1 (bottom)). Assuming the product quantization-noise  $\{e_p(n)\}$  is uniformly distributed in the range  $[-2^{-W_m}, 2^{-W_m}]$ , is spectrally white and is uncorrelated with the product  $\rho_k(n)$ , the variance of  $\{e_p(n)\}$  can be calculated to be  $\sigma_p^2 = 2^{-2W_m}/3$  [66] (pp. 564-568 and 753-756).

The product quantization error caused by each multiplier in the MD filter structure contributes to quantization noise of the final output. However, the scale of the noise contribution at a particular multiplier is determined by the transfer function between that multiplier output and the final output of the MD filter [65](pp. 638-640). In other words, the filter structure determines the contribution of product quantization-noise in the MD filter output. Given that the proposed beamforming MD FIR filters can be implemented

as parallel connected array of 1D FIR filters, the structure of the 1D FIR filters determines the quantization noise contribution at the final output of the beamformer.

### 6.2.3 Filter Coefficient Quantization

Coefficient-quantization leads to *deterministic distortions* in the frequency transfer function of the beamforming MD FIR filters and in general reduces the stopband attenuation and increases the passband ripple [66](pp. 578-582). However for linear-phased FIR filters, the linear-phase property is not affected by the rounding-quantization of filter coefficient [66](pp. 579-580). At the output of beamforming MD FIR filters, the reduction in stopband attenuation increases the power of the interfering signals where as the increase in the passband ripple increases the distortion of the desired signal. As in the case of product quantization-noise, the 1D FIR filter structure used in the parallel connected arrays of beamforming MD FIR filters determines the effect of coefficient-quantization at the final output of the beamformer. Examples of transfer function distortion due to filter coefficient quantization are given in section 6.3.

### 6.2.4 1D Filter Structures and Their Significance in the Product Quantization Noise and the Effects of Coefficient Quantization at the Output

The three main filter structures used in the implementation of 1D FIR filters are shown in Figure 6.2. They are; (a) the direct-form (including the transposed form), (b) the cascade-form and (c) the lattice-form. The direct-form and the cascade-form structures for 1D FIR filters have essentially the same computational complexity in terms of the number of multiplications and additions per output sample is concerned [66](pp. 503-505). However, direct-form structures in general, yield lower product quantization noise compared to equivalent cascade-form structures [210][211]. On the other hand, cascade-form structures can be designed to have lower distortions of the frequency transfer function due to coefficient quantization compared to the equivalent direct-form structure [212][213].

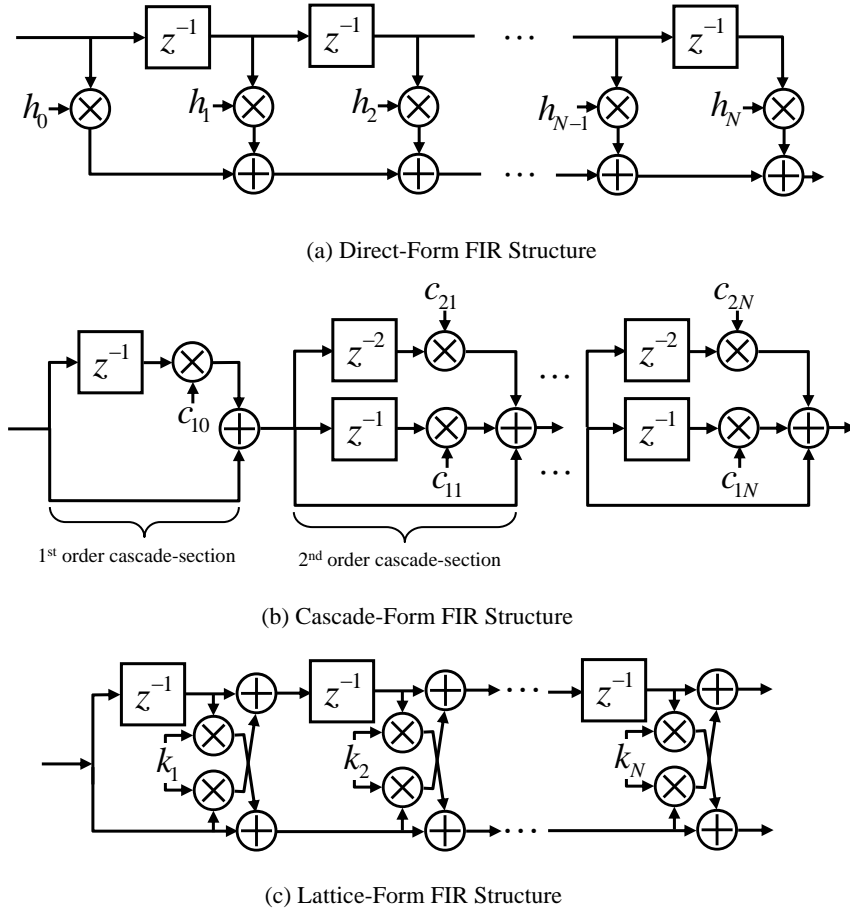


Figure 6.2: The most common structures employed in the implementation of 1D FIR filters; (a) the direct-form, (b) the cascade-form and (c) the lattice-form.

In order to minimize the product quantization noise in cascade-form structures, an exhaustive search method has been proposed in [214] that finds the optimum “sequence” of the cascading sections. However, the cascade-form structure optimization and sequencing algorithms are too time consuming to be used in most broadband beamforming applications, which requires instant adaptation [47].

Nevertheless, the lattice-form structure is mainly used in adaptive filter implementation [215] and according to Figure 6.2 (c), it requires twice as much as multiplications and additions to evaluate one output sample compared to the direct-form and the cascade-form structures. Due to the increase of computational complexity, the lattice-structure is

not considered in the implementation of parallel connected 1D FIR filters in beamforming MD FIR filters for computationally-intensive broadband-beamforming applications. Hence, the direct-form implementation is considered in the implementation of parallel connected 1D FIR filters in beamforming MD FIR filters for computationally-intensive broadband-beamforming applications for the remainder of this chapter.

### 6.2.5 Adder-Overflow Errors

The effect of adder overflow-errors on the output of the beamformer is significant because such errors are associated with the most-significant-bits<sup>4</sup> of the partial-sums. Hence, *the chance of occurring an adder overflow-error must be avoided* by assigning sufficient number of bits for the registers that retain partial-sums.

The partial-sum  $y_P(n)$  of a parallel connected direct-form 1D FIR filter, which is shown in Figure 6.2 (a), may be given by

$$y_P(n) = \sum_{k=0}^N h_k x_D(n-k), \quad (6.5)$$

where  $h_k$ ;  $k = 0, 1, \dots, N$  are the filter-coefficients of the 1D FIR filter of order ( $N$ ) and  $\{x_D(n)\}$  is the input data-sequence. Assuming both  $h_k$  and  $x_D(n)$  are normalized; i.e.  $|h_k| \leq 1$  for  $\forall k$  and  $|x_D(n)| \leq 1$  for  $\forall n$ , it can be shown that the magnitude of each  $y_P(n)$  is bounded such that

$$|y_P(n)| \leq L = \sum_{k=0}^N |h_k|. \quad (6.6)$$

Given the products from multipliers are bounded  $|h_k \cdot x_D(n-k)| \leq 1$  and stored in  $W_m$ -bit registers, adding  $\lceil \log_2(L) \rceil$ -bits<sup>5</sup> left of the binary-point annihilates any chance of overflow at the outputs of the adder-trees. Therefore, the outputs of the adder-trees should be assigned with

$$W_a = W_m + \lceil \log_2(L) \rceil - \text{bits}, \quad (6.7)$$

long registers in order to avoid adder-overflow errors.

---

<sup>4</sup>i.e the left-most bits of the code-word.

<sup>5</sup>The operation of rounding-up to the nearest integer is denoted by  $\lceil \cdot \rceil$ .

### 6.3 The Distortions of the Transfer Functions of Beamforming MD FIR Filters due to Coefficient Quantization

#### 6.3.1 Examples of Transfer Function Distortions in Beamforming Polyphase 2D FIR Double-Trapezoidal Filters

Given the beamforming polyphase 2D FIR double-trapezoidal filter has not been presented in the previous chapters, a brief review of it is given in the following. A reader can find more detailed treatment of the design of the beamforming polyphase 2D FIR double-trapezoidal filter in [59][63]<sup>6</sup>.

#### **The Beamforming Polyphase 2D FIR Double-Trapezoidal Filters: A Review**

The polyphase 2D FIR double-trapezoidal filter enables the selective enhancement (i.e. beamforming) of *double sideband modulated (DSM) temporally-broadband-bandpassed* (BB-BP) spatio-temporal (ST) plane-waves (PWs)<sup>7</sup> based on their directions of arrivals (DOAs) [59]. This design achieves significant enhancement of the signal associated with the PW arriving from the desired direction compared to co-channel interfering signals arriving from different directions. Numerical simulations conducted in MATLAB with floating-point number representation show that the signal-to-interference ratio (SIR) of the desired signal at the output of the beamformer is typically improved by more than 55 dB [59].

In order to selectively enhance a desired *space-time sampled* PW, the ideal double-trapezoidal-shaped passband  $IH_{\text{TR-D}}(e^{j\omega_x}, e^{j\omega_t})$  (Figure 6.3 -  $ABCD \cup A'B'C'D'$ ) of the beamforming 2D FIR filter is arranged to closely enclose the region-of-support (ROS) of the spectrum  $PW_{\text{IF-D}_R}(e^{j\omega_x}, e^{j\omega_t})$  of the desired sampled PW. Spatial sampling of the propagating PWs is achieved using a 1D uniformly distributed sensor array (1D-UDSA)

---

<sup>6</sup>Note that in case a reader wishes to follow the original publication [59], labels used in [59] are used in the following review.

<sup>7</sup>For brevity, for the remainder of this chapter, DSM BB-BP ST-PWs are referred simply as PWs.



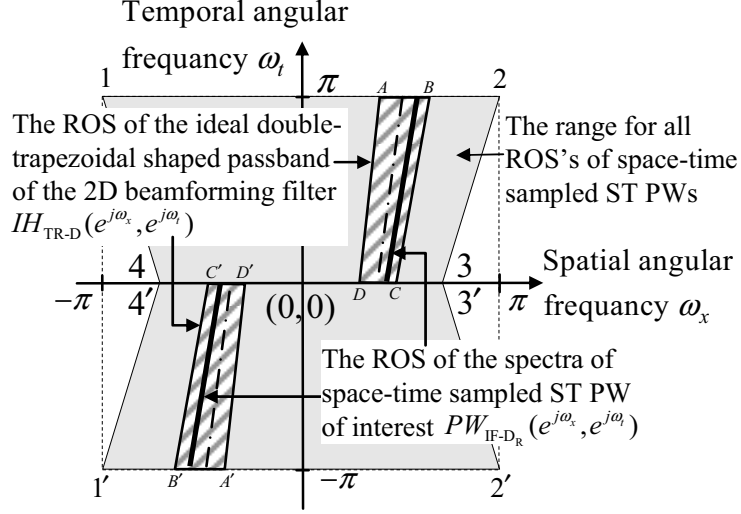


Figure 6.3: The ROS of the ideal passband of the 2D double-trapezoidal filter that closely enclose the ROS of the spectrum of the space-time sampled ST PW of interest.

consisting of  $2N_x + 1$ ;  $N_x \in \mathbb{Z}$ , sensors. Prior to temporal sampling, the sensor signals are *pre-filtered and frequency translated to an IF band* employing the real IF tri-stage temporal sampler array [59]. If the bandwidth of the temporal DSM signal associated with the PW of interest is  $BW$ , then the synchronous temporal sampling rate of the real IF tri-stage temporal sampler array is  $f_s = 2BW$ . However, according to Shannon's sampling theory [66] (pp. 738-746), in order to avoid temporal aliasing in sampling a DSM signal of bandwidth  $BW$ , the minimum required sampling rate is  $f'_s = BW$ . Note that the over-sampling of sensor signals by a factor of 2 at the real IF tri-stage temporal sampler array leads to 50% reduction in the complexity of the pre-processing hardware compared to comple-quadrature sampling [59].

Given that the impulse response of the 2D FIR double-trapezoidal filter is denote by  $h_{\text{TR-D}}(n_x, n_t)$  and the 2D space-time sampled sequence of PWs is denoted by  $x(n_x, n_t)$ , the 1D output sequence  $y(0, n_t)$  of the 2D FIR double-trapezoidal filter is given by

$$y(0, n_t) = y(n_x, n_t)_{\{n_x=0\}} = [x(n_x, n_t) ** h_{\text{TR-D}}(n_x, n_t)]_{\{n_x=0\}}, \quad (6.8)$$

where  $**$  denotes the 2D discrete domain convolution operation. According to [142], over-

sampling of the sensor signals can be compensated by down-sampling the 1D output sequence  $y(0, n_t)$  by a factor of 2. However, down-sampled signal is required to be modulated with  $(-1)^{n_t}$  to correct the spectral orientation of the recovered signal [59]. Hence, the output sequence of the beamformer  $y_B(n_t)$  is given by

$$y_B(n_t) = (-1)^{n_t} [[y(0, n_t)] \downarrow 2], \quad (6.9)$$

where  $\downarrow 2$  denotes the temporal-down-sampling by a factor of two.

In order to increase computational efficiency [59], the beamforming 2D FIR double-trapezoidal filter is implemented using a polyphase structure, where the down-sampling is done prior to filtering [142]. For a beamforming polyphase 2D FIR double-trapezoidal filter  $H_{\text{TR-D}}(z_x, z_t)$  of spatial order  $2N_x$  and temporal order  $8N_{pp}$ ;  $N_{pp} \in \mathbb{Z}$ , the difference-equations for the polyphase implementation is given by,

$$\begin{aligned} [y(0, n_t)] \downarrow 2 &= \sum_{m_x=-N_x}^{+N_x} \sum_{m_t=0}^{4N_{pp}} x_{-m_x,0}(m_t) g_{m_x,0}(n_t - m_t) \\ &+ \sum_{m_x=-N_x}^{+N_x} \sum_{m_t=0}^{4N_{pp}-1} x_{-m_x,1}(m_t) g_{m_x,1}(n_t - m_t), \end{aligned} \quad (6.10)$$

where the filter coefficients for each phase are defined according to [142], as

$$g_{m_x,0}(m_t) \triangleq h_{\text{TR-D}}(m_x, 2m_t); \text{ for } 0 \leq m_t \leq 4N_{pp} \quad (6.11a)$$

$$g_{m_x,1}(m_t) \triangleq h_{\text{TR-D}}(m_x, 2m_t + 1); \text{ for } 0 \leq m_t \leq 4N_{pp} - 1, \quad (6.11b)$$

for  $m_x = -N_x, \dots, 0, \dots, N_x$ . Also, according to [142], the down-sampled polyphase signals from each sensor  $m_x$  are given by

$$x_{m_x,0}(m_t) = [x(m_x, m_t)] \downarrow 2, \quad \text{Input Phase 0} \quad (6.12a)$$

$$x_{m_x,1}(m_t) = z_t^{-1} \{x(m_x, m_t)\} \downarrow 2, \quad \text{Input Phase 1} \quad (6.12b)$$

where the operator  $z_t^{-1} \{\cdot\}$  denotes a single temporal delay.

### The Proposed Polyphase 1D FIR Building Block

A filter structure having  $(2N_x + 1)$  parallel-connected polyphase 1D FIR building blocks (see Fig. 9 of [59]) has been proposed for real-time implementation of the beamforming polyphase 2D FIR double-trapezoidal filter [59]. The proposed polyphase 1D FIR building block that realizes the  $m_x^{\text{th}}$ -branch of the difference-equation, which is given by

$$y_{m_x}(n_t) = \sum_{m_t=0}^{4N_{pp}} x_{-m_x,0}(m_t) g_{m_x,0}(n_t - m_t) + \sum_{m_t=0}^{4N_{pp}-1} x_{-m_x,1}(m_t) g_{m_x,1}(n_t - m_t), \quad (6.13)$$

is shown in Figure 6.4. As shown there, the two polyphase components  $x_{m_x,0}(m_t)$  and  $x_{m_x,1}(m_t)$  from each sensor  $m_x \in [-N_x, N_x]$  are filtered using two congruent 1D FIR polyphase filters, labeled as Phase 0 and Phase 1. The polyphase 1D FIR building block is implemented using two conventional direct-form (or transposed direct-form) 1D FIR filter structures for Phase 0 and Phase 1. The structure for Phase 0 consists of  $(4N_{pp} + 1)$  parallel multipliers and a  $(4N_{pp})$ -input adder-tree where as the structure for Phase 1 consists of  $(4N_{pp})$  parallel multipliers and a  $(4N_{pp} - 1)$ -input adder-tree. Note that each product  $\{x_{-m_x,0/1}(m_t) \cdot g_{m_x,0/1}(n_t - m_t)\}$  is quantized into a  $W_m$ -bit word at the output of each multiplier.

### Distortions in the Magnitude Transfer Functions of Beamforming Polyphase 2D FIR Double-Trapezoidal Filters

As mentioned in subsection 6.2.3, the coefficient quantization leads to deterministic distortions of the frequency transfer function of beamforming polyphase 2D FIR double-trapezoidal filters  $H_{\text{TR-D}}(z_x, z_t)$ . However, the linear phase property of  $H_{\text{TR-D}}(z_x, z_t)$  is preserved under rounding-quantization because, *rotational symmetry* [41] (ch. 5), of corresponding filter coefficients  $h_{\text{TR-D}}(n_x, n_t)$ , remains unchanged after quantization. Hence, in the following the analysis is limited to the distortions in the magnitude response of beamforming polyphase 2D FIR double-trapezoidal filters due to coefficient quantization.

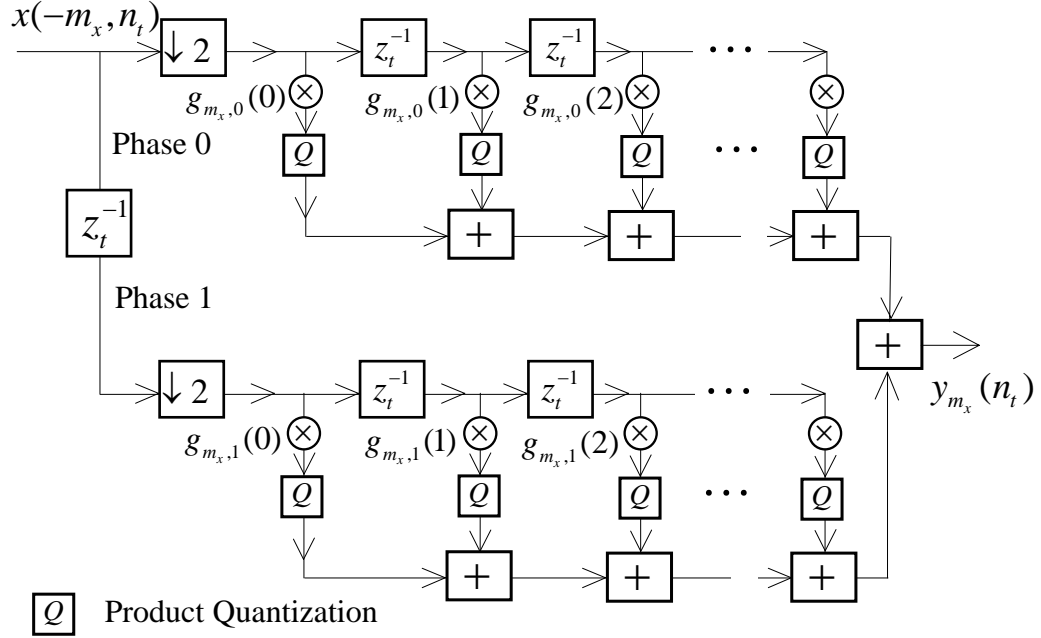


Figure 6.4: The proposed hardware architecture of a polyphase 1D FIR building block of the beamforming polyphase 2D FIR double-trapezoidal filter.

Let's consider the polyphase 2D FIR double-trapezoidal filter  $\bar{H}_{\text{TR-D}}(z_x, z_t)$ , of order  $(32 \times 32)$  that is designed to selectively enhance the wavefront signals associated with PWs of bandwidth spread-factor<sup>8</sup>  $K = 0.1$ , arriving in the general direction  $\bar{\phi} = 55^\circ$ , within the angular range  $\bar{\phi} \in [50^\circ, 60^\circ]$ , with respect to the 1D-UDSA [59]. For this particular 2D FIR filter  $\bar{H}_{\text{TR-D}}(z_x, z_t)$ , the corresponding filter coefficients  $\bar{h}_{\text{TR-D}}(n_x, n_t)$ , are evaluated according to (24) of [59], where the expressions for  $Ih_{\text{TR-D}}(n_x, n_t)$  are given in Appendix III of [59].

In order to effectively utilize the available dynamic range  $[-1, 1 - 2^{-W_c+1}]$  of  $W_c$ -bit two's complement representation, coefficients  $h_{\text{TR-D}}(n_x, n_t)$  are scaled before being

<sup>8</sup>Bandwidth spread factor ( $K$ ) is the ratio between the temporal bandwidth  $BW$ , and twice the maximum temporal frequency  $2f_{\text{max}}$  as defined in [59] and in chapter 4.

quantized. The scaling-factor  $\beta > 0$  is defined as

$$\beta \triangleq \begin{cases} \frac{(1-2^{-W_c})}{\max[\bar{h}_{\text{TR-D}}(n_x, n_t)]}; & \text{if } \max[\bar{h}_{\text{TR-D}}(n_x, n_t)] \geq \min[\bar{h}_{\text{TR-D}}(n_x, n_t)] , \\ \frac{-1}{\min[\bar{h}_{\text{TR-D}}(n_x, n_t)]}; & \text{if } \min[\bar{h}_{\text{TR-D}}(n_x, n_t)] \geq \max[\bar{h}_{\text{TR-D}}(n_x, n_t)] . \end{cases} \quad (6.14)$$

The scaled coefficients are given by

$$\hat{h}_{\text{TR-D}}(n_x, n_t) = \beta \cdot \bar{h}_{\text{TR-D}}(n_x, n_t). \quad (6.15)$$

Here, the scaled coefficients  $\hat{h}_{\text{TR-D}}(n_x, n_t)$  are subjected to rounding quantization and represented with  $W_c = 8, 10, 12, 14, 16$  and 18-bit two's complement format. The MATLAB Fixed-Point Toolbox has been employed in evaluating  $W_c$ -bit two's complement filter coefficients. Note that for floating point represented scaled filter coefficients  $\hat{h}_{\text{TR-D}}(n_x, n_t)$ , the corresponding frequency transfer function is denoted by  $\bar{H}_{\text{TR-D[FP]}}(e^{j\omega_x}, e^{j\omega_t})$ . Also note that the  $W_c$ -bit quantized coefficient set is denoted by  $\hat{h}_{\text{TR-D}[W_c]}(n_x, n_t)$  and the corresponding set of transfer functions is denoted by  $\bar{H}_{\text{TR-D}[W_c]}(e^{j\omega_x}, e^{j\omega_t})$ .

In this example, the cross-sectional magnitude responses taken across and along the passbands (see Figure 6.3) of the transfer function  $\bar{H}_{\text{TR-D[FP]}}(e^{j\omega_x}, e^{j\omega_t})$  corresponding to floating-point coefficients and the transfer functions  $\bar{H}_{\text{TR-D}[W_c]}(e^{j\omega_x}, e^{j\omega_t})$  corresponding to two's complement coefficients of word-length  $W_c = 8, 10, 12, 14, 16$  and 18-bits, are shown in Figure 6.5, Figure 6.6 and Figure 6.7. According to Figure 6.5 and Figure 6.7, where the cross-sectional magnitude responses are evaluated on the line  $\omega_t = 0.5\pi$  for  $\omega_x \in (-0.4\pi, -0.2\pi)$ , the *effective stopband attenuation* of  $\bar{H}_{\text{TR-D}[W_c]}(e^{j\omega_x}, e^{j\omega_t})$  for  $W_c = 8$  is much lower than that of  $\bar{H}_{\text{TR-D[FP]}}(e^{j\omega_x}, e^{j\omega_t})$ , where the effective stopband attenuation of  $\bar{H}_{\text{TR-D}[W_c]}(e^{j\omega_x}, e^{j\omega_t})$  for  $W_c = 10$  is moderately lower than that of  $\bar{H}_{\text{TR-D[FP]}}(e^{j\omega_x}, e^{j\omega_t})$ . However, the effective stopband attenuations of  $\bar{H}_{\text{TR-D}[W_c]}(e^{j\omega_x}, e^{j\omega_t})$  for  $W_c = 12$  and  $W_c = 14$  closely approximate that of  $\bar{H}_{\text{TR-D[FP]}}(e^{j\omega_x}, e^{j\omega_t})$  where as the effective stopband attenuations of  $\bar{H}_{\text{TR-D}[W_c]}(e^{j\omega_x}, e^{j\omega_t})$  for  $W_c = 16$  and  $W_c = 18$  are almost identical to that of  $\bar{H}_{\text{TR-D[FP]}}(e^{j\omega_x}, e^{j\omega_t})$ .

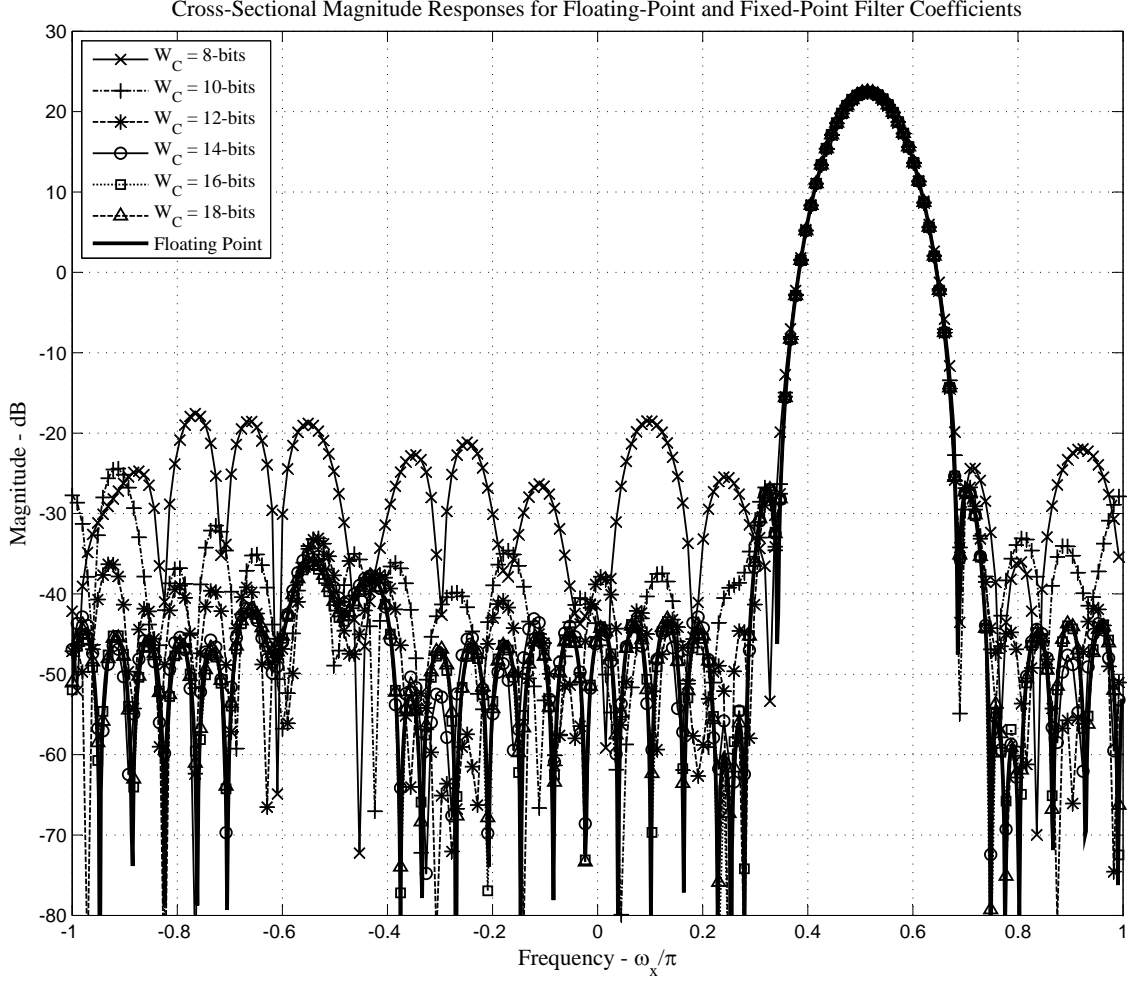


Figure 6.5: The cross-sectional magnitude responses evaluated on  $\omega_t = 0.5\pi$  across the passbands of  $\bar{H}_{\text{TR-D}[W_c]}(e^{j\omega_x}, e^{j\omega_t})$  for  $W_c = 8, 10, 12, 14, 16$  and 18-bits and  $\bar{H}_{\text{TR-D}[FP]}(e^{j\omega_x}, e^{j\omega_t})$ .

For the transfer function  $\bar{H}_{\text{TR-D}[FP]}(e^{j\omega_x}, e^{j\omega_t})$  corresponding to floating point filter coefficients and the transfer functions  $\bar{H}_{\text{TR-D}[W_c]}(e^{j\omega_x}, e^{j\omega_t})$  corresponding to two's complement filter coefficients of word-lengths  $W_c = 8, 10, 12, 14, 16$  and 18-bits, the *normalized effective passband gains*  $\text{PB}/\text{mean}[\text{PB}]$ , which are evaluated for 85% spectral occupancy in  $\omega_t$ , are shown in Figure 6.6. Here, PB is evaluated by averaging the magnitude frequency response along the line  $\omega_x = (2K(\omega_t - \pi) + \pi) \cos(\bar{\phi})$  for  $\omega_t \in (0, 0.85\pi)$  for the positive frequency band and the magnitude frequency response along the line  $\omega_x = (2K(\omega_t + \pi) - \pi) \cos(\bar{\phi})$  for  $\omega_t \in (-0.85\pi, 0)$  for the negative frequency band

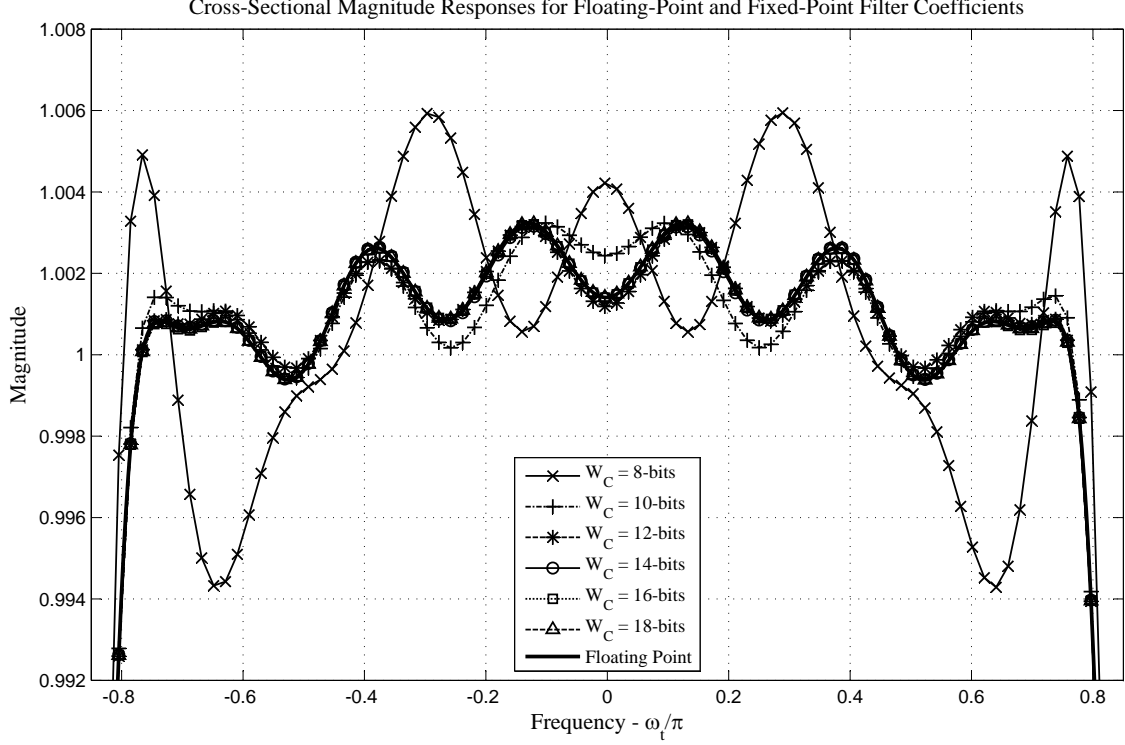


Figure 6.6: The normalized effective passband gains  $PB/\text{mean}[PB]$ , evaluated by averaging the magnitude responses on the lines  $\omega_x = (2K(\omega_t - \pi) + \pi)\cos(\bar{\phi})$  and  $\omega_x = (2K(\omega_t + \pi) - \pi)\cos(\bar{\phi})$  along the positive and negative frequency bands of  $\bar{H}_{\text{TR-D}[W_c]}(e^{j\omega_x}, e^{j\omega_t})$  for  $W_c = 8, 10, 12, 14, 16$  and  $18$ -bits and  $\bar{H}_{\text{TR-D}[FP]}(e^{j\omega_x}, e^{j\omega_t})$ .

where  $\bar{\phi} = 55^\circ$ . According to Figure 6.6, the passband ripple of  $\bar{H}_{\text{TR-D}[W_c]}(e^{j\omega_x}, e^{j\omega_t})$  for  $W_c = 8$  is higher than that of  $\bar{H}_{\text{TR-D}[FP]}(e^{j\omega_x}, e^{j\omega_t})$  where as the passband ripple of  $\bar{H}_{\text{TR-D}[W_c]}(e^{j\omega_x}, e^{j\omega_t})$  for  $W_c = 10$  closely approximates that of  $\bar{H}_{\text{TR-D}[FP]}(e^{j\omega_x}, e^{j\omega_t})$ . Note that the passband ripple of  $\bar{H}_{\text{TR-D}[W_c]}(e^{j\omega_x}, e^{j\omega_t})$  for  $W_c = 12, W_c = 14, W_c = 16$  and  $W_c = 18$  are almost identical to that of  $\bar{H}_{\text{TR-D}[FP]}(e^{j\omega_x}, e^{j\omega_t})$ .

### 6.3.2 Examples of Transfer Function Distortions in Beamforming Complex-Coefficient 2D FIR Asymmetric-Trapezoidal Filters

In chapter 4, the complex-coefficient 2D FIR asymmetric-trapezoidal filters have been proposed for the real-time adaptive broadband beamforming in CR systems. The design of beamforming complex-coefficient 2D FIR asymmetric-trapezoidal filters are explained

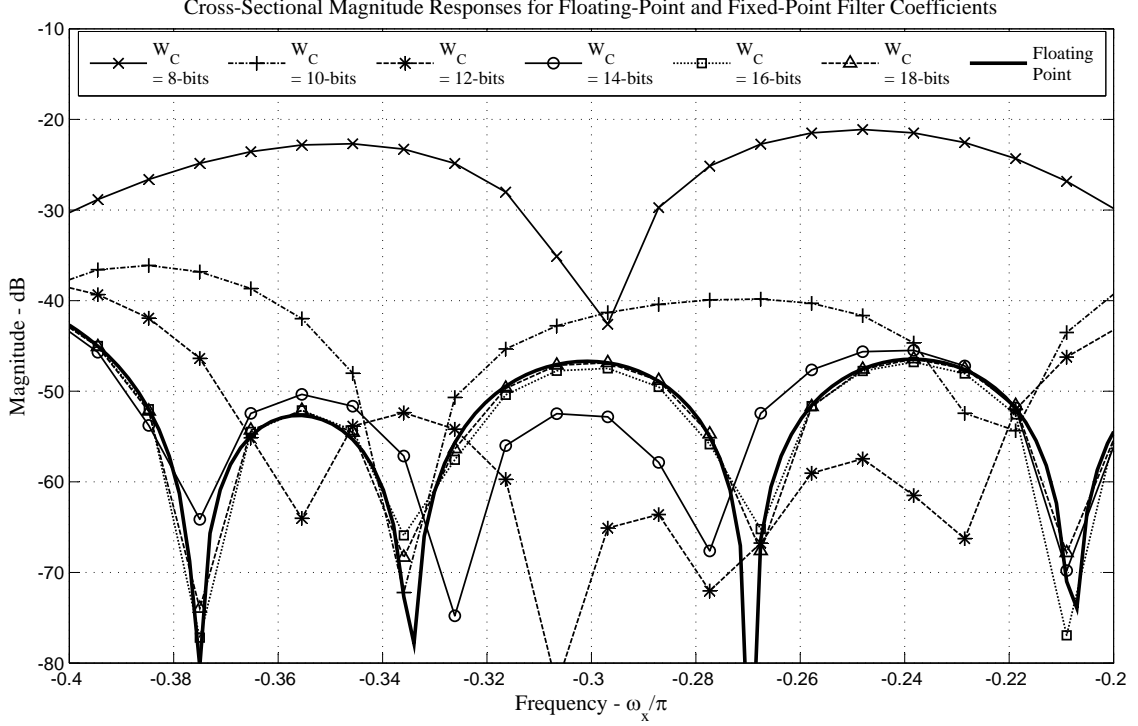


Figure 6.7: The expanded cross-sectional magnitude responses evaluated on  $\omega_t = 0.5\pi$  for  $\omega_x \in (-0.4\pi, -0.2\pi)$  across the passbands of  $\bar{H}_{\text{TR-D}[W_c]}(e^{j\omega_x}, e^{j\omega_t})$  for  $W_c = 8, 10, 12, 14, 16$  and  $18$ -bits and  $\bar{H}_{\text{TR-D}[FP]}(e^{j\omega_x}, e^{j\omega_t})$ .

in detail in section 4.5 of chapter 4. The distortions of the magnitude frequency response of beamforming complex-coefficient 2D FIR asymmetric-trapezoidal filters  $G(z_x, z_t)$ , due to coefficient quantization are studied in the following. Note that the linear phase property of  $G(z_x, z_t)$  is also preserved under rounding quantization because, *rotational conjugate-symmetry* [41] (ch. 5), of corresponding filter coefficients  $\tilde{g}(n_x, n_t)$ , remains unchanged after quantization.

Let's consider the beamforming complex-coefficient 2D FIR asymmetric-trapezoidal filter  $\bar{G}(z_x, z_t)$ , of order  $(32 \times 40)$  that is designed to meet the specifications  $\bar{\phi}_0 = 70^\circ$ ,  $\Delta\bar{\phi} = 3.5^\circ$ ,  $K_I = 0.125$  and  $L_I = 1$ . Following chapter 4,  $\bar{G}(z_x, z_t)$  may be employed in order to selectively enhance the wavefront signals associated with propagating EM BB-BP ST PWs that are arriving in the general direction  $\bar{\phi} = 70^\circ$ , within the angular range  $\bar{\phi} \in [66.5^\circ, 73.5^\circ]$ , with respect to the 1D-UDAA. For  $\bar{G}(z_x, z_t)$ , the corresponding filter



coefficients  $\bar{g}(n_x, n_y)$ , are determined by the closed-form design expressions specified in (1.57(a)) - (1.57(f)) and (4.58) in chapter 4. Following (6.14) and (6.15), the filter coefficients  $\bar{g}(n_x, n_y)$  are scaled before being quantized. The scaled coefficients  $\hat{g}(n_x, n_t)$  are subjected to rounding quantization and represented with  $W_c = 8, 10, 12, 14, 16$  and 18-bit two's complement format. Note that for floating point represented scaled filter coefficients  $\hat{g}(n_x, n_t)$ , the corresponding frequency transfer function is denoted by  $\bar{G}_{[\text{FP}]}(e^{j\omega_x}, e^{j\omega_t})$ . Also note that the  $W_c$ -bit quantized coefficient set is denoted by  $\hat{g}_{[W_c]}(n_x, n_t)$  and the corresponding set of transfer functions is denoted by  $\bar{G}_{[W_c]}(e^{j\omega_x}, e^{j\omega_t})$ .

In this example, the cross-sectional magnitude responses taken across and along the trapezoidal-shaped passbands (see Figure 4.7, page 151) of the filters  $\bar{G}_{[W_c]}(z_x, z_t)$  corresponding to two's complement coefficients of word-length  $W_c = 8, 10, 12, 14, 16$  and 18-bits and the filter  $\bar{G}_{[\text{FP}]}(z_x, z_t)$  corresponding to floating-point coefficients, are shown in Figure 6.8 and Figure 6.9, respectively. According to Figure 6.8, where the cross-sectional magnitude responses are evaluated on the line  $\omega_t = 0$  for  $\omega_x \in (-\pi, \pi)$ , the effective stopband attenuations of  $\bar{G}_{[W_c]}(e^{j\omega_x}, e^{j\omega_t})$  for  $W_c = 8$  and  $W_c = 10$  are much lower than that of  $\bar{G}_{\text{TR-D}[\text{FP}]}(e^{j\omega_x}, e^{j\omega_t})$ . However, the effective stopband attenuations of  $\bar{H}_{\text{TR-D}[\text{W}_c]}(e^{j\omega_x}, e^{j\omega_t})$  for  $W_c = 12$  and  $W_c = 14$  closely approximate that of  $\bar{G}_{\text{TR-D}[\text{FP}]}(e^{j\omega_x}, e^{j\omega_t})$  where as the effective stopband attenuations of  $\bar{G}_{\text{TR-D}[\text{W}_c]}(e^{j\omega_x}, e^{j\omega_t})$  for  $W_c = 16$  and  $W_c = 18$  are almost identical to that of  $\bar{G}_{\text{TR-D}[\text{FP}]}(e^{j\omega_x}, e^{j\omega_t})$ .

For floating point filter coefficients  $\hat{g}(n_x, n_t)$ , and two's complement filter coefficients  $\hat{g}_{[W_c]}(n_x, n_t)$ , of word-lengths  $W_c = 8, 10, 12, 14, 16$  and 18-bits, the normalized effective passband gains PG, which are evaluated for 90% spectral occupancy in  $\omega_t$ , are shown in Figure 6.9. Here, PG represent the average of  $\text{Avg}(\omega_t)$ , the magnitude frequency response along the line  $\omega_x = L_1(K_1(\omega_t - \pi) + \pi) \cos(\bar{\phi})$  for  $\omega_t \in (-0.9, 0.9\pi)$  and the first order polynomial of  $\omega_t$  approximating  $[\text{Avg}(\omega_t)]^{-1}$ , for  $\bar{\phi} = 70^\circ$ . According to Figure 6.9, the passband ripple of  $\bar{G}_{[W_c]}(e^{j\omega_x}, e^{j\omega_t})$  for  $W_c = 8$  is higher than that of  $\bar{G}_{[\text{FP}]}(e^{j\omega_x}, e^{j\omega_t})$

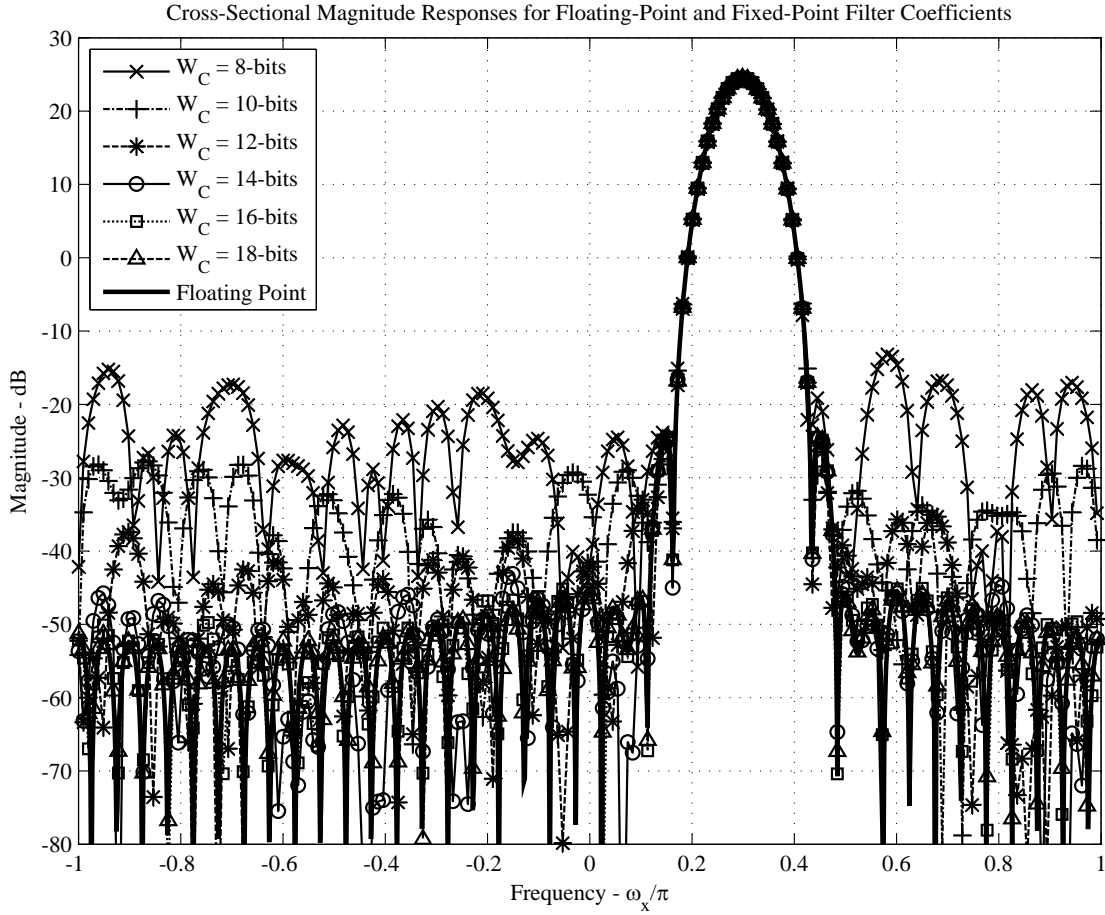


Figure 6.8: The cross-sectional magnitude responses evaluated on  $\omega_t = 0.5\pi$  across the passbands of  $\bar{G}_{[W_c]}(e^{j\omega_x}, e^{j\omega_t})$  for  $W_c = 8, 10, 12, 14, 16$  and  $18$ -bits and  $\bar{G}_{[FP]}(e^{j\omega_x}, e^{j\omega_t})$ .

where as the passband ripple of  $\bar{G}_{[W_c]}(e^{j\omega_x}, e^{j\omega_t})$  for  $W_c = 10$  closely approximates that of  $\bar{G}_{[FP]}(e^{j\omega_x}, e^{j\omega_t})$ . Note that the passband ripple of  $\bar{G}_{[W_c]}(e^{j\omega_x}, e^{j\omega_t})$  for  $W_c = 12, W_c = 14, W_c = 16$  and  $W_c = 18$  are almost identical to that of  $\bar{G}_{[FP]}(e^{j\omega_x}, e^{j\omega_t})$ .

### 6.3.3 Examples of Transfer Function Distortions in Beamforming Complex-Coefficient 3D FIR Frustum Filters

In chapter 5, the complex-coefficient 3D FIR frustum filters have been proposed for the broadband beamforming of FPA signals for applications in pulsar timing and profile studies. The design of beamforming complex-coefficient 3D FIR frustum filters is explained in detail in section 5.4 of chapter 5. The distortions of the magnitude frequency response

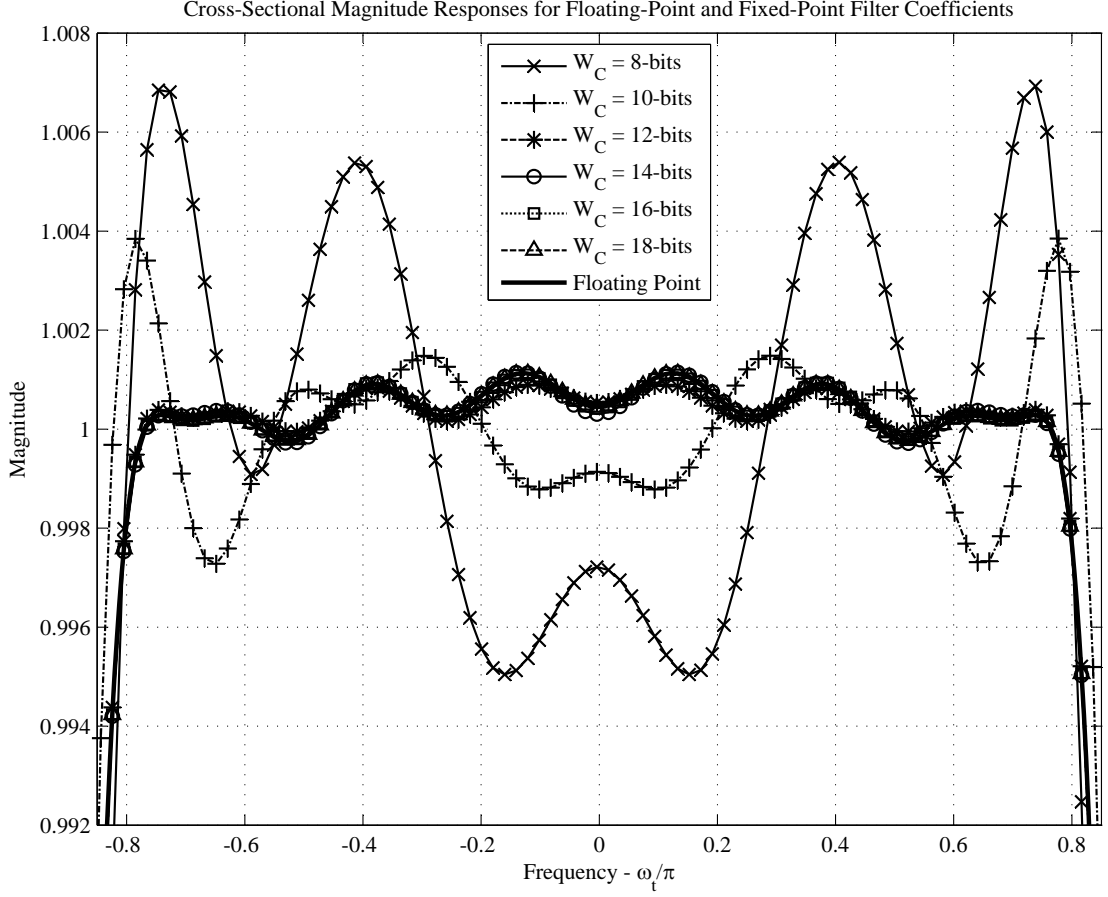


Figure 6.9: The normalized effective passband gains  $\text{PB}/\text{mean}[\text{PB}]$ , evaluated on the line  $\omega_x = L_I(K_I(\omega_t - \pi) + \pi) \cos(70^\circ)$  along the passband of  $\tilde{G}_{[W_c]}(e^{j\omega_x}, e^{j\omega_t})$  for  $W_c = 8, 10, 12, 14, 16$  and 18-bits and  $\tilde{G}_{[\text{FP}]}(e^{j\omega_x}, e^{j\omega_t})$ , for  $\omega_t \in (-0.9, 0.9\pi)$ .

of beamforming complex-coefficient 2D FIR asymmetric-trapezoidal filters  $H(z_x, z_y, z_t)$ , due to coefficient quantization are studies in the following. Note that the linear phase property of  $H(z_x, z_y, z_t)$  is also preserved under rounding quantization because, *rotational conjugate-symmetry* [41] (ch. 5), of corresponding filter coefficients  $\tilde{h}(n_x, n_y, n_t)$ , remains unchanged after quantization.

Let's consider the beamforming complex-coefficient 3D FIR frustum filter  $\bar{H}(z_x, z_y, z_t)$ , of order  $[16, 16, 10]$  that is designed to selectively enhance the broadband pulsar signals received by the FPA from a pulsar at the angular position  $(\theta = 0^\circ, \phi = 0^\circ)$  (i.e. directly along the axis of the paraboloidal reflector). In order to suppress RFI and ground thermal

noise, the beamforming 3D FIR frustum filter  $\bar{H}(z_x, z_y, z_t)$  is designed to meet the specifications  $F_C = 1.1$  GHz,  $BW = 1.2$  GHz, which leads to  $K = 0.353$ , and half-cone angle  $\alpha_{\max} = 30^\circ$ . The corresponding the filter coefficients  $\bar{h}(n_x, n_y, n_t)$  are determined following the combined 3D window-based and frequency sampling filter design method specified in subsection 5.4.2. Following (6.14) and (6.15), the filter coefficients  $\bar{h}(n_x, n_y, n_t)$  are scaled before being quantized. The scaled coefficients  $\hat{h}(n_x, n_y, n_t)$  are subjected to rounding quantization and represented with  $W_c = 6, 8, 10, 12, 14$  and 16-bit two's complement format. Note that for floating point represented scaled filter coefficients  $\hat{h}(n_x, n_y, n_t)$ , the corresponding frequency transfer function is denoted by  $\bar{H}_{[\text{FP}]}(e^{j\omega_x}, e^{j\omega_y}, e^{j\omega_t})$ . Also note that the  $W_c$ -bit quantized coefficient set is denoted by  $\hat{h}_{[W_c]}(n_x, n_y, n_t)$  and the corresponding set of transfer functions is denoted by  $\bar{H}_{[W_c]}(e^{j\omega_x}, e^{j\omega_y}, e^{j\omega_t})$ .

In this example, the cross-sectional magnitude response taken along the line of intersection of two planes  $\omega_t = -0.5\pi$  and  $\omega_y = 0$ , in 3D frequency-space, of the transfer function  $\bar{H}_{[W_c]}(e^{j\omega_x}, e^{j\omega_y}, e^{j\omega_t})$  corresponding to two's complement coefficients of word-length  $W_c = 6, 8, 10, 12, 14$  and 16-bit and the transfer function  $\bar{H}_{[\text{FP}]}(e^{j\omega_x}, e^{j\omega_y}, e^{j\omega_t})$  corresponding to floating-point coefficients, are shown in Figure 6.10. Following a series of cross-sectional magnitude response evaluated along different lines in the **PNC**, it is observed that the effective stopband attenuations of  $\bar{H}_{[W_c]}(e^{j\omega_x}, e^{j\omega_y}, e^{j\omega_t})$  for  $W_c = 6$  is much lower than that of  $\bar{H}_{[\text{FP}]}(e^{j\omega_x}, e^{j\omega_y}, e^{j\omega_t})$ . However, the effective stopband attenuations of  $\bar{H}_{[W_c]}(e^{j\omega_x}, e^{j\omega_y}, e^{j\omega_t})$  for  $W_c = 8$  closely approximate that of  $\bar{H}_{[\text{FP}]}(e^{j\omega_x}, e^{j\omega_t})$  where as the effective stopband attenuations of  $\bar{H}_{[W_c]}(e^{j\omega_x}, e^{j\omega_y}, e^{j\omega_t})$  for  $W_c = 10, W_c = 12, W_c = 14$  and  $W_c = 16$  are almost identical to that of  $\bar{G}_{\text{TR-D}[\text{FP}]}(e^{j\omega_x}, e^{j\omega_t})$ .

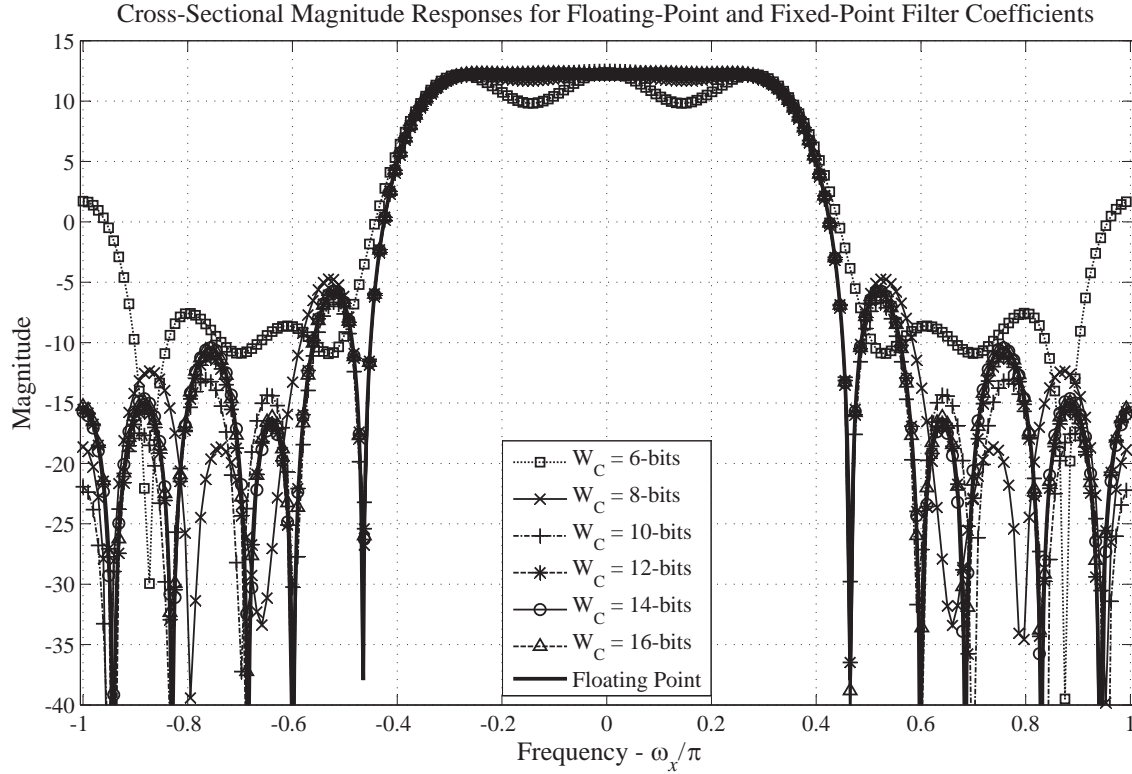


Figure 6.10: The cross-sectional magnitude responses evaluated on the line of intersection between the plane  $\omega_t = -0.5\pi$  and  $\omega_y =$  across the passbands of  $\bar{H}_{[W_c]}(e^{j\omega_x}, e^{j\omega_y}, e^{j\omega_t})$  for  $W_c = 6, 8, 10, 12, 14$  and 16-bits and  $\bar{H}_{[FP]}(e^{j\omega_x}, e^{j\omega_y}, e^{j\omega_t})$ .

#### 6.4 The Degradation of the SNDR of Beamforming MD FIR Filters due to Finite-Word-Length Digital Arithmetics

In section 6.3, the examples of the cross sectional magnitude frequency responses taken across and along the passbands of beamforming MD FIR filters, where the coefficients are represented with floating-point and  $W_c$ -bits two's complement formats, indicate that with proper assignment of register length for filter coefficients, distortions of the transfer functions can be minimized. As mentioned in section 6.2, in addition to the transfer function distortions the quantization noise generated at the outputs of ADCs and the outputs of multipliers contaminate the beamformer output lowering the maximum achievable SNDR.

In the following, a typical procedure taken for estimating the finite-word-length effects

of the SNDR at the output of beamforming MD FIR filters is outlined considering the example of the beamforming polyphase 2D FIR double-trapezoidal filter. First, a theoretical model is developed for estimating SNDRs of the beamformer output for different DSP configurations, i.e. the word-lengths for input-data, filter-coefficients, multiplier-products and partial-sums. Next, Monte Carlo simulations have been conducted using the MATLAB Fixed-Point Toolbox in determining the averaged SNDRs under the same DSP configurations. The empirically evaluated SNDRs are compared with the estimated SNDRs in order to verify the theoretical model. The combined theoretical and empirical process has been used to configure the DSP hardware architecture for the beamforming polyphase 2D FIR double-trapezoidal filter. This hardware architecture is used in implementing the beamforming polyphase 2D FIR double-trapezoidal filter of order  $(32 \times 32)$  on Xilinx Virtex-4 Sx35 ff668-10 FPGA chips. An example of the partial FPGA implementation of this 2D filter is given in section 6.5.

#### 6.4.1 A Theoretical Model for the SNDR at the Output of the Beamformer

Following (4.69) in subsection 4.5.4 and (5.43) in subsection 5.4.4, the signal to noise plus distortion ratio (SNDR) at the output of the beamformer is defined as

$$\text{SNDR}_{\text{dB}} \triangleq 10 \cdot \log_{10} \frac{\sigma_S^2}{\sigma_N^2 + \sigma_D^2}, \quad (6.16)$$

where  $\sigma_S^2$  and  $\sigma_N^2$  are the variances of the recovered signal  $y_B(n_t)$  and the contaminating noise  $\eta(n_t)$  at the output of the beamformer, respectively. Also,  $\sigma_D^2$  is the variance of the signal distortion

$$y_D(n_t) = x_0(n_t) - y_B(n_t), \quad (6.17)$$

of  $y_B(n_t)$  with respect to the desired-signal  $x_0(n_t)$ . Therefore, the variance of the signal distortion  $y_D(n_t)$  can be given by  $\sigma_D^2 = \gamma \cdot \sigma_S^2$ , where  $\gamma$  is the *normalized mean-square passband-ripple* of the beamforming 2D double-trapezoidal filter  $H_{\text{TR-D}}(z_x, z_t)$ . Here,  $\gamma$

is given by

$$\gamma = \text{mean} \left[ 1 - \frac{\text{PB}}{\text{mean}[\text{PB}]} \right]^2, \quad (6.18)$$

where PB is the *effective passband gain* that is evaluated by averaging the magnitude responses on the axis of the positive frequency band and on the axis of the negative frequency band (see Figure 6.3) of the passband of  $H_{\text{TR-D}}(z_x, z_t)$  of order  $(2N_x \times 8N_{pp})$ .

The contaminating noise  $\eta(n_t)$  at the beamformer output is consisted of the accumulated product quantization noise, the residual co-channel interference and the residual input quantization noise. Hence, the variance  $\sigma_N^2$  of  $\eta(n_t)$  may be given by

$$\sigma_N^2 = \sigma_{Ap}^2 + \sigma_{\text{RInt}}^2 + \sigma_{Ri}^2, \quad (6.19)$$

where  $\sigma_{Ap}^2$ ,  $\sigma_{\text{RInt}}^2$  and  $\sigma_{Ri}^2$  are the variances of the accumulated product quantization noise, the residual co-channel interfering signals and the residual input quantization noise at the beamformer output, respectively.

In the direct-form structure shown in Figure 6.2(a), the product quantization noise components generated at the outputs of multiplier are directly accumulated in the filter output. Given the product quantization noise components are uncorrelated, the variance of the accumulated product quantization noise at the output of the direct-form polyphase 1D FIR building block shown in Figure 6.11 is  $M_{M_x} \sigma_p^2$ . Here,  $M_{M_x}$  is the *actual number of quantizations* occurred in the polyphase 1D FIR building block in evaluating one output sample and  $\sigma_p^2$  is the variance of the product quantization noise at the output of each multiplier as defined in the subsection 6.2.2 [210]. Considering the parallel connected array of  $(2N_x + 1)$  polyphase 1D FIR building blocks, the variance of product quantization noise at the output of the beamformer is  $\sigma_{Ap}^2 = M \sigma_p^2$ , where  $M$  is the total number of quantizations occur in evaluating one output sample of  $H_{\text{TR-D}}(z_x, z_t)$ . Here,  $M$  is approximated with the number of non-zero coefficients of  $H_{\text{TR-D}}(z_x, z_t)$ . In general  $M \leq (2N_x + 1) \times (8N_{PP} + 1)$  for  $H_{\text{TR-D}}(z_x, z_t)$ , because some coefficients are inherently zero where as some coefficients are approximated to zero by the coefficient quantization

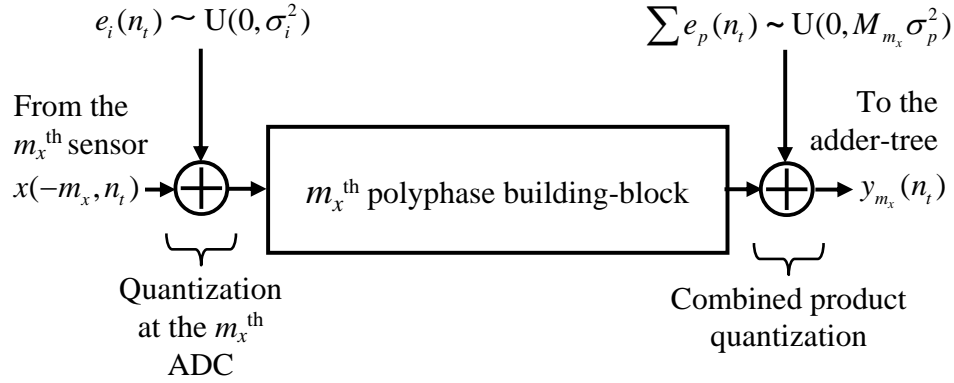


Figure 6.11: The noise-model for the polyphase 1D FIR building block of the beamforming polyphase 2D FIR double-trapezoidal filter.

process.

Assuming the co-channel interfering signals are at the stopband of  $H_{\text{TR-D}}(z_x, z_t)$ , the variance  $\sigma_{\text{Int}}^2$  of the residual co-channel interference signals at the output of the beamformer is  $\sigma_{\text{RInt}}^2 = a \cdot \sigma_{\text{Int}}^2$ , where  $\sigma_{\text{Int}}^2$  is the variance of the co-channel interference at the input and where  $a$  is given by

$$a = \iint_{(\omega_x, \omega_t) \in \text{Stopband}} H_{\text{TR-D}}(e^{j\omega_x}, e^{j\omega_t})^2 d\omega_x d\omega_t. \quad (6.20)$$

Note in (6.20),  $H_{\text{TR-D}}(e^{j\omega_x}, e^{j\omega_t})$  is the frequency transfer function of the beamforming polyphase 2D FIR double-trapezoidal filter  $H_{\text{TR-D}}(z_x, z_t)$  of order  $(2N_x \times 8N_{pp})$  and its “stopband” corresponds to the area  $(122'1') - (ABCD \cup A'B'C'D')$  in Figure 6.3.

Given that the input quantization noise  $\{e_i(n_t)\}$  at the outputs of  $(2N_x + 1)$  ADCs are uncorrelated both temporally and spatially, the power spectral density of the input quantization noise is uniform and equals to  $(2N_x + 1)\sigma_i^2/4\pi^2$  inside the principle Nyquist-square (i.e. the square denoted by 122'1' in Figure 6.3 such that  $[\omega_x, \omega_t] \in [-\pi, \pi]$  [44]) where  $\sigma_i^2$  is the variance of the input quantization noise at each ADC output as defined in the subsection 6.2.1. Therefore, the variance  $\sigma_{\text{Ri}}^2$  of the residual input quantization noise at



the beamformer output is  $\sigma_{Ri}^2 = \kappa \cdot \sigma_i^2$ , where  $\kappa$  is given by

$$\kappa = \frac{(2N_x + 1)}{4\pi^2} \iint_{[\omega_x, \omega_t] \pi} H_{\text{TR-D}}(e^{j\omega_x}, e^{j\omega_t})^2 d\omega_x d\omega_t . \quad (6.21)$$

Hence, the theoretical estimate of the SNDR at the output of the beamforming 2D double-trapezoidal filter  $H_{\text{TR-D}}(z_x, z_t)$  is given by

$$[\text{SNDR}_{\text{dB}}]_{\text{Estimate}} = 10 \cdot \log_{10} \frac{\sigma_S^2}{M \cdot \sigma_p^2 + a \cdot \sigma_{\text{Int}}^2 + \kappa \cdot \sigma_i^2 + \gamma \cdot \sigma_S^2} . \quad (6.22)$$

#### 6.4.2 Estimation of the SNDR at the Output of a Particular Beamformer

In order to estimate the SNDR of a particular beamformer following (6.22), first, the parameters  $a$ ,  $M$ ,  $\kappa$ ,  $\gamma$ ,  $\sigma_S^2$ ,  $\sigma_p^2$ ,  $\sigma_i^2$  and  $\sigma_{\text{Int}}^2$  should be evaluated. In case of beamforming polyphase 2D FIR double-trapezoidal filters  $H_{\text{TR-D}}(z_x, z_t)$ , the parameters  $a$ ,  $M$ ,  $\kappa$  and  $\gamma$  of (6.22) depend on the order  $(2N_x + 1) \times (8N_{pp} + 1)$  of a particular 2D FIR double-trapezoidal  $\bar{H}_{\text{TR-D}}(z_x, z_t)$ , which is specified by the bandwidth spread factor  $K$ , beam direction  $\bar{\phi}$  and the angular range  $\Delta\phi$  [59], and on the assigned word-lengths ( $W_c$ ) for the filter coefficients. For estimating the parameters  $a$ ,  $M$ ,  $\kappa$  and  $\gamma$  of a typical beamforming polyphase 2D FIR double-trapezoidal filter, let's reconsider  $\bar{H}_{\text{TR-D}}(z_x, z_t)$ , which has been introduced in subsection 6.3.1. Recall that  $\bar{H}_{\text{TR-D}}(z_x, z_t)$ , of order  $(32 \times 32)$  has been designed to meet the specifications  $K = 0.1$ ,  $\bar{\phi} = 55^\circ$  and  $\Delta\phi = 5^\circ$ . As mentioned in subsection 6.3.1, the scaled filter coefficients  $\hat{h}_{\text{TR-D}}(n_x, n_t)$ , of  $\bar{H}_{\text{TR-D}}(z_x, z_t)$  are represented in floating point format and in two's complement format having coefficient word-lengths  $W_c = 8, 10, 12, 14, 16$  and 18-bits. The parameters  $\gamma$ ,  $a$  and  $\kappa$  evaluated for  $\bar{H}_{\text{TR-D}[W_c]}(e^{j\omega_x}, e^{j\omega_t})$  where  $W_c = 8, 10, 12, 14, 16$  and 18 and for  $\bar{H}_{\text{TR-D}[FP]}(e^{j\omega_x}, e^{j\omega_t})$ , following (6.18), (6.20) and (6.21), are listed in Table 6.1. As mentioned earlier,  $M$  is estimated with the number of non-zero filter coefficients of  $\bar{H}_{\text{TR-D}[W_c]}(z_x, z_t)$  and  $\bar{H}_{\text{TR-D}[FP]}(z_x, z_t)$ .

Table 6.1: Estimated  $\gamma$ ,  $a$ ,  $\kappa$  and  $M$  of  $\bar{H}_{\text{TR-D}[W_c]}(z_x, z_t)$  for  $W_c = 8, 10, 12, 14, 16$  and  $18$  and  $\bar{H}_{\text{TR-D}[FP]}(z_x, z_t)$ .

Parameters	$W_c=8$	$W_c=10$	$W_c=12$	$W_c=14$	$W_c=16$	$W_c=18$	Floating Point
$\gamma$ - dB	-45.1	-45.6	-45.7	-45.7	-45.7	-45.6	-45.6
$a$ - dB	-26.6	-34.3	-40.3	-41.6	-41.7	-41.7	-41.7
$\kappa$	299	303	304	304	304	304	304
$M$	401	639	833	959	1031	1049	1073

Assume that the DSP configuration for the particular beamforming polyphase 2D FIR double-trapezoidal filter  $\bar{H}_{\text{TR-D}[W_c]}(z_x, z_t)$  is selected as follows,

- Word-length of filter-coefficients  $W_c = 12$ -bits
- Word-length of input-data  $W = 12$ -bits
- Word-length of multiplier-output  $W_m = 14$ -bits
- Word-length of adder-output  $W_a = 19$ -bits (following (6.7)).

Now the SNDR at the output of  $\bar{H}_{\text{TR-D}[W_c]}(z_x, z_t)$ , can be estimated with (6.22) by substituting the parameters  $a$ ,  $M$ ,  $\kappa$  and  $\gamma$  that correspond to  $W_c = 12$ -bits where the variance of input-data quantization noise  $\sigma_i^2 = 2^{-2W}/3$  (see subsection 6.2.1) and the variance of the product quantization noise  $\sigma_p^2 = 2^{-2W_m}/3$  (see subsection 6.2.2). Note that the input signal power  $\sigma_S^2/\beta^{29}$  and input co-channel interference signal power  $\sigma_{\text{Int}}^2$  are specified by the *input signal-to-interference-ratio* (ISIR) that is defined as

$$[\text{ISIR}_{\text{dB}}] = 10 \log_{10} \frac{\sigma_S^2}{\beta^2 \sigma_{\text{Int}}^2} \quad , \quad (6.23)$$

where  $\beta$  is the coefficient scaling factor that is defined in (6.14). Here, it is assumed that the front-end automatic-gain-control (AGC) systems of the receiver keep the total signal and interference power at a constant level at the input of the ADCs such that  $\sigma_S^2/\beta^2 +$

---

<sup>9</sup>Due to the scaling of the filter coefficients by  $\beta$ , the output signal power  $\sigma_S^2$  is  $\beta^2$  higher than the signal power at the input.

$\sigma_{\text{Int}}^2 = 1/9$ . Hence according to [61], the probability of sampled unquantized sequence  $\{x_{\text{C}}(n_t T) \mid x_{\text{C}}(n_t T) \in [-1, 1]\}$  is 0.997 and the probability of saturation of ADCs, which are having the input range  $[-1, 1]$ , is 0.003. With the selected DSP configuration and an input sequence of ISIR = -40 dB, according to (6.22) the estimated SNDR for this particular beamforming polyphase 2D FIR double-trapezoidal filter  $\bar{H}_{\text{TR-D}[\text{W}_c]}(z_x, z_t)$  is 18.05 dB.

### Estimating the SNDR at the Outputs of a Series of Beamforming Polyphase 2D FIR Double-Trapezoidal Filters

Now let's consider a series of beamforming polyphase 2D FIR double-trapezoidal filters  $H_{\text{TR-D}}(z_x, z_t)$ , of order  $(32 \times 32)$  that are designed to meet the specifications  $K = 0.1$ ,  $\phi \in [30^\circ, 150^\circ]$  and  $\Delta\phi = 5^\circ$ , which enables the selectively enhancement of the desired signals arriving in the angular-range  $[\phi - 5^\circ, \phi + 5^\circ]$  for  $\phi \in [30^\circ, 150^\circ]$ . For the series of  $H_{\text{TR-D}}(z_x, z_t)$ , the computed values for the parameters  $a$ ,  $\gamma$ ,  $\kappa$  and  $M$  are presented in Figure 6.12, Figure 6.13, Figure 6.14 and Figure 6.15, respectively. Hence, in order to estimate the SNDR at the output of any particular beamforming 2D FIR double-trapezoidal filter of order  $(32 \times 32)$ , which is designed to selectively enhance the desired signals arriving in the angular-range  $[\phi - 5^\circ, \phi + 5^\circ]$  for  $\phi \in [30^\circ, 150^\circ]$ , the parameters  $a$ ,  $\gamma$ ,  $\kappa$  and  $M$  corresponding to the beamformer associated with the particular  $\phi$  are substituted into (6.22) along with other parameters  $\sigma_i^2$ ,  $\sigma_p^2$ ,  $\sigma_S^2$  and  $\sigma_{\text{Int}}^2$ . In the following subsection, the estimated SNDRs for different DSP configurations of the beamforming 2D FIR double-trapezoidal filter of order  $(32 \times 32)$ , which is designed to selectively enhance the signals arriving from the angular range  $[30^\circ, 40^\circ]$ , are compared with the calculated SNDRs using Monte Carlo simulations.

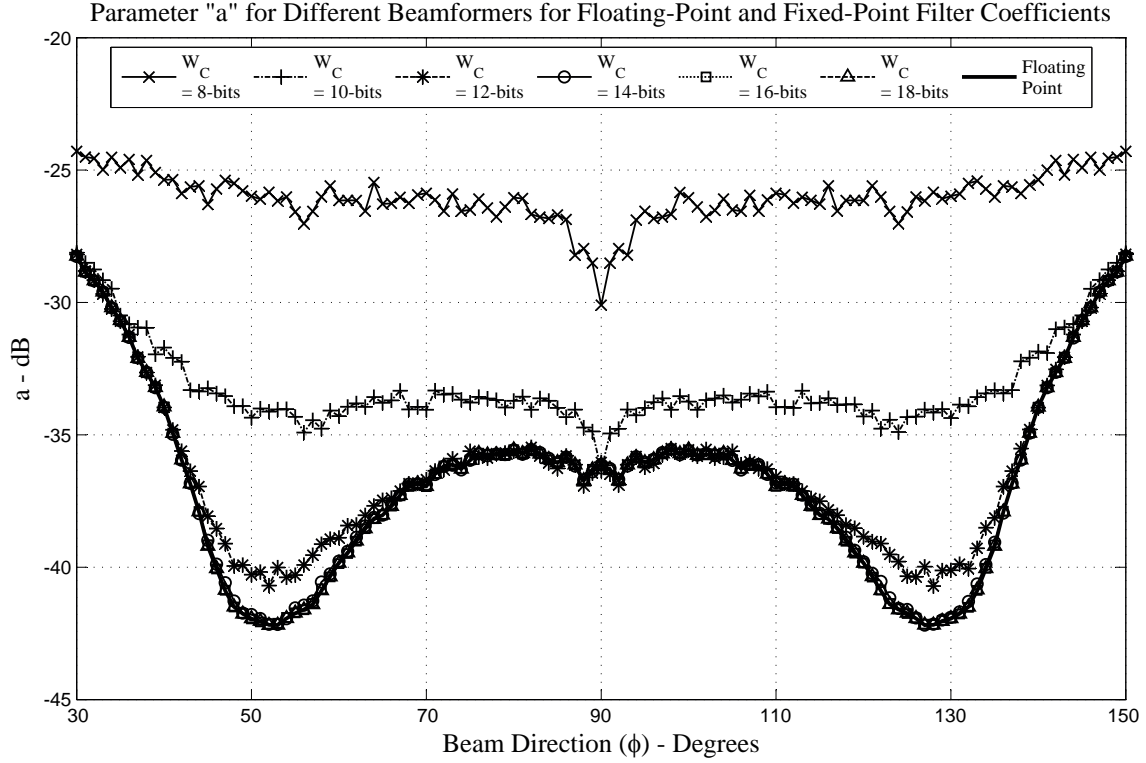


Figure 6.12: The parameter “ $a$ ” evaluated for different beamformers directed at  $\phi$  for  $\phi \in [30^\circ, 150^\circ]$  where the corresponding filter coefficients are represented with two’s complement format with  $W_c = 8, 10, 12, 14, 16$  and 18-bits and the floating point format.

#### 6.4.3 Comparison Between Estimated SNDRs and Calculated SNDRs with the Monte Carlo Simulations

Consider the following scenario where the desired signal, which is arriving along the direction specified by  $\bar{\phi} = 55^\circ$  from the broadside of the 1D-UDSA, is contaminated by four co-channel interfering signals, which are arriving along the directions specified by  $\phi = 15^\circ$ ,  $\phi = 80^\circ$ ,  $\phi = 105^\circ$  and  $\phi = 160^\circ$ , respectively. For all 5 signals, the bandwidth spread factor ( $K$ ) is 0.1 with 85% spectral-occupancy. Note that with respect to the desired signal arriving along  $\bar{\phi} = 55^\circ$  the SIR is as low as -40 dB. The beamforming polyphase 2D FIR double-trapezoidal filter [59] of order  $(32 \times 32)$  has been designed to selectively enhance the signals arriving in the angular range  $[50^\circ, 60^\circ]$  for the recovery of the desired signal. In this case, the SNDR at the beamformer output  $y_B(n_t)$  required to

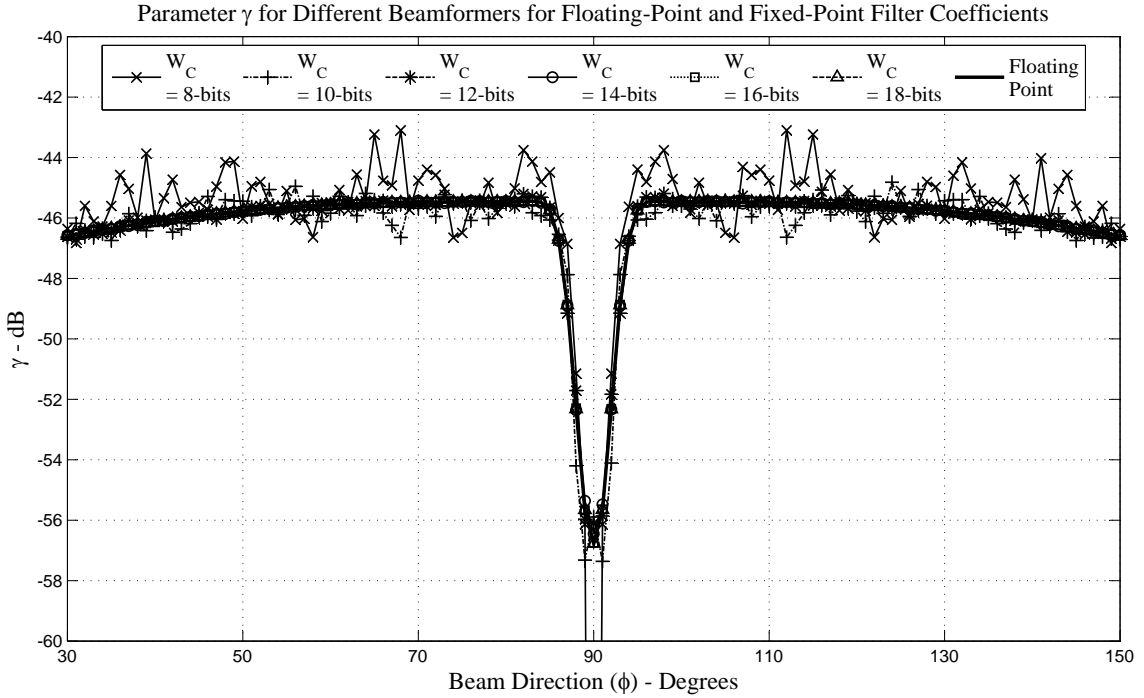


Figure 6.13: The parameter “ $\gamma$ ” evaluated for different beamformers directed at  $\phi$  for  $\phi \in [30^\circ, 150^\circ]$  where the corresponding filter coefficients are represented with two’s complement format with  $W_c = 8, 10, 12, 14, 16$  and 18-bits and the floating point format.

be better than 20 dB.

In order to evaluate the SNDR of  $y_B(n_t)$  for the above scenario, a series of Monte Carlo simulations have been carried out using MATLAB Fixed-Point Toolbox for different DSP configurations in implementing of the beamforming polyphase 2D FIR double-trapezoidal filter  $\bar{H}_{\text{TR-D}[W_c]}(z_x, z_t)$ . Here, filter coefficients of  $W_c = 12$ -bits are selected because according to Table 6.1, it is the smallest word-length that closely approximate the effective stopband attenuation and the effective passband ripple of a transfer function of the floating-point represented filter coefficients. In these Monte Carlo simulations, the register-lengths of the outputs of multipliers are varied such that  $W_m = 10, 11, \dots, 16$ . Hence, according to (6.7), the outputs of adders should be assigned with  $W_a = W_m + 5$ -bit registers to avoid adder-overflow errors because  $\lceil \log_2(|\bar{h}_{\text{TR-DI}[W_c]}(z_x, z_t)|) \rceil = 5$ , for  $W_c = 12$ -bit filter-coefficients. The *complex tri-stage sampled* test sequences of size  $(33 \times 1000)$  that correspond to different SIR levels are synthesized using Equation (17) of

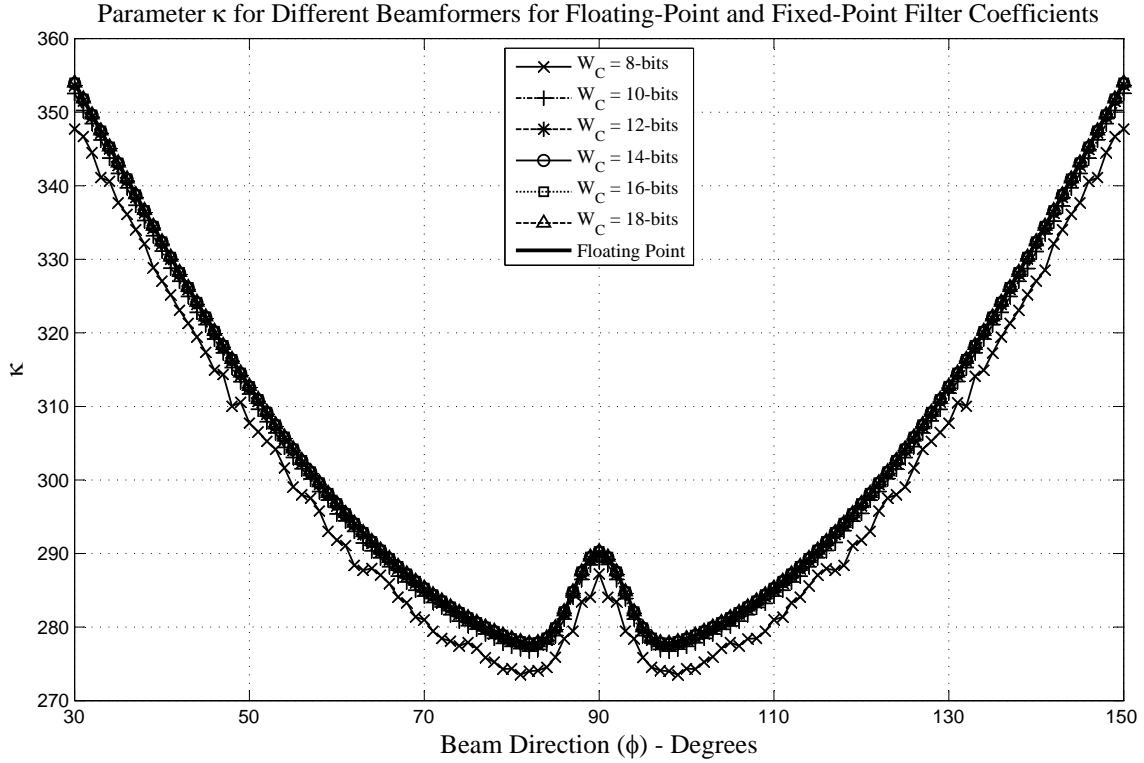


Figure 6.14: The parameter “ $\kappa$ ” evaluated for different beamformers directed at  $\phi$  for  $\phi \in [30^\circ, 150^\circ]$  where the corresponding filter coefficients are represented with two’s complement format with  $W_c = 8, 10, 12, 14, 16$  and  $18$ -bits and the floating point format.

[59] and represented with  $W = 12$ -bit two’s complement format. For different input SIR levels, the calculated SNDRs of  $y_B(n_t)$  with the Monte Carlo simulations are plotted in Figure 6.16 along with the SNDRs estimated with (6.22).

The estimated SNDR (dashed-line) and calculated average SNDR (circles-o) with Monte Carlo simulations for the floating-point represented beamforming filter are shown in Figure 6.16 (a). As shown there, the close agreement between the estimated SNDR and calculated averaged SNDR for the floating-point represented beamforming filter confirms the validity of the theoretical model. The estimated SNDRs (solid) and the calculated average SNDRs (o) with Monte Carlo simulations for fixed-point implemented beamforming filter with  $W_m = 10, 11, 12, 13, 14, 15$  and  $16$ -bits are shown in Figure 6.16 (b) - (h), respectively. Note that the estimated SNDR (dashed-line) for floating-point represented beamforming filter is also plotted in filter Figure 6.16 (b) - (h), which is considered as

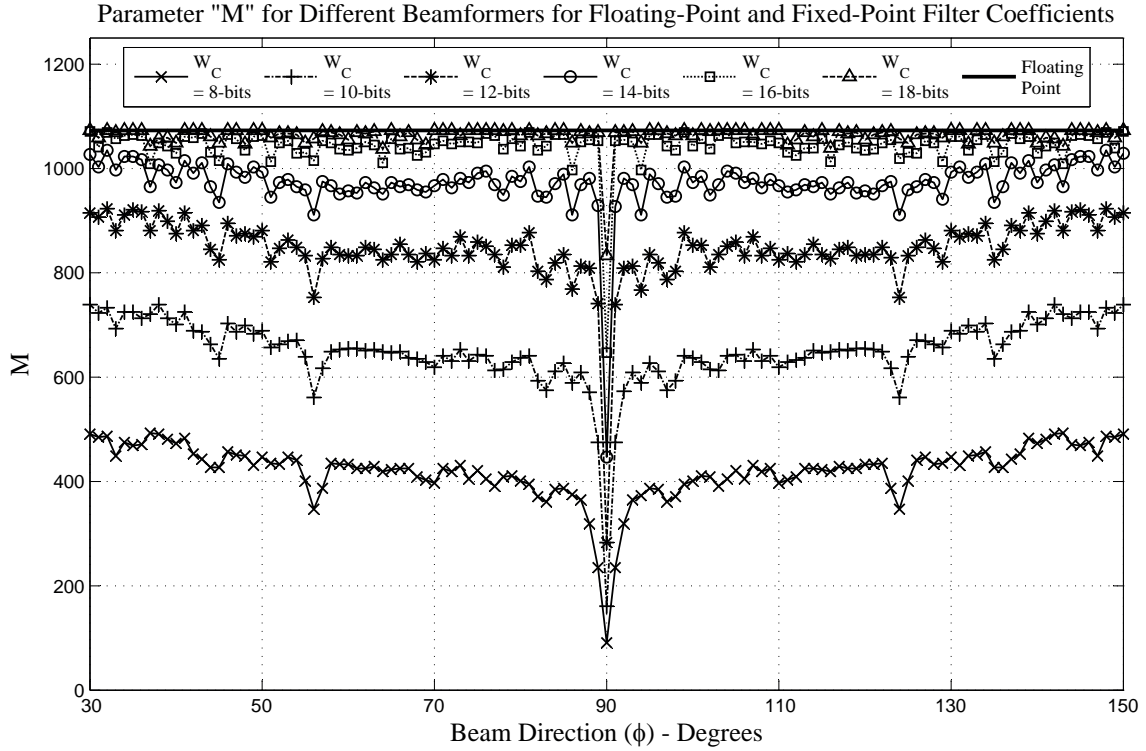


Figure 6.15: The parameter “ $M$ ” evaluated for different beamformers directed at  $\phi$  for  $\phi \in [30^\circ, 150^\circ]$  where the corresponding filter coefficients are represented with two’s complement format with  $W_c = 8, 10, 12, 14, 16$  and 18-bits and the floating point format.

the upper limit for the SNDRs achieved with fixed-point representation. As expected the SNDR for  $W_m = 10$  is the worst among the tested cases because of the accumulated product quantization noise at the output. According to Figure 6.16 (f), (g) and (h), for  $W_m = 14, 15$  and 16, the maximum degradations of both the estimated and calculated SNDRs compared to the floating-point implemented filter are -3 dB, -0.5 dB and -0.2 dB, respectively. Therefore, the polyphase 2D FIR double-trapezoidal filter-based beamformer implemented with the DSP configuration of  $W = 12$ -bit input-data samples,  $W_c = 12$ -bit filter-coefficients,  $W_m = 14$ -bit multiplier=products and  $W_a = 19$ -bit partial-sums, is capable of achieving the SNDR within 3 dBs of the maximum achievable value with floating point representation.

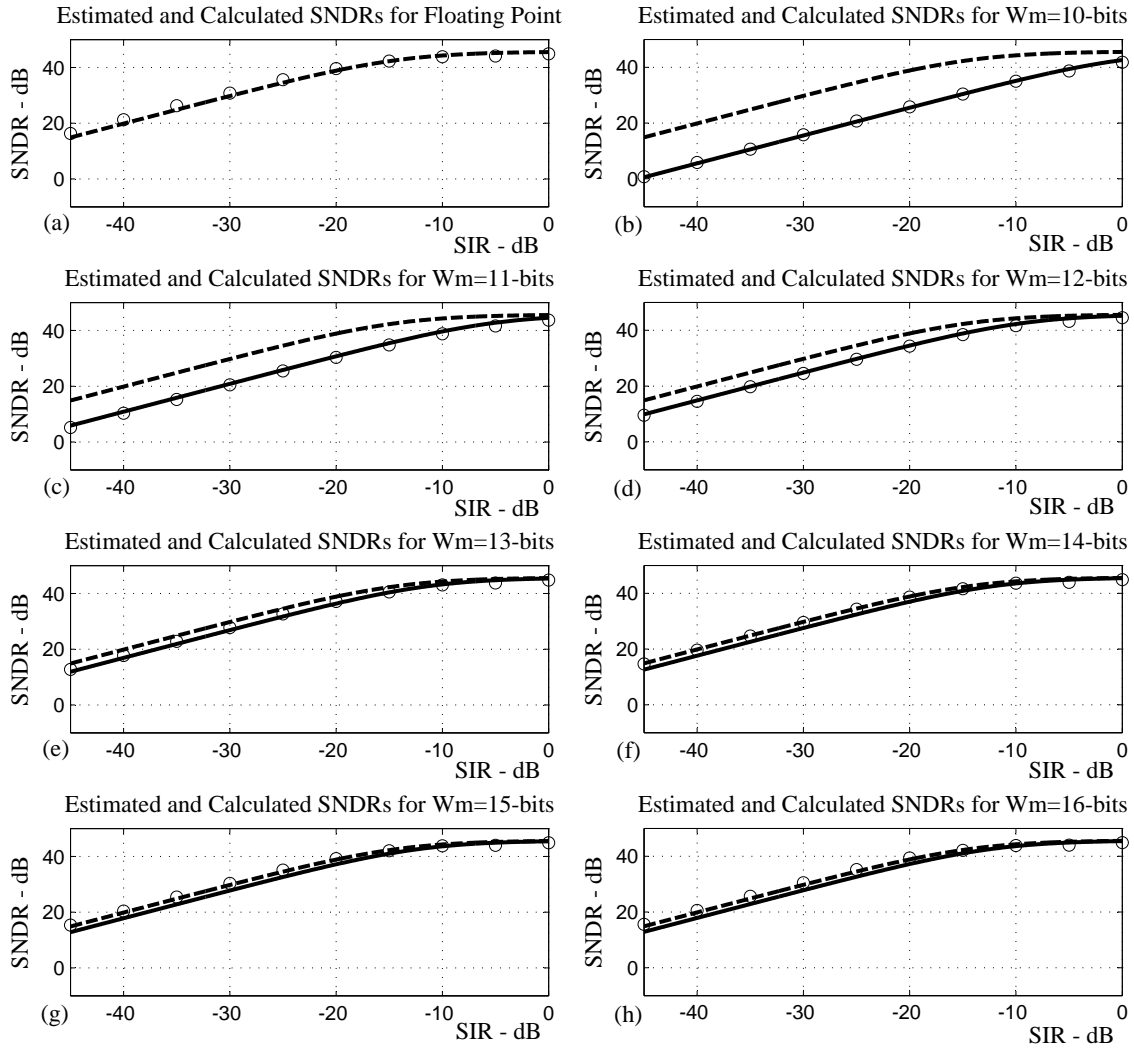


Figure 6.16: The comparison between the estimated SNDRs and the calculated SNDRs for  $W_m = 10, 11, 12, 13, 14, 15$  and  $16$ -bits and floating point represented filters for different input SIR levels. The estimated SNDRs (dashed) for the floating-point implemented beamforming filter are shown in Figures (a) - (h). The estimated SNDRs (solid) for fixed point implemented beamforming filter with  $W_m = 10, 11, 12, 13, 14, 15$  and  $16$ -bits are shown in Figures (b) - (h). The calculated SNDRs (o) with Monte Carlo simulations for floating point and fixed point (with  $W_m = 10, 11, 12, 13, 14, 15$  and  $16$ -bits) implemented beamforming filters are shown in Figures (a) - (h), respectively.



## 6.5 An Example of FPGA Implementation of Beamforming Polyphase 2D FIR Double-Trapezoidal Filter

The proposed FPGA architecture for the real-time implementation of the beamforming polyphase 2D FIR double-trapezoidal filter [68] maintains the hardware complexity at a tolerable level while limiting the reduction of SNDR that is within 3 dB of the ideal case with the floating-point representation. It is estimated that the full implementation of the beamforming 2D FIR filter of order  $(32 \times 32)$  with  $W = 12$ -bit input-data,  $W_c = 12$ -bit filter-coefficients,  $W_m = 14$ -bit multiplier-products and  $W_a = 19$ -bit partial-sums requires seven Xilinx Virtex-4 Sx35 ff668-10 FPGAs. However, the proposed filter is only partially<sup>10</sup> prototyped in a single Xilinx Virtex-4 Sx35 ff668-10 FPGA using XtremeDSP Kit-4 system. The full-filter responses for the test sequences are generated using on-chip “hardware-in-the-loop” testing that is associated with the hardware co-simulation feature of the Xilinx System Generator.

### 6.5.1 The FPGA Implementation of the Polyphase 1D FIR Building Block

The polyphase 1D FIR building block shown in Figure 6.4 (see page 244) is implemented using two reusable IP cores, which consist of two conventional direct-form (or transposed direct-form) 1D FIR filter structures for phase 0 and phase 1. The structure for phase 0 consists of 17 parallel multipliers and a 16-input pipelined adder-tree where as the structure for phase 1 consists of 16 parallel multipliers and a 15-input pipelined adder-tree.

---

<sup>10</sup>Due to the limited availability of FPGAs.

### 6.5.2 Throughput and Computational Complexity of the Polyphase 1D FIR Building Block

Given that  $f_S$  is the sampling rate of the analog-to-digital converter (A/D), a single polyphase 1D FIR building block, operating at the clock frequency of  $f_{CLK} = f_S/2$ , has a real-time throughput of  $C_M = 33 \cdot f_{CLK}$  parallel multiplications per second, and  $C_{A/S} = 32 \cdot f_{CLK}$  parallel additions per second. The total computational throughput of the beamforming polyphase 2D FIR double-trapezoidal filter, for 33 sensors, is  $33 \cdot C_M$  multiplications per second, and  $33 \cdot (C_{A/S} + 1) - 1$  additions per second.

### 6.5.3 Estimated FPGA Resources for Filter Designs for Different $W_m$

Five FPGA designs has been considered for the beamforming polyphase 2D FIR double-trapezoidal filter of order  $(32 \times 32)$  using bit-true cycle-accurate Xilinx System Generator and MATLAB/SIMULINK design and simulation tools. In these designs the register lengths for input-data and filter-coefficients were set to  $W = 12$ -bits and  $W_c = 12$ -bits, respectively while the register lengths for multiplier-products and partial-sums are changed such that  $W_m = 11, 12, 13, 14$  and  $15$ -bits and  $W_a = W_m + 5$ -bits, respectively. The FPGA resources that are required for the full implementation of the beamforming polyphase 2D FIR trapezoidal filter for above 5 designs are estimated using the Xilinx System Generator tool “Resource Estimator”. A summary of the required recourses is given in Table 6.2.

### 6.5.4 Design Partitioning and a Multiple-FPGA Physical Implementation

According to the estimates of the FPGA recourses required for the full implementation of the beamforming polyphase 2D FIR double-trapezoidal filter given in the previous subsection, the selected designs are too resource intensive for the currently available single-FPGA. However, the implementation may be partitioned across several high-capacity FPGAs such as Xilinx LX200 or Xilinx SX55. Here, the Xilinx Sx35 ff668-10 FPGA-chip

Table 6.2: Estimated FPGA Resources For the Beamforming Polyphase 2D FIR Double-Trapezoidal Filters with Different Word-Lengths Combinations.

$W_m$	Slices	(FFs)	(LUTs)	IOBs	Embedded Mults
11	90156	97680	129558	1336	1089
12	92466	99762	134914	1402	1089
13	97680	101904	141371	1468	1089
14	99990	104016	147840	1534	1089
15	104082	106128	153186	1600	1089
16	106392	108240	158614	1666	1089

was selected<sup>11</sup> and 5 polyphase 1D FIR building blocks (see Figure 6.4) of the beamforming polyphase 2D FIR double-trapezoidal filter have been physically implemented on the FPGA. In this physical-implementation, the register lengths are selected as  $W = 12$ ,  $W_c = 12$ ,  $W_m = 14$  and  $W_a = 19$ -bits for input-data, filter-coefficients and the output of the multipliers and adder-trees, respectively.

The 5-block physical-implementation on Xilinx Sx35 ff668-10 FPGA-chip consumed 10809 slices (out of 15360), 11911 flip-flops (FFs) (out of 30720), 15201 4-input look up tables (LUTs) (out of 30720), 110 bonded input-output blocks (IOBs) (out of 448), and 165 embedded DSP48 type  $18 \times 18$  multipliers (out of 192). The post place-and-route timing analysis yielded critical timing corresponding to 9.7 ns, implying a maximum real-time clock frequency of 103 MHz. The critical path delays are estimated by the xflow tool in the Xylinx ISE suite and are given by the parameters sysgen\_clk and dsp\_clk in the xflow.results file were 0.599 ns and 0.415 ns, with maximum delays of 3.144 ns, and 2.959 ns, respectively.

---

<sup>11</sup>The FPGA chip that was available for the MDSP Group.

### 6.5.5 Some Results of the On-chip Stepped Hardware Co-Simulations of the Modeled FPGA Implementation

The FPGA physical-implementation proposed in the previous subsection has been tested and verified using the “hardware-in-the-loop” feature of the hardware co-simulation testing of the Xilinx System Generator. In the following example, the beamforming polyphase 2D FIR double-trapezoidal filter of order  $(32 \times 32)$ , which is designed to selectively enhance the signals of bandwidth spread factor  $(K)$  [59] = 0.1 arriving in the angular range  $[50^\circ, 60^\circ]$ , has been modeled in Xilinx System Generator with the register lengths selected as  $W = 12$ ,  $W_c = 12$ ,  $W_m = 14$  and  $W_a = 19$ -bits for input-data, filter-coefficients and the output of the multipliers and adder-trees, respectively. This beamformer model has been employed in recovering the desired signal contaminated by four co-channel interfering signals each having 20 dB higher power level compared to the desired signal. In this example, the desired signal is arriving from  $55^\circ$  from the broadside of the 1D-UDSA where the four interfering signals are arriving from  $15^\circ$ ,  $70^\circ$ ,  $95^\circ$  and  $155^\circ$  from the broadside of the 1D-UDSA, respectively. Here, the 5 test signals are selected to be sinc pulses of 85% spectral occupancy, where each pulse is having a different initiation-delay.

A typical comparison of the outputs of the modeled beamformer in response to the above test signal is shown in Figure 6.17. According to Figure 6.17 (top), which shows the signals recovered without beamforming, the desired signal is irrecoverably suppressed if either of these interfering signals overlaps in time with the desired signal. The output  $y_{B[\text{FP}]}(n_t)$  of the floating-point implementation of the polyphase 2D FIR double-trapezoidal filter-based beamformer is shown in Figure 6.17 (middle). The SNDR of  $y_{B[\text{FP}]}(n_t)$  is 40.78 dB. However, the output  $y_{B[\text{WC}]}(n_t)$  of the modeled beamformer with the proposed fixed-point implementation, which is shown in Figure 6.17 (bottom), is 37.86 dB. This illustrates the effective recovery of the desired signal with the proposed fixed-point implementation. The bit-true cycle-accurate simulations showed that the

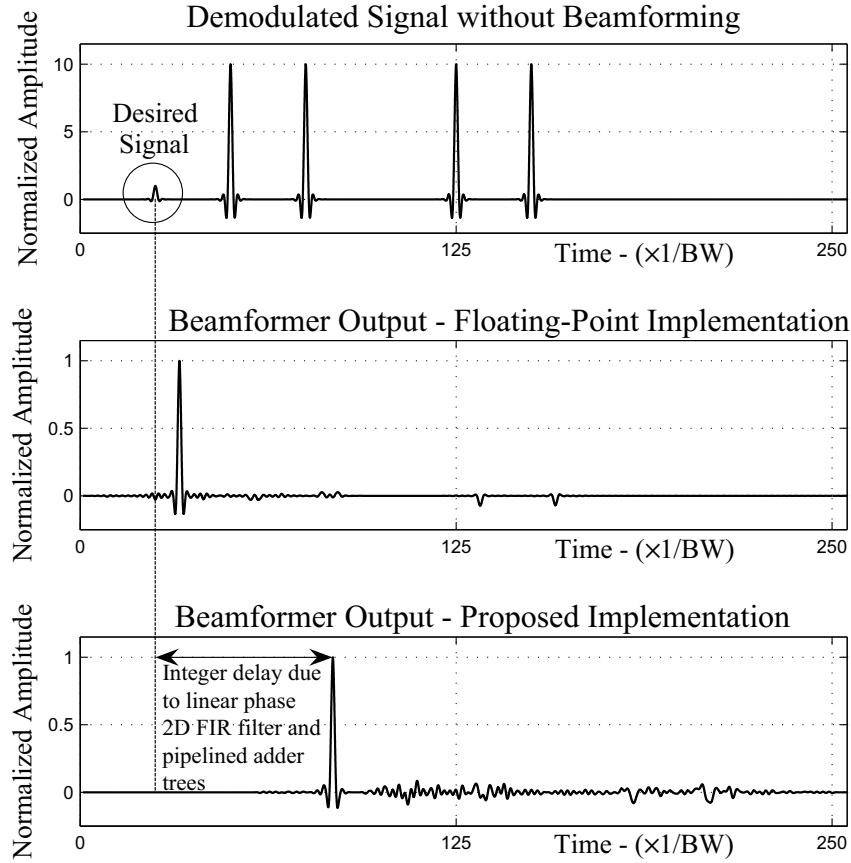


Figure 6.17: The demodulated signal without beamforming (top), output of the beamformer with ideal floating point implementation (middle) and the output of the beamformer with proposed fixed point implementation (bottom).

achieved SNDR of  $y_B(n_t)$  is 37.86 dB, which is only 2.92 dB less than the SNDR achieved with the floating point implementation. Such degradation is acceptable for most applications including for wireless smart antennas, radar, sonar and ultrasound imaging [23][45].

## 6.6 Summary

In this chapter, an analysis of the finite-word-length effects of beamforming MD FIR filters has been given. Here, it is assumed that the beamforming MD FIR filters are implemented with a parallel connected 1D/2D arrays of 1D direct-form FIR filters. The main contribution of this chapter is the proposed theoretical model that estimates the

SNDR of the output of MD FIR filter-based beamformers having a specific DSP configuration. Also, an example of an FPGA implementation of a typical beamforming polyphase 2D FIR double-trapezoidal filter has been outlined in this chapter.

A review of the quantization noise generation in the ADCs and the outputs of digital multipliers, transfer function distortion due to coefficient quantization, adder overflow errors and different 1D FIR filter structures have been given in section 6.2. Assuming the MD FIR filter-based beamformers are implemented with parallel connected 1D/2D arrays of direct-form (or transposed direct-form) 1D FIR filter structures, a theoretical model has been derived in section 6.4 in order to estimate the SNDR at the output of the beamformer. In subsection 6.4.2, the derivation of parameters for a particular beamformer is demonstrated by taking the example of a polyphase 2D FIR double-trapezoidal filter-based beamformer. A series of Monte Carlo simulations has been conducted for different DSP configurations of the same polyphase 2D FIR double-trapezoidal filter-based beamformer. It has been observed that the calculated SNDRs from the Monte Carlo simulations closely agree with the estimated SNDRs from the theoretical model. Based on these results, an FPGA implementation of the beamforming polyphase 2D FIR double-trapezoidal filter is proposed in section 6.5. Here, the objective is to minimize the hardware complexity while keeping the signal degradation at the output of the beamformer, due to noise and distortion, at an acceptable level (e.g. within 3 dB of the ideal, in this case). The bit-true cycle-accurate simulation results also confirm that the fixed-point hardware implementation of the polyphase 2D FIR double-trapezoidal filter-based beamformers are capable of achieving SNDR levels at the output within 3 dB of the SNDR levels achieved using the floating point implementation for SNR levels at least up to -40 dB.

## Chapter 7

### Conclusions and Future Work

#### 7.1 Conclusions

Two MD FIR filter-based beamforming methods have been proposed for propagating temporally-broadband-bandpassed signals received by 1D/2D uniformly distributed antenna arrays. In the first method, a real-time adaptive filter design method has been proposed for the beamforming complex-coefficient 2D FIR asymmetric-trapezoidal filter for the front-end broadband-bandpass beamforming in CR systems having SDR front-ends. The performance of the proposed beamformer has been compared with other broadband beamforming methods such as the digital DFT beamformer [138], the digital interpolation delay-and-sum beamformer [101] and the Sekiguchi-method [139], which can be employed for broadband beamforming in CR systems. According to the simulation results given in sections 4.6 and 4.7, compared to the broadband-beamforming methods [101][138][139] and many other similar methods, the proposed 2D FIR trapezoidal filter-based method achieves the best overall performance for a CR system considering instantaneous adaptability, lower distortion of the desired signal and higher attenuation of the co-channel interference signals with given computational complexity.

In the second method, a 3D FIR frustum filter-based beamformer has been proposed for the real-time pre-processing of FPA signals for broadband detection applications of the SKA such as pulsar timing observations and pulsar profile studies using coherent de-dispersion [175]. Here, a combined frequency-sampling and 3D window-based design method has been proposed in order to approximate the ideal 3D frustum-shaped transfer function such that the dominant spectral components of receiver noise, off-dish RFI

and ground thermal noise are suppressed in the stopband while the dominant spectral components of the SOIs are enhanced in the passband. The numerical analysis presented in section 5.5, has confirmed that the proposed 3D FIR frustum filter-based beamformer achieves lower distortion compared to the conventional 2D spatial-only beamformer and the 3D CFM beamformer. The 2D spatial-only beamformer resulted in the highest distortion because its passband is designed considering the properties of only the center frequency of the SOIs. On the other hand for the 3D CFM beamformer, the spatio-temporal characteristics of SOIs for the entire operational bandwidth have been considered in its design however, it does not consider the spatio-temporal characteristics of off-dish RFI and ground thermal noise.

The Focal Field Synthesizer (FFS), a GPU accelerated computer program, has been proposed to evaluate the electric field in the focal region of a paraboloidal reflector. The accuracy of the electric fields evaluated with the FFS has been verified using the GRASP9 [58], which is a widely used EM field evaluation software for analyzing reflector antennas. According to the Huygens' Principle Approximation, it has been deduced in chapter 3, that the ROS the spectra of focal-plane electric-fields is given by a 3D frustum. In subsection 3.2.2, this has been verified using the focal-plane electric-fields evaluated using the FFS. Also in the design of complex-coefficient 3D FIR frustum filters in subsection 5.4.2 of chapter 5, FFS has been used in generating the ideal 3D phase-response of the focal field for the design of 3D FIR frustum filters. Further in section 5.5, the FFS has been employed in generating the test sequences for evaluating the performance of the FPA beamforming methods.

A combined theoretical and empirical process has been used in section 6.4, in order to study the degradation of SNDR at the outputs of beamforming MD FIR filters due to finite-word-length-effects. Using the example of beamforming polyphase 2D FIR double-trapezoidal filter that has been implemented with an array of direct-form 1D FIR filters,



a theoretical model has been proposed to estimate the SNDR at the output for a given DSP configuration. Monte Carlo simulations have been conducted to evaluate the average SNDRs at the output of the same beamforming polyphase 2D FIR double-trapezoidal filter implemented with the identical FIR structure for the given DSP configuration, which has been used in the estimation. It has been shown in Figure 6.16, that the calculated SNDRs from the Monte Carlo simulations closely agree with the estimated SNDRs from the theoretical model. Following the estimated and calculated SNDRs achieved with a particular DSP configuration of a particular beamforming polyphase 2D FIR double-trapezoidal filter, an FPGA implementation of the parallel connected direct-form 1D FIR filter structure has been proposed in section 6.5. The results achieved with bit-true cycle-accurate on-chip stepped hardware co-simulations imply that by proper assignment of register-lengths for input-data, filter-coefficients, multiplier-outputs and adder-tree-outputs, the degradation of the SNDR at the output of the beamformer can be minimized.

## 7.2 Future Work

It has been mentioned in chapter 5 that full sampling focal plane arrays (FPAs) have been proposed for the lower-mid frequency-band (i.e. 0.5 - 1.7 GHz) of the SKA, as a means of increasing the field-of-view (FoV) of the paraboloidal reflector based receiver system [19][110][111]. Regarding the narrowband beamforming required in aperture synthesis imaging, significant progress has been achieved recently in understanding the signal characteristics in FPAs [216] and in designing optimum narrowband beamformers for FPAs [217]. However, still engineers are not satisfied with the sensitivity achieved with the FPAs for applications in radio astronomy. Therefore, the FPA receivers are not included in the Phase-I of the SKA engineering implementation that is scheduled to commence in year 2016 [178][179]. Nevertheless, full-sampling FPAs may have other applications in

microwave-imaging, remote-sensing, space-science, deep-space communications, satellite broadcasting and satellite communications [104][105][106][107][108][109]. With proper understanding of the noise spectral density of the FPA signals, the proposed broadband 3D FIR frustum filter-based beamforming method can be optimized to achieve the best sensitivity for pulse type broadband signals. An accurate estimate of the noise spectral density in the **PNC** can be achieved with simulations by extending the concept of “SNR element-patterns”, which has been proposed in [54][192]. It would be worth to use the models of wideband elemental antennas given in [218] in order to simulate the noise coupling and to estimate the noise spectral density in the **PNC** that in turn leads to the optimal design of beamforming 3D FIR frustum filters.

Also according to chapter 5, it is expected that most of the time the SKA will be operating in the aperture synthesis mode observing the spectral densities corresponding to the red-shifted HI-line. The typical architecture for the front-end signal processing stages that have been proposed to be used in the aperture synthesis mode is shown in Figure 5.5 (see page 190). As shown there, prior to beamforming, the broadband signals at the outputs of the LNAs are divided in to large number of channels (e.g. 512, 1024) using a polyphase analysis filter-bank (e.g. maximally-decimated polyphase-DFT filter-bank) [142]. Then, narrowband beamforming methods [180][186][217], are applied to sub-groups of FPA signals for each individual channel in order to form narrowband sky-beams spanning the FoV. Note that different sets of beamforming coefficients are required to form channel-specific sky-beams for each sub-group of FPA signals. It has been proposed that by exploiting *perfect-reconstruction techniques* [142], the beamformed narrowband channel signals can be recombined such that the original broadband signal corresponding to the celestial source is reconstructed with minimum distortion. With this approach to broadband beamforming, the front-end signal processing architecture of the SKA receivers can be kept unchanged for both narrowband (e.g. HI surveys)

and broadband (e.g. pulsar timing- and profile- studies) observations. Hence, such an architecture can facilitate a number of simultaneous astronomical surveys that include both narrowband and broadband observations. However, it is believed that in the VLSI implementation of the analysis- and synthesis- polyphase filter-banks may require longer register-lengths for multiplier-outputs in order to maintain the SNDR at a tolerable level compared to direct implementation. Hence, it would be an interesting future project to compare the computational complexity required by the VLSI implementations of the 3D FIR frustum filter-based beamformer and the perfect-reconstruction analysis-synthesis filter-bank-based beamformer in order to achieve a specified SNDR at the output.

## Bibliography

- [1] J. Schiller, *Mobile Communications*, 2nd ed. Addison Wesley, Sep. 2003.
- [2] T. S. Rappaport, *Wireless Communications: Principles and Practice*, 2nd ed. Prentice Hall, Jan. 2002.
- [3] J. L. Yen, “Image reconstruction in synthesis radio telescope arrays,” in *Array Signal Processing*, S. Haykin, Ed. Prentice-Hall Inc., Englewood Cliffs, New Jersey 07632, 1985.
- [4] T. L. Wilson, K. Rohlf, and S. Httmeister, *Tools of Radio Astronomy*. Springer, Nov. 2010.
- [5] J. Eaves and E. Reedy, *Principles of Modern Radar*. Springer Publisher, Ltd., 1987.
- [6] S. Haykin, “Radar signal processing,” *IEEE ASSP Magazine*, vol. 2, no. 2, part 1, pp. 2–18, 1985.
- [7] N. L. Owsley, “Sonar array processing,” in *Array Signal Processing*, S. Haykin, Ed. Prentice-Hall Inc., Englewood Cliffs, New Jersey 07632, 1985.
- [8] R. P. Hodges, *Underwater Acoustics: Analysis, Design and Performance of Sonar*, 1st ed. Wiley, Aug. 2010.
- [9] K. M. Mudry, R. Plonsey, and J. D. B. (Editors), *Biomedical Imaging*. CRC Press, Boca Raton, FL., 2003.
- [10] A. C. Kak, “Tomographic imaging with diffracting and non-diffracting sources,” in *Array Signal Processing*, S. Haykin, Ed. Prentice-Hall Inc., Englewood Cliffs, New Jersey 07632, 1985.

- [11] A. Gilloire, F. Khalid, and J. Jullien, "Microphone array for sound pickup in teleconference systems," *Journal of Audio Engineering Society*, vol. 42, no. 9, pp. 691–700, 1994.
- [12] M. Brandstein and D. Ward, *Microphone Arrays: Signal Processing Techniques and Applications*, 1st ed. Springer, Jun. 2001.
- [13] H. Arslan, *Cognitive Radio, Software Defined Radio, and Adaptive Wireless Systems*. Springer, 2007.
- [14] I. Cosovic, F. K. Jondral, M. M. Buddhikot, and R. Kohno, *Cognitive Radio and Dynamic Spectrum Sharing Systems*. Hindawi Publishing Corp US SR, Apr. 2008.
- [15] B. A. Fette and B. Fette, *Cognitive Radio Technology*. Newnes, 2006.
- [16] L. E. Doyle, *Essentials of Cognitive Radio*, 1st ed. Cambridge University Press, May 2009.
- [17] M. Dillinger, K. Madani, and N. Alonistioti, *Software Defined Radio: Architectures, Systems and Functions*. Wiley, Jul. 2003.
- [18] P. Hall, *The Square Kilometre Array: An Engineering Perspective*. SpringerLink, 2005. [Online]. Available: <http://dx.doi.org/10.1007/1-4020-3798-8>
- [19] P. Hall, R. Schilizzi, P. Dewdney, and J. Lazio, "The Square Kilometer Array (SKA) radio telescope: Progress and technical directions," *The Radio Science Bulletin*, no. 326, pp. 4–19, September 2008.
- [20] B. Veidt and P. Dewdney, "A Phased-Array feed demonstrator for radio telescopes," in *Proc. of General Assembly, International Union of Radio Science (URSI)*, 2005. [Online]. Available: [http://www.ursi.org/Proceedings/ProcGA05/pdf/B04.10\(0638\).pdf](http://www.ursi.org/Proceedings/ProcGA05/pdf/B04.10(0638).pdf)

- [21] Y. Bhattacharjee, "Radio Astronomers Take Arms Against a Sea of Signals," *Science*, vol. 330, no. 6003, pp. 444–445, 2010. [Online]. Available: <http://www.sciencemag.org>
- [22] B. V. Veen and K. Buckley, "Beamforming: a versatile approach to spatial filtering," *ASSP Magazine, IEEE*, vol. 5, no. 2, pp. 4–24, Apr. 1988.
- [23] J. Liberti and T. Rappaport, *Smart Antennas for Wireless Communications-IS-95 and Third Generation CDMA Applications*. Prentice-Hall, 1999.
- [24] T. S. Rappaport, *Smart Antennas: Adaptive Arrays, Algorithms, & Wireless Position Location*. Institute of Electrical & Electronics Engineer, Oct. 1998.
- [25] A. Ardenne, H. Butcher, J. de Vaate, A. Boonstra, B. J. D. Bregman, Woestenburg, K. van der Schaaf, P. N. Wilkinson, and M. A. Garrett, "The aperture array approach for the Square Kilometre Array," ASTRON, Netherlands, Tech. Rep., May 2003.
- [26] J. Thorner, "Approaches to sonar beamforming," in *Southern Tier Technical Conference, 1990., Proceedings of the 1990 IEEE*, 1990, pp. 69–78.
- [27] K. Farrell, R. Mammone, and J. Flanagan, "Beamforming microphone arrays for speech enhancement," in *International Conference on Acoustics, Speech, and Signal Processing*, Mar. 1992.
- [28] D. L. Jones, "Four-dimensional sound source recovery from arbitrary acoustic arrays," in *Intl. Conf. on Multimedia and Expo, ICME'03*, vol. 3, 2003, pp. 41–44.
- [29] T. H. Hankins, J. S. Kern, J. C. Weatherall, and J. A. Eilek, "Nanosecond radio bursts from strong plasma turbulence in the Crab pulsar," *Nature*, vol. 422, no. 6928, pp. 141–143, 2003.

- [30] M. Bailes, "The art of precision pulsar timing," *Proceedings of the International Astronomical Union*, vol. 5, no. S261, pp. 212–217, 2009.
- [31] H. Burchett and M. Upton, "Application of broadband radar to volumetric sensing and distance measurement," *Sensor Review*, vol. 18, no. 2, pp. 111 –114, 1998.
- [32] I. G. Cumming and F. H. Wong, *Digital Processing Of Synthetic Aperture Radar Data: Algorithms And Implementation*. Artech House Publishers, 2005.
- [33] F. Nekoogar, *Ultra-wideband Communications: Fundamentals and Applications*. Prentice Hall PTR, 2006.
- [34] Y. Huang, "WiMAX dynamnic beamforming antenna," *Aerospace and Electronic Systems Magazine, IEEE*, vol. 23, pp. 26–31, 2008.
- [35] P. Ramamoorthy and L. Bruton, "Design of stable 2-Dimensional analog and digital filters with applications in image processing," *Circuit Theory and Applications - John Wiley and Sons, Ltd*, vol. 7, pp. 229–245, 1979.
- [36] L. Bruton, *RC-Active Circuits:Theory and Design*. Prentice-Hall, Englewood Cliffs, N.J. 07632, 1980.
- [37] M. Mani, "Analog 2D Spatio-Temporal filters for plane wave array processing," Ph.D. dissertation, University of Calgary, Apr. 2006.
- [38] S. Stergiopoulos, *Advanced Signal Processing Handbook*. CRC, 2001.
- [39] S. M. Kuo and W. S. Gan, *Digital Signal Processors: Architectures, Implementations, and Applications*. Prentice Hall, Apr. 2004.
- [40] S. M. Kuo, B. H. Lee, and W. Tian, *Real-Time Digital Signal Processing: Implementations and Applications*. Wiley, Jun. 2006.

- [41] L. T. Bruton, “Multidimensional signal processing course notes,” 2003.
- [42] D. Dudgeon and R. Mersereau, *Multidimensional Digital Signal Processing*. Prentice-Hall Inc., Englewood Cliffs, New Jersey 07632, 1984.
- [43] D. H. Johnson and D. E. Dudgeon, *Array Signal Processing: Concepts and Techniques*. Prentice Hall PTR, Feb. 1993.
- [44] H. Schroder and H. Blume, *One-and-Multidimensional Signal Processing: Algorithms and Applications in Image Processing*. John Wiley & Sons, Dec. 2000.
- [45] H. L. V. Trees, *Optimum Array Processing; Detection, Estimation and Modulation Theory, Part IV*. John Wiley and Sons, Inc., NY, 2002.
- [46] J. W. Woods, *Multidimensional Signal, Image, and Video Processing and Coding*, 1st ed. Academic Press, Mar. 2006.
- [47] T. Gunaratne and L. Bruton, “Adaptive complex-coefficient 2D FIR trapezoidal filters for broadband beamforming in cognitive radio systems,” *Circuits, Systems, and Signal Processing*, vol. 30, pp. 587–608, 2011, 10.1007/s00034-010-9246-9. [Online]. Available: <http://dx.doi.org/10.1007/s00034-010-9246-9>
- [48] —, “Broadband beamforming of bandpass plane waves using 2D FIR trapezoidal filters at baseband,” in *Circuits and Systems, 2006. APCCAS 2006. IEEE Asia Pacific Conference on*, 2006, pp. 546–549.
- [49] —, “Tracking broadband plane waves using 2D adaptive FIR fan filters,” in *Circuits and Systems, 2006. ISCAS 2006. Proceedings. 2006 IEEE International Symposium on*, 2006, p. 4 pp.
- [50] J. Cordes, “The Square Kilometre Array as a radio synoptic survey telescope: Widefield surveys for transients, pulsars and ETI,” SKA Memo 97, Tech.



- Rep., April 20, 2009. [Online]. Available: [http://www.skatelescope.org/uploaded/55809\\_97\\_memo\\_Cordes.pdf](http://www.skatelescope.org/uploaded/55809_97_memo_Cordes.pdf)
- [51] K. W. Martin, “Complex signal processing is not complex,” *IEEE Transactions on Circuits and Systems-1, Regular Papers*, vol. 51, no. 9, pp. 1823–1836, 2004.
- [52] R. Hansen, *Phased array antennas*. Wiley-Interscience, 2009.
- [53] A. Bhattacharyya, *Phased array antennas and subsystems: Floquet analysis, synthesis, BFNs, and active array systems*. John Wiley and Sons, Mar. 2006.
- [54] C. Craeye, B. Parvais, and X. Dardenne, “MoM simulation of signal-to-noise patterns in infinite and finite receiving antenna arrays,” *Antennas and Propagation, IEEE Transactions on*, vol. 52, no. 12, pp. 3245–3256, 2004. [Online]. Available: <http://ieeexplore.ieee.org/stamp/stamp.jsp?tp=&arnumber=1364140>
- [55] T. Gunaratne and L. Bruton, “Broadband beamforming of dense aperture array (DAA) and focal plane array (FPA) signals using 3D spatio-temporal filters for applications in aperture synthesis radio astronomy,” *Multidimensional Systems and Signal Processing*, vol. 22, pp. 213–236, 2011, 10.1007/s11045-010-0130-3. [Online]. Available: <http://dx.doi.org/10.1007/s11045-010-0130-3>
- [56] T. Gunaratne, L. Bruton, and P. Agathoklis, “Broadband beamforming of focal plane array (fpa) signals using real-time spatio-temporal 3d fir frustum digital filters,” *Antennas and Propagation, IEEE Transactions on*, vol. PP, no. 99, p. 1, 2011.
- [57] J. W. Baars, *The Paraboloidal Reflector Antenna in Radio Astronomy and Communication: Theory and Practice (Astrophysics and Space Science Library)*. Springer, Jul. 2007.

- [58] TICRA, GRASP9 - General reflector and antenna farm analysis software. [Online]. Available: [http://www.ticra.com/script/site/page.asp?artid=166&cat\\_id=148](http://www.ticra.com/script/site/page.asp?artid=166&cat_id=148)
- [59] T. Gunaratne and L. Bruton, "Beamforming of Broad-Band bandpass plane waves using polyphase 2-D FIR trapezoidal filters," *Circuits and Systems I: Regular Papers, IEEE Transactions on*, vol. 55, no. 3, pp. 838–850, 2008.
- [60] S. Kung, "VLSI array processors," *ASSP Magazine, IEEE*, vol. 2, no. 3, pp. 4–22, 2003.
- [61] B. Widrow and I. Kollr, *Quantization Noise: Roundoff Error in Digital Computation, Signal Processing, Control, and Communications*. Cambridge University Press, Jul. 2008.
- [62] M. D. Ercegovac and T. Lang, *Digital Arithmetic*. Morgan Kaufmann Publishers, 2004.
- [63] T. K. Gunaratne, "Beamforming of temporally broadband bandpass plane waves using 2D FIR trapezoidal filters," Master's thesis, University of Calgary, Dec. 2006.
- [64] T. Gunaratne and L. Bruton, "Beamforming of Temporally-Broadband-Bandpass plane waves using real polyphase 2-D FIR trapezoidal filters," in *Circuits and Systems, 2007. ISCAS 2007. IEEE International Symposium on*, 2007, pp. 589–592.
- [65] A. Antoniou, *Digital Signal Processing: Signals, Systems, and Filters*. McGraw-Hill Professional, Oct. 2005.
- [66] J. E. Proakis and D. G. Manolakis, *Digital Signal Processing; Principle, Algorithms and Applications*. Prentice-Hall Inc., Englewood Cliffs, New Jersey 07458, 1996.

- [67] F. Rivoallon, “Achieving Breakthrough Performance in Virtex-4 FPGAs,” *Xilinx Inc., San Jose, CA [Online]. Available: [www.xilinx.com](http://www.xilinx.com), WP218, ver. v1*, vol. 4, pp. 1–9, 2006.
- [68] T. Gunaratne, H. Madanayake, and L. Bruton, “An FPGA architecture for real-time polyphase 2D FIR double-trapezoidal plane-wave filters,” in *Circuits and Systems, 2008. APCCAS 2008. IEEE Asia Pacific*, 2008, pp. 984–987.
- [69] C. G. Someda, *Electromagnetic Waves*, 2nd ed. CRC Press, Jan. 2006.
- [70] S. Drabowitch, A. Papiernik, H. Griffiths, J. Encinas, and B. Smith, *Modern Antennas*, 2nd ed. Springer, Dec. 2005.
- [71] A. B. Carlson, P. B. Crilly, and J. Rutledge, *Communication Systems: An Introduction to Signals and Noise in Electrical Communication*. McGraw-Hill, 1986.
- [72] Wikipedia, “Hypercone — wikipedia, the free encyclopedia,” 2010, [Online; accessed 21-March-2011]. [Online]. Available: <http://en.wikipedia.org/w/index.php?title=Hypercone&oldid=369403194>
- [73] —, “Frustum — wikipedia, the free encyclopedia,” 2011, [Online; accessed 24-March-2011]. [Online]. Available: <http://en.wikipedia.org/w/index.php?title=Frustum&oldid=419945783>
- [74] A. V. Ardenne, “The technology challenges for the next generation radio telescopes,” in *Perspectives on Radio Astronomy - Technologies for Large Antenna Arrays*, Netherlands Foundation for Research in Astronomy, 1999, pp. x–xviii.
- [75] G. Matthaei, E. M. T. Jones, and L. Young, *Microwave Filters, Impedance-Matching Networks, and Coupling Structures*. Artech House, Inc., 1985.
- [76] G. Gonzalez, *Microwave Transistor Amplifiers: Analysis and Design*, 2nd ed. Prentice Hall, Aug. 1996.

- [77] D. M. Pozar, *Microwave Engineering*, 3rd ed. Wiley, Jan. 2004.
- [78] J. H. Reed, *An Introduction to Ultra Wideband Communication Systems*. Prentice Hall, Apr. 2005.
- [79] M. Neiman, “The principle of reciprocity in antenna theory,” *Proceedings of the IRE*, vol. 31, no. 12, pp. 666–671, 1943.
- [80] A. De Hoop, “A reciprocity relation between the transmitting and the receiving properties of an antenna,” *Applied Scientific Research*, vol. 19, no. 1, pp. 90–96, 1968.
- [81] D. Pozar, “The active element pattern,” *Antennas and Propagation, IEEE Transactions on*, vol. 42, no. 8, pp. 1176–1178, 1994.
- [82] M. Kragalott, W. Pickles, and M. Kluskens, “Design of a 5:1 bandwidth stripline notch array from FDTD analysis,” *IEEE Trans. on Antennas and Propagation*, vol. 48, pp. 1733–1741, 2000.
- [83] C. Craeye, T. Gilles, X. Dardenne, and R. Sarkis, “Fast Impedance and Pattern Evaluation for Phased Arrays Made of Complex Elements Involving Finite Dielectric Material,” in *The Second European Conference on Antennas and Propagation, (EuCAP 2007)*. IET, 2007, pp. 1–6.
- [84] S. Licul and W. Davis, “Unified frequency and time-domain antenna modeling and characterization,” *Antennas and Propagation, IEEE Transactions on*, vol. 53, no. 9, pp. 2882 – 2888, sept. 2005.
- [85] N. Farahat, V. Prakash, and R. Mittra, “Analysis of a Vivaldi phased array antenna using the conformal finite difference time domain (CFDTD) method,” in *Antennas and Propagation Society International Symposium, 2002. IEEE*, vol. 1. IEEE, 2002, pp. 516–519.

- [86] D. Schaubert, J. Aas, M. Cooley, and N. Buris, "Moment method analysis of infinite stripline-fed tapered slot antenna arrays with a ground plane," *Antennas and Propagation, IEEE Transactions on*, vol. 42, no. 8, pp. 1161–1166, Aug. 1994.
- [87] M. Cooley, D. Schaubert, N. Buris, and E. Urbanik, "Radiation and scattering analysis of infinite arrays of endfire slot antennas with a ground plane," *Antennas and Propagation, IEEE Transactions on*, vol. 39, no. 11, pp. 1615–1625, Nov. 1991.
- [88] P. Simon, K. McInturff, R. Jobsky, and D. Johnson, "Full-wave analysis of an infinite, planar array of linearly polarized,stripline-fed, tapered notch elements," in *Antennas and Propagation Society International Symposium Digest*, vol. 1, Jun. 1991, pp. 334–337.
- [89] H. Holter, T. Chio, and D. Schaubert, "Experimental results of 144-Element dual polarized endfire tapered slot phased arrays," *IEEE Trans. on Antennas and Propagation*, vol. 48, pp. 1707–1718, Nov. 2000.
- [90] M. Ivashina and J. Bregman, "Experimental synthesis of a feed pattern with a dense focal plane array," in *Microwave Conference, 2002. 32nd European*, sept. 2002, pp. 1–4.
- [91] M. Ivashina, J. Bregman, L. Li, and A. Parfitt, "Experimental results for a focal plane array, synthesized with conjugate field method," in *Antennas and Propagation Society International Symposium, 2004. IEEE*, vol. 1. IEEE, 2004, pp. 21–24.
- [92] B. Veidt, T. Burgess, R. Messing, G. Hovey, and R. Smegal, "The DRAO phased array feed demonstrator: Recent results," in *Antenna Technology and Applied Electromagnetics and the Canadian Radio Science Meeting, 2009. ANTEM/URSI 2009. 13th International Symposium on*, feb. 2009, pp. 1–4.

- [93] H. Nakano, *Wiley Encyclopedia of Electrical and Electronics Engineering*. John Wiley & Sons, Inc., 1993, ch. Receiving Antennas, pp. 270–273. [Online]. Available: <http://dx.doi.org/10.1002/047134608X.W1234>
- [94] R. E. Blahut, *Theory of Remote Image Formation*. Cambridge University Press, Jan. 2005.
- [95] D. S. Filipovic and T. Cencich, *Antenna Engineering Handbook*. McGraw-Hill, 2007, ch. 13 : Frequency Independent Antennas, pp. 13–1 – 13–67.
- [96] T. S. Bird and A. W. Love, *Antenna Engineering Handbook*. McGraw-Hill, 2007, ch. 14 : Horn Antennas, pp. 14–1 – 14–74.
- [97] J. S. Lim, *Two-dimensional Signal and Image Processing*. Prentice Hall, 1990.
- [98] T. S. Huang, “Two dimensional windows,” *IEEE Trans. Audio Electroacoust.*, vol. 20, no. 01, pp. 88–89, Mar. 1972.
- [99] J. F. James, *A Student’s Guide to Fourier Transforms: With Applications in Physics and Engineering*, 2nd ed. Cambridge University Press, Feb. 2003.
- [100] J. J. Benedetto and P. J. Ferreira, *Modern Sampling Theory*, 1st ed. Birkhuser Boston, Feb. 2001.
- [101] R. G. Pridham and R. A. Mucci, “Digital interpolation beamforming for low-pass and bandpass signal,” *Proceedings of the IEEE*, vol. 67, no. 6, pp. 904–919, Jun. 1979.
- [102] B. F. Burke and F. Graham-Smith, *An Introduction to Radio Astronomy*. Cambridge University Press, 2002.
- [103] D. A. Pujara, S. B. Sharma, and S. B. Chakrabarty, “Improving the beam efficiency of an off-set parabolic reflector antenna for space-borne radiometric

- applications,” *Progress In Electromagnetics Research C*, vol. 10, pp. 143–150, 2009. [Online]. Available: <http://www.jpier.org/PIERC/pier.php?paper=09080103>
- [104] P. W. Gaiser, K. M. S. Germain, E. M. Twarog, G. A. Poe, W. Purdy, D. Richardson, W. Grossman, W. L. Jones, D. Spencer, G. Golba, J. Cleveland, L. Choy, R. M. Bevilacqua, and P. S. Chang, “The WindSat spaceborne polarimetric microwave radiometer: sensor description and early orbit performance,” *Geoscience and Remote Sensing, IEEE Transactions on*, vol. 42, no. 11, pp. 2347–2361, Nov. 2004. [Online]. Available: [http://ieeexplore.ieee.org/xpls/abs\\_all.jsp?arnumber=1356050](http://ieeexplore.ieee.org/xpls/abs_all.jsp?arnumber=1356050)
- [105] J. Kero, C. Szasz, A. Pellinen-Wannberg, G. Wannberg, A. Westman, and D. D. Meisel, “Determination of meteoroid physical properties from tristatic radar observations,” *Annales Geophysicae*, vol. 26, no. 8, pp. 2217–2228, Aug. 2008. [Online]. Available: <http://adsabs.harvard.edu/abs/2008AnGeo..26.2217K>
- [106] M. Blanc et. al., “LAPLACE: a mission to europa and the jupiter system for ESA’s cosmic vision programme,” *Experimental Astronomy*, vol. 23, no. 3, pp. 849–892, Jan. 2009. [Online]. Available: <http://adsabs.harvard.edu/abs/2009ExA...23..849B>
- [107] J. M. Gomez, *Satellite Broadcast Systems Engineering*, 1st ed. Artech House, Mar. 2002.
- [108] D. Roddy, *Satellite Communications, Fourth Edition*, 4th ed. McGraw-Hill Professional, Jan. 2006.
- [109] J. Bergmann, R. C. Brown, P. J. Clarricoats, and H. Zhou, “Synthesis of shaped-beam reflector antenna patterns,” *Microwaves, Antennas and Propagation, IEE Proceedings H*, vol. 135, no. 1, pp. 48–53, Feb. 1988. [Online]. Available: [http://ieeexplore.ieee.org/xpls/abs\\_all.jsp?arnumber=6663](http://ieeexplore.ieee.org/xpls/abs_all.jsp?arnumber=6663)

- [110] P. E. Dewdney, P. J. Hall, R. T. Schilizzi, and T. J. Lazio, "The Square Kilometre Array," *Proceedings of the IEEE*, vol. 97, no. 8, pp. 1482–1496, Aug. 2009. [Online]. Available: [http://ieeexplore.ieee.org/xpls/abs\\_all.jsp?arnumber=5136190](http://ieeexplore.ieee.org/xpls/abs_all.jsp?arnumber=5136190)
- [111] R. T. Schilizzi, P. E. F. Dewdney, and T. J. W. Lazio, "The square kilometre array," in *Ground-based and Airborne Telescopes II*, Marseille, France, 2008, pp. 70 121I–70 121I–13. [Online]. Available: [http://spie.org/x648.html?product\\_id=786780](http://spie.org/x648.html?product_id=786780)
- [112] C. R. Scott, *Modern Methods of Reflector Antenna Analysis and Design*. Artech House Publishers, Mar. 1990.
- [113] D. V. Griffiths and I. M. Smith, *Numerical Methods for Engineers: A Programming Approach*, 1st ed. CRC-Press, Mar. 1991.
- [114] A. W. Love, *Reflector Antennas*. John Wiley & Sons Inc, Dec. 1978.
- [115] E. Kreyszig, *Advanced Engineering Mathematics*, 8th ed. Wiley, 1998.
- [116] V. Galindo-Israel and R. Mittra, "A new series representation for the radiation integral with application to reflector antennas," *Antennas and Propagation, IEEE Transactions on*, vol. 25, no. 5, pp. 631–641, 1977.
- [117] R. Mittra, W. Ko, and M. Sheshadri, "A transform technique for computing the radiation pattern of prime-focal and cassegrainian reflector antennas," *Antennas and Propagation, IEEE Transactions on*, vol. 30, no. 3, pp. 520–524, 1982.
- [118] P. Lam, S. Lee, C. Hung, and R. Acosta, "Strategy for reflector pattern calculation: Let the computer do the work," *Antennas and Propagation, IEEE Transactions on*, vol. 34, no. 4, pp. 592–595, 1986.
- [119] C. Hung and R. Mittra, "Secondary pattern and focal region distribution of reflector antennas under wide-angle scanning," *Antennas and Propagation, IEEE Transactions on*, vol. 31, no. 5, pp. 756–763, 1983.



- [120] Y. Rahmat-Samii, *Antenna Engineering Handbook*, 4th ed. McGraw-Hill, 2007, ch. 15 Reflector Antennas, pp. 15–1 – 15.63.
- [121] R. Schneider, L. Turner, and M. Okoniewski, “Application of fpga technology to accelerate the finite-difference time-domain (fdtd) method,” in *Proceedings of the 2002 ACM/SIGDA tenth international symposium on Field-programmable gate arrays*. ACM, 2002, pp. 97–105.
- [122] J. Durbano, F. Ortiz, J. Humphrey, P. Curt, and D. Prather, “Fpga-based acceleration of the 3d finite-difference time-domain method,” in *12th Annual IEEE symposium on field-programmable custom computing machines*, 2004, pp. 156–163.
- [123] M. Inman and A. Elsherbeni, “Programming video cards for computational electromagnetics applications,” *Antennas and Propagation Magazine, IEEE*, vol. 47, no. 6, pp. 71–78, 2005.
- [124] S. Adams, J. Payne, and R. Boppana, “Finite difference time domain (FDTD) simulations using graphics processors,” in *Proceedings of the 2007 DoD High Performance Computing Modernization Program Users Group Conference*, ser. HPCMP-UGC ’07. Washington, DC, USA: IEEE Computer Society, 2007, pp. 334–338.
- [125] Y. Tao, H. Lin, and H. Bao, “Gpu-based shooting and bouncing ray method for fast rcs prediction,” *Antennas and Propagation, IEEE Transactions on*, vol. 58, no. 2, pp. 494–502, 2010.
- [126] M. Pharr and R. Fernando, *GPU Gems 2: Programming Techniques for High-Performance Graphics and General-Purpose Computation*. Addison-Wesley Professional, Mar. 2005.
- [127] H. Nguyen, *GPU Gems 3*. Addison-Wesley Professional, Aug. 2007.

- [128] *CUDA Programming Guide Version 2.2.1*, NVIDIA, 2009. [Online]. Available: [http://developer.download.nvidia.com/compute/cuda/2.21/toolkit/docs/NVIDIA\\_CUDA\\_Programming\\_Guide\\_2.2.1.pdf](http://developer.download.nvidia.com/compute/cuda/2.21/toolkit/docs/NVIDIA_CUDA_Programming_Guide_2.2.1.pdf)
- [129] *Jacket User Guide*, Accelereyes, 2009. [Online]. Available: <http://www.accelereyes.com/doc/JacketUserGuide.pdf>
- [130] *GPUMat User Guide*, 0th ed., GP-You.Org, 2009. [Online]. Available: [http://gp-you.org/download/PDF/GPUMat\\_User\\_Guide\\_0.1.pdf](http://gp-you.org/download/PDF/GPUMat_User_Guide_0.1.pdf)
- [131] W. Rusch and P. Potter, *Analysis of Reflector Antennas*. Academic Press, 1970.
- [132] A. Ludwig, "Computation of radiation patterns involving numerical double integration," *Antennas and Propagation, IEEE Transactions on*, vol. 16, no. 6, pp. 767–769, 1968.
- [133] W. Stutzman, S. Gilmore, and S. Stewart, "Numerical evaluation of radiation integrals for reflector antenna analysis including a new measure of accuracy," *Antennas and Propagation, IEEE Transactions on*, vol. 36, no. 7, pp. 1018–1023, 1988.
- [134] S. Haber, "Numerical evaluation of multiple integrals," *SIAM review*, vol. 12, no. 4, pp. 481–526, 1970.
- [135] M. Ivashina and K. van t Klooster, "Focal fields in reflector antennas and associated array feed synthesis for high efficiency multi-beam performances," in *25th ESA Antenna Workshop on Satellite Antenna Technology*, September 2002.
- [136] D. Hayman, T. Bird, K. Esselle, and P. Hall, "Encircled power study of focal plane field for estimating focal plane array size," in *Antennas and Propagation Society International Symposium, 2005 IEEE*, vol. 3. IEEE, 2005, pp. 371–374.
- [137] *GRASP9 - Reference Manual*. [Online]. Available: <http://support.ticra.com/public/grasp9.3.01-se.exe>.

- [138] B. Maranda, “Efficient digital beamforming in the frequency domain,” *The Journal of the Acoustical Society of America*, vol. 86, no. 5, p. 1813, 1989. [Online]. Available: [http://asadl.org/jasa/resource/1/jasman/v86/i5/p1813\\_s1](http://asadl.org/jasa/resource/1/jasman/v86/i5/p1813_s1)
- [139] T. Sekiguchi, R. Miura, A. Klouche-Djedid, and Y. Karasawa, “A method of designing two-dimensional complex coefficient FIR digital filters for broadband digital beamforming antennas by a combination of spectral transformation and a window method,” *Electronic and Telecommunications in Japan; Part 3*, vol. 81, no. 3, pp. 22–34, 1998.
- [140] Wikipedia, “United states 2008 wireless spectrum auction — wikipedia, the free encyclopedia,” 2011, [Online; accessed 23-June-2011]. [Online]. Available: [http://en.wikipedia.org/w/index.php?title=United\\_States\\_2008\\_wireless\\_spectrum\\_auction&oldid=432778707](http://en.wikipedia.org/w/index.php?title=United_States_2008_wireless_spectrum_auction&oldid=432778707)
- [141] P. Golding, *Next generation wireless applications*. John Wiley and Sons, Jul. 2004.
- [142] P. Vaidyanathan, *Multirate Systems and Filter Banks*. Prentice-Hall, 1992.
- [143] G. L. DeMuth, “Frequency domain beamforming techniques,” in *Proceedings of IEEE International Conference on Acoustics, Speech, and Signal Processing (ICASSP 77)*, May 1977, pp. 713–715.
- [144] M. Palmese and A. Trucco, “Chirp zeta transform beamforming for three-dimensional acoustic imaging,” *The Journal of the Acoustical Society of America*, vol. 122, no. 5, pp. EL191–195, Nov. 2007, PMID: 18189455. [Online]. Available: <http://www.ncbi.nlm.nih.gov/pubmed/18189455>
- [145] R. G. Pridham, “A novel approach to digital beamforming,” *The Journal of the Acoustical Society of America*, vol. 63, no. 2, p. 425, 1978. [Online]. Available: [http://asadl.org/jasa/resource/1/jasman/v63/i2/p425\\_s1](http://asadl.org/jasa/resource/1/jasman/v63/i2/p425_s1)

- [146] R. A. Mucci, "Digital interpolation beamforming for bandpass signals," *The Journal of the Acoustical Society of America*, vol. 63, no. S1, p. S48, 1978. [Online]. Available: [http://asadl.org/jasa/resource/1/jasman/v63/iS1/pS48\\_s3](http://asadl.org/jasa/resource/1/jasman/v63/iS1/pS48_s3)
- [147] D. C. M. Hovatt, J. S. Bird, and M. M. Goulding, "True Time-Delay bandpass beamforming," *IEEE Journal of Oceanic Engineering*, vol. 17, no. 2, pp. 185–192, Apr. 1992.
- [148] D. E. Dudgeon, "Fundamentals of digital array processing," *Proceedings of the IEEE*, vol. 65, no. 6, pp. 898–904, Jun. 1977.
- [149] R. A. Mucci, "Impact of beam steering errors on shifted sideband and phase shift beamforming techniques," *The Journal of the Acoustical Society of America*, vol. 69, no. 5, p. 1360, 1981. [Online]. Available: [http://asadl.org/jasa/resource/1/jasman/v69/i5/p1360\\_s1](http://asadl.org/jasa/resource/1/jasman/v69/i5/p1360_s1)
- [150] D. B. Ward, "Theory and design of broadband sensor arrays with frequency invariant far-field beam patterns," *The Journal of the Acoustical Society of America*, vol. 97, no. 2, p. 1023, 1995. [Online]. Available: <http://adsabs.harvard.edu/abs/1995ASAJ...97.1023W>
- [151] D. Scholnik and J. Coleman, "Optimal design of wideband array patterns," in *Radar Conference, 2000. The Record of the IEEE 2000 International*, 2000, pp. 172–177.
- [152] D. Scholink and J. Coleman, "Formulating wideband array-pattern optimizations," in *Phased Array Systems and Technology, 2000. Proceedings. 2000 IEEE International Conference on*, 2000, pp. 489–492.
- [153] S. Yan, Y. Ma, and C. Hou, "Optimal array pattern synthesis for broadband arrays," *The Journal of the Acoustical Society of America*, vol. 122, no. 5, p.

- 2686, 2007. [Online]. Available: [http://asadl.org/jasa/resource/1/jasman/v122/i5/p2686\\_s1](http://asadl.org/jasa/resource/1/jasman/v122/i5/p2686_s1)
- [154] S. Yan, C. Hou, X. Ma, and Y. Ma, "Convex optimization based time-domain broadband beamforming with sidelobe control," *The Journal of the Acoustical Society of America*, vol. 121, no. 1, p. 46, 2007. [Online]. Available: [http://asadl.org/jasa/resource/1/jasman/v121/i1/p46\\_s1](http://asadl.org/jasa/resource/1/jasman/v121/i1/p46_s1)
- [155] K. Nishikawa, T. Yamamoto, K. Oto, and T. Kanamori, "Wideband beamforming using fan filter," in *Proceedings of IEEE International Symposium of Circuits and Systems*, 1992, pp. 533–536.
- [156] T. Sekiguchi and Y. Karasawa, "Wideband beamspace adaptive array utilizing FIR fan filters for multibeam forming," *Signal Processing, IEEE Transactions on [see also Acoustics, Speech, and Signal Processing, IEEE Transactions on]*, vol. 48, no. 1, pp. 277–284, 2000.
- [157] K. Nishikawa, H. Ohno, X. Tang, T. Kanamori, and H. Naono, "A design method of 2D FIR fan filters for wideband beam forming by means of 2D fourier series approximation," *Electronic and Telecommunications in Japan; Part 3*, vol. 85, no. 7, pp. 38–49, 2002.
- [158] W. Lu and A. Antoniou, *Two-dimensional Digital Filters*. CRC, Jul. 1992.
- [159] J. H. McClellan, "The design of two-dimensional digital filters by transformations," in *7th Annual Princeton Conference on Information Science and Systems*, 1973, pp. 247–251.
- [160] P. J. Hall, "The Square Kilometre Array: An international engineering perspective," *Experimental Astronomy*, vol. 17, no. 1-3, pp. 5–16, Jun. 2004.

- [161] J. Cordes and M. McLaughlin, “Searches for fast radio transients,” *The Astrophysical Journal*, vol. 596, p. 1142, 2003.
- [162] J. Fisher and R. Bradley, “Full-Sampling Focal Plane Arrays,” in *Imaging at Radio Through Submillimeter Wavelengths*, vol. 217, 2000, p. 11.
- [163] A. van Ardenne, J. Bregman, W. van Cappellen, G. Kant, and J. de Vaate, “Extending the field of view with phased array techniques: Results of European SKA research,” *Proceedings of the IEEE*, vol. 97, no. 8, pp. 1531–1542, 2009.
- [164] D. DeBoer, R. Gough, J. Bunton, T. Cornwell, R. Beresford, S. Johnston, I. Feain, A. Schinckel, C. Jackson, M. Kesteven *et al.*, “Australian SKA pathfinder: A high-dynamic range wide-field of view survey telescope,” *Proceedings of the IEEE*, vol. 97, no. 8, pp. 1507–1521, 2009.
- [165] W. Van Cappellen, J. de Vaate, M. Ivashina, L. Bakker, and T. Oosterloo, “Focal plane arrays evolve,” in *Proceedings of the XXIXth General Assembly of the International Union of Radio Science (URSI GA)*, 2008, pp. 1–4.
- [166] S. Hay, J. O’Sullivan, J. Kot, C. Granet, A. Grancea, A. Forsyth, and D. Hayman, “Focal plane array development for ASKAP (Australian SKA Pathfinder),” in *The Second European Conference on Antennas and Propagation (EuCAP 2007)*. IET, 2007, pp. 1–5.
- [167] P. Patel, D. Kant, E. Wal, and A. van Ardene, “Phased array antennas demonstrator as a radio telescope - EMBRACE,” in *Antennas and Propagation Society International Symposium, 2008. AP-S 2008. IEEE*. IEEE, 2008, pp. 1–4.
- [168] D. Lorimer and M. Kramer, *Handbook of pulsar astronomy*. Cambridge Univ Pr, 2005.

- [169] C. Carilli and S. Rawlings, Eds., *Science with the Square Kilometre Array*, ser. New Astronomy Reviews. Elsevier, Dec. 2004.
- [170] The SKA Program Development Office, “The SKA Brochure,” Mar. 2011, [Online; accessed 21-July-2011]. [Online]. Available: [http://www.skatelescope.org/wp-content/uploads/2011/03/SKA-Brochure\\_web.pdf](http://www.skatelescope.org/wp-content/uploads/2011/03/SKA-Brochure_web.pdf)
- [171] R. Smits, M. Kramer, B. Stappers, D. R. Lorimer, J. Cordes, and A. Faulkner, “Pulsar searches and timing with the square kilometre array,” *Astronomy and Astrophysics*, vol. 493, no. 3, pp. 1161–1170, 2009.
- [172] B. W. Stappers et. al., “Observing pulsars and fast transients with LOFAR,” *Astronomy & Astrophysics*, vol. 530, p. A80, May 2011. [Online]. Available: <http://adsabs.harvard.edu/abs/2011arXiv1104.1577S>
- [173] L. Dddario, “Searching for dispersed transient pulses with ASKAP,” SKA Memo 124, Tech. Rep., Mar 2010. [Online]. Available: <http://www.skatelescope.org/PDF/memos/124.Memo.D’Addario.pdf>
- [174] —, “ASKAP surveys for transients: Which observing mode is best?” SKA Memo 123, Tech. Rep., Apr 2010. [Online]. Available: [http://www.skatelescope.org/PDF/memos/123\\_Memo\\_D’Addario.pdf](http://www.skatelescope.org/PDF/memos/123_Memo_D’Addario.pdf)
- [175] T. Hankins and B. Rickett, *Pulsar signal processing*, ser. Radio Astronomy. Academic Press, 1975, vol. 14, pp. 55–129.
- [176] B. R. Carlson, P. E. Dewdney, T. A. Burgess, R. V. Casorso, W. T. Petrachenko, and W. H. Cannon, “The s2 VLBI correlator: A correlator for space VLBI and geodetic signal processing,” *Proceedings of the Astronomical Society of the Pacific*, vol. 111, pp. 1025–1047, 1999.

- [177] B. Carlson and P. Dewdney, “Efficient wideband digital correlation,” *Electronics Letters*, vol. 36, no. 11, pp. 987 – 988, may 2000.
- [178] M. Garrett, J. Cordes, D. D. Boer, J. Jonas, S. Rawlings, and R. T. Schilizzi, “Concept design for SKA Phase 1 SKA<sub>1</sub>,” SKA Memo 125, Tech. Rep., August, 2010, SSEC SKA Phase 1 Sub-committee. [Online]. Available: [http://www.skatelescope.org/uploaded/27414\\_125\\_Memo\\_Garrett.pdf](http://www.skatelescope.org/uploaded/27414_125_Memo_Garrett.pdf)
- [179] P. Dewdney, J.-G. bij de Vaate, K. Cloete, A. Gunst, D. Hall, R. McCool, N. Roddis, and W. Turner, “SKA Phase 1: Preliminary system description,” SKA Memo 130, Tech. Rep., November 22, 2010. [Online]. Available: [http://www.skatelescope.org/uploaded/21705\\_130\\_Memo\\_Dewdney.pdf](http://www.skatelescope.org/uploaded/21705_130_Memo_Dewdney.pdf)
- [180] B. Jeffs, K. Warnick, J. Landon, J. Waldron, D. Jones, J. Fisher, and R. Norrod, “Signal processing for phased array feeds in radio astronomical telescopes,” *Selected Topics in Signal Processing, IEEE Journal of*, vol. 2, no. 5, pp. 635–646, 2008.
- [181] P. J. Hall, *The Square Kilometre Array: An International Engineering Perspective*. Springer, 2005, ch. The Square Kilometre Array: An International Engineering Perspective, pp. 5–16.
- [182] E. Woestenburg and J. Kuenen, *Low Noise Performance Perspectives Of Wideband Aperture Phased Arrays*. Springer, 2005, pp. 89–99.
- [183] L. Belostotski and J. Haslett, “Two-port noise figure optimization of source-degenerated cascode CMOS LNAs,” *Analog Integrated Circuits and Signal Processing*, vol. 55, no. 2, pp. 125–137, 2008.
- [184] D. Jones, “Characterization of a phased array feed model,” Master’s thesis, Brigham Young University, Provo, Utah, US, 2008.



- [185] K. Warnick and B. Jeffs, "Efficiencies and system temperature for a beamforming array," *Antennas and Wireless Propagation Letters, IEEE*, vol. 7, pp. 565–568, 2008.
- [186] J. Landon, M. Elmer, J. Waldron, D. Jones, A. Stemmons, B. D. Jeffs, K. F. Warnick, J. R. Fisher, and R. D. Norrod, "Phased array feed calibration, beamforming, and imaging," *The Astronomical Journal*, vol. 139, no. 3, p. 1154, 2010. [Online]. Available: <http://stacks.iop.org/1538-3881/139/i=3/a=1154>
- [187] K. Warnick and M. Jensen, "Optimal noise matching for mutually coupled arrays," *Antennas and Propagation, IEEE Transactions on*, vol. 55, no. 6, pp. 1726–1731, 2007.
- [188] K. Warnick, B. Woestenburg, L. Belostotski, and P. Russer, "Minimizing the noise penalty due to mutual coupling for a receiving array," *Antennas and Propagation, IEEE Transactions on*, vol. 57, no. 6, pp. 1634–1644, 2009.
- [189] R. Maaskant and E. Woestenburg, "Applying the active antenna impedance to achieve noise match in receiving array antennas," in *Antennas and Propagation Society International Symposium, 2007 IEEE*. IEEE, 2007, pp. 5889–5892.
- [190] D. Pozar, "A relation between the active input impedance and the active element pattern of a phased array," *Antennas and Propagation, IEEE Transactions on*, vol. 51, no. 9, pp. 2486–2489, 2003.
- [191] J. Weem and Z. Popovic, "A method for determining noise coupling in a phased array antenna," in *Microwave Symposium Digest, 2001 IEEE MTT-S International*, vol. 1. IEEE, 2001, pp. 271–274.
- [192] C. Craeye, "Including spatial correlation of thermal noise in the noise model of high-sensitivity arrays," *Antennas and Propagation, IEEE Transactions*

- on, vol. 53, no. 11, pp. 3845–3848, 2005. [Online]. Available: <http://ieeexplore.ieee.org/stamp/stamp.jsp?tp=&arnumber=1528759>
- [193] N. Liyanage, “3D space-time digital filtering for radio astronomy,” Master’s thesis, University of Victoria. Victoria, BC, Canada, 2009.
- [194] J. L. Volakis, *Antenna Engineering Handbook*. McGraw-Hill, 2007.
- [195] L. T. Bruton, “Three dimensional cone filter banks,” *IEEE Transactions on Circuits and Systems-1, Fundamental Theory and Applications*, vol. 50, no. 2, pp. 208–216, Feb. 2003. [Online]. Available: <http://ieeexplore.ieee.org/stamp/stamp.jsp?tp=&arnumber=1183644>
- [196] L. Khademi, “Reducing the computational complexity of FIR 2D fan and 3D cone filters,” Ph.D. dissertation, University of Calgary, Oct. 2004.
- [197] B. Kuenzle and L. Bruton, “3-D IIR filtering using decimated DFT-polyphase filter bank structures,” *Circuits and Systems I: Regular Papers, IEEE Transactions on*, vol. 53, pp. 394–408, 2006.
- [198] N. Liyanage, L. Bruton, and P. Agathoklis, “On the attenuation of interference and mutual coupling in antenna arrays using 3D space-time filters,” in *Communications, Computers and Signal Processing, 2009. PacRim 2009. IEEE Pacific Rim Conference on*. IEEE, 2009, pp. 146–151.
- [199] A. Madanayake and L. Bruton, “A high performance distributed-parallel-processor architecture for 3D IIR digital filters,” in *Proceedings of IEEE 2005 Intl. Symp. on Circuits and Systems (ISCAS’2005)*, vol. 2, 2005, pp. 1457–1460.
- [200] P. J. Davis and P. Rabinowitz, *Methods of Numerical Integration: Second Edition*, 2nd ed. Dover Publications, Oct. 2007.

- [201] MATLAB, “quad; MATLAB<sup>®</sup> function help,” 2011a. [Online]. Available: <http://www.mathworks.com/help/techdoc/ref/quad.html>
- [202] J. Ahn, C. Lim, D. Han, and H. Oh, “Adaptive hybrid beamformer for mobile reception of ATSC DTV,” *Broadcasting, IEEE Transactions on*, vol. 51, pp. 296–304, 2005.
- [203] A. V. Ardenne, “Concepts of the Square Kilometre Array; toward the new generation radio telescopes,” in *IEEE 2000 Intl. Symp. on Antennas and Propagation*, vol. 1, 2000, pp. 158–161.
- [204] S. Kung, *VLSI Array Processors*. Prentice-Hall, Englewood Cliffs, N.J., 1988.
- [205] —, “VLSI array processors: Designs and applications,” in *1988 IEEE International Symp. on Circuits and Systems, ISCAS’88*, vol. 1, 1988, pp. 313–320.
- [206] K. K. Parhi, *VLSI Digital Signal Processing Systems: Design and Implementation*. John Wiley and Sons, 1999.
- [207] M. Zajc, R. Serbec, and J. Tasic, “Array processors for DSP: implementation considerations,” in *10th Mediterranean Electrotechnical Conference, 2000, MELECON 2000*, vol. 2, 2000, pp. 790–793.
- [208] “System generator user guides,” 2008. [Online]. Available: [http://www.xilinx.com/support/sw\\_manuals/sysgen\\_bklist.pdf/](http://www.xilinx.com/support/sw_manuals/sysgen_bklist.pdf/)
- [209] Maxim, “Analog-to-Digital converters; product tree,” Online, 2010. [Online]. Available: <http://para.maxim-ic.com/index.mvp?tree=adconverters>
- [210] D. Chan and L. Rabiner, “Analysis of quantization errors in the direct form for finite impulse response digital filters,” *Audio and Electroacoustics, IEEE Transactions on*, vol. 21, no. 4, pp. 354–366, 2003.

- [211] D. S. K. Chan and L. R. Rabiner, "Theory of roundoff noise in cascade realizations of finite impulse response digital filters," *The Bell Systems Technical Journal*, vol. 52, no. 3, pp. 329 – 345, Mar. 1973. [Online]. Available: <http://ieeexplore.ieee.org/stamp/stamp.jsp?arnumber=01162497>
- [212] M. Bhattacharya, R. C. Agarwal, and S. C. D. Roy, "Cascade realization of linear phase FIR filters with low sensitivity," *Signal Processing*, vol. 9, no. 4, pp. 245 – 251, 1985. [Online]. Available: <http://www.sciencedirect.com/science/article/B6V18-48V2637-9T/2/5609a89caa99a7d2fe8a52978e70de8f>
- [213] H. Honma, Y. Mori, and M. Sagawa, "Low-sensitivity realization of linear-phase FIR digital filters using cascade form," *Electronics and Communications in Japan (Part I: Communications)*, vol. 71, no. 11, pp. 13–23, 1988. [Online]. Available: <http://dx.doi.org/10.1002/ecja.4410711102>
- [214] L. Montgomery Smith and J. Henderson, M.E., "Roundoff noise reduction in cascade realizations of fir digital filters," *Signal Processing, IEEE Transactions on*, vol. 48, no. 4, pp. 1196 – 1200, Apr. 2000.
- [215] S. Haykin, *Adaptive Filter Theory*, 4th ed. Prentice Hall, 9 2001.
- [216] B. Veidt, G. Hovey, T. Burgess, R. Smegal, R. Messing, A. Willis, A. Gray, and P. Dewdney, "Demonstration of a dual-polarized phased-array feed," *Antennas and Propagation, IEEE Transactions on*, vol. 59, no. 6, pp. 2047 –2057, June 2011. [Online]. Available: [http://ieeexplore.ieee.org/xpls/abs\\_all.jsp?arnumber=5722995](http://ieeexplore.ieee.org/xpls/abs_all.jsp?arnumber=5722995)
- [217] M. Ivashina, O. Iupikov, R. Maaskant, W. van Cappellen, and T. Oosterloo, "An optimal beamforming strategy for wide-field surveys with phased-array-fed reflector antennas," *Antennas and Propagation, IEEE Transactions on*, vol. 59, no. 6, pp. 1864 –1875, June 2011. [Online]. Available: <http://ieeexplore.ieee.org/stamp/stamp.jsp?tp=&arnumber=5725169>

- [218] C. Craeye, A. Garcia, E. Munoz, and R. Sarkis, “An open-source code for the calculation of the effects of mutual coupling in arrays of wires and for the asm-mbf method,” *International Journal of Antennas and Propagation*, vol. 2010, 2010. [Online]. Available: <http://downloads.hindawi.com/journals/ijap/2010/137903.pdf>

## Appendix A

### The Evaluation of MD Continuous-Domain Fourier Transform (CDFT) of a MD BB-BP ST PW

#### A.1 The Evaluation of 4D CDFT of a 4D BB-BP ST PW

The novel approach taken in this thesis to evaluate the 4D-CDFT of the 4D BB-BP ST PW is given in the following. According to (2.11), the 4D CDFT of a 4D BB-BP ST PW  $pw_{4C}(x, y, z, t)$ , is given by

$$PW_{4CP}(f_x, f_y, f_z, f_t) = \iiint\limits_{x,y,z,t=-\infty}^{+\infty} w_{CP} \left( t + c^{-1}(d_x x + d_y y + d_z z) \right) e^{-j2\pi(f_x x + f_y y + f_z z + f_t t)} dx dy dz dt, \quad (A.1)$$

where  $w_{CP}(\tau)$ ;  $\forall \tau = t + c^{-1}(d_x x + d_y y + d_z z) \in \mathbb{R}$  is the 1D BB-BP temporal primary function. Matrix notation can be used to achieve more compact expression for (A.1).

Let the 4-element column vectors  $\mathbf{x}_4$ ,  $\boldsymbol{\nu}_4$  and  $\mathbf{f}_4$  are defined such that  $\mathbf{x}_4^T \triangleq [t \ x \ y \ z]$ ,  $\boldsymbol{\nu}_4^T \triangleq [1 \ c^{-1}d_x \ c^{-1}d_y \ c^{-1}d_z]$  and  $\mathbf{f}_4^T \triangleq [f_t \ f_x \ f_y \ f_z]$ , (2.11) can be rewritten as

$$PW_{4CP}(f_x, f_y, f_z, f_t) = \iiint\limits_{\mathbf{x}_4 \in \mathbb{R}^4} w_{CP} \boldsymbol{\nu}_4^T \cdot \mathbf{x}_4 e^{-j2\pi(\mathbf{f}_4^T \cdot \mathbf{x}_4)} d\mathbf{x}_4. \quad (A.2)$$

Consider the following *linear-transformation* of the original space-time variables  $\mathbf{x}_4$  into  $\boldsymbol{\psi}_4$ ,

$$\boldsymbol{\psi}_4 = \Gamma_4 \mathbf{x}_4, \quad (A.3)$$

where  $\boldsymbol{\psi}_4^{\mathbf{T}} \triangleq [\lambda \ \mu \ \kappa \ \gamma]$  and where

$$\Gamma_4 \triangleq \begin{bmatrix} 1 & c^{-1}d_x & c^{-1}d_y & c^{-1}d_z \\ c^{-1}d_x & -(1 + c^{-2}(d_y^2 + d_z^2)) & c^{-2}d_xd_y & c^{-2}d_xd_z \\ c^{-1}d_y & c^{-2}d_xd_y & -(1 + c^{-2}(d_x^2 + d_z^2)) & c^{-2}d_yd_z \\ c^{-1}d_z & c^{-2}d_xd_z & c^{-2}d_yd_z & -(1 + c^{-2}(d_x^2 + d_y^2)) \end{bmatrix}. \quad (\text{A.4})$$

Note that the first row-vector of  $\Gamma_4$  is  $\boldsymbol{\nu}_4^{\mathbf{T}}$  in (A.2) and therefore with this linear-transform

$$t + c^{-1}(d_x x + d_y y + d_z z) = \lambda. \quad (\text{A.5})$$

Also note that  $\Gamma_4$  is a symmetric matrix and the first column-vector (or row-vector) is orthogonal to the second, third, and fourth column-vectors (or row-vectors). The inverse of  $\Gamma_4$  is given by

$$\Gamma_4^{-1} = \frac{1}{(1 + c^{-2})} \begin{bmatrix} 1 & c^{-1}d_x & c^{-1}d_y & c^{-1}d_z \\ c^{-1}d_x & -1 & 0 & 0 \\ c^{-1}d_y & 0 & -1 & 0 \\ c^{-1}d_z & 0 & 0 & -1 \end{bmatrix}, \quad (\text{A.6})$$

which is also a symmetric matrix where the first column-vector (or row-vector) is orthogonal to the second, third, and fourth column-vectors (or row-vectors). Further, the first column-vector (or row-vector) of  $\Gamma_4^{-1}$  is a scaled version of  $\boldsymbol{\nu}_4$  (or  $\boldsymbol{\nu}_4^{\mathbf{T}}$ ) (i.e. the first column-vector (or row-vector) of  $\Gamma_4$ ). According to [41](ch. 06),

$$d\mathbf{x}_4 = \det(\Gamma_4^{-1}) d\boldsymbol{\psi}_4 = \frac{d\boldsymbol{\psi}_4}{(1 + c^{-2})^3}. \quad (\text{A.7})$$

Substituting (A.5), (A.6) and (A.7) into (A.2) results,

$$PW_{4\text{CP}}(f_x, f_y, f_z, f_t) = \iiint\limits_{\boldsymbol{\psi}_4 \in \mathbb{R}^4} w_{CP}(\lambda) e^{-j2\pi(\mathbf{f}_4^{\mathbf{T}} \Gamma_4^{-1} \boldsymbol{\psi}_4)} \frac{d\boldsymbol{\psi}_4}{(1 + c^{-2})^3}. \quad (\text{A.8})$$

Given that

$$\begin{aligned}
 \mathbf{f}_4^T \Gamma_4^{-1} \boldsymbol{\psi}_4 &= \frac{[f_t \ f_x \ f_y \ f_z]}{(1+c^{-2})} \begin{bmatrix} 1 & c^{-1}d_x & c^{-1}d_y & c^{-1}d_z \\ c^{-1}d_x & -1 & 0 & 0 \\ c^{-1}d_y & 0 & -1 & 0 \\ c^{-1}d_z & 0 & 0 & -1 \end{bmatrix} \begin{bmatrix} \lambda \\ \mu \\ \kappa \\ \gamma \end{bmatrix}, \\
 &= \frac{1}{(1+c^{-2})} \begin{pmatrix} (f_t + c^{-1}d_x f_x + c^{-1}d_y f_y + c^{-1}d_z f_z)\lambda \\ + (c^{-1}d_x f_t - f_x)\mu \\ + (c^{-1}d_y f_t - f_y)\kappa \\ + (c^{-1}d_z f_t - f_z)\gamma \end{pmatrix}, \tag{A.9}
 \end{aligned}$$

(A.8) can be expressed as a product of four 1D integrals of respective variables  $\lambda$ ,  $\mu$ ,  $\kappa$  and  $\gamma$ , such that

$$\begin{aligned}
 PW_{4\text{CP}}(f_x, f_y, f_z, f_t) &= \int_{\lambda=-\infty}^{+\infty} w_{\text{CP}}(\lambda) e^{-j2\pi \frac{f_t + c^{-1}d_x f_x + c^{-1}d_y f_y + c^{-1}d_z f_z}{1+c^{-2}} \lambda} d\lambda \\
 &\times \int_{\mu=-\infty}^{+\infty} e^{-j2\pi \frac{c^{-1}d_x f_t - f_x}{1+c^{-2}} \mu} \frac{d\mu}{1+c^{-2}} \\
 &\times \int_{\kappa=-\infty}^{+\infty} e^{-j2\pi \frac{c^{-1}d_y f_t - f_y}{1+c^{-2}} \kappa} \frac{d\kappa}{1+c^{-2}} \\
 &\times \int_{\gamma=-\infty}^{+\infty} e^{-j2\pi \frac{c^{-1}d_z f_t - f_z}{1+c^{-2}} \gamma} \frac{d\gamma}{1+c^{-2}}. \tag{A.10}
 \end{aligned}$$

According to [44](pp.10),

$$\int_{t=-\infty}^{+\infty} 1 \cdot e^{-j2\pi f_t t} dt = \delta(f_t), \tag{A.11}$$

where  $\delta(f_t)$  is the *1D continuous-domain unit impulse function*. Also  $W_{\text{CP}}(f_t)$ , the 1D-CDFT of  $w_{\text{CP}}(t)$  with respect to the variable  $t$ , is defined by

$$W_{\text{CP}}(f_t) \triangleq \int_{t=-\infty}^{+\infty} w_{\text{CP}}(t) e^{-j2\pi f_t t} dt. \tag{A.12}$$



Following (A.11) and (A.12), (A.10) can be evaluated such that

$$PW_{4CP}(f_x, f_y, f_z, f_t) = W_{CP} \frac{f_t + c^{-1}d_x f_x + c^{-1}d_y f_y + c^{-1}d_z f_z}{1 + c^{-2}} \cdot \delta(c^{-1}d_x f_t - f_x) \cdot \delta(c^{-1}d_y f_t - f_y) \cdot \delta(c^{-1}d_z f_t - f_z). \quad (\text{A.13})$$

Because  $PW_{4CP}(f_x, f_y, f_z, f_t) = 0$  if  $(c^{-1}d_x f_t - f_x = 0)$  and  $(c^{-1}d_y f_t - f_y = 0)$  and  $(c^{-1}d_z f_t - f_z = 0)$ ;  $\forall (f_x, f_y, f_z, f_t) \in \mathbb{R}^4$ , substituting  $f_x = c^{-1}d_x f_t$  and  $f_y = c^{-1}d_y f_t$  and  $f_z = c^{-1}d_z f_t$  into the  $W_{CP} \frac{f_t + c^{-1}d_x f_x + c^{-1}d_y f_y + c^{-1}d_z f_z}{1 + c^{-2}}$  term of (A.13) yields a more simplified version

$$PW_{4CP}(f_x, f_y, f_z, f_t) = W_{CP} f_t \cdot \delta(c^{-1}d_x f_t - f_x) \cdot \delta(c^{-1}d_y f_t - f_y) \cdot \delta(c^{-1}d_z f_t - f_z). \quad (\text{A.14})$$

## A.2 The Evaluation of 3D CDFT of a 3D BB-BP ST PW

According to (2.21), the 3D CDFT of a 3D BB-BP ST PW  $pw_{3C}(x, y, t)$ , is given by

$$PW_{3CP}(f_x, f_y, f_{ct}) = \iiint_{x,y,t=-\infty}^{+\infty} w_{CP}(t + c^{-1}(d_x x + d_y y)) e^{-j2\pi f_x x} e^{-j2\pi f_y y} e^{-j2\pi c f_{ct} t} dx dy dt. \quad (\text{A.15})$$

Using the compact matrix-notation, (A.15) can be rewritten as

$$PW_{3CP}(f_x, f_y, f_{ct}) = \iiint_{\mathbf{x}_3 \in \mathbb{R}^3} w_{CP} \boldsymbol{\nu}_3^T \cdot \mathbf{x}_3 e^{-j2\pi(\mathbf{f}_3^T \cdot \mathbf{x}_3)} d\mathbf{x}_3, \quad (\text{A.16})$$

where the 3-element column vectors  $\mathbf{x}_3$ ,  $\boldsymbol{\nu}_3$  and  $\mathbf{f}_3$  are defined such that  $\mathbf{x}_3^T \triangleq [t \ x \ y]$ ,  $\boldsymbol{\nu}_3^T \triangleq [1 \ c^{-1}d_x \ c^{-1}d_y]$  and  $\mathbf{f}_3^T \triangleq [c f_{ct} \ f_x \ f_y]$ .

Consider the following linear-transformation of the original space-time variables  $\mathbf{x}_3$  into  $\boldsymbol{\psi}_3$ ,

$$\boldsymbol{\psi}_3 = \Gamma_3 \mathbf{x}_3, \quad (\text{A.17})$$

where  $\boldsymbol{\psi}_3^{\mathbf{T}} \triangleq [\lambda \ \mu \ \kappa]$  and where

$$\Gamma_3 \triangleq \begin{bmatrix} 1 & c^{-1}d_x & c^{-1}d_y \\ c^{-1}d_x & -(1 + c^{-2}d_y^2) & c^{-2}d_xd_y \\ c^{-1}d_y & c^{-2}d_xd_y & -(1 + c^{-2}d_x^2) \end{bmatrix}. \quad (\text{A.18})$$

Note that the first row-vector of  $\Gamma_3$  is  $\boldsymbol{\nu}_3^{\mathbf{T}}$  in (A.15) and therefore with this linear-transform

$$t + c^{-1}(d_x x + d_y y) = \lambda. \quad (\text{A.19})$$

The inverse of  $\Gamma_3$  is given by

$$\Gamma_3^{-1} = \frac{1}{(1 + c^{-2}(d_x^2 + d_y^2))} \begin{bmatrix} 1 & c^{-1}d_x & c^{-1}d_y \\ c^{-1}d_x & -1 & 0 \\ c^{-1}d_y & 0 & -1 \end{bmatrix}. \quad (\text{A.20})$$

Note that  $\Gamma_3$  and  $\Gamma_3^{-1}$  are symmetric matrices where the first column-vectors (or row-vectors) are orthogonal to respective the second and third column-vectors (or row-vectors). According to [41](ch. 06),

$$d\mathbf{x}_3 = \det(\Gamma_3^{-1}) d\boldsymbol{\psi}_3 = \frac{d\boldsymbol{\psi}_3}{(1 + c^{-2}(d_x^2 + d_y^2))^2}. \quad (\text{A.21})$$

Substituting (A.19), (A.20) and (A.21) into (A.15) results,

$$PW_{3\text{CP}}(f_x, f_y, f_{ct}) = \iiint_{\boldsymbol{\psi}_3 \in \mathbb{R}^3} w_{\text{CP}}(\lambda) e^{-j2\pi(\mathbf{f}_3^{\mathbf{T}} \Gamma_3^{-1} \boldsymbol{\psi}_3)} \frac{d\boldsymbol{\psi}_3}{(1 + c^{-2}(d_x^2 + d_y^2))^2}. \quad (\text{A.22})$$

Given that

$$\begin{aligned} \mathbf{f}_3^{\mathbf{T}} \Gamma_3^{-1} \boldsymbol{\psi}_3 &= \frac{[cf_{ct} \ f_x \ f_y]}{(1 + c^{-2}(d_x^2 + d_y^2))} \begin{bmatrix} 1 & c^{-1}d_x & c^{-1}d_y \\ c^{-1}d_x & -1 & 0 \\ c^{-1}d_y & 0 & -1 \end{bmatrix} \begin{bmatrix} \lambda \\ \mu \\ \kappa \end{bmatrix}, \\ &= \frac{1}{(1 + c^{-2}(d_x^2 + d_y^2))} \begin{pmatrix} (cf_{ct} + c^{-1}d_x f_x + c^{-1}d_y f_y)\lambda \\ + (d_x f_{ct} - f_x)\mu \\ + (d_y f_{ct} - f_y)\kappa \end{pmatrix}, \end{aligned} \quad (\text{A.23})$$

(A.22) can be expressed as a product of three 1D integrals of respective variables  $\lambda$ ,  $\mu$  and  $\kappa$ , such that

$$\begin{aligned}
 PW_{3CP}(f_x, f_y, f_{ct}) &= \int_{\lambda=-\infty}^{+\infty} w_{CP}(\lambda) e^{-j2\pi \frac{cf_{ct}+c^{-1}d_x f_x+c^{-1}d_y f_y}{1+c^{-2}(d_x^2+d_y^2)} \lambda} d\lambda \\
 &\times \int_{\mu=-\infty}^{+\infty} e^{-j2\pi d_x f_{ct}-f_x \frac{\mu}{1+c^{-2}(d_x^2+d_y^2)}} \frac{d\mu}{1+c^{-2}(d_x^2+d_y^2)} \\
 &\times \int_{\kappa=-\infty}^{+\infty} e^{-j2\pi d_y f_{ct}-f_y \frac{\kappa}{1+c^{-2}(d_x^2+d_y^2)}} \frac{d\kappa}{1+c^{-2}(d_x^2+d_y^2)}. \quad (A.24)
 \end{aligned}$$

Following (A.11) and (A.12), (A.24) can be evaluated such that

$$PW_{3CP}(f_x, f_y, f_{ct}) = W_{CP} \frac{cf_{ct}+c^{-1}d_x f_x+c^{-1}d_y f_y}{1+c^{-2}(d_x^2+d_y^2)} \cdot \delta(d_x f_{ct}-f_x) \cdot \delta(d_y f_{ct}-f_y). \quad (A.25)$$

Because  $PW_{3CP}(f_x, f_y, f_{ct}) = 0$  if  $(d_x f_{ct}-f_x = 0)$  and  $(d_y f_{ct}-f_y = 0)$ ;  $\forall (f_x, f_y, f_{ct}) \in \mathbb{R}^3$ , substituting  $f_x = d_x f_{ct}$  and  $f_y = d_y f_{ct}$  into the  $W_{CP} \frac{cf_{ct}+c^{-1}d_x f_x+c^{-1}d_y f_y}{1+c^{-2}(d_x^2+d_y^2)}$  term of (A.25) yields a more simplified version

$$PW_{3CP}(f_x, f_y, f_{ct}) = W_{CP} cf_{ct} \cdot \delta(d_x f_{ct}-f_x) \cdot \delta(d_y f_{ct}-f_y). \quad (A.26)$$

### A.3 The Evaluation of 2D CDFT of a 2D BB-BP ST PW

According to (2.31), the 2D CDFT of a 2D BB-BP ST PW  $pw_{2C}(x, t)$ , is given by

$$PW_{2CP}(f_x, f_y, f_{ct}) = \iint_{x,t=-\infty}^{+\infty} w_{CP}(t+c^{-1}d_x x) e^{-j2\pi f_x x} e^{-j2\pi cf_{ct}t} dx dt. \quad (A.27)$$

Using the compact matrix-notation, (A.27) can be rewritten as

$$PW_{2CP}(f_x, f_{ct}) = \iint_{\mathbf{x}_2 \in \mathbb{R}^2} w_{CP} \boldsymbol{\nu}_2^T \cdot \mathbf{x}_2 e^{-j2\pi(\mathbf{f}_2^T \cdot \mathbf{x}_2)} d\mathbf{x}_2, \quad (A.28)$$

where the 2-element column vectors  $\mathbf{x}_2$ ,  $\boldsymbol{\nu}_2$  and  $\mathbf{f}_2$  are defined such that  $\mathbf{x}_2^T \triangleq [t \ x]$ ,  $\boldsymbol{\nu}_2^T \triangleq [1 \ c^{-1}d_x]$  and  $\mathbf{f}_2^T \triangleq [cf_{ct} \ f_x]$ .

Consider the linear-transformation of the original space-time variables  $\mathbf{x}_2$  into  $\boldsymbol{\psi}_2$ ,

$$\boldsymbol{\psi}_2 = \Gamma_2 \mathbf{x}_2, \quad (A.29)$$

where  $\boldsymbol{\psi}_2^{\mathbf{T}} \triangleq [\lambda \ \mu]$  and where

$$\Gamma_2 \triangleq \begin{bmatrix} 1 & c^{-1}d_x \\ c^{-1}d_x & -1 \end{bmatrix}. \quad (\text{A.30})$$

Note that the first row-vector of  $\Gamma_2$  is  $\boldsymbol{\nu}_2^{\mathbf{T}}$  in (A.28) and therefore with this linear-transform

$$t + c^{-1}d_x x = \lambda. \quad (\text{A.31})$$

The inverse of  $\Gamma_2$  is given by

$$\Gamma_2^{-1} = \frac{1}{(1 + c^{-2}d_x^2)} \begin{bmatrix} 1 & c^{-1}d_x \\ c^{-1}d_x & -1 \end{bmatrix}. \quad (\text{A.32})$$

Note that  $\Gamma_2$  and  $\Gamma_2^{-1}$  are symmetric matrices where the first column-vectors (or row-vectors) are orthogonal to respective the second column-vectors (or row-vectors). According to [41](ch. 06),

$$d\mathbf{x}_2 = \det(\Gamma_2^{-1}) d\boldsymbol{\psi}_2 = \frac{d\boldsymbol{\psi}_2}{(1 + c^{-2}d_x^2)}. \quad (\text{A.33})$$

Substituting (A.31), (A.32) and (A.33) into (A.28) results,

$$PW_{2\text{CP}}(f_x, f_{ct}) = \iint_{\boldsymbol{\psi}_2 \in \mathbb{R}^2} w_{\text{CP}}(\lambda) e^{-j2\pi(\mathbf{f}_2^{\mathbf{T}} \Gamma_2^{-1} \boldsymbol{\psi}_2)} \frac{d\boldsymbol{\psi}_2}{(1 + c^{-2}d_x^2)}. \quad (\text{A.34})$$

Given that

$$\begin{aligned} \mathbf{f}_2^{\mathbf{T}} \Gamma_2^{-1} \boldsymbol{\psi}_3 &= \frac{[cf_{ct} \ f_x]}{(1 + c^{-2}d_x^2)} \begin{bmatrix} 1 & c^{-1}d_x \\ c^{-1}d_x & -1 \end{bmatrix} \begin{bmatrix} \lambda \\ \mu \end{bmatrix}, \\ &= \frac{1}{(1 + c^{-2}d_x^2)} \begin{pmatrix} (cf_{ct} + c^{-1}d_x f_x)\lambda \\ + (d_x f_{ct} - f_x)\mu \end{pmatrix}, \end{aligned} \quad (\text{A.35})$$

(A.34) can be expressed as a product of two 1D integrals of respective variables  $\lambda$  and  $\mu$ , such that

$$\begin{aligned} PW_{2\text{CP}}(f_x, f_{ct}) &= \int_{\lambda=-\infty}^{+\infty} w_{\text{CP}}(\lambda) e^{-j2\pi \frac{cf_{ct} + c^{-1}d_x f_x}{1 + c^{-2}d_x^2}} \lambda d\lambda \\ &\times \int_{\mu=-\infty}^{+\infty} e^{-j2\pi \frac{d_x f_{ct} - f_x}{1 + c^{-2}(d_x^2 + d_y^2)}} \frac{d\mu}{1 + c^{-2}d_x^2}. \end{aligned} \quad (\text{A.36})$$

Following (A.11) and (A.12), (A.36) can be evaluated such that

$$PW_{2\text{CP}}(f_x, f_{ct}) = W_{\text{CP}} \frac{cf_{ct} + c^{-1}d_x f_x}{1 + c^{-2}d_x^2} \cdot \delta(d_x f_{ct} - f_x). \quad (\text{A.37})$$

Because  $PW_{2\text{CP}}(f_x, f_{ct}) = 0$  if  $(d_x f_{ct} - f_x = 0)$ ;  $\forall (f_x, f_{ct}) \in \mathbb{R}^2$ , substituting  $f_x = d_x f_{ct}$  into the  $W_{\text{CP}} \frac{cf_{ct} + c^{-1}d_x f_x}{1 + c^{-2}d_x^2}$  term of (A.37) yields a more simplified version

$$PW_{2\text{CP}}(f_x, f_{ct}) = W_{\text{CP}} cf_{ct} \cdot \delta(d_x f_{ct} - f_x). \quad (\text{A.38})$$